MISSOURI S&T

CENTER FOR TRANSPORTATION INFRASTRUCTURE AND SAFETY

Spalling Solution of Precast - Prestressed Bridge Deck Panels

by

Lesley Sneed, Ph.D., P.E.
Abdeldjelil "DJ" Belarbi, Ph.D., P.E.
Young-Min You, Ph.D., P.E.

A National University Transportation Center at Missouri University of Science and Technology

Disclaimer

The contents of this report reflect the views of the author(s), who are responsible for the facts and the accuracy of information presented herein. This document is disseminated under the sponsorship of the Department of Transportation, University Transportation Centers Program and the Center for Transportation Infrastructure and Safety NUTC program at the Missouri University of Science and Technology, in the interest of information exchange. The U.S. Government and Center for Transportation Infrastructure and Safety assumes no liability for the contents or use thereof.

Technical Report Documentation Page

1. Report No.	2. Government Accession No.	3. Recipient's Catalog No.
NUTC R234		

4. Title and Subtitle	5. Report Date
Spalling Solution of Precast - Prestressed Bridge Deck Panels	October 2010
	6. Performing Organization Code

7. Author/s	8. Performing Organization Report No.
Lesley Sneed, Ph.D., P.E., Abdeldjelil "DJ" Belarbi, Ph.D., P.E., Young-Min You, Ph.D., P.E.	00022972

9. Performing Organization Name and Address	10. Work Unit No. (TRAIS)
Center for Transportation Infrastructure and Safety/NUTC program Missouri University of Science and Technology 220 Engineering Research Lab Rolla, MO 65409	11. Contract or Grant No. DTRT06-G-0014

12. Sponsoring Organization Name and Address	13. Type of Report and Period Covered
U.S. Department of Transportation Research and Innovative Technology Administration 1200 New Jersey Avenue, SE Washington, DC 20590	Final
	14. Sponsoring Agency Code

15. Supplementary Notes

16. Abstract

This research has examined spalling of several partial-depth precast prestressed concrete (PPC) bridge decks. It was recently observed that some bridges with this panel system in the MoDOT inventory have experienced rusting of embedded steel reinforcement and concrete spalling issues in the deck panels. The objectives of this research were to investigate the causes of spalling in precast-prestressed panels and propose cost-effective alternative solutions including improved design options for new construction, as well as suggest mitigation methods for existing deteriorated bridge decks. A survey of transportation agencies and a series of bridge deck investigations were conducted to determine the nature and causes of spalling. Panel deck system modifications were proposed and evaluated for potential use in new construction. These modifications were investigated in terms of structural performance and serviceability with respect to the current design. Panel deck system modifications evaluated included an increase in tendon side cover, the addition of fibers or corrosion inhibitor to the panel concrete mixture, an increase in reinforcement in the cast-in-place concrete topping, and the substitution of edge tendons with epoxy-coated steel or carbon fiber reinforced polymer tendons. Efficiency of the proposed solutions was examined and validated through fundamental laboratory studies and numerical simulations using finite element modeling. Finally, recommendations are provided for new and existing construction to mitigate the spalling problem.

17. Key Words	18. Distribution Statement
Corrosion, Bridge Evaluation, Precast-Prestressed Concrete Bridge Decks, Spalling	No restrictions. This document is available to the public through the National Technical Information Service, Springfield, Virginia 22161.

19. Security Classification (of this report)	20. Security Classification (of this page)	21. No. Of Pages	22. Price
unclassified	unclassified	468	

Form DOT F 1700.7 (8-72)

FINAL REPORT

PROJECT 1B

SPALLING SOLUTION OF PRECAST-PRESTRESSED BRIDGE DECK PANELS

Prepared for
Missouri Department of Transportation
Organizational Results

by

Lesley Sneed, Ph.D., PE
Assistant Professor
Department of Civil, Architectural & Environmental Engineering
Missouri University of Science and Technology

Abdeldjelil "DJ" Belarbi, Ph.D., P.E.
Chair and Hugh Roy and Lillie Cranz Cullen Distinguished Professor
Department of Civil & Environmental Engineering
University of Houston
&
Young-Min You, Ph.D., P.E.
Research Associate
Department of Civil & Environmental Engineering
University of Houston

AUGUST 2010

TECHNICAL REPORT DOCUMENTATION PAGE

1. Report No.	2. Government Accession No.	3. Recipient's Catalog No.
4. Title and Subtitle		5. Report Date
		6. Performing Organization Code
7. Author(s)		8. Performing Organization Report No.
9. Performing Organization Name and Address Missouri Department of Transportation Research, Development and Technology P. O. Box 270-Jefferson City, MO 65102		10. Work Unit No.
		11. Contract or Grant No.
12. Sponsoring Agency Name and Address Missouri Department of Transportation Research, Development and Technology P. O. Box 270-Jefferson City, MO 65102		13. Type of Report and Period Covered Final Report
		14. Sponsoring Agency Code

15. Supplementary Notes
The investigation was conducted in cooperation with the U. S. Department of Transportation, Federal Highway Administration.

16. Abstract

This research has examined spalling of several partial-depth precast prestressed concrete (PPC) bridge decks. It was recently observed that some bridges with this panel system in the MoDOT inventory have experienced rusting of embedded steel reinforcement and concrete spalling issues in the deck panels. The objectives of this research were to investigate the causes of spalling in precast-prestressed panels and propose cost-effective alternative solutions including improved design options for new construction, as well as suggest mitigation methods for existing deteriorated bridge decks.

A survey of transportation agencies and a series of bridge deck investigations were conducted to determine the nature and causes of spalling. Panel deck system modifications were proposed and evaluated for potential use in new construction. These modifications were investigated in terms of structural performance and serviceability with respect to the current design. Panel deck system modifications evaluated included an increase in tendon side cover, the addition of fibers or corrosion inhibitor to the panel concrete mixture, an increase in reinforcement in the cast-in-place concrete topping, and the substitution of edge tendons with epoxy-coated steel or carbon fiber reinforced polymer tendons. Efficiency of the proposed solutions was examined and validated through fundamental laboratory studies and numerical simulations using finite element modeling. Finally, recommendations are provided for new and existing construction to mitigate the spalling problem.

17. Key Words	18. Distribution Statement

Corrosion, Bridge Evaluation, Precast-Prestressed Concrete Bridge Decks, Spalling		No restrictions. This document is available to the public through National Technical Information Center, Springfield, Virginia 22161	
19. Security Classification (of this report) Unclassified	20. Security Classification (of this page) Unclassified	21. No. of Pages	22. Price

EXECUTIVE SUMMARY

This research has examined spalling of several partial-depth precast prestressed concrete (PPC) bridge decks. It was recently observed that some bridges with this panel system in the MoDOT inventory have experienced rusting of embedded steel reinforcement and concrete spalling issues in the deck panels. Hence, an investigation was initiated to determine the causes and development of solutions including alternate design options for these panels.

As part of this research, a survey of transportation agencies was conducted to determine the extent of use of precast-prestressed concrete bridge deck panels and to compare the behavior of these systems. To comprehend fully and define accurately the cause of the spalling problem observed in partial-depth PPC bridge deck panels, a series of investigations of bridge decks with the bridge deck paneling systems was also conducted. Findings from the field investigations indicated that spalling observed in the PPC panels is the result of the penetration of water and chlorides through the transverse reflective cracking in the cast-in-place (CIP) topping at the panel joint locations, to the interface between the CIP topping and the PPC panels, then through the PPC panels to the prestressing tendons located near the panel joints. Because of the deicing frequency and tactics used by MoDOT, routing and sealing treatment was recommended on a regular basis for transverse reflective cracks at the panel joint locations. This treatment is particularly critical for full-depth transverse cracks and at the girder positive moment regions, where relatively lower levels of CIP topping reinforcement are used (compared with negative moment regions).

Panel deck system modifications evaluated for potential use in new construction included an increase in tendon side cover, the addition of fibers or corrosion inhibitor to the panel concrete mixture, an increase in reinforcement in the cast-in-place concrete topping, and the substitution of edge tendons with epoxy-coated steel or carbon fiber reinforced polymer tendons. These modifications were investigated in terms of structural performance and serviceability with respect to the current design. Efficiency of the proposed solutions was examined and validated through fundamental laboratory studies and numerical simulations using finite element modeling. Of the system modifications evaluated in this research, increase in side cover was found to be the most effective for new construction in terms of cost and constructability. Increase in reinforcement in the cast-in-place concrete topping slab and substitution of panel edge tendons with epoxy-coated steel or carbon fiber reinforced polymer tendons were also found to be effective, although more costly.

This research was performed by Missouri University of Science and Technology and The University of Houston. The report fully documents the research. Supplemental data are included in the appendices.

TABLE OF CONTENTS

LIST OF FIGURES

LIST OF TABLES

1 INTRODUCTION

1.1 Research Motivation

The use of precast-prestressed concrete panels is popular in the construction of concrete bridge decks. For composite decks consisting of precast panels and cast-in-place topping, partial-depth precast-prestressed concrete panels can serve as formwork for the cast-in-place concrete slabs and accelerate the construction of bridge decks in a cost-effective way. Traditionally these panels are reinforced with mild steel temperature reinforcement in the traffic direction along with low-relaxation seven wire steel prestressing strands perpendicular to the traffic direction (along the span length of the panel).

MoDOT began using precast concrete panel decks in 1973 and has been using them on a regular basis since the 1980s. Of 10,335 bridges in MoDOT's current inventory, 1,712 include bridge decks constructed with partial depth precast panels with a cast-in-place topping slab. These decks typically consist of precast-prestressed 3 in. thick deck panels with 5.5 in. thick cast-in-place concrete on top of the panels. The girder system is either steel (27.5%) or prestressed concrete (72.5%).

It was recently observed that some bridges with this panel system in the MoDOT inventory have experienced rusting of embedded steel reinforcement and concrete spalling issues in the deck panels. The plausible reasons for spalling observed in many bridges currently in service likely include corrosion of the steel in the panels due to use of deicing salts, permeability/cracking in the panels, and inadequate concrete cover. Corrosion of steel reinforcement can be detrimental as it can result in shorter life spans for the deck panels.

Since the use of stay-in-place deck panels has proven to be a very cost-effective practice for concrete bridge deck constructions in Missouri, it is of interest to examine ways to mitigate spalling and the resulting service-life reduction associated with corrosion of embedded reinforcement in these panels. Hence, an investigation was initiated to determine the causes and development of solutions including alternate design options for these panels.

1.2 Scope and Objectives

The primary objectives of this project were to investigate the causes for spalling in precast-prestressed panels and propose cost-effective alternative solutions including improved design options for new construction, as well as suggest mitigation methods for existing deteriorated bridge decks. Efficiency of the proposed solutions was examined and validated through fundamental laboratory studies and numerical simulations using finite element modeling. Recommendations were provided for new construction to eliminate the spalling problem. Field implementation and performance monitoring of the bridge deck panel on new construction and/or replacement of existing bridge decks could constitute future Phase II of the project (not included in this report).

1.3 Selection of Proposed Systems

Based on the results from the Questionnaire Survey discussed in Chapter 3 and the Field Investigations discussed in Chapter 4, eight plausible systems were proposed to the MoDOT project Technical Advisory Panel (TAP) members. The systems proposed are summarized in Table 1-1. After discussions with TAP members about the cost, feasibility, and practicality of

systems, five were selected for further investigation (Systems 1, 2, 3, 4, and 6). The three that were disregarded (Systems 5, 7 and 8) were considered uneconomical and/or impractical. Most of the selected systems were examined through experimental and analytical approaches with respect to durability and structural performance (Chapters 5 and 6, respectively). Proposed System No. 4, enhancement of reinforcement in CIP topping concrete, was examined through analysis supplemented by observations from field investigations (Chapters 6 and 4, respectively).

Table 1-1 Systems Proposed

Proposed System	Test Approach
1. Increase side cover of prestressing tendons	O, Δ
2. Use enhanced concrete using FRC	O
3. Use corrosion-free concrete using corrosion inhibitor	O
4. Enhance the reinforcement in CIP topping concrete deck	Δ
5. Substitute 2 epoxy-coated steel or CFRP tendons for all steel tendons	X
6. Substitute 2 epoxy-coated steel or CFRP tendons for 2 steel tendons each edge	O
7. Use re-shaped panel	X
8. Add surface protection	X

* O : Examine Experimentally, Δ : Examine analytically, X : Disregard

1.4 Organization of the Report

Chapter 1 presents the motivation, objectives, methodology, and tasks of this project. Chapter 2 provides the background for this project including a literature review for precast-prestressed panel systems and previous research works related to spalling problems in reinforced concrete (RC) structures. Chapter 3 presents the results of a nationwide questionnaire survey for spalling problems in precast-prestressed concrete deck panel systems. Chapter 4 summarizes the findings of field investigations conducted on representative bridges in the state of Missouri. Chapters 5 and 6 present the summary of the experimental and analytical works. Chapter 7 presents the recommendation of repair methods for spalled precast panels. Chapter 8 provides the summary of findings, construction implications, and recommendations based on the findings of this project. This main body of the report serves as the summary of the major research findings while detailed information is provided in the Appendices.

2 BACKGROUND

2.1 Overview of Precast Prestressed Concrete Deck Panel Systems

Increasing traffic volume and congestion requires a significant demand for the development of innovative bridge systems that can be constructed quickly while maintaining the equal or better qualities of the conventional bridge systems. In this context, the use of precast concrete structures in bridge construction can be a promising alternative to cast-in-place concrete structures. Previous precast concrete applications have proven their efficiency with respect to reduction in construction time and decrease in traffic impacts. Besides these beneficial construction aspects, precast concrete components have many other advantages as well. Precast concrete members are often more durable and more uniformly constructed than their cast-in-place concrete counterparts because of the controlled fabrication environment and stringent quality control in precast concrete production plants. A study on bridge durability found that a smaller percentage of prestressed concrete bridges were "structurally deficient" than cast-in-place bridges of similar age and span length (Dunker and Rabbat 1992). Precast components also reduce the time during which workers are exposed to high-speed traffic and other on-site construction hazards, increasing work-zone safety. Precast concrete components are advantageous for bridges being constructed over water, wetlands, and other sensitive sites where environmental concerns and regulations discourage the use of cast-in-place concrete. Precast concrete systems also require significantly less formwork than cast-in-place concrete. This provides an additional advantage for situations in which clearance is limited and sufficient room is not available for formwork extending below the bridge superstructure.

Most superstructure and substructure bridge components such as piers, decks, and girders are available in precast concrete. For superstructure systems, two types of precast-prestressed concrete deck panel systems are widely used. The first is a full-depth precast concrete deck panel system, and the second is a partial-depth precast concrete deck panel system. Each system is briefly addressed below with respect to its concept, usage, and issues based on works by Hieber et. al. (2005). Since partial-depth precast concrete deck panel systems are the focus of this study, this system description is more detailed.

2.1.1 Full-depth Precast Concrete Deck Panels

Full-depth precast concrete deck panels are used for both new bridge construction and replacement of deteriorated, cast-in-place concrete decks on existing bridges. A typical system is shown in Figure 2-1. This system typically consists of precast concrete panels, approximately 8-in. thick, placed adjacent to one another on bridge girders. Panels typically span the full width of the bridge deck and are approximately 10 ft long.

Grouted shear keys are used in the transverse joints between adjacent panels. The panels are typically connected to the girders using shear pocket connectors, which consist of mechanical connectors (such as shear studs or reinforcing bars) encapsulated in grouted pockets. These connections cause the panels to develop composite action with the girders. Panel reinforcement configuration varies among applications. Some applications use pretensioning in the bridge transverse direction, while others use mild steel reinforcement. Most recent applications contain post-tensioning in the longitudinal direction of the bridge. The post-tensioning induces compression in the transverse joints between panels to improve durability and promote monolithic behavior. Full-depth panels do not necessarily require a wearing course.

Nonetheless, in many applications, asphalt, latex modified concrete, or micro-silica modified concrete wearing course is applied to create a smooth riding surface.

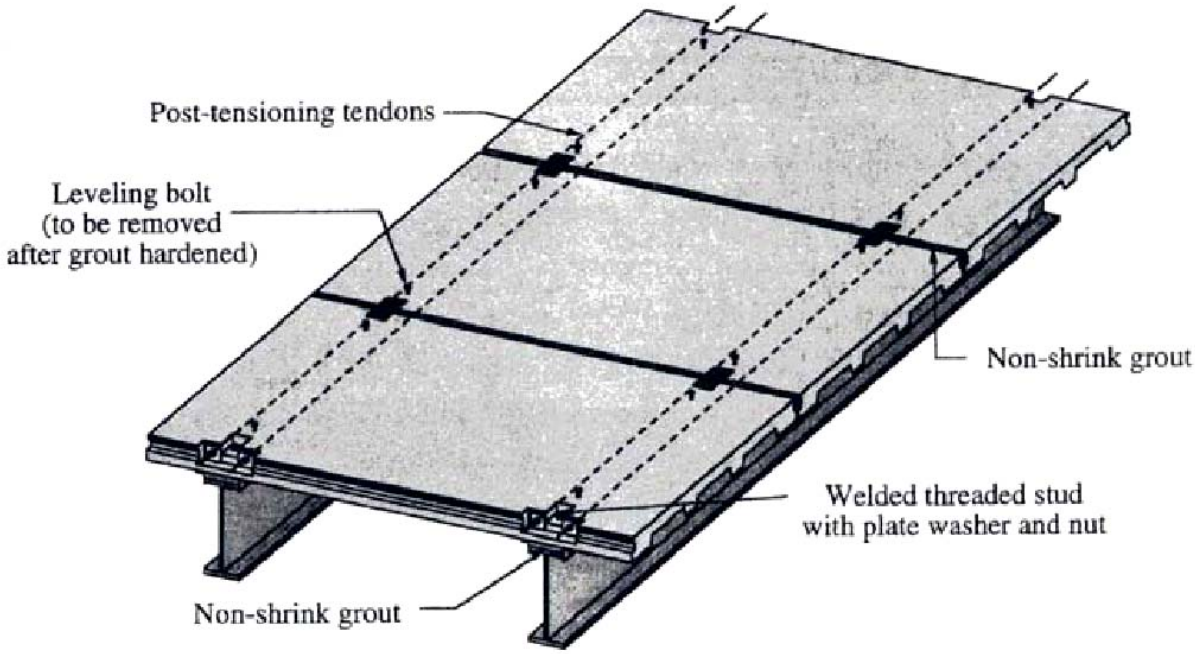

Figure 2-1 Typical Full-depth Precast Concrete Deck Panel Application on Steel Girders (Yamane et al. 1998)

Full-depth panels have been used since the early 1960s (Biswas et al. 1984). They were originally used for non-composite construction. The first application of full-depth panels for full composite construction was in 1973 (Biswas 1986). Use of full-depth panels has been documented in over 18 states, as well as in Japan, Great Britain, Canada, and Mexico (Issa et al. 1995 and Matsui et al. 1994). As mentioned previously, full-depth panels have been used primarily for the replacement of deteriorated, cast-in-place concrete decks; however, they have also been used in the construction of new bridges.

The majority of the previous applications have been on steel girder bridges. One possible explanation for this is because most prestressed concrete girder bridges are not old enough to require a deck replacement, which is the most common use for panels (Slavis 1982). Another possible explanation is that connections between panels and steel girders are simpler than between panels and prestressed concrete girders. Some research contends that full-depth panels perform better on prestressed concrete girders because of their larger stiffness relative to steel girders (Issa et al. 1995). The increased stiffness of precast girders may reduce cracking and fatigue problems associated with decks supported on steel girders.

Full-depth panels are versatile and can be used on a variety of bridge geometries and bridge lengths. Panel dimensions can be altered to accommodate skewed and curved bridges. Deteriorated decks can be replaced in stages with full-depth panels, allowing a bridge to be redecked with only night-time and weekend closures. Partial width redecking (one or two lanes

of traffic at a time) is also possible, allowing bridges to remain open with a reduced traffic volume.

Despite extensive efforts to improve the durability and constructability of full-depth panel systems, some problems still remain. Even with improvements in joint details and the inclusion of longitudinal post-tensioning in design, the long-term serviceability of this system is still questionable. Deterioration problems, particularly associated with the transverse joints, have been reported in previous applications. Many current full-depth panel designs have openings in the top of the slab for shear pocket connectors in locations of maximum negative moment. This reduces the flexural cracking capacity of the panels in the area of maximum demand. The pockets cause cracks to initiate, resulting in decreased deck durability. Alterations in design to eliminate these pockets should be explored further. The system also requires a large quantity of grouting, which can be time consuming in the field. In addition, it is difficult to produce consistently a high quality grout and to fill the gaps between the slab and girders completely. Many serviceability problems can result when the grout is low quality or there are gaps or voids in the grout.

2.1.2 Partial-depth Precast Concrete Deck Panels

Partial-depth precast concrete deck panels are the focus of this research study, and more specifically, the spalling problems associated with this system. Therefore, the main features of this system are described and discussed in detail in this section.

2.1.2.1 System Description

Partial-depth precast concrete deck panels, shown in Figure 2-2, are thin prestressed concrete panels that span between girders and serve as stay-in-place (SIP) forms for the cast-in-place (CIP) concrete deck. Typical geometries of panels are 3.5 in. thick, 8 ft long in the longitudinal direction of the bridge, and sufficiently wide to span transversely between the girders, although their geometries differ from state to state. The panels are pretensioned with strands located at mid-depth oriented in the bridge's transverse direction. The panels are placed adjacent to each other along the length of the bridge. The panels are not connected to one another at the transverse joints. The prestressing strands in the panels serve as the bottom layer of reinforcement in the bridge deck. After the panels are in place, the top layers of reinforcing steel are placed, and the cast-in-place concrete portion of the deck (typically 4.5 in. thick) is placed on top of the panels. The cast-in-place concrete and panels act as a composite deck slab.

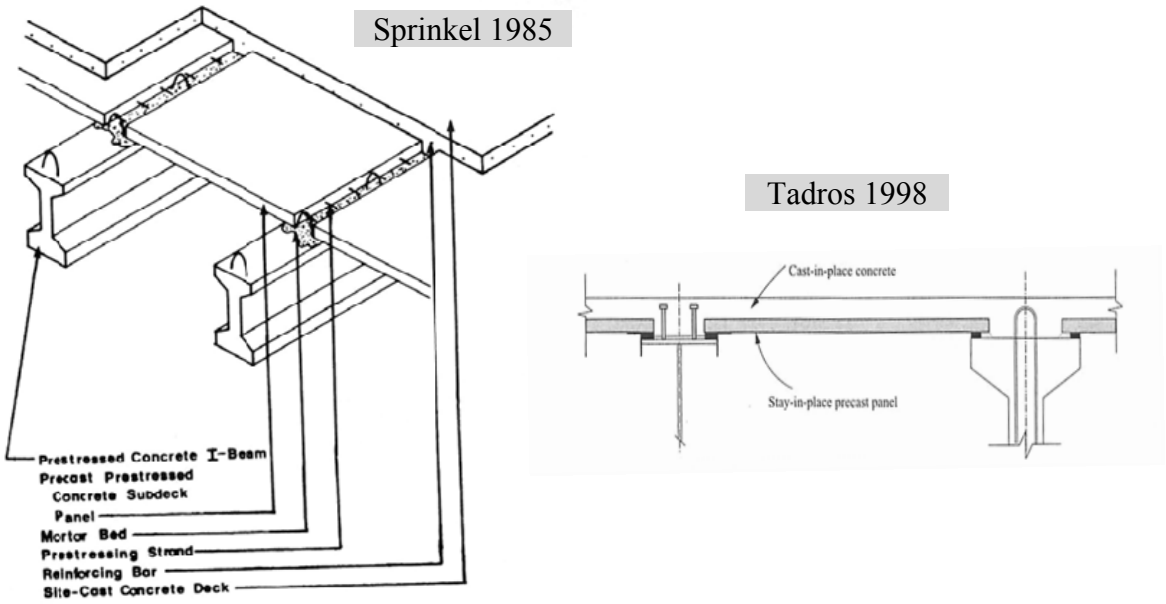

Figure 2-2 Typical Partial-depth Precast Concrete Deck Panel

2.1.2.2 Summary of Usage

Partial-depth deck panels were first used in the 1950s for bridges on the Illinois Tollway project. In the late 1960s and early 1970s, many other states began to incorporate them into their bridges (Goldberg 1987). Such panels have been used in at least 28 U.S. states and Canadian provinces (Goldberg 1987). Partial-depth panels have been used in a variety of applications, both for deck replacement and new construction. They have also been used on both steel girders and precast prestressed concrete girders.

Partial-depth panels have been used in the state of Missouri since 1973, and 90% of concrete bridge decks in Missouri are currently constructed with this system. Significant changes in MoDOT design guidelines have been incorporated since this system was incorporated in Missouri bridges. Panel thickness reduced from 3.5 in. to 3.0 in. to increase cast-in-place concrete thickness from 5.0 in. to 5.5 in. in an attempt to reduce reflective cracking at the transverse joints. Specified compressive strength of concrete was increased from 5,000 psi to 6,000 psi in order to increase corrosion protection to the strands by means of increasing the tensile strength and decreasing the permeability of concrete. In addition, minimum joint filler increased from ¾ in. to 1 in. to permit better concrete consolidation and firm bearing.

2.1.2.3 Durability Problems

The most common problem reported with the use of partial-depth deck panels is cracking in the cast-in-place concrete portion of the deck at both the transverse joints between panels and at the locations where the panels are supported on the girders. Although cracks have been observed in the deck surface directly above the transverse joints between panels, investigation of these decks has revealed that the cracks usually extend only part-way through the cast-in-place portion of the deck slab. The cause of these reflective cracks can be attributed mainly to the concentration of shrinkage of cast-in-place concrete at the joints between the precast panels. The cracks are not

believed to affect significantly the structural performance of the deck slab (Goldberg 1987 and Sprinkel 1985). However, these reflective cracks raise a deterioration concern because they permit the ingress of moisture and corrosion agents to the reinforcement in the deck. Especially when reflective cracks extend through the full thickness of the cast-in-place slab, the ingress of moisture and corrosion agents can be concentrated at the panel joint locations, evidenced by water staining and corrosion issues within the panels. This is a serious concern in highly corrosive environments such as coastal areas or regions where deicing salts are used, such as the state of Missouri. To minimize this type of cracking, some states restrict the use of partial-depth slabs only in positive moment regions of the bridge deck, because it is believed that compressive stress in top of cast-in-place slab caused by the positive moment can compensate for the tensile stress in this region causing the transverse cracks. In other words, the use of partial-depth slabs is prohibited in the negative moment regions due to the presence of tension in the top of the slab that can promote the development of the transverse cracks. Alternatively, other states including Missouri aim to minimize this kind of cracking by enhancing the longitudinal reinforcement along the traffic direction in the negative moment region. Although these efforts could reduce the occurrence of reflective cracks in the negative moment regions, reflective cracks are still observed even in the positive moment regions. Since occurrence of these cracks is strongly related with the subject of this project, this problem is also deeply discussed in this report.

2.1.2.4 Key Issues

Several substantial key issues are critical for the performance of partial-depth precast concrete deck panel systems:

Placement of Panels on Girders

When partial-depth panels are placed on the supporting girders, not only should a solid and uniform bearing be provided to produce acceptable performance, but also the panels must be firmly bedded in grout or concrete on the supporting girders. Improper bearing using soft bearing material such as fiberboard and imperfect infill in the void between the panels and the girder flanges can cause severe problems including,

- Simple span behavior of the bridge deck between girders instead of continuity over girders,
- Delamination of the ends of the panels from the cast-in-place concrete near the joints (Faundo et al. 1985, Ross Bryan Associates, Inc. 1988, Abendroth 1991),
- Transfer of all of the live load shear to cast-in-place concrete, and
- Formation of cracks in the cast-in-place concrete over the joints.

Besides the requirements of bearing and infill, current design specifications also require careful detailing of leveling bolts, grout dams, and adhesives to prevent adverse effects of these parameters on the performance of the panels.

Prestressing Strand Extensions

The effectiveness of prestressing strand extensions in increasing the performance of partial-depth panels is currently under debate. Several research projects examining the effects of strand extensions have found that the strand extensions did not significantly affect the behavior of the deck system (Fagundo et al. 1985, Goldberg 1987, Klingner and Bieschke 1988, and Ross Bryan

Associates, Inc. 1988). Research performed at the University of Texas at Austin showed that there is no difference in the size of cracks in decks constructed from panels with or without strand extensions (Tadros and Baishya1998). AASHTO states that prestressing strands and/or reinforcing bars in the panel need not extend into the cast-in-place concrete above the beams (AASHTO LRFD 9.7.4.3.2 1998). In contrast, research performed in Florida showed that a 6 in. projection of prestressing strands from the ends of the panels is required to anchor the panels to the cast-in-place deck (Tadros 1998). Although the AASHTO LRFD Specification does not require extensions, it does mention in the commentary that the absence of extended reinforcement may affect transverse load distribution because of a lack of negative moment continuity over the beams. This could result in reflective longitudinal cracking where the panels rest on the girders. It is important to protect reinforcing steel in the deck slab in case longitudinal cracks do develop, especially in areas where deicing salts are used (AASHTO LRFD C9.7.4.3.2 1998). If extensions are to be used, PCI-NER (2001) recommends using a minimum extension of 4 inches. It is also important to verify that there is no conflict between the prestressing extensions and the girder web reinforcement (Sprinkel 1985).

Development of Prestressing within Panels

The span of partial-depth panels is limited to the distances between bridge girders. In most cases, this limitation causes a short span length of the panels resulting in insufficient development length of prestressing tendons required by AASHTO specifications. Because of the limited development length, nominal moment capacity of the panel is decreased by a reduction of nominal strength of the prestressing tendon, f_{ps}, specified by the AASHTO specification. In addition, it is not desirable to decrease the development length too much because small development lengths can also increase the potential for splitting at the panel ends. Therefore, it is important to avoid additional adverse conditions that could affect the bond behavior between the strand and the concrete such as use of dirty strands or sudden release of prestressing force.

Composite Action between CIP Concrete and Precast Panel

Partial-depth panels must be capable of developing sufficient composite action with the cast-in-place concrete to be an effective bridge deck system. As a composite deck system, the cast-in-place concrete and the partial-depth panels create the total thickness of the slab, with the panel's reinforcing steel serving as the positive moment reinforcement in the transverse direction of the bridge. To ensure full bond between the cast-in-place concrete and panels, it is recommended by AASHTO specification (1998) that the top surface of the panel is intentionally roughened before the placement of the cast-in-place concrete. In addition, the surface must also be cleaned by removing the laitance or other contaminates on the surface.

Certain recommended limitations exist regarding the partial-depth panel thickness relative to total deck thickness. AASHTO LRFD (1998) and PCI-NER (2001) recommend that the panels neither exceed 55 percent of the finished deck depth nor be less than 3.5 inches. This requirement helps to minimize the development of cracks in the cast-in-place concrete over the panel joints and to ensure that composite action will develop.

2.1.3 Advanced Technology in Precast Prestressed Concrete Deck Panels

Recent research studies have focused on overcoming weaknesses of precast-prestressed concrete deck panels in terms of materials and structural systems. Because corrosion of embedded steel

reinforcement is considered a primary cause of spalling problems associated with reinforced concrete structures, several studies focus on eliminating or minimizing the factors causing the corrosion problems in precast deck panels. Accordingly, representative advanced technologies are introduced in this section with an emphasis on topics related to the concrete spalling problem.

2.1.3.1 Alternative Materials

Two approaches are possible to reduce the possibility of the spalling problem on deck panels via employing alternative materials. The first is to prevent the corrosion of reinforcement by substituting traditional uncoated steel reinforcement with corrosion-resistant or corrosion-free reinforcement. The second is to enhance the system such that it is capable of enduring the effects of corrosion that occurs. There are several conventional options for these approaches. They include altering the concrete mixture with admixtures such as corrosion inhibitors, application of electrochemical techniques such as cathodic protection or chloride removal, or replacement of uncoated steel reinforcement with corrosion-resistant reinforcement such as galvanized, epoxy coated, stainless steel reinforcement, or FRP reinforcement. All these methods have a place as design alternatives and some are now standard practice. They offer a number of advantages over traditional systems with uncoated steel reinforcement including an increased time to initiation of steel corrosion and a reduced risk of cracking and spalling of the concrete, which leads to an increase in service life of the structure and a reduction in the frequency and extent of repairs. Following is a brief introduction about some materials that were considered in the proposed deck panels.

Epoxy-coated Prestressing Strands

The purpose of the epoxy coating is to isolate and insulate the prestressing steel from a corrosive environment. Initially, epoxy-coated seven-wire prestressing strand was developed to be used in bridge decks, where the risk of chloride-induced corrosion exists. Experiences have shown that epoxy-resin coatings are able to provide long-term corrosion protection, ASTM A882 (2004) specifies the requirements for epoxy-coated prestressing steel strands, which are in addition to the requirement for uncoated steel strands, to achieve this performance. Coating thickness and defect-free coatings are of importance in order to reduce permeation of oxygen and moisture to steel. For optimal corrosion protection, ASTM A822 specifies a coating thickness between 650 and 1150 μm. The minimum thickness of the epoxy layer is present at the crown of the outer wires and amounts to about 800 to 1000 μm. A great part of the space between the outer wires is filled up with epoxy, thus changing the initial cross-sectional shape of the strand. As shown in Figure 2-3, the space between the center wire and the outer wires is not filled. Thick coatings require proper preparation of the steel surface for ensuring bond between coating and steel to avoid a damaging split. The application of a primer is recommended. In addition, epoxy coating should be as tight and ductile as possible to withstand mechanical and environmental influences on site.

The most critical issue in the use of epoxy-coated strands is the interface behavior between strand and surrounding concrete to ensure composite behavior. Many researchers (Dorsten et al. 1984, Cousins et al. 1986; 1990; 1993, Brearley et al. 1990) have revealed that epoxy-coated tendon without any treatment has virtually no bond strength resulting in slippage of strands from concrete. Application of grit to the epoxy resolved this problem by enhancing the bond properties between them. A clear difference between uncoated and grit-impregnated epoxy-

coated strands is observed with respect to the interface after the occurrence of slip. While the concrete face is smooth in the case of uncoated strands, it is scratched when coated strands are used, thus showing that the harder grit particles plough though the mortar layer near the interface. This can be interpreted in terms of a higher coefficient of friction.

Figure 2-3 Epoxy-Coated Strands

Dorsten et al. (1984) reported results of comparative pull-out and development length tests with grit impregnated epoxy coated and uncoated 12.7 mm diameter strands. Immediately after prestress release, the coated strand showed a 16% longer transmission length than the uncoated one. After 14 months, transmission length of the coated strand increased 20%, while transmission length of the uncoated strand increased only 3%. Cousins et al. (1990) also studied the development length of epoxy-coated strands with respect to strand diameter (9.5, 12.7 and 15.2 mm) and strand surface condition: UN-uncoated, CP-coated without grit, and coated with various grit densities (CL, CM and CH, for low, middle and high density, respectively; thickness of coating =1.1 mm). Results were similar to those of Dorsten et al. (1984). At prestress release, the two CP-specimens showed that there was virtually no bond. UN specimens had a longer development length than CL specimens. Increasing grit density resulted in a shorter development length. Based on research efforts on this issue, most of manufacturers currently provide a grit-impregnated epoxy-coated strand.

FRP Tendons

Development of FRP tendons for prestressing concrete took place in Holland, Germany, and Japan in the early 1980s. This was also motivated primarily by the desire to reduce corrosion in prestressed concrete elements, similar to epoxy-coated steel strands. Since its introduction, a large number of research works (Dolan 1990, Nanni 1992, Currier 1995, Ehsani et al. 1997, Lu et al. 2000, Bakis et al. 2001) have been conducted during past decades to examine its applicability on various structures.

Since FRP composite materials have a higher material cost than conventional steel reinforcement, hybrid systems containing both materials can be developed to combine the benefits of each in a cost-effective way. The use of hybrid systems can also help to build confidence in engineers and owners who are more comfortable with conventional materials than with FRP composite materials.

High strength corrosion resistant FRP tendons are showing great potential in prestressed applications. Use of FRP tendons with high performance concrete can eliminate corrosion problems and increase the service life of concrete members with respect to members with

conventional steel prestressing tendons. One successful first generation application in pre- and post-tensioned concrete Tee beams shows that FRP can be designed to overcome its non-ductile behavior. Although FRP components behave linear-elastic until rupture, they can be designed to behave in a ductile manner in a structural system. Grace and Abdel-Sayed (1998) demonstrated that a hybrid concrete/FRP tendon structural system can be designed to fail with large deflection by combining bonded internal tendons with unbounded externally draped tendons in double-Tee prestressed concrete beams.

While there is a substantial volume of laboratory test and field installation results in this area, a number of research areas remain to be investigated. ACI Committee 440 (2004) indicated the following major challenges with respect to prestressed applications of FRP tendons:

- Tendon and anchorage systems —The lack of commercial tendon and anchorage systems remains a major impediment to the industry. Without a commercial system, every project remains a research endeavor. This concern extends to the economics of FRP tendons. The current price premium makes them uneconomical for many applications.
- Anchorages—Anchorages need additional development in several areas. Field and construction-friendly anchorages are needed. The fatigue effects at anchorages for unbonded systems need evaluation.
- Fire protection — Even though carbon fibers may be heat resistant to 1000 °C (1800 °F), the resins are generally sensitive to heat. Fire protection of anchorages is also of concern.
- Harping devices —The larger radii needed to limit stresses make commercial push-down and roller-harping devices unsuitable. New harping devices and saddles need to be developed.
- Long-term bond —The FRP tendon bond depends on the resin surface. While there is some experience with epoxy-coated steel bars, the long-term durability behavior of bond in FRP prestressing tendons is not yet defined.
- Galvanic action —Carbon fibers are higher on the galvanic table than steel, creating a potential corrosion problem. The resin bonding agents may preclude this effect, but research is needed to investigate this behavior and provide design guidance.
- External post-tensioning for rehabilitation —FRP has potential for rehabilitation applications. The lower elastic modulus of FRP makes stressing short tendons more attractive. The lack of tendon-anchorage systems remains a key application issue.
- Tendon replacement —FRP replacement tendons for corroded structures are an application area with high potential. The design of a tendon to fit in the existing duct and to function over tendon bend points in the reinforcement needs to be resolved.
- Circular prestressed tanks —Design guides for prestressing circular “wire- and strand-wrapped” tanks using FRP tendons need to be developed.
- Stressing procedure — Guidelines for stressing procedure/methods need to be developed.
- Reliability assessment —The strength-reduction factors require recalibration to ensure conformance with the load factors in ACI 318-08.
- Shear capacity —Shear design guidelines for FRP prestressed beams with FRP stirrups need further development.
- Bond and development —Protocols for validation of FRP tendon transfer and development lengths are needed. (ACI 440 2004).

Several issues related to bond behavior of FRP prestressing tendons as mentioned above are applicable to the application in precast prestressed deck panels. As explained previously, insufficient development length of prestressing tendons can decrease the moment capacity of panels as well as increase the potential for splitting at the panel ends. It is hoped that higher strength of FRP tendons can compensate for this problem and will be investigated as part of this project.

Fiber-Reinforced Concrete (FRC)

Fiber reinforced concrete (FRC) is concrete containing fibrous material that increases the mechanical properties and structural integrity of concrete. FRC contains short discrete fibers that are uniformly distributed and randomly oriented. A thin and short fiber (short hair-shaped glass fiber for example) can be effective during the first hours after placing the concrete by reducing cracking while the concrete stiffens, but it cannot increase the concrete tensile strength. However, a larger size fiber (for instance, 1 mm diameter and 45 mm length) can also increase the load-carrying capability by increasing the concrete tensile strength when the modulus of elasticity of the fiber is higher than the matrix (concrete or mortar binder). Thus, geometry of fiber such shape, dimension, and length is a very important factor to determine the final properties of FRC. In addition, fibers also lower the permeability of concrete and thus reduce bleeding of water, which helps to mitigate corrosion problems. Some types of fibers produce greater impact, abrasion, brittle, and shatter resistance in concrete. Thus, adoption of FRC to precast-prestressed panels can be an alternative way to make a corrosion-resistant system.

Fibers types include steel, glass, synthetic, and natural materials. Table 2-1 shows the mechanical properties of various fiber types that may be used in FRC (ACI 549.2R 2004). The general characteristics of representative fibers are briefly introduced below.

- Steel fiber —Steel fiber is a commonly used material in FRC. It is proven to increase both the tensile strength and ductility of concrete. However, it is not suitable for a corrosion free structure, so this fiber is not further considered in this project.
- Glass fiber — Many types of glass fiber have been used in glass fiber-reinforced concrete (GFRC) since the 1960s. In terms of long-term durability, alkali-resistant (AR) glass fibers have shown the best results. The mechanical properties of GFRC depend on many factors: fiber content, polymer content (if used), water-cement ratio, porosity, sand content, fiber orientation, fiber length, and method of curing. Changes in the dimensions and mechanical properties can occur when GFRC is exposed to severe environment. The addition of polymer to the fiber mix has been shown to reduce fiber embrittlement and improve strength retention in natural weathering conditions (ACI 544 2009). Other ways are being developed to improve strength retention such as adding coatings to the glass fibers as well as altering the cement matrix. No alterations to GFRC are needed for freeze-thaw durability.
- Synthetic fibers —Synthetic fibers include any fabricated materials that are not steel, glass, or natural fibers. Concrete with synthetic fibers is known as synthetic fiber-reinforced concrete or SNFRC. Acrylic fiber is a type of synthetic fiber that can have tensile strength up to 145 ksi. Aramid (aromatic polyamide) fiber has a high tensile strength and tensile modulus. This fiber is two and a half times stronger than E-glass fibers and five times stronger than steel fiber. Aramid fiber can resist creep and does not

change dimensions with temperatures under 392 degrees Fahrenheit. The mechanical properties of aramid fiber are very attractive for reinforced concrete; however, its high cost is a major problem to be resolved. Carbon fiber has similar qualities to aramid fiber, but its mechanical properties tend to vary depending on the types of materials used. Although high cost is also a main issue in the use of carbon fibers, this can be compensated somewhat by using cheaper materials. For instance, carbon fiber made from petroleum and coal pitch is cheaper than carbon fiber made from polyacrylonitrile. Nylon fiber has good long-term performance, toughness, and elastic recovery qualities. It is resistant to a wide variety of organic and inorganic materials including strong alkalis. Currently, two types of nylon fiber are produced for reinforced concrete, Nylon 6 and Nylon 66. These fibers have been proven to sustain and increase the load carrying capability of concrete following first cracking, and decrease shrinkage of concrete. Polyester fiber exhibits different physical and chemical characteristics depending on manufacturing technique. All polyester fibers used in concrete belong to the thermoplastic polyester sub-group. Thermoplastics are very sensitive to temperature. Accordingly, the characteristics of polyester fiber in concrete can be changed when concrete is exposed to high temperatures. Polyester fibers bond mechanically with concrete because they are hydrophobic. Like polyester fiber, polypropylene fiber is hydrophobic and bonds with concrete mechanically. The melting point and the elastic modulus of this fiber are lower than the other fibers. Therefore, polypropylene fiber does not significantly increase compressive or tensile strength of concrete, although it can induce a more ductile failure of concrete. In addition to the ongoing pursuit mentioned above, the need for further research was emphasized by ACI Committee 544 (2009) in following areas such as the effect of the addition of various fiber types on control joint spacing for concrete flatwork, the effectiveness of fibers as temperature and shrinkage reinforcement, standardized test procedures for impact and fatigue loadings, design methodology for composite application using conventional reinforcement in FRC, and fire resistant properties of fiber reinforced composites.

- Natural fiber —Natural fibers can be easily obtained at low cost energy in local areas. Such fibers are used in the manufacture of low fiber content FRC and occasionally have been used in the manufacture of thin sheet with high fiber content FRC. Fibers that have not been processed are typically referred to as unprocessed natural fibers (UNF). Other natural fibers that have been processed to enhance their properties are also available. These fibers are made from wood by a chemical process and are referred to as processed natural fibers (PNF). Although historically many fibers have been used to reinforce various building materials, until recently little scientific effort has been devoted to the use of natural fibers for reinforcement. The use of some of the best-known natural fibers such as sisal, coconut, sugarcane bagasse, plantain (banana), palm, etc., has mostly been limited to the production of fabrics, ropes, mats, etc. ACI Committee 544 (2009) recommends further investigation with respect to: i) durability and performance of unprocessed natural fiber reinforced concrete, and ii) potential for embritttlement under exposure to some aggressive environments of processed natural FRC.

Table 2-1 Mechanical Properties of Various Fibers (ACI 549.2R 2004)

	Tensile strength (Mpa)	Modulus of Elasticity (Gpa)	Tensile Strain (%) (max-min)	Fiber Diameter (mm)	Adhesion to Matrix (relative)	Alkali Resistance (relative)
Asbestos	600-3600	69-150	0.3-0.1	0.02-30	excellent	excellent
Carbon	590-4800	28-520	2-<1	7-18	poor to good	excellent
Aramid	2700	62-130	4-3	11-12	fair	good
Polypropylene	200-700	0.5-9.8	15-10	10-150	poor to good	excellent
Polyamide	700-1000	3.9-6	15	10-50	good	nc
Polyester	800-1300	up to 15	20-8	10-50	fair	nc
Rayon	450-1100	up to 11	15-7	10-50	good	fair
Polyvinyl alcohol	1150-1470	21-36	15	4-14	good	good
Polyacrylonitrile	850-1000	17-18	9	19	good	good
Polvethylene	400	2-4	400-100	40		excellent
Polyethylene Pulp Oriented	-	-	-	1-20	good	excellent
Carbon Steel	3000	200	2-1	50-85	excellent	excellent
Stainless Steel	3000	200	2-1	50-85	excellent	excellent
AR Glass	1700	72	2	12-20	excellent	good

2.1.3.2 Advanced Types of Panels

New types of precast deck panel systems have been recently introduced to overcome some of the performance problems with conventional deck panel systems indicated in previous sections. It is of interest to review these systems to consider and incorporate the good aspects of new systems into the proposed system. This section introduces some of the newly developed precast deck panel systems available in literature.

NUDECK Panel

The NUDECK system is a hybrid system utilizing aspects from both partial-depth deck systems and full-depth deck systems developed by the University of Nebraska-Lincoln. This system was developed to eliminate some of the drawbacks found in the conventional partial-depth deck system including reflective cracks over both the transverse joints and above the girders and the need to utilize traditional forming techniques for the overhangs. This system utilizes precast partial-depth panels (4.5 in. thick) that extend over the entire width of the bridge connected in the transverse direction by both prestressed and nonprestressed reinforcement. Units are connected in the longitudinal direction by reinforcement that is not post-tensioned as in the conventional full depth precast deck panel, allowing the system to be continuous in both the transverse and longitudinal directions. Badie et al. (1998) showed that this continuity helped to reduce cracking as well as increase the flexural capacity compared to the conventional SIP system. Figure 2-4 and Figure 2-5 show a cross-section and plan view of this panel system.

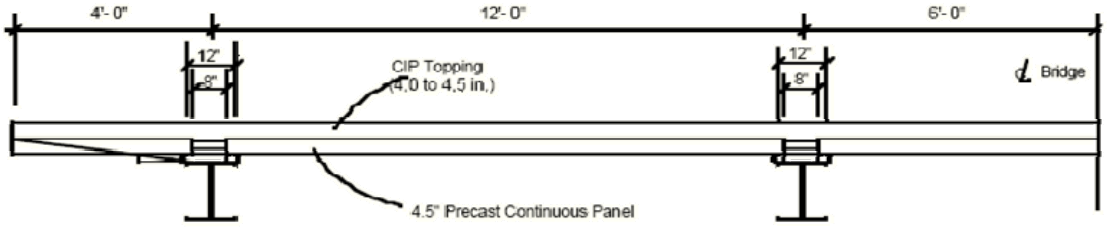

Figure 2-4 Cross-section of a Bridge with the NUDECK Panel System (Badie et al. 1998)

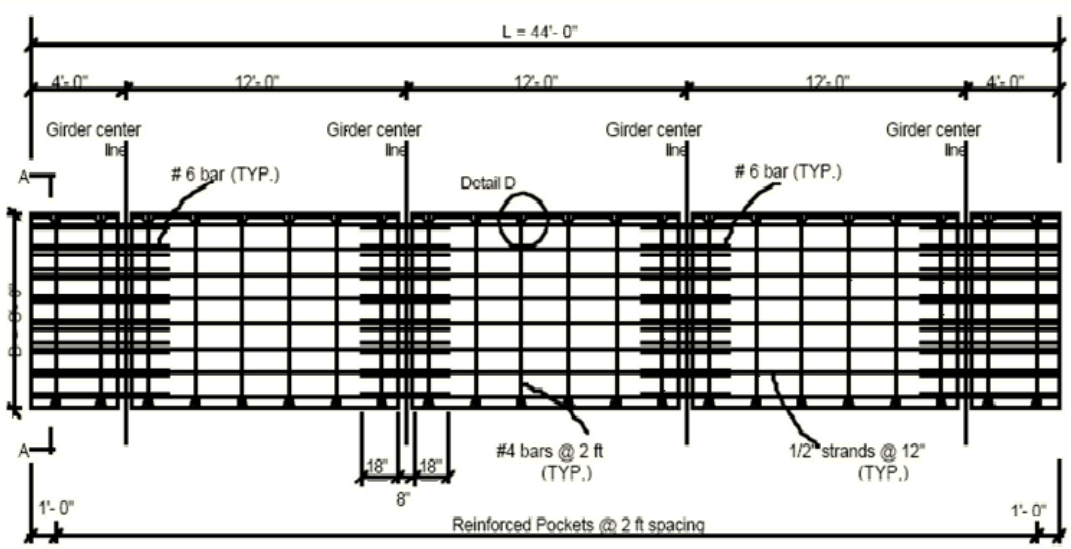

Figure 2-5 Plan View of the NUDECK SIP Panel (Badie et al. 1998)

Steel Free Deck Systems

Bowen (2006) introduced this steel free deck system by combining the steel free deck with partial depth precast panels. The slab is constructed of two elements. The lower element is the partial depth precast concrete panel, which is constructed with a bottom mat of crack control reinforcement and steel straps required for this system. The upper element consists of cast-in-place concrete with no reinforcement in the positive moment regions of the bridge deck. The concept of a steel free deck is achieved by providing no reinforcement in the upper layer of the deck in the positive moment regions and utilizing noncorrosive reinforcement in the lower layer of the bridge deck. A schematic drawing of this system is shown in Figure 2-6. Once the deck is complete, the system acts monolithically. The panels are pre-fabricated, delivered to the construction site, and placed on top of the girders between the girder lines. Forming is required at the longitudinal ends of the structure and may or may not be required at a cantilever depending on its width. Continuity between the panels and the cast-in-place portion of the bridge deck is achieved by roughening the top surface of the panels to improve bond and by extending the steel straps with shear connectors over the girder flange that also has shear connectors. Composite action is achieved in this manner.

Static testing of this system revealed that the partial depth precast concrete panels resisted load primarily in bending. The steel straps acted as external reinforcement and laterally restrained the supporting girders during loading. The strain in the transverse GFRP bars was negligible under service wheel loading and thus did not contribute to the ultimate capacity of the deck. The grid of GFRP reinforcement cast within the deck provided crack control during the panel and deck testing. In addition, the testing program verified that the partial depth precast concrete panels can safely withstand transportation and construction loading for the span arrangement. Finally, the deck system failed in a punching shear under static wheel load.

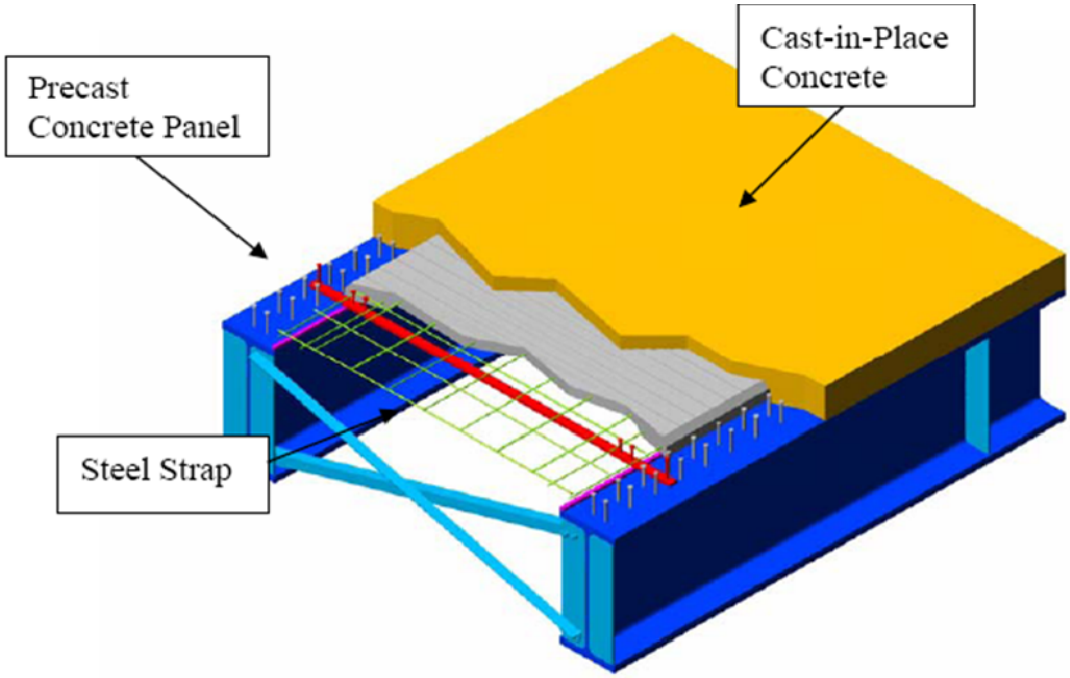

Figure 2-6 Bridge Deck Showing the Precast Panels and Completed Deck Concrete in the Steel Free Deck System (Bowen 2006)

Stay-in-Place Metal Forms

A stay-in-place metal form is a permanent formwork made of thin, corrugated sheets of galvanized steel referred to as SIPMFs as shown in Figure 2-7. Similar to precast-prestressed SIP panels systems, this system eliminates the need for temporary formwork during deck construction. Since the introduction of SIPMFs to the concrete bridge deck construction industry, a few studies (Cady and Renton 1976, Grace et al. 2004, Frost 2006) have been published evaluating their effect on bridge deck performance. However, there is consensus on advantages and disadvantages associated with the use of SIPMFs. The advantages include reduction of the overall cost and time associated with bridge deck construction, as well as exposure of workers to elevated levels of risk. The principle disadvantages include: i) the presence of SIPMFs may accelerate deck deterioration by causing higher moisture and salt contents within the deck, ii) the metal forms may corrode over time, causing unsightliness and possible danger to the traveling public, iii) the presence of SIPMFs prevents bridge inspectors from viewing the underside of the bridge deck. These three reasons have been cited as the primary limiting factors for the use of SIPMFs in the United States.

Figure 2-7 Bottom View of an SIPMF (Frost 2006)

Fiber-reinforced Polymer Panels

In recent years, fiber-reinforced polymer (FRP) composite deck systems have emerged as an alternative to conventional reinforced concrete (RC) slabs. Engineers are hoping to benefit from: i) relatively light weight of FRP deck panels to reduce dead loads, which comprise a major portion of design loads in typical bridges; ii) shorter construction time due to quick and easy installation; and iii) increased service life because of enhanced durability of FRP panels. A combination of these three features make FRP panels particularly appealing for urban bridges with high traffic volumes where construction times should be minimized as much as possible. The low dead load level of the deck system provides upgradability of existing bridges to higher live load capacities or potential for addition of new traffic lanes. In spite of their advantages and versatility, however, FRP composite has not seen widespread use in civil engineering due to high initial cost, restricted design, limited experience, and lack of long-term performance data. According to the results of a survey study by Hastak et al. (2006), only three out of 38 state Departments of Transportation (DOTs) currently not using FRP bridge deck panels have plans for installing them within the next 5 years.

Figure 2-8 Fiber Reinforced Polymer (FRP) Deck Panel (Ralls 2005)

2.2 Spalling Problems in Reinforced Concrete

2.2.1 Physical Observations and Experimental Studies

This section provides background information on corrosion and spalling of bridge decks based on previous inspections and experimental work from the literature. The works are summarized individually by the researcher or research sponsor, and key conclusions are presented.

2.2.1.1 Portland Cement Association (State Highway Departments et al. 1970)

The Portland Cement Association completed one of the earliest studies on characterization of bridge decks deterioration. The main objectives of the study were to determine the types and the extent of the durability problems, determine the causes of different deterioration types, improve the durability of future bridges, and develop mitigation options for the existing bridge decks experiencing deterioration. The study included a survey study of 1000 bridges in eight states, in-depth investigation of 70 bridges in four states, and an analytical study of the vibration characteristics of 46 bridges.

The study began in 1961 with a random survey on more than 1000 bridges built between 1940 and 1962. A summary of the types and the extent of the bridge deterioration was the main purpose of the random survey. Scaling, types of cracking, rusting, surface and joint spalling, and pop outs were the types of deterioration recorded. In addition, different relationships and observations were generated as a function of deck age, bridge type, traffic volume, etc. The results of the random survey showed that decks with non-air-entrained concrete experienced scaling. Transverse cracking was the dominant cracking type in two thirds of the bridge decks. In addition, the transverse cracking increased with age, span length, and was more prevalent in continuous spans and bridges built on steel girders.

In-depth investigations were made on 70 bridges from four states. Determining causes of bridge deck deterioration was the primary purpose of the in-depth investigations. The study included

documentation of deterioration of each bridge, collection of concrete cores for laboratory study, and examination of construction and design documentation. Scaling, cracking, and surface spalling were categorized from the field investigations and the laboratory tests. Scaling was found to be most severe on the bridge decks with non-air-entrained concrete. Based on the laboratory tests for air content and air void distribution, the scaling was found to be caused by localized deficiencies. There was no correlation between the scaling and the chloride content tests. Chloride content analysis showed that the transverse cracking typically occurred above the reinforcement locations. Transverse cracking occurred more frequently in the steel girder bridge decks. Diagonal cracking was typically observed on skewed bridges, which was considered to be caused by structural deformation from the loading. In addition, random cracking was found on most of the bridge decks. The wheel loads, temperature and shrinkage, reactive aggregates, and small imperfections in the concrete were considered as the causes of the random cracking.

The final phase of the PCA study included determining the vibration characteristics for each bridge. Empirical equations developed by Nieto-Ramierez and Veletsos (1966) were used to calculate the theoretical vibration characteristics for 46 bridges. Calculations of the natural frequency, the speed parameter, and the impact value were used to compare with the level of deck deterioration and structure type. In conclusion, the vibration characteristics for the bridge decks were found not to be the major factor of the concrete bridge deck deterioration.

2.2.1.2 Dakhil, Cady, and Carrier (Dakhil et al. 1975)

Dakhil, Cady, and Carrier studied experimentally the effects of cover depth, concrete slump, and reinforcing bar size on fresh concrete cracks over reinforcement leading to corrosion and spalling. Photoelastic techniques were used to study the tensile stresses above the reinforcement, and a corrosion study was performed to investigate the effects of subsistence cracks on the corrosion process.

Results from this research showed that the occurrence and severity of subsistence cracking decrease with larger covers, lower slumps, and smaller bar size. Cover depth was found to be the most significant of these factors in crack formation. Photoelastic results showed that tensile stresses were greatest directly over the reinforcement. Corrosion results showed that corrosion potential was higher in areas with subsistence cracking than without cracking, indicating that subsistence cracking enhances corrosion of embedded reinforcement.

2.2.1.3 North Carolina State (Cheng and Johnston 1985 and Perfetti et al. 1985)

Two groups of investigators at North Carolina State completed a two-part study on the effects of construction, materials, and structural parameters on transverse cracking of bridge decks. Fifty-two bridges with steel girders and 20 bridges with prestressed girders were evaluated between 1972 and 1981. Thirty-five of the bridges were simple span, and 37 bridges were continuous and simple span or continuous span only.

In Cheng and Johnston (1985), data from plans, construction diaries, and weather and test records were collected and compared with transverse cracking obtained from field surveys. The number of major and minor transverse cracks were recorded and used to quantify the number of cracks per linear foot of the bridge deck. The field surveys showed results similar to the PCA study (PCA 1970). The main findings were that most of the transverse cracks occurred above the

top reinforcement, and more severe transverse cracking occurred on bridges with continuous spans than simple spans and on steel girders than prestressed girders. Recommendations were made with respect to casting sequence on continuous girders to help reduce the flexural tension and associated transverse cracking in the negative moment regions.

In Perfetti, Johnston, and Bingham (1985), potential influence of bridge vibration characteristics, casting sequence, and structure type were studied with respect to the transverse cracking data from the Cheng and Johnston study (1985). From both studies, three main observations were made: 1) decks supported on simple spans and prestressed girders showed the least transverse cracking; 2) maximum concrete tensile stresses from combined dead and live load should be limited to 250 psi, and 3) alternating placement sequence was recommended for decks supported on continuous span girders.

2.2.1.4 MoDOT (Wenzlick 2005)

In 2005, a follow-up inspection was made on a 32 bridges originally inspected in 1987 by FHWA Missouri division. Fourteen of the bridge decks inspected were conventional CIP concrete construction, and 18 bridges used precast-prestressed SIP panels. The bridges were built on either steel or prestressed I girders. The age of these bridges at the time of the first inspection was 22-32 years old. The objective of the follow-up inspection was to evaluate the performance of the bridge decks using SIP panels compared to conventional bridge decks. The inspection included mapping of cracks, areas of seepage, and other special conditions. Chloride samples were also acquired at crack locations.

Results indicated that there was little change from the 1987 inspection results, with all bridges rated "Fair" to "Excellent." Performance of decks with CIP concrete and SIP panels was similar. Deck cracking of steel girder bridges was found to be greater than on prestressed I girders. Sounding inspection showed no indication of debonding at the SIP panel-CIP topping interface.

2.2.1.5 MoDOT (Wenzlick 2008)

A special inspection was made by MoDOT in 2008 on four steel girder bridges with SIP panels reportedly experiencing concrete spalling problems on the underside of the deck (bridges A4709, A4067, A4704, and A4729). The inspection included mapping of cracking, staining rusting, spalling, and efflorescence observed on the bottom surface of the deck. Reflective cracking was documented in the top of the deck in the same pattern as most of the panel joints. Concrete samples were taken from spalled locations to determine the chloride content.

Results from this investigation showed high chloride content at the spalled locations, which indicated severe deterioration at the joint cracks. It was also noted that the spalling problem occurred in steel girder bridges with long spans, which may increase the severity of the corrosion issues. Based on the findings, increased side cover of the panels was recommended to delay the corrosion process. Other recommendations included potential replacement of the SIP panel edge tendons with noncorrosive or less corrosive materials including epoxy-coated steel or carbon fiber reinforced polymer tendons in new construction.

2.2.2 Mechanical and Numerical Models

2.2.2.1 Corrosion Models

Corrosion has been identified as one of the main causes of bridge deterioration. Durability and serviceability of a bridge structure are affected by corrosion propagation, which can result in spalling in the concrete. Many mechanical and numerical models have been developed to provide information about the service life of new and existing bridges. This section provides a review of analytical and numerical models related to corrosion and spalling damage.

Many models have been developed to predict the behavior of corrosion cracking or spalling of concrete caused by chloride diffusion induced steel corrosion. Such models are typically presented within the literature in terms of factors that cause concrete cracking and spalling such as the expansive pressure at embedded steel location. Due to the special characteristics of corrosion cracking, principles of fracture mechanics are usually employed.

Bazant (1979) proposed the first analytical model capable of predicting the time from the corrosion initiation state to corrosion-induced cracking state. A simplified corrosion model was suggested to estimate the time for corrosion cracking based on volume expansion of rust. Model assumptions included: 1) oxygen and chloride ions diffuse through concrete in quasi-stationary and one-dimensional direction, 2) the expansive rust layer starts from the depassivation time, and 3) type of rust that most significantly influences concrete cracking, red rust, is used.

Under steady state corrosion with constant rate, the time for the cracking state can be related to the steady state corrosion by Equation 2-1,

$$t_{cr} = \rho_{cor} \times \frac{D \cdot \Delta D}{S \cdot j_r} \tag{2-1}$$

where S is the perimeter of the bar, D is the diameter of bars, ΔD is the change in diameter of bars, j_r is the instantaneous corrosion rate ($g/cm^2/s$), and ρ_{cor} is the combined density factor for steel and rust.

Bazant's model expressed the relationship of time to corrosion cracking in terms of geometrical and mechanical parameters. Corrosion rate was the most influential parameter in estimating the time of corrosion cracking. Banzat's model did not agree well with experimental and field results and was found to underestimate the time to corrosion cracking.

Liu and Weyers (1998) enhanced Bazant's model (1979) by including the time to fill the porous zone around the reinforcement by the corrosion products. The Liu and Weyers model estimated time for the corrosion cracking by calculating the critical rust weight and the rate of steel loss (or the corrosion rate) expressed in Equations 2-2 and 2-3, respectively.

$$W_{crit} = \rho_{rust} \left\{ \pi \left[\frac{C f_t^{'}}{E_{ef}} \left(\frac{a^2 + b^2}{b^2 - a^2} \right) + \upsilon_c \right) + d_o \right] D + \frac{W_{st}}{\rho_{st}} \right\} \tag{2-2}$$

In Equation 2-2, W_{crit} is the critical amount of corrosion products, ρ_{rust} is the density of the corrosion product, C is the cover depth of concrete, $f_t^{'}$ is the tensile strength of concrete, E_{ef} is the effective modulus of elasticity, a and b are geometrical parameters related to the thickness pore band around the steel/concrete interface (d_o), D is the steel diameter, W_{st} is the mass of corroded steel, and ρ_{st} is the density of steel.

$$t_{cr} = \frac{(W_{crit})^2}{2k_p} \tag{2-3}$$

In Equation 2-3, $k_p = 0.098(1/\alpha)\pi D i_{cor}$ where α is related to the type of rust products and icor is the annual mean corrosion rate (mA/ft^2).

The Liu and Weyers model overestimated the time of corrosion cracking due to underestimation of the amount of steel loss compared to Faraday's law.

Bahargava et al. (2005) proposed an analytical model to anticipate the time required for cover cracking and determine the weight loss of the steel reinforcing bar. The model considered the stiffness contribution of the steel reinforcing bar, the expansive rust layer, and the residual strength of cracked concrete. They assumed a cylinder consisting of two isotropic linearly elastic materials with different elastic moduli as shown in Figure 2-9. The cracked concrete was expressed as a reduced modulus of elasticity compared with the inner cracked cylinder.

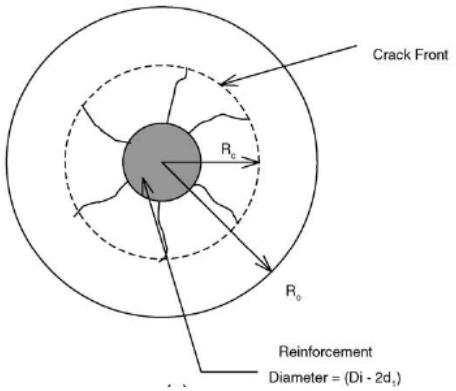

Figure 2-9 Propagation of Radial Splitting Cracks Through Cover Concrete Due to Corrosion Process (Bahargava 2005)

Although the analytical results showed a good agreement with test results, insufficient explanation about modeling of boundary area is a drawback for their model. In addition, the modulus of elasticity in the radial direction was not defined.

Li et al. (2006) proposed an analytical model to investigate corrosion induced cracking by employing fracture mechanics for stress and strain calculations around the reinforcing bar location (Figure 2-10). The smeared crack concept was used to simulate the corrosion cracking assuming quasi-brittle material property for concrete.

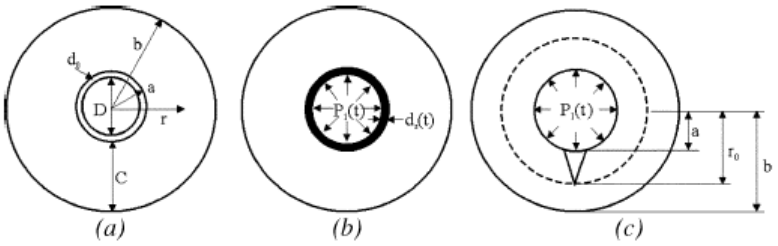

Figure 2-10 Schematic of Corrosion-induced Cracking Process (Li et al. 2006)

The model revealed that time of the cracking and the width of crack width was mainly dependent on the corrosion rate ($i_{corr.}$). However, and similar to Bahargava et al. (2006) model, the compatibility of stresses and strains on the boundary between the two materials were not provided, since the changing in the modulus of elasticity in the tangential direction was depending only in the average strains.

El Maaddawy and Soudki (2007) proposed a model to estimate the time from corrosion initiation to corrosion cracking based on Bazant's (1979) and Liu and Weyers's (1998) models. The main concept of this model was developing a relationship between the internal radial pressure caused by expansion of corrosion product (rust) and the steel mass loss by using thick walled cylinder concept as shown in Figure 2-11. Model assumptions included: 1) uniform distribution of corrosion products around the steel bar, 2) development of internal pressure after filling of the porous zone around the bar, 3) strain associated with corrosion product expansion in the concrete only, and 4) occurrence of cracks after exceeding concrete tensile strength. Once the critical internal radial pressure was determined, the estimated time from corrosion initiation to corrosion cracking was calculated using Faraday's law.

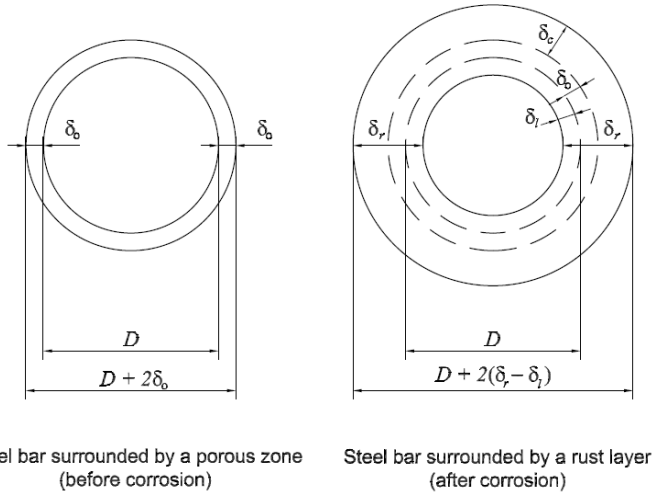

Figure 2-11 Change in reinforcing bar diameter caused by corrosion
(El Maaddawy and Soudki 2007)

The time from corrosion initiation to corrosion cracking T_{cr} is expressed in Eq. 2-4:

$$T_{cr} = [\frac{7117.5(D+2\delta_o)(1+\upsilon+\psi)}{iE_{eff}}][\frac{2Cf_{ct}}{D} + \frac{2\delta_0 E_{eff}}{(1+\upsilon+\psi)(D+2\delta_0)}] \quad (2\text{-}4)$$

where i is the current density ($\mu A/cm^2$) and f_{ct} is tensile strength of concrete, $\psi = \frac{D'^2}{2C(C+D')}$, $D' = D + 2\delta_o$, C is the concrete cover, E_{eff} is the effective modulus of elasticity, D is the steel bar diameter, υ is Poisson's ratio, δ_o is thickness of porous zone, ρ_s is the mass density of steel, and ρ_s is the mass density of rust.

Morinaga (1988) developed an empirical equation to estimate the time for corrosion cracking based on field and laboratory data as shown in Eq. 2-5.

$$Q_{cr} = 0.602D(1+\frac{2C}{D})^{0.85} \quad (2\text{-}5)$$

where Q_{cr} is amount of corrosion required to cause cracking ($10^{-4} g/cm^2$), C is the reinforcement cover (mm), and D is the steel bar diameter (mm). For steady state corrosion, the time to initiate cracking can be estimated by Eq. 2-6.

$$t_{cr} = \frac{Q_{cr}}{i_{cor}} \quad (2\text{-}6)$$

where i_{cor} is the corrosion rate ($10^{-4} g/cm^2/day$), and t_{cr} is the cracking time (days).

Because this model only considered the geometrical aspects without consideration of material properties of concrete, it is not versatile for all corrosion cases.

Liang et al. (2002) proposed a model to predict the service life of an existing bridge. The model discussed both stages for corrosion initiation and propagation time. The service life was calculated by adding these two periods. Bazant (1979) and Amey et al. (1998) methods were suggested to estimate the initiation and propagation times, respectively. The model proposed modified Bazant's equation for corrosion cracking time. The model was expected to provide reasonable times for an initial stage of repair, strengthening, and replacement. Analytical results showed a reasonable agreement with field study results. It was recommended that the parameters should be tested carefully to provide accurate prediction.

Pantazopoulou and Papoulia (2001) formulated a model based on the mechanical response of concrete to the rust expansion around the reinforcing bar. The governing equations were provided in terms of concrete cover, material properties around the reinforcing bar, the rust product properties, and the rate of the rust. Two alternatives were used to model the rust accumulation. The first model was a linear model derived from the Faraday's law, while the

second model was a nonlinear model considering a barrier that restrains the chloride diffusion. The nonlinear simulation provided better prediction of the service life than the linear model. In addition, the cover cracking was a function of the reinforcement stresses.

Zhao and Jin (2006) modeled the amount of corrosion product required for concrete cracking. The process of the steel corrosion was assumed as three stages: free expansion of the rust product, stress initiation, and concrete cover cracking. The summation of the steel loss in each stage represented the total amount of corrosion for concrete cover cracking. The model concluded that the ratio of cover to reinforcing bar was the main factor determining the amount of corrosion to induce the cracking.

2.2.2.2 Numerical Models

Numerical models can provide valuable information to gain better understanding of the mechanisms of damage propagation due to corrosion of reinforcement, delamination, and spalling of concrete structures. Thus, during past decades, countless research efforts have been devoted to estimating deterioration caused by reinforcement corrosion and predicting the service life of the reinforced concrete structures using finite element methods of numerical modeling. Most studies on this area, however, have focused on characterizing the mechanism of damage by utilizing the effective material properties and geometry of a member, and consequent element behavior. This is an inevitable situation in FE modeling. Therefore, it is necessary to optimize the modeling options to fit into the purpose of this particular study. In this section, some representative research works related to this project are presented.

In general, deterioration problems were investigated by two-or three-dimensional (2D or 3D) FE analysis with respect to local areas considering a variety of configurations (Dagher and Kulendran 1992, Chen and Mahadevan 2008, Richard et. al. 2010), while serviceability of the deteriorated concrete structures was simulated by 2D FE models for global area (Lee et. al. 1999, Coronelli and Gamarova 2004, Saetta 2005). In 2D FE analysis of local sections, plane stress or strain elements are mostly used and corrosion induced forces are modeled by a uniform pressure of dilatation. The same concept of corrosion-induced force is also applied in 3D FE analysis for local sections with different finite elements.

Regardless of the geometry of the FE model, adoption of proper material models is an important factor to develop an accurate model. There are many established concrete models based on strength and fracture mechanic criteria with respect to tensile and compressive behavior of concrete. It is difficult to say which one is a perfect one, because proper material models can be varied according to purpose of FE analysis. Presently, most commercial FE programs include these material models as built-in option.

The most critical feature in modeling reinforced concrete structures is the cracking model of FE elements. In finite element analysis, reinforced concrete cracking has long been modeled using either the smeared crack model or the discrete crack model. The smeared crack model, initially proposed by Rashid (1968), characterizes cracking as systems of parallel cracks continuously distributed over the finite elements. Since its conception, the smeared crack model has been successfully utilized by many researchers and has undergone a number of refinements. Important contributions to the classical smeared crack model were offered by Bazant (1979, 1983, 1984),

leading to what is now referred to as the cracked band model. In contrast with the smeared model, the discrete crack model proposed by Ngo and Scordelis (1967) uses discrete cracks that form between the elements. Each concept has its own advantages and disadvantages. Although the discrete crack model has been successfully implemented in large finite element programs, the smeared crack model offers a clear computational advantage, since only the material properties of the cracked elements are modified to account for the crack. In the discrete crack model, a node must be separated into two nodes to allow the crack to form, thereby increasing the number of nodes, changing the topological connectivity of the mesh, and destroying the band structure of the structural stiffness matrix. In addition, the discrete crack model cannot easily incorporate an unknown crack direction, since this may necessitate repositioning the nodes when the new crack direction does not closely coincide with existing element lines. Besides being more convenient to implement in a computer code, the crack band model was found to be essentially equivalent to the inter-element crack model endowed with a softening cohesion zone near the crack tip. For this reason, most FE analyses have adopted the smeared crack model. Due to important features of these crack models, the literature review in this section addresses both the smeared crack model and the discrete crack model and serves as the basis for the numerical simulations presented in Chapter 6.

Smeared Crack Model

Dagher and Kulendran (1992) visualized crack propagation and mechanism of final damage. The researchers compared smeared-versus-discrete crack models, local-versus-nonlocal continuum approaches, and strength-versus-fracture mechanics criteria for crack initiation and extension. Finally, they developed a 2D FE model to assess the durability of a concrete bridge deck as shown in Figure 2-12 using the smeared crack model, local continuum approaches, and strength criteria. They examined the effects of reinforcing details such as spacing of reinforcing bars and concrete cover on the progression of corrosion damage in concrete bridge decks. Only the top part of the deck section was modeled, because cracking in the region between and above the two bars shown in the figure was of interest. The bottom boundary of the mesh is located 2 in. clear below the bars, and is restrained along its entire length, representing an inner section of deck. The vertical boundaries of the mesh are located at a distance from the center of a bar equal to the bar spacing, and are considered fixed. The top surface of the mesh is always unrestrained. Corrosion induced forces were modeled by a uniform dilation. The model showed that as little as 0.0003 in. of uniform radial bar expansion can cause a plane of delamination to form in a deck. This initial visualized FE model was considered as a typical 2D model, and most researchers followed this approach in terms of modeling techniques as well as adopted concepts.

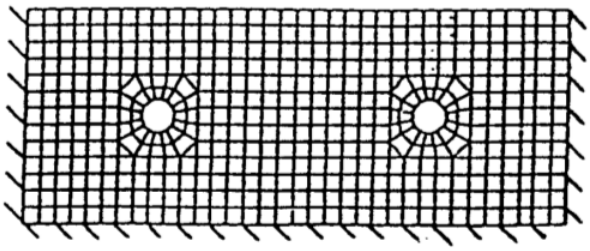

Figure 2-12 Two-Dimensional FE Model of Bridge Deck (Dagher and Kulendran 1992)

Molina et al. (1993) also developed a 2D FE analysis using the smeared crack model to compare their experimental results. A different approach for modeling of corrosion-induced force, however, was used in their model. Corrosion was modeled by a combination of initial strains and change of elastic properties, which are respectively equivalent to the expansion and softening of the steel elements at the rebar surface when rust forms. Finally, they quantitatively assessed the effect of the crack-width rate of the specific volume of the rust being formed.

Zhou et al. (2005) investigated the corrosion-induced damage of RC bridge decks via a 2D FE model as shown in Figure 2-13. They made the following assumptions in developing their model; (1) the concrete deck was modeled in a state of plane strain ($\varepsilon_z = 0$), which corresponds to stress conditions associated with a splitting mode of failure; (2) the geometry of the corrosion products was assumed to be a uniform build-up around the surface of the rebar; and, (3) the concrete material properties were assumed to be time-independent. Based on these assumptions, the accumulation of corrosion products on the bar was simulated by imposing a uniform radial displacement along the surface of the reinforcing bar. From the analysis, they found that different failure modes (longitudinal cracking, spalling, and delamination) governed corrosion-induced damage depending on the geometry of the deck, concrete cover and configuration of the reinforcing bars.

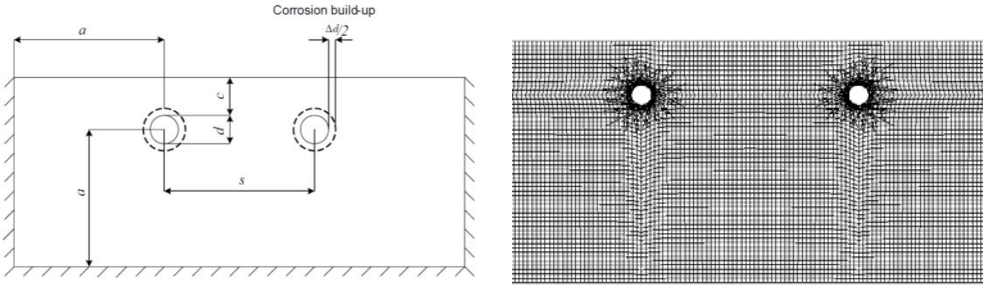

Figure 2-13 Geometry of RC Bridge Deck Model and Corresponding FE Model (Zhou et al. 2005)

Bohner and Muller (2006) investigated the influence of shrinkage and creep on the development of concrete cracking in the early propagation stage of reinforcement corrosion by developing a 2D FE model as shown in Figure 2-14. They focused on the damage progress in the propagation stage caused by reinforcement corrosion combining the shrinkage and creep effects on the stress condition within the concrete cover. They also estimated the level of stresses and the chronology of appearance of cracks inside the concrete cover, which were caused by shrinkage and creep of the concrete and later by the corrosion of the reinforcement.

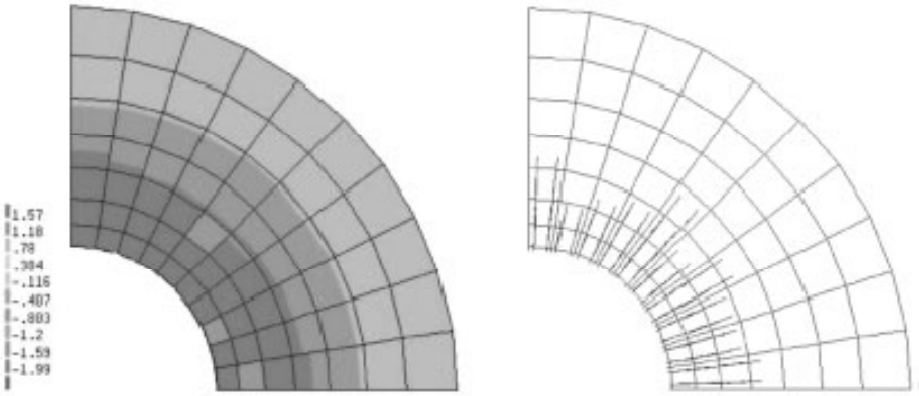

Figure 2-14 Two-Dimensional FE Model of a Corrosion Cylinder (Bohner and Muller 2006)

Du et. al. (2006) examined two approaches of assuming the corrosion-induced force as internal pressure and as radial expansion via a 2D FE model. Predictions were compared with test results for reinforced concrete accelerated corrosion specimens. They found that that the radial expansion of corroded reinforcement caused concrete cover to crack in four different stages: internal cracking, external cracking, penetration cracking and ultimate cracking. In addition, they could use FE analytical results to explain qualitatively the experimentally determined the relationship between amount of corrosion for concrete cracking and ratio of concrete cover to bar diameter, as well as that between reinforcement bond strength and amount of corrosion.

Ahmed et al. (2007) developed a 2D FE model to simulate the corrosion-induced cracking on ordinary concrete, ductile fiber-reinforced cementitious composite (DFRCC), and engineered cementitious composites (ECC). Applicability of the FE model on response of different concrete materials by corrosion of reinforcement was an important feature of this study. They compared the strains obtained from the FE models with those measured by a fiber-optic strain sensor (FOSS) gauge, which is placed between longitudinal steel bars at mid-span of RC beams during the accelerated corrosion test as shown in Figure 2-15. From the comparison, they found that the FE model could predict the corrosion-induced damage tolerance of ECC and DFRCC materials, which were several times higher than that of ordinary concrete. In addition, the FE model could predict the uniform damage in the ECC and DFRCC materials due to corrosion compared with localized damage in ordinary concrete resulting in the delamination of the cover of the RC beams containing ECC/DFRCC materials. This delamination occurred at a higher level of steel loss compared with that of an ordinary concrete beam. Finally, they concluded that the better performance exhibited by the RC beam containing ECC/DFRCC materials was due to their higher tensile strain capacity, strain hardening, and multiple cracking behavior.

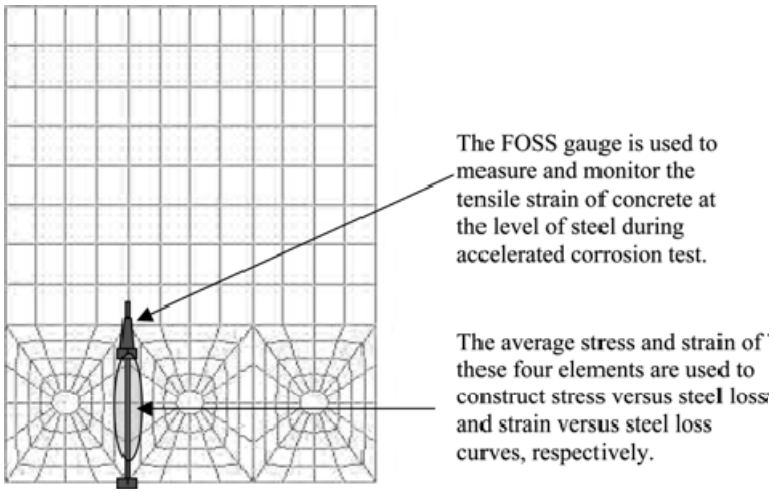

Figure 2-15 Mesh Diagram for FE Model of Beam Cross Section (Ahmed et al. 2007)

Chen and Mahdevan (2008) tried to simulate the entire degradation process from chloride penetration to reinforcement rust expansion to concrete cracking by developing a 3D FE model as shown in Figure 2-16 . The characteristics of this study are development of a 3D FE model and simulation of time-dependent analysis. The reinforcement corrosion model was based on Faraday's law, and the rust expansion was represented in the finite element analysis by an equivalent time-varying radial displacement boundary condition. Two established corrosion rate models – the constant model and the dynamic model – were combined with the proposed method. The simulation results and the predicted crack patterns for a reinforced concrete slab exposed to a constant chloride environment were mechanically reasonable.

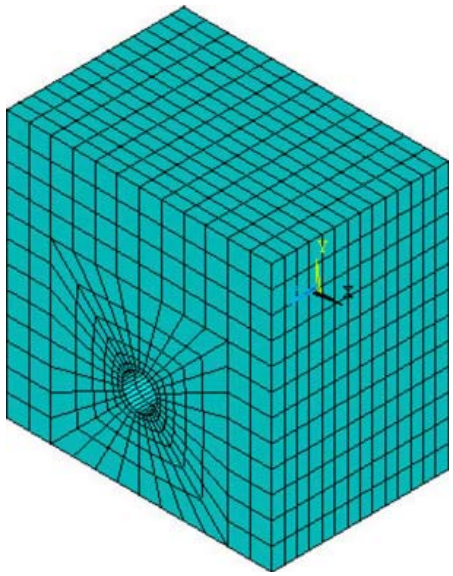

Figure 2-16 Three-Dimensional FE Model (Chen and Mahdevan 2008)

Val et. al. (2009) focused on quantifying the proportion of corrosion products that are dissipated within the concrete pores and cracks resulting from the pressure exerted by corrosion products on

the surrounding concrete. They developed a 2D FE model and compared results with experimental data on crack initiation and propagation obtained from accelerated corrosion tests of reinforced concrete slabs. A comparison of FE model results and experimental data was used to estimate the amount of corrosion products penetrating into concrete pores and cracks, which is an essential parameter for prediction of corrosion initiation and propagation. They found that the amount of corrosion products penetrating into the concrete pores before crack initiation was larger than that obtained by other researchers. In addition, corrosion products did not fully fill corrosion-induced cracks in concrete immediately after their initiation as the cracks were being filled gradually over time.

Jang and Oh (2010) investigated the effects of non-uniform corrosion on cracking behavior of the concrete cover via 2D FE analysis as shown in Figure 2-17. They also considered the effects of cover-to-reinforcing diameter ratio and concrete compressive strength on the cracking pressure of concrete cover. They found that the pressures causing cracking of the concrete cover under non-uniform corrosion conditions were much smaller than those under uniform corrosion conditions. Additionally, cover-to-reinforcing bar diameter ratio and concrete compressive strength greatly affect the cracking pressure of concrete cover. They derived the equations on the cracking pressure of concrete cover based on FE results and compared with test data.

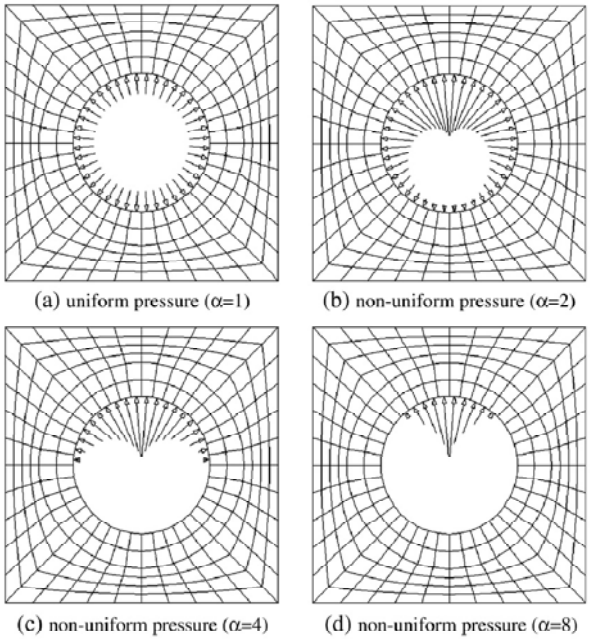

Figure 2-17 Uniform and Non-Uniform Pressure Distributions Around a Rebar (Jang and Oh 2010)

Richard et al. (2010) tried to develop a new constitutive law for modeling the steel/concrete interface by including main corrosion effects as shown in Figure 2-18. They developed 3D FE model incorporating the new constitutive law. In order to show its efficiency, they simulated the pull-out tests with and without the presence of corrosion. They found the effects of corrosion on failure loads are clearly in accordance with experimental results with respect to the damage pattern and the crack path.

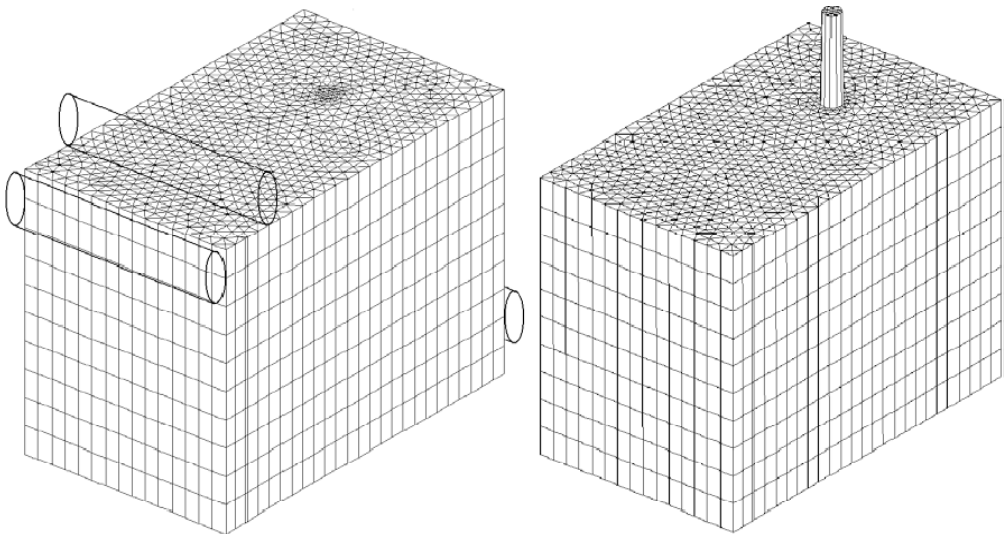

Figure 2-18 3D FE Model of Pull-Out Tests (Richard et al 2010)

Discrete Crack Model

A relatively small number of research works on FE simulation adopting the discrete crack model has been conducted compared to those of the smeared crack model. Reasons for this are due to the drawbacks of the discrete crack model mentioned above.

Noghabai (1999) investigated the cracking mechanism in concrete covers due to corrosion of reinforcement by developing a 2D FE model adopting the discrete crack model as shown in Figure 2-19 . He examined the cross-section geometry and the material properties by varying the different cover thicknesses and adopting properties of both plain and fibrous concrete. He found that the fibers enhanced the post-tensile-strength or the tension softening behavior of concrete. The cover thickness and its splitting capacity governed occurrence of the splitting cracks. For the examined covers, the fibers used had no significant influence on the appearance of the first crack. However, they effectively arrested further widening of arisen cracks. Although the main dominating cracks in covers of plain and fibrous concrete might develop similarly in time, he found that fibers might postpone or prevent a complete cover spalling, due to redistribution of strains among the arisen cracks.

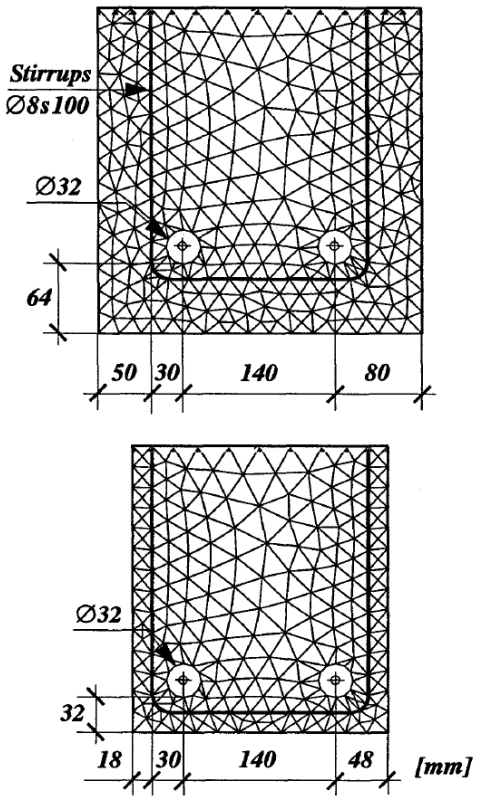

Figure 2-19 2D FE Model Incorporating Discrete Crack Model

Hansen and Saouma (1999) developed a 2D FE model based on the discrete crack model to simulate the deterioration of a concrete bridge deck induced by steel corrosion. They assumed a three-node plain strain element with linear elastic material properties for concrete and a four-node interface element for cracks as shown in Figure 2-20 . They assumed two crack paths, a single vertical crack path and five crack paths as shown in the figure. Finally, they examined the applicability of nonlinear fracture mechanics on cracks and validated their model against companion test results.

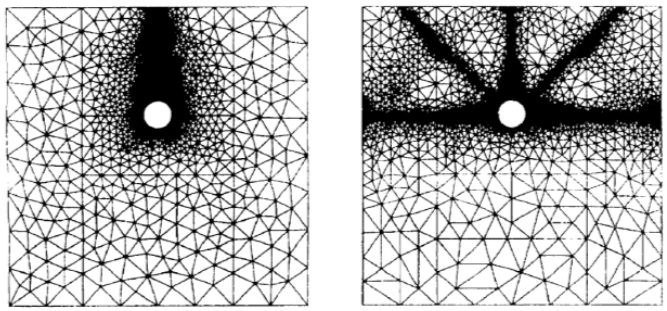

Figure 2-20 2D FE Element Meshes for Concrete Fracture: Single and Multiple Crack Cases

3 QUESTIONNAIRE SURVEY

3.1 Description and Methodology

Fifty-two transportation agencies were surveyed to determine the extent of use of precast-prestressed concrete bridge deck panels and to compare the behavior of these systems. The purpose of this survey was to collect objective data with regard to spalling problems observed in the soffit of the PPC bridge deck panels and to request information about field data and/or research studies related to this issue. Results discussed in Section 3.3 provided direction for this research in developing the field investigation, experimental, and analytical works described in Chapters 4, 5 and 6, respectively.

The survey consisted of 20 questions or requests divided into four separate sections. The first section requested design guidelines and specifications for construction of precast-prestressed concrete panels (if available).The second section questions were used to determine the type of bridge decks in current use by the agency and general information, such as dimensions and material properties of the PPC panels. The third section requested information about current problems and mitigation methods. The final section requested any information the agency may have available related to this subject. A copy of the survey is included in Appendix A.

3.2 Discussion of Survey Results

The survey yielded 29 of 52 responses. Thirteen of 29 states responding reported no or minimal use of precast-prestressed bridge deck panels (full or partial-depth). Four agencies reported interest in the implementation of these panels systems but stated that more research or an increase in familiarity with the systems is needed before implementation would be possible. In contrast, six agencies reported using precast panel systems but only in a very limited number of bridges. For instance, Arkansas has used partial-depth PPC panels in one bridge deck. The bridge is a newly-constructed cable stay bridge and was not yet open to traffic at the time of the survey. Of the 16 agencies that reported use of prestressed PPC panel systems, Nebraska and Alaska were the only two states that predominately use full-depth precast panels. Table 3-1 summarizes information received from the 14 agencies that reportedly use partial-depth PPC panels pertaining to deck age, design and deterioration observed. Design parameters and deterioration problems reported were compared in an attempt to determine the factors that are critical to the spalling problem. The most important of these factors are discussed in this section. Analyses of the other factors are also included in Appendix A.

Because spalling of concrete is strongly related to chronological changes of material properties, the age of precast prestressed deck panel systems in bridges is an important factor to consider when evaluating effects of other parameters. According to the survey results presented in Table 3-1, the use of partial-depth panels ranges from 5-40 years. As shown in Figure 3-1, six states have been using partial-depth PPC deck systems less than 20 years, three states have been using them for up to 30 years, and three states (including Missouri, Florida and Tennessee) have been using them for up to 40 years. Missouri has the second oldest bridges with partial-depth PPC panels.

Table 3-1 Summary of Survey Responses and Partial-depth PPC Panel Usage

State	PPC Panel			CIP Topping		Age (years)	Girder Type (%)		Problems Observed
	Thickness (in)	Reinforcement Type	f'c (psi)	Curing Method	f'c (psi)		Steel	Precast	
Kansas	3-3.5	PR, EC	4000	MC	4000	20	5	10	TC,LC
Florida	NR	PR	NR	NR	NR	40	0	100	LC
Minnesota	3.5	PR,EC,WWR	6000	MC	4000	8	0	100	TC,LC
Texas	4	PR	5000	MC,WC	4000	25	5	95	TC,LC
Oklahoma	4	PR	5000	MC	4000	15	50	50	TC
Tennessee	3.5-4	PR	4000	MC,LM	4000	33	30	50	TC
Arkansas	NR	EC	5800	MC	5800	0	100	0	None
Hawaii	3.5	PR,MR	6000	MC,LM	4000	14	0	100	None
Michigan	NR	EC	4000	MC	4000	NR	0	100	TC,LC,PC,SJ
Iowa	3.5	PR,EC,MR	10000	WC	3500	25	20	80	None
Georgia	6	PR,MR	5000	MC,WC	3500	28	0	100	None
Missouri	3	PR	6000	MC,LM	4000	35	30	70	TC,LC,PC,SJ, EJ,RS,CS,CR
Kentucky	NR	PR,EC		MC	5000	10	100	0	None
Colorado	NR	PR,MR	5000	LM,WC	5000	16	10	90	TC,PC,SJ,EJ

PR= Prestressing reinforcement, EC= Epoxy-coated reinforcement, WWR=Welded wire reinforcement, MR= Uncoated mild reinforcement, LC= Longitudinal cracking, SJ= Seepage at panel joints, RS= Rust stains along tendons in panels, CR= Corrosion of prestressing reinforcement, MC= Moist curing, WC= Waterproof cover, LM= Liquid membrane curing, TC= Transverse cracking, PC= Panel cracking, EJ= Efflorescence at panel joints, CS= Concrete spalling at panel joints, NR= Not reported

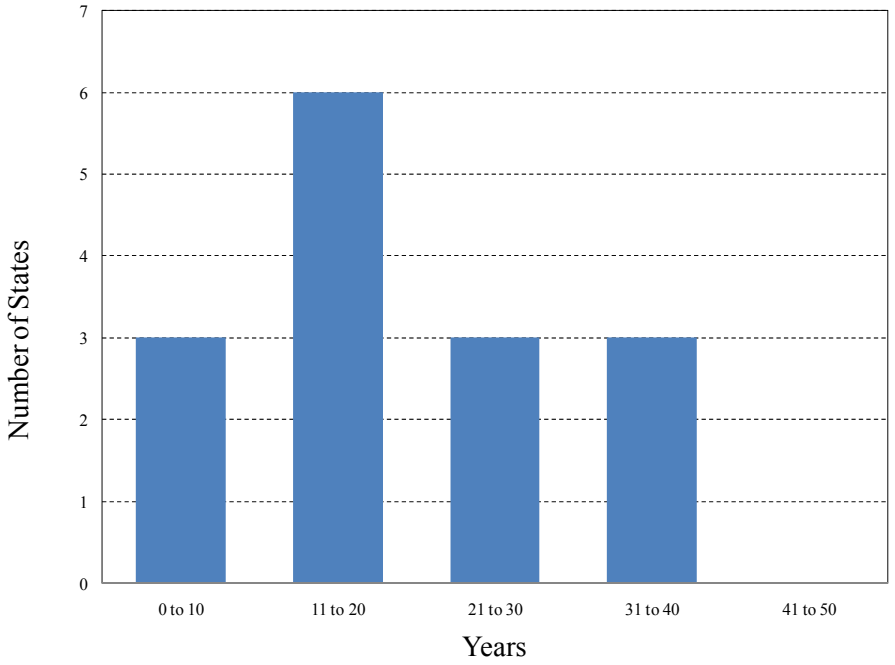

Figure 3-1 Usage Years of Precast Prestressed Deck Panel Systems

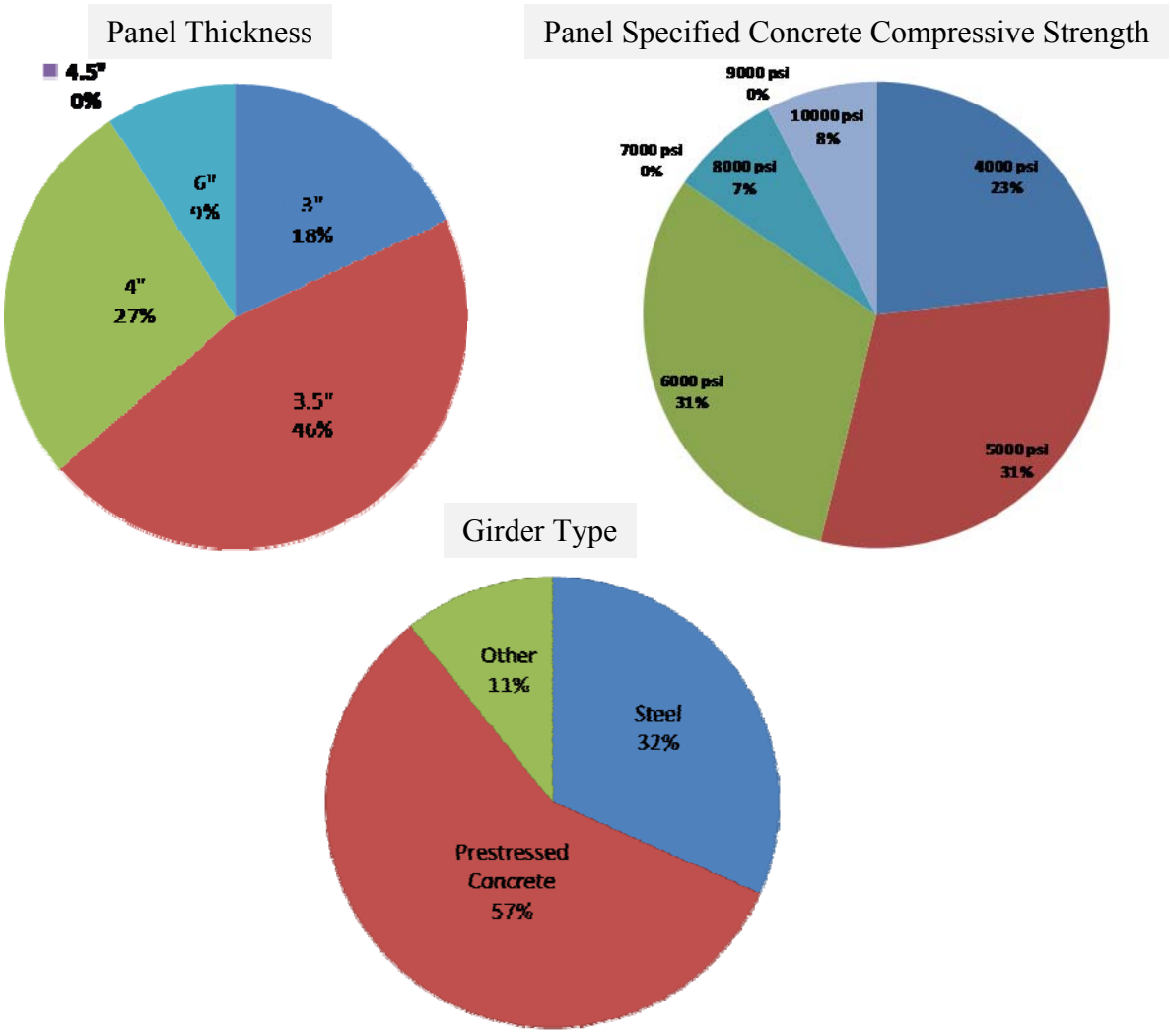

Figure 3-2 Summary of Reported Panel Thickness, Concrete Strength, and Bridge Girder Type

Panel thickness is also an important factor in the strength and serviceability of the system. In the overall structural behavior of a composite bridge deck, partial-depth PPC deck panels are in the tension region of the cross-section in locations of positive bending moment. Therefore, structural performance of the composite deck slab is strongly dependent on panel thickness. Variation of thickness can directly affect the moment arm between the internal tension and compression forces within the composite section. This moment arm governs the ultimate capacity of the composite section. Thickness of concrete cover also influences the serviceability of the panels, since cover provides protection from environmental conditions, such as the progression of chloride ions, which may lead to cracking and spalling. Typical thickness of panels is 3.5 in. according to AASHTO LRFD; however, panel thicknesses vary from state to state. According to the survey responses shown in Table 3-1, partial-depth panels range in thickness from 3-6 in. Results are also illustrated in Figure 3-2. It should be noted that Missouri is the only state besides Kansas that specifies a panel thickness of 3 in., the smallest thickness reported. Several state

agencies noted that they have changed the specified thickness of panels since implementing this system, including Missouri, to fit their needs and requirements.

Specified 28-day compressive strength of panel concrete ranges from 4000-10,000 psi, while CIP topping concrete compressive strength ranges from 3500-5800 psi. Both panel and CIP topping concrete compressive strengths specified in Missouri fall within the ranges of other states. Variation in specified panel concrete compressive strength can be seen Figure 3-2. Survey analysis indicates that panel specified compressive strength tends to be related to panel thickness. In general, as the specified compressive strength of panel increases, the panel thickness decreases. It is difficult to say which combination of compressive strength and panel thickness provides the best performance because of the numerous aspects to be considered for evaluating performance of bridge systems in terms of both structural and serviceability performance. However, further studies on quantifying the effects of concrete strength and thickness seem to be necessary for optimized design.

Most bridges in Missouri experiencing the spalling problem are reportedly constructed with steel girders (Figure 3-2). MoDOT currently has approximately 470 bridge decks with steel girders in its bridge inventory that use partial-depth PPC panels. In contrast, approximately 1240 bridge decks constructed with partial-depth PPC deck panels use prestressed concrete girders. Six other states use both steel and prestressed concrete girders for supporting the precast paneling systems; however, only one (Alaska) reported the percentage of steel girders higher than the percentage of prestressed concrete girders. Steel girders are more flexible than prestressed concrete girders resulting in more deflection in the bridge deck. The difference in deflection along the girders could be a contributor to the reflective cracking seen over the panel joints in the bridge decks; however, this was not proven in this research.

Figure 3-3 and Figure 3-4 show a summary of problems reported in PPC bridge decks (full and partial-depth). Transverse cracks (reflective cracks) and longitudinal cracks appearing in the CIP portion of the deck are the most prominent deterioration problem reported in these partial-depth PPC bridge decks. Eight agencies reported transverse cracking and six states longitudinal cracking as problems observed on the top surface of bridge decks with these systems. As explained in Section 2.1.2, the cause of transverse cracks is mainly attributed to the concentration of shrinkage of the cast-in-place concrete at the joints between the precast panels. Thus, appearance of transverse cracks is not strongly related to age of deck, properties of the panels, and girder type. Appearance of longitudinal cracks, however, appears to be more prevalent in states that predominately use prestressed concrete girders as opposed to steel girders regardless of age and concrete properties. Because the longitudinal cracks are structural cracks caused by negative moment over the girder supports, it is believed that prestressed concrete girders can provide a better performance than steel girders due to their increased stiffness. Other factors may be contributing to this tendency, and further investigation is needed for confirmation.

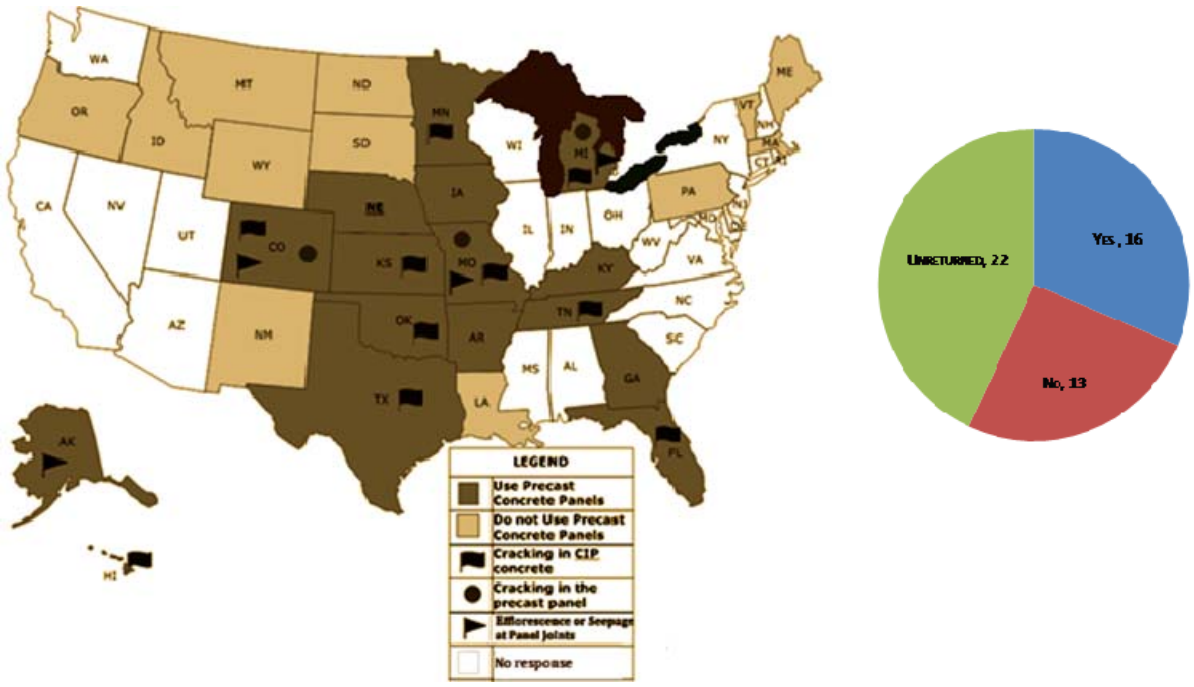

Figure 3-3 Use of Precast Concrete Bridge Deck Systems

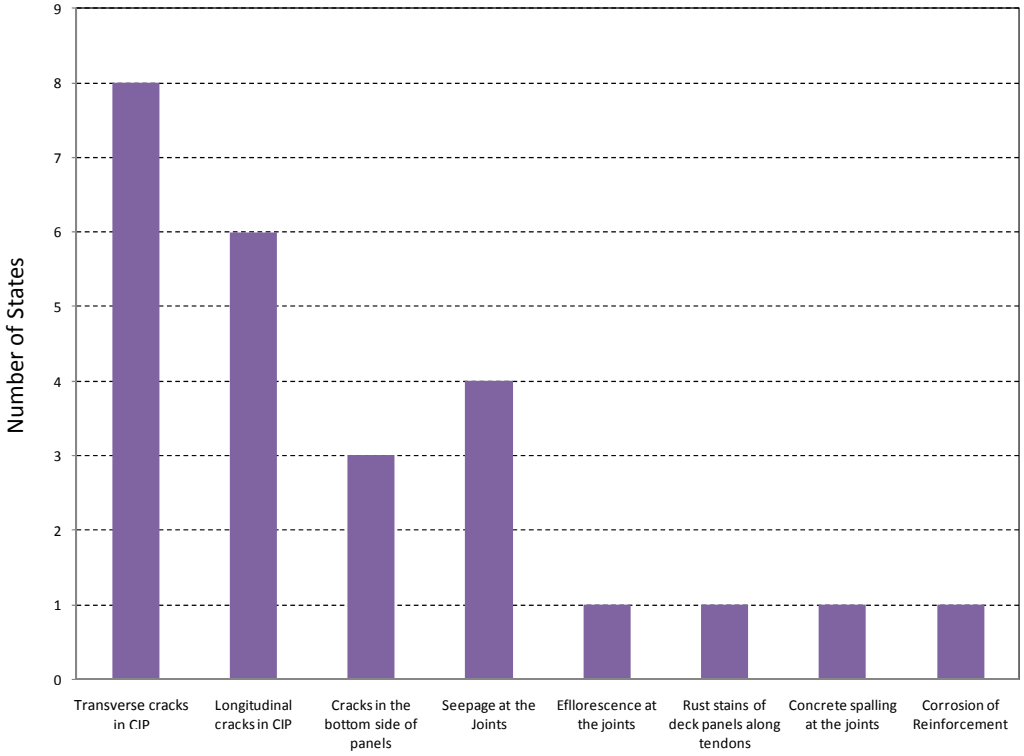

Figure 3-4 Deterioration Problems Reported

The remaining reported problems in Table 3-1 pertain to problems observed on the bottom surface of the deck associated with the panels, including panel cracking and water seepage at panel joints. Michigan, Colorado and Missouri were the only states that reported deterioration in

the partial depth panels as well as the CIP topping. Although it is difficult to correlate the results of these three states, a common characteristic is annual climate change. In particular, these states commonly use deicing materials including salts in the winter due to heavy snow. It is interesting to note that all three states report transverse cracking in the CIP topping as well as water seepage at the panel joints. This would indicate that water is progressing through the deck slab at the joint locations. Efflorescence at the panel joints was reported by Missouri and Colorado. All three states also reported panel cracking as well. Follow up information from Michigan and Colorado regarding the nature of panel cracking; however, indicates there is not a direct correlation with the panel cracking observed in Missouri as explained in the paragraphs that follow.

According to the survey response, partial-depth precast panels are used in Michigan but only as replacement decks. A report on their use of the panels, "Investigation of Precast Deck Panels Used in Spread Box Beam Bridges," included an investigation performed by MDOT to determine if possible alternative formwork used on spread box beam bridges was acceptable (Till 1997). Alternatives included concrete SIP form-only panels that made no structural contribution to the bridge deck capacity and structural SIP precast panels that were designed to contribute to the overall bridge deck capacity. Three different decks built in the early 1990s were chosen for this research assignment, one using precast panels as SIP formwork only (built in 1995), another using precast panels as structural SIP forms (built in 1994), and the last using conventional formwork (built in 1993). All three bridge decks were evaluated in the field after being subjected to traffic loadings and environmental effects. Mapping of cracks on the top and underside of the bridge decks was performed and served as the basis for comparison to determine whether the system was an acceptable alternative. Due to the extent of the cracking observed in the bridge decks built with the structural SIP forms, it was concluded that the only acceptable alternative to conventional plywood forms was form-only precast panels. No additional information was available on the nature of the panel deterioration, and further attempts to contact MDOT to inquire about their panel designs were unsuccessful.

Figure 3-5 Cracking Observed in Colorado's Partial Depth Precast-prestressed Concrete Panels

Colorado was also contacted in regards to cracking reported in their partial-depth concrete panels. Photographs sent by an agency representative indicate a much different cracking problem than that observed in Missouri bridges. The agency's panels included a type of plastic shrinkage cracking. Figure 3-5 shows one of the photographs sent. Based on the comments from one of Colorado's engineers, cracking issues are most likely a result of "hot mixture concrete and quick

evaporation of moisture" in the panels and shrinkage cracking due to the curing process. This was not a deterioration problem, so there was no further investigation performed.

The two state agencies most similar to Missouri in terms of climate and age of bridges are Tennessee and Kansas. Since these states did not report problems in partial-depth PPC panels, a comparison was performed to determine differences in design between their design specifications and those of MoDOT.

Tennessee's only recorded problem was transverse cracking, and these bridges are approximately 33 years old. Tennessee uses epoxy coated U-bars for lifting hooks, which would help prevent these bars from corroding and increasing internal pressures in the concrete. Shrinkage reinforcement is also provided in the panels that is alternately placed on the top and bottom of the prestressing strands and has a smaller spacing specification on the ends of the panels. In order for the panels to encompass this many layers of steel, the specified minimum panel thickness is 3.5 inches. In addition, the prestressing strands extend 3 inches beyond the edges of panels and over the girder. Extending the prestressing strands over the girders and into the CIP topping increases continuity in the system, which would help decrease cracking in the CIP topping in this location.

Kansas specifies many similar parameters to Tennessee. For instance, epoxy-coated shrinkage reinforcement is specified with reduced spacing increments at the ends of the panels. Kansas also extends prestressing reinforcement beyond the edge of the panel over the girders a minimum length of 4 inches. Missouri does not specify the prestressing steel to be extended out of the panels or the use of epoxy-coated U-bars; however, most panels fabricated for Missouri bridge decks now include these designs. Egyptian Concrete in Bonne Terre, Missouri and Coreslab Structures in Marshall, Missouri are the main producers of the partial-depth precast-prestressed panels in Missouri, and a review of their construction process revealed the use of epoxy-coated U-bars, epoxy-coated welded wire reinforcement or No. 3 rebar spaced at 6 inches on center, and extension of prestressing strands beyond the edge of the panels.

Of the states that reported use of partial-depth bridge deck systems, Hawaii, Georgia, Kentucky, and Iowa were the states that did not record problems on either the top or bottom surface of the deck. According to the National Climate Data Center, Georgia and Hawaii receive less than two inches of annual snow and ice, Kentucky receives approximately 17 inches, Iowa receives 35 inches and Missouri averages 20 inches of snow and ice on an annual basis (NCDC 2008). The lower snowfall averages in Kentucky, Georgia and Hawaii result in fewer deicing salt encounters for their bridge decks. Iowa, however, has a greater annual snowfall (35 inches) than that of Missouri, thus it can be expected to have more deicing occurrences per year. Iowa began using PPC panels in the 1980s, similar to Missouri, so Iowa DOT standard drawings were examined in more detail. Compared with Missouri, the main differences in design between Missouri and Iowa panels are prestressing strand spacing and specified panel thicknesses. The reinforcement used in the Iowa panels include 3/8 in. prestressing strands spaced at 3 in. with 3 in. side cover and either No. 3 reinforcing bars at 12 in. on center or 6 in. × 6 in. welded wire reinforcement. Iowa panel thickness is 3.5 in. In comparison, Missouri uses 3/8 in. prestressing strand at 4-4.5 in. spacing and specifies a minimum side cover of 1.5 in. Panel thickness is 3 in.

In addition to reviewing Iowa's specifications, a report written in 1991 about research sponsored by the Iowa DOT entitled, "Composite Precast Prestressed Concrete Bridge Slabs," was reviewed (Abendroth 1991). The report included a questionnaire sent to 121 different transportation design agencies and research performed on the composite design of the stay-in-place precast forms and the CIP topping. The questionnaire received responses from 69 agencies, and 29 of those agencies had specialized use of PPC panels. With respect to the types of bridge girders, 16 agencies specified that the panels are to be supported by precast concrete girders only, 3 agencies specified steel girders only and 9 specified either concrete or steel girders. Bridge investigations performed during the research revealed that single and sometimes multiple hairline cracks running parallel to the panel span (parallel with traffic) are located within the center half of affected panels and occur below prestressing strands. This cracking was thought to have been caused by "shrinkage of the concrete in the topping slab, thermal expansion or contraction of the cast-in-place topping slab relative to the precast panels, and tensile strains along the bridge length induced by wheel loads." In addition, the research team observed discoloration beneath the strands ranging from small shades of darker gray to 6 to 12 in. long rust stains. The possible cause for the concrete discoloration beneath the strands was thought to be initial corrosion of the prestressing strands initiated by moisture penetrating through the hairline cracking observed along the bottom side of the panels. It should be noted that at the time of this report, the thickness of the panels used was 2.5 in. As seen from Table 3-1, Iowa reported the use of a 3.5 in. thick panel, indicating an increase in panel thickness in their current bridge specifications.

3.3 Summary and Conclusions

3.3.1 Summary

The following summarizes the survey responses in terms of PPC panel usage, structural system, and deterioration reported:

- PPC panel usage:
  Of the 29 agencies responding, 16 reported use of PPC deck panels, 14 of which use partial-depth panels. Thirteen agencies reported no or minimal use of PPC panels (full or partial-depth).
- Structural system:
  Partial-depth panels range in age from 5-40 years and in thickness from 3-6 in. Missouri has the second oldest bridges with partial-depth PPC panels and is the only state besides Kansas that specifies a panel thickness of 3 inches. Specified 28-day compressive strengths of panel concrete range from 4000-10,000 psi, while CIP topping concrete compressive strengths range from 3500-5800 psi. Both panel and CIP topping concrete strengths specified in Missouri fall between the ranges of other states. Ten states use more precast concrete girders than steel girders.
- Deterioration:
  Eight states reported transverse cracking, and six states longitudinal cracking on the top surface of the deck. Only three states (Missouri, Michigan and Colorado) reported deterioration in the partial-depth panels. Water seepage at the panel joint locations and panel cracking was reported by all three states, and efflorescence at the panel joints was

reported by Missouri and Colorado. The nature of panel cracking reported in Michigan and Colorado was not similar to panel cracking observed in Missouri.

3.3.2 Conclusions

Based on the analysis of the questionnaire survey responses, the following conclusions were developed to serve as the basis for work described in subsequent chapters of this report:

- Longitudinal cracks and transverse (reflective) cracks appearing on the top deck surface are the most prominent deterioration problem reported in partial-depth PPC bridge decks. Longitudinal cracking appears to be more prevalent in states that predominately use prestressed concrete girders as opposed to steel girders regardless of age and concrete properties. Transverse cracking appears to be independent of girder type.
- Of the states reporting problems on the bottom deck surface (Missouri, Michigan and Colorado), a common trend is transverse cracking in the CIP topping as well as water seepage at the panel joints. This would indicate water progression through the deck slab at the panel joint locations. While Michigan and Colorado have not experienced the panel cracking similar to that observed in Missouri, their panels have not been in service as long.
- The combination of design parameters, age, environmental conditions, and problems reported in Missouri bridges with partial-depth PPC panels is unique with respect to the other respondents. Thus, a comprehensive field investigation is required to determine the specific cause of deterioration and mechanism of spalling reported in Missouri bridges with partial-depth PPC panels (Chapter 4).
- Most of the reported deterioration problems with the PPC panel system appear to be related to environmental conditions resulting in corrosion of embedded steel rather than structural issues. Missouri panels have the smallest thickness reported (3 in.) and have been in service longer than most other states (35 years). Relatively shallow concrete cover associated with the use of a relatively thin panel and small specified edge distance would appear to exacerbate the long-term effects of environmental conditions. Thus, numerical simulation and corrosion tests that simulate the in situ environmental conditions in Missouri bridges are needed to provide fundamental knowledge on the deterioration behavior of the panels. This knowledge is critical in the development of proposed system modifications for new construction that is corrosion-free (Chapter 5) and spalling mitigation strategies in existing structures (Chapter 6).

4 FIELD INVESTIGATIONS

4.1 Overview of Field Investigations

In order to comprehend fully and define accurately the cause of the spalling problem observed in partial-depth PPC bridge deck panels, a series of investigations of bridge decks with the bridge deck paneling systems was conducted. Table 4-1 is a reference table of bridges investigated during this research, each of which were identified by MoDOT as showing signs of spalling. Bridge A4709 was identified by MoDOT bridge engineers as having the most advanced degree of spalling of all bridge decks of this type in MoDOT's inventory. Section 4.2 discusses the preliminary study on Bridges A4704, A4705, A4375 and A4067, which served as the basis for the comprehensive study of Bridge A4709 summarized in Section 4.3. (Additional results from the Bridge A4709 investigation are provided in Appendix B). Follow-up study on Bridges A4067 and A4705 is discussed in Section 4.4. Based on the findings from each field investigation, key findings regarding the spalling mechanism are presented in Section 4.5.

Table 4-1 Bridges Investigated

Bridge Number	Construction Date	Number of Spans	Orientation	Prestressing Spacing	Panel thickness
A4067	1986	3	N to S	4.5 in. o.c	3.5 in.
A4375	1985	2	NE to SW	4.5 in. o.c.	3.5 in.
A4704	1990	2	N to S	4 in. o.c.	3 in.
A4705	1990	4	NE to SW	4.5 in. o.c	3 in.
A4709	1991	2	NW to SE	4 in. o.c	3 in.

4.2 Bridges A4067, A4375, A4704 and A4705

A visual investigation was conducted on Bridges A4067, A4375, A4704 and A4705 in St. Louis, MO on December 10, 2008. The objective of these investigations was to identify visually problems in the bridge decks and to gain a better understanding of the nature of problems occurring in the partial-depth PPC bridge decks. These investigations would also serve as the basis for establishing the protocol for the comprehensive bridge investigation described in Section 4.3. The bridges contain partial-depth PPC panel bridge systems that were identified as having the panel spalling problem and serve as overpasses to major highways. In each case, panels are supported on continuous steel plate girders spanning two to four spans. St. Louis had received approximately 0.5 in. of rainfall and 0.3 in. of snow the week before the investigations.

Deterioration conditions observed were similar in nature in each bridge deck. Transverse cracking extended over the entire bridge deck in a "zigzag" fashion and in many cases extended through the concrete barriers. Transverse cracks appear to be reflective cracks that formed directly over the panel joints. Figure 4-1 shows examples of the cracking observed in the bridge decks. Observed water stains, efflorescence, rust seepage and spalling at the bottom surface of many panels indicate deterioration and corrosion of steel is occurring. Its main cause is most likely due to the ingress of carbonation and chlorides into the concrete. Figure 4-2 shows three different panel joints with water staining and efflorescence surrounding the spalled area, which exposes much of the panel reinforcement at the panel edge. The transverse cracks above provide a direct route for chlorides to reach prestressing tendons embedded in the prestressed panel. No

significant longitudinal cracks were observed along the girder lines in any of the St. Louis bridge decks investigated.

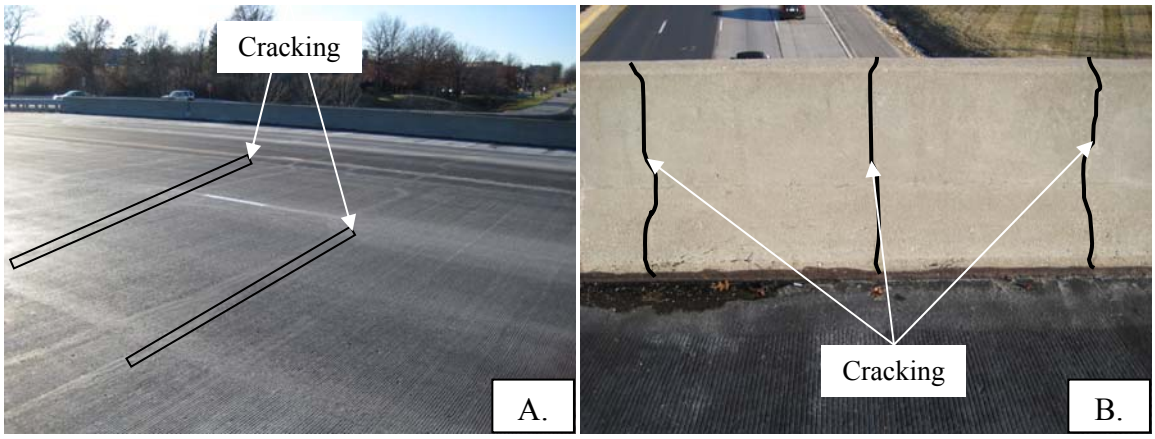

Figure 4-1 Crack Propagation in Bridge Deck (A. Cracking in the CIP topping, B. Cracking from the CIP topping extending to the concrete barrier (highlighted for clarity)) (Bridge A4704)

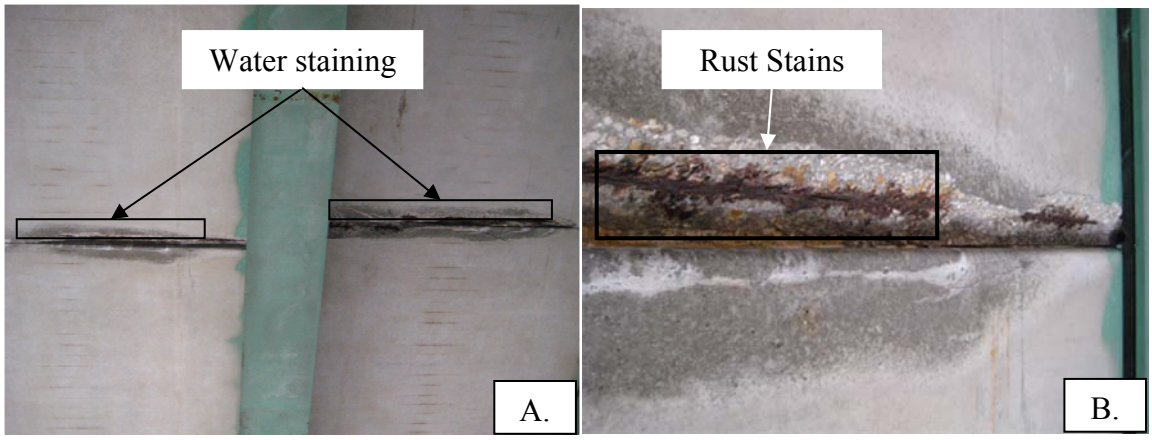

Figure 4-2 Spalling, Efflorescence, Water Staining and Rust Stains Observed in PPC panels (A. Adjacent panel joints, B. Close-up shot of panel joint) (Bridge A4704)

Rust colored stains were also observed on the surface of many panels as shown in Figure 4-3. The spacing of these stains is approximately 4 in. and is consistent with tendon spacing. No cracking was observed in the panels at or near the discoloration lines.

Figure 4-4 and Figure 4-5 show exposed tendons and spalled concrete sections. In Figure 4-4, the spall thickness is approximately 2.5 in. deep. The spalling not only exposes the prestressing but also the mild reinforcement spaced at 6 in. on center. Partially or completely ruptured tendons, shown in Figure 4-5, indicate the extent of corrosion in these systems.

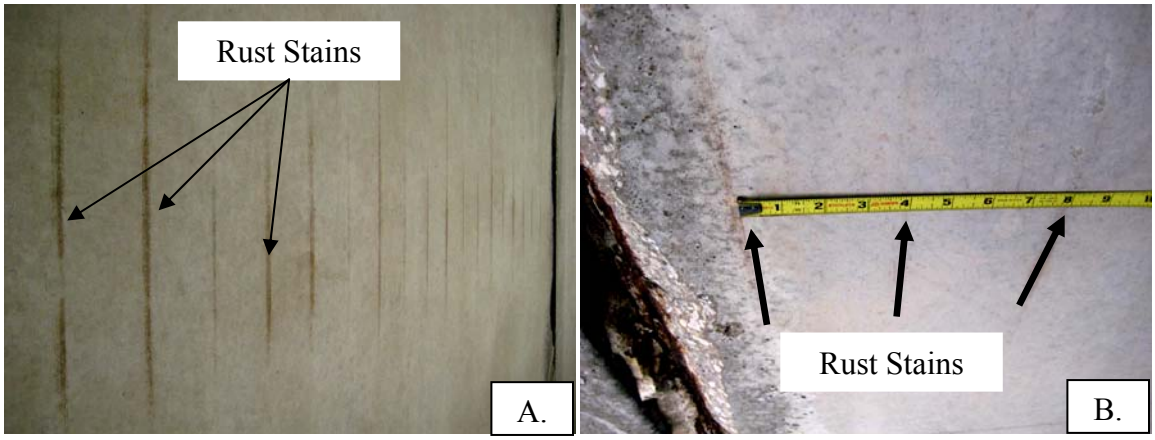

Figure 4-3 Rust Stains Observed on the Panel Surface (A. Rust stains along the entire width of the panel, B. Rust stain spacing at 4 in. on center) (Bridge A4704)

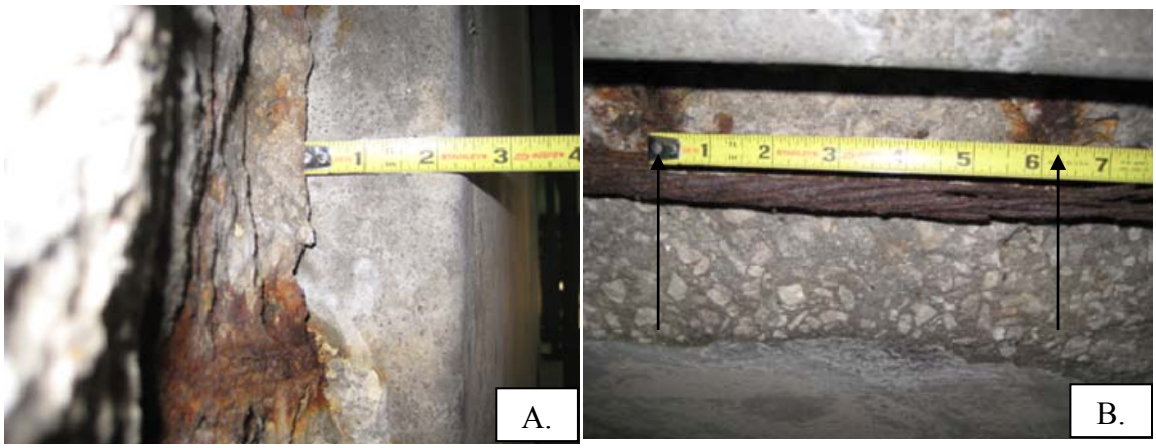

Figure 4-4 Spalled Sections of PPC Panels (A. Depth of a spalled section, B. Exposed mild reinforcement in a spalled section) (Bridge A4067)

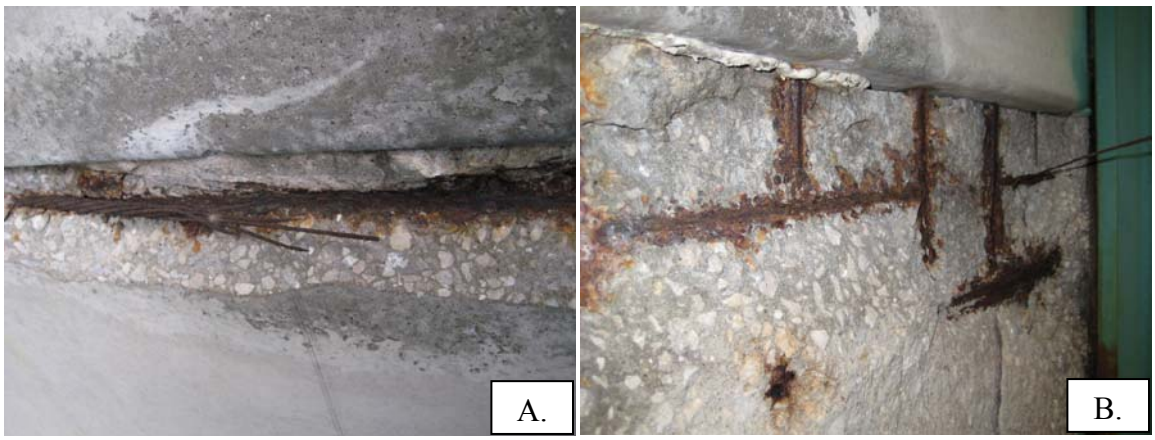

Figure 4-5 Ruptured Tendons in Spalled Section (A. Partially ruptured tendon, B. Completely ruptured tendon) (Bridge A4067)

4.3 Bridge A4709

4.3.1 Introduction

A comprehensive investigation was performed on Bridge A4709 located in Mexico, MO over the course of three days, August 10 and 11, 2009 and April 1, 2010. Bridge A4709 was selected for the detailed investigation because it was identified by MoDOT bridge engineers as having the most advanced degree of spalling of all bridge decks of this type in MoDOT's inventory. The objective of this bridge investigation was to gain information on the in-situ bridge deck properties and to determine the causes of spalling in the PPC panels. The goal was to examine thoroughly each side of the bridge deck using various non-destructive techniques to gain a full understanding of the deck and the deterioration. To achieve the objective, the following information was sought: 1) reason for differences in deterioration occurring in the PPC panels in various locations of the deck; 2) mechanism by which water and chlorides were progressing through the CIP topping and into the panels; and 3) relative corrosion amongst the tendons within a given panel. Various techniques were selected based on the background review described in Wieberg (2010). No recorded rain occurred during the week before August 10, 2009 except for small showers on the night of August 9, 2009 and the morning of August 10, 2009. Recorded rainfall during the week before the April 1, 2010 bridge investigation was approximately 0.75 in. with no rain occurring within three days of the investigation.

Bridge A4709 was built in 1991 and serves as an overpass bridge to US 54. The bridge slab consists of 3 in. thick partial-depth PPC panels and 5.5 in. CIP topping containing epoxy-coated reinforcing steel bars. The spacing of the 3/8 in. prestressing tendons in the panels is 4 in. The construction drawings indicate a change in the CIP reinforcement spacing in the negative moment areas of the bridge deck with respect to the remainder of the deck. Longitudinal reinforcement in the positive moment regions of the bridge deck span is spaced at 15 in., and longitudinal reinforcement in the negative moment portion of the bridge deck span is spaced at 5 in. Long span steel plate girders with two spans of 127 ft. and 120 ft support the deck. The bridge has 116 panel joints, defined herein as the joint between two adjacent panels in the longitudinal direction (direction of traffic).

No history of repair was available on the bridge deck, but in a previous in-depth investigation report performed by MoDOT bridge investigators, Wenzlick reported "the top of the deck appeared to have been sealed with Pavon In-deck probably two to three years earlier and the bigger cracks poured with oil some time since then" (Wenzlick 2008). Wenzlick performed a visual inspection on the bridge in which reflective cracking was noted in the top of the deck in the same pattern as most of the panel joints. This can result in salt and moisture intrusion through the cracks that can penetrate the panels, making them susceptible to corrosion. From the bottom side of the bridge deck, 6% of the panel joints reportedly exhibited visible signs of spalling. The spalled sections ranged from 3 to 16 in. long and 2 to 3 in. wide on the ends of the PPC panels. Wenzlick's site investigation took place just after a rain that kept the deck wet for several days allowing him to make several other observations: about one third of the panels had water saturation 3 to 6 in. back from the panel joints with over 44% of the joints leaking water. In addition, 25% of the panel joints were starting to show efflorescence.

In the present study, the bridge deck was first investigated on August 10-11, 2009 on the upper and lower surface of the bridge deck by conducting an in-depth visual inspection and using several other non-destructive techniques: GPR, half-cell potential, resistivity, and rebound hammer. The second investigation took place on April 1, 2010 and included the use of GPR on the top surface of the deck only. Each test was performed according to its corresponding ASTM and AASHTO standards, as well as ACI recommendations (ACI 201.1 1992). Figure 4-6 indicates the different labeling rubric used in this investigation. The (project) west lane of traffic included Panel Lines A and B, and the (project) east lane of traffic included Panel Lines C and D. The protocol for each technique used is described in Sections 4.3.2-4.3.7. Key findings and results are discussed in Section 4.3.8.

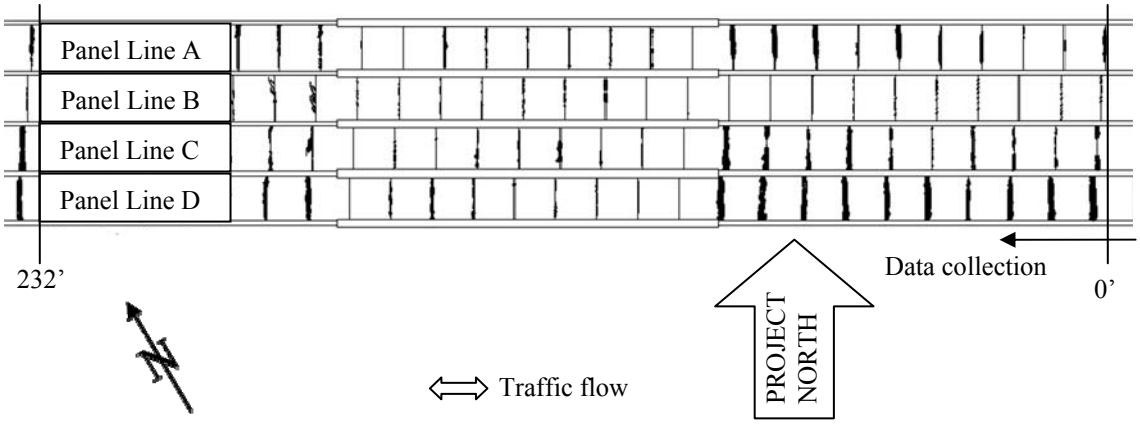

Figure 4-6 Labeling Rubric Used for Bridge A4709 Bridge Site Investigation

4.3.2 Visual Inspection

An in-depth visual inspection was performed on the upper and lower portions of the bridge deck. Cracking in the CIP portion of the deck was measured and mapped. The visual inspection of the bridge top surface confirmed the reflective cracking described by Wenzlick (2008). Crack widths were unable to be measured due to the crack sealant that was applied to the cracks to prevent water ingress. Transverse cracking observed in the CIP topping stretched in a diagonal "zig-zag" across the bridge deck, as highlighted in Figure 4-1, and extended to the concrete barriers located at the edges of the deck. These cracks looked to be a result of reflective cracking above the panel joints. No longitudinal cracking was observed in the bridge deck.

At the time of this investigation, 15 of the 116 total panel joints (13%) have started to spall, and an additional 19 joints have begun cracking at the edges, an early stage of spalling. Spalling was limited to the south side of the bridge, Panel Lines C and D. Panel Line D included nine of the spalled joints, and Panel Line C included six spalled joints. The extent of the spalling in Panel Line C is not as advanced as that found in Panel Line D. Figure 4-7 shows a full bridge deck bottom surface view of the spalled panel joints. Of the 15 spalled joints, tendons were exposed in 14 joints. Measurements at spalled sections showed edge distance to tendon ranged from 1.5 to 2.0 in. (center of tendon to edge of concrete). Cracking in the panels was limited to Panel Line A, C and D at the panel joint locations. Figure 4-7 also shows the locations of panel joints with cracking but no spalling. No additional cracking was observed in the other portions of the panels.

Efflorescence observed in 88 panel joints tended to be less prevalent in the panels placed in the middle and at the ends of the bridge deck. The same is true for water stains observed at the panels joints with the exception of panel joints located in Panel Line B. Only four of the 29 panel joints in Panel Line B contained water stains. Of the 116 full size panels, 96 included discoloration lines in the middle of the panels that had a spacing of 4 in. on center. Most of these lines had a grayish or rust colored tint to them. No cracking was observed along these lines.

Mapping of all deterioration observed from the top and bottom surfaces of the bridge deck (cracking, spalling, water staining, efflorescence, and discoloration lines) is compiled in Appendix B.

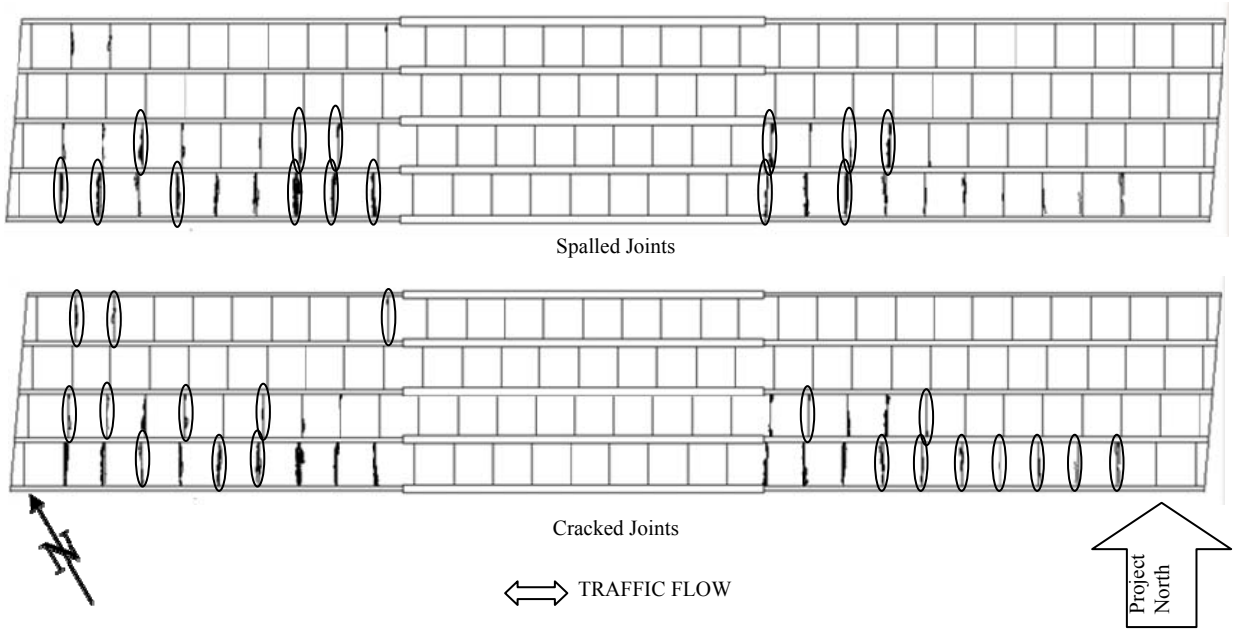

Figure 4-7 Panel Spalling and Cracking Locations

4.3.3 Half-cell Potential

Half-cell potential and resistivity data (Section 4.3.4) were acquired on the bridge deck with the objective of estimating the corrosion rate of the prestressing tendons. Half-cell potential data were also acquired on representative panels to complement the GPR control. Half-cell data were obtained on August 11, 2009 using a Canin Corrosion Analyzing Instrument from Proceq. The average temperature during data acquisition was 85 degrees Fahrenheit. Due to time constraints, the half-cell potential test was only performed near tendons that were already exposed due to spalling. The half-cell potential was performed on six different tendons. Readings taken over these tendons approximated a corrosion rate by indicating the severity of corrosion. Some of the tendons were fully exposed and partially fractured while others were only partially exposed. Each tendon tested provided readings indicating that corrosion was a high probability (Canin 2007). As expected, higher corrosion values were found on the fully exposed tendons versus the partially exposed tendons. See Table B-1 in Appendix B for compiled half-cell potential data.

4.3.4 Resistivity

Resistivity measurements were gathered only from the underside of the panels. Resistivity testing was attempted on the CIP portion of the bridge deck but was unsuccessful in obtaining a

good electrical connection to the topping, presumably due to a coating applied to the bridge deck. The Canin Corrosion Analyzing Instrument from Proceq was used for the resistivity data acquisition by attaching the four-prong probe device. Resistivity measurements obtained on August 11, 2009 on 22 representative panels showed only one panel having the possibility of corrosion (Canin 2007). See Table B-2 in Appendix B for compiled resistivity data. The one panel with a voltage reading low enough to indicate that corrosion was possible (D22-23) exhibited spalling in both panel joints. This panel was one of the worst case panels found during the bottom deck visual inspection (Section 4.3.2).

4.3.5 Rebound Hammer

The rebound hammer test was performed on August 10-11, 2009 on 27 representative panels to determine an approximate concrete strength value as well as relative concrete strengths between the panels. Testing was performed on the bottom side of the bridge deck surface in the vertical direction. A total of 8-12 readings were obtained on various locations of each panel tested. Rebound hammer test data are summarized in Table B-3 in Appendix B.

4.3.6 Ground Penetrating Radar

GPR measurements were taken from both top and bottom surfaces of the bridge deck using a GSSI 1.5 GHz antenna. GPR data are typically not acquired from the bottom surface of the bridge deck due to the inconvenience of having to couple the GPR antenna to the bridge deck surface. The reason for taking measurements from both surfaces, however, was to attempt to obtain a better image of the cross section because the deck consists of two layers of concrete as well as multiple layers of reinforcement. Additionally, it was of particular interest to image the bottom surface to examine the condition of the prestressing tendons, which are critical to the load-carrying capacity of the deck. Reinforcement can best be detected by acquiring the GPR data perpendicular to its axial orientation. Therefore, data were acquired along longitudinal traverses on the bottom surface of the deck with a special apparatus consisting of a small survey wheel and the antenna attached to an extended handle. Data were acquired at the panel ends next to the girders as well as in the middle of each panel. GPR data acquisition on the top surface of the bridge deck consisted of two different scans in 24 in. intervals, one in the longitudinal direction of the bridge deck and one in the transverse direction. The longitudinal investigation consisted of 19 scan lines 232 feet long. The transverse investigation consisted of 124 different scan lines 38 feet long. Because the orientation of the upper mat of steel was not clear and information about the prestressing tendons was needed, the longitudinal direction scan was performed first. The longitudinal scan was performed on August 10, 2009 in an attempt to locate delaminations within the CIP and panel interface and to determine relative corrosion levels of the prestressing tendons. The longitudinal data obtained consisted of numerous anomalies, which made it impossible to determine depths of reinforcement. As a result, a second GPR scan in the transverse direction, conducted on April 1, 2010, was performed to develop a deterioration map of the bridge deck. In all cases, data were acquired using the distance sampling technique. Individual GPR profiles were processed using GSSI RADAN 6.5 bridge assessment module.

Rain that had occurred the night of August 9, 2009 resulted in a wet top surface of the deck and caused possible water build-up inside the slab. For this reason, the dielectric property of moist concrete, 6.25, was used for the top bridge deck investigation with a sampling depth of 20 in in

the longitudinal scan. A sampling depth of 12 in. was selected for the transverse GPR scan, and a dielectric constant of 6.25 was used.

Panel joints could be located accurately on the longitudinal GPR profiles obtained from the top surface of the bridge deck, in large part because they are characterized by deteriorated concrete and propagate in the transverse direction across the bridge deck. Figure 4-8 shows GPR data acquired along the top surface of the deck along Panel Line D; the locations of two joints are highlighted in the figure. Anomalously high travel times (large apparent depths) and anomalously low amplitudes characterize the GPR image of reinforcing bar in immediate proximity to the panel joints. Both features are normally indicative of concrete degradation. In addition, the arrival time (apparent depth) of the reflection from the base of the concrete slab is anomalously high, presumably because of deterioration of the concrete. These interpretations are consistent with the visual inspection data. As described in Section 4.3.2, reflective cracking was observed in the CIP portion of the bridge deck, and water stains and cracking were observed in the PPC panels of the bridge deck in these locations.

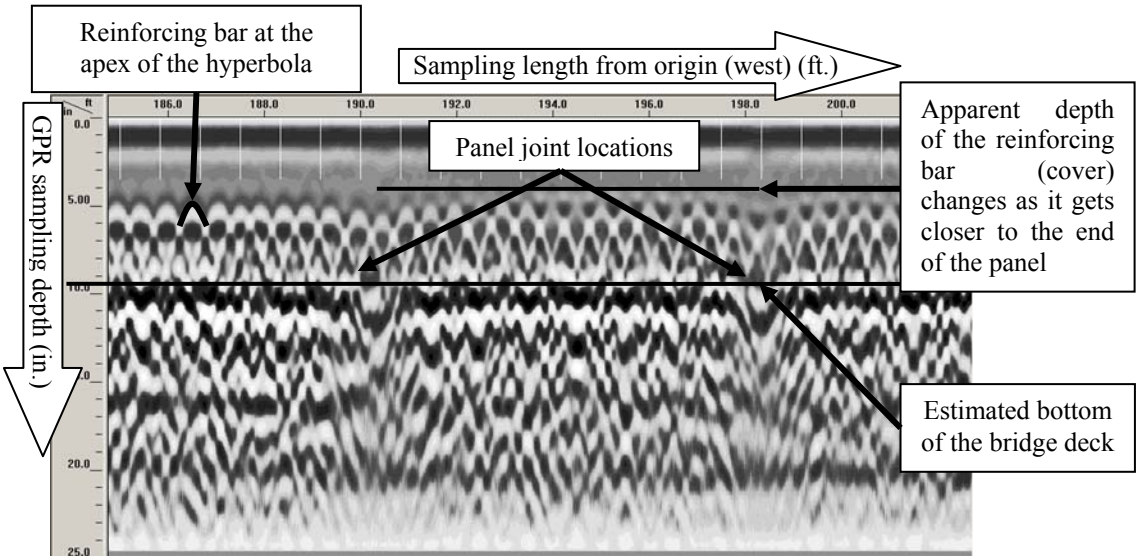

Figure 4-8 GPR Data Acquired on the Top Surface of the Deck Along Panel Line D During the Longitudinal Scan

Pulse magnitudes were also reviewed at key segments of the data profile. The pulse magnitude indicates the amount by which dielectric properties differ. The larger the pulse magnitude is the greater the difference in dielectric permittivity of the two materials. Figure 4-9 depicts GPR data acquired in the longitudinal direction from the top surface of the bridge deck over Panel Line C. The graph to the right of the profile depicts pulse magnitude along the horizontal axis versus travel time along the vertical axis. The wavelet encircled by the solid line in Figure 4-9A is the reflected signal from the bottom of the bridge deck in the middle of a panel where there is little to no visual evidence of degradation. It has maximum amplitude of ±0.4. In comparison, Figure 4-9B shows the GPR reflection from the bottom of the bridge deck near a panel joint where there is visual evidence of degradation. The relatively low pulse amplitude supports the hypothesis that degradation is occurring in proximity to the joint.

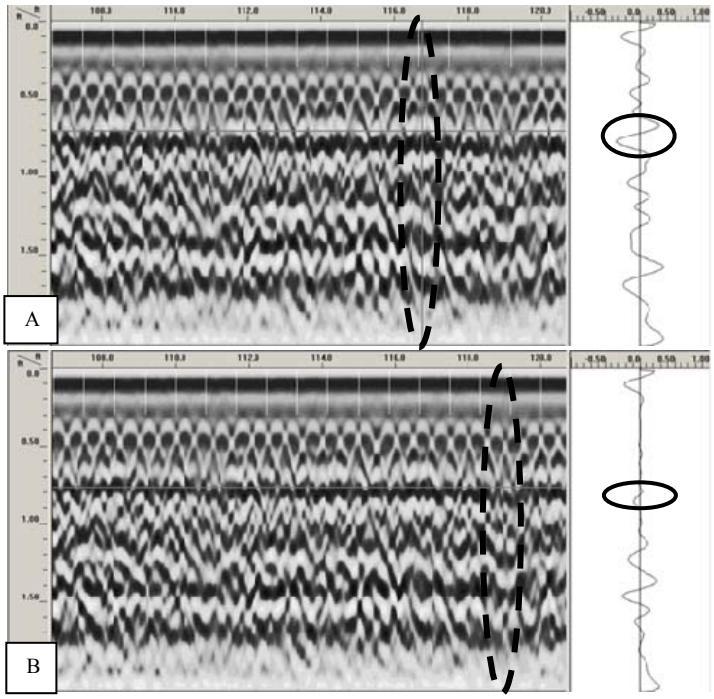

Figure 4-9 GPR Data Obtained During the Longitudinal Scan, and Graph Showing Pulse Magnitude vs. Travel Time (A. Non-degraded or non-delaminated area, B. Degraded or delaminated area)

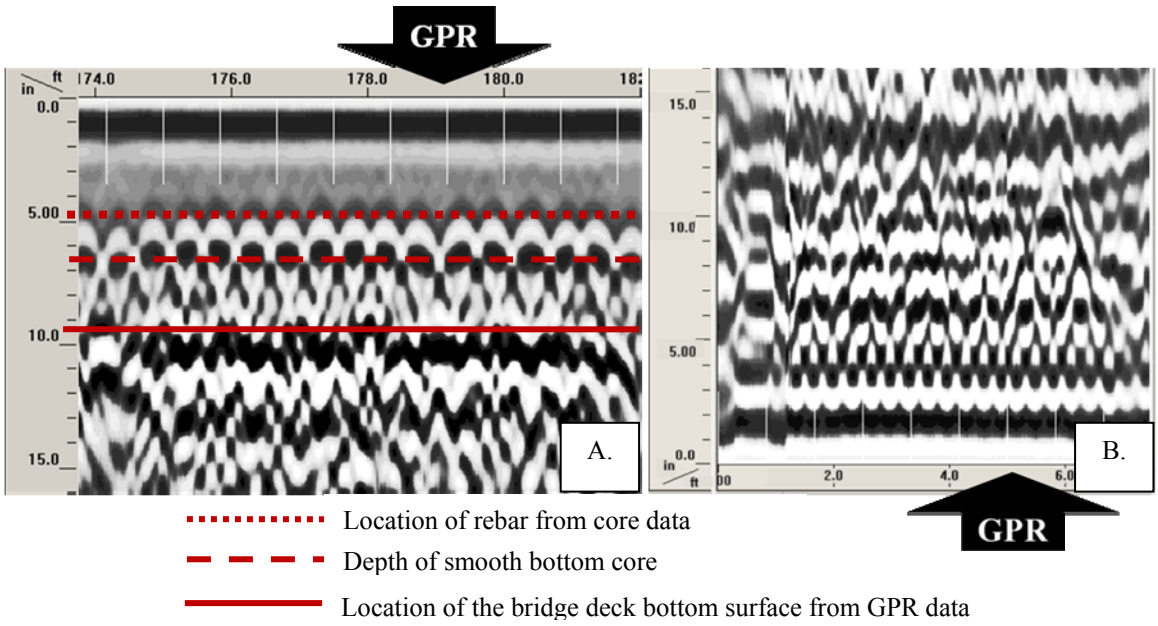

Figure 4-10 GPR Data Acquired on August 11, 2009 (A. Data acquired from the top surface of the bridge deck, B. Data acquired from the bottom surface of the bridge deck)

In an attempt to examine deterioration within the thickness of the bridge deck, data acquired from the top and bottom surfaces of the bridge deck were compared. Figure 4-10 shows data acquired from both the top and bottom surfaces of the bridge deck on August 11, 2009. Figure 4-10A shows data acquired from the top surface of the bridge deck in the longitudinal direction

over a length of 8 ft. Figure 4-10B shows data acquired from the bottom surface of the bridge deck of the 8 ft. wide panel located in the area corresponding to Figure 4-10A. Both figures show increasing depths to reinforcement near the edges of the data (panel joint locations) indicating degradation at the panel joints.

The varying degree of degradation from one panel line to the next can be seen in Figure 4-11. This figure shows GPR data taken in the longitudinal direction from the top of the bridge deck in the four different panel lines at the same location measured along the length of the bridge. The solid lines indicate the GPR representation (apparent location) of the bottom of the bridge deck in that area. When the data for the four panel lines are compared, varying (apparent) reinforcing bar depths and concrete thicknesses are observed. As expected, apparent reinforcing depths and concrete thicknesses are greatest on Panel Line D because it is the most deteriorated based on the visual inspection data.

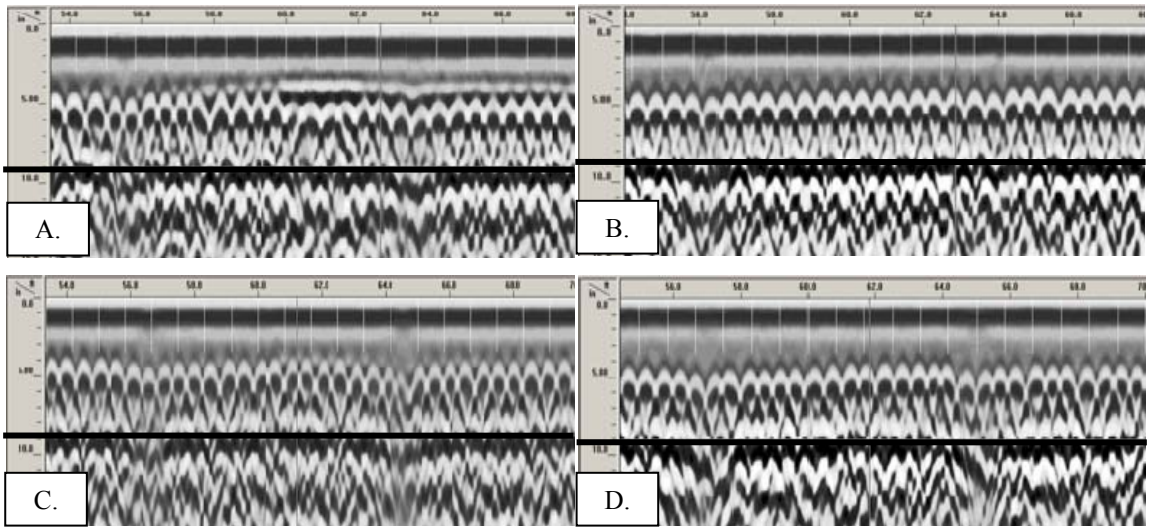

Figure 4-11 Apparent Depth of Deck from GPR Shots Obtained on Top of the Bridge Deck in the Longitudinal Direction Over Varying Panel Lines (A. Panel Line A = 9.2 in, B. Panel Line B = 8.7 in., C. Panel Line C = 8.8 in., D. Panel Line D = 9.3 in.)

Additional graphical representation of relative deterioration was depicted in contour maps using RADAN interpretation software (GSSI 2007). The contour map of the rebar reflection amplitudes from the upper mat of rebar is shown in Figure 4-12. Once the EM energy is emitted into the concrete, the energy can be absorbed, refracted or reflected back to the antenna. The amount by which the energy is absorbed, reflected or refracted depends greatly on the complex permittivity of the material. The permittivity of the material is influenced by the temperature, moisture content and salt content of the material as well as the material pore structure and the EM energy pulse frequency (Maierhofer 2003). This map, based on data obtained in the transverse direction, shows that relatively higher amplitude signals exist in the ends of the bridge deck. The amplitude of the signal is a measurement of dielectric permittivity contrasts between the concrete and the rebar and is recorded in decibels (dB). Smaller amplitudes indicate areas of increased deterioration. According to the contour map, less deterioration is occurring at the ends and middle portions of the bridge deck.

A contour map of the travel times to the upper mat of rebar is also presented in Figure 4-12 that shows the signal travel times to the upper mat of rebar in nanoseconds (ns). The velocity at which EM energy travels through a material is dependent upon the material dielectric constant, or dielectric permittivity. As the dielectric constant of the material increases, the velocity at which EM energy propagates through the given material decreases. Normally, the longer travel times would indicate more deterioration in the system.

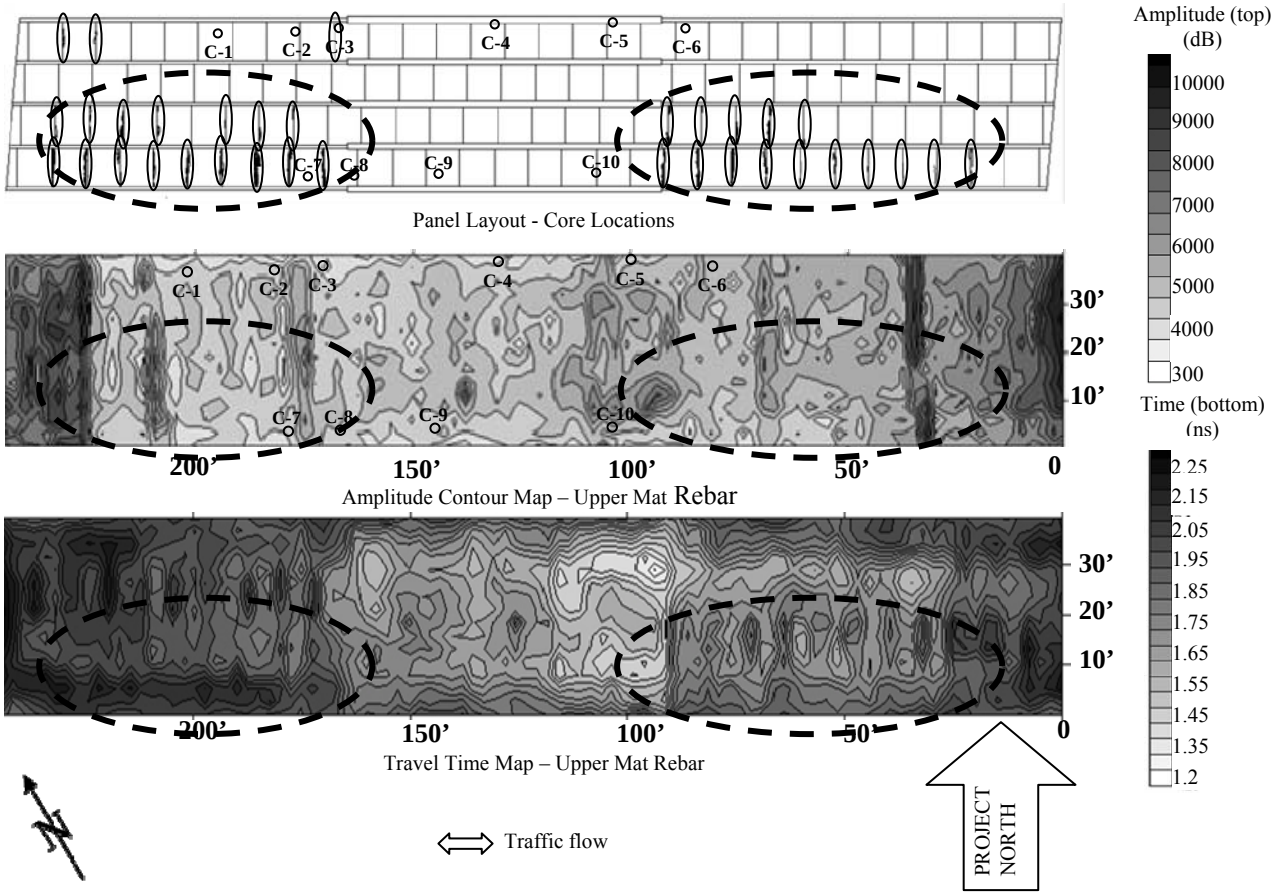

Figure 4-12 Visual Inspection Results and GPR Contour Map Comparison

4.3.7 Cores

Cores were taken from ten different locations in the CIP portion of the bridge deck to serve as ground truth for the GPR data. The GPR data were used to designate the location of the cores shown in Figure 4-12 by identifying anomalous areas in the bridge deck. The presence of both chloride and moisture correlates with rebar corrosion, so the cores were tested for chloride ion content and carbonation. A summary of core data is presented in Table B-4 in Appendix B.

4.3.8 Discussion of Results

As discussed in Section 4.3.1, the following information was needed to achieve the objective of this investigation: 1) reason for differences in deterioration occurring in the PPC panels in various locations of the deck; 2) mechanism by which water and chlorides were progressing through the CIP topping and into the panels; and 3) relative corrosion amongst the tendons within a given panel. The following sections discuss the results in these contexts.

4.3.8.1 Relative Deterioration of Concrete

Visual inspection findings indicated a nonuniform distribution of deterioration occuring in the panels of the bridge decks. Spalling was limited to Panel Lines D and C (Figure 4-7), and more importantly, panels located in the middle of the bridge deck (in the longitudinal direction) had little to no signs of deterioration. GPR and rebound hammer data confirm this relationship as explained below. All data indicate that panels located in the region of the deck with increased longitudinal reinforcement in the CIP slab are less deteriorated, which is likely the result of a lesser amount of chlorides because the additional reinforcement provides improved transverse crack control.

GPR data obtained on the top surface of the bridge deck in both the longitudinal and transverse directions indicated areas of less deterioration in locations similar to those observed in the visual inspection data. Data obtained in the longitudinal GPR scans clearly show an anomaly in the middle of the bridge deck. This anomaly is due to the presence of additional longitudinal reinforcement placed in the CIP topping slab in areas of higher negative moment in the bridge girders. Longitudinal GPR scan results show that the apparent depth of the reinforcement within this anomaly region is less than the apparent depth of the reinforcement outside the anomaly region. Additionally panel joint regions located outside the anomaly show more degradation than the joints located within the anomaly. Based on these observations, longitudinal GPR results indicate that the region with additional CIP reinforcement has less overall degradation.

Lesser degredation of concrete within the anomoly region is confirmed with the GPR scan in the transverse direction. Figure 4-13 shows the variation in apparent reinforcement depths in two scan lines, Lines 45 and 47, in the transverse scan. Line 45 is located just outside the anomoly region, and Line 47 is located just inside the anomoly region. The figure shows a decrease in apparent reinforcement depth as the spacing of the reinforcement decreases. Since the actual depth of reinforcement is the same in both cases, the decrease in apparent reinforcement depths indicates less deteriorated concrete.

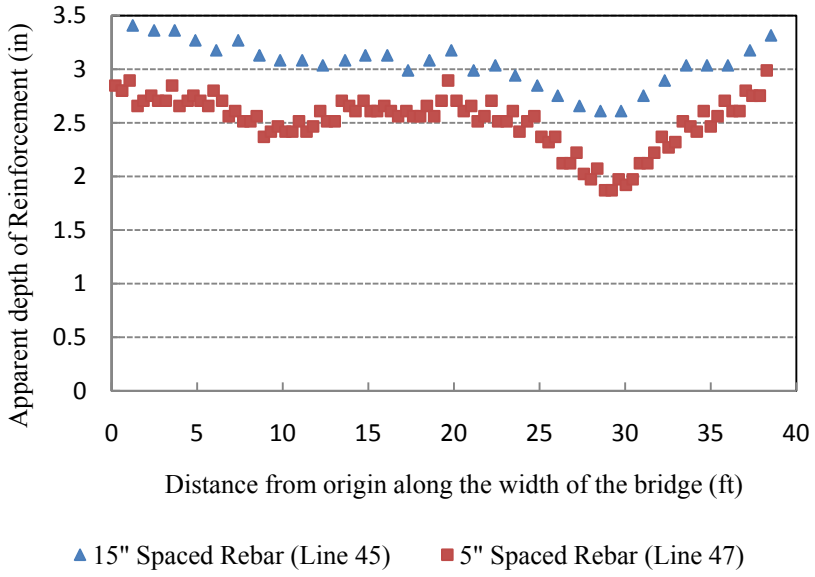

Figure 4-13 Apparent Reinforcement Depth - Transverse GPR Scan Lines 45 and 47

The location of the GPR anomoly (additional reinforcement) was mapped along with the spalling, cracking, efflorescence and water staining visual inspection results. Figure 4-14 shows a portion of the bottom surface of the bridge deck at the transition between 15 in. spaced reinforcement, located on the right side figure, and 5 in. spaced reinforcement, located on the left side of the figure. The CIP reinforcement overlays the panel mapping for visual aid. Note the spalled and waterstained joints in Panel Line D. The area with the closer spaced reinforcement shows less signs of water stains and no spalling or cracking. The locations of spalled and water stained joints clearly show that more deterioration is occurring in areas with decreased reinforcement.

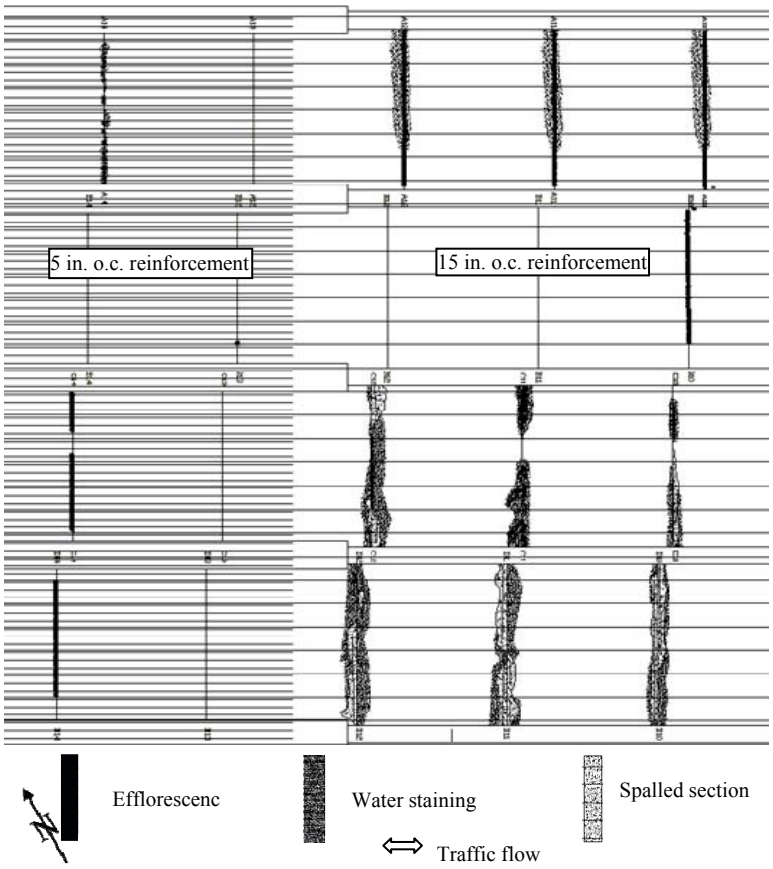

Figure 4-14 Relationship Between Longitudinal Reinforcement Spacing in CIP topping and PPC Panel Deterioration (A. 5 in. spacing, B. 15 in. spacing)

Rebound hammer data also correlated well with overall visual inspection results. The rebound hammer data presented in Table B-3, acquired from a selection of panels with varying degrees of deterioration, can be used to compare relative concrete strengths of the panels. The two lowest average rebound numbers (concrete strengths) were acquired from the panels with the worst cases of spalling located in Panel Line D. Panels with the highest rebound numbers were also located in Panel Line D, the panel line subjected with the worst spalling conditions; however, these readings were taken on panels with little to no signs of degradation. In Table B-3, panels designated by 1's and 2's in their superscripts have cracking and/or spalling at the panel edges. Panels with no superscripts show little sign of deterioration and degradation. It can be seen from the table that panels exhibiting serious deterioration overall had lower concrete strength values.

Two exceptions were panels C12-13 and D12-13. These panels had one seriously deteriorated edge while the other edge showed minimal efflorescence and water staining. These panels were located in the area below the transition between 5 in. spaced reinforcement and 15 in. spaced reinforcement in the CIP topping, which could indicate why one-side-deteriorated panels experienced higher average strengths than most 2-side-deteriorated panels.

4.3.8.2 Delamination Locations

Results from the previous section show that areas of the bridge deck with less reinforcement crossing the transverse reflective cracking in the CIP topping are more prone to panel joint deterioration; however, more information was needed to determine how water and chlorides were progressing through the deck once inside the CIP topping slab. Because delaminations occurring within the bridge deck cross-section cannot be seen during a visual inspection, GPR and core data were used to determine where delaminations were located.

Two contour maps were created from the GPR data to display possible areas of deterioration and delaminations (Figure 4-12). Visual inspection results are also shown in the figure for comparison. Figure 4-12 shows the GPR interpretation of deterioration in the bridge deck through the reinforcement reflection amplitude and signal travel time contour maps versus the visual inspection results from the bottom side of the bridge deck. The circled portions of each diagram correspond to the locations with the worst case of spalling and cracking observed in the panels on the bridge deck. These areas should presumably correspond to the worst delaminating areas in the CIP topping slab because the CIP topping slab is the concrete through which the chlorides are progressing to allow tendon corrosion.

GPR data gathered in the area of the dashed circles located on the east side of the bridge correlates well with the visual inspection data for both contour maps. The amplitude map shows lower areas of reinforcement reflection amplitudes (lighter sections), and the travel time map shows longer travel times (darker sections) in the circled area especially close to the east end of the bridge deck. There is, however, a “strip” of darker area in the reinforcement reflection amplitude map located inside of the circle, indicating less deteriorated concrete. This area is directly over the mid-width of a panel and not near a panel joint. This confirms that most of the deteriorated concrete is concentrated over the panel joints alone, and that there are no additional delaminations occurring between the panel joints in the CIP topping.

GPR data on the west side of the bridge deck show excessively long travel times in the signal travel time map, indicating deterioration, and some areas of lower reinforcement reflection amplitudes in the amplitude map. Again, the amplitude map includes “strips” of relatively high amplitudes. The “sinkhole” areas of longer travel times in the signal travel time map likely correspond to the reflective cracking in the CIP topping over the panel joints observed during the visual inspection. The scan lines in the west portion of the deck appear to have acquired data over the reflective cracking occurring over Panel Lines B and D, and the scan lines acquired in the east portion of the bridge deck appear to have acquired data over the reflective cracking occurring over Panel Line C.

In some areas, such as the area located just west of the eastern circle, the maps complement each other. The amplitude map shows higher amplitudes, and the travel time map shows shorter travel

times, which are both an indication of less deteriorated concrete. In contrast, the two contour maps produce some contradicting results, particularly at the outer ends of the bridge deck. The reinforcement reflection amplitude map shows higher amplitude signals at the ends of the bridge deck indicating less deterioration. The travel time contour map, however, shows longer travel times at these same locations, which is an indication of deterioration assuming the thickness of the concrete and the placement of the reinforcement is the same throughout the entire bridge deck. Varying reinforcement placement and concrete thickness are possible explanations for this discrepancy.

Cores taken from the CIP topping slab were used to correlate GPR findings in terms of delamination locations. Core locations were superimposed on GPR data obtained in the longitudinal scan to compare apparent reinforcement levels and measured chloride ion contents and to obtain more information on delamination locations. Figure 4-15 shows cores obtained in Panel Lines A and D and indicates core chloride ion contents given in Table B-4. Note that cores with higher chloride ion values, cores C-2, C-3, and C-10, were taken in areas that appear to be anomalous sections compared to the other cored areas. A solid line marks the apparent location of the bottom surface of the bridge deck with respect to each core location. Longer travel times or deeper apparent thicknesses are normally indicative of increased deterioration. By comparing the apparent thickness of each core location, a relative comparison of deterioration was obtained. For instance, when comparing the apparent thicknesses at locations of cores C-3 and C-2, C-3 area has an apparent thickness of 10 in. and C-2 has an apparent thickness of 9.7 in. As shown in Table B-4, chloride ion levels in C-3 were higher than levels found in C-2; thus, the GPR data is consistent with chloride ion data found.

In addition, C-2 and C-3 had a smooth bottom surface when extracted from the topping slab. Cores with smooth bottom surfaces were used as a control to determine areas of delamination. These cores were easy to extract from the concrete deck indicating that the CIP and PPC panels had little to no bond between the two surfaces. Furthermore, the depth of core corresponds to the thickness of the CIP topping slab in these locations. Core C-2 had a length of 5.5 in., and core C-3 had a length of 6.125 in. The apparent thickness at the location of core C-3 should appear thicker because the bridge deck is thicker in that area. For these cores, the information obtained from the GPR data was consistent; however, because the apparent thickness of the slab changed with an increase in chloride ion content of the concrete, these data do not prove that GPR can accurately detect increasing chloride ion contents.

The shortest smooth bottom core obtained was 5.5 in. long, which is the specified thickness according to the construction documents. The longest smooth bottom core obtained was 6.5 in. long, while the longest broken bottom core obtained was 7.125 in. long. Core C-9 was 7 in. long with a broken bottom. This gives evidence that the bridge deck varies in total thickness from 8.5 in. to at least 10.125 in. In addition, core lengths appeared to increase toward the middle of the bridge deck. Variations of thicknesses in the CIP topping may have been used to achieve a level bridge deck or to create a crown in the bridge deck cross-section.

GPR data obtained in the longitudinal direction from the top and bottom surface of the bridge decks were also correlated with findings from core C-7. The location of core C-7 with respect to the GPR data is shown in Figure 4-10 from the upper and lower deck views. This core had a

smooth bottom surface and included reinforcement. The depth of the reinforcement and core were mapped on the GPR data obtained from the top of the bridge deck. This core, taken in the middle of a spalled panel, contained a measured chloride ion content suggesting corrosion was not probable in the CIP portion of the bridge deck; however, some delamination was most likely occurring in the area because of the smooth bottom surface of the core. Figure 4-10A shows GPR data acquired from the top surface, and Figure 4-10B shows GPR data acquired from the bottom surface of the bridge deck in this region. Apparent depth of reinforcement and slab thickness shown on the GPR data obtained on the top surface of the bridge deck correlates well with the core data, which indicates little to no delaminations; however, little information pertaining to the cross-section of the bridge deck could be obtained from the bottom surface GPR data due to the close spacing of the tendons (4 in. spacing).

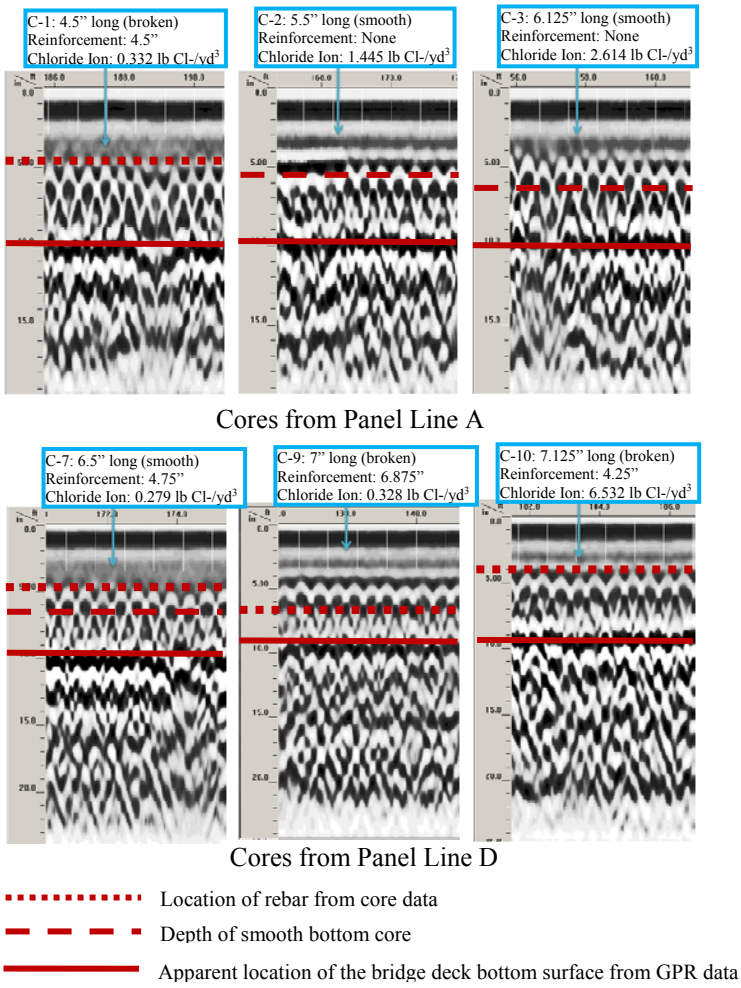

Figure 4-15 Core Comparison

For additional comparison, each core was plotted on the amplitude contour map. Figure 4-12 shows the locations of the cores with respect to the amplitude contour map created from the transverse scan GPR data. The amplitude values for each core location were then compared with the amplitude values with the highest chloride ion content found in each core (Figure 4-16). GPR data yielded results that did not always correlate with the chloride ion values measured in each

core. For example, core C-10 had the highest chloride ion value, but was not in an area of the lowest amplitude. Core C-10, taken directly over a reflective crack in the CIP topping, is a spot measurement, and the crack would allow more chlorides to ingress into the concrete at that spot. GPR data, however, indicates the concrete integrity in a given area and the concrete area around core C-10 may be very sound.

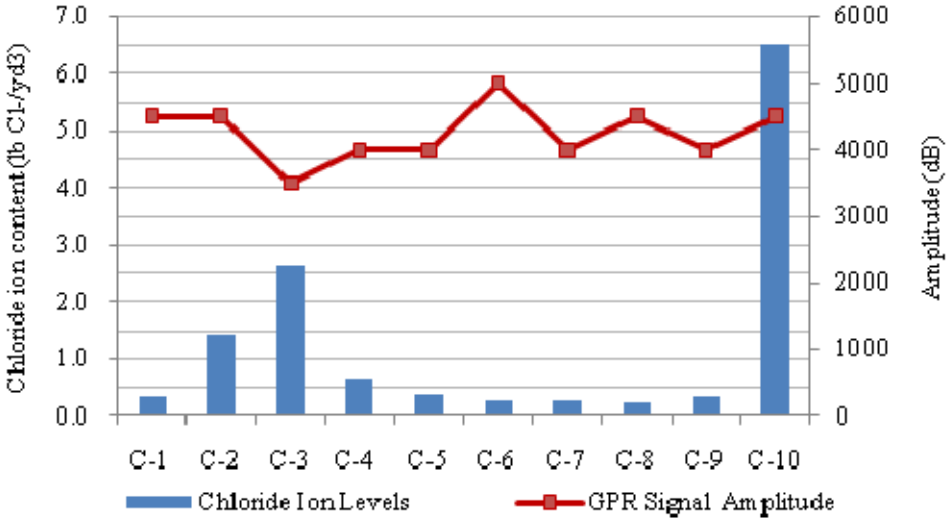

Figure 4-16 Chloride Ion Levels of Each Core Versus the Amplitude Measurement of Each Core

A closer look at C-10 on the GPR data obtained in the longitudinal scan provided better correlation to the core data. Core C-10 exhibited the worst deterioration in the concrete because it was taken from the concrete directly over a panel joint. As expected, the chloride ion content was higher in this core relative to the others. The panel joint at the location of core C-10 had no spalling and minimal water stains, but the GPR data in the longitudinal scan indicated some degradation. Figure 4-17 shows the screen shot at the location of core C-10. As indicated in the figure, there is slight degradation, change in anomaly depths, at this location. This shows that GPR can locate areas of degradation before spalling occurs. The correlation between core and GPR data also shows that GPR can accurately locate areas of delamination.

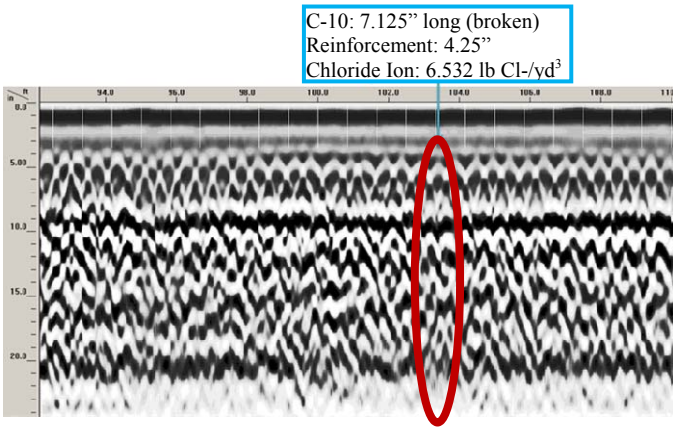

Figure 4-17 Screen Shot of Core C-10 in GPR Data Obtained in the Longitudinal Scan

4.3.8.3 Relative Deterioration of PPC Panel Reinforcement

Visual inspection results indicated discoloration lines in the middle of various panels in all of the bridge decks observed. These lines varied in color from gray to a rust brown. Rust stains could indicate corrosion is occurring in the prestressing strands and that the rust is permeating through the concrete to be visible on the bottom surface of the panel; however, rust would also create an increase in stresses in the concrete and cause cracking. Similar discoloration lines were reported in an Iowa study described in Section 3.2, which were thought to be initial corrosion of the prestressing strands initiated by moisture penetrating through the hairline cracking observed along the bottom side of the panels. Iowa panels were 2.5 in. thick.

As mentioned in Section 4.3.2, the only cracking occurring in the panels was observed at the panel joint locations. In the previous section it was shown that locations of delaminations were occurring in the CIP topping slab mostly in the reflective cracking locations. Further investigation on relative tendon deterioration was performed to determine if chlorides were accessing the middle tendons as well as the outer tendons on each panel.

As mentioned in Section 4.3.3, half-cell and resistivity testing were conducted to determine the corrosion rates of the prestressing tendons as well as correlate GPR data. Results indicate that corrosion was indeed occurring in the tendons located nearest to the panel joints and either partially or fully exposed in many places. The resistivity results, however, indicated that there were no suitable combinations of porosity, permeability, moisture content and salinity in any of the panels except one to indicate corrosion was a possibility in the middle of the panels.

GPR data were obtained on the bottom surface of the bridge deck in an attempt to determine the relative condition of the prestressing tendons. Unfortunately, because of the apparatus used and difficulty in maneuvering in the lifts, the antenna was not always directly coupled to the surface of the panel resulting in changes of the angle of the antenna with respect to the panel. As a result, much of the data obtained was unusable in comparing relative panel-to-panel deterioration, but the general relationship of the data proved useful. Through the use of the reinforcement reflection-picking tool in RADAN, the amplitude of each tendon reflection was acquired for all panels selected for the GPR data acquisition located in Panel Line D, which exhibited the worst case of spalling. Figure 4-18 shows the average amplitudes recorded for each tendon reflection acquired on selected panels. As shown in the graph, many of the panels had varying amplitudes, but most had the general relationship of lower amplitudes at the panel ends, near the joints, and higher amplitudes in the middle of the panels. Data were often not available at the edges of the panels due to how the wheel was configured. Lower amplitudes at the joints indicate that more deterioration is occurring in tendons at the edges than within the middle of the panels.

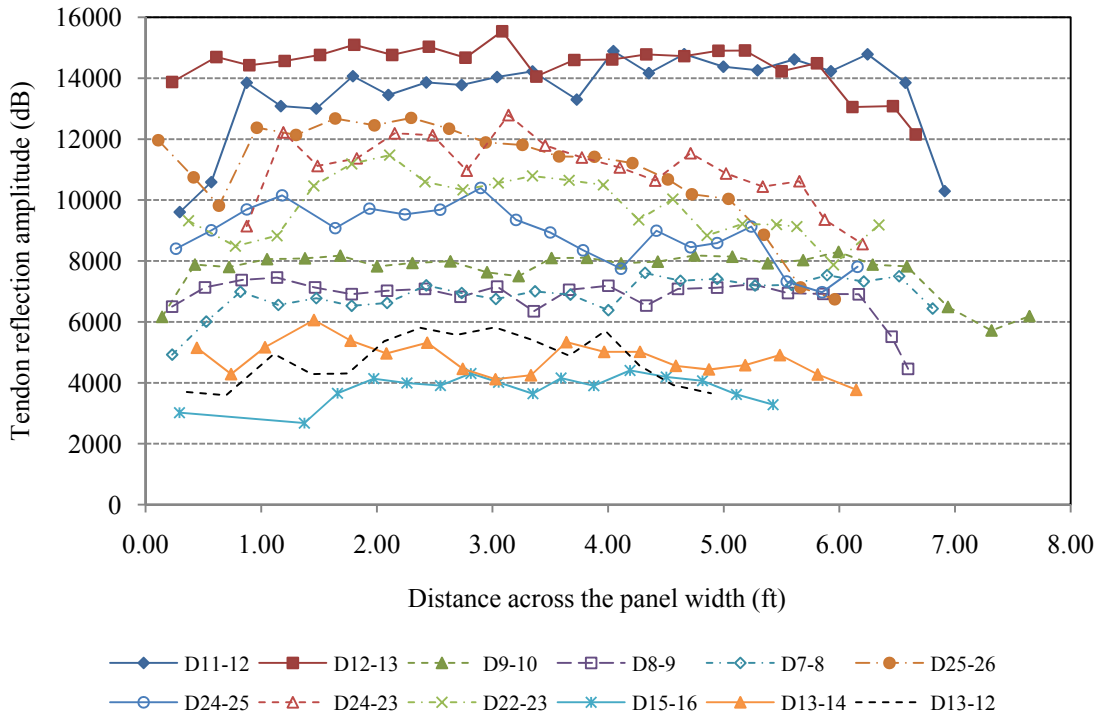

Figure 4-18 Average Tendon Reflection Amplitudes on Panels Located in Panel Line D

All of the panels shown in Figure 4-18 have discoloration lines on the bottom surface, so an additional plot of tendon reflection amplitude data from panels in Panel Line C is shown in Figure 4-19. Dotted lines were used to connect the data points acquired on panels without the discoloration lines (Panels C5-6 and C13-12), and solid lines were used to connect the data points acquired on panels with discoloration lines (Panels C7-8 and C9-10). The figure shows similar relationships between plots of data acquired from panels with the discoloration lines and the panels without the lines. This indicates that no additional corrosion is occurring in panels with the discoloration lines; therefore, there is no evidence supporting the assumption that the discoloration lines are indicative of corrosion occurring in the tendons.

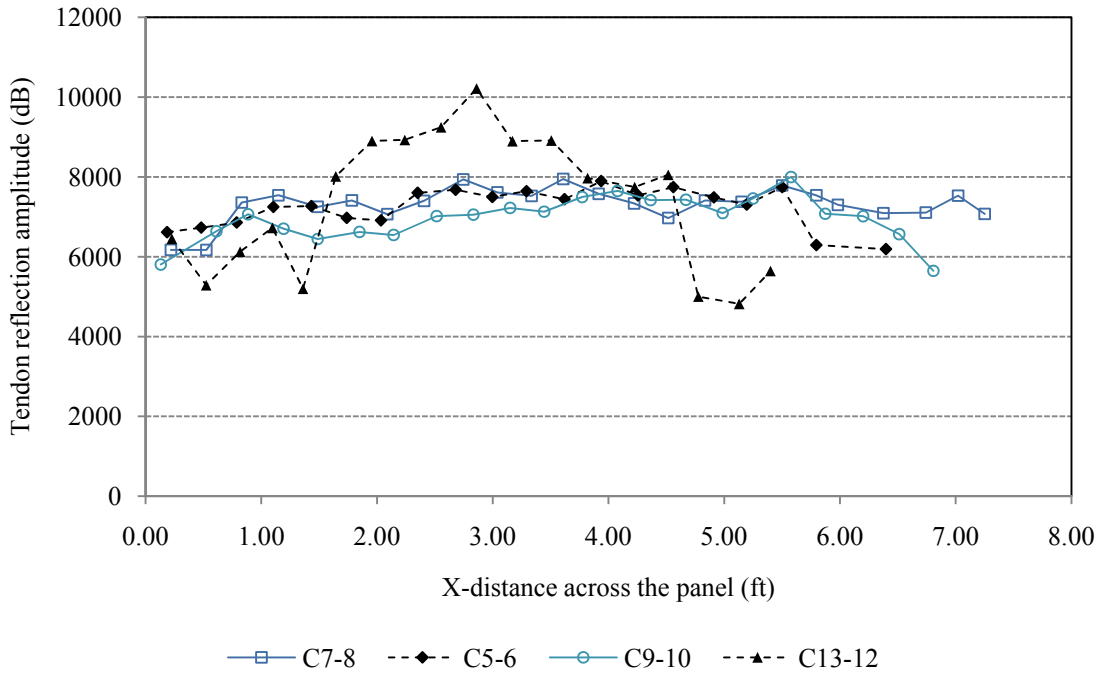

Figure 4-19 Average Tendon Reflection Amplitudes on Panels Located in Panel Line C

4.4 Bridges A4067 and A4705

Follow-up investigations were conducted on Bridges A4067 and A4075 with the objective of correlating findings from the Bridge A4709 investigation described in Section 4.3 regarding the significance of additional negative moment reinforcement in CIP topping in the negative moment regions of the deck. As discussed in Section 4.3, results showed less deterioration occurred in panels located under this additional reinforcement. Because Bridge A4709 has only 2 spans, additional bridges with more than 2 spans were selected for this investigation with the expectation that more deterioration would be seen in the areas without the additional reinforcement in multiple locations of the bridge deck.

Bridge A4067, constructed in 1986, serves as an over pass to MO-141 and consists of three spans. Bridge A4705, constructed in 1990, serves as an over pass to Route 40/I-64 and consists of four spans. Both bridges use partial-depth PPC panels as structural stay-in-place formwork for a 5.5 in. CIP topping. A panel thickness of 3.5 inches is specified for Bridge A4067, and a panel thickness of 3 in. is specified in the drawings for Bridge A4705. Panels in each bridge deck are reinforced with 3/8 in. prestressing strands spaced at 4.5 in. Long span steel plate girders support each bridge deck. The upper mat of reinforcement in the CIP topping changes from a 15 in. spacing in the positive moment regions of the bridge deck to a 5 in. spacing in the negative moment regions of the bridge deck. St. Louis received approximately 1 in. of rainfall the week preceding the bridge investigations.

The objective of the bridge investigation was accomplished by viewing as many panels as possible from behind the guardrail or from one lane closure. These positions allowed a clear viewing of all of the panels within 50 feet of each pier. Figure 4-20 shows the panel layout of Bridge A4067 with the labeling rubric used for the investigation. Figure 4-21 shows the panel

layout for Bridge A4705. The figures also highlight locations of additional reinforcement in the CIP bridge deck topping as specified in the bridge drawings. Span length dimensions as well as lengths of areas with extra reinforcement are also shown. Due to the limited number of spalled panel joints observed, joints with water staining deterioration were dually observed and recorded. on each of the figures. Observed spalled joints are circled, and water stained joints are marked with a dotted line. Only two spalled panel joints were identified in Bridge A4067 and three in Bridge A4705. No spalled or water stained joints were observed in panel joints located under the areas containing the additional negative moment reinforcement in the CIP topping.

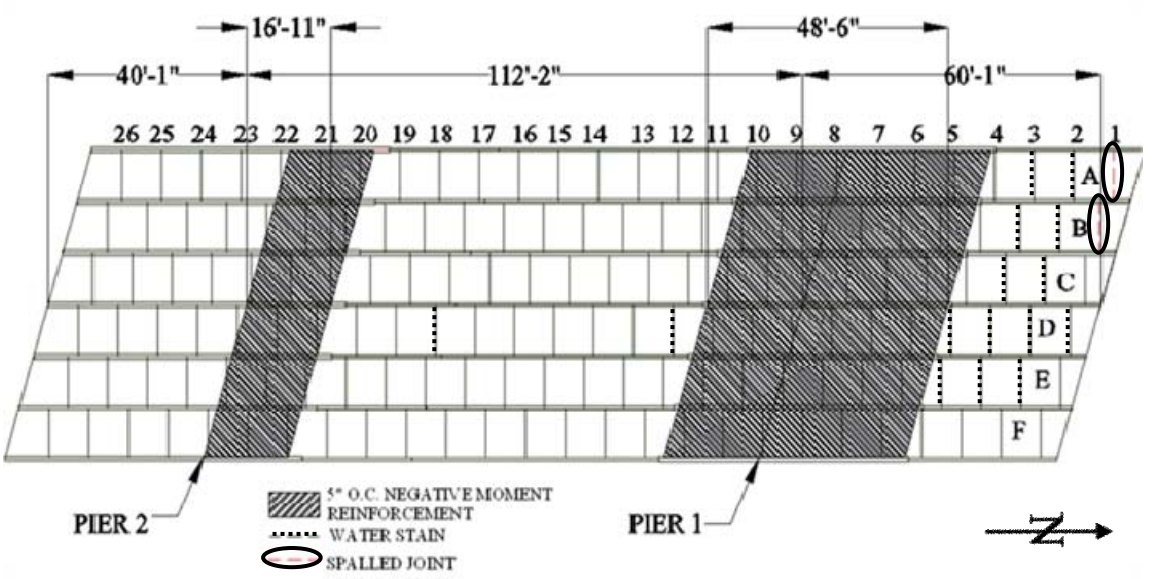

Figure 4-20 Visual Inspection Results for Bridge A4067

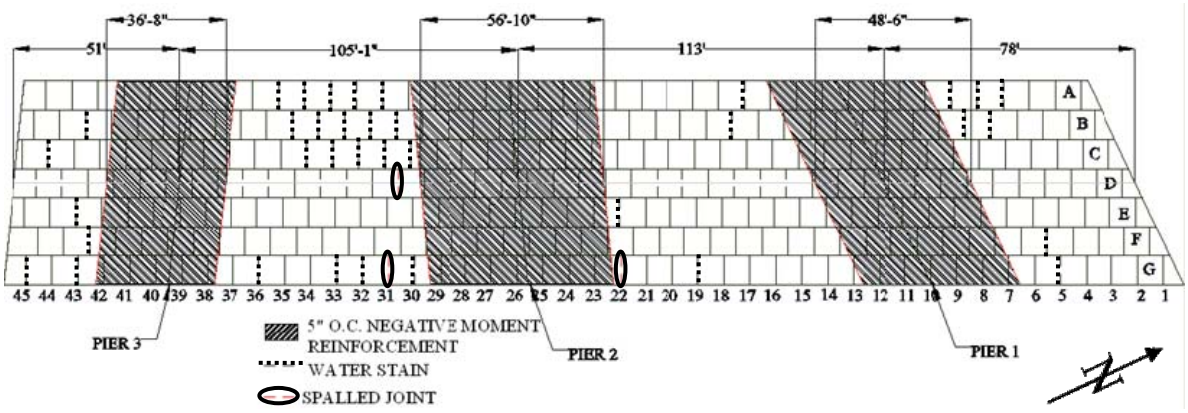

Figure 4-21 Visual Inspection Results for Bridge A4705

Figure 4-22 shows the worst case spalling found in Bridge A4067. The outermost tendon is completely ruptured, and several sections of rebar are fully exposed. The worst deterioration on this bridge deck occurred at the edge of the west abutment. The bridge deck slopes downward from west to east at a grade of -5.00%. Given this slope, it is logical to conclude that the excess deterioration is not caused by the ponding of water in this area.

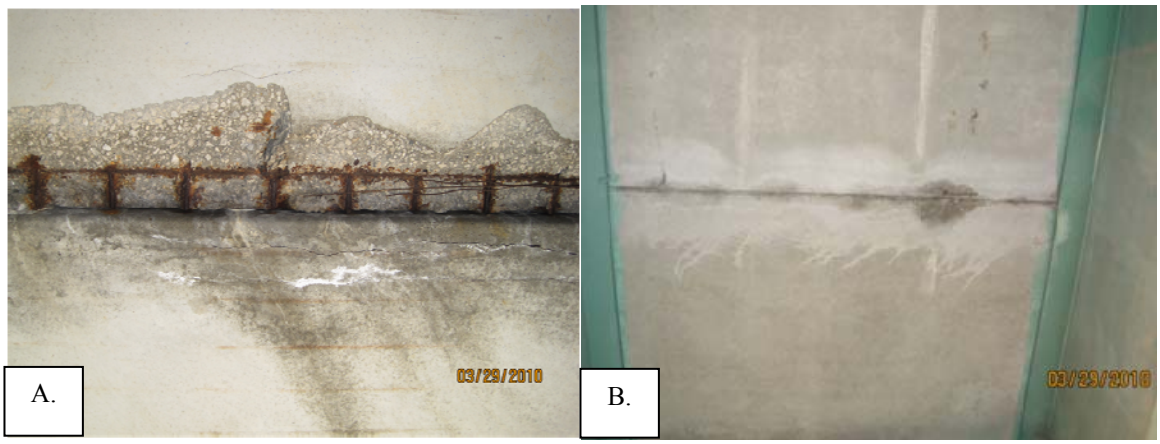

Figure 4-22: Images of Bridge Deterioration from St. Louis Bridge Investigations (A. Worst case spalling found in Bridge A4067, B. Panel joint experiencing waterstaining and efflorescence in Bridge A4705)

4.5 Summary and Key Observations

The objective of the field investigations was to determine from physical evidence the nature and mechanism of spalling observed in partial-depth PPC bridge decks. Based on the results from the investigations described in Section 4.2-4.4, the following conclusions are made:

- Spalling observed in the PPC panels is the result of the penetration of water and chlorides through the transverse reflective cracking in the CIP topping, to the interface between the CIP topping and the PPC panels, then through the PPC panels to the prestressing tendons located near the panel joints.
- Visual inspection results from the bottom surface of the A4079 bridge deck indicated an uneven distribution of deterioration in the bridge deck panels. GPR and rebound hammer results indicate that panels located under the area with increased negative moment reinforcement (i.e. girder interior supports) were less deteriorated. Further investigation of Bridges A4067 and A4705 confirmed this relationship. Thus, increased longitudinal CIP reinforcement, which serves as transverse crack control, was found to be significant in increasing the concrete integrity and delaying the onset of spalling at the panel joints.
- Reflective cracking over the panel joints allows water and chlorides entrance into and, in many cases, through the CIP topping. GPR results showed most deterioration in Bridge A4709 is occurring near the area of reflective cracking in the CIP topping and not in the area of concrete over the middle of the panels.
- Smooth bottom cores, acquired at various locations along the panels in Bridge A4709 indicate that some delamination has occurred at the interface between the CIP topping and PPC panels, particularly at panel joint locations, despite the roughened PPC panel surface.
- Acquiring GPR data from the bottom surface of the bridge deck was a labor intensive and time-consuming technique. Unfortunately, the data acquired from the bottom surface of the bridge deck was not helpful in terms of determining areas of delaminations, and the close spacing of the prestressing tendons made it difficult for the electromagnetic energy to navigate to the rest of the bridge deck. These data were, however, helpful in evaluating relative tendon deterioration.

- Discoloration lines observed across the middle of the panels during the visual inspection of the underside of the bridge decks initially appeared to be rust stains caused by the rusting of the middle tendons and the permeation of the rust through the prestressed concrete panel. High resistivity readings obtained from the panel concrete indicates a very low possibility of corrosion. In addition, GPR data obtained from the bottom side of the bridge deck showed that prestressing tendons located in the middle of the panels were less degraded than the outer most tendons. As a result, the field investigations yielded no evidence to indicate that discoloration lines are caused by corroding tendons.

5 EXPERIMENTS

5.1 Overview

This chapter discusses the results of physical experiments conducted to identify and examine potential spalling mitigation solutions. The structural performance of proposed panel types was investigated by testing 12 full-size panels subjected to static and dynamic loadings described in Section 5.2. Durability experiments summarized in Section 5.3 aimed to investigate the environmental effects of parameters suspected of influencing the spalling problem. Key results are summarized in Sections 5.2.4.3 and 5.3.5.

5.1.1 Systems Studied Through Experimental Approaches

As discussed in Section 1.3, five proposed systems in Table 5-1 were selected for further investigation (Systems 1, 2, 3, 4, and 6). Of these, Systems 1, 2, 3, and 6 were examined through experimental approaches with respect to durability and structural performance (Numerical analysis of these systems is discussed in Chapter 6).

Table 5-1 Systems Proposed

Proposed System	Test Approach
1. Increase side cover of prestressing tendons	O, Δ
2. Use enhanced concrete using FRC	O
3. Use corrosion-free concrete using corrosion inhibitor	O
4. Enhance the reinforcement in CIP topping concrete deck	Δ
5. Substitute CFRP or epoxy-coated tendons for all steel tendons	X
6. Substitute 2 CFRP or epoxy-coated tendons for 2 steel tendons each edge	O
7. Use re-shaped panel	X
8. Add surface protection	X

* O : Examine Experimentally, Δ : Examine analytically, X : Disregard

5.1.2 Test Objectives and Methodology

The objective of the experiments was to study the structural behavior and durability characteristics of the systems discussed in Section 5.1.1 with respect to the current design specified by MoDOT. To achieve this objective, two types of experiments were conducted in this study: structural behavior of full-scale unit panel specimens, and durability characteristics of small-scale specimens. The experiment types are illustrated in Table 5-2. Detailed information on the unit panel experiments and durability experiments is presented in Sections 5.2 and 5.3, respectively.

Table 5-2 Experiment Types

Test Type	Specimen Type	Purpose	Parameters
Structural Behavior	Unit panels	Investigate structural behavior of SIP panels with alternative materials	▪ Addition of fibers to concrete mixture (FRC) ▪ Substitution of epoxy-coated steel tendons for steel tendons (2 each end) ▪ Substitution of CFRP tendons for steel tendons (2 each end)
Durability	Small-scale specimens	Investigate the effects of considered parameters for mitigating spalling problem	▪ Contents of NaCl ▪ Fiber reinforced concrete (FRC) ▪ Admixture (Corrosion inhibitors) ▪ Various side cover ▪ Existence of prestressing force in tendon ▪ Size effect ▪ Environmental conditions

5.2 Unit Panel Experiments

5.2.1 Introduction

This section presents and discusses the key test results of the unit panel experiments. Detailed information about the mechanical properties of the materials used, test specimens, test procedure, and results of each test specimen are presented in Appendix C.

As presented in Table 5-2, the purpose of the unit panel experiments is to investigate the structural behavior of SIP panels with different materials than those currently specified by MoDOT. Proposed Systems 2, 5, and 6 from Table 5-1 modify the existing SIP panel by including the use of fibers in the concrete mixture, or substituting either epoxy-coated steel tendons or CFRP tendons for the steel tendons at the panel edges, respectively. These experiments aim to study the structural response, at both service and ultimate states, due to these modifications. Due to the nature of the loading of the SIP panels in service, both static and fatigue response was explored. Testing of fatigue response was important to study stiffness degradation and structural behavior in response to cyclic loading that is representative of the transient live load experienced by bridges due to traffic flow.

The unit panel test matrix includes a total number of 12 unit panels as shown in Table 5-3. Parameters tested were edge tendon type, concrete mixture type, and loading type. A three-term notation system is used to identify the variables of each test specimen. The first term refers to the edge tendon type: steel, epoxy-coated steel, or CFRP tendons. The second term indicates the concrete type: normal or fiber reinforced concrete. The third term is the loading type: static or fatigue loading. The design of Panels ST-NC-SL and ST-NC-FL is consistent with the panels currently specified by MoDOT. Thus Panels ST-NC-SL and ST-NC-FL were the control specimens for the static and fatigue loading tests, respectively.

Table 5-3 Unit Panel Experiments Test Matrix

Test Specimen	Edge Tendon Type			Concrete Type		Loading Type	
	Steel	Epoxy-coated Steel	CFRP	Normal	FRC	Static	Fatigue
ST-NC-SL	O			O		O	
ST-FRC-SL	O				O	O	
ECST-NC-SL		O		O		O	
ECST-FRC-SL		O			O	O	
CFRPT-NC-SL			O	O		O	
CFRPT-FRC-SL			O		O	O	
ST-NC-FL	O			O			O
ST-FRC-FL	O				O		O
ECST-NC-FL		O		O			O
ECST-FRC-FL		O			O		O
CFRPT-NC-FL			O	O			O
CFRPT-FRC-FL			O		O		O

5.2.2 Test Specimens

5.2.2.1 Specimen Design

12 full-scale unit panels were designed according to current MoDOT specifications (2004).

5.2.2.2 Dimensions and Material Properties

Specimen dimensions and material properties are summarized in Table 5-4. Detailed information is provided in Appendix C.

Table 5-4 Unit Panel Dimensions and Material Properties Summary

Test Specimen	Width (in.)	Length (in.)	Height (in.)	Tendon Spacing (in.)	f_c (psi)	Tendon f_y		Tendon f_u		
						ST (psi)	ECT (psi)	ST (psi)	ECT (psi)	CFRPT (psi)
ST-NC-SL	996	96	3	4.5	6,360	252,000	-	274,000	-	-
ST-FRC-SL	996	96	3	4.5	5,580	252,000	-	274,000	-	-
ECST-NC-SL	996	96	3	4.5	5,900	260,000	273,000	279,000	290,000	-
ECST-FRC-SL	996	96	3	4.5	6,460	260,000	273,000	279,000	290,000	-
CFRPT-NC-SL	996	96	3	4.5	7,000	260,000	-	279,000	-	
CFRPT-FRC-SL	996	96	3	4.5	6,390	260,000	-	279,000	-	
ST-NC-FL	996	96	3	4.5	6,380	252,000	-	274,000	-	-
ST-FRC-FL	996	96	3	4.5	7,710	252,000	-	274,000	-	-
ECST-NC-FL	996	96	3	4.5	6,200	260,000	273,000	279,000	290,000	-
ECST-FRC-FL	996	96	3	4.5	7,600	260,000	273,000	279,000	290,000	-
CFRPT-NC-FL	996	96	3	4.5	6,040	260,000	-	279,000	-	
CFRPT-FRC-FL	996	96	3	4.5	6,080	260,000	-	279000	-	

5.2.3 Test Procedure

5.2.3.1 Test Setup

Unit panel specimens were subjected to a distributed line load on simply supported boundary conditions to investigate the flexural capacity as shown in Figure 5-1. Because the predominant internal force in the panel in service is bending moment, testing the punching shear capacity of the proposed panels was not considered in this study. It should be noted, however, that panels can be subjected to such loading conditions during the construction stage. The results of these tests are intended to provide information on the strength, serviceability, and behavior of the different panel types under static and fatigue loads.

The test setup was designed for the system to be stable during both static and fatigue loading. Supports consisted of two W12×96 structural steel beams connected to one another by steel straps that were connected to the ground floor by prestressed Dywidag bars. Specimens were supported on two 6 in. wide continuous steel plates that were supported on continuous steel rods. One support plate was welded to the rod to simulate a pin support, while the other support plate merely rested on the rod so that the rod was free to move laterally to simulate a roller support.

5.2.3.2 Instrumentation

To investigate global and local behavior of the unit panel, each specimen was instrumented with a combination of sensors used to measure force, displacement, and strain at key locations. The applied load was measured by a load cell within the hydraulic actuator. Displacement and strain were measured by sensors described in the following paragraphs. All devices were connected to a data acquisition system controlled by a personal computer.

Displacement

Displacement was measured at nine locations on each panel. Displacement measurements were acquired by eight DC voltage transformers (DCVTs) and one additional linear variable differential transformer (LVDT) within the actuator at locations shown in Figure 5-2 to measure the displacement of the panel. Since the panel is symmetric, measurements were taken over half the panel (right side of Figure 5-2). The right side of the panel was instrumented to avoid congestion with the concrete surface gage locations described in the next section. Grids E and F correspond to locations where strain gages are also attached to the prestressing tendons described in the next section, while Grid E' has no strain gages. The DCVTs were attached to the top surface of the panel due to space limitations beneath the panel.

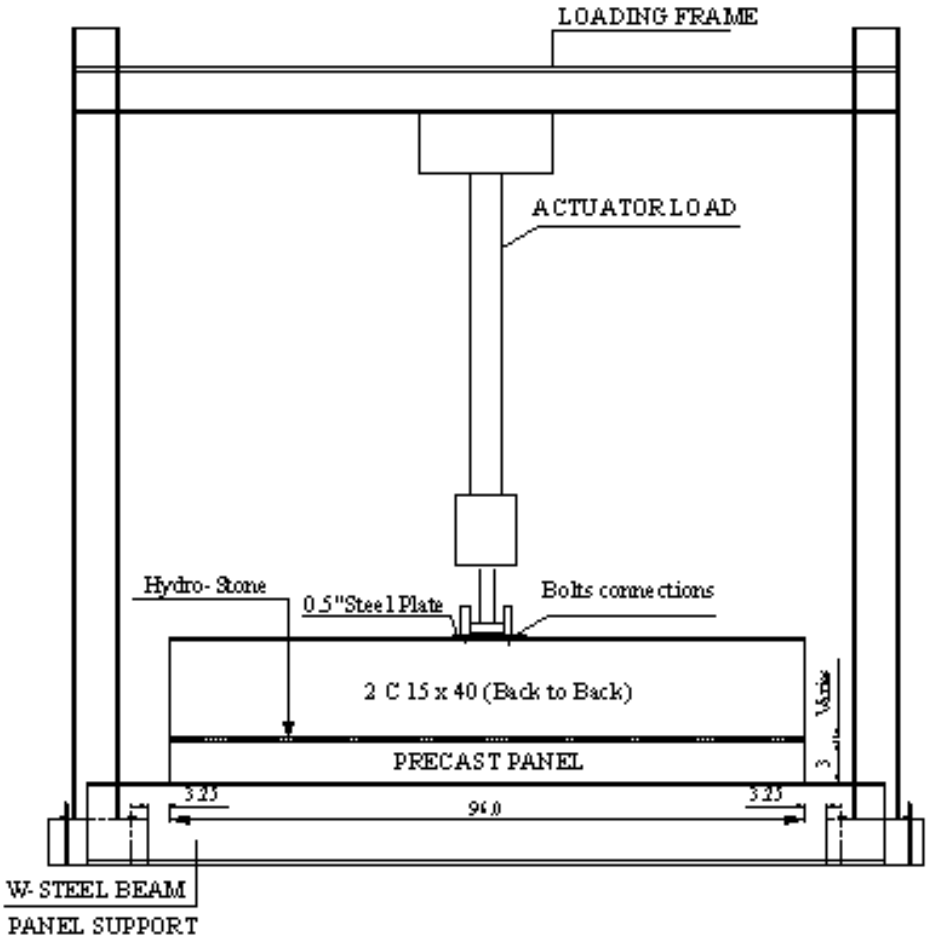

LONGITUDINAL CROSS SECTION THROUGH TEST SETUP
Dimensions in inches

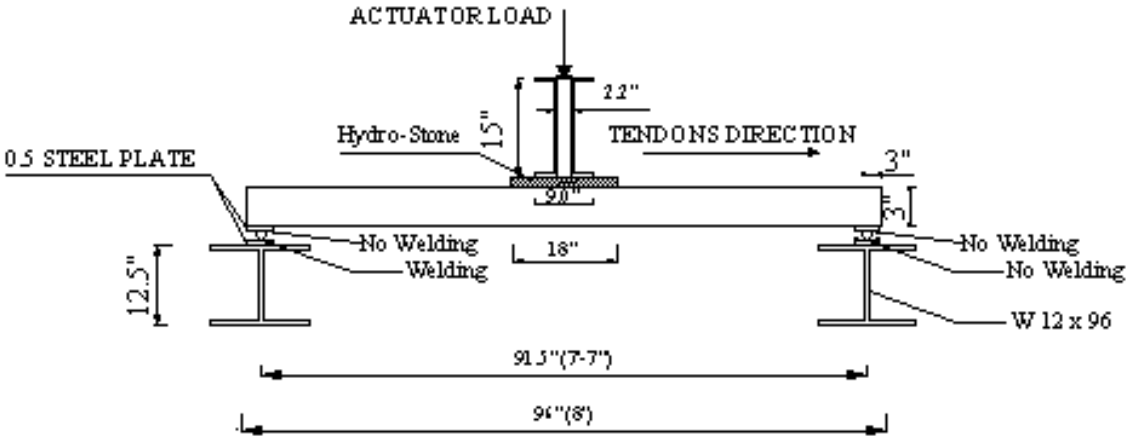

TRANSVERSE CROSS SECTION THROUGH TEST SETUP

Figure 5-1 Test Set-Up for Unit Panel Test

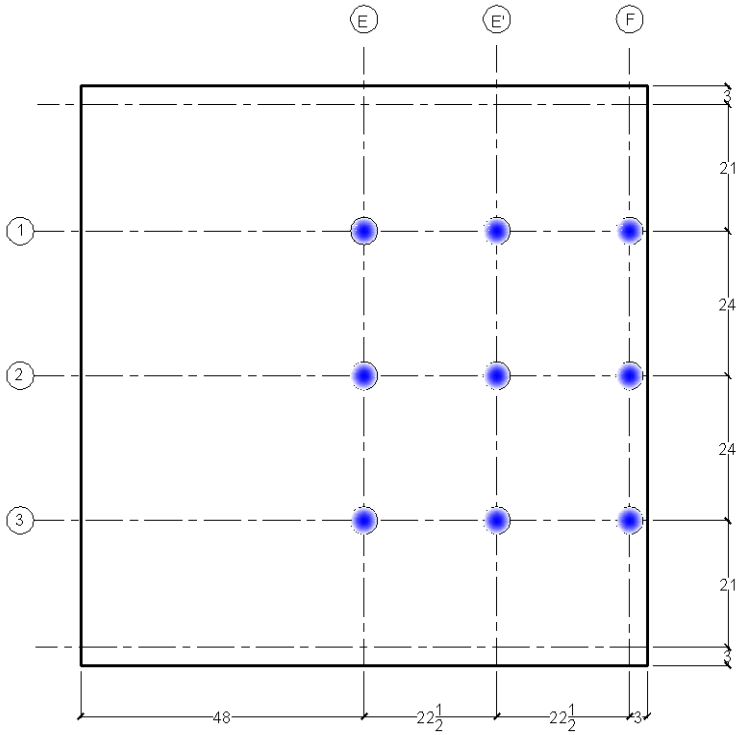

Note: dimensions are in inches
Figure 5-2 Displacement Instrumentation Layout

Strain Gages

Eighteen uniaxial electric resistance strain gages were applied to the prestressing tendons at various locations of each panel as shown in Figure 5-3. Locations correspond to one-half and one quarter of the panel length in the span direction. Strain was measured at different locations along the span length to observe the difference in strain as a function of moment along the span. As mentioned in Section 2.1.2.4, transfer and development length in the prestressed panel is an important issue because it effects the tensile stress distribution along tendons. Thus, distribution of strain gages along the tendon was designed to observe this issue. Use of different prestressing materials at the panel ends is a key parameter in the unit panel experiments requiring detailed observation. Thus, several different tendons were instrumented to observe variations in strain between different prestressing materials. As shown in Figure 5-3, Grids A, B, and F correspond to edge tendons that are steel, epoxy-coated steel, or CFRP depending on the specimen. Grids C, D, and E are steel tendons. Grid E also corresponds to the panel mid-width.

A total of 18 uniaxial electric resistance strain gages were also applied at both the top and bottom surfaces of the concrete along the Grids A, D, and E as shown in Figure 5-3. Locations of the concrete surface gages correspond to the locations of the strain gages on the tendons as discussed in the previous paragraph so that the strain profile could be determined at these locations.

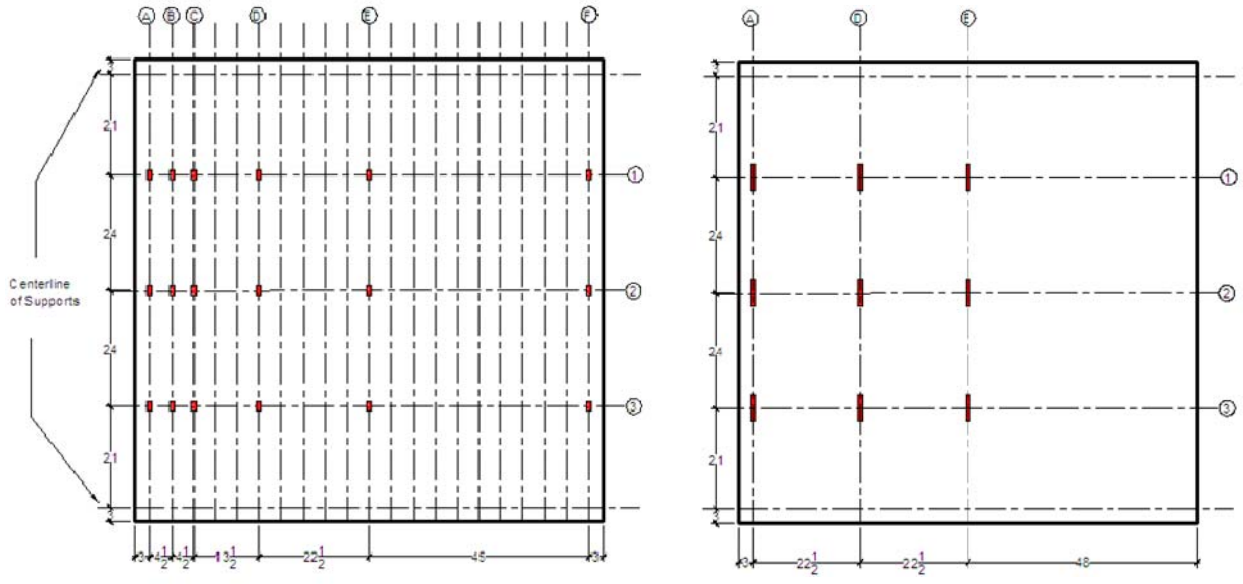

Tendon Strain Gage Layout Concrete Surface Strain Gage Layout

Note: dimensions are in inches

Figure 5-3 Strain Gage Layout

5.2.3.3 Loading Protocol

The load was applied by a single fatigue-rated hydraulic actuator (MTS 244.41) with a capacity of 110 kips located at midspan that was suspended on the loading frame (Figure 5-1). A 2C15×40 back-to-back steel spreader beam was attached to the actuator and was used to distribute the load across the panel width. The footprint of the spreader beam was approximately 18 in. (corresponding to the width of loading), and the length was longer than the width of the panel specimen. The spreader beam was secured to the test specimens with a 0.5-1.0 in. continuous layer of Hydrostone cast in place between the spreader beam and the specimen to increase the uniformity of the loading and to level the spreader beam on the panel surface. The weight of the spreader beam was 1.85 kips. This weight, in addition to the self-weight of the specimens, was applied to the specimens but was not registered by the load cell.

Static load test specimens were loaded under displacement control. Displacement was increased by 0.05 in. at each load step until failure. The loading process was temporarily paused and held constant at different load intervals to observe cracks and take photographs during testing.

Fatigue load test specimens were loaded under displacement control. The target displacement range was determined based on a target load range of 2-12 kips. The maximum load (and corresponding displacement) corresponds to the service dead and live load on the panel, which was taken as 60% of the average maximum load for all panels based on results of the static load tests described in Section 5.2.4.1. This load range corresponds to approximately 0.05 in. and 0.25 in. displacement based on results from the static load tests. The minimum load (and corresponding displacement) selected corresponds to self-weight of the CIP concrete topping with zero live load. The maximum load (and corresponding displacement) is less than the cracking load and displacement based on results of the static load tests; thus, macro cracking was

not expected to occur. Prior fatigue testing, the panel was tested under displacement control to a displacement of 0.25 in. to provide a baseline to evaluate stiffness degradation. Two million load cycles were applied to each panel at 4 Hz. Testing was paused after each 500,000 cycles to perform a quasi-static load test up to 0.25 in. displacement. After 2,000,000 cycles were completed, panels were tested to failure under quasi-static load. Quasi-static test protocol was the same as the static test protocal.

5.2.4 Test Results

5.2.4.1 Static Load Tests

This section summarizes the overall results for the six static load test specimens in terms of failure mode, cracking behavior, load-displacement response, and load strain-response. Detailed results for each panel are included in Appendix C.

5.2.4.1.1 Cracking Behavior and Failure Mode

During testing of all panels, flexural cracks first developed on the extreme tension face, which increased in length and number with increasing applied load. All six panels failed by concrete crushing in the compression zone (the top surface of the panel) as the failure crack penetrated the flexural compression zone. The typical failure mode is shown in Figure 5-4. No tendons were yielding at the maximum load. First cracking and maximum loads and the respective displacements for each panel are listed in Table 5-5.

Due to the nature of the test setup, the bottom surface of the test specimens was not visible during testing. Thus, cracks were observed and marked on the two side surfaces during testing. The cracking loads reported in Table 5-5 were determined by the change in load-displacement and load-strain behavior as discussed in Sections 5.2.4.1.2 and 5.2.4.1.3. The cracking load for all panels was ranged from 13.79 kips to 14.99 kips, and the cracking displacement was 0.35 in. for all panels. Cracks were visible on the side surfaces at load and displacement levels slightly higher than these values. The initial cracks were flexural cracks that appeared beneath the spreader beam location. As the applied displacement (and resulting applied load) was increased, additional flexural cracks appeared and existing cracks propagated upward. At the maximum load, the cracks near the edge of the loading zone propagated through the entire thickness of the panel penetrating the flexural compression zone. At failure, Panel CFRPT-NC-SL had the most cracks observed while Panel ECST-NC-SL had the fewest cracks of the six panels. Crack patterns for each specimen are shown in included in Figure 5-5 and Appendix C (Note that crack patterns were not available for Panel ST-NC-SL and are not shown).

Table 5-5 Summary of Applied Load and Displacement at Cracking and Failure – Static Load Panels

Test Specimen	Cracking Load (kips)	Cracking Displacement at Midspan (in.)	Maximum Load (kips)	Displacement Corresponding to Maximum Load at Midspan (in.)
ST-NC-SL	13.92	0.35	22.08	2.14
ST-FRC-SL	13.79	0.35	20.25	1.65
ECST-NC-SL	14.19	0.35	18.49	1.05
ECST-FRC-SL	14.25	0.35	21.10	1.70
CFRPT-NC-SL	14.99	0.35	21.05	1.35
CFRPT-FRC-SL	14.06	0.35	20.70	1.70

Figure 5-4 Typical Flexural Failure at Midspan by Concrete Crushing of Simply Supported Panels (Panel ST-NC-SL shown)

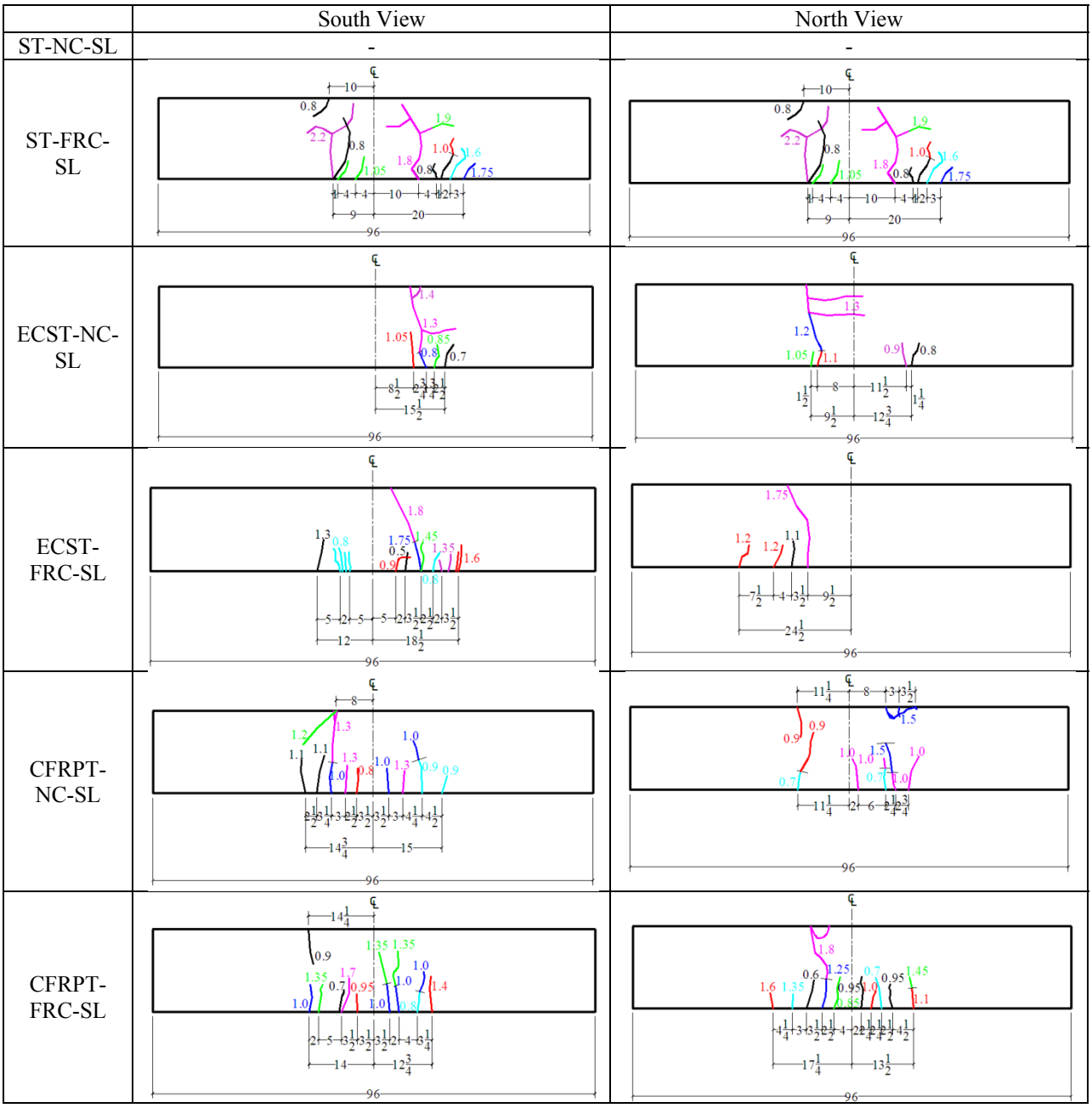

Figure 5-5 Crack Patterns – Static Load Panels

5.2.4.1.2 Load-Displacement Response

Figure 5-6 shows the measured displacements along the panel length at Grid E for all specimens. Grid locations are defined in Figure 5-2. Displacements are shown at five locations along the span (three points instrumented with DCVTs and two support points) at different applied load levels. Figure 5-7 shows the applied load–displacement response for each test specimen. From both figures, it can be observed that measured displacements increased gradually with the increasing applied load until the cracking load, after which displacements increased more rapidly with increasing applied load. Figure 5-7 also shows a bilinear load-displacement relationship for all the panels. Before cracking, the displacement at the quarter span is almost half of the

displacement at midspan. After cracking, the displacement at the quarter span is almost sixty percent of the displacement at midspan. Midspan displacements at cracking and maximum loads are summarized in Table 5-5.

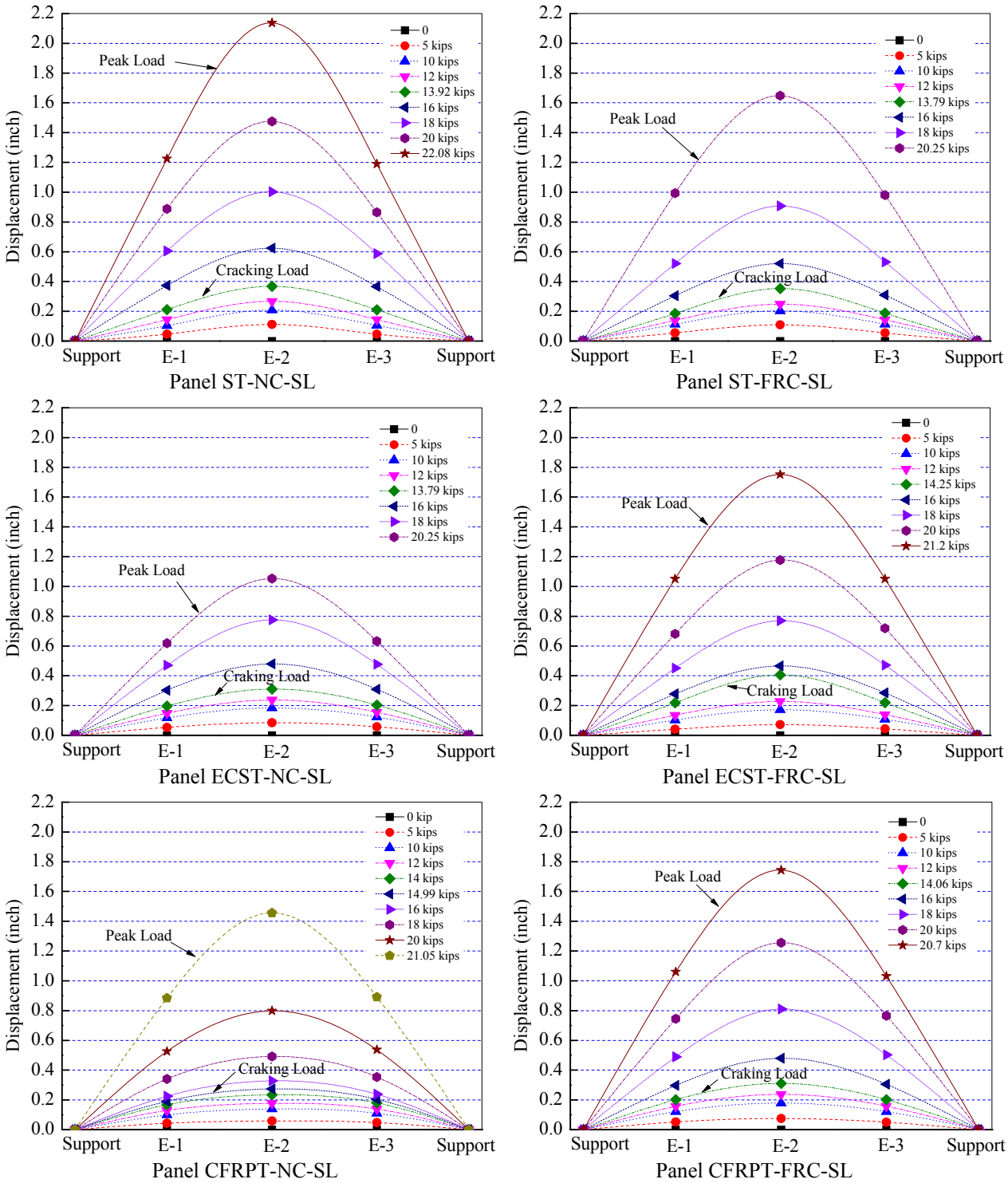

Figure 5-6 Measured Displacement along Panel Length at Grid E

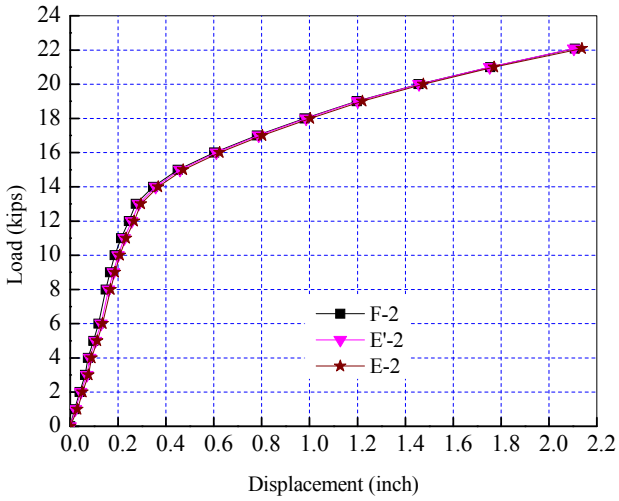

Panel ST-NC-SL

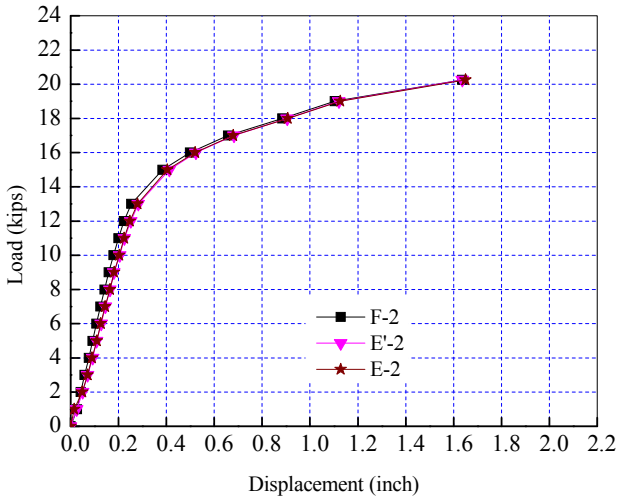

Panel ST-FRC-SL

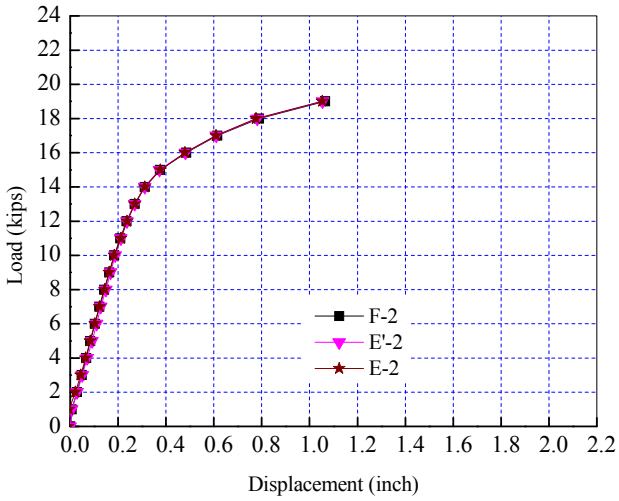

Panel ECST-NC-SL

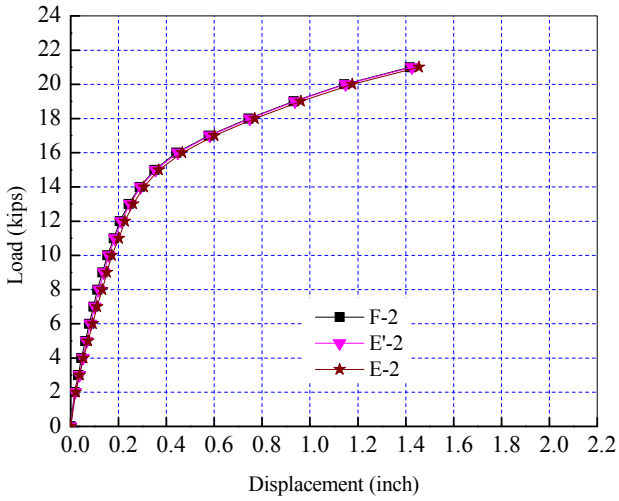

Panel ECST-FRC-SL

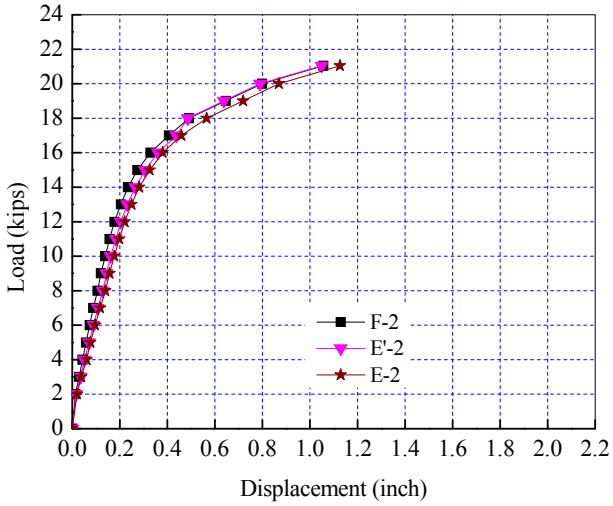

Panel CFRPT-NC-SL

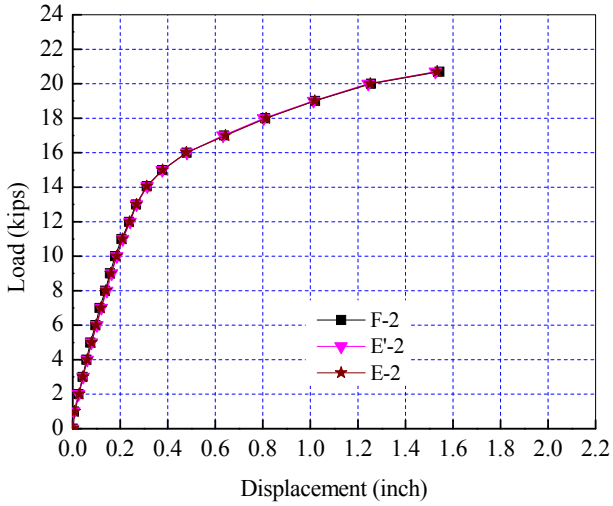

Panel CFRPT-FRC-SL

Figure 5-7 Typical Midspan Load-displacement Relationships

All six panels were expected to have similar stiffness before cracking because they had the same geometry and similar compressive (and tensile) strength of concrete. Figure 5-8 shows the load-displacement relationship for all six panels at location E-2 (center of panel). The figure shows that the stiffness of the panels is the same up to cracking; however, panels had different stiffness after cracking.

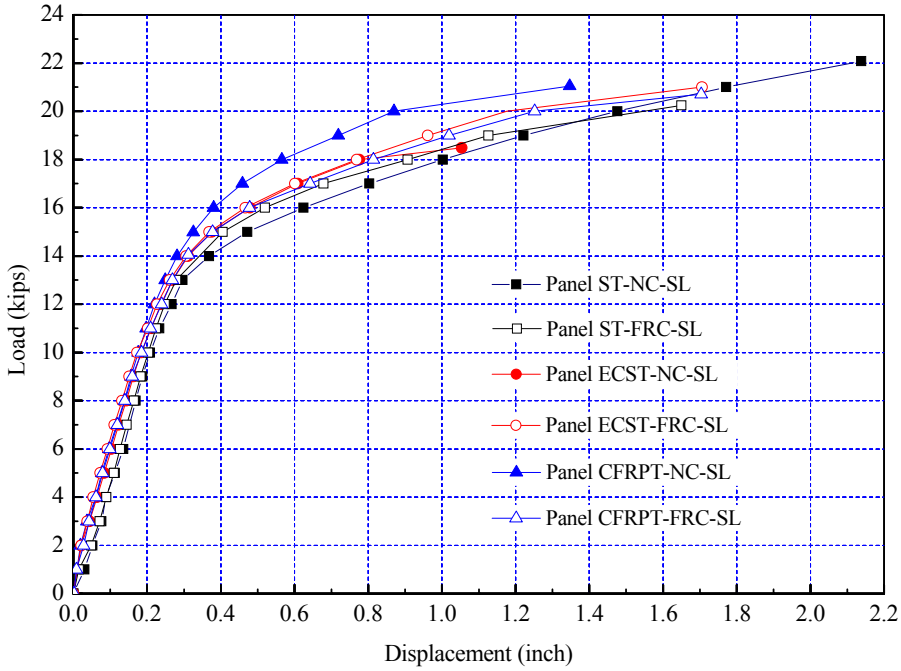

Figure 5-8 Comparison of Applied Load-displacement Relationship at E-2 for All Panels

To study the influence of tendon type on panel behavior, the load-displacement relationships were compared for panels having the same type of concrete (normal concrete or FRC). Comparison results are discussed in the following sections.

Comparison of load-displacement relationships for panels with normal concrete

Panels ST-NC-SL, ECST-NC-SL, and CFRPT-NC-SL were constructed with normal concrete as shown in Table 5-3. Panel ST-NC-SL was the control specimen with all steel tendons, while Panels ECST-NC-SL and CFRPT-NC-SL contained epoxy-coated steel or CFRP edge tendons, respectively. The load-displacement response for these three panels is compared in Figure 5-9. As shown in Figure 5-9, the load-displacement response is approximately linear for all the three panels until the cracking load (approximately 14 kips) is reached. This applied load corresponds to a displacement of 0.35 in. for all panels; thus the stiffness of each panel in this range is approximately the same. For loads greater than the cracking load, the response of each panel is different from the initial response with a marked decrease in stiffness. Panel ST-NC-SL has a nearly constant post-cracking stiffness until the maximum load is achieved, while Panels ECST-NC-SL and CFRPT-NC-SL show progressively decreasing post-cracking stiffness until the maximum load is achieved.

Of the panels with normal concrete, Panel ST-NC-SL has the greatest ductility, while Panel ECST-NC-SL has the lowest ductility. This can be explained through the required development length of different tendons. Steel tendons require the shortest development length while the epoxy tendons require the longest development length.

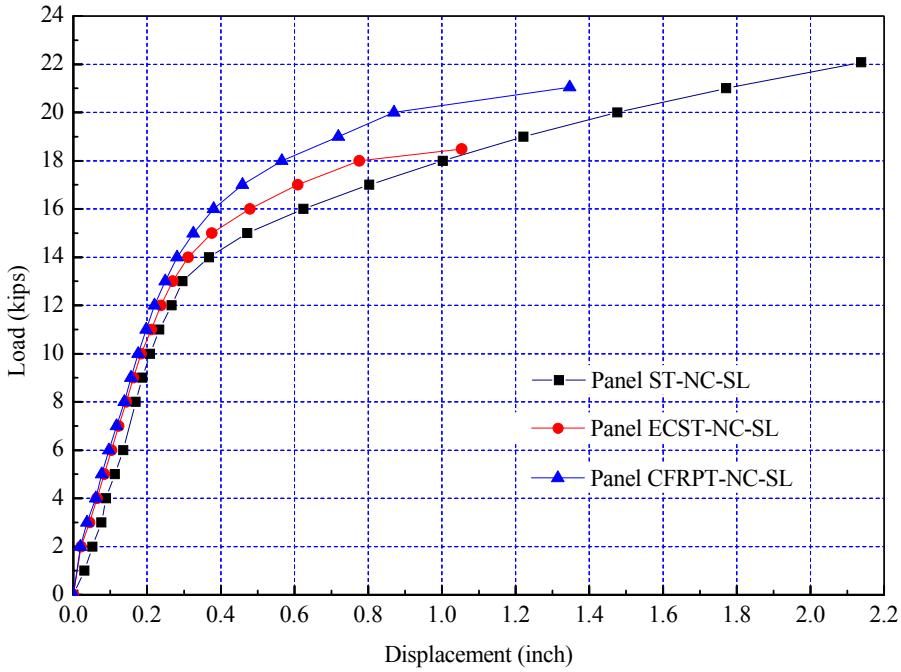

Figure 5-9 Comparison of Applied Load-displacement Relationships at E-2 for Panels with Normal Concrete

Comparison of load-displacement relationships for panels with fiber reinforced concrete

Panels ST-FRC-SL, ECST-FRC-SL, and CFRPT-FRC-SL were constructed with fiber reinforced concrete. Panel ST-FRC-SL contained all steel tendons, while Panels ECST-FRC-SL and CFRPT-FRC-SL contained epoxy-coated steel or CFRP edge tendons, respectively. The load-displacement response for these three panels is compared in Figure 5-10. As shown in Figure 5-10, the load-displacement response is approximately linear for all the three panels until the cracking load (approximately 14 kips) is reached. This applied load corresponds to a displacement of 0.35 in. for all panels; thus the stiffness of each panel in this range is approximately the same. For loads greater than 14 kips, the response of each panel is different from the initial response with a marked decrease in stiffness. Additionally, the post-cracking stiffness of all three panels is approximately the same.

Moreover, all three FRC panels have similar ductility and ultimate strength. Based on the results, it appears that when fiber reinforced concrete is used, the different tendon distribution had little consequence with respect to stiffness, ductility, and ultimate strength of panels.

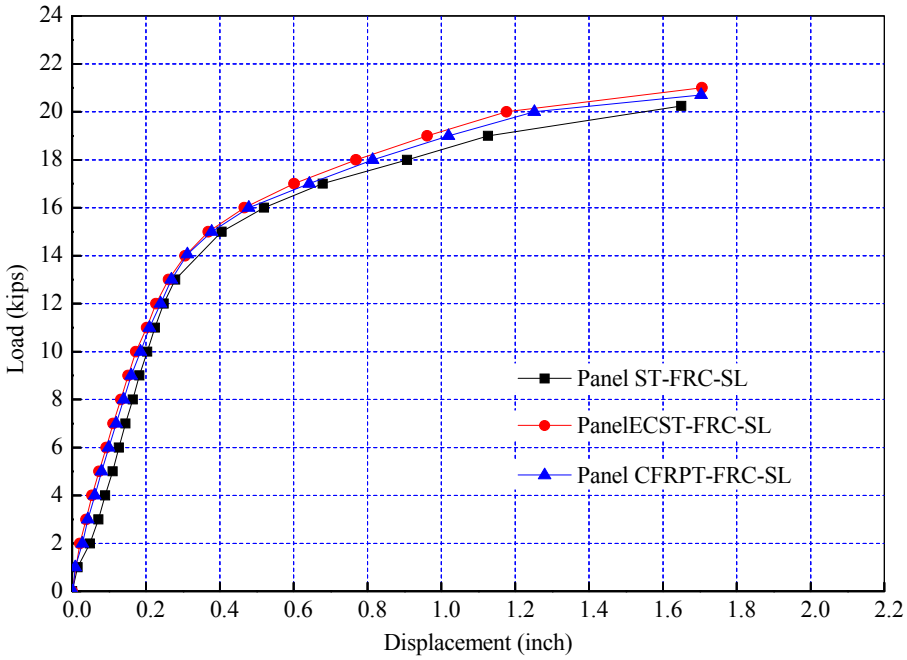

Figure 5-10 Comparison of Applied Load-displacement Relationships at E-2 for Panels with FRC

Load-Strain Response

Figure 5-11 shows the strain profiles at different load levels measured at the quarter span and midspan locations in representative Panel ST-NC-SL. Compression strain is shown as negative while tension strain is shown as positive for both concrete and tendons. The strain behavior along individual tendons for Panel ST-NC-SL is similar to and representative of the other five panels. Strain values were measured by strain gages applied to the prestressed tendons and top and bottom surfaces of the concrete as described in Section 5.2.3.2. Locations A-1 and A-3 correspond to quarter span, and location A-2 corresponds to midspan. At quarter span locations (A-1 and A-3), Figure 5-11 shows that the strains are linearly distributed within the section for all applied load levels. Strains measured on the top and bottom surfaces have the same values but with opposite signs, and the strains measured on the tendons are almost zero. Tendons are located at panel midheight. Thus, the neutral axis is located at the midheight of the section, i.e. at the center of the tendons during the entire test. At midspan (A-2), Figure 5-11 shows that the strains are linearly distributed, and the neutral axis is located at the midheight of the section until the applied load reaches a specific value corresponding to the cracking load (13.92 kips in the figure). When the applied load exceeds this specific value, the strains measured on the bottom surface are greater than those measured on the top surface. With increasing load, the neutral axis shifts progressively upward away from the geometric centroid indicating that the section has cracked. It should be noted that concrete surface gages on the bottom surface of the panel stopped working after flexural cracks occurred at the gage location; thus, measured strain in these locations is reported only until the respective gage stopped working.

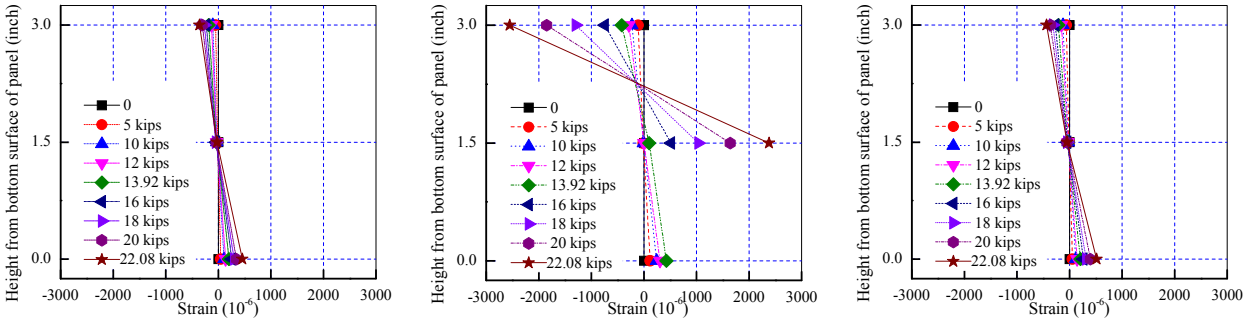

A-1 A-2 A-3

Figure 5-11 Measured Strain Profile Along Tendon (Panel ST-NC-SL, Tendon A Shown)

	A-2	E-2
ST-NC-SL	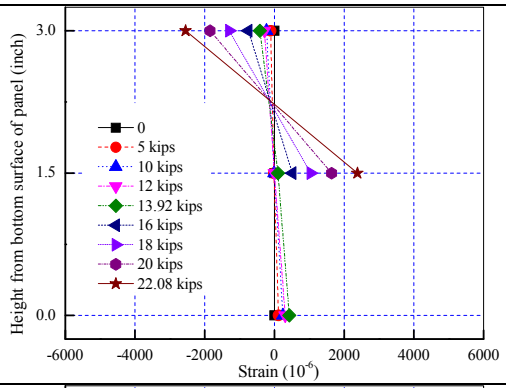	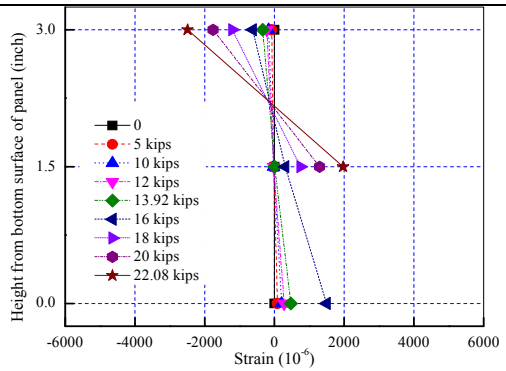
ECST-NC-SL	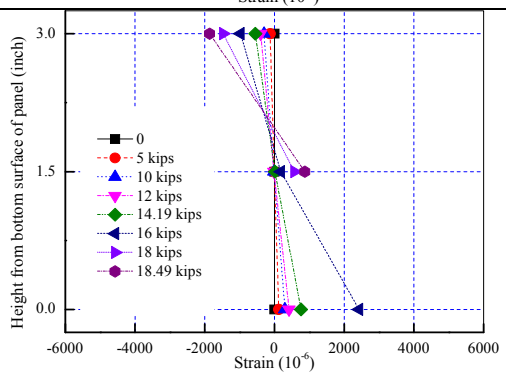	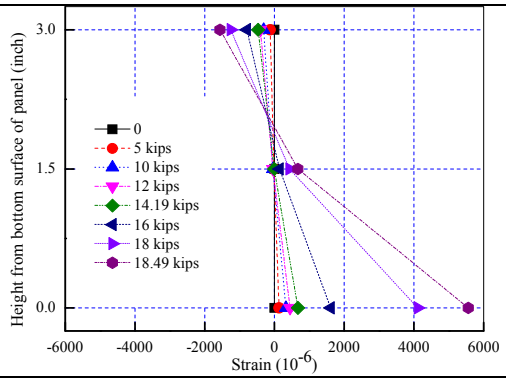
CFRPT-NC-SL	Gages A-T-2 and A-B-2 are broken	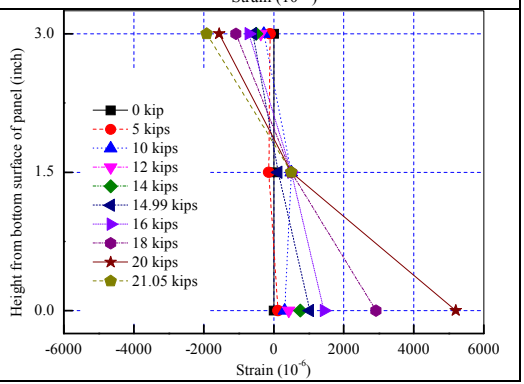

Figure 5-12 Comparison of Strain Profiles at A-2 and E-2 of Panels with Normal Concrete

Strain profiles of center and edge tendons at midspan in panels constructed with normal concrete are compared in Figure 5-12 for different load levels up to maximum load. (Center tendons are uncoated steel, and edge tendons vary based on the panel.) In Panel ST-NC-SL, strain profiles at edge and center were similar at each load level. At each load level beyond the cracking load, the neutral axis at edge and center tendons were approximately the same depth from the extreme compressive fiber of the section as indicated by the strain profiles.

In Panel ECST-NC-SL, strain profiles at edge and center were also observed to be similar under different load levels. At each load level beyond the cracking load, the neutral axis at edge and center tendons were approximately the same depth from the extreme compressive fiber of the section as indicated by the strain profiles (tendons on Panel CFRPT-NC-SL are not compared because surface gages at tendon A were not working).

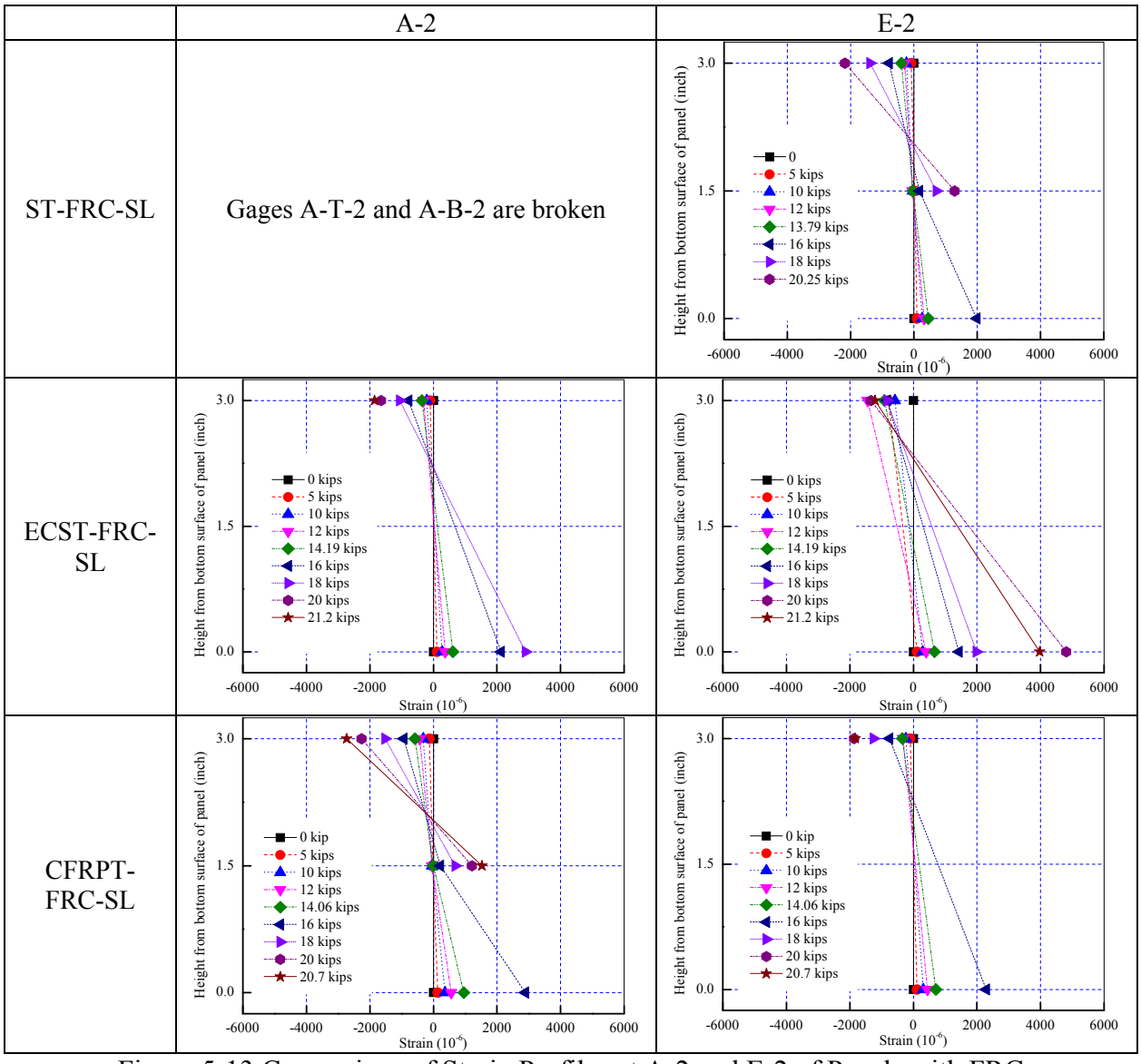

Figure 5-13 Comparison of Strain Profiles at A-2 and E-2 of Panels with FRC

Strain profiles of center and edge tendons at midspan in panels constructed with FRC are compared in Figure 5-13. (Tendons on Panel ST-FRC-SL are not compared because surface gages at tendon A were not working.) In Panel ECST-FRC-SL, for applied loads greater than the cracking load, the neutral axis shifted up at both edge and center with increasing load. When the applied load was near maximum load, however, the neutral axis at the edge is deeper at the edge (tendon E, the epoxy-coated steel tendon) than that at center (tendon A, the uncoated steel tendon). If no bond slip occurred, the profiles at these two locations should be the same as observed in Panel ST-NC-SL in Figure 5-12 since the epoxy-coated tendon has the same modulus as the uncoated steel tendon. A plausible explanation for the different strain profiles may be the bond slip between the epoxy-coated tendon and FRC, although this phenomenon was not observed with the normal concrete panels in Figure 5-12.

In panel CFRPT-FRC-SL, for applied loads greater than the cracking load, again the neutral axis shifted up at both edge and center tendons with increasing applied load. However, when the applied load was near maximum load, the neutral axis is deeper at the edge tendon than at the center tendon. Regardless of the lack of tendon strain data at the center tendon, the strain profiles can be approximately drawn by connecting concrete surface strains at different load levels with straight lines, based on which a comparison of strain profiles can be made. For a given load level, the CFRP tendon had a higher strain value than the steel tendon. If no bond slip occurred, this phenomenon can be explained by the lower modulus of elasticity of the CFRP tendons compared with steel tendons (the modulus of elasticity of the CFRP tendons is 18,000 ksi provided by the manufacturer).

Summary and Key Observations

In Section 5.2.4.1, the static load test data were analyzed to investigate and compare the static behavior of six panels including the failure mode and cracking behavior, load-displacement relationships, and load-strain relationships. Based on the discussions from Sections 5.2.4.1.1-5.2.4.1.3, the following key observations are made:

(1) All panels behaved similarly in the uncracked elastic region. Panels had similar stiffness and had similar cracking loads and displacements despite the difference in concrete and edge tendon materials. Since in situ panel service load levels fall within this range, all panels are expected to behave similarly under service load conditions.
(2) The failure mode of all panels was crushing of the concrete in the flexural compression zone. Failure occurred prior to tendon yielding or rupture.
(3) The load-displacement relationship for all panels was approximately bilinear, with a marked decrease in stiffness after cracking.
(4) Panels with normal concrete had similar stiffness in the uncracked elastic range but different stiffness after cracking. Panel ST-NC-SL with only steel tendons has the highest ultimate strength and the greatest ductility. Panel ECST-NC-SL had the lowest ultimate strength and lowest ductility.
(5) Panels with FRC had similar stiffness in the uncracked elastic range as well as after cracking. Panels with FRC also had similar ultimate strength and ductility, despite different tendon types.

5.2.4.2 Fatigue Load Tests

This section summarizes the representative test results of six fatigue load test specimens in terms of overall behavior of test specimens (ultimate and cracking strength, failure mode, load-displacement relations, and stiffness degradation) and local response of materials (load-strain relationships and S-N curve). Detailed results for each panel are included in Appendix C.

As mentioned in Section 5.2.3.3, testing was paused to perform a quasi-static load test up to 0.25 in. displacement after each 500,000 cycles and finally up to failure after 2 million cycles. Overall behavior of test specimens and local response of each material are mostly described using results of a quasi-static load test after 2 million cycles.

Cracking Behavior and Failure Mode

All panels were able to withstand the prescribed two million cycles without failure. No cracks were observed in any of the specimens during the fatigue load cycles and the quasi-static test at each 500,000 cycle increment.

After completion of two million cycles, all fatigue test specimens were tested until failure under monotonic static conditions similarly to the static load specimens described in Section 5.2.4.1. All six panels failed by concrete crushing in the compression zone (the top surface of the panel) as the failure crack penetrated the flexural compression zone similar to failure modes of static test specimens. The typical failure mode is shown in Figure 5-14. No tendons were yielding at the maximum load. Cracking and maximum loads are summarized in Table 5-6 with corresponding displacements.

The cracking loads reported in Table 5-6 were determined by the change in load-displacement and load-strain behavior as discussed in the following sections. The cracking load for all panels ranged from 13.00 kips to 15.50 kips, and the cracking displacement ranged from 0.30 in. to 0.42 in. for all panels. The maximum load ranged from 17.49 kips to 22.10 kips, and the corresponding displacement ranged from 1.02 in. to 1.76 in.

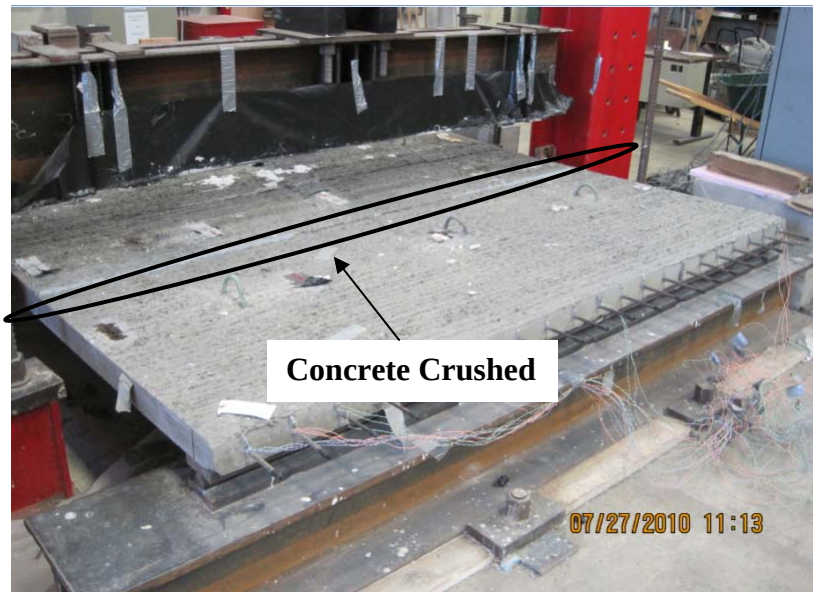

Figure 5-14 Typical Flexural Failure at Midspan by Concrete Crushing of Simply Supported Panels (Panel CFRPT-FRC-FL shown)

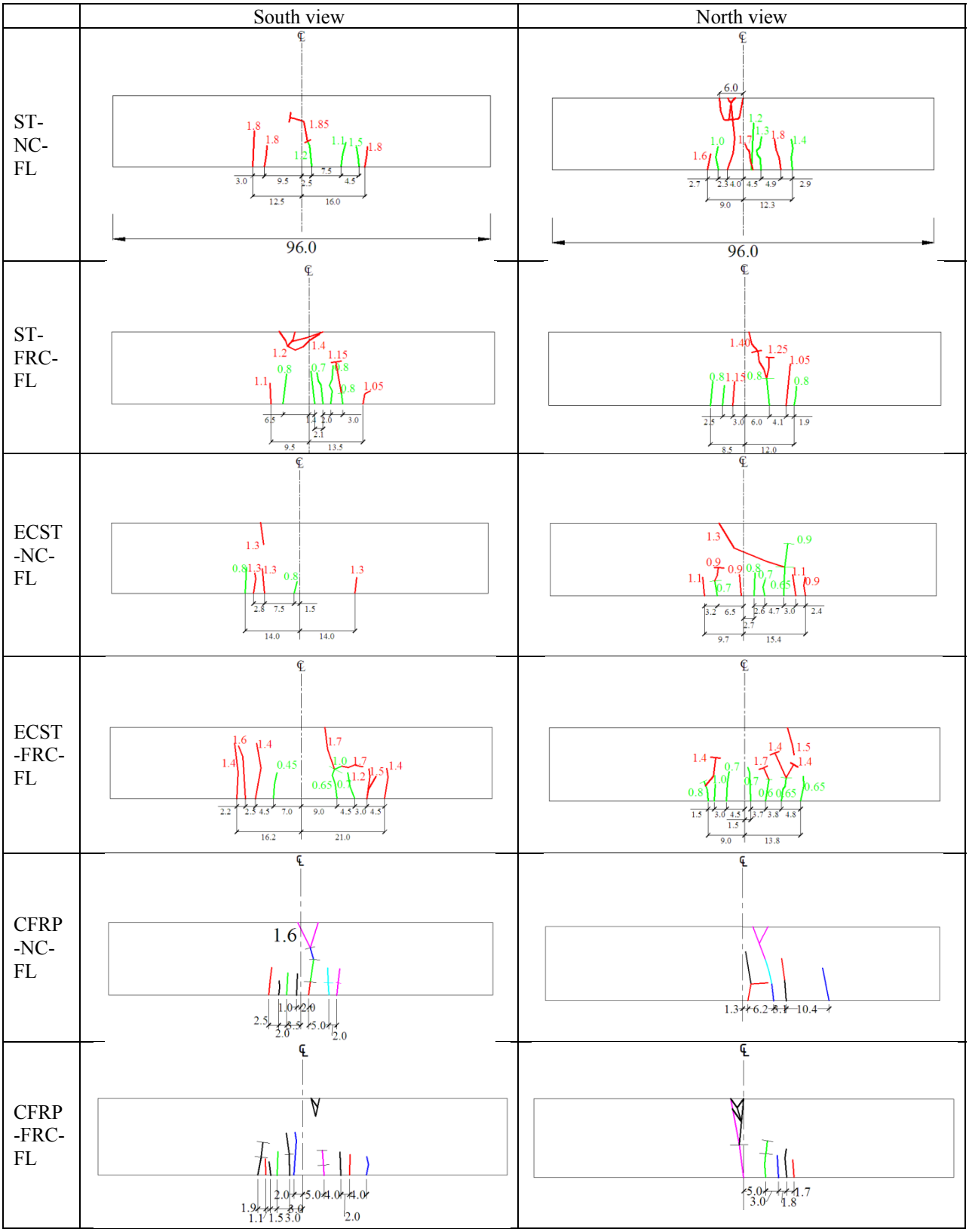

Figure 5-15 Crack Patterns from Quasi-static Test after 2 Million Cycles

Due to the nature of the test setup, the bottom surface of the test specimens was not visible during testing. Thus, cracks were observed and marked on the two side surfaces during testing. Cracks were visible on the side surfaces at load and displacement levels slightly higher than these values. The initial cracks were flexural cracks that appeared beneath the spreader beam location. As the applied displacement (and resulting applied load) was increased, additional flexural cracks appeared and existing cracks propagated upward. At the maximum load, the cracks near the edge of the loading zone propagated through the entire thickness of the panel penetrating the flexural compression zone. Crack patterns for each specimen are shown in Figure 5-15 and Appendix C.

Table 5-6 Summary of Applied Load and Displacement at Cracking and Failure – Fatigue Load Panels

Test Specimen	Cracking Load (kips)	Cracking Displacement at Midspan (in.)	Maximum Load (kips)	Displacement at Midspan Corresponding to Maximum Load (in.)
ST-NC-FL	13.98	0.32	22.10	1.76
ST-FRC-FL	14.00	0.33	20.70	1.63
ECST-NC-FL	15.50	0.42	19.00	1.12
ECST-FRC-FL	13.25	0.30	19.49	1.40
CFRPT-NC-FL	13.70	0.35	17.49	1.02
CFRPT-FRC-FL	13.00	0.35	17.95	1.33

Load-Displacement Response

Representative load-displacement relationships after two million cycles for all fatigue test specimens are illustrated in Figure 5-16 at the point of application of the load (E-2 in Figure 5-2). As observed in Figure 5-16, differences were observed for the six panels before and after cracking. Unlike the static load test results discussed in Section 5.2.4.1.2, different cracking and maximum load and corresponding displacements were observed. Accordingly, these differences are investigated by detailed analysis of load-displacement relationships with respect to parameters considered and observation of stiffness degradation after each 500,000 cycles.

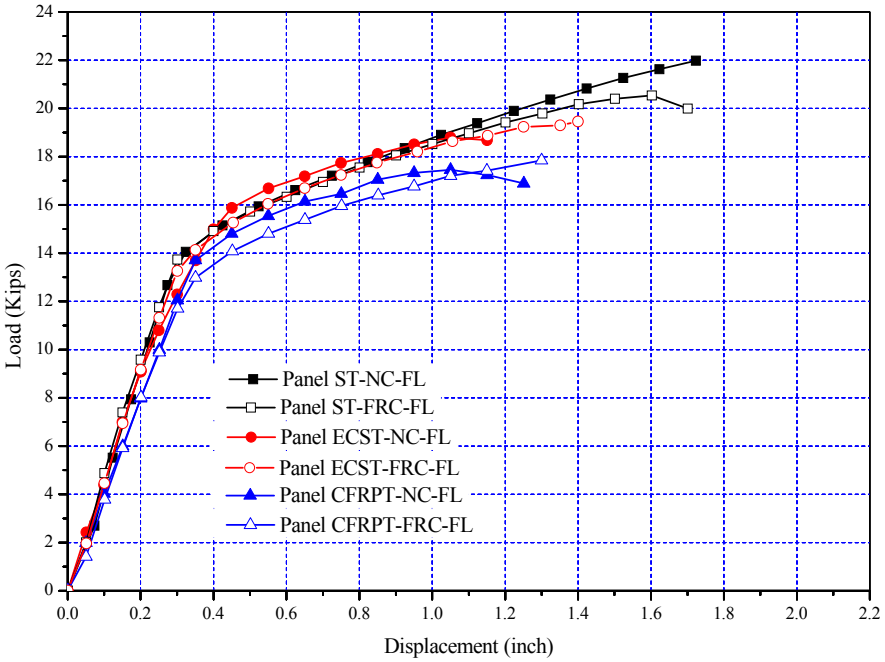

Figure 5-16 Applied Load-displacement Relationship at E-2 during Quasi-static Load Test after 2 Million Fatigue Cycles

Comparison of load-displacement relationships for panels with different materials

The load-displacement relationships of quasi-static tests were compared for panels having the same type of concrete (normal concrete or FRC) to study the influence of tendon type on panel behavior. A similar comparison was also conducted for panels having the same type of edge tendons (steel, epoxy-coated steel, and CFRP) for investigating the effects of different concrete.

Panels ST-NC-FL, ECST-NC-FL, and CFRPT-NC-FL were constructed with normal concrete as shown in Table 5-3. Panel ST-NC-FL is the control specimen with steel tendons, while Panels ECST-NC-FL and CFRPT-NC-FL contain either epoxy-coated steel or CFRP edge tendons, respectively. Figure 5-17 shows the difference in the load-displacement response for the three normal concrete panels for the quasi-static test after two million cycles. Significant differences between the three panels are maximum load and ductility. As shown in Figure 5-17, the load-displacement response is approximately linear for all three panels until the cracking load is reached. Different cracking loads and corresponding displacements were observed due to stiffness degradation as discussed later. For loads greater than the cracking load, the response of each panel is different from the initial response with a marked decrease in stiffness. Panels ST-NC-FL, ECST-NC-FL, and CFRPT-NC-FL show similar post-cracking behavior as their corresponding static load panels discussed in Section 5.2.4.1.2, with main differences in the ductility and the ultimate capacity due to the cyclic loading. Panel ST-NC-FL shows a difference in the ductility only (maximum displacement), and no maximum load change is observed. Panel ST-NC-FL has a nearly constant post-cracking stiffness until the maximum load is achieved, while Panels ECST-NC-FL and CFRPT-NC-FL show progressively decreasing post-cracking stiffness until the maximum load is achieved. Panel ST-NC-FL has the greatest ductility of the three normal concrete panels.

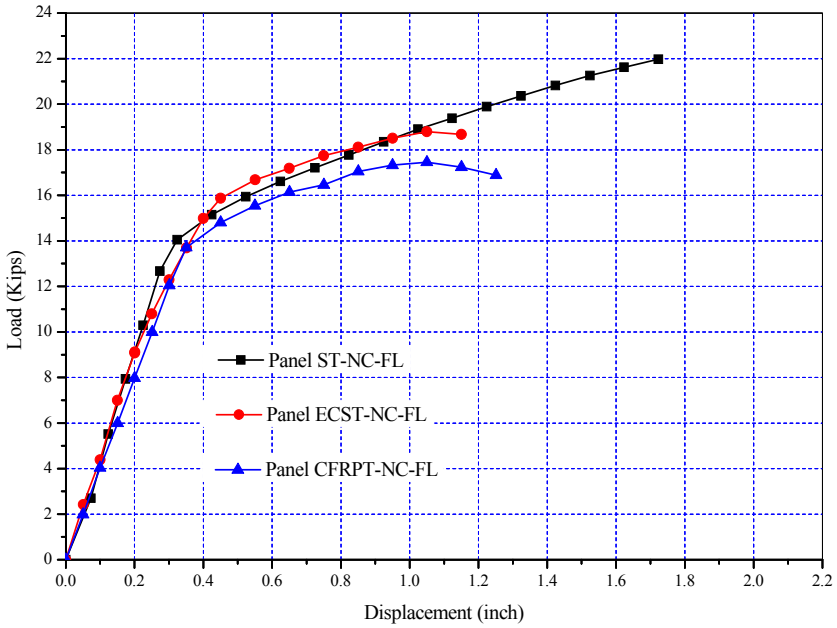

Figure 5-17 Applied Load-displacement Relationship at E-2 of Panels with Normal Concrete during Quasi-static Load Test after 2 Million Fatigue Cycles

Panels ST-FRC-FL, ECST-FRC-FL, and CFRPT-FRC-FL were constructed with fiber reinforced concrete. Panel ST-FRC-FL contained steel tendons, while Panels ECST-FRC-FL and CFRPT-FRC-FL contained either epoxy-coated steel or CFRP edge tendons, respectively. The load-displacement response for these three panels is compared in Figure 5-18. Initial stiffness and cracking load of Panel CFRPT-FRC-FL is slightly lower than the other panels. However, post-cracking behavior, which is mainly governed by the reinforcements, is similar for each panel in terms of stiffness. Panel ST-FRC-FL has the greatest ductility of all three FRC panels.

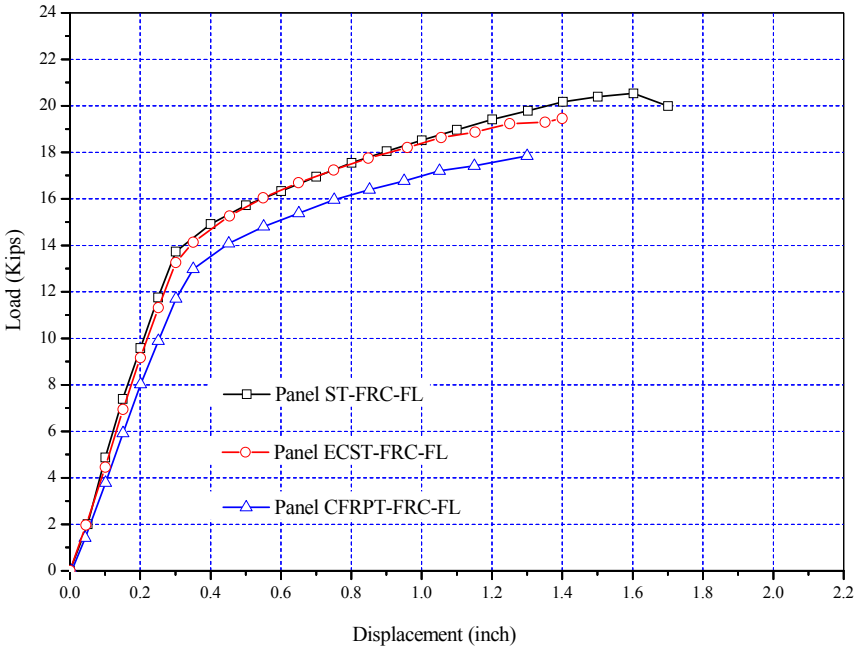

Figure 5-18 Applied Load-displacement Relationship at E-2 of Panels with FRC during Quasi-static Load Test after 2 Million Fatigue Cycles

Figure 5-19, Figure 5-20, and Figure 5-21 show the load-displacement relationships for panels with the same tendon profiles but different concrete (normal or fiber reinforced) at the 2 million quasi-static load test. Figure 5-19 shows the load-displacement relationship for panels with steel edge tendons. It can be observed that before cracking, Panels ST-NC-FL and ST-FRC-FL have the same stiffness and similar cracking loads and displacements. Panel ST-NC-FL has a slightly higher maximum load and larger peak displacement, however, which indicates a higher strength and ductility. Figure 5-20 shows the load-displacement relationship for panels with epoxy-coated steel edge tendons. It can be observed that before cracking, Panels ECST-NC-FL and ECST-FRC-FL have the same stiffness, but panel ECST-NC-FL has a higher cracking load and cracking displacement. Panel ECST-FRC-FL has a slightly higher maximum load and larger maximum displacement, however, thus higher strength and ductility. Figure 5-21 shows the load-displacement relationship for panels with CFRP edge tendons. It can be observed that before cracking Panels CFRPT-NC-FL and CFRPT-FRC-SL have the same stiffness and similar cracking loads and displacements. Panel CFRP-FRC-FL, however, has slightly higher maximum load and maximum displacement, which indicates higher strength and ductility.

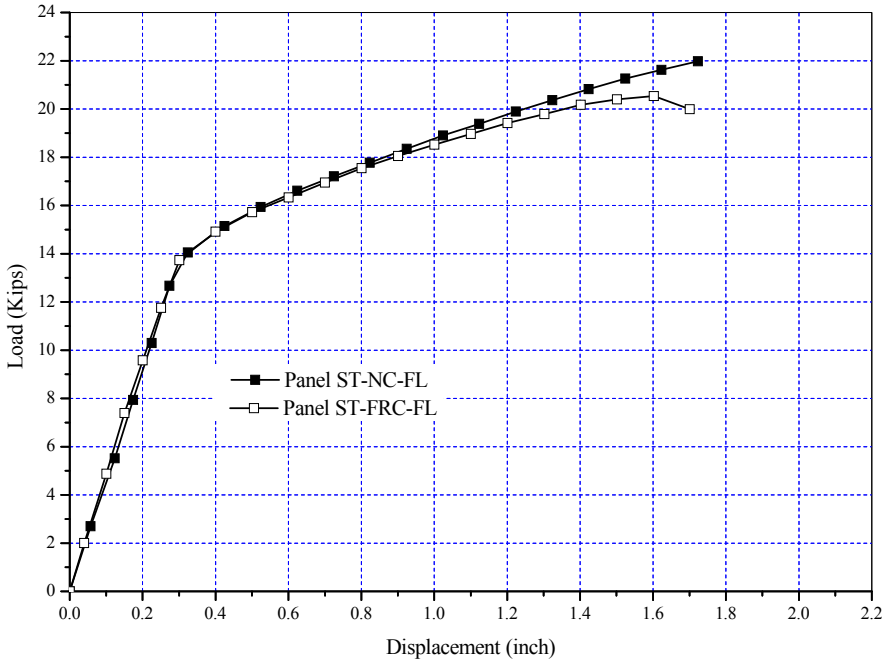

Figure 5-19 Applied Load-displacement Relationship at E-2 of Panels with Steel Edge Tendons during Quasi-static Load Test after 2 Million Fatigue Cycles

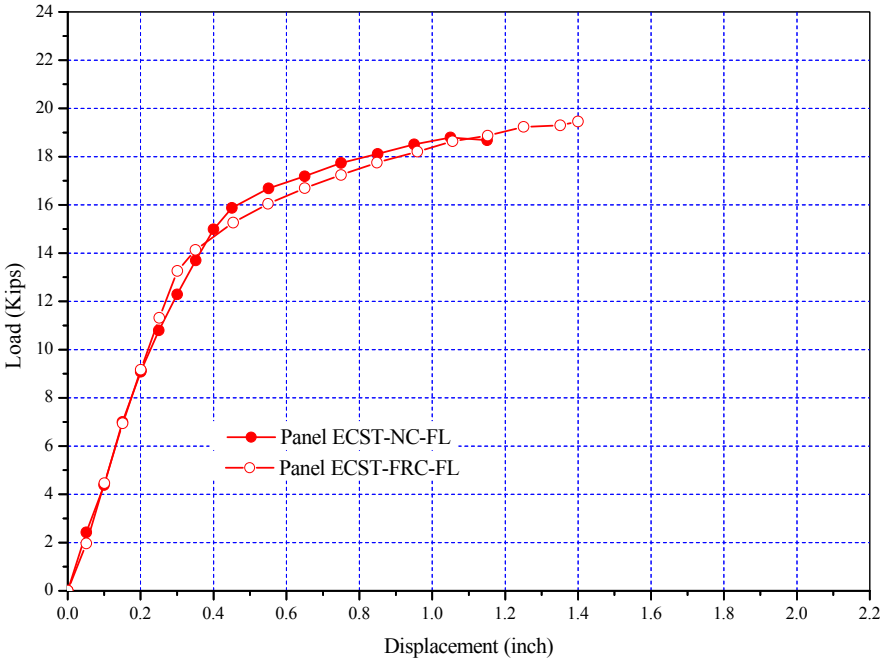

Figure 5-20 Applied Load-displacement Relationship at E-2 of Panels with Epoxy Coated Steel Edge Tendons during Quasi-static Load Test after 2 Million Fatigue Cycles

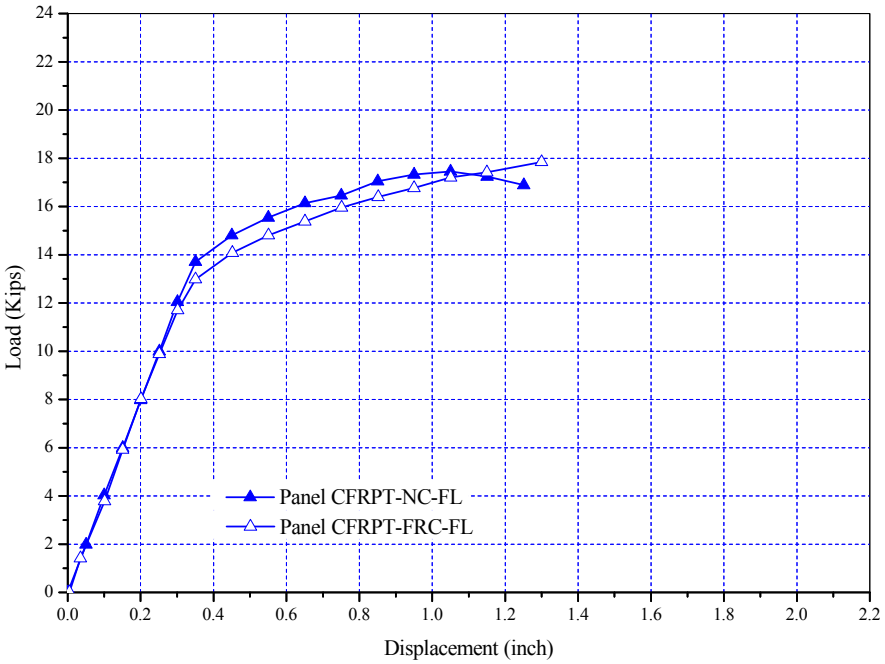

Figure 5-21 Applied Load-displacement Relationship at E-2 of Panels with CFRP Edge Tendons during Quasi-static Load Test after 2 Million Fatigue Cycles

Figure 5-22 shows the measured displacements along the panel length at Grid E for all specimens at the two million cycle quasi-static load test. Grid locations are defined in Figure 5-2.

Displacements are shown at five locations along the span (three points instrumented with DCVTs and two support points) at different applied load levels. In general, it can be observed that measured displacements increased gradually with the increasing applied load until the cracking load, after which displacements increased more rapidly with increasing applied load.

In addition, Figure 5-23, Figure 5-24, and Figure 5-25 compare the displacement profiles between test specimens with normal and FRC concrete at ultimate. Figure 5-23 shows the measured displacements at maximum load along panel length for panels with steel tendons only. As shown in the figure, the midspan displacement of Panel ST-NC-FL is about 30% higher than that of Panel ST-FRC-FL, while the quarter span displacement is about 25% higher. The slope of the displacement curve of Panel ST-NC-FL is also larger than that of Panel ST-FRC-FL. Figure 5-24 shows the measured displacements at maximum load along panel length for panels with epoxy-coated steel edge tendons. As shown in the figure, the midspan displacement of Panel ECST-NC-FL is about 8% smaller than that of Panel ECST-FRC-SL, while the quarter span displacement is about 14% lower. The slope of the displacement of Panel ECST-NC-FL is also smaller than that of Panel ECST-FRC-SL. Figure 5-25 shows the measured displacements at maximum load along panel length for panels with CFRP edge tendons. As shown in the figure, the midspan displacement of Panel CFRPT-FRC-FL is about 18% higher than of Panel CFRPT-NC-FL, while the quarter span displacement is about 25% higher. The slope of the displacement curve of Panel CFRPT-FRC-FL is also larger than that of Panel CFRPT-NC-FL.

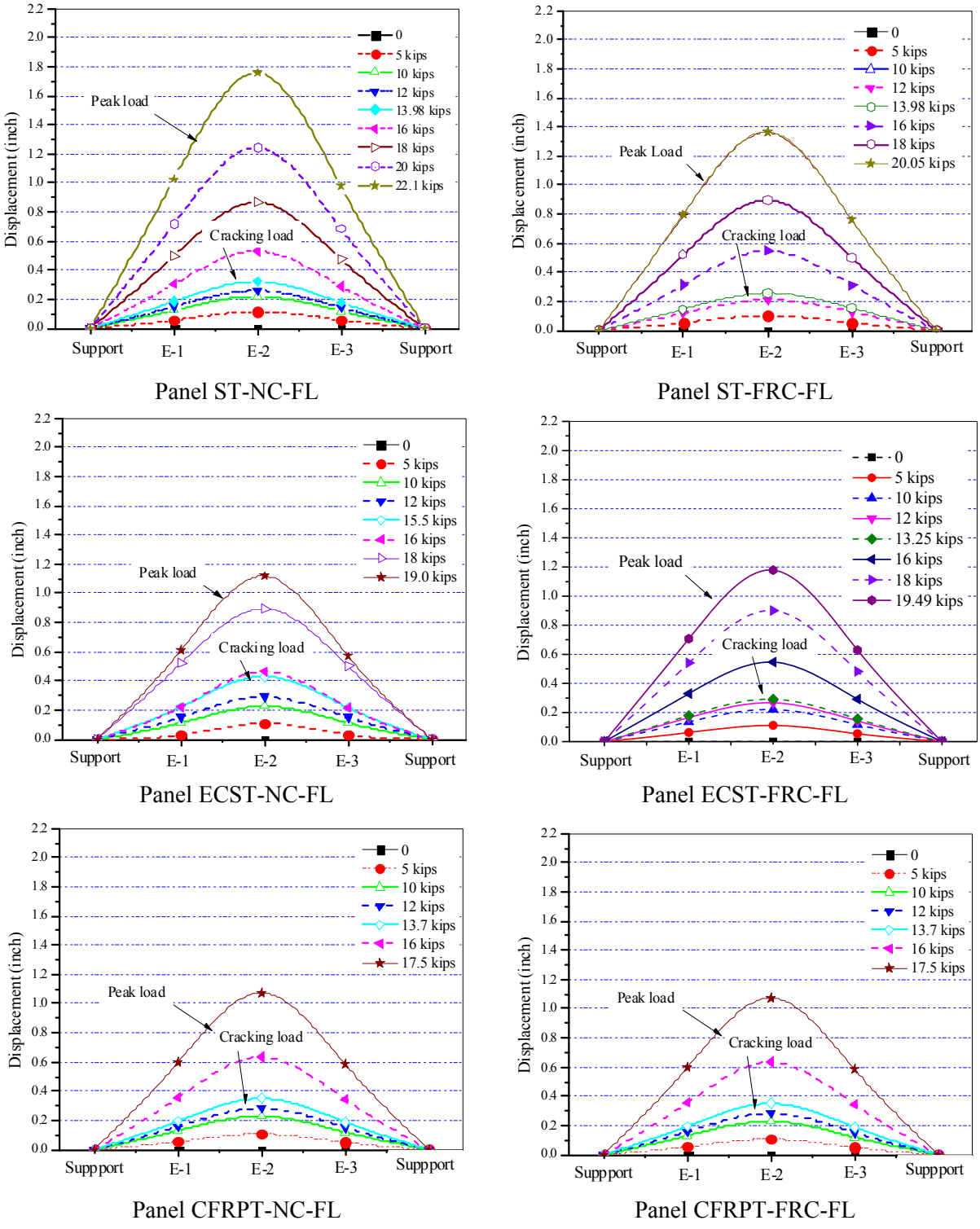

Figure 5-22 Measured Displacements along Panel Length at Grid E at 2 Million Cycle Quasi-static Load Test

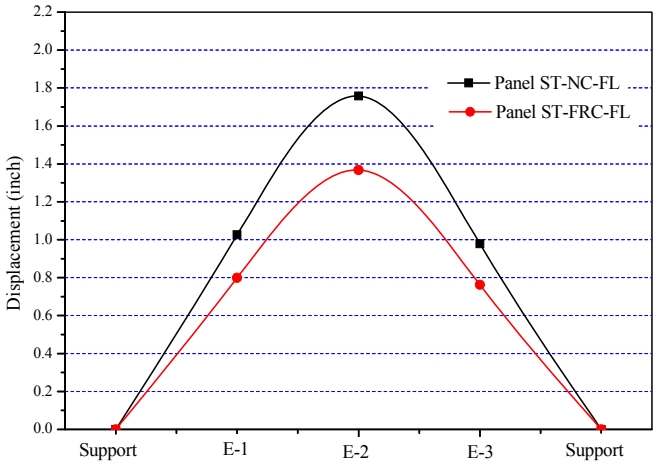

Figure 5-23 Measured Displacements at Maximum Load Along Panel Length for Panels with Steel Edge Tendons

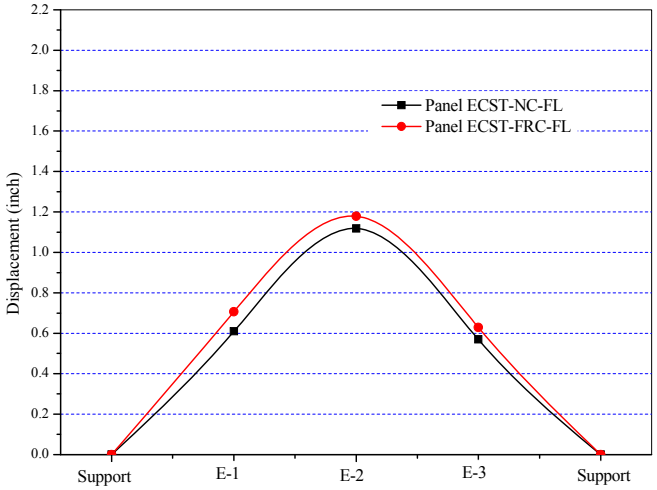

Figure 5-24 Measured Displacements at Maximum Load Along Panel Length for Panels with Epoxy-coated Steel Edge Tendons

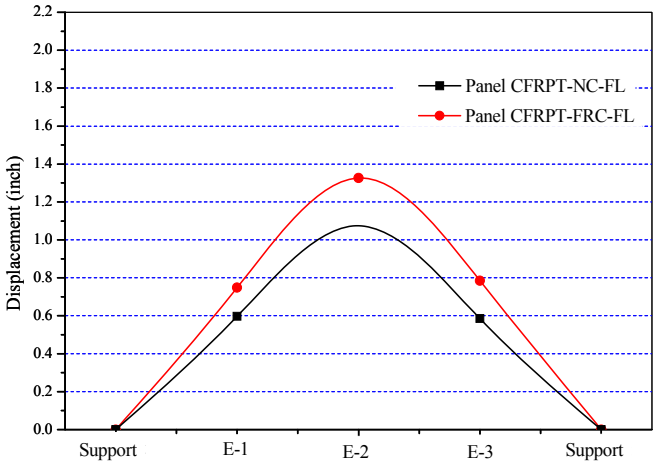

Figure 5-25 Measured Displacements at Maximum Load Along Panel Length for Panels with CFRP Edge Tendons

Stiffness degradation

Reduction in stiffness with successive cycles, or stiffness degradation, is indicated in Figure 5-26 as a reduction in slope of the load-displacement relationship. Stiffness degradation as a function of 500,000 cycle increment is summarized in Table 5-7 for each panel. Stiffness values given in the table were calculated based on linear regression of the load-displacement relationships. Stiffness degradation values given in the table are based on comparison with the baseline measurement (i.e. zero cycles with the exception of panel ST-NC-FL, which was one million cycles).

Figure 5-27 shows the stiffness degradation of all test specimens for each 500,000 cycle increment. In general, all specimens show a decreasing trend in the stiffness with increase of loading cycles except for panel CFRPT-FRC-FL. Relatively larger degradations are observed in both ranges of 0~0.5 million and 1.5~2 million than the other ranges. In particular, Panel ECST-NC-FL shows a significant decrease at initial loading cycle, while Panel CFRPT-NC-FL does at the last loading cycle range. From this discussion, it is difficult to distinguish the effects of the different materials. However, comparison of final stiffness degradation illustrated in Figure 5-28 indicates that stiffness degradation is the lowest in panel ECST-NC-FL and the highest in Panel CFRPT-FRC-FL.

Table 5-7 Stiffness Degradation of Fatigue Load Specimens

Test Specimen	0 Cycles		500,000 Cycles		1,000,000 Cycles		1,500,000 Cycles		2,000,000 Cycles	
	Stiffness (kips/in.)	Degradation[1] (%)	Stiffness (kips/in.)	Degradation[1] (%)	Stiffness (kips/in.)	Degradation[1] (%)	Stiffness (kips/in.)	Degradation[1] (%)	Stiffness (kips/in.)	Degradation[1] (%)
ST-NC-FL	(Note 2)	(Note 2)	(Note 2)	(Note 2)	52.4	-	51.4	-	50.0	-
ST-FRC-FL	51.3	0	49.8	-2.9	49.6	-3.3	48.7	-5.1	47.3	-7.8
ECST-NC-FL	59.8	0	50.9	-14.9	50.0	-16.4	49.7	-16.9	47.7	-20.2
ECST-FRC-FL	49.2	0	48.0	-2.4	46.3	-5.9	46.4	-5.9	45.7	-7.1
CFRPT-NC-FL	51.3	0	48.0	-6.4	46.9	-8.6	46.2	-9.9	42.8	-16.6
CFRPT-FRC-FL	42.2	0	41.6	-1.4	43.4	2.8[3]	42.8	1.4[3]	41.0	-2.8

Notes 1. Degradation reported is compared with initial measurement.
2. Measurements unavailable at the corresponding number of cycles.
3. Degradation in the range of -3%~3% can be regarded as negligible.

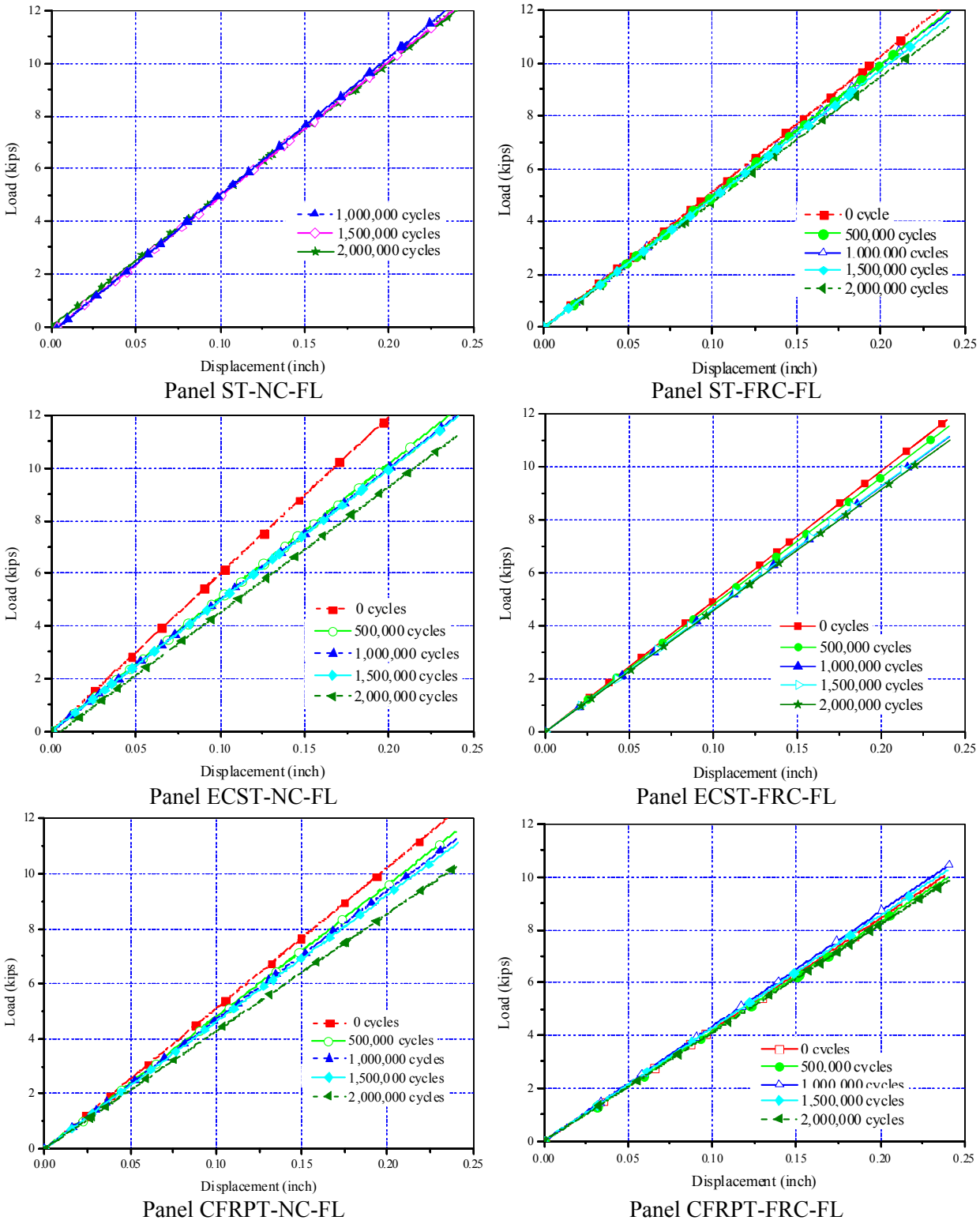

Figure 5-26 Load-displacement Relationship at Different Cycle Increments

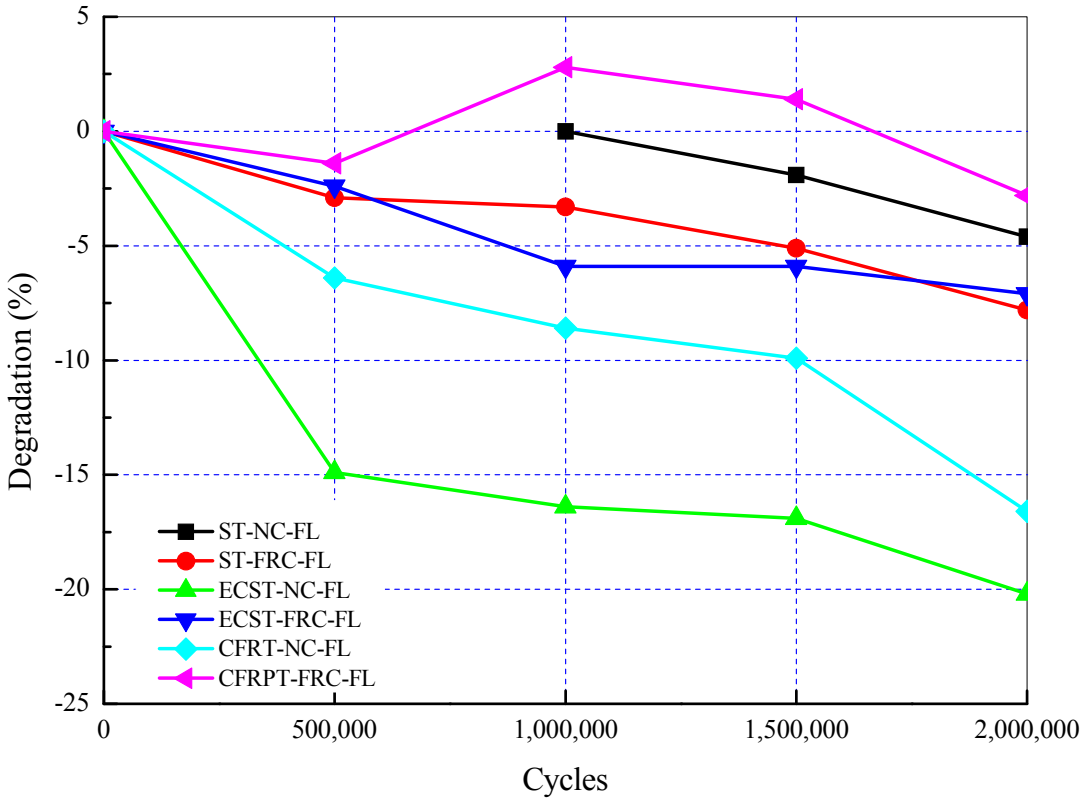

Figure 5-27 Stiffness Degradation versus Cycles

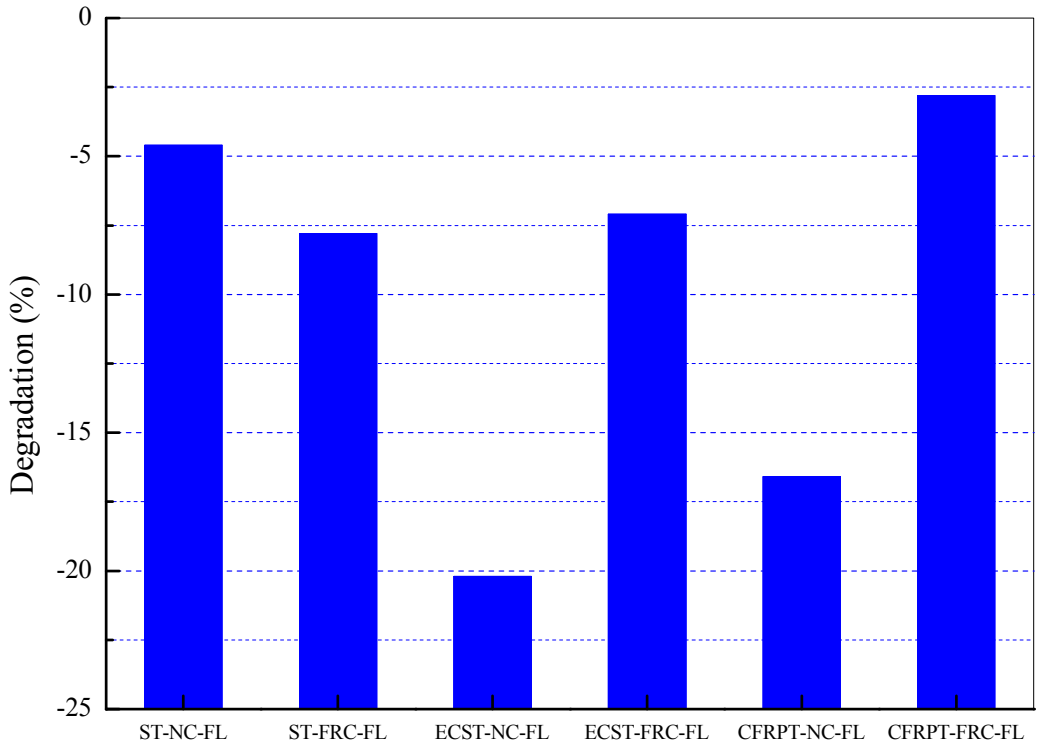

Figure 5-28 Stiffness Degradation Comparison after 2 Million Cycles

Load-Strain Response

This section presents a discussion of the measured load-strain relationships to investigate local behavior of each component. Fatigue behavior of tendons is characterized by S-N curves. Load-strain relationships are utilized to investigate the effects of different materials as well as strain variation across the panel section. This information can support the explanation for the final failure modes and overall behavior of the panel discussed in Section 5.2.4.2.1 This section describes the representative data only, while detailed data is included in Appendix C.

S-N curves

Figure 5-29 shows a typical tendon strain-test cycles relationship at quarter span and midspan. It can be observed that regardless of the test cycles, the tendon strains at both quarter and mid spans remain values near zero. This indicates that the neutral axis of the cross sections at midspan and quarter span remains at the centroid of tendon, based on which the fact that no cross sections experience cracking can be confirmed. Thus, there is no doubt about the serviceability of the tested panel. Furthermore, all the other tested panels have the similar S-N curves as shown in Figure 5-29, which proved the serviceability of the proposed panel systems.

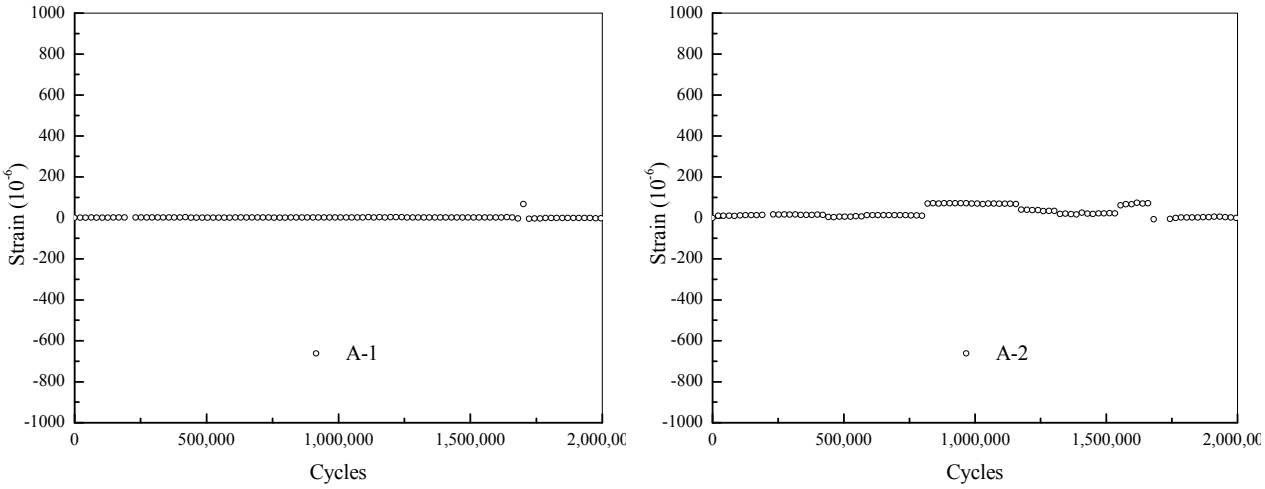

Figure 5-29 Typical Maximum Tendon Strain per Cycle vs. Test Cycles at Quarter Span and Midspan (Panel ST-NC-FL shown)

Load-strain relationships

This section presents the representative load-strain relationship of the quasi-static test after two million cycles for Panel ST-NC-SL. Figure 5-29 shows the applied load-strain relationships for all concrete surface gages, while relationships for all tendons are illustrated in Figure 5-30. The same sign convention is used for the strain values as provided in Section 5.2.4.2.1. Compression strain is taken as negative while tension strain is taken as positive for both concrete and tendons.

Most of the load-strain relationships for the concrete surface gages in Figure 5-29 show a consistent tendency with respect to measuring points except for the E-T-2 gage located on the center of the panel. Load-strain relationships at midspan show a clear non-linear behavior of concrete after cracking load in both top and bottom surface, while relationships at the quarter-spans show a symmetric linear behavior up to the maximum load with respect to top and bottom strains. From this observation, not only can local behavior of the concrete be examined, but

overall behavior of the panel such as the final failure mode can also be detected. It is obvious that the midspan area is the predominant area to govern the final behavior, while the other areas along the panel length are still in the elastic range resulting in no significant effect on the failure mode. Similar tendencies are observed in load-strain relationships for tendons as illustrated in Figure 5-30. Measured tendon strains along midspan are almost zero before cracking load because they are located at the neutral axis. When the load is greater than this level, the strains begin to increase linearly until failure of the panel without yielding. Meanwhile, no significant increases are observed in the other strains. This information supplements the conclusion about the final failure mode made by observation of overall behavior. Assured evidence for the final failure mode can be obtained from relative relationships between concrete and tendon strain values across the section as discussed in the following sections.

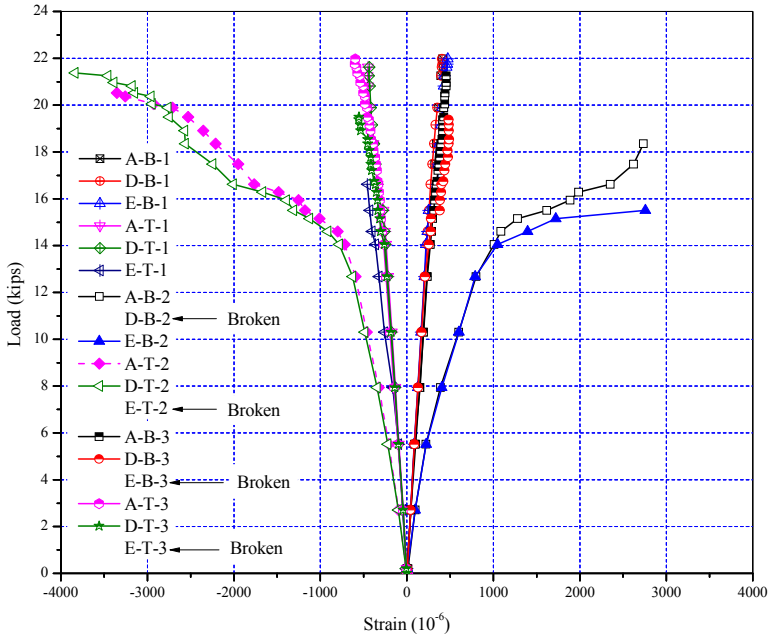

Figure 5-30 Typical Load-concrete Surface Strain Relationship (Panel ST-NC-FL)

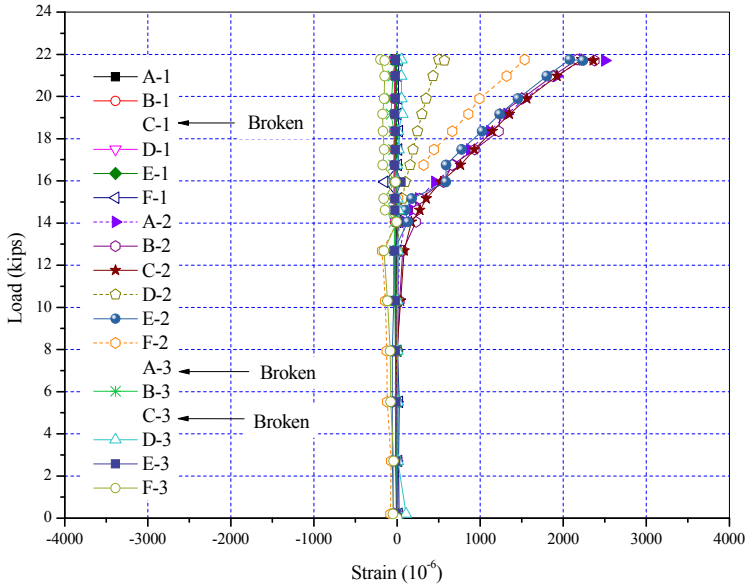

Figure 5-31 Typical Applied Load-tendon Strain Relationship (Panel ST-NC-FL Shown)

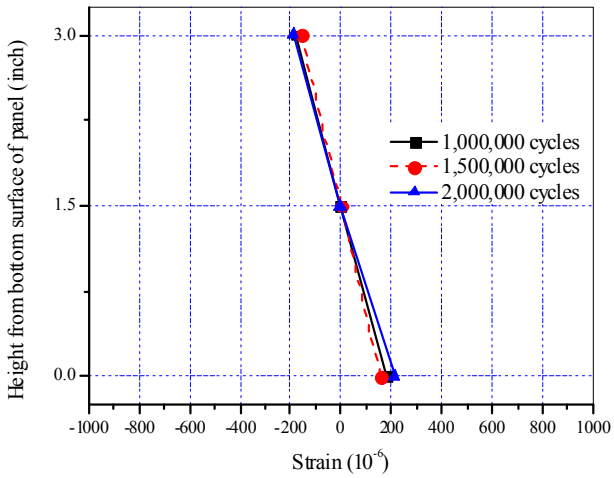

Panel ST-NC-FL

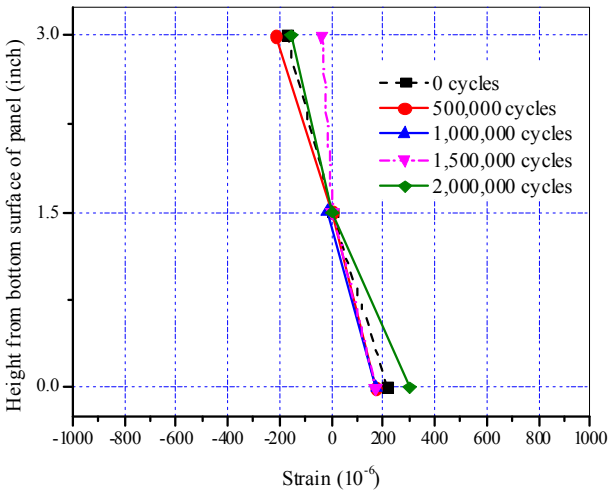

Panel ST-FRC-FL

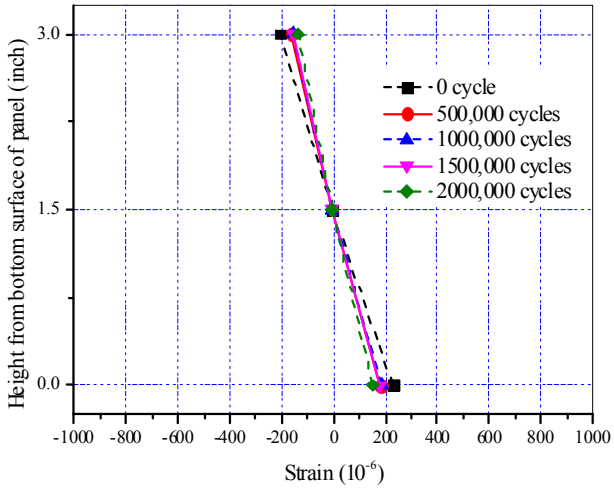

Panel ECST-NC-FL

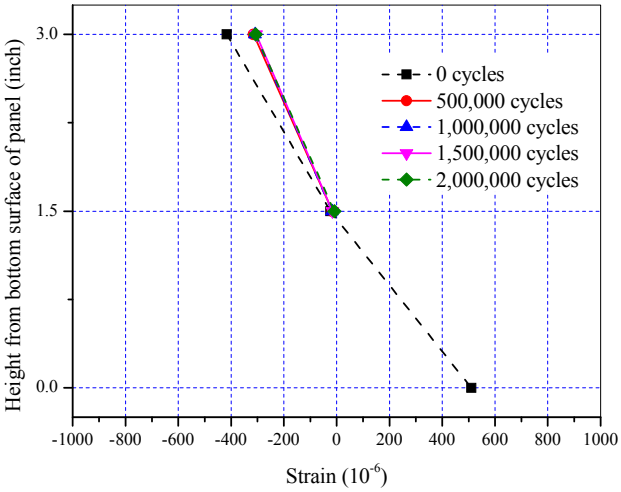

Panel ECST-FRC-FL

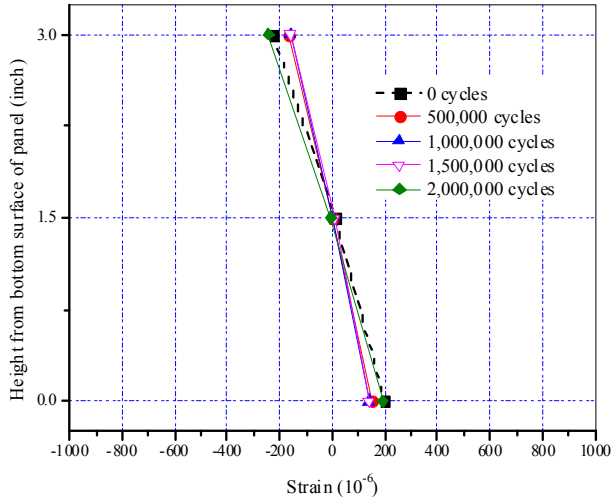

Panel CFRPT-NC-FL

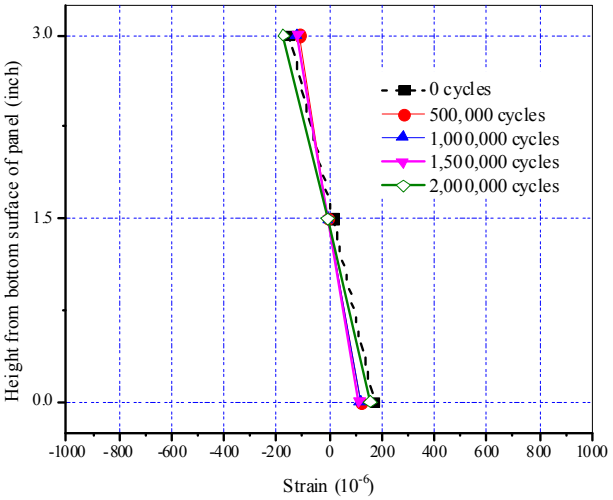

Panel CFRPT-FRC-FL

Figure 5-32 Measured Strain Profile at A-1 After Each 500,000 Cycles

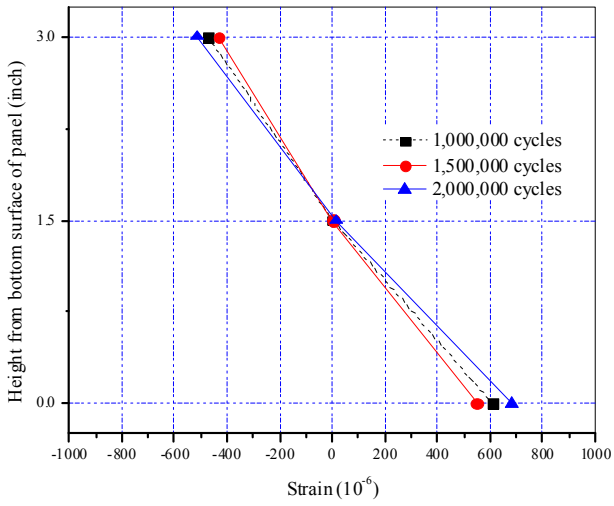

Panel ST-NC-FL

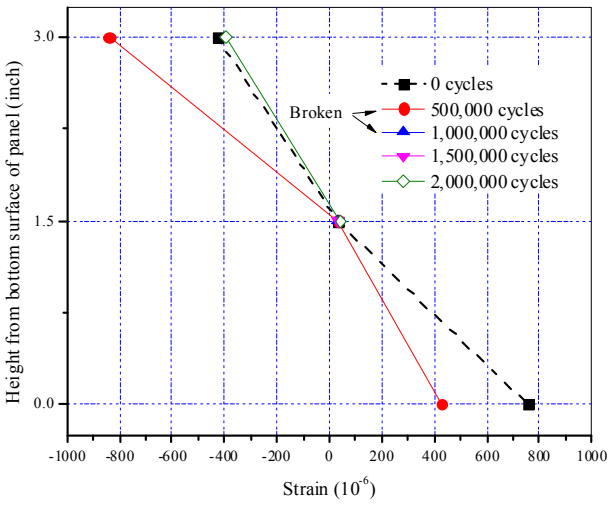

Panel ST-FRC-FL

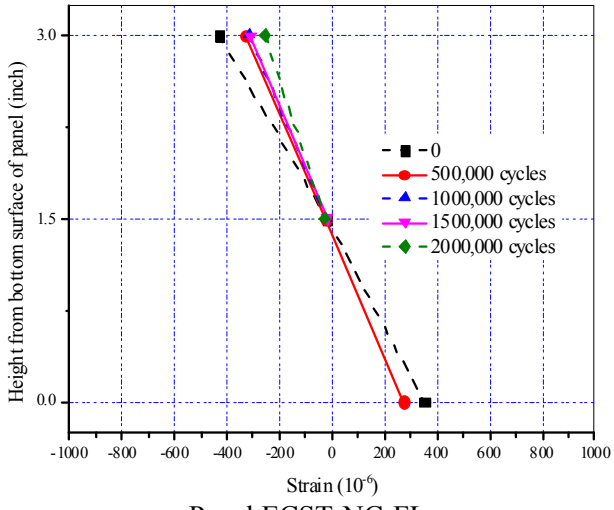

Panel ECST-NC-FL

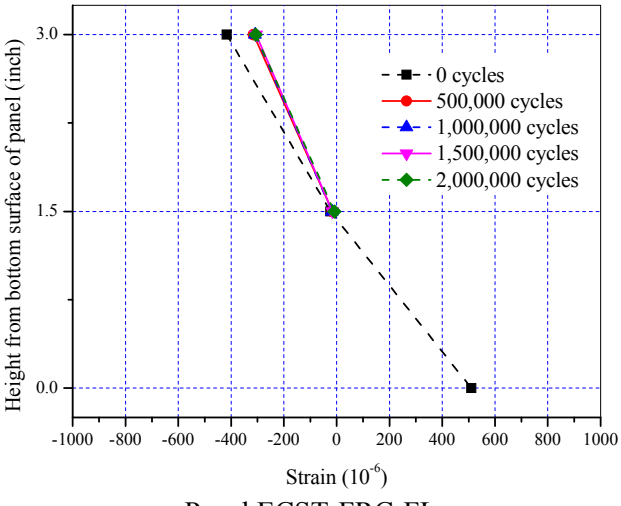

Panel ECST-FRC-FL

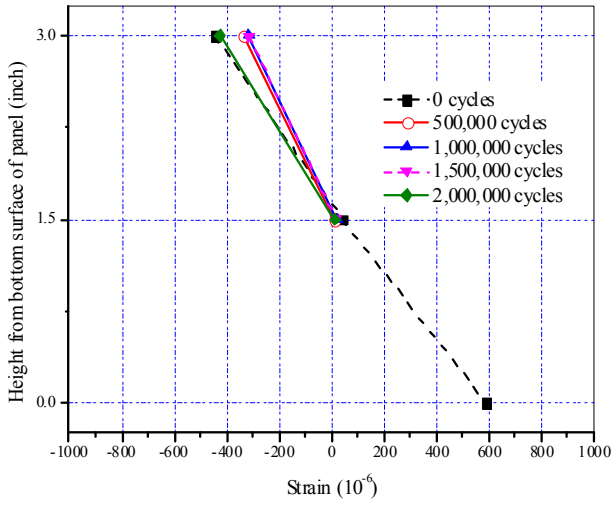

Panel CFRPT-NC-FL

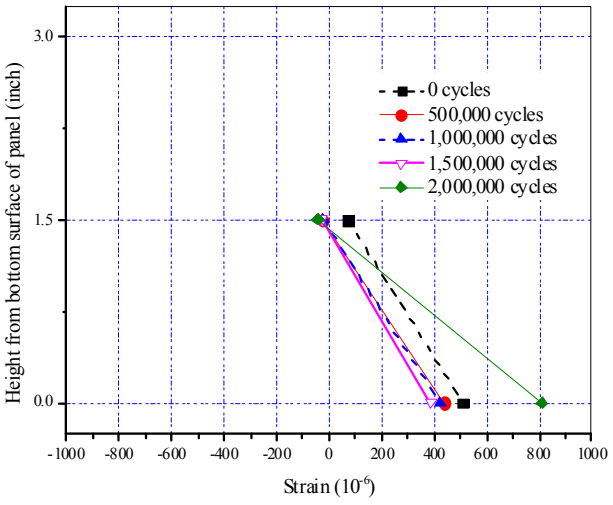

Panel CFRPT-FRC-FL

Figure 5-33 Measured Strain Profile at A-2 After Each 500,000 Cycles

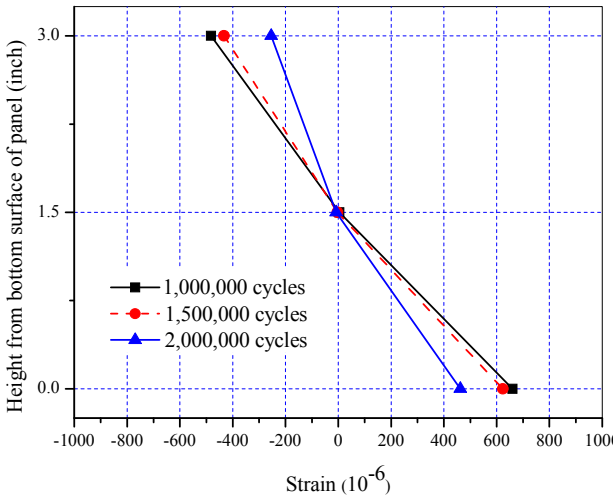

Panel ST-NC-FL

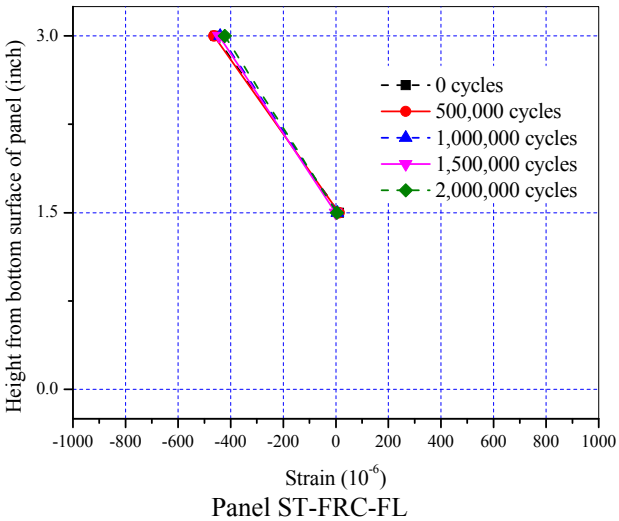

Panel ST-FRC-FL

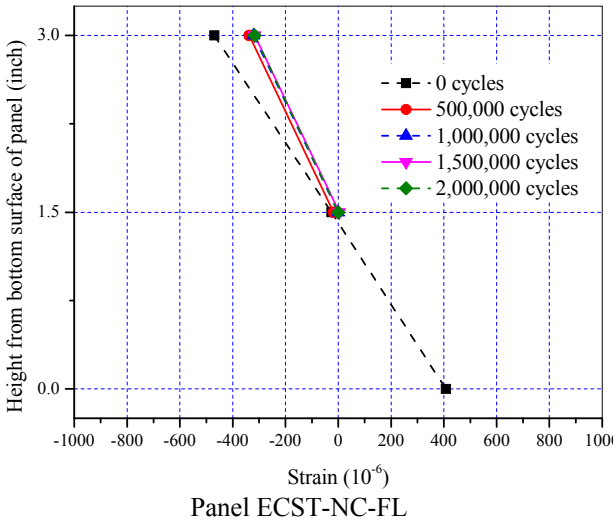

Panel ECST-NC-FL

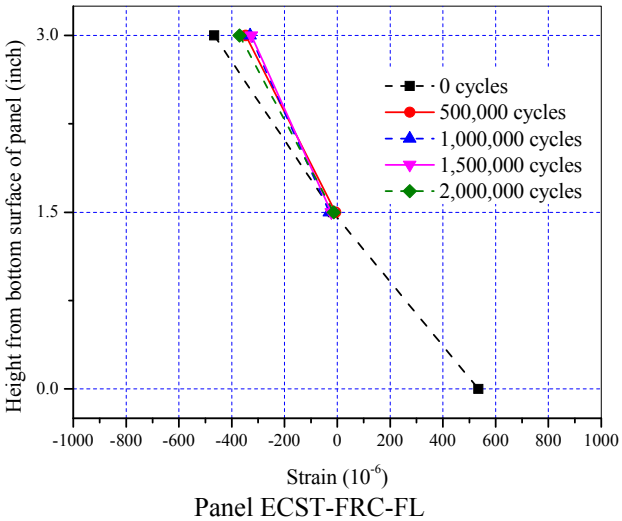

Panel ECST-FRC-FL

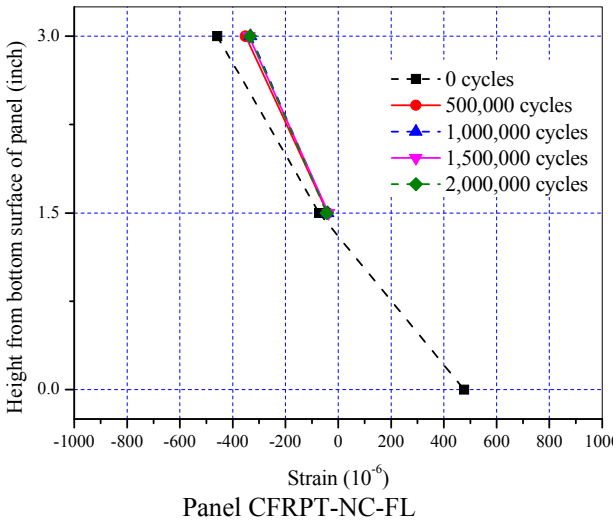

Panel CFRPT-NC-FL

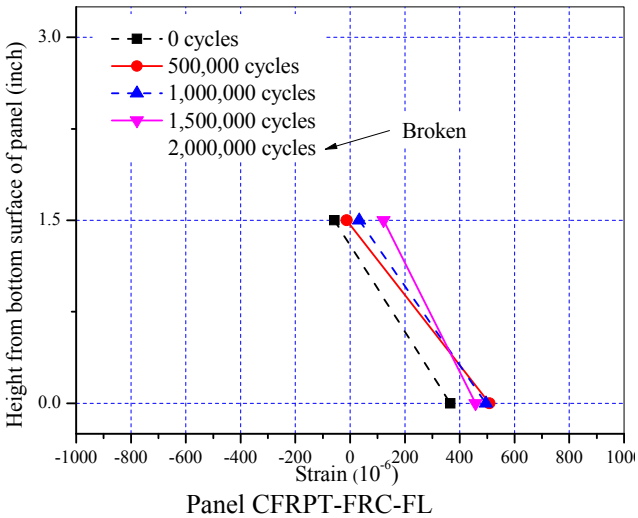

Panel CFRPT-FRC-FL

Figure 5-34 Measured Strain Profile at E-2 After Each 500,000 Cycles

Strain variations across the section

Figure 5-31, Figure 5-32, and Figure 5-33 show the representative strain profiles of all fatigue panels at the maximum applied load after each 500,000 cycles with respect to locations A-1, A-2 and E-2. Figure 5-31 and Figure 5-32 are intended to investigate the different behavior of steel, epoxy-coated steel, and CFRP edge tendons with respect to fatigue loading effect, while Figure 5-33 is provided to examine the effects of different materials on overall behavior.

Figure 5-34 and Figure 5-35 show the strain profile of all panels at locations of A-2 and E-2 with respect to the quasi-static load test after 2 million cycles. From these observations, final fatigue loading effects can be examined.

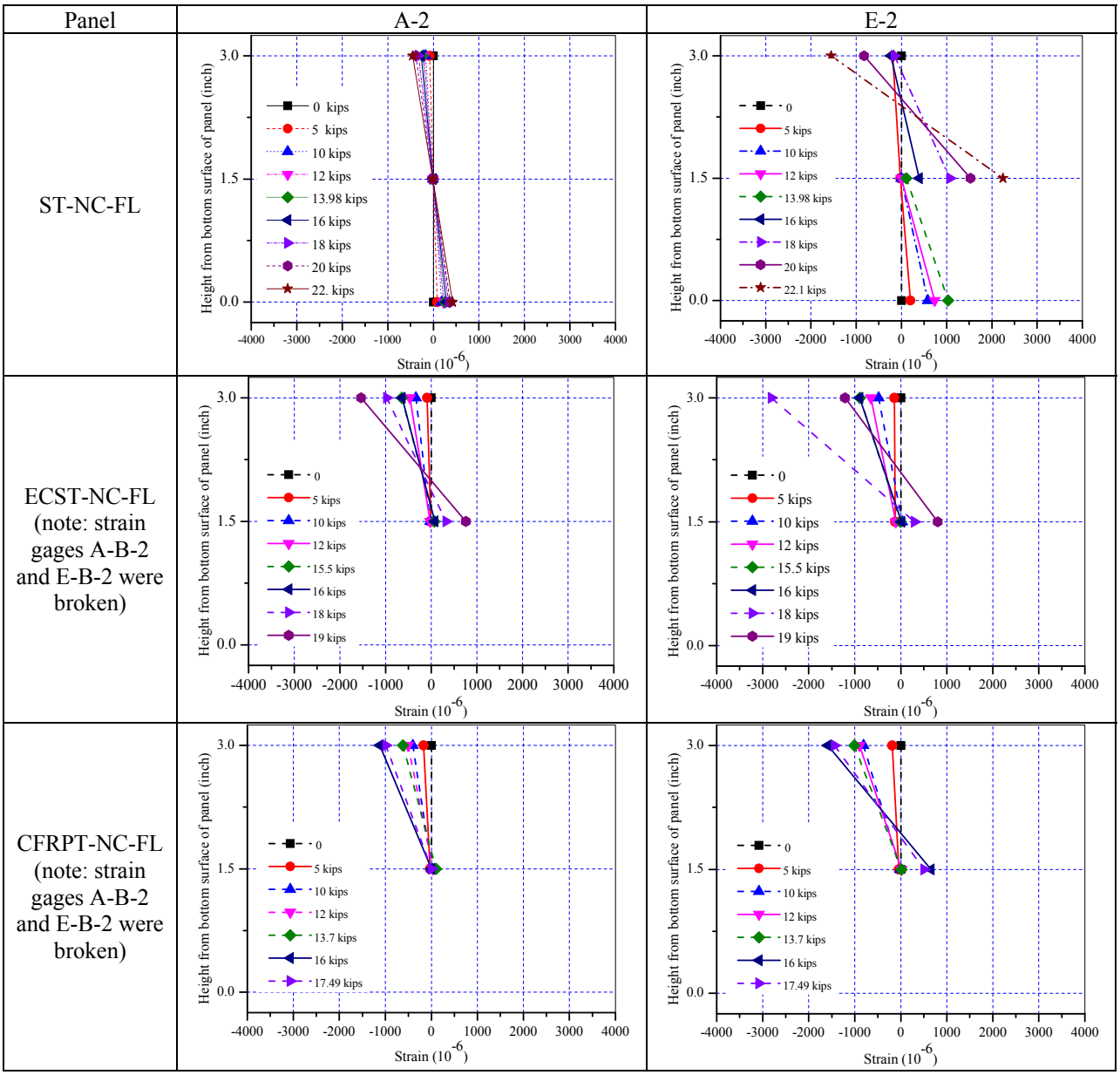

Figure 5-35 Measured Strain Profile During Quasi-static Test After 2 Million Cycles for Panels with Normal Concrete

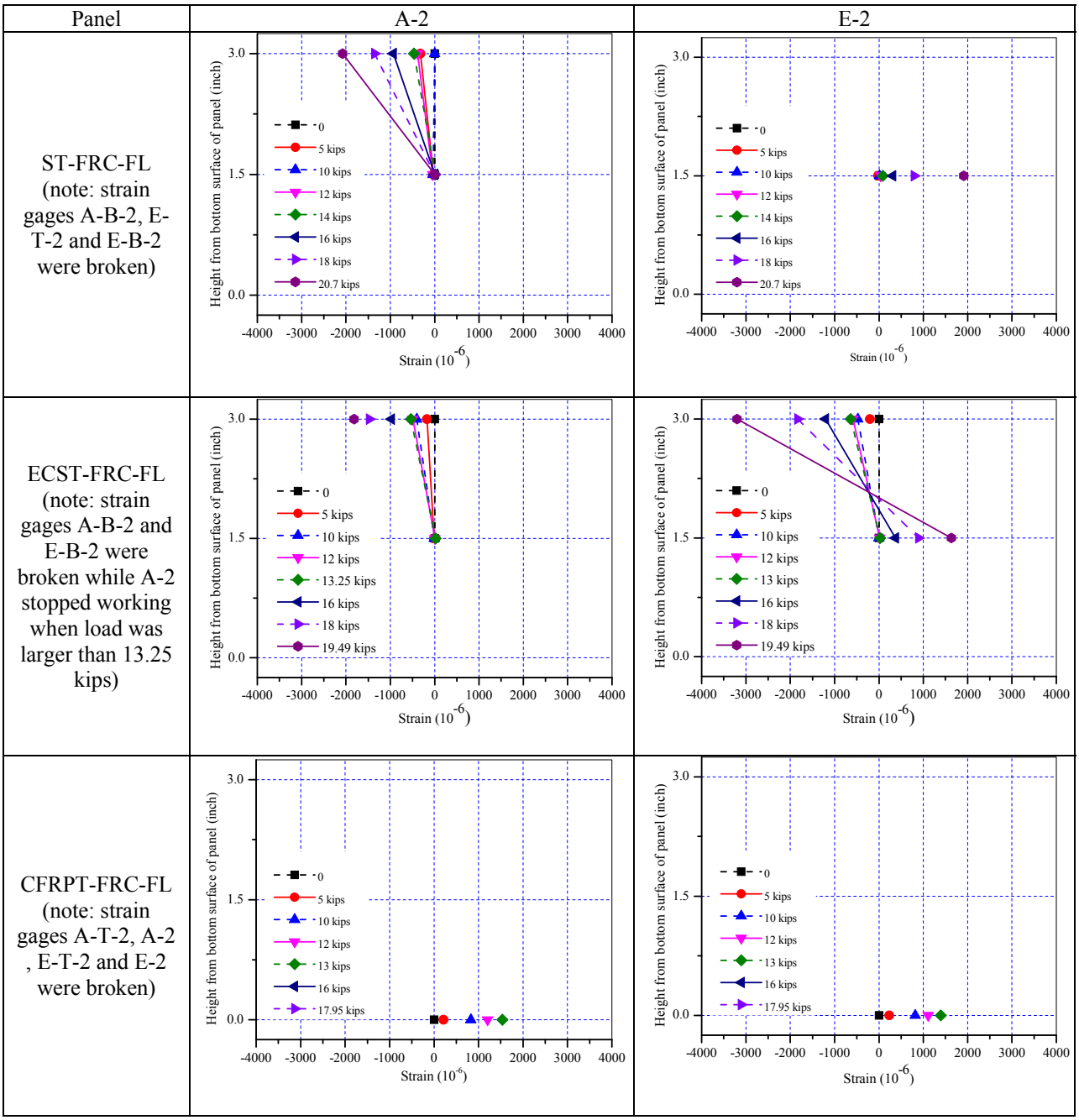

Figure 5-36 Measured Strain Profile During Quasi-static Test After 2 Million Cycles for Panels with FRC

Summary and Key Observations

In Section 5.2.4.2, the fatigue load test data were analyzed to investigate and compare the fatigue behavior of six panels including the failure mode and cracking behavior, load-displacement relationships, stiffness degradation, and load-strain relationships. Based on the discussions from Sections 5.2.4.2.1-5.2.4.2.3, the following key observations are made:

(1) All panels were able to withstand the prescribed two million cycles without failure. No cracks were observed in any of the specimens during the fatigue load cycles and the quasi-static test at each 500,000 cycle increment.
(2) At the 2 million cycle quasi-static load test to failure, the failure mode of all panels was crushing of the concrete in the flexural compression zone. Failure occurred prior to tendon yielding or rupture.
(3) Representative load-displacement relationships after two million cycles for all fatigue test specimens showed differences in panel behavior both before and after cracking. Unlike the static load test results discussed in Section 5.2.4.1.2, different cracking and maximum load and corresponding displacements were observed. These differences are attributed to stiffness degradation.
(4) Panels with normal concrete showed more stiffness degradation than panels with FRC.

5.2.4.3 Discussion

Comparison of Static and Fatigue Behavior

Table 5-8 summarizes the maximum and cracking loads and displacements for all 12 unit panel specimens (static and fatigue load panels) when tested to failure. Results in Table 5-8 compare the panel behavior in terms of ultimate performance, before and after being subjected to 2 million cycles of service load. As can be seen from the table, panels with steel and epoxy-coated steel edge tendons showed no significant differences between static and fatigue test specimens with respect to cracking and maximum load. In contrast, panels with CFRP edge tendons showed a marked reduction in maximum load. After being subjected to 2 million cycles, panels with CFRP edge tendons and normal concrete showed a 17% reduction in ultimate capacity, while panels with CFRP tendons and FRC showed a 13% reduction in ultimate capacity.

Table 5-8 Summary of Applied Load and Displacement at Cracking and Failure – Static and Fatigue Load Panels

Test Specimen	**Cracking Load (kips)**	**Cracking Displacement at Midspan (in.)**	**Maximum Load (kips)**	**Displacement at Midspan Corresponding Maximum Load (in.)**
ST-NC-FL(SL)	13.98 (13.92)	0.32 (0.35)	22.10 (22.08)	1.76 (2.14)
ST-FRC-FL(SL)	14.00 (13.79)	0.33 (0.35)	20.70 (20.25)	1.63 (1.65)
ECST-NC-FL(SL)	15.50 (14.19)	0.42 (0.35)	19.00 (18.49)	1.12 (1.05)
ECST-FRC-FL(SL)	13.25 (14.25)	0.30 (0.35)	19.49 (21.10)	1.40 (1.70)
CFRPT-NC-FL(SL)	13.70 (14.99)	0.35 (0.35)	17.49 (21.05)	1.02 (1.35)
CFRPT-FRC-FL(SL)	13.00 (14.06)	0.35 (0.35)	17.95 (20.70)	1.33 (1.70)
AVERAGE	**13.91 (14.20)**	**0.35 (0.35)**	**19.46 (20.61)**	**1.38 (1.60)**

Results in Table 5-8 show marked reductions in maximum displacement for all panels after being subjected to 2 million cycles. This phenomenon can be attributed to the accumulated damage in the fatigue test specimens. Detailed explanation and background data about this phenomenon is discussed in Section 5.2.4.2 in terms of serviceability performance for each individual fatigue test panel, since panels were cycled within the elastic range.

Figure 5-36 (a)-(f) shows the load-displacement comparison of static and fatigue unit panels. The displacement is shown for location E-2 (center of panel). One main difference in behavior is the ductility of the panels with most fatigue panels exhibiting a decrease in displacement corresponding to maximum load than their corresponding static panels. The decrease in maximum displacement is more marked in panels with normal concrete than those with FRC.

As shown in Figure 5-36 (a), Panel ST-NC-SL and Panel ST-NC-FL have similar stiffness before cracking, with similar cracking loads and corresponding displacements. Panel ST-NC-SL has a larger maximum displacement than ST-NC-FL, however, although they have similar maximum loads. As shown in Figure 5-36 (b), Panel ST-FRC-SL and Panel ST-FRC-FL have similar stiffness before cracking, with similar cracking loads and corresponding displacements. Additionally, they have similar maximum loads and corresponding displacements. As shown in Figure 5-36 (c), Panel ECST-NC-FL has a smaller stiffness before cracking than Panel ECST-NC-SL with similar maximum loads and corresponding displacements. As shown in Figure 5-36 (d), Panel ECST-FRC-FL has a slightly smaller stiffness before cracking than Panel ECST-FRC-SL. In addition, Panel ECST-FRC-FL has 7% lower maximum load and 18% smaller corresponding displacement, which indicates that it has lower strength and ductility. As shown in Figure 5-36 (e), Panel CFRPT-NC-FL has a slightly smaller stiffness before cracking than Panel CFRPT-NC-SL, while cracking loads and displacements are almost the same for these two panels. In addition, Panel CFRPT-NC-FL has 14% lower maximum load and 13% smaller maximum displacement than Panel CFRPT-NC-SL. As shown in Figure 5-36 (f), Panel CFRPT-FRC-FL has a slightly smaller stiffness before cracking than CFRPT-FRC-SL, while cracking loads and displacements are almost the same for these two panels. In addition, Panel CFRPT-FRC-FL has 14% lower strength and 24% smaller maximum displacement than Panel CFRPT-NC-SL.

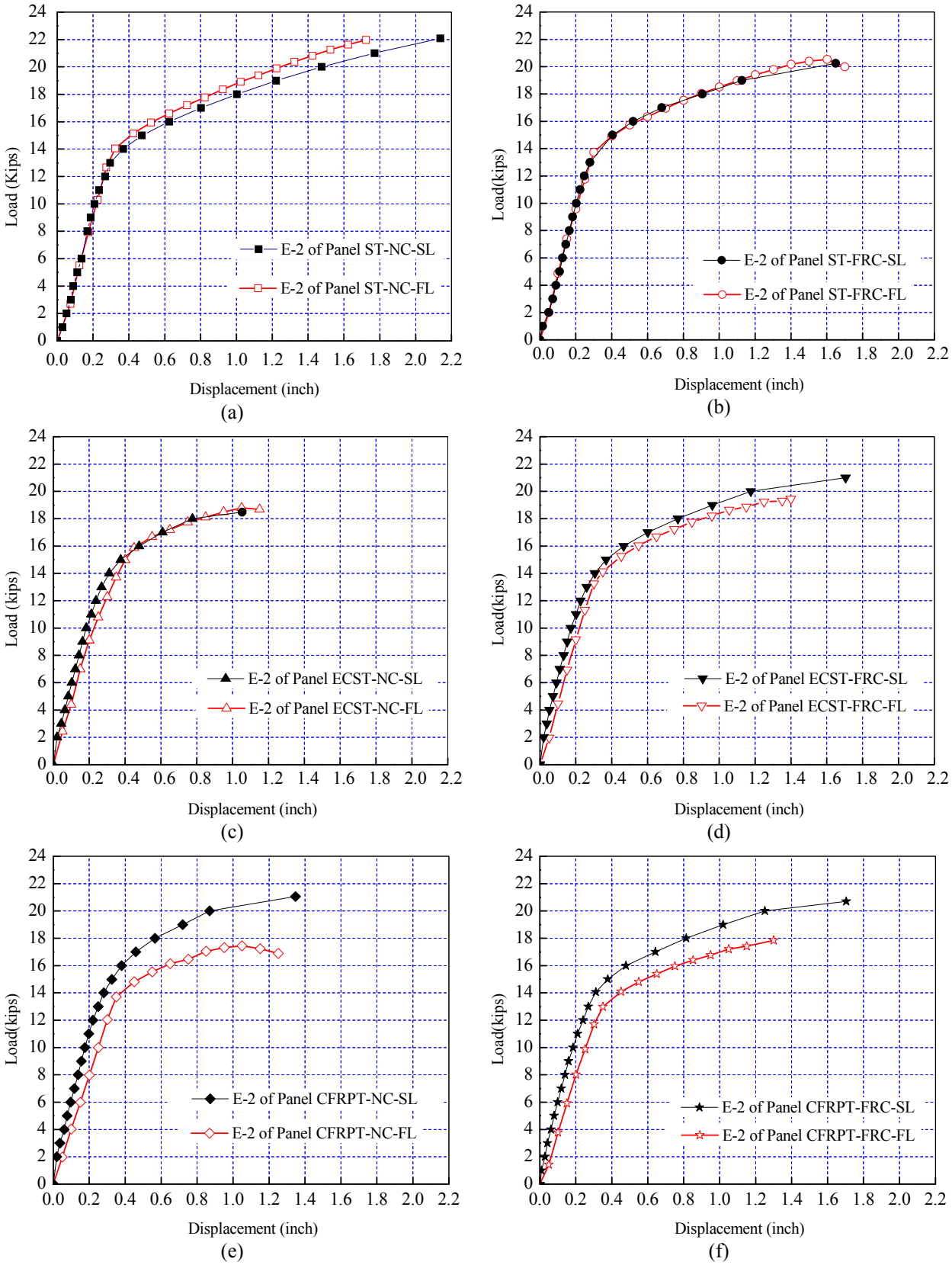

Figure 5-37 Load-displacement Comparison of Static and Fatigue Unit Panels

Comparison of Panels with Different Edge Tendon Types

With respect to the panels with epoxy-coated steel edge tendons, results show that the static and fatigue structural performance under service load conditions of panels with epoxy-coated steel edge tendons is comparable to the panels with steel edge tendons. Similar to the panels with steel edge tendons, panels with epoxy-coated steel edge tendons were able to withstand the prescribed two million cycles without failure. No cracks were observed during the fatigue load cycles and the quasi-static test at each 500,000 cycle increment. When tested to failure, the failure mode for the static and fatigue specimens was the same as that of the control specimens. Panels with epoxy-coated steel edge tendons, however, showed a marked reduction in maximum load, maximum displacement, and ductility as compared to the panels with steel edge tendons (with the exception of ECST-FRC-SL).

Panels with epoxy-coated steel edge tendons showed no significant differences between static and fatigue test specimens with respect to cracking and maximum load. Marked reductions in maximum displacement were observed after the panels had been subjected to 2 million cycles. This phenomenon is attributed to the accumulated damage in the fatigue test specimens. Panels with normal concrete showed more stiffness degradation than panels with FRC.

For panels with CFRP edge tendons, results show that the static and fatigue structural performance under service load conditions of panels with CFRP edge tendons is comparable to the panels with steel edge tendons. Similar to the panels with steel edge tendons, panels with CFRP edge tendons were able to withstand the prescribed two million cycles without failure. No cracks were observed during the fatigue load cycles and the quasi-static test at each 500,000 cycle increment. When tested to failure, the failure mode for the static and fatigue specimens was the same as that of the control specimens. Panels with CFRP edge tendons, however, showed a marked reduction in maximum load, maximum displacement, and ductility as compared to the panels with steel edge tendons.

Panels with CFRP edge tendons showed a marked reduction in maximum load after being subjected to 2 million cycles. Panels with CFRP edge tendons and normal concrete showed a 17% reduction in ultimate capacity, while panels with CFRP tendons and FRC showed a 13% reduction in ultimate capacity. Marked reductions in maximum displacement were also observed after the panels had been subjected to 2 million cycles. This phenomenon is attributed to the accumulated damage in the fatigue test specimens. Panels with normal concrete showed more stiffness degradation than panels with FRC.

5.3 Durability Experiments

5.3.1 Introduction

The goal of the durability experiments was to investigate the effects of the parameters considered, including edge distance to reinforcement, fiber usage, and corrosion inhibitor usage, on the durability of the panel. In addition, other parameters of interest were influence of NaCl content, wet-dry cycle effects, and time. Two types of tests, initiation corrosion and accelerated corrosion tests, were planned and carried out to accommodate all parameters considered as shown in Table 5-9.

Table 5-9 Test Matrix for Durability Experiments

Specimen Type	Parameter		Purpose(s)	Variables	Number of Specimens
Accelerated Corrosion Specimens	NaCl Content		▪ Acceleration of corrosion ▪ Representation of carbonized concrete	▪ 3 %	1
	Edge distance		▪ Prohibition of horizontal crack propagation	▪ 1.5 in. ▪ 2.5 in. ▪ 3.5 in.	3
	Concrete	Normal Concrete	▪ Comparison with enhanced concrete mixtures (FRC and corrosion inhibitor)	-	3
		FRC	▪ Reduction of crack propagation by increasing tensile strength of concrete	-	
		Corrosion Inhibitor	▪ Retard corrosion	-	
	BASIC NUMBER OF TEST SPECIMENS				**9**
	Testing Time Increments		▪ Investigation of corrosion rate and crack propagation	▪ 6 months	2
	NUMBER OF TEST SPECIMENS				***18***
Corrosion Initiation Specimens with Wet/Dry Cycles	NaCl Content		▪ Acceleration of corrosion ▪ Representation of carbonized concrete	▪ 0 %	1
	Edge distance[1]		▪ Prohibition of horizontal crack propagation	▪ 1.5 in. ▪ 2.5 in. ▪ 3.5 in.	3
	Concrete	Normal Concrete	▪ Comparison with enhanced concrete mixtures (FRC and corrosion inhibitor)	-	3
		FRC	▪ Block the concrete voids and retard corrosion	-	
		Corrosion Inhibitor	▪ Retard corrosion	-	
	Testing Time Increments		▪ Measure the chloride content	▪ 2 months ▪ 4 months ▪ 6 months	3
	NUMBER OF TEST SPECIMENS				***27***
TOTAL NUMBER OF TEST SPECIMENS					***45***

5.3.2 Test Specimens

The corrosion initiation test was carried out to investigate the effects of the parameters considered on time of corrosion initiation indicated as $t_{initiation}$ in Figure 5-38. The accelerated corrosion test was purposed to investigate the corrosion process after $t_{initiation}$, and especially the end state of corrosion, $t_{spalling}$. It was expected that the addition of corrosion inhibitor would be mostly effective for retarding the initial corrosion resulting in an increase in the length of the 1st phase (i.e. increase in $t_{initiation}$), while usage of FRC would be more effective in the 2nd and 3rd phases. The increase in edge distance was expected to increase the length of the 3rd phase resulting in an increase in $t_{spalling}$.

A total of forty-five test specimens were fabricated for the corrosion initiation and accelerated corrosion tests. All specimens were 11 in. long and 3 in. high with different widths to accommodate a variation in edge distance to the centerline of the reinforcement (1.5, 2.5, 3.5 in.). Specimen height was consistent with the MoDOT specified panel thickness (3 in.). Specimen length (11 in.) was consistent with the standard specimen size of ASTM G 109-07. Detailed information about the specimen dimensions is provided in Appendix C.

Specimen ID was assigned according to edge distance, type of concrete, and specimen number in the form of "SP edge distance – concrete type – specimen number". In the first term, SP 1, 2 or 3 corresponded to the edge distance of 1.5 in., 2.5., or 3.5 in., respectively. In the second term, normal, fiber reinforced, or corrosion inhibitor concrete were labeled as NC, FRC, or CI, respectively. Third term represents the specimen number within the set of duplicate test specimens.

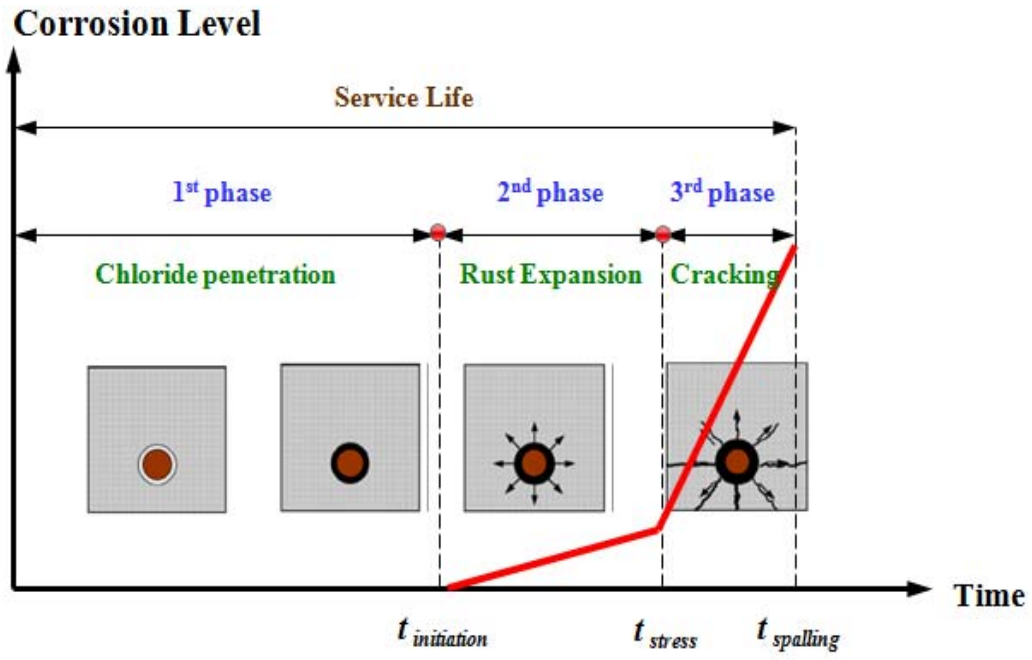

Figure 5-38 Corrosion Process as a Function of Time

5.3.3 Test Procedure

5.3.3.1 Test Setup

Twenty-seven test specimens were included in the corrosion initiation test. In this test program, content of NaCl was excluded from the inventory of parameters to examine only the effects of geometrical conditions and different materials. Test specimens were submerged in 5% NaCl solution as shown in Figure 5-39 to simulate a severe environmental condition. This test setup was developed based on experimental works by Hamid (2004). Waterproof epoxy coatings (Fosroc-Nitoflor FC 140 and Duromar 2510) were used to coat both the top and bottom surface of the test specimens to promote uniform chloride penetration within the immersed portion of the specimens. The corrosion initiation test specimens were also subjected to wet/dry cycles, where each cycle lasted seven days. The specimens were kept in solution for four days, then dried in an oven for three days at 104 ºF, which corresponds to the average highest temperature in Missouri during the summer.

Accelerated corrosion testing was performed on eighteen specimens containing 3% NaCl in the concrete mixture subjected to 0.4 mA of current for 4400 hours submerged in a 5% NaCl solution. The corrosion process was accelerated by inducing a current into the specimens using the anode and the cathode electrochemical concept. Embedded steel tendons were used as an anode, and 0.5 in. graphite rods were used as a cathode as shown in Figure 5-39. In this test, the epoxy coating was applied only to the bottom surface of the test specimen to prohibit the chloride ingress from the bottom surface as well as to ensure ingress from the side surfaces. The applied current was determined from typical current densities ranging from 200 to 3,000 μA/cm^2 (1,290 to 19,355 μA/in^2) based on the study by Tamer and Khaled (2003).

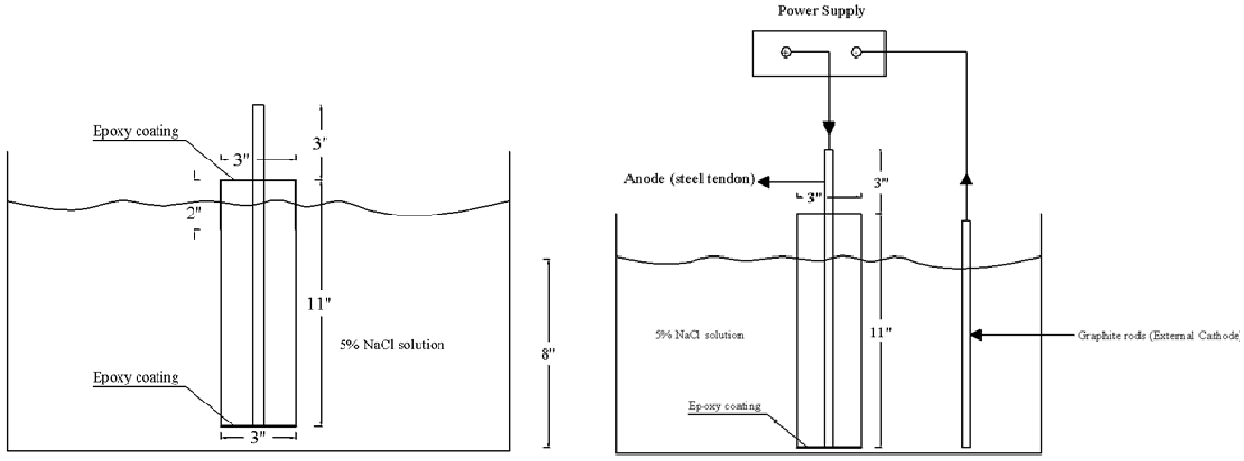

Corrosion initiation test Accelerated corrosion test

Figure 5-39 Test Set-Ups for Corrosion Initiation and Accelerated Corrosion Tests

5.3.3.2 Measurement systems

Half-cell potential and chloride ion content measurements are the most common methods used in measuring the corrosion initiation state. Thus for the corrosion initiation specimens, the half-cell potential test was conducted every two weeks, and chloride content was measured every two months by taking sample cores from all test specimens according to ASTM C1218/ C 1218M-99. After 6 months of wet/dry cycles in the corrosion initiation test, steel loss was measured by a

gravimetric method together with a visual inspection. In the accelerated corrosion test, a weekly visual inspection was carried out to record the cracking and spalling time. Steel loss was also measured at the end of the accelerated corrosion test.

Half-Cell Potential Test

The corrosion process is an electrochemical process that induces current flow from the anode to the cathode. From this current flow, electrical potentials can be measured by the half-cell potential test according to the method specified in ASTM C876-91. Measurements were conducted every two weeks, and Table 5-10 was used to interpret the results.

Table 5-10 Interpretation of Half-Cell Potential Results (ASTM C876-91)

E (Cu/CuSO4)	Probability of Corrosion
>- 200 mV	Corrosion probability is less than 5%
-350 to -200 mV	Corrosion probability equals 50%
< -350 mV	Corrosion probability is more than 90%

Chloride Ion Content Analysis

When the chloride concentration reaches a threshold value, corrosion can initiate. Sohanghpurwala (2006) reported this threshold value as 0.025% to 0.033% of concrete weight, while Smith and Virmani (2000) reported a threshold value of 0.71 kg/m^3 (1.2 lb/yd^3). In case of absence of an initial corrosion record, the chloride profile (chloride concentration variation with depth) can provide important information about the diffusion rate, which is used to calculate the required time for exceeding the threshold value of corrosion initiation.

There are two main types of chloride ion tests. The first is the acid soluble test, which is used to determine the total chloride content in the concrete. The second is the water-soluble test, which is used to provide the chloride ion content in the pore water. In this test program, the water soluble test was used to measure the chloride content at different depths according to ASTM C1218/ C 1218M- 99. Measuring the chloride at different depths provides important information for availability of chloride amount required to initiate corrosion and source of chloride in the concrete.

Gravimetric Method

The gravimetric method was applied to both the corrosion initiation and accelerated corrosion specimens. The gravimetric method requires measuring the weight of the steel before concrete casting and after testing. The current and the time duration of the accelerated corrosion test were then used to determine the corrosion rate.

5.3.4 Test Results

This section includes a summary of the experimental results of the durability test specimens. Additional information is included in Appendix C.

5.3.4.1 Corrosion Initiation Test

Visual Inspection

After six months of wet/dry cycles, a visual inspection was conducted to observe the concrete deterioration. The main types of concrete deterioration observed in the visual inspection were efflorescence, rust, and cracking. Table 5-11 shows the deterioration observed in specimens with 1.5 in. edge distance. All test specimens showed the efflorescence on the surface due to the salt solution as shown in Figure 5-40. Rust was also observed in most of specimens, while cracks were observed in all specimens except those with normal concrete. As shown in the Figure 5-41, superficial cracks were observed on either the side or bottom surfaces. Because these cracks did not propagate from the steel location, they were believed to be shrinkage cracks due to wet/dry cycles, not corrosion-induced cracks.

Table 5-11 Visual Inspection for Corrosion Initiation Specimens with 1.5 in. Edge Distance

Specimen Designation	Concrete Deterioration		
	Efflorescence	Rust	Cracking
SP1-NC-1	X		
SP1-NC-2	X	X	
SP1-NC-3	X	X	
SP1-CI-1	X	X	X
SP1-CI-2	X	X	X
SP1-CI-3	X	X	X
SP1-FRC-1	X	X	X
SP1-FRC-2	X	X	X
SP1-FRC-2	X	X	X

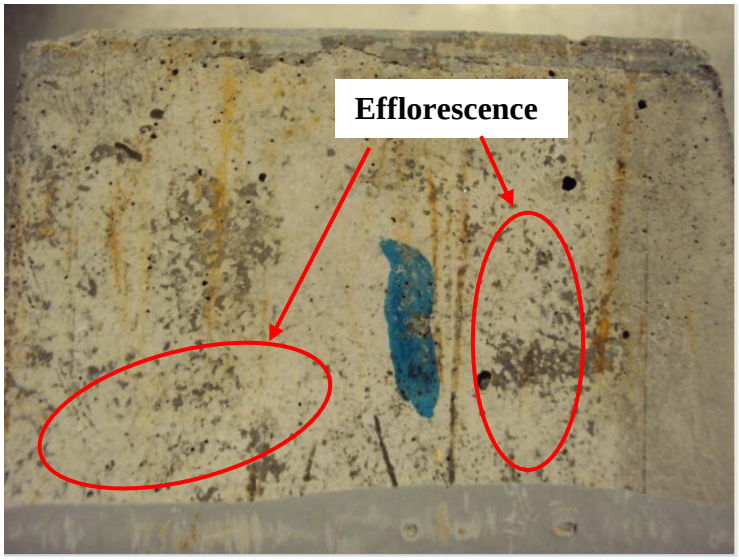

Figure 5-40 Efflorescence in Corrosion Specimen (SP1-NC-2)

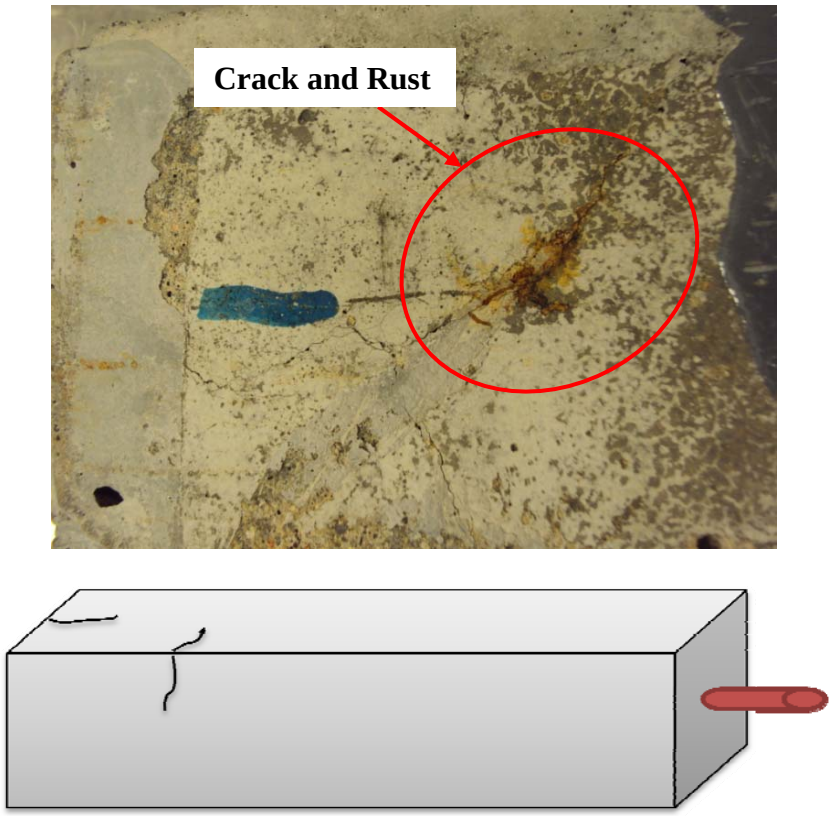

Figure 5-41 Rust and Crack in Corrosion Specimen (SP1-FRC-1)

Table 5-12 shows the deterioration observed in specimens with 2.5 in. edge distance. Similar to the test specimens with 1.5 in. edge distance, all specimens showed efflorescence at the surface as shown in Figure 5-42. Rust and cracks were observed only in specimens containing corrosion inhibitor. Crack patterns observed in SP2-CI-7 was similar to that observed in the test specimens with 1.5 in. edge distance as shown in Figure 5-43.

Table 5-12 Visual Inspection for Corrosion Initiation Specimens with 2.5 in. Edge Distance

Specimen Designation	Concrete Deterioration		
	Efflorescence	Rust	Cracking
SP2-NC-5	X		
SP2-NC-6	X		
SP2-NC-7	X		
SP2-CI-5	X	X	
SP2-CI-6	X		
SP2-CI-7	X	X	X
SP2-FRC-5	X		
SP2-FRC-6	X		
SP2-FRC-7	X		

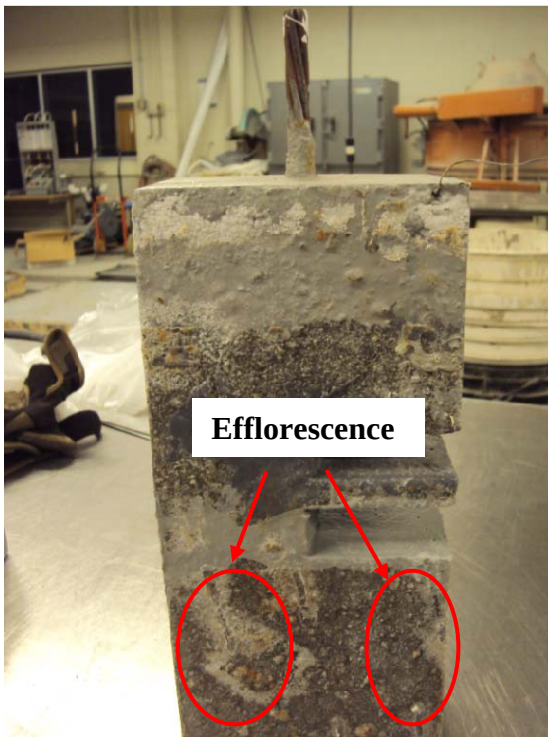

Figure 5-42 Efflorescence in Corrosion Specimen (SP2-NC-5)

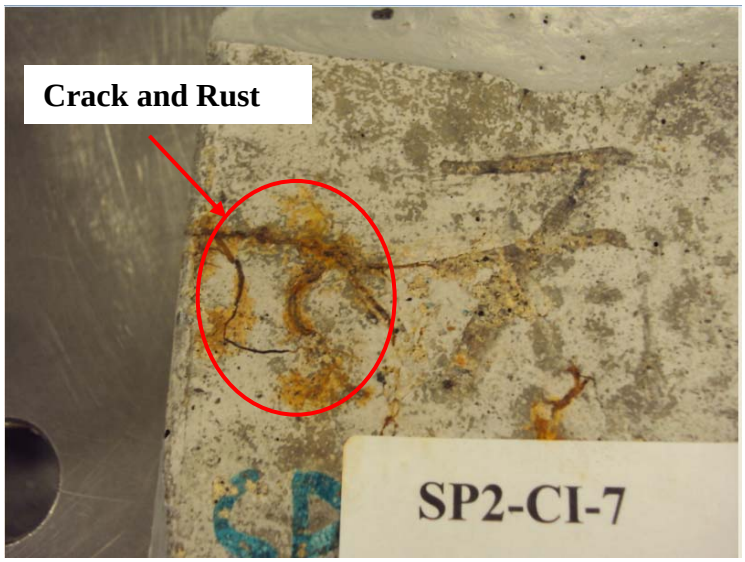

Figure 5-43 Rust and Crack in Corrosion Specimen (SP2-CI-7)

As shown in Table 5-13, specimens with edge distance of 3.5 in. showed results similar to the specimens with 2.5 in. edge distance. Efflorescence was observed in all specimens as shown in Figure 5-44. Only specimens containing corrosion inhibitor showed rust and cracks as shown in Figure 5-45.

Table 5-13 Visual Inspection for Corrosion Initiation Specimens with 3.5 in. Edge Distance

Specimen Designation	Concrete Deterioration		
	Efflorescence	Rust	Cracking
SP3-NC-9	X		
SP3-NC-10	X		
SP3-NC-11	X		
SP3-CI-9	X	X	X
SP3-CI-10	X	X	
SP3-CI-11	X		
SP3-FRC-9	X		
SP3-FRC-10	X		
SP3-FRC-11	X		

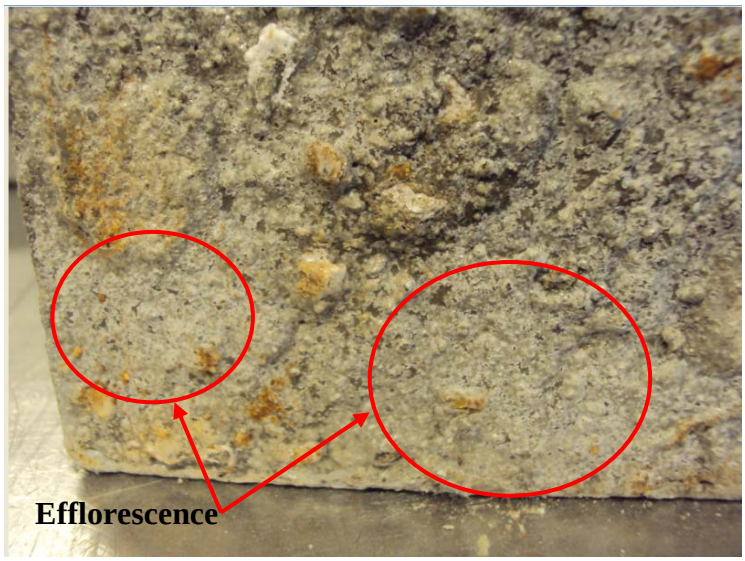

Figure 5-44 Efflorescence in Corrosion Specimen (SP3-CI-10)

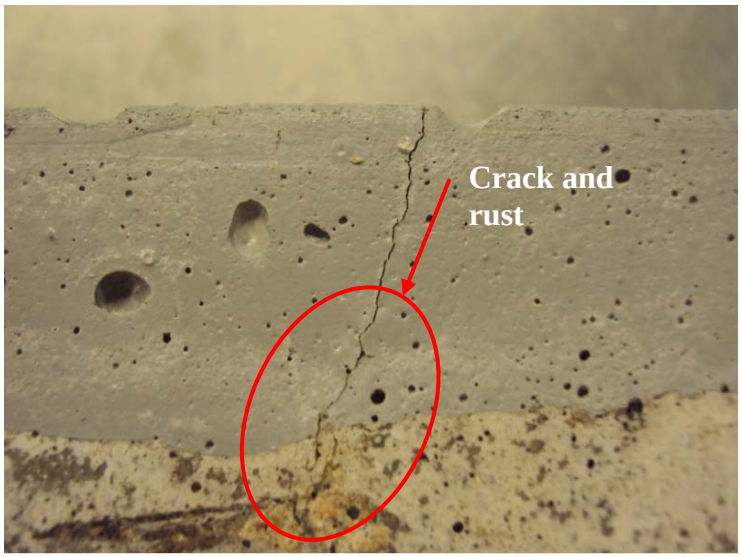

Figure 5-45 Rust and Crack in Corrosion Specimen (SP3-CI-9)

Based on observations from all corrosion initiation specimens, it is apparent that the addition of corrosion inhibitor affects the environmental response of the concrete. In comparison to specimens with corrosion inhibitor, specimens with FRC showed better environmental performance. These different performances can be attributed to the inherent material characteristics. Corrosion inhibitor changes the chemical composition of the concrete, while fiber changes the mechanical properties of the concrete. Thus, careful usage of corrosion inhibitor in severe weather condition is required.

Gravimetric Study

Although corrosion-induced cracks were not observed in the corrosion initiation test specimens, corroded tendons were retrieved and measured to determine the corrosion level. Cleaning and preparing the steel tendons followed the method given in ASTM G1-03. Table 5-14 summarizes test results. As shown in the Table 5-14, steel losses in all test specimens are mostly negligible to induce the cracking around the tendons. Broomfield (2007) suggested a threshold value for corrosion-induced cracking of 100 μm/cm. None of initiation corrosion test specimens reached this value, and no significant corrosion cracks were observed in this test.

Table 5-14 Steel Loss Calculations for Corrosion Initiation Specimens

Specimen I.D.	Initial Mass lb (g)	Final Mass lb (g)	Loss (%)
SP1-NC-1	0.313 (142.0)	0.311 (141.1)	1
SP1-NC-2	0.313 (142.0)	0.307 (139.3)	2
SP1-NC-3	0.313 (142.0)	0.313 (142.0)	0
SP1-CI-1	0.313 (142.0)	0.312 (141.5)	0
SP1-CI-2	0.310 (140.6)	0.310 (140.6)	0
SP1-CI-3	0.313 (142.0)	0.310 (140.6)	1
SP1-FRC-1	0.310 (140.6)	0.310 (140.6)	0
SP1-FRC-2	0.313 (142.0)	0.313 (142.0)	0
SP1-FRC-3	0.309 (140.2)	0.309 (140.2)	0
SP2-NC-5	0.309 (140.2)	0.310 (140.6)	0
SP2-NC-6	0.313 (142.0)	0.310 (140.6)	1
SP2-NC-7	0.310 (140.6)	0.307 (139.3)	1
SP2-CI-5	0.312 (141.5)	0.311 (141.1)	0
SP2-CI-6	0.312 (141.5)	0.312 (141.5)	0
SP2-CI-7	0.312 (141.5)	0.312 (141.5)	0
SP2-FRC-5	0.312 (141.5)	0.311 (141.1)	0
SP2-FRC-6	0.313 (142.0)	0.311 (141.1)	1
SP2-FRC-7	0.311 (141.1)	0.309 (140.2)	1
SP3-NC-9	0.310 (140.6)	0.308 (139.7)	1
SP3-NC-10	0.313 (142.0)	0.311 (141.1)	1
SP3-NC-11	0.311 (140.6)	0.310 (140.6)	0
SP3-CI-9	0.312 (141.5)	0.311 (140.6)	0
SP3-CI-10	0.313 (142.0)	0.313 (142.0)	0
SP3-CI-11	0.310 (140.6)	0.310 (140.6)	0
SP3-FRC-9	0.313 (142.0)	0.312 (141.5)	0
SP3-FRC-10	0.314 (142.4)	0.312 (141.5)	1
SP3-FRC-11	0.312 (141.5)	0.310 (140.6)	1

Half-Cell Potential Measurement

Half-cell potential measurements were conducted every two weeks to determine the probability of corrosion according to ASTM C876-91. Figure 5-46 shows the relationship between corrosion potential and time for test specimens constructed with the same concrete type. Values above the dashed horizontal line in the figure have a corrosion probability of less than 5%, values between the dashed and solid lines have a 50% corrosion probability, while values lower than the solid horizontal line have a corrosion probability of more than 90% in accordance with Table 5-10. Irrespective of material properties, all test specimens showed values lower than the threshold value of 5% corrosion probability. That is, all specimens had at least 50% corrosion probability. As time increased, some specimens showed 90% corrosion probability, especially specimens

containing corrosion inhibitor after 8 weeks. Although there are some fluctuations in the data, increasing edge distance showed beneficial effects overall.

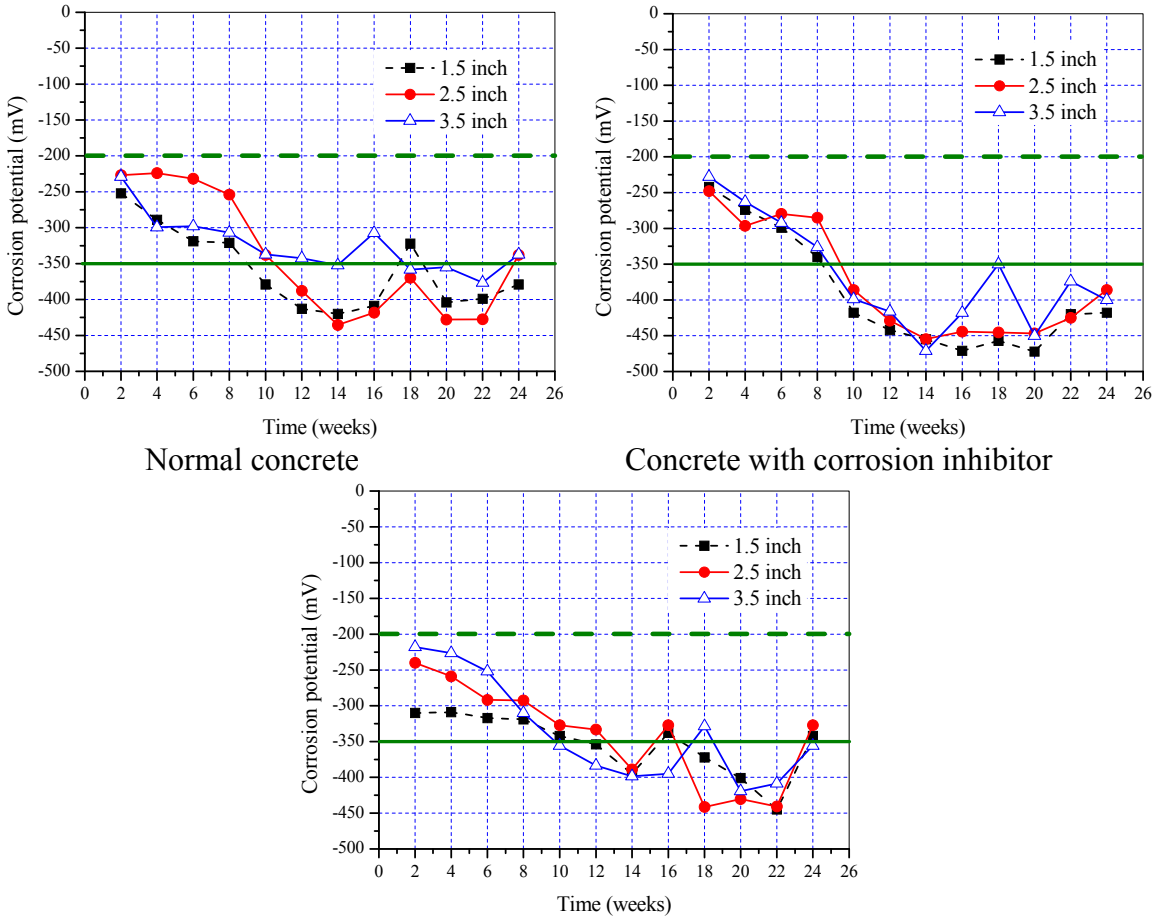

Normal concrete

Concrete with corrosion inhibitor

Concrete with fibers

Figure 5-46 Corrosion Potential vs. Time Curve for Concrete Property

Figure 5-47 shows the relationship between corrosion potential and time for specimens with the same edge distance. Specimens containing the corrosion inhibitor showed the highest corrosion probability, while there are no significant differences between normal and fiber reinforced concrete.

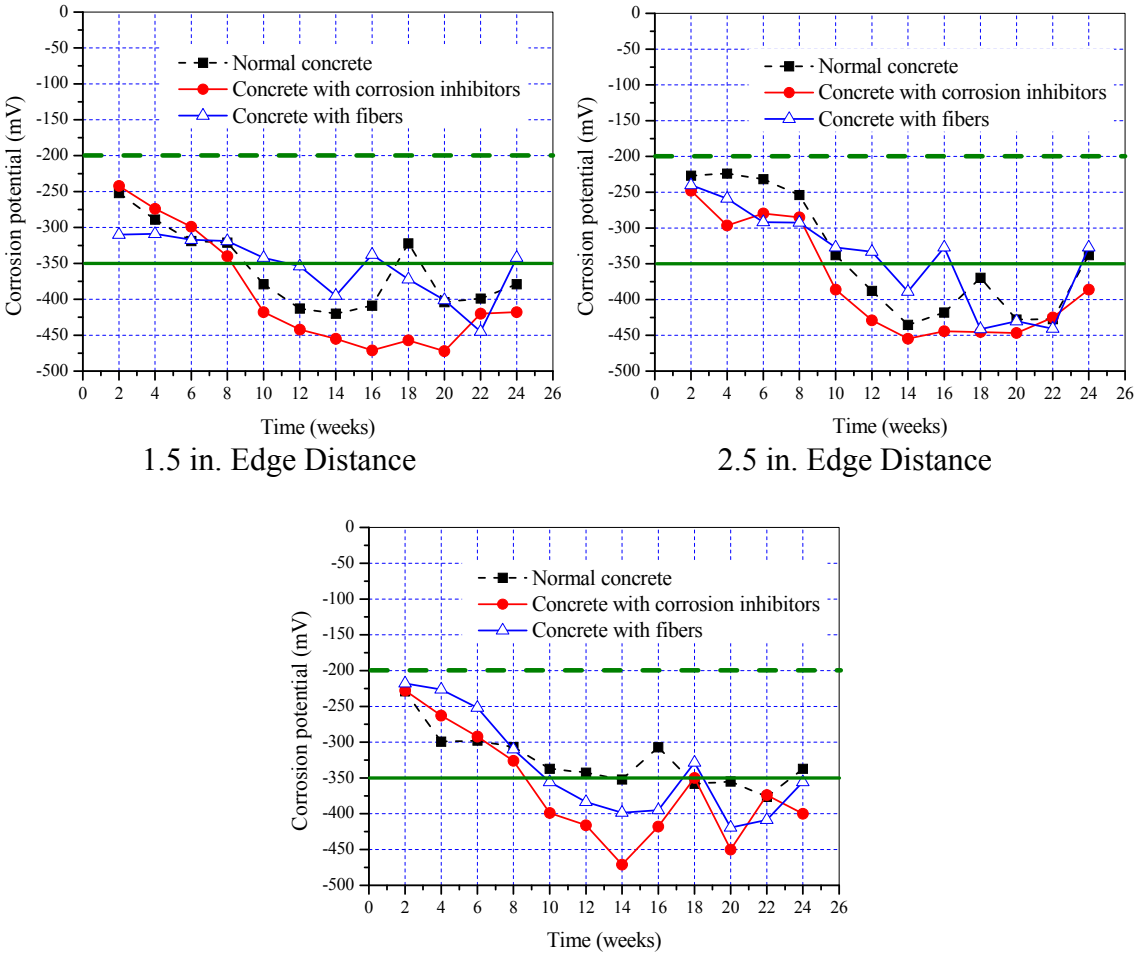

Figure 5-47 Corrosion Potential vs. Time Curve for Edge Distance

Analysis of Chloride Ion Test

It is significant to measure the chloride content at different times to examine whether the chloride content is enough to initiate corrosion of the reinforcement. Detailed analysis was made by measuring the chloride content every two months at different locations including 0.5 in. from the surface, mid-distance between the surface and steel location, and at the steel location.

The chloride ion content test at two months was conducted by MoDOT. Chloride contents at different distances from the exposed surface were reported as parts per million (ppm) of chloride. ACI 222R (2001) specifies that at least 330 ppm of chloride in concrete is required to initiate corrosion in concrete.

Table 5-15 shows the chloride contents at 0.5 in. from the exposed surface and at the steel tendon locations. The table shows that all specimens exceeded the threshold value of corrosion initiation.

Table 5-15 Chloride Content in Concrete at Two Months

Specimen I.D.	Chloride at 0.5 in. Depth (ppm)	Chloride at Steel Location (ppm)
SP1-NC	5,061	X
SP1-CI	4,098	731
SP1-FRC	4,301	X
SP2-NC	2,981	1,228
SP2-CI	5,352	4,616
SP2-FRC	6,276	3,206
SP3-NC	1,867	1,911
SP3-CI	2,542	1,868
SP3-FRC	2,266	693

Four-month chloride tests were conducted in Missouri S&T using rapid chloride test (RCT) equipment. The unit of measurement used in this chloride test was percentage of chloride by concrete weight. The threshold range for corrosion initiation is 0.025% to 0.033% (Ali 2006). As shown in the Table 5-16, all of the specimens exceeded the threshold ranges regardless of location.

Table 5-16 Chloride Content in Concrete at Four Months

Specimen I.D.	Chloride at 0.5 in. Depth (%)	Chloride at Steel Location (%)
SP1-NC	0.210	0.090
SP1-CI	0.380	0.056
SP1-FRC	0.250	0.019
SP2-NC	0.210	0.110
SP2-CI	0.400	0.080
SP2-FRC	0.300	0.076
SP3-NC	0.260	0.056
SP3-CI	0.500	0.014
SP3-FRC	0.270	0.037

Six-month chloride tests were also conducted at Missouri S&T. Significant increases in chloride contents at both 0.5 in. depth and steel locations were observed as shown in Table 5-17.

.

Table 5-17 Chloride Content in Concrete at Six Months

Specimen I.D.	Chloride at 0.5 in. Depth (%)	Chloride at Steel Location (%)
SP1-NC	0.360	0.150
SP1-CI	0.450	0.370
SP1-FRC	0.370	0.310
SP2-NC	0.450	0.230
SP2-CI	0.460	0.180
SP2-FRC	0.420	0.160
SP3-NC	0.360	0.300
SP3-CI	0.480	0.250
SP3-FRC	0.340	0.056

Figure 5-48 summarizes the chloride content tests of four and six months with respect to the parameters considered. Results of the two month test were excluded in this figure to make a comparison of data with consistent units of measurement. All specimens showed an increase in chloride contents from 4 months to 6 months. While the data show some significant scatter, in general it can be seen that gaps between the two curves tend to decrease with increasing edge distance for each concrete material. In other words, increase of edge distance can retard the chloride diffusion in concrete. Specimens with concrete containing corrosion inhibitor showed relatively higher chloride content values than the specimens with normal concrete or fibers with respect to each edge distance. This observation is consistent with results from the half-cell potential test.

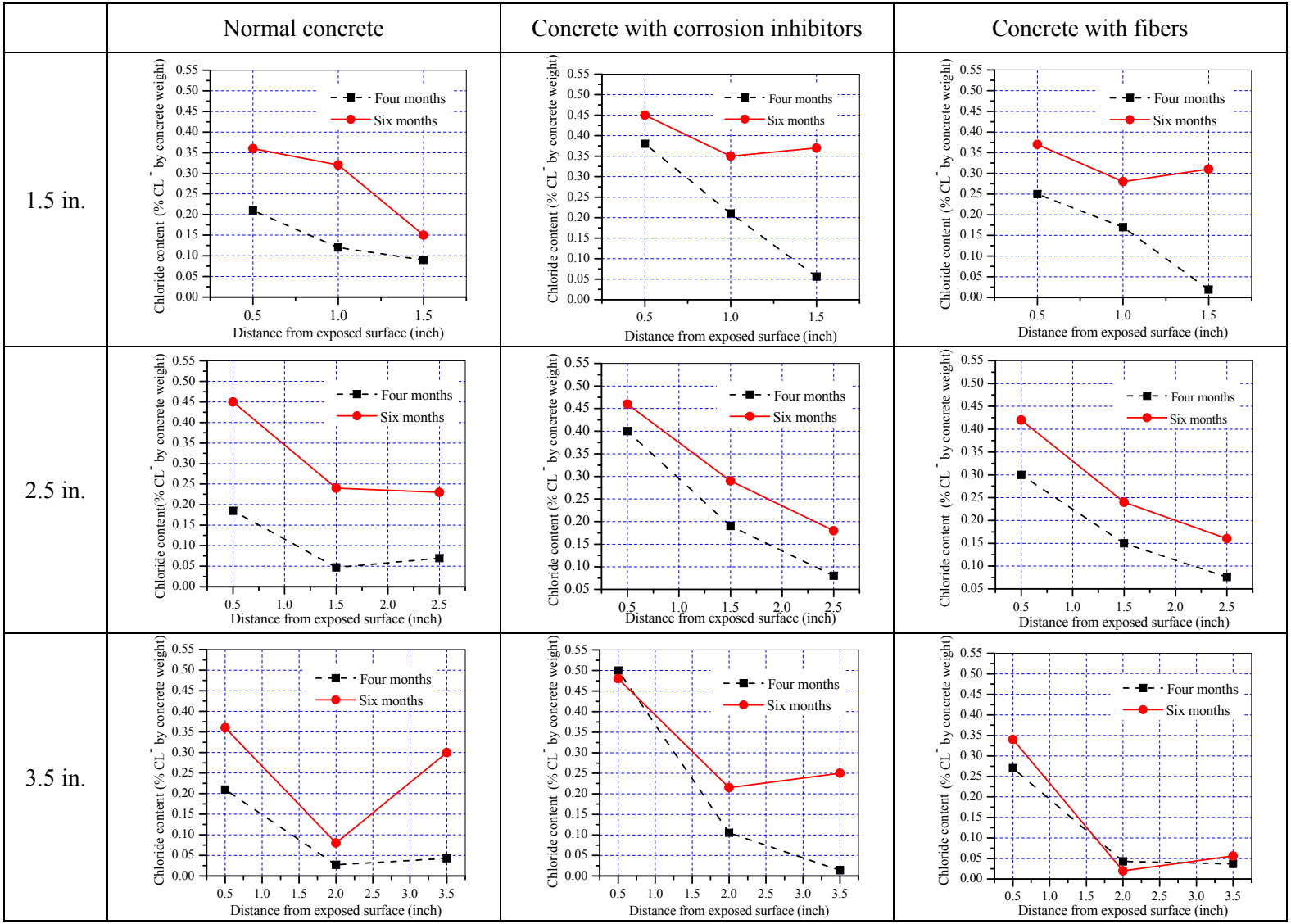

Figure 5-48 Comparison of Chloride Profiles

5.3.4.2 Accelerated Corrosion Test

Visual Inspection

Table 5-18 shows the visual inspection results for specimens with 1.5 in. edge distance. The table shows that the specimens experienced deterioration including rust, cracking, and spalling. Rust and cracks were observed in most specimens at different locations on the surface. Rust in all specimens was observed in all four surfaces since the distance to each surface was the same (because of the square cross-section). Spalling was assumed when corrosion-induced cracks propagated to two or more surfaces.

Table 5-18 Visual Inspection of the Accelerated Corrosion Test Specimens with 1.5 in. Edge Distance

Specimen Designation	Concrete Deterioration			
	Rust	Cracking	Spalling	Special observation
SP1-NC-13			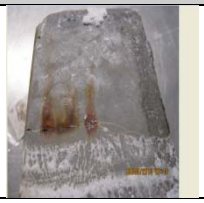	None observed
SP1-NC-14			None observed	
SP1-CI-13			None observed	None observed
SP1-CI-14				
SP1-FRC-13			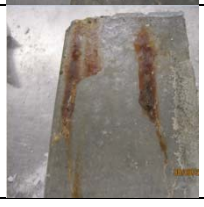	None observed
SP1-FRC-14			None observed	

Table 5-19 shows the results of visual inspection for the specimens with 2.5 in. edge distance. Rust was observed in all specimens on the surface that had the shortest distance from the steel tendon, while cracks were observed in only three specimens. Similar to the results of the 1.5 in. edge distance specimens, it is difficult to distinguish the effects of different concrete because they showed the same deterioration levels. It is apparent, however, that increasing the edge distance prohibited the propagation of corrosion-induced cracks observed in 1.5 in. test specimens.

Table 5-19 Visual Inspection of the Accelerated Corrosion Test Specimens with 2.5 in. Edge Distance

Specimen Designation	Concrete Deterioration			
	Rust	Cracking	Spalling	Special observation
SP2-NC-17			None observed	
SP2-NC-18		None observed	None observed	
SP2-CI-17			None observed	
SP2-CI-18		None observed	None observed	None observed
SP2-FRC-17			None observed	
SP2-FRC-18		None observed	None observed	None observed

Table 5-20 summarizes the visual inspection results for test specimens with 3.5 in. edge distance. Rust and cracks were observed only in test specimens with normal concrete, while no deterioration was observed in specimens containing corrosion inhibitor and fibers. As discussed earlier, these results show effects of corrosion inhibitors and fibers. Compared with the results of specimens with 1.5 and 2.5 in. edge distance, it is apparent that increasing edge distance significantly affected the durability of concrete.

Table 5-20 Visual Inspection of the Accelerated Corrosion Test Specimens with 3.5 in. Edge Distance

Specimen Designation	Concrete Deterioration			
	Rust	Cracking	Spalling	Special observation
SP3-NC-21		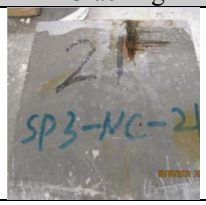	None observed	
SP3-NC-22		None observed	None observed	None observed
SP3-CI-21	None observed	None observed	None observed	None observed
SP3-CI-22	None observed	None observed	None observed	None observed
SP3-FRC-21	None observed	None observed	None observed	None observed
SP2-FRC-22	None observed	None observed	None observed	None observed

5.3.4.3 Gravimetric Study

After the 6-month visual inspection was completed, tendons were retrieved to record corrosion area and measure steel loss. No fractures were found in any of the retrieved tendons. All tendons showed corroded areas of different lengths. Figure 5-49 shows a representative corroded tendon for SP1-FRC-13.

Figure 5-49 Example of Corrosion Area (SP1-FRC-13)

The gravimetric study was performed after 7 months. Faraday's law was used to calculate the steel losses, and the results are summarized in Table 5-21:

$$M_1 = \frac{M \cdot I \cdot T}{z \cdot F}$$

where M_1 is the mass of steel loss (g) with time T (in seconds), I is the corrosion current (A), F is Farady's constant (96,500 A·s), z is the ionic charge (2 for anode reaction), and M is the atomic mass of metal (56 g for Fe).

Table 5-21 Predicted Steel Loss using Faraday's law

Constants	Tendon area in^2 (cm^2)	Applied current (mA)	Applied current density(mA/cm^2)	Predicted steel loss (g)	Predicted steel loss (%)
Values	0.085 (0.55)	0.4	0.72	1.9	1.3 – 1.4

Table 5-22 summarizes the test results and corrosion rate using the equation given in ASTM G1-03, which can be used for calculating the corrosion rate as follows:

$$\text{Corrosion rate} = (K \times W)/(A \times T \times D)$$

where K is a constant, T is the time of exposure (hours), A is the area (cm^2), W is the mass loss (g), and D is the density of steel (g/cm^2).

The values in Table 5-22 show a significant amount of variability. In general, increasing edge distance mostly reduced the mass loss (and thus decreased the corrosion rate). It was difficult to distinguish effects of the different concrete types on the corrosion rate.

Table 5-22 Steel Loss Calculations for Corrosion Initiation Specimens

Specimen I.D.	Initial Mass lb (g)	Final Mass lb (g)	Mass Loss (g)	Corrosion Rate (μm/year)
SP1-NC-13	0.312 (141.5)	0.308 (139.7)	1.80	4,164
SP1-NC-14	0.313 (142.0)	0.308 (139.7)	2.30	5,320
SP1-CI-13	0.309 (140.2)	0.306 (138.8)	1.40	3,239
SP1-CI-14	0.309 (140.2)	0.297 (134.7)	5.50	12,723
SP1-FRC-13	0.312 (141.5)	0.306 (138.8)	2.70	6,246
SP1-FRC-14	0.310 (140.6)	0.305 (138.3)	2.30	5,320
SP2-NC-17	0.310 (140.6)	0.304 (137.9)	2.70	6,246
SP2-NC-18	0.308 (139.7)	0.302 (137.0)	2.70	6,246
SP2-CI-17	0.309 (140.2)	0.302 (137.0)	3.20	7,402
SP2-CI-18	0.310 (140.6)	0.309 (140.2)	0.40	925
SP2-FRC-17	0.309 (140.2)	0.298 (135.2)	5.00	11,566
SP2-FRC-18	0.308 (139.7)	0.295 (133.8)	5.90	13,648
SP3-NC-21	0.308 (139.7)	0.306 (138.8)	0.90	2,082
SP3-NC-22	0.313 (142.0)	0.310 (140.6)	1.40	3,239
SP3-CI-21	0.313 (142.0)	0.312 (141.5)	0.50	1,157
SP3-CI-22	0.308 (139.7)	0.306 (138.8)	0.90	2,082
SP3-FRC-21	0.314 (142.4)	0.310 (140.6)	1.80	4,164
SP3-FRC-22	0.311 (141.1)	0.303 (137.4)	3.70	8,559

5.3.5 Summary

The durability test results presented in this chapter provide important information about the effectiveness of edge distances and enhanced concrete on improving the corrosion resistance of concrete. The following conclusions can be made from the results:

- Visual inspection in the corrosion initiation test indicated that the concrete deterioration level decreases with increasing edge distance. Most concrete deterioration was observed in specimens with 1.5 in. edge distance, while specimens with 3.5 in. edge distance showed no significant concrete deterioration.
- Chloride content analyses in the corrosion initiation test indicated that the chloride content at the steel location decreased as the edge distance increased for all specimens. Concrete containing corrosion inhibitor showed relatively higher chloride content than the normal concrete or concrete with fibers.
- Visual inspection in the accelerated corrosion test indicated that increasing edge distance retarded crack initiation as well as crack propagation. Most specimens with 1.5 in. edge distance showed corrosion-induced cracks, and some of them spalled. In contrast, only some of specimens with thicker covers showed cracking.
- In general, increasing edge distance mostly reduced the mass loss (and thus decreased the corrosion rate).

6 NUMERICAL ANALYSES OF SIP PANEL SYSTEMS

6.1 Introduction

This chapter summarizes the results of numerical analyses performed to investigate various aspects of SIP panel systems. Simulations presented in this chapter were carried out using the commercial finite element (FE) program, DIANA (de Witte and Kikstra 2003). FE simulations presented in Section 6.2 are aimed at investigating the causes of spalling in the SIP panels and the effects of spalling on the panel capacity. FE simulations described in Section 6.3 examine the behavior of the proposed SIP-CIP deck system modifications investigated in this study. Detailed results for each analysis are provided in Appendix D. A summary of findings is presented in Section 6.4.

6.2 Simulation of SIP Panel Spalling

This section presents the results of the FE simulation conducted to investigate the causes of spalling in the SIP panels and effects on the panel capacity. From the field investigations conducted in this project, corrosion of embedded steel reinforcement and degradation of concrete are believed to be the main sources of the spalling problem in the panel based on explicit phenomenological evidence discussed in Chapter 4. However, the mechanism of the spalling could not be detected from this explicit evidence. Accordingly, FE simulation was conducted to simulate the causes and determine the mechanism of the spalling in the panel as discussed in Section 6.2.1. Section 6.2.2 presents results of the FE simulation performed to examine the resulting effects on panel capacity.

6.2.1 Simulation of Spalling Causes

As observed in the Chapter 4 field investigations, corrosion of embedded steel reinforcement at the panel edges near the panel joints is a main reason for spalling problems in the SIP panel. Corrosion of reinforcement develops internal pressure along the reinforcement, resulting in cracking of the surrounding concrete that finally triggers the spalling of concrete as described in Chapter 4. Thus, geometrical conditions at the spalled region of the panel, including concrete cover and arrangement of reinforcement specified in MoDOT specifications (2004), are important factors for this issue. Accordingly, a 2-dimensional (2D) FE analysis was carried out to investigate the effects of geometrical conditions of edge reinforcement on the nature of crack development and propagation.

Due to the model complexity and number of parameters involved, the FE simulation was performed in two stages: preliminary and final. The preliminary FE simulation was first conducted to examine several important parameters including boundary conditions and geometrical conditions before developing the final FE model. The purpose of the preliminary simulation was to investigate the effects of these parameters on the cracking behavior. The preliminary model was based on a typical FE model used by most of the researchers in this area (Dagher and Kulendran 1992, Zhou et al. 2005, Ahmed et al. 2007, Chen and Mahdevan 2008). As shown in Table 6-1, local panel behavior was considered by modeling panel sections of different widths that include the corresponding number of reinforcements. Section thickness and spacing of reinforcement were consistent with current MoDOT specifications (2004). Two different boundary conditions were adopted in these models to represent the restraint conditions of the panel within the overall bridge deck. Cases P1 and P3 represent an interior section of the panel having three-side fixed boundaries along both sides and top surface, while Cases P2 and P4

represent an edge section of the panel having two-side fixed boundaries along one side and top surface. Although the spalling problem is observed only at the panel edges (ref. Chapter 4), the corrosion process within the interior sections is also of interest to study the degradation level in the middle of the panel and to compare differences between interior and edge sections.

In the preliminary model, incremental internal pressure representing the increasing internal pressure induced by rust expansion of the reinforcement was applied to each hole. The final stage of the corrosion process is summarized in Table 6-1 with respect to Von Misses stress variations and crack patterns. The final stage of the corrosion process was determined as the time when the iterative FE analysis terminated (i.e. convergence was no longer possible). As shown in Table 6-1, there are no significant differences between one and two sections in terms of stress variation and crack propagation. These findings indicate that enough distance between adjacent reinforcement, 4.5 in. spacing in this case, can prohibit lateral crack propagation to adjacent reinforcement. Results also revealed that the cracking process is affected by the boundary conditions. Interior sections having three-sided fixed boundary conditions on top and both surfaces, while the bottom surface is free, (Cases P1 and P3) show that crack propagation to the bottom surface is less severe than that of edge sections (Cases P2 and P4) having two-sided fixed boundary conditions on top and right surfaces as shown in the figure. It is obvious that more constraint effects in the internal section restrain the crack propagation in both horizontal and vertical directions. Thus, it is clear that edge sections are more vulnerable to corrosion-induced cracking effects than interior sections.

While the preliminary FE analysis was able to simulate distinct differences in crack propagation to the bottom surface in edge versus interior sections, crack propagation to the side surface was not triggered in this simulation. Thus there are other factors that likely contribute to the spalling problem. Based on review of MoDOT SIP panel specifications (2004) and other literature, two other potential factors were identified: flexible arrangement of reinforcement and potential butting of adjacent panels at the panel joint locations. The effects of these two factors were investigated through 2D FE simulation with respect to various parameters and are discussed in Sections 6.2.1.1 and 6.2.1.2.

Table 6-1 Preliminary FE Analysis of Corrosion Process

Case	Parameter	Boundary Conditions	Von Mises Stress Variations	Crack Propagation
P1	One Section	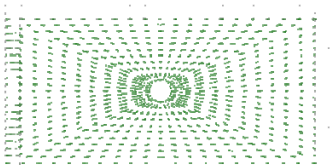	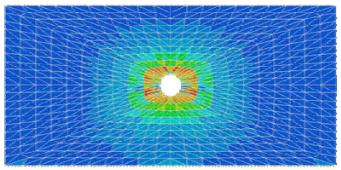	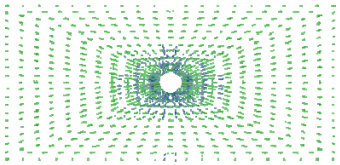
P2	One Section	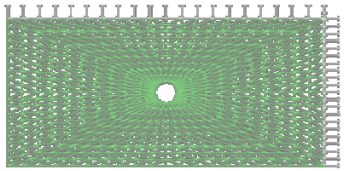	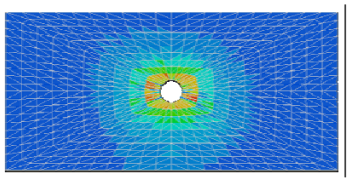	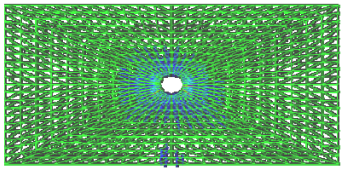
P3	Two Sections	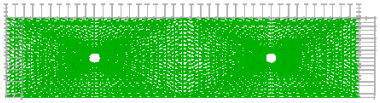	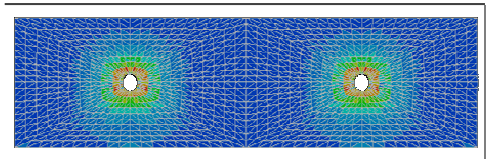	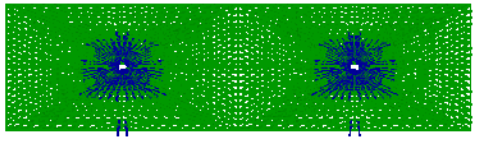
P4	Two Sections	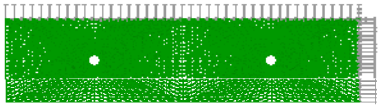	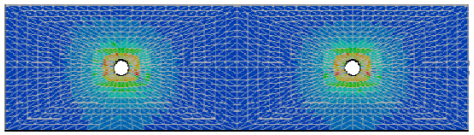	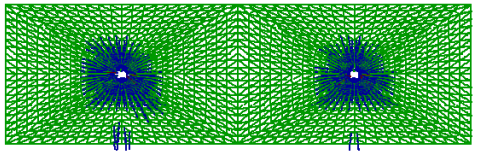
P5	Full Panel (All Sections)		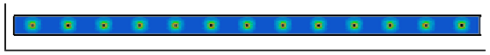	

6.2.1.1 Reinforcement Arrangement Effects

Current MoDOT design specifications shown in Figure 6-1 show that the side cover to the prestressed reinforcement can range from 1.5 in. to 3 in., and the location of lifting hooks (labeled as U1 in the figure) can vary. Accordingly, 2D FE analysis was carried out with respect to different side covers and different arrangements of reinforcement with respect to the location of the U1 bar. Figure 6-2 illustrates the configuration of the panel simulated in the FE models. As illustrated in the figure, only the local area of the panel was considered in the FE analysis due to symmetry of the panel. Assumptions were made in the FE model with respect to boundary conditions, loading conditions, and elements as explained in the following discussion.

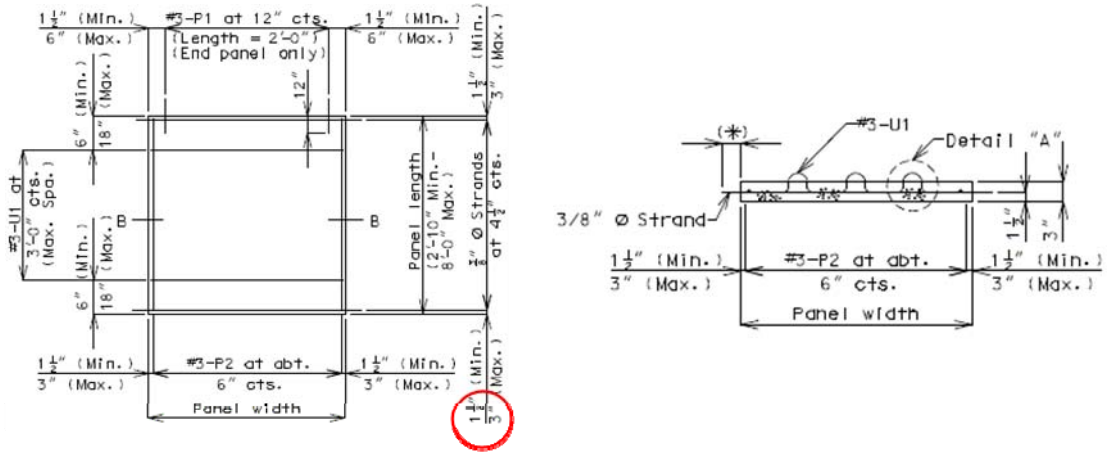

Figure 6-1 Details of MoDOT Partial-Depth PPC Panel (MoDOT 2004)

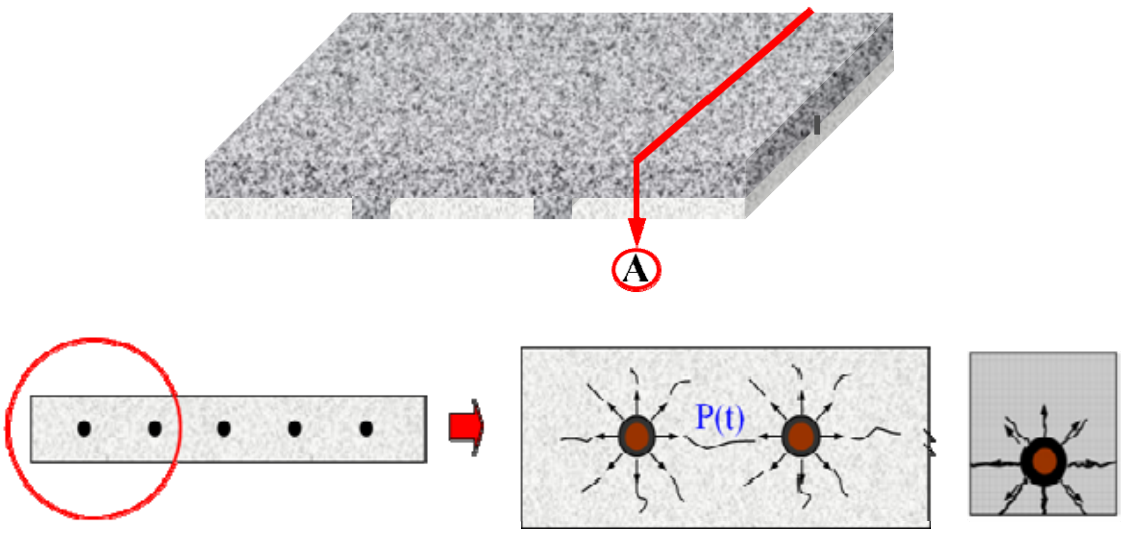

Figure 6-2 Configuration of Edge Reinforcement in the Panel

Figure 6-3 shows the configuration of the FE models illustrating the considered parameters. A three-node triangular isoparmetric plane stress element (T6MEM in DIANA) was used in the FE model as illustrated in the figure. Each hole in the model represents the location of embedded reinforcing steel of the same size as the corresponding reinforcement. The same incremental internal pressure was applied to each hole assuming the same corrosion level of all reinforcement. It should be noted that although this assumption is not realistic, it is a critical situation to simulate the spalling problem in the panel. The right surface of the model is modeled as a fixed boundary condition to simulate the continuity of the section. The top surface of the model is also modeled as a fixed boundary condition assuming full composite action between the SIP panel and CIP concrete deck. When this interface cannot achieve perfect composite action due to delamination as was observed in the field investigation (ref. Section 4.3.8), other specified boundary conditions can be considered.

Two main parameters related to geometrical effects on the spalling problem are considered in this FE analysis based on results from the preliminary FE analysis: the location of the U1 bar and the side cover. Location of the U1 bar is the distinction between the two FE models shown in Figure 6-3 6-3. For convenience, the FE models are labeled Case I and II for the upper and bottom figures, respectively. The Case I figure illustrates the FE model considering U1 bar located between the first and second tendons, with a tendon spacing of 4 in. on center. With the U1 bar in the center of the tendons, the spacing between reinforcement is 2 in. In the Case II figure, the U1 bar is located between the second and third tendons, and the tendons are spaced at 4.5 in. on center. Thus with the U1 bar in the center of the tendons, the spacing between reinforcement is 2.25 in. Case I represents a critical configuration of reinforcement arrangement that can occur, while Case II represents a typical reinforcement arrangement. Side cover was varied from 1.5 in. to 4 in. in both FE models.

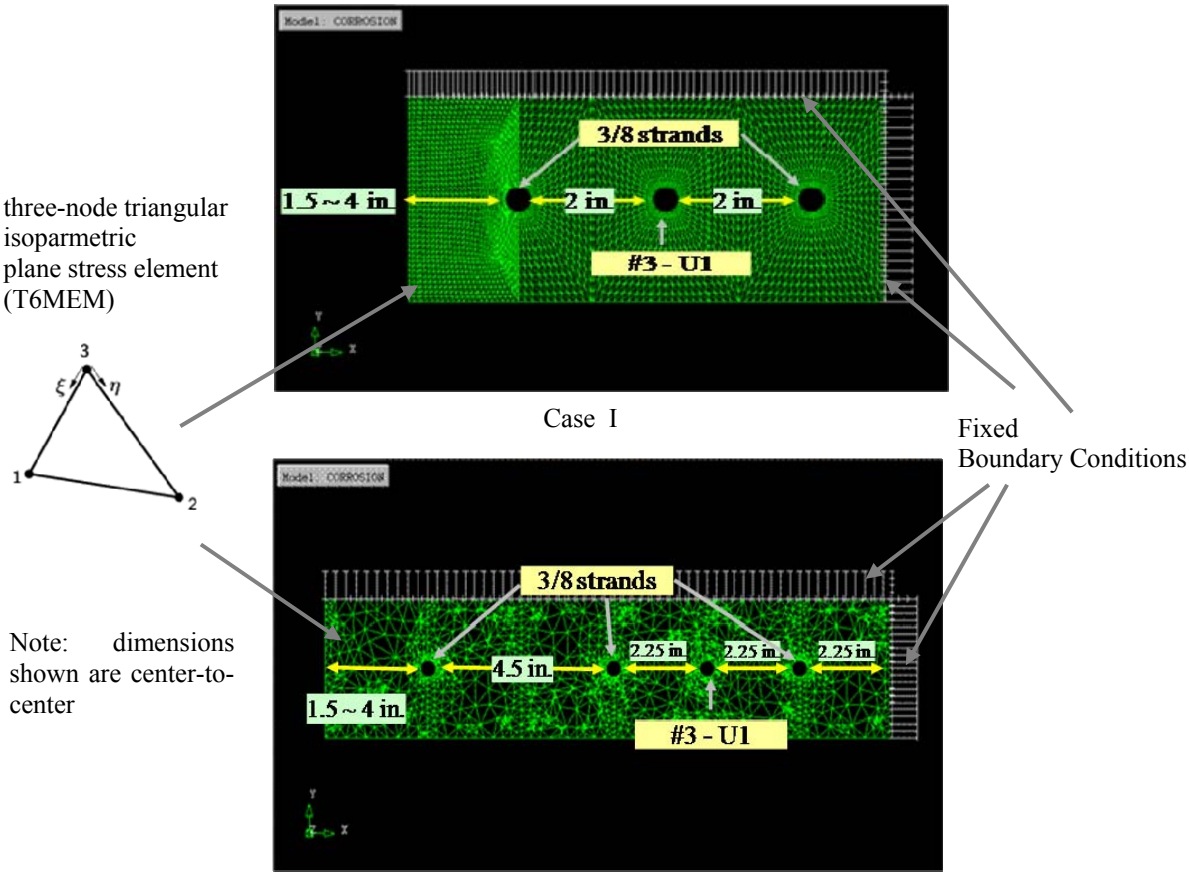

Figure 6-3 Two-Dimensional FE Models for Corrosion Process

Figure 6-4 shows a representative crack propagation of Case I having 1.5 in. side cover with respect to incremental internal pressure. First cracking is observed in this simulation when the internal pressure reaches 400 psi. As the internal pressure increases, cracks propagate around the reinforcement locations similarly to the preliminary FE analysis described in Section 6.2.1. A very interesting phenomenon happens when the internal pressure exceeds 2,000 psi. Cracks at the U1 bar location propagate laterally to both adjacent reinforcement locations and finally join with cracks from the adjacent reinforcement. This kind of crack propagation is usually called a "bridging crack". After formation of this bridging crack at 2,200 psi, cracks propagate in random directions at 2,400 psi. Cracks finally reach the bottom surface and almost approach the side surface. This final stage of crack propagation can be considered to represent spalling of the section. Therefore, it can be concluded that the bridging crack can trigger spalling in the panel. The same phenomenon is observed in other Case I FE models at the final stage as shown in Figure 6-5. This figure shows only crack patterns at the critical loading stages, while detailed data including stress variation and crack propagation are available in Appendix D. Excessive crack propagation is observed in each FE model after formation of the bridging crack. However, propagation of cracks from the edge tendons to the side surface is not observed as side cover increases over 2.0 in. in the models. In addition, cracks directed to the bottom surface are also significantly diminished with increasing side cover. There is no doubt that increasing concrete

cover increases the corrosion protection of embedded reinforcement. This simulation shows that concrete cover side also plays a critical role in arresting bridging crack propagation to the side surface of the panel.

Figure 6-6 shows crack patterns of the Case II FE analysis at the final stage. The crack patterns are very different from the crack patterns of Case I and are similar with those of the preliminary FE analysis shown in Table 6-1. Increased distance between adjacent reinforcement is shown to prohibit the crack propagation between reinforcement resulting in bridging cracks. In addition, effects of different side cover are found to be insignificant in this case.

It should be noted that although MoDOT specifications allow a somewhat flexible arrangement of reinforcement in terms of side cover and location of lifting hooks, the Case I situation is unlikely to occur in typical construction. Case II situations are more common and were observed in the field investigations discussed in Chapter 4 and in the construction of the unit panel specimens in Chapter 5. In the field investigations, however, concrete spalling was in fact observed. Although the Case II model does not explain this phenomenon, the significance of the bridging crack in the Case I model is a key finding. In this analysis, this crack was formed from pure crack propagation between closely-spaced reinforcement induced by corrosion. However, another mechanism exists to aid in the formation of the bridging crack. As illustrated in Figure 6-7, corrosion of temperature reinforcement oriented perpendicular to the tendon direction can induce cracks along the temperature reinforcement playing a similar role as the bridging crack. Although this phenomenon was not simulated in this 2D analysis, there is convincing physical evidence of a link between corrosion of temperature reinforcement and the bridging crack. Most of the spalled panels observed in the field survey exposed heavily corroded temperature reinforcement with corroded edge tendons as shown in the corresponding section (see Figure 4-4B and Figure 4-5B). Thus from both an analytical approach and through field investigation, it can be concluded that the bridging crack is a primary agency for the corrosion-induced spalling problem in the panel.

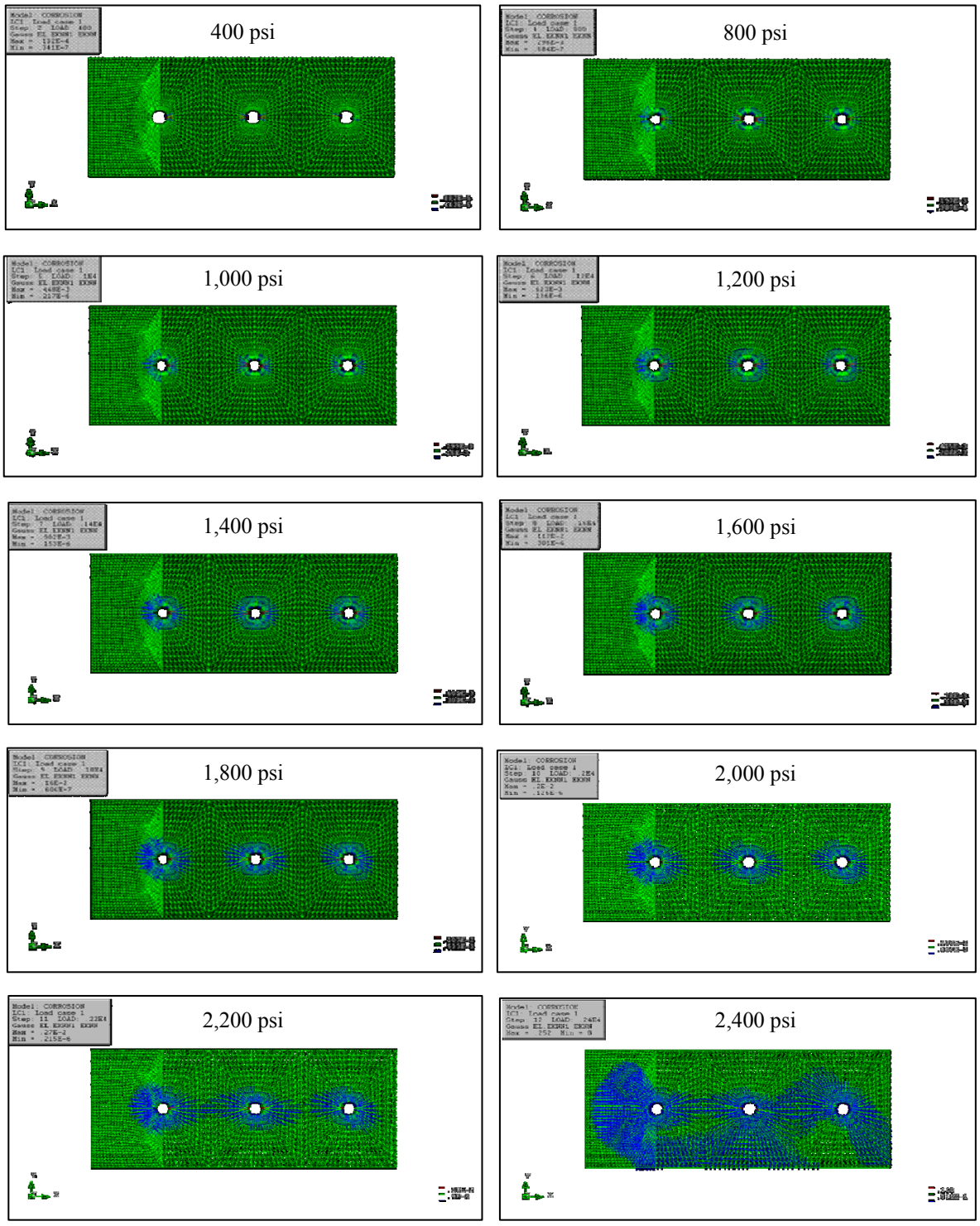

Figure 6-4 Crack Propagation of Case I FE Model (Cover = 1.5 in.)

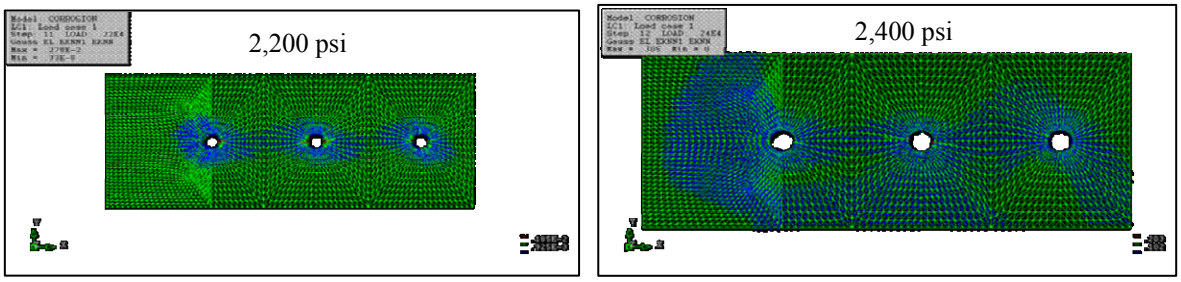

(a) Side Cover = 2.0 in.

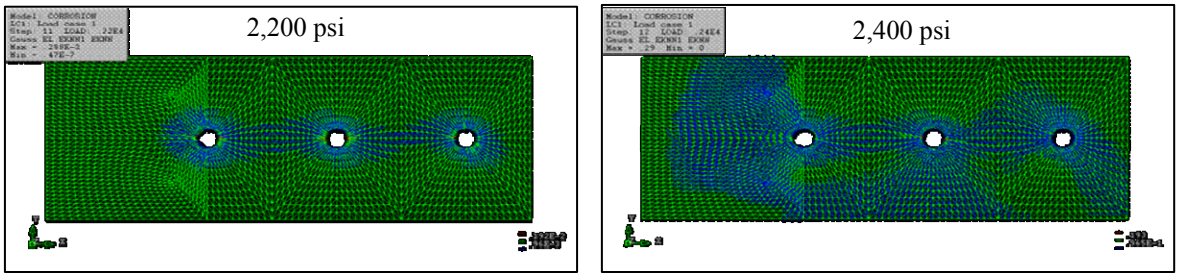

(b) Side Cover = 2.5 in.

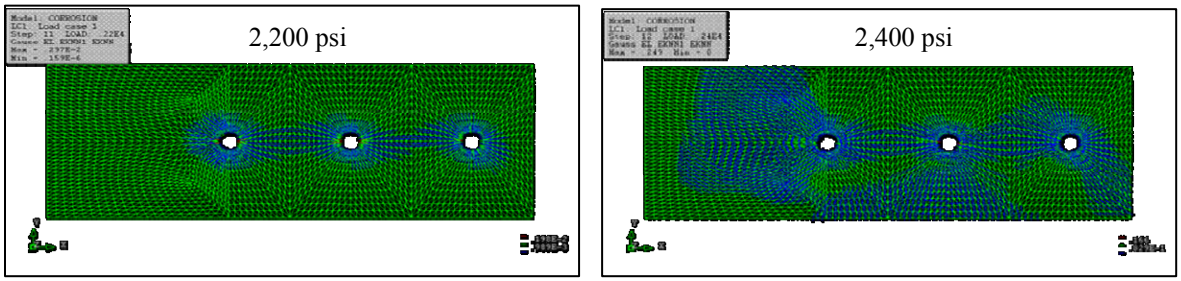

(c) Side Cover = 3.0 in.

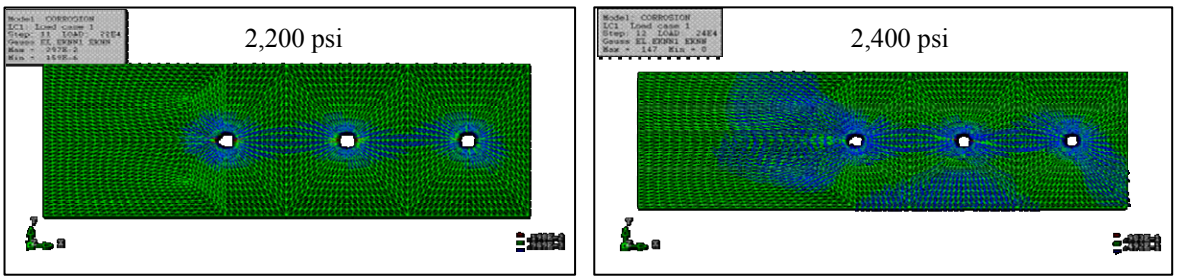

(d) Side Cover = 4.0 in.

Figure 6-5 Crack Patterns of Case I FE Model (Cover = 2.0, 2.5, 3.0, and 4.0 in.)

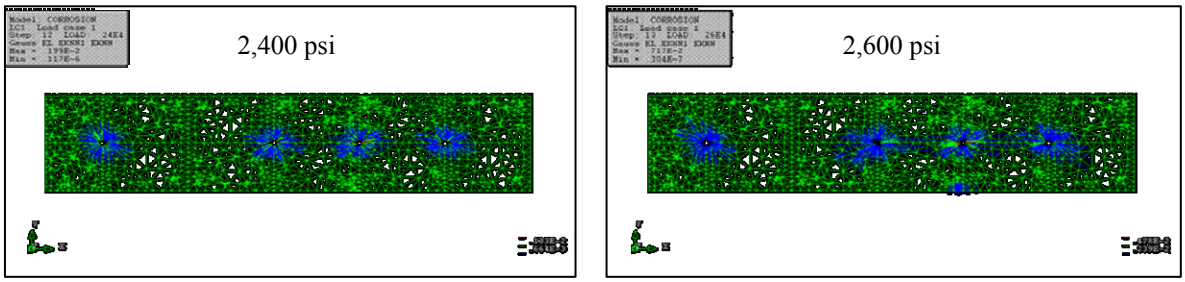

(a) Side Cover = 1.5 in.

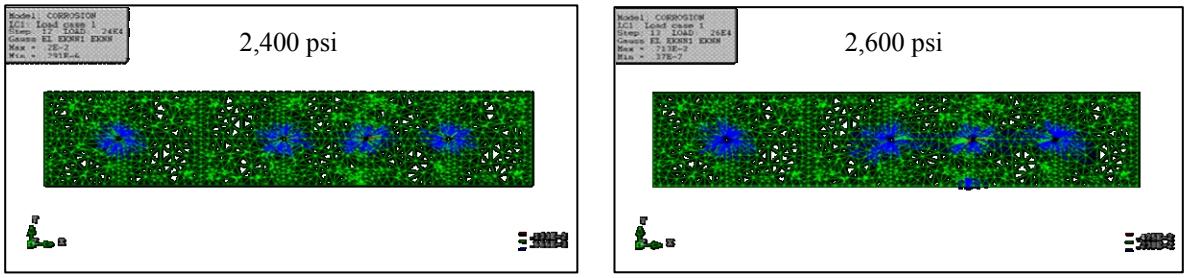

(b) Side Cover = 2.0 in.

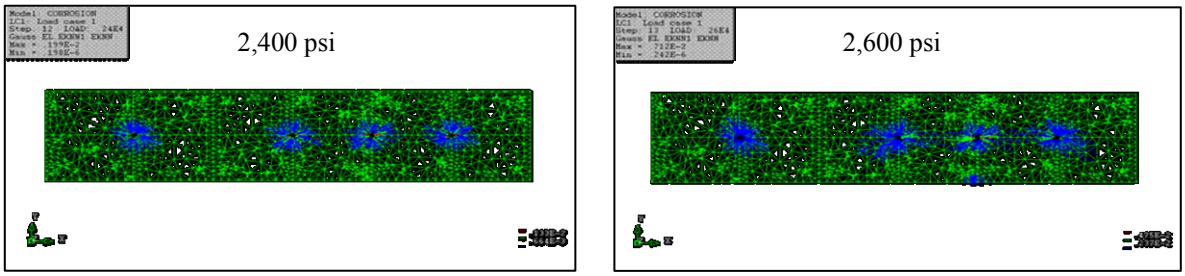

(c) Side Cover = 2.5 in.

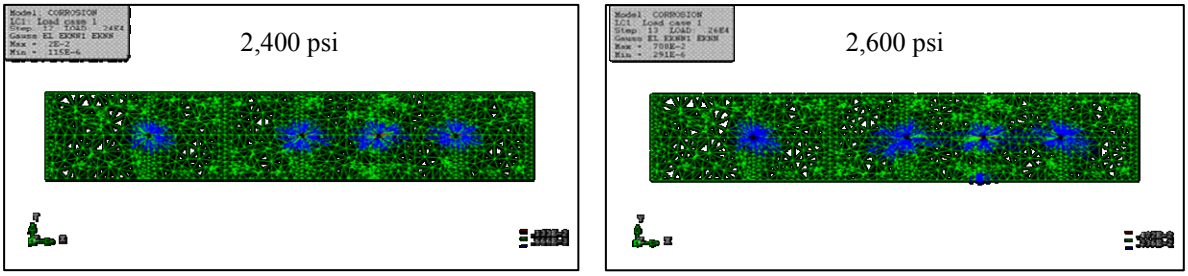

(d) Side Cover = 3.0 in.

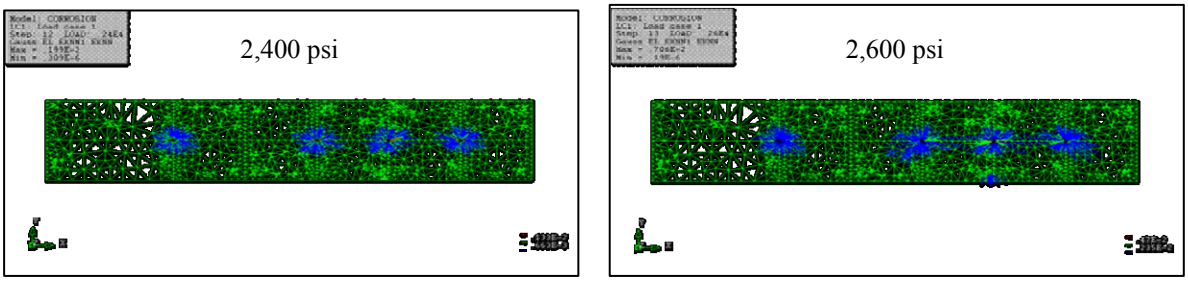

(e) Side Cover = 3.0 in.

Figure 6-6 Crack Patterns of Case II FE Model (Cover = 1.5, 2.0, 2.5, 3.0, and 4.0 in.)

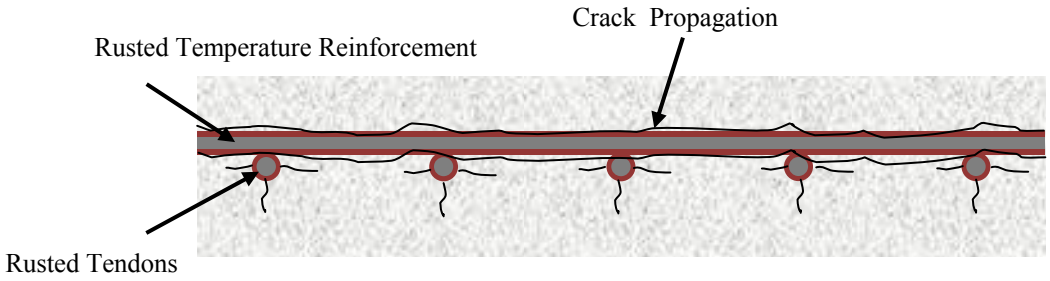

Figure 6-7 Schematic Illustration of Bridging Crack

6.2.1.2 Butting Effects

Besides the effects of corrosion of embedded reinforcing steel, another external source exists to trigger a spalling problem in the panel as reported by many researchers (Goldberg 1987, Hieber 2005). Case II in Section 6.2.1.1 showed that spalling may not occur at the concrete edges with minor crack propagation, unless another mechanism exists to form the critical bridging crack. In this section, external impact on panel edges was investigated to determine whether butting effects can contribute to concrete spalling in combination with internal cracks induced by corrosion of embedded reinforcement. Inherent discontinuity of the partial depth precast panel system discussed in Section 2.1.2 can result in external impact on the panel at the panel joints by butting of adjacent panels. Butting problems at the panel joints are mostly attributed to construction errors such as an insufficient gap between the panels or misalignment of adjacent panels shown in Figure 6-8.

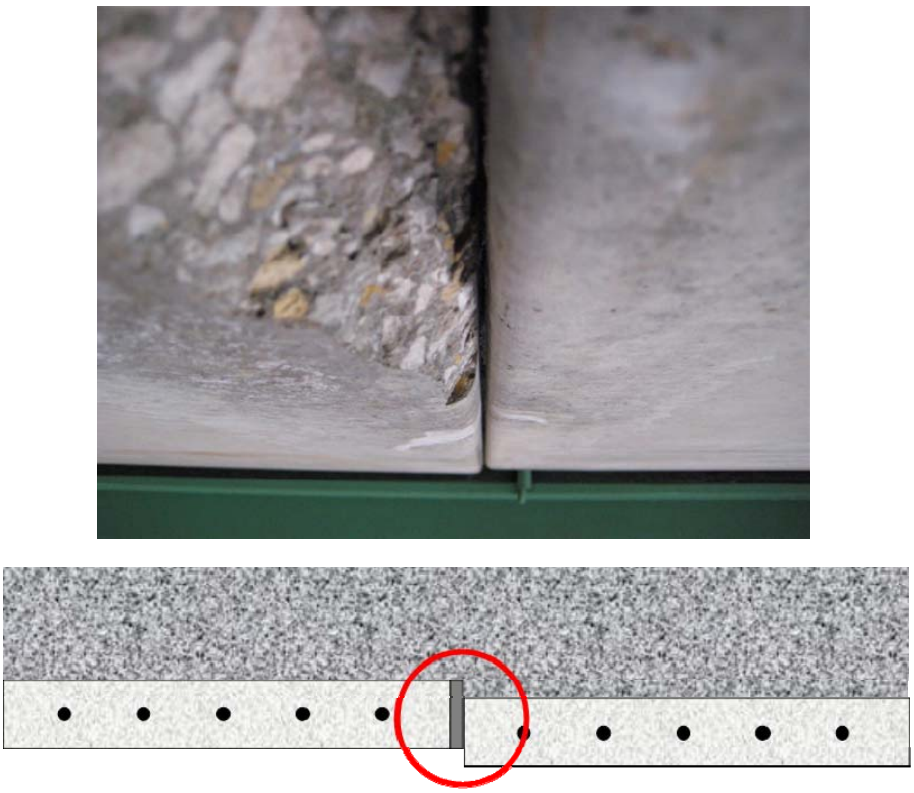

Figure 6-8 Possible Causes of Butting

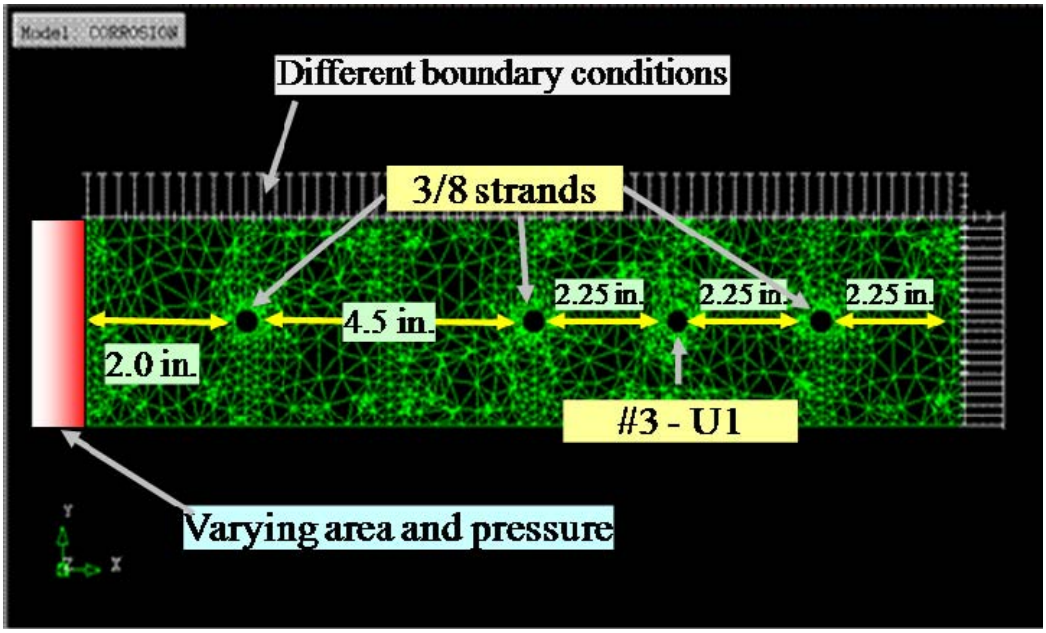

Figure 6-9 2D FE Butting Model

To encompass various conditions of the butting problem, several parameters were taken into account as shown in Figure 6-9. A FE simulation was conducted on the Case II FE model in the corrosion analysis described in Section 6.2.1.1 to emphasize the butting effect. Based on results of the Case II FE analysis, 50% of the ultimate internal pressure, 1,300 psi, was applied at each reinforcement location to simulate a small amount of corrosion. Impact load induced by butting of the adjacent panel was modeled by incremental pressure of varying area on the panel joint side of the panel to account for varying misalignment of the panels. In this analysis, delamination at the top surface corresponding to the interface region between the SIP panel and CIP deck was considered by releasing the horizontal restraint at the upper surface of the model as discussed in the previous section. While the assumption of free horizontal movement is somewhat extreme in representing the delamination in this region, it serves to achieve the goal of maximizing the effects of butting on spalling. Further detailed analysis for the delamination phenomenon is possible when addtional data are available.

Based on the model described above, final crack patterns are shown in Figure 6-10. Detailed results are also available in Appendix D. As shown in Figure 6-10, models having a fixed boundary condition at the top surface (corresponding to full composite action) show local failure at the top edge surface regardless of loading type. In contrast, models having a released boundary condition at the top surface (corresponding to complete delamination at the SIP-CIP interface) are strongly affected by loading types with a variation of failure modes. It is difficult to determine the most critical case among the models with a released boundary condition because ultimate pressures are also varied with respect to loading types, and it is difficult to estimate the external pressure induced by butting of the adjacent panel. However, it clear that delamination of the SIP-CIP interface plays a key role in the contribution of butting to the spalling problem.

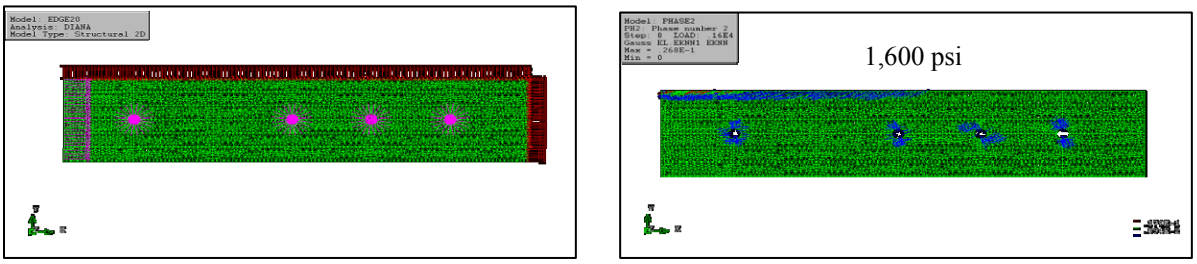

(a) Fixed boundary + Full pressure

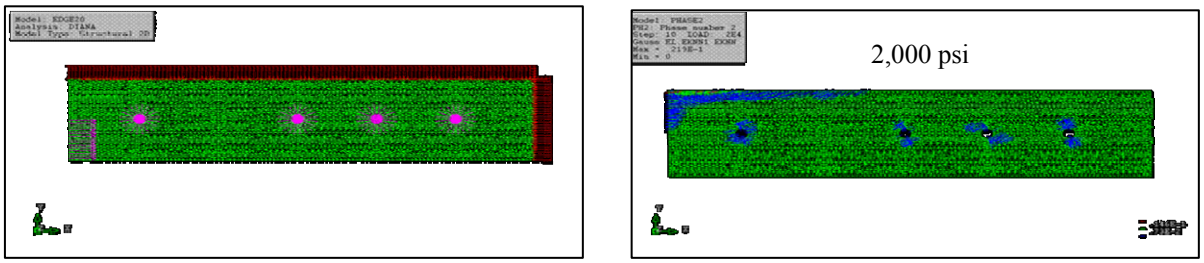

(b) Fixed boundary + Half pressure

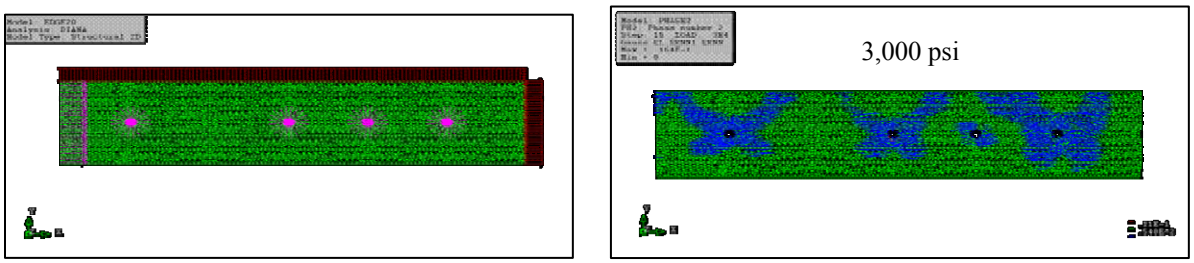

(c) Released boundary + Full pressure

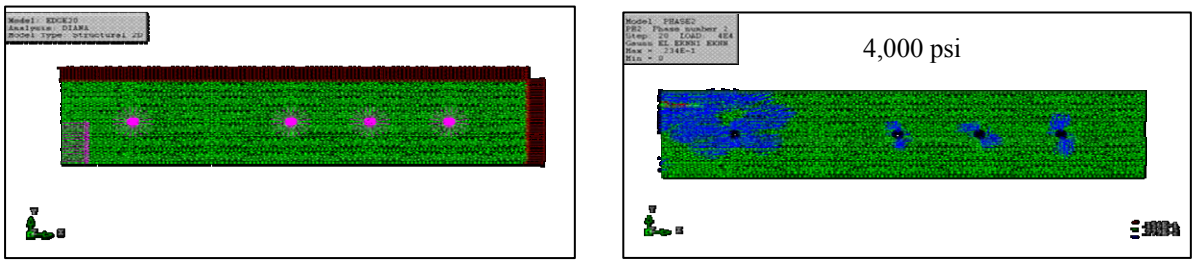

(d) Released boundary + Half pressure

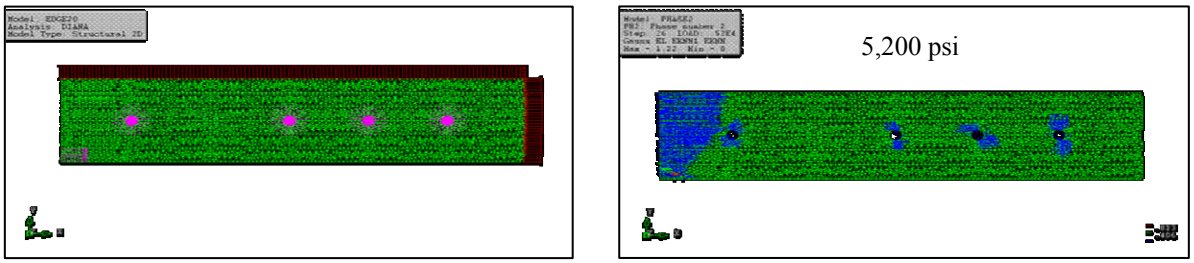

(e) Released boundary + Edge pressure

Figure 6-10 Final Crack Pattern of 2D FE Butting Analysis

6.2.2 Simulation of Deteriorated Panel Capacity

This section describes three-dimensional (3D) nonlinear FE analyses carried out to investigate the capacity of deteriorated SIP panels. Since the ultimate capacity of the partial-depth panel system is based on composite action with the CIP concrete deck, only serviceability of the deteriorated panel is investigated in this analysis through a simplified FE model. Figure 6-11 shows the configuration of the FE model used in this analysis. This configuration follows the MoDOT specification with respect to geometrical conditions. Distance between supports is determined from the distance between bearings used to support the panel over the girders. To highlight the response of the deteriorated panel, simple span behavior of the panel was achieved by assuming the pinned boundary conditions on both supporting areas. Dead and live load was applied to the top surface of the panel as a distributed pressure load. Deterioration levels were simulated by eliminating tendons located at the edge and center regions.

The eight-node isoparametric solid brick element (HX24L in DIANA) was used to model the concrete and supporting plate. The prestressing tendon was modeled as embedded bar elements specialized by DIANA. Main characteristics of the bar elements are as follows:

- Reinforcements are embedded in structural elements, the so-called mother elements.
- Reinforcements do not have degrees of freedom of their own.
- Reinforcement strains are computed from the displacement field of the mother elements. This implies perfect bond between the reinforcement and the surrounding material.

Table 6-2 summarizes the results of the FE simulation with respect to Von Mises stress variations. Each deteriorated panel shows higher stress concentration in the middle section of the panel with a wide range of stress variations compared to the non-deteriorated panel. This phenomenon is clearly observed from the stress variation on the cut section at the center of the panel. No significant differences are observed in the deteriorated panels with respect to the stress range. Although stress variations are slightly different between each panel considered depending on location of eliminated tendons, they are not significant. Thus, deterioration caused by losing edge tendons does not appear to affect significantly the serviceability of the panel.

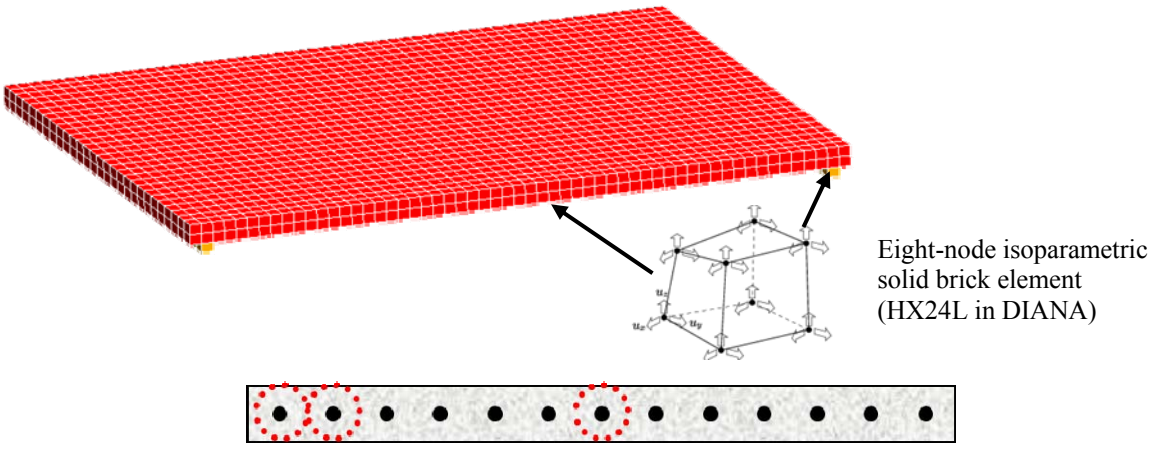

Figure 6-11 3D FE Model of Deteriorated Panel

Table 6-2 Von Mises Stress Variations of Deteriorated Panels

Parameter	Upper Surface	Lower Surface	Cut Section at the Center
Full Tendons	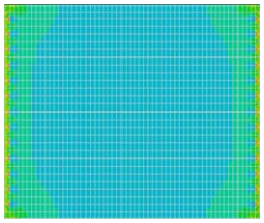	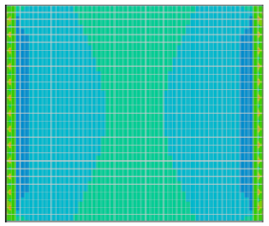	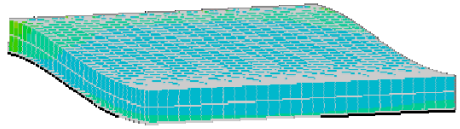
1 Center Tendon	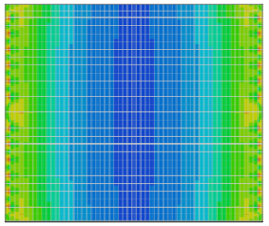	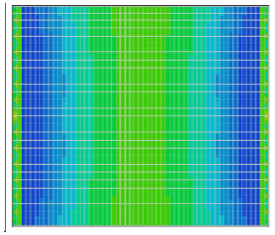	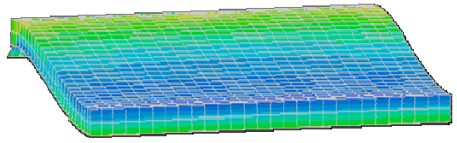
1 Edge Tendon	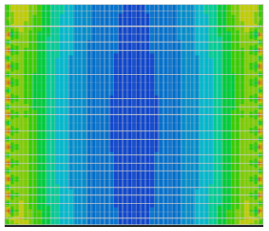	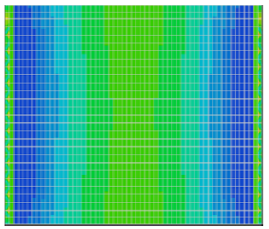	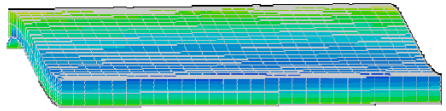
2 Edge Tendons	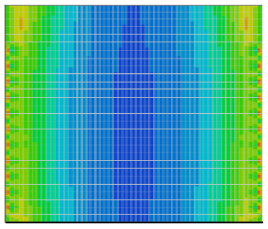	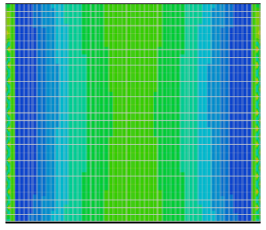	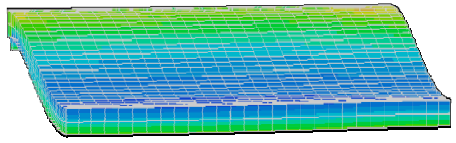

6.3 Numerical Analysis of Proposed Systems

This section presents the results of FE analyses and simulations carried out to examine the behavior of the proposed SIP-CIP deck system modifications investigated in this study. Because of the composite nature of the deck system, simulations are approached and presented in three parts: 1) simulation of unit panel behavior of proposed SIP panel types, 2) composite deck behavior of proposed SIP panel types composite with the CIP concrete topping, 3) deck behavior with proposed CIP concrete topping modifications. Section 6.3.1 examines the behavior of SIP panel types proposed and examined experimentally in Chapter 5. In addition to validating the experimental behavior of the Section 5.2 unit panel specimens, additional analysis is performed to estimate the structural capacity of deteriorated panels with different levels of tendon corrosion. Section 6.3.2 examines the behavior of proposed SIP panels in the composite deck system subjected to the typical design truckload to investigate the serviceability of the composite system. In addition, future performance of the composite system is also estimated by assuming a specified corrosion level of steel tendons. Section 6.3.3 presents results of FE simulation of the deck behavior when proposed modifications are made to the CIP topping reinforcement to reduce the occurrence of transverse reflective cracks at panel joint locations.

6.3.1 Simulation of Unit Panel Behavior

Three-dimensional (3D) nonlinear FE simulations were conducted to validate the performance of the unit panel static load test specimens discussed in Section 5.2. A total number of 8 simulations were carried out consisting of 4 simulations of test specimen behavior and 4 simulations of panel behavior with different levels of tendon corrosion. (Of the six static load panel specimens in Section 5.2, panels with epoxy-coated steel tendons were excluded from the simulation due to inapplicability of interface elements between concrete and epoxy-coated steel tendons within 3D FE simulation of a global structure. This kind of simulation is usually conducted on a local region of the structure to examine the bond stress-slip relationship between concrete and reinforcement and requires excessive computational effort, especially for 3D models. In addition, verification of the interface behavior between concrete and epoxy coated steel tendons was outside the scope of this study.)

6.3.1.1 FE Model Configuration

Besides calibration of FE models with respect to mechanical properties, FE simulation for prestressed concrete structures requires a special modeling technique due to their specific configurations. To demonstrate the different loading conditions of specimens under construction or loading history, a phased analysis technique is usually employed in the simulation. Between each phase, the model is updated by addition or removal of elements and constraints. In each phase a separate analysis is performed in which the results from previous phases are used as initial values. This technique makes it possible to predict the response with respect to the time-dependent behavior of elements or materials. The software program used in this study, DIANA, has the capability for phased analysis that highlights the suitability of this program for this study.

As illustrated in Figure 6-12, the two phases in the analysis of the test panels are: (a) a prestressing phase (Phase I), and (b) a loading phase (Phase II) following the same loading protocol conducted in the Section 5.2 experiments. In the model, tendons in panels are unbonded to the embedding elements, namely the mother elements, during the prestressing process. After the prestressing process, tendons are assumed to be perfectly bonded to the embedding elements

similar to the other reinforcing steels. Because this simulation requires a time-dependent analysis, the phased analysis technique is considered an appropriate analytical method for modeling the prestressing effects.

(a) Phase I: Prestressing (b) Phase II: Loading State

Figure 6-12 Finite Element Models of Each Phase

Figure 6-13 illustrates the configuration of a representative FE model of the unit panel. The eight-node isoparametric solid brick element (HX24L in DIANA) was used for modeling the panel, supporting plate, and loading plate. Both the temperature reinforcement and tendons were modeled as embedded bar elements specified by DIANA. As mentioned previously, reinforcements in the panel are assumed to be perfectly bonded to concrete in the Phase II analysis.

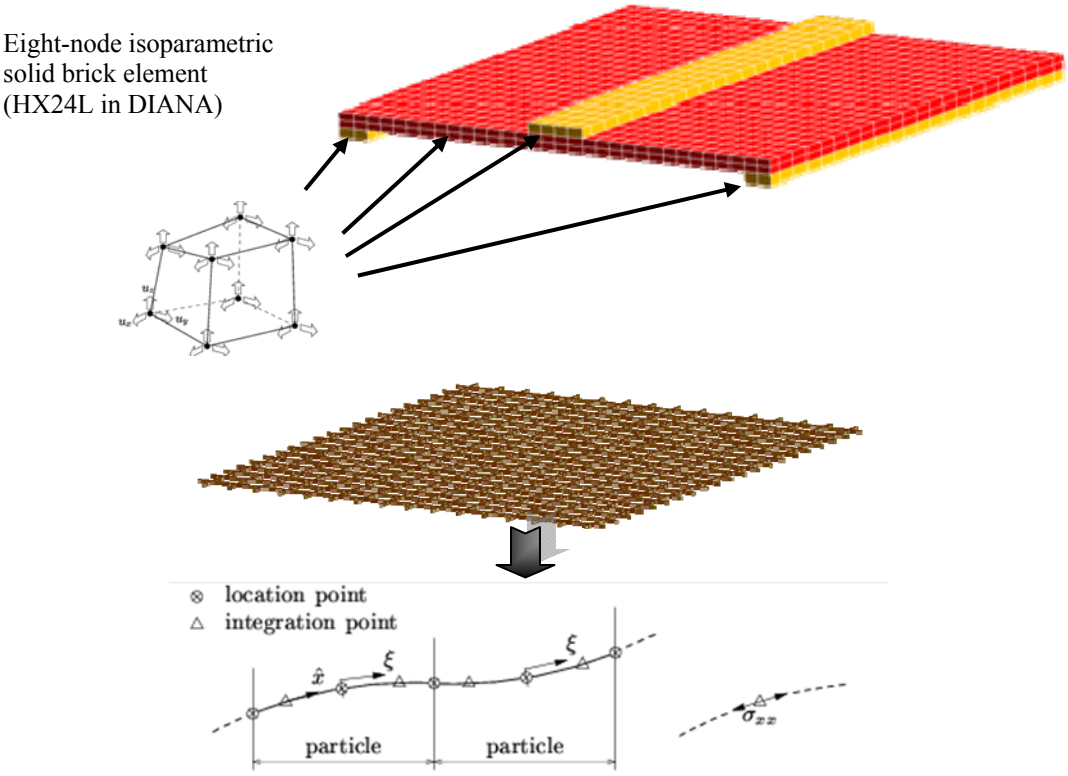

Figure 6-13 Configuration of FE Models for Test Specimens

For nonlinear analyses, the embedded formulation with perfect bond may be too coarse. For such cases, employing separate truss elements for the reinforcement and connecting them to the

surrounding structural elements via interface elements makes them capable of representing the bond stress-slip relationships between reinforcement and concrete. However, this method requires an excessive computational effort especially for 3D FE models. Thus, models developed in this section assume perfect bond between concrete and reinforcements, even for CFRP tendons.

The FE model developed in this study is based on the smeared crack model that employs the rotating crack model concept using Thorenfeldt's (1987) uniaxial model for the concrete compressive behavior and an exponential softening relationship for the concrete tensile behavior based on fracture energy related to a crack bandwidth as commonly adopted in smeared crack models. As mentioned in Section 2.2.2.2, the discrete crack model is unsuitable for blind prediction since it requires excessive assumptions in FE modeling in terms of material properties as well as FE model itself. The material properties for the fiber reinforced concrete (FRC) followed the specifications provided by the manufacturer.

Both the reinforcing steel and prestressing steel tendons in the FE models were assumed to follow an elastic-perfectly plastic behavior, while prestressing CFRP tendons were assumed linear elastic up to failure. Supporting and loading plates were assumed to be of linear elastic material having a very high stiffness to avoid secondary effects from these elements.

6.3.1.2 Results and Discussion

Comparison of unit panel test and numerical analysis results

Based on the model configuration described in Section 6.2.1.1, FE analysis results including overall behavior, ultimate strength, failure modes, and stress variations on each component are summarized and compared with test results from Section 5.2 to validate the performance of the proposed panels. Important data are presented in this section, while additional information is included in Appendix D.

Overall Behavior and Ultimate Strength

The experimental load-displacement relationships at the point of application of the load (E-2 in Figure 5-2) are compared with FE analysis results as shown in Figure 6-14. Ultimate strengths and corresponding displacements are summarized in Table 6-3.

FE analytical results shown in Figure 6-14 show reasonable agreement with test results regarding the overall behavior. Most of the experimental results, however, show less ductile behavior than FE analytical results with the exception of the control panel, ST-NC-SL. There are several reasons for this phenomenon. First, this phenomenon is mainly attributed to different material properties of concrete between the experiments and FE analysis. As observed in the experiments, most test specimens failed by concrete crushing at the top fiber at the ultimate state (ref. Section 5.2). Thus, the failure mode is governed substantially by the compressive strength of concrete. In particular, significant differences between test and analytical results for specimens using FRC, Figure 6-14 (b) and (d), can be explained by this reason. As mentioned above, concrete material properties adopted in the FE models were based on the manufacturer's recommendation, which indicated a 10% and 2% increase in compressive and flexural strength, respectively, from that of corresponding concrete without fibers. These differences make a large difference between experimental and analytical results as shown in the graphs. As observed in Figure 6-14 (a),

which shows good agreement between experiment and analysis, the FE analysis can give good agreement in the overall behavior when appropriate material properties are assumed in the FE models. Secondly, mechanical assumptions adopted in the FE modeling have a significant meaning for FE simulations. The smeared crack model used in the simulations (ref. Section 6.2.1.1) distributes stresses into surrounding elements resulting in reduction of stress concentration at a critical crack. This behavior is in contrast to that of the test specimens' cracking, which was featured by a few critical flexural cracks at the loading location (ref. Section 5.2). This phenomenon can be observed in the discussion that follows describing crack patterns. Thirdly, effective prestress can be another source for disagreement at ultimate state. As mentioned above, because failure of the panel is governed by concrete crushing at the top fiber of the concrete, the stress state of the panel induced by the prestressing force is an important factor governing the behavior. In this analysis, effective prestress was calculated considering short- and long-term prestress losses based on conventional methods and was applied in the FE models assuming perfect bond between concrete and tendons. Moreover, different bond-slip relationships between each material can affect the effective prestress of tendons. That is, bond-slip relationships between different tendons and different concrete can reduce or increase the effective prestress in tendons resulting in varying stress levels in the whole panel during the loading process. In addition, insufficient transfer length of the panel can amplify this effect. The difference in load-displacement relationships for panel CFRPT-NC-SL, Figure 6-14 (c), can be a result of this effect. From stress variations on each component in the following sections, this phenomenon can be explained.

As a result, FE analysis was found to overestimate the ultimate strengths and corresponding displacements of the unit panel specimens. As shown in Table 6-3, the average ratio of ultimate strength (P_{EXP}/P_{FE}) is 0.87 with a maximum ratio of 0.95 and a minimum ratio of 0.82. FE analyses for both FRC specimens significantly overestimate both ultimate strengths and displacements. If the exact stress-strain relationship of FRC were available, this discrepancy would most likely be resolved. Good agreement (5%) between experimental and FE results of panel ST-NC-SL is explicit evidence for this explanation.

Although FE analysis somewhat overestimated the ultimate strengths and corresponding displacements, good agreement was found in the behavior before the ultimate state including cracking load, initial (uncracked) stiffness, and post-cracking behavior. The following discussions on crack patterns and stress variations on each component further address the efficiency and limitations of these analyses.

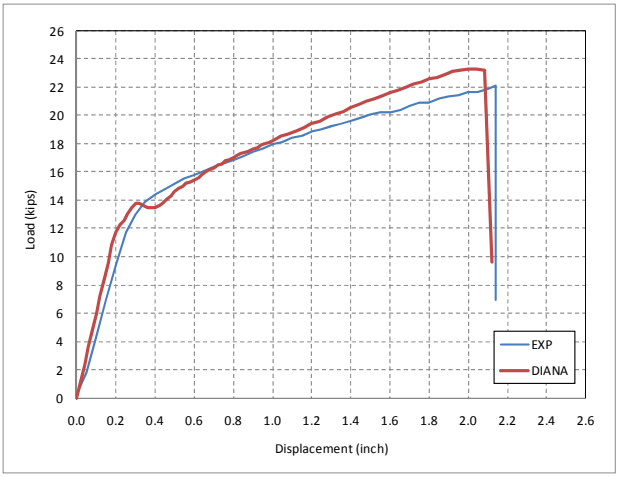

(a) ST-NC-SL

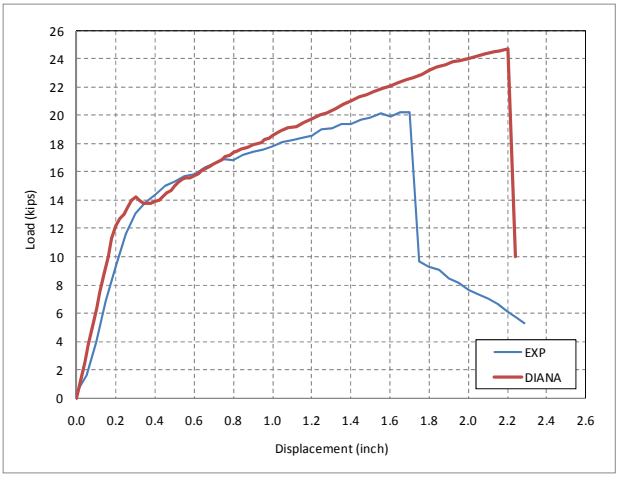

(b) ST-FRC-SL

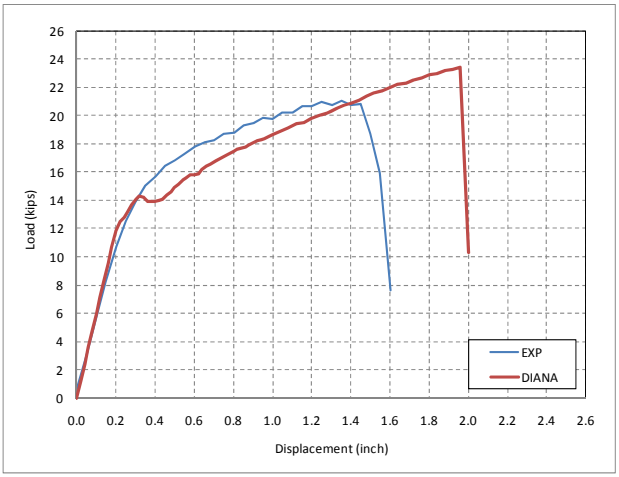

(c) CFRPT-NC-SL

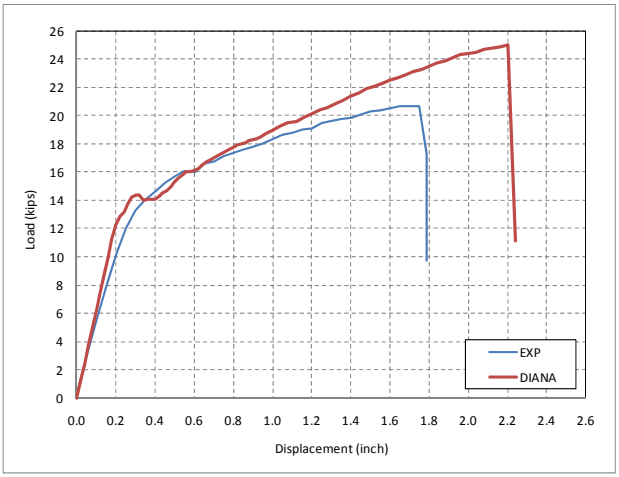

(d) CFRPT-FRC-SL

Figure 6-14 Comparison of Load-Displacement Relationships at Loading Point Location

Table 6-3 Comparison of Ultimate Strength and Displacement for Unit Panels Specimens

Unit Panel	Corresponding Figures	Ultimate Strength (kips)		Exp/FE	Displacement (in.)	
		EXP	FE		EXP	FE
ST-NC-SL	Figure 6-15 (a)	22.08	23.30	0.95	2.14	2.04
ST-FRC-SL	Figure 6-15 (b)	20.21	24.70	0.82	1.70	2.20
CFRPT-NC-SL	Figure 6-15 (c)	21.05	23.40	0.90	1.55	1.96
CFRPT-FRC-SL	Figure 6-15 (d)	20.70	24.90	0.83	1.79	2.16
AVERAGE	-	**21.01**	**24.08**	**0.87**		

Failure Mode and Cracking Behavior

Comparison of failure modes can shed light on the efficiency of the FE models. Because the developed models adopt the concept of the smeared crack model discussed in Section 6.3.1.1, models cannot depict the exact crack patterns of test specimens at the failure state, which are usually governed by a few critical, primary cracks—the so-called discrete cracks—but can give an indication of the overall failure mode. Crack patterns at ultimate state are summarized in Table 6-4 with respect to experimental and FE analytical results. Crack patterns of FE analysis were illustrated for both side and bottom surfaces. As discussed previously, cracks in the FE analysis are more distributed along the tendon direction for all specimens, while most of the test results show several critical flexural cracks located under the loading point. These critical cracks mainly govern overall behavior of the test specimens and finally induce more brittle failure at ultimate state than what is modeled in the FE simulation.

Table 6-4 Crack Patterns at Ultimate State

	South View	North View
ST-NC-SL	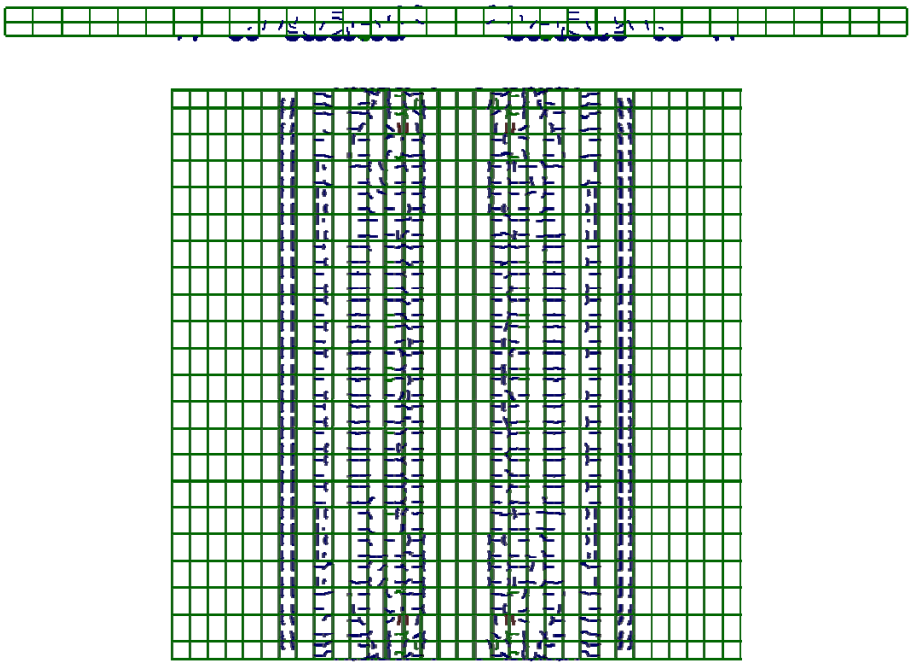 (FE results)	
ST-FRC-SL	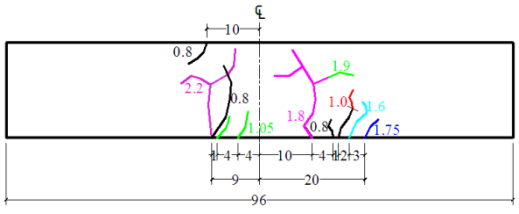 (Experimental results)	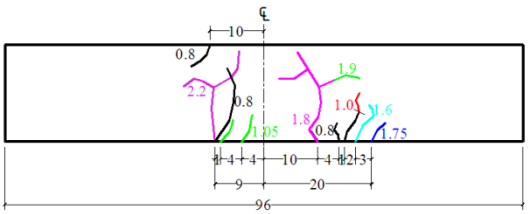 (Experimental results)

	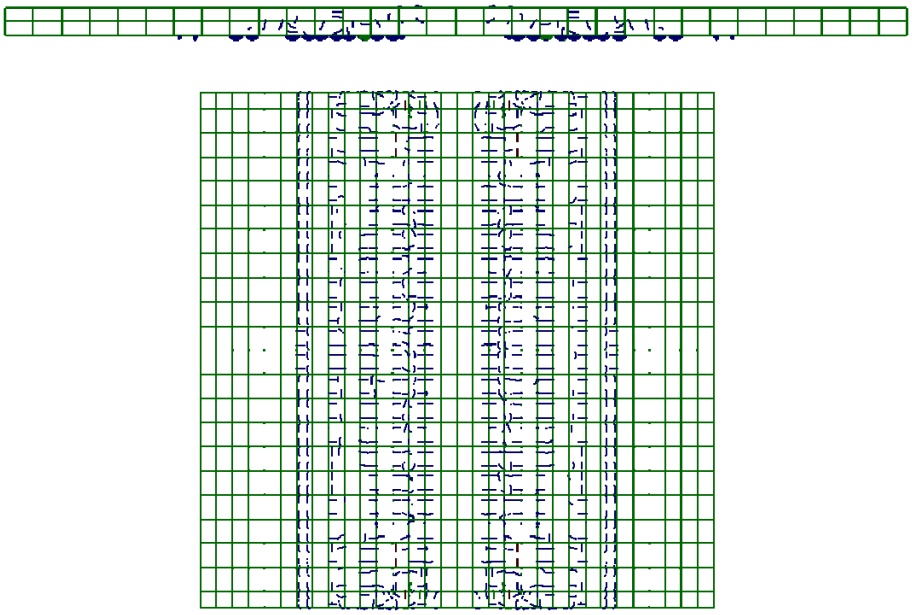 (FE results)
CFRPT-NC-SL	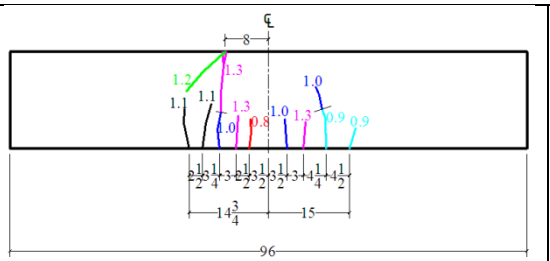 (Experimental results) 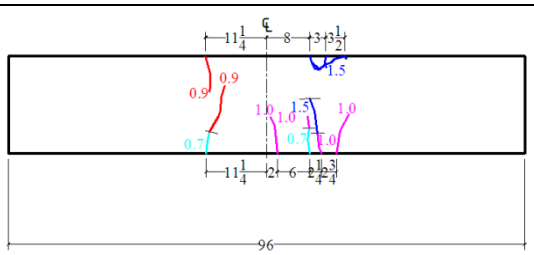 (Experimental results) 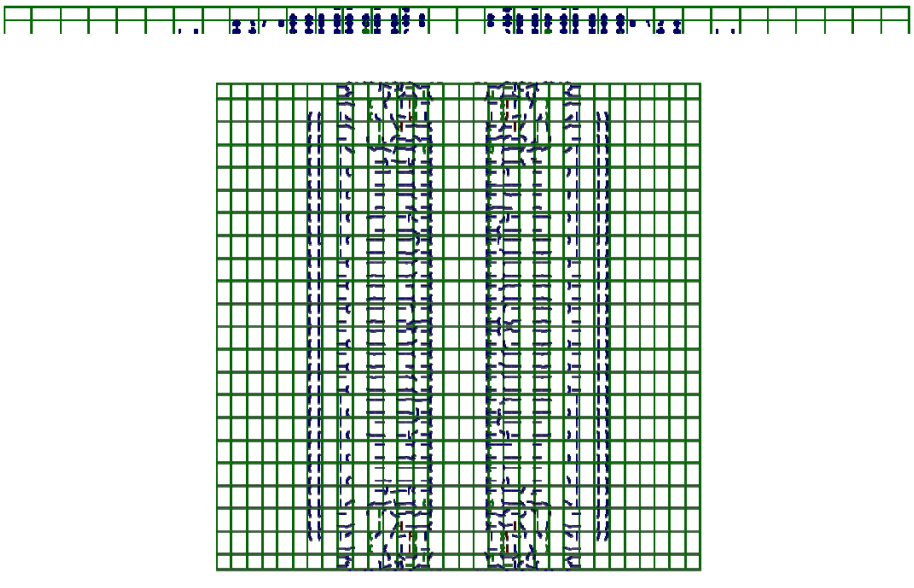 (FE results)

CFRPT-FRC-SL	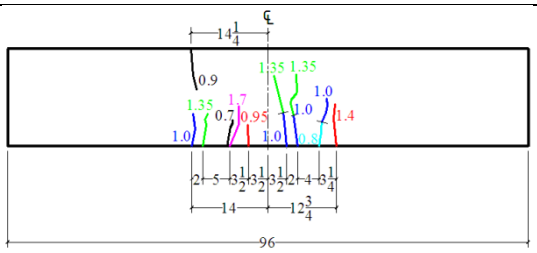 (Experimental results)	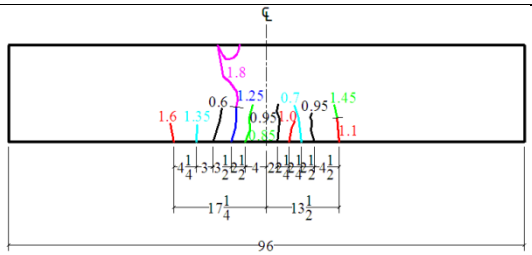 (Experimental results)
	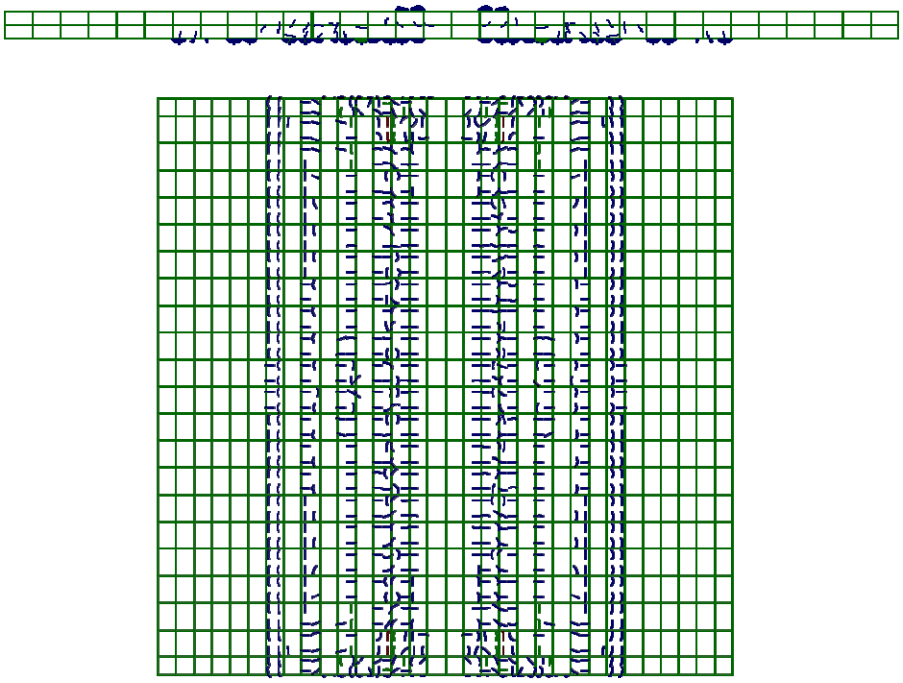 (FE results)	

Stress and Strain Variations

A beneficial aspect of FE analysis is the feasibility of investigating the detailed local behaviors of different components, which are impossible to observe through experiments alone. This section describes detailed information about the local behavior of concrete and tendon components with respect to stress and strain variations. These results can provide supplementary information for the failure mode as well as insight into the role of each component.

Figure 6-15 illustrates Von Mises Stress variations on concrete on both bottom and top surfaces. Usually Von Mises stress variations are used to determine the critical local region under severe conditions. As shown in the figure, all analytical results show stress concentrations at both edge regions of the loading beam. Normal stress variations along the tendon direction are presented in Figure 6-16 with respect to the top and bottom surface. Stress values of these variations range from compressive strength on the top surface to tensile strength of concrete on the bottom surface. Thus, the failure mode of each specimen can be clearly observed from these variations. 6-17 shows strain variations across the section at midspan at ultimate state. This data can be used to compare with measured test data as well as to calculate panel curvature.

	TOP SURFACE	BOTTOM SURFACE
ST - NC - SL	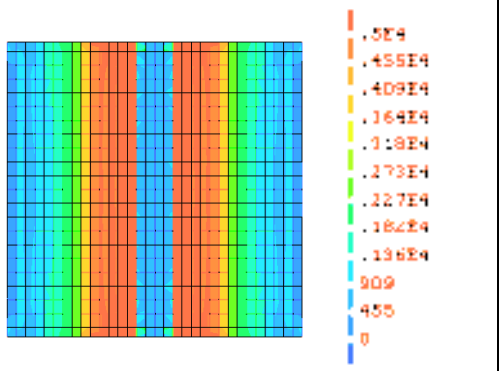	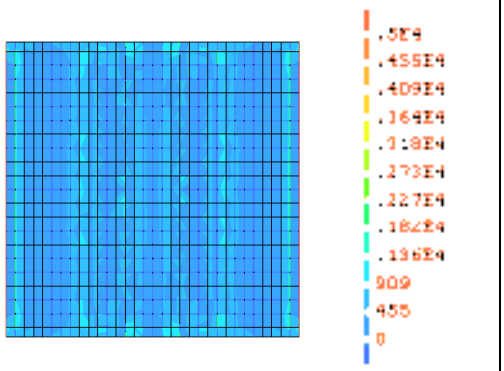
ST - FRC - SL	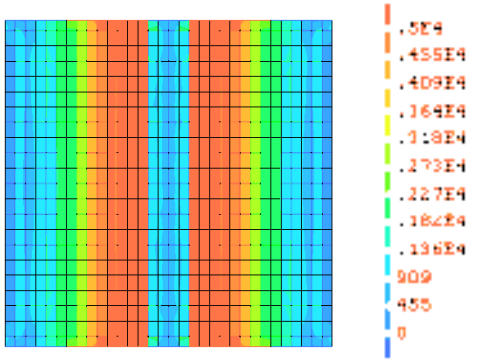	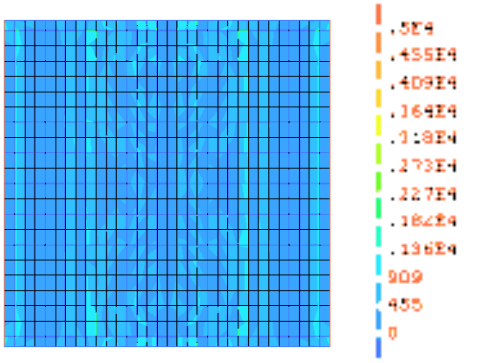
CFRPT - NC - SL	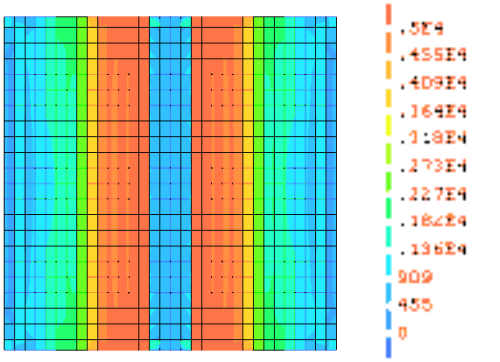	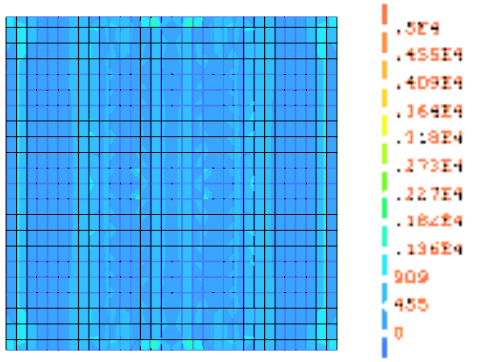
CFRPT - FRC - SL	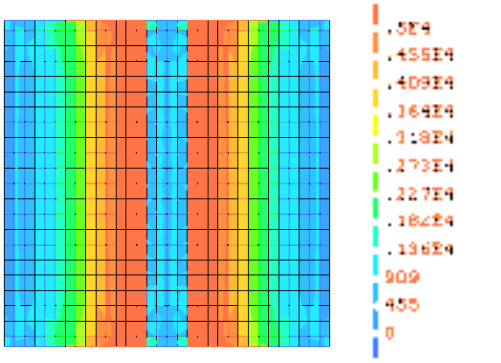	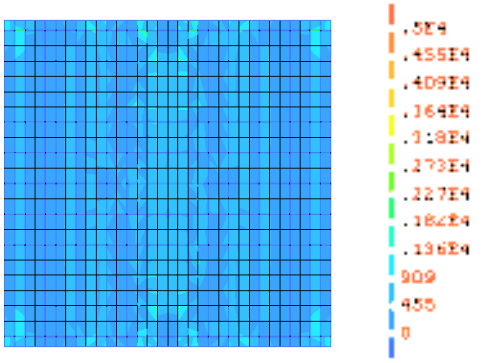

Figure 6-15 Von Mises Stress Variations on Concrete Surfaces at Ultimate State

	TOP SURFACE	BOTTOM SURFACE
ST - NC - SL	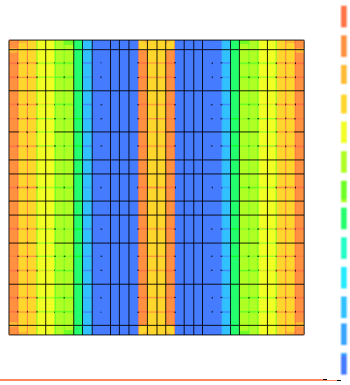	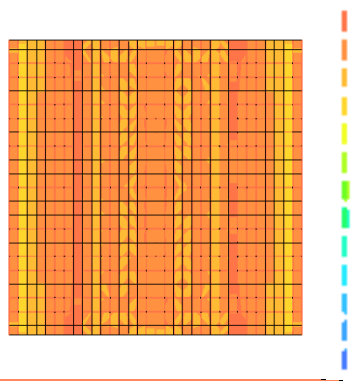
ST - FRC - SL	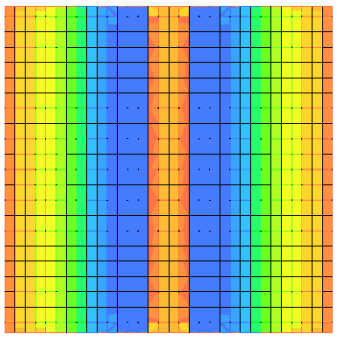	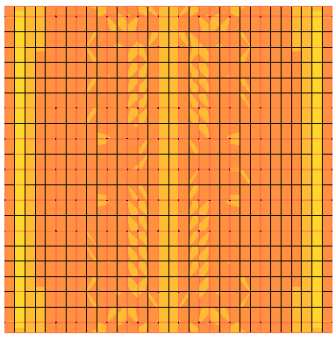
CFRPT - NC - SL	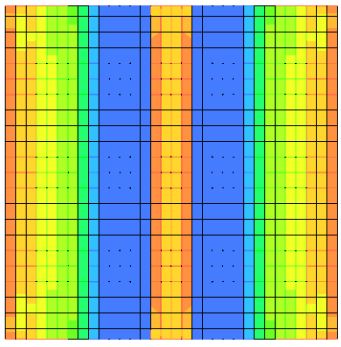	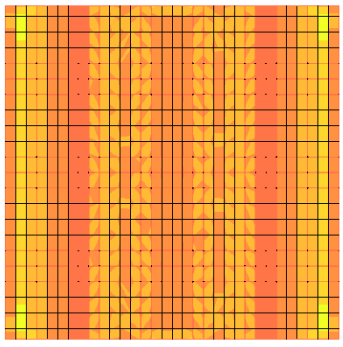
CFRPT - FRC - SL	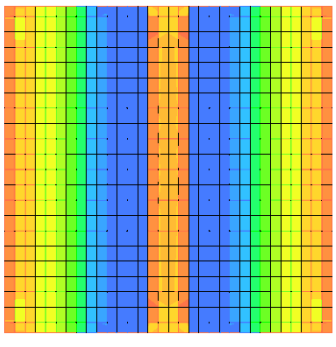	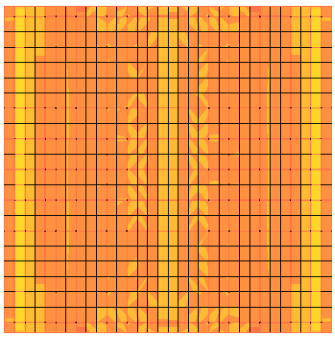

Figure 6-16 Stress Variations on Concrete Surfaces along Tendon Direction at Ultimate State

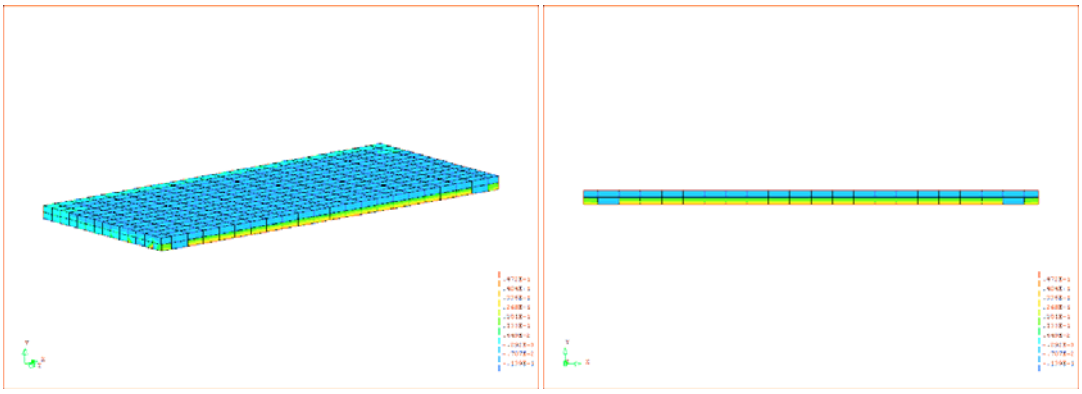

(a) ST-NC-SL

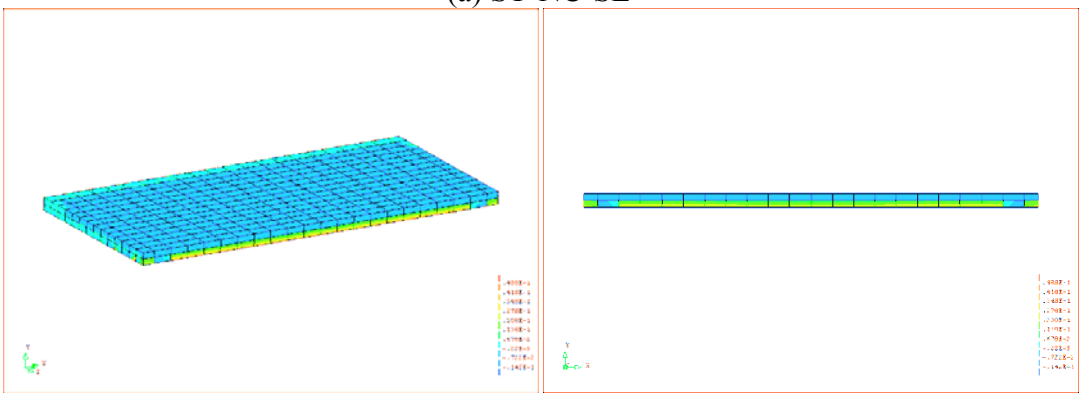

(b) ST-FRC-SL

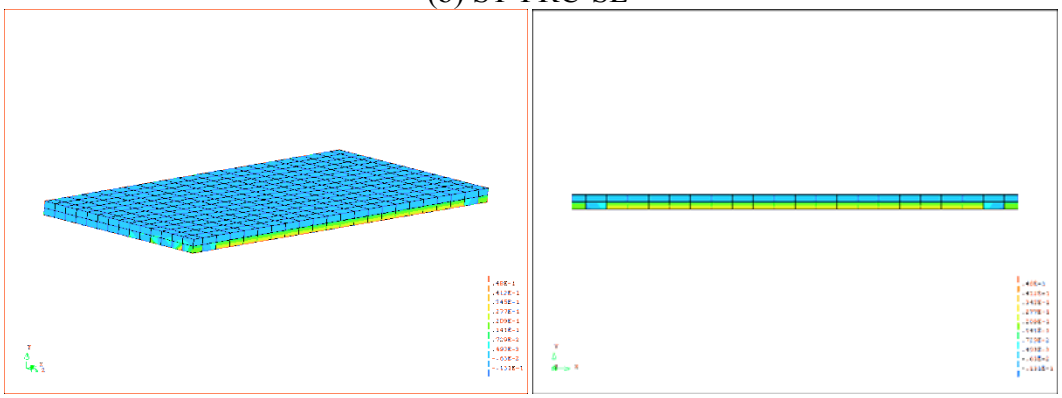

(c) CFRPT-NC-SL

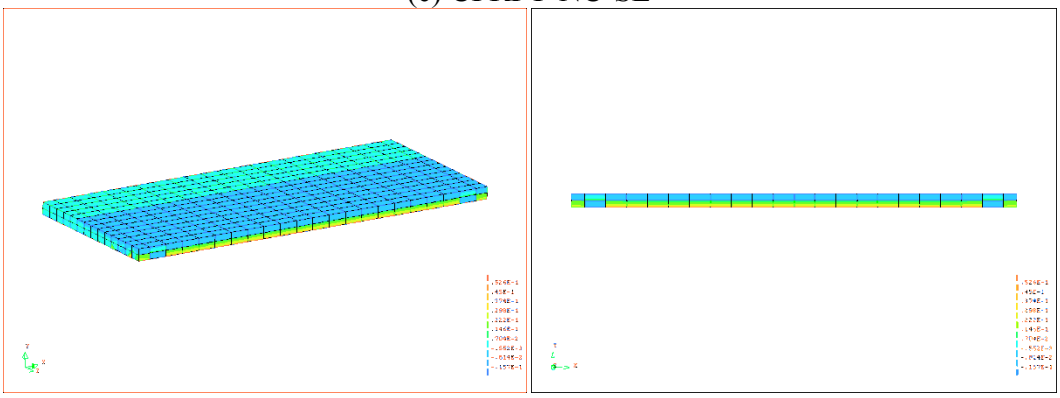

(d) CFRPT-FRC-SL

Figure 6-17 Strain Variations across the Section at Ultimate State

Stress variations of reinforcement are important to determine which material governs the final failure mode and investigate the effects of using different materials. Figure 6-18 illustrates the principal tensile stress variations on tendons at ultimate state with detailed values depicted in legend. Although stress levels are somewhat different for a given panel, all values are below the tendon yield strength. From this observation, it is clear that failure is governed by concrete crushing and not by yielding of reinforcement. In addition, comparison between normal and fiber reinforced concrete reveals that relatively higher stress values are observed in FRC specimens due to higher loading capacity of these members. CFRP tendons participate less in the load-carrying capacity than steel tendons. Accordingly, CFRP tendons can have more reserve to withstand further loading increase than steel tendons with respect to their strengths.

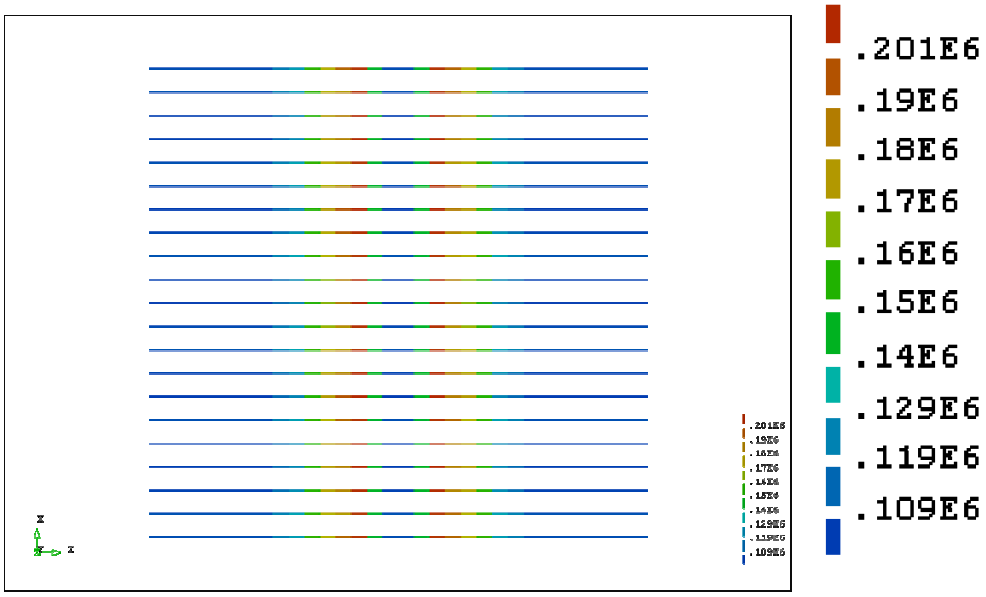

(a) ST-NC-SL

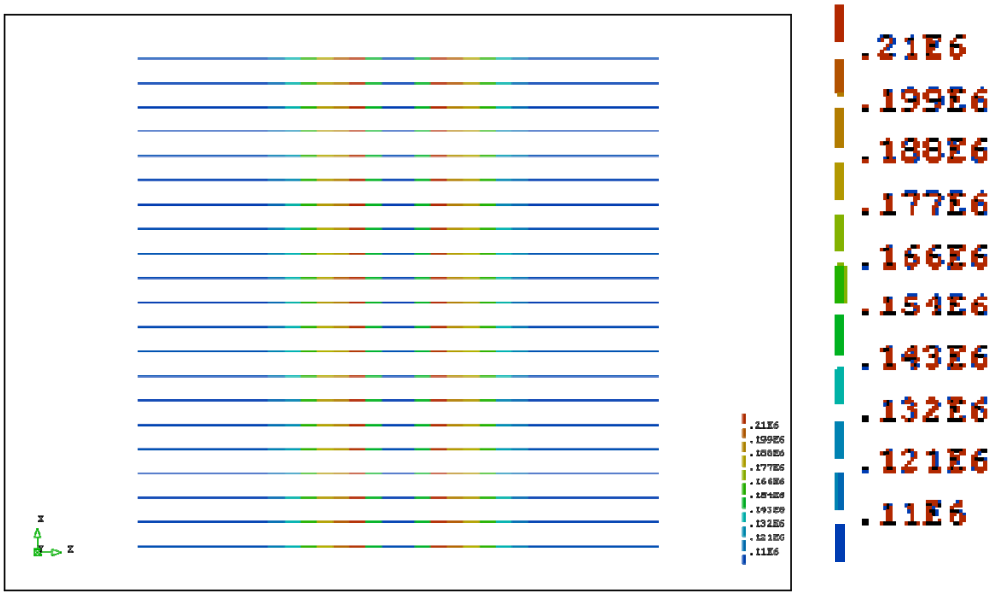

(b) ST-FRC-SL

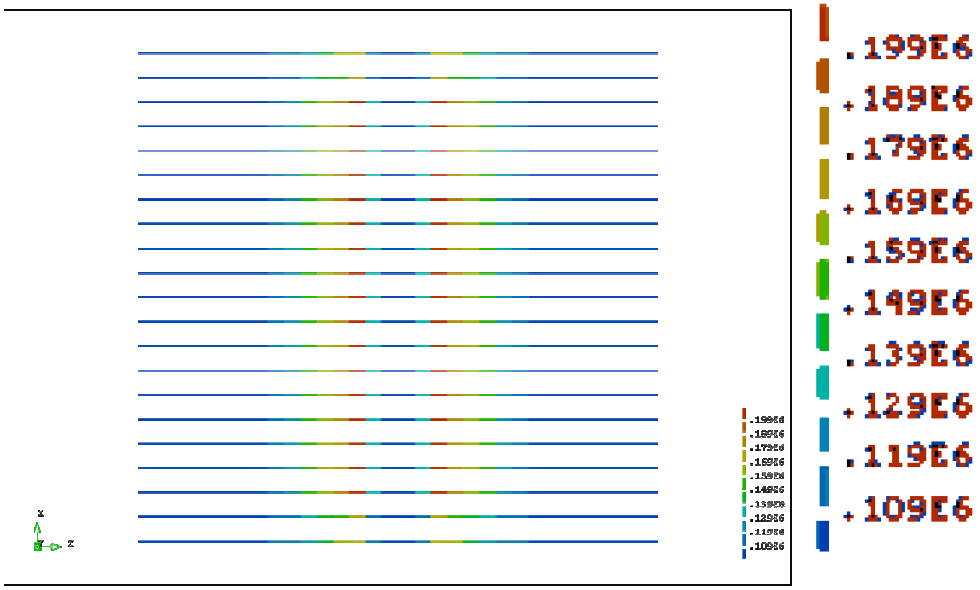

(c) CFRPT-NC-SL

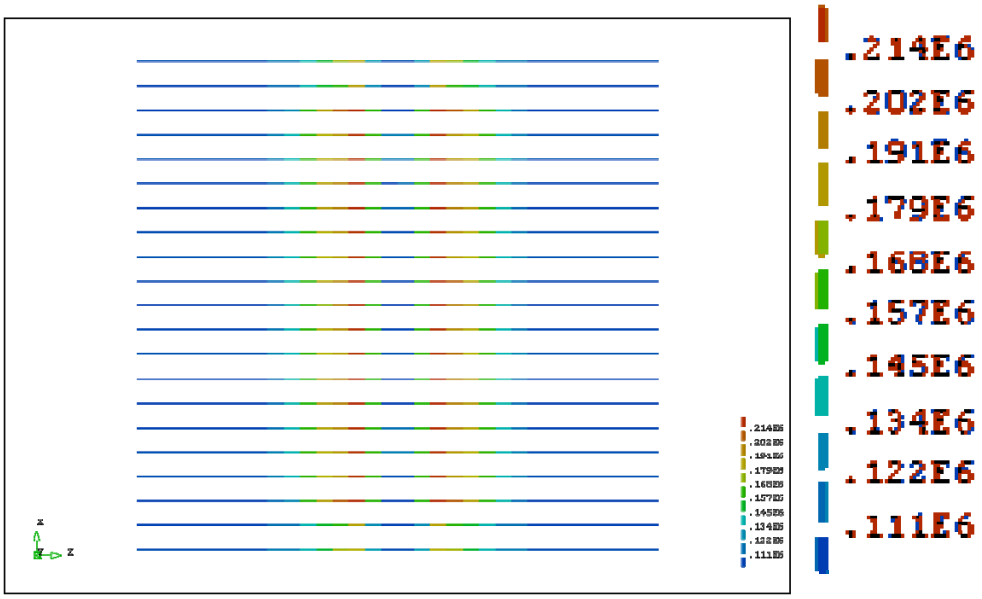

(d) CFRPT-FRC-SL

Figure 6-18 Principal Tensile Stress Variations on Tendons at Ultimate State

Simulation of Deteriorated Unit Panel Capacity

While the previous FE simulation in Section 6.2 focused on the serviceability and cracking aspects of deteriorated panels, the simulation in this section was aimed at estimating the remaining capacity of panels with corroded tendons as observed in the Chapter 4 field investigations. The remaining capacity of corroded panels was examined by FE simulation assuming various corrosion levels. Although this analysis can not exactly reflect real configurations of the panel in situ, it can provide valuable information about future performance of panel types proposed in this study. Configuration of FE models in this analysis follows the

configuration of panel specimen ST-NC-SL with respect to panel design, modeling techniques, and loading process. The option within DIANA software of estimating time-dependent corrosion of embedded steel reinforcement was utilized. This analysis process is performed by assigning a time range and assuming reduction factors for reinforcement cross-section at the corresponding times. In this analysis, FE simulation was carried out on panel ST-NC-SL with predefined reduction factors 0.9, 0.8, 0.7, and 0.6 for all tendons irrespective of time.

Figure 6-19 shows load-displacement relationships for all analytical models. As shown in the figure, cracking and ultimate strengths are significantly decreased with decreasing reduction factors (corresponding to decreasing cross-section). Especially, a marked decrease in ultimate strength is observed in reduction factor, 0.7, with respect to test results as indicated in Table 6-5. Therefore, it is necessary to investigate failure modes from stress variations on concrete and reinforcement.

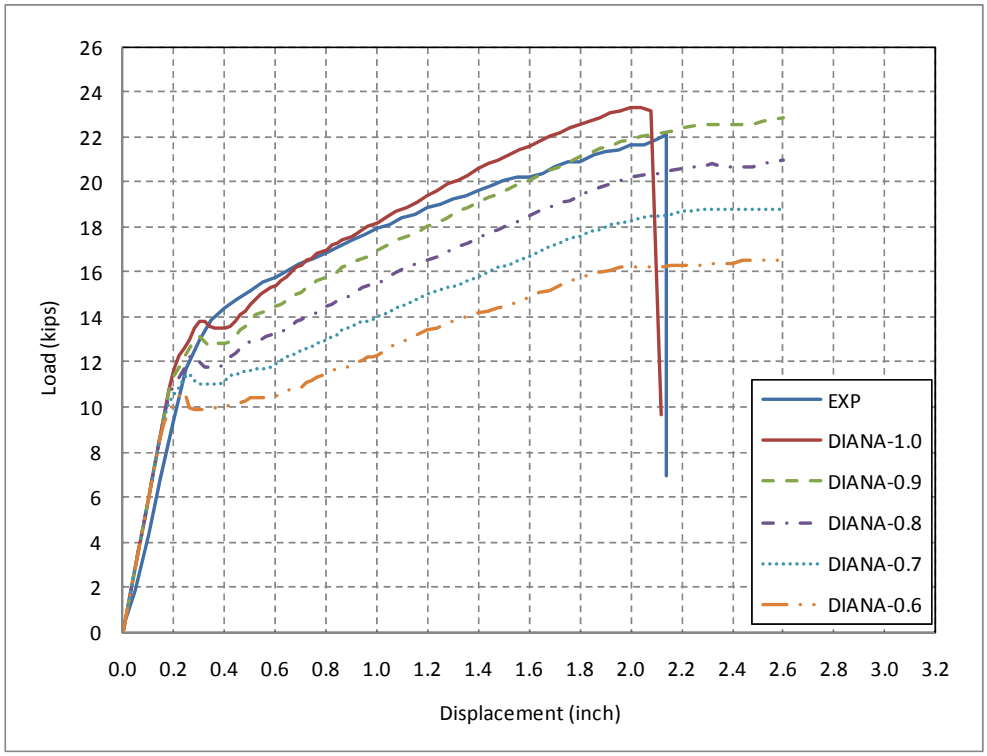

Figure 6-19 Load-Displacement Relationships of Corroded Panels

Figure 6-20 shows normal stress variations at the top surface of the concrete and principal tensile stress variations on the tendons at ultimate state. Significant stress changes are observed in both concrete and tendons between reduction factors 0.8 and 0.7. After reduction factor 0.8, prestressing tendons start to yield and concrete does not reach its compressive strength. That is, yielding of the prestressing tendons governs the failure mode. Therefore, severe corrosion levels of prestressing tendons, with reduction in cross-section roughly estimated between 0.8 and 0.7, can cause substantial degradation of the ultimate capacity of the SIP panel as well as alter the failure mode.

Table 6-5 Comparison of Ultimate Strength of Corroded Panels

Simulation I.D.	Ultimate Strength (kips)	FE/EXP
ST-NC-SL	22.08	1.00
FE – 1.0	23.30	1.05
FE – 0.9	22.90	1.04
FE – 0.8	21.00	0.95
FE – 0.7	18.80	0.82
FE – 0.6	16.50	0.75

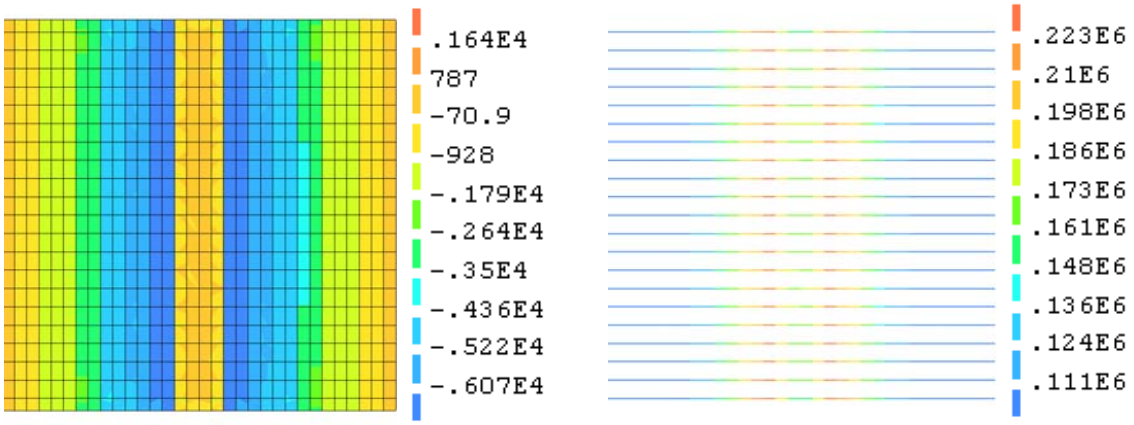

(a) Reduction factor = 0.9

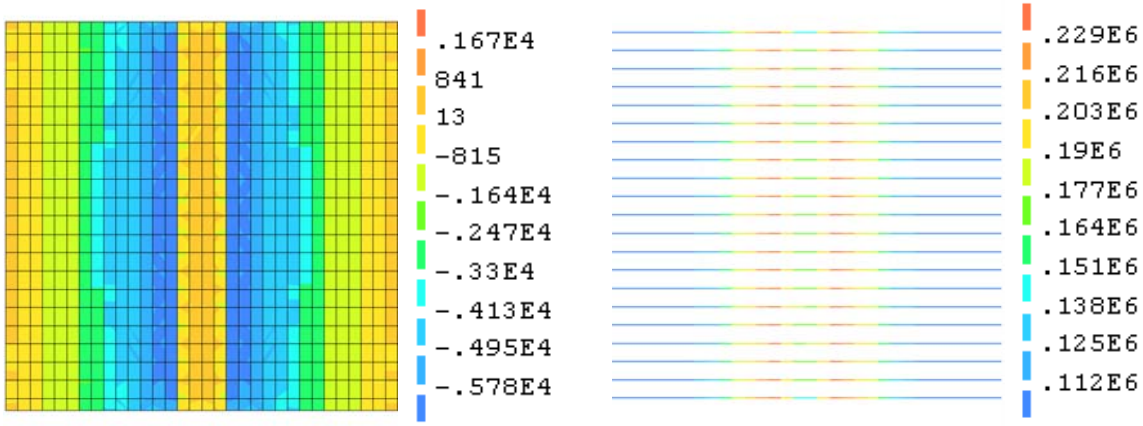

(b) Reduction factor = 0.8

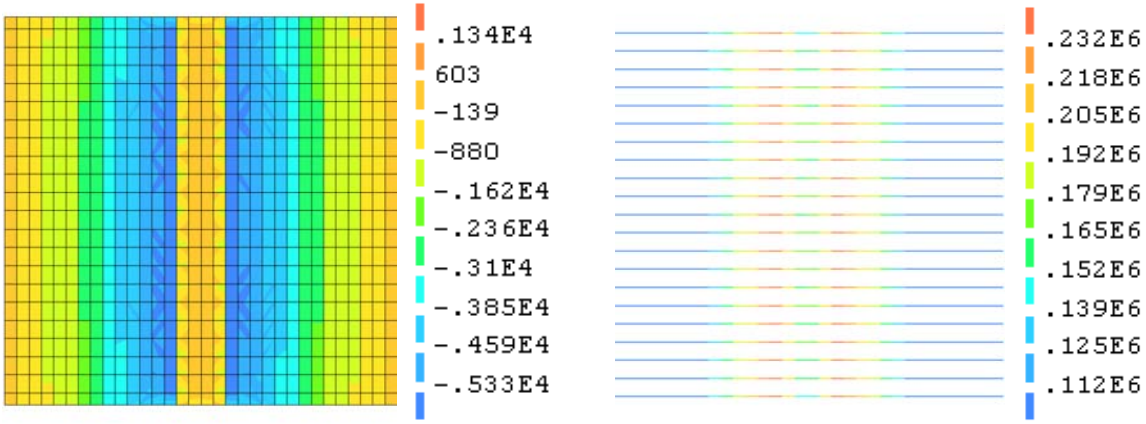

(c) Reduction factor = 0.7

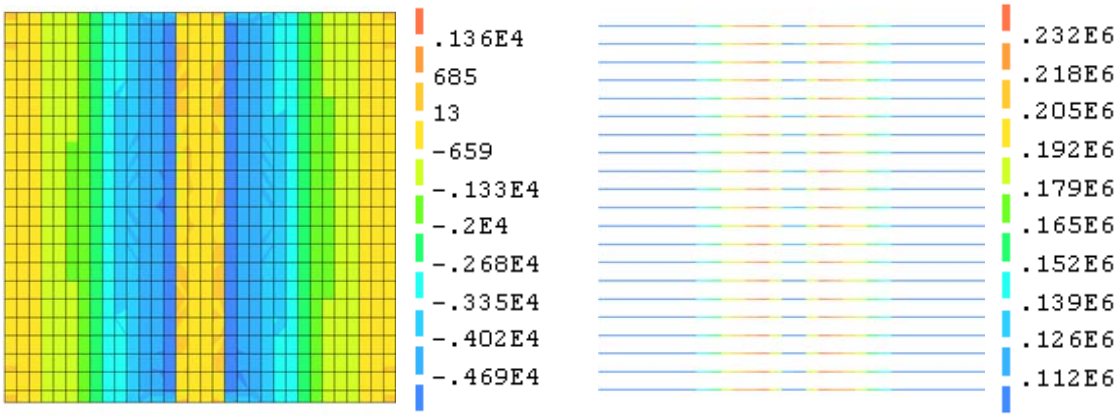

(d) Reduction factor = 0.6

Figure 6-20 Stress Variations for Corroded Panels

6.3.2 Simulation of Composite Deck Behavior

This section presents FE results to simulate the composite bridge deck systems composed of the proposed unit panels composite with a CIP concrete topping. The configuration of Bridge A4709, located in Mexico, MO, was considered in the FE analysis. Figure 6-21 shows a cross-section of the bridge. (Comprehensive field investigation of Bridge A4709 is discussed in Section 4.3.) One half of the cross-section was considered in this analysis due to geometrical symmetry. To maximize loading effects on the panels, one layer of panels along the direction perpendicular to traffic flow is considered in this analysis. A total number of 8 FE simulations were carried out consisting of four simulations for the composite deck systems adopting the proposed panels and the other four simulations for corrosion effects for the corresponding systems. (Of the six static load panel specimens in Section 5.2, panels with epoxy-coated steel tendons were excluded from the simulation for reasons discussed in Section 6.3.1.) Based on results from the analysis discussed in Section 6.3.1.2, the corrosion level on the FE models was assumed as a reduction factor of 0.7 for all tendons. Analytical cases are summarized in Table 6-6.

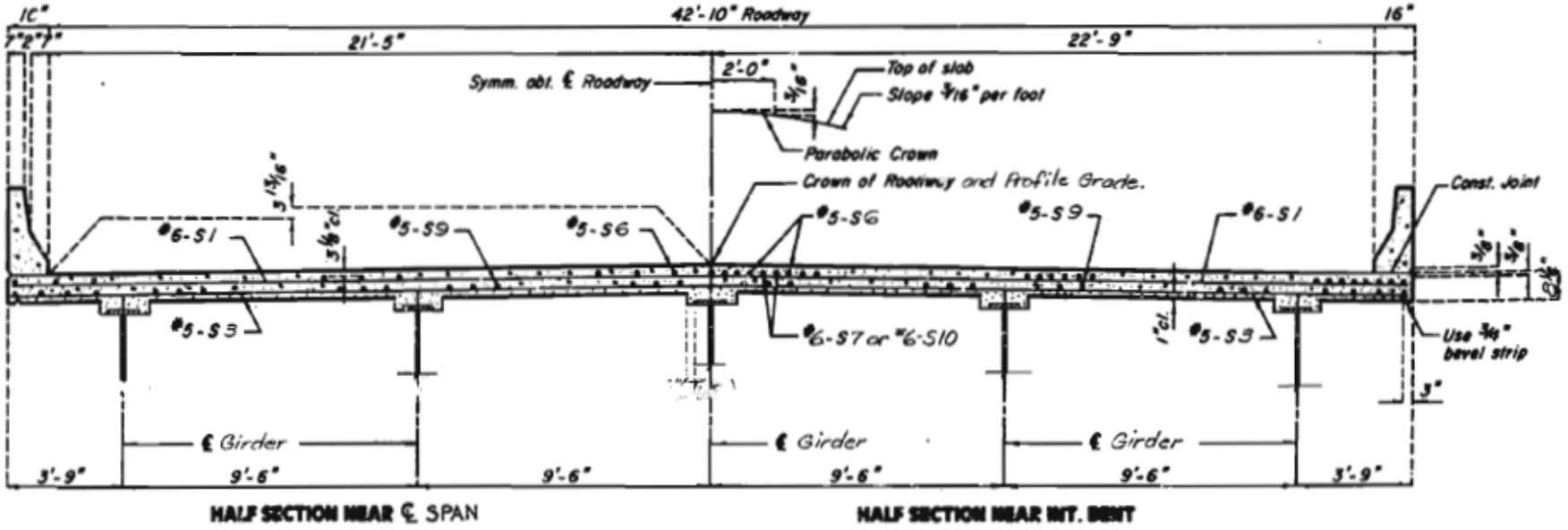

Figure 6-21 Cross-Section of Bridge A4709 (Mexico, MO)

Table 6-6 Analysis Cases for Hybrid Composite Deck

Simulation ID	Concrete		Tendon		Corrosion
	NC	FRC	STEEL	CFRP	
H-ST-NC	O		O		
H-ST-FRC		O	O		
H-ST-NC-CO	O		O		O
H-ST-FRC-CO		O	O		O
H-CFRP-ST-NC	O		O	O	
H-CFRP-ST-FRC		O	O	O	
H-CFRP-ST-NC-CO	O		O	O	O
H-CFRP-ST-FRC-CO		O	O	O	O

6.3.2.1 FE Model Configuration

Typical phase analysis was carried out in two phases, which include a prestressing phase denoted as Phase I and a loading phase as Phase II as shown in Figure 6-22. In the prestressing phase, only the prestressing process was simulated in the SIP panels without any boundary conditions or additional elements. Phase II represents the final stage of the FE model considering all loads, boundary conditions, and additional elements. Dead load in Phase II was automatically calculated in DIANA, while live load was assumed as pressure load by dividing the wheel load by tire contact area. To maximize the loading effect to the panel, one wheel load was located in the center of the second span as illustrated in Figure 6-22(c), while the other wheel load was located near the first interior girder.

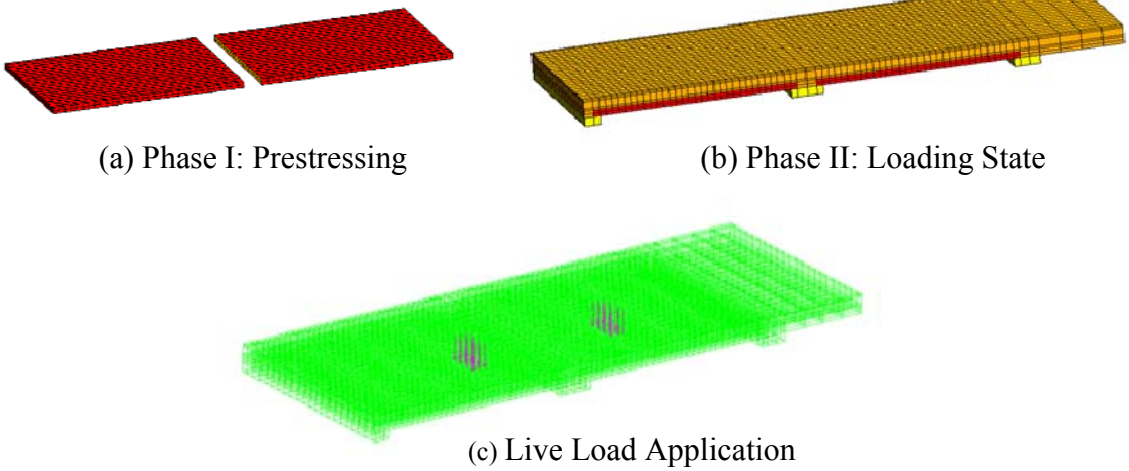

(a) Phase I: Prestressing

(b) Phase II: Loading State

(c) Live Load Application

Figure 6-22 FE Models on Each Phase for Hybrid Deck System

Figure 6-23 illustrates the configuration of a representative FE model. The eight-node isoparametric solid brick element (HX24L in DIANA) was used for modeling the SIP panel, CIP topping concrete, and supporting plates which represent the upper flange of the steel girder. As assumed in the design process, locations of supporting girders were assumed as pinned boundary conditions, while cross section at the axis of symmetry was assumed as fixed boundary conditions. Both temperature reinforcement and tendons were modeled as embedded bar elements specified by DIANA assuming a perfect bond.

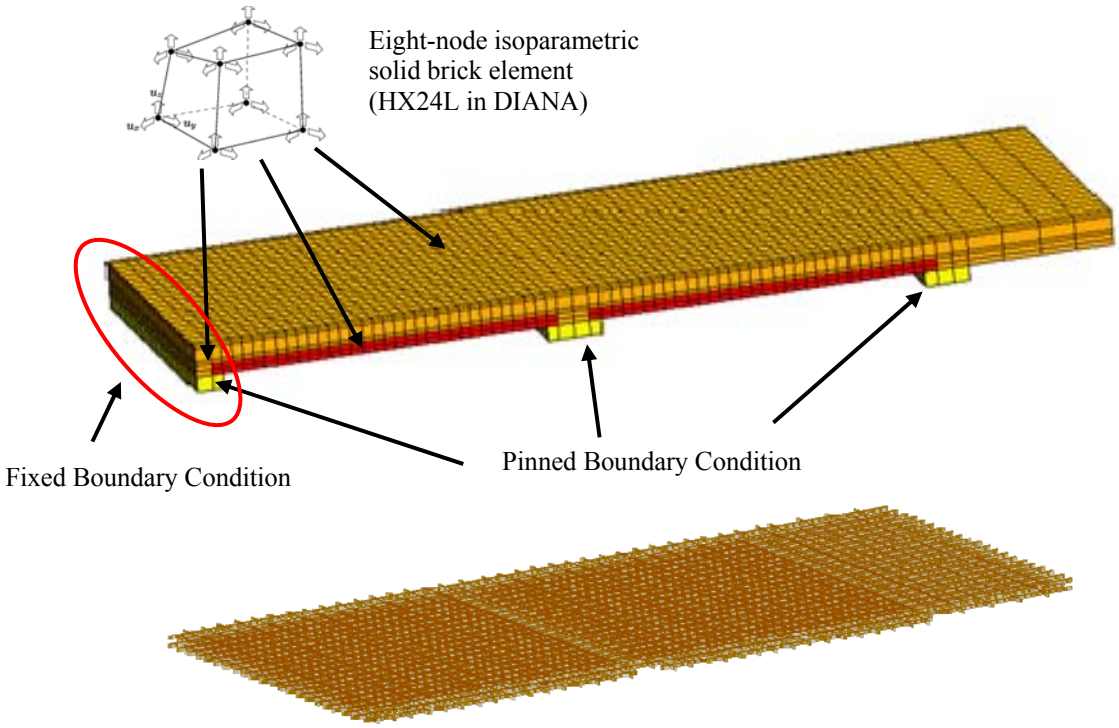

Figure 6-23 Configurations of FE Models Hybrid Deck System

6.3.2.2 Results and Discussion

Representative stress variations in each phase for the panel and composite deck system of H-ST-NC are illustrated in Figure 6-24 through Figure 6-28 . As shown in the figures, serviceability of the composite system can be estimated not only for the panel but also for the deck system according to time-dependent loading conditions. From Figure 6-24, Figure 6-26, and Figure 6-28, normal stress changes in the panel can be observed. To focus on investigating the capability of the proposed panel in the composite system, normal stress variations on the panel under combined loads and corresponding principal tensile stress variations on tendons are summarized in this section. Detailed results are also available in Appendix D.

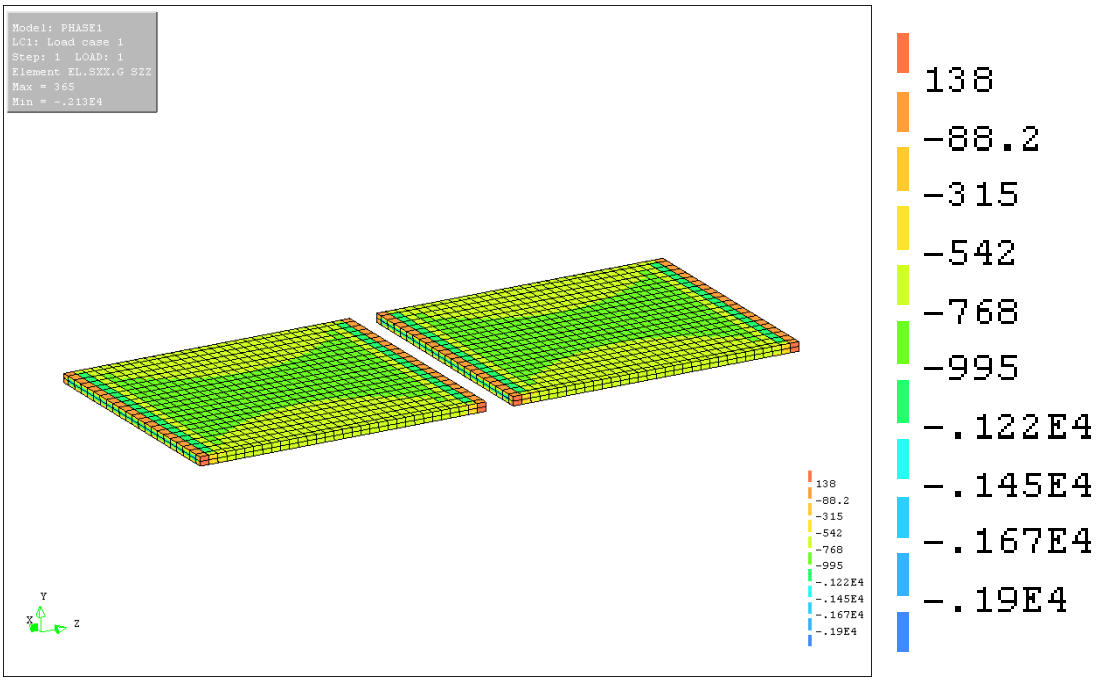

Figure 6-24 Normal Stress Variations on Panel at Phase I

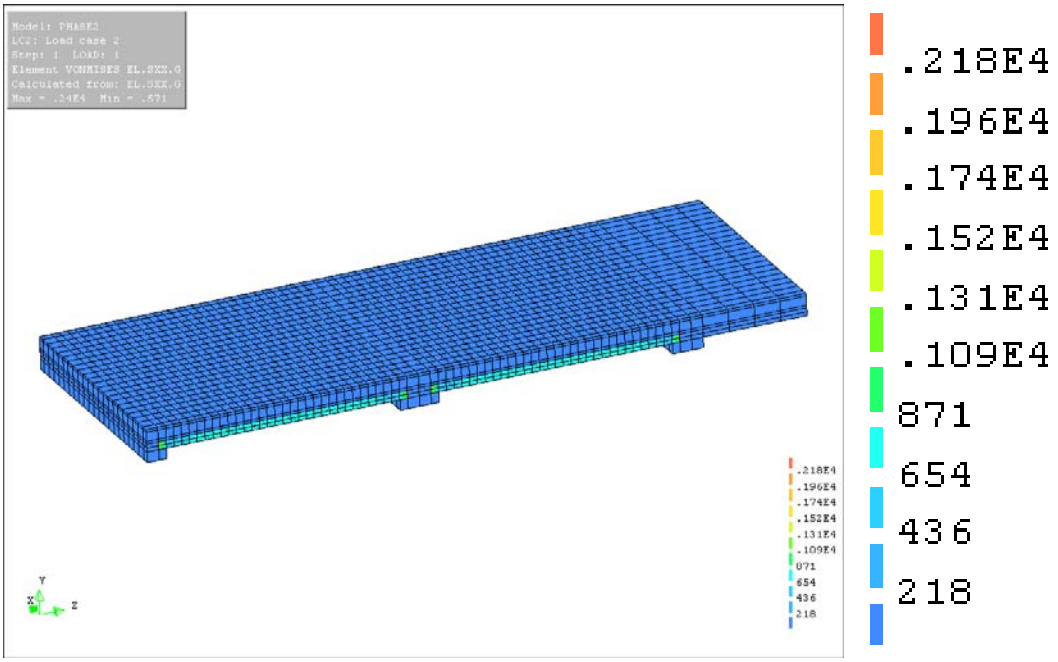

Figure 6-25 Von Mises Stress Variations in Composite Deck System under Dead Load at Phase II

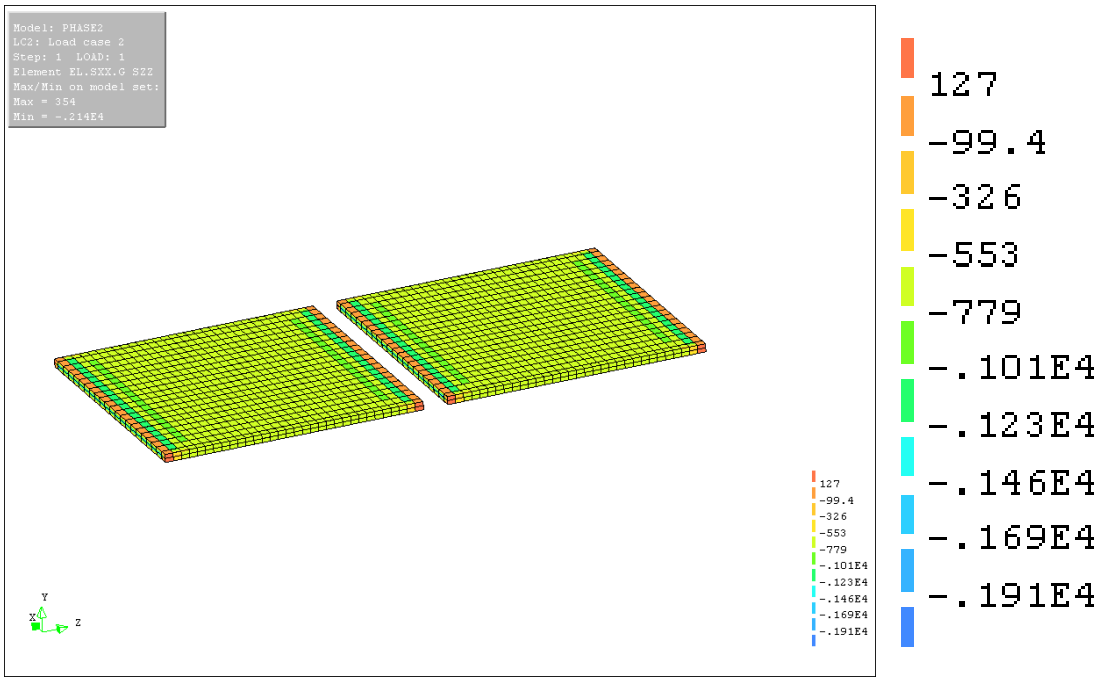

Figure 6-26 Normal Stress Variations in Panel under Dead Load at Phase II

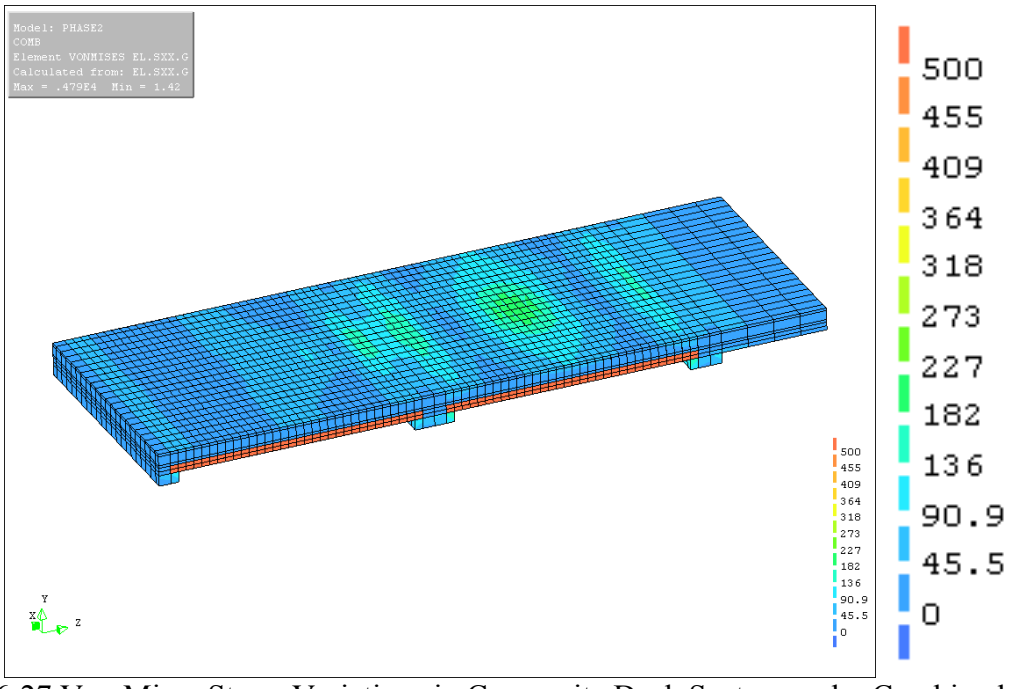

Figure 6-27 Von Mises Stress Variations in Composite Deck System under Combined Load at Phase II

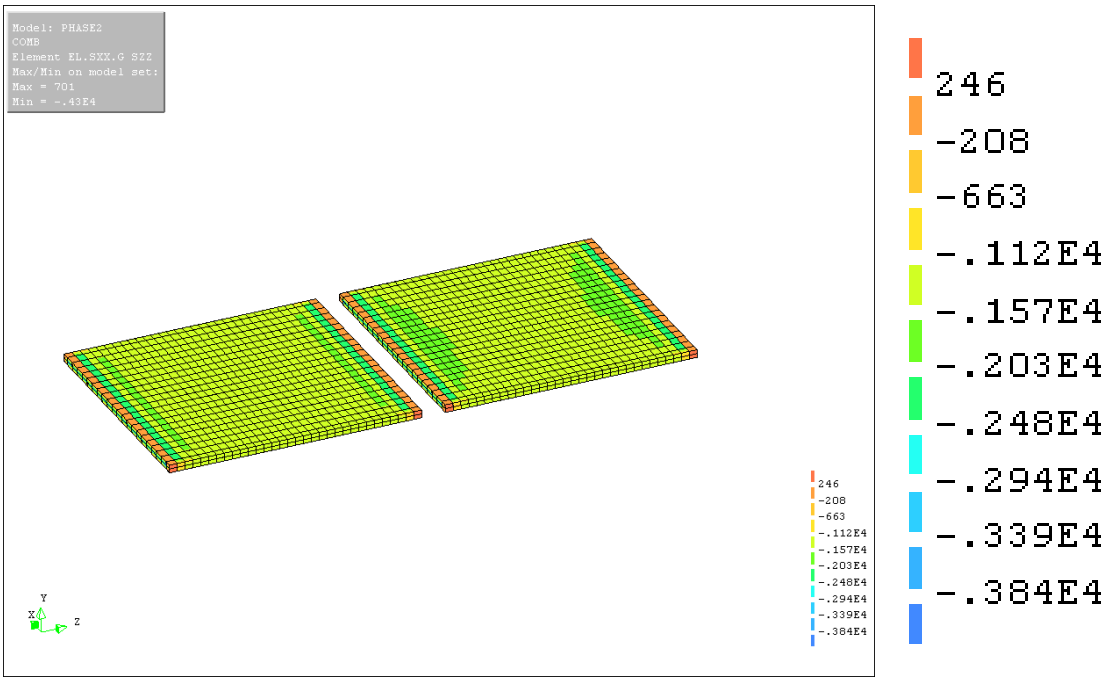

Figure 6-28 Normal Stress Variations on Panel under Combined Load at Phase II

Normal stress variations on concrete for all analytical cases are presented in Figure 6-29 with respect to both the top and bottom surfaces. As can be seen from the figure, all panels, even corroded panels, are able to sustain the compressive stress state under combined dead and live loads. Because SIP panels are participating in the tensile portion of the composite deck system, this low stress state indicates further capacity of the panel to withstand excess load. While the use of FRC does not seem to affect significantly the structural performance of the panel at the service state, adoption of CFRP tendons at the edge regions somewhat affects the serviceability performance. Unequal prestressing effects for the panel cross-section can be a reason for this phenomenon. As a result, local stress concentration is observed at the location of the wheel load on the bottom surface as shown in Figure 6-29(e) and (f). Although compressive stress ranges are somewhat less than those of panels with only steel tendons, it is not significant. When steel tendons are corroded, however, significant stress redistribution is observed as shown in Figure 6-29(g) and (h). This phenomenon is caused by loss of loading-capacity of corroded tendons resulting in increased participation of CFRP tendons.

Corresponding principal tensile stress variations on tendons are illustrated in Figure 6-30. A very interesting phenomenon is observed in these results. As shown in the figure, most of the tendons have similar stress variations and values for all analysis cases. These results are very different from the results of the FE analysis for the Section 6.3.1.2 unit panel test specimens because of different loading configurations. As discussed in Section 6.3.1.2, stress concentrations were observed in the unit panel analysis under the loading frame with different effects on each tendon, while uniform stress distribution was observed in this analysis regardless of tendon types. Thus, use of CFRP tendons makes no difference in the serviceability of the composite deck system. As a result, concrete properties are found to be more influential in the serviceability of the composite system similar to results of the Section 6.3.1.2 unit panel analysis.

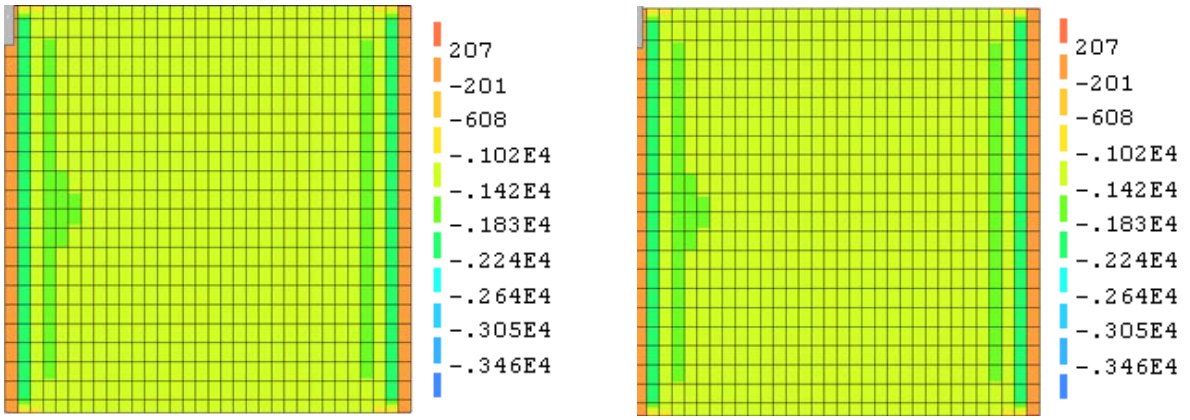

(a) H-ST-NC

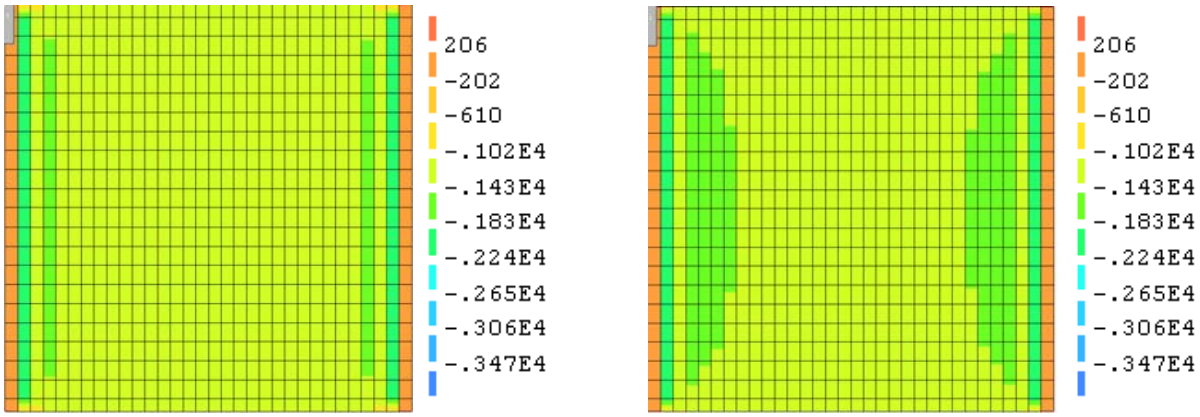

(b) H-ST-FRC

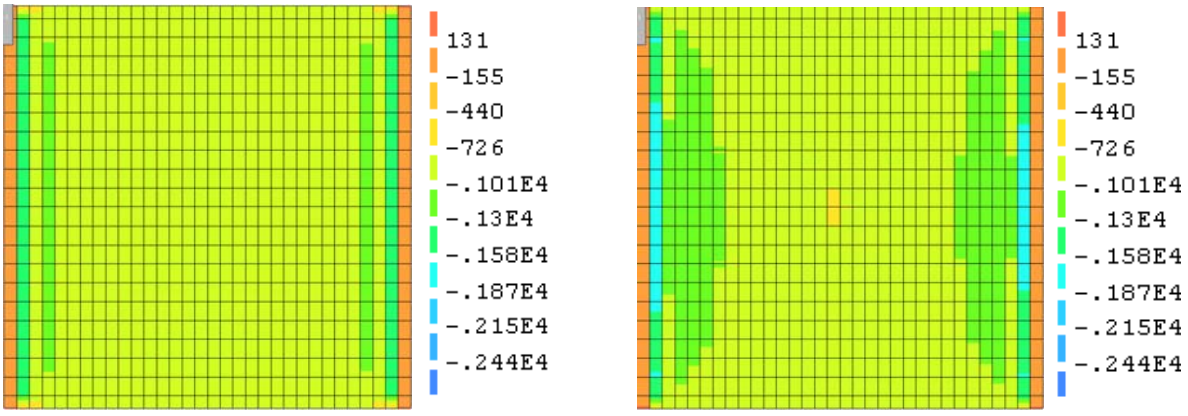

(c) H-ST-NC-CO

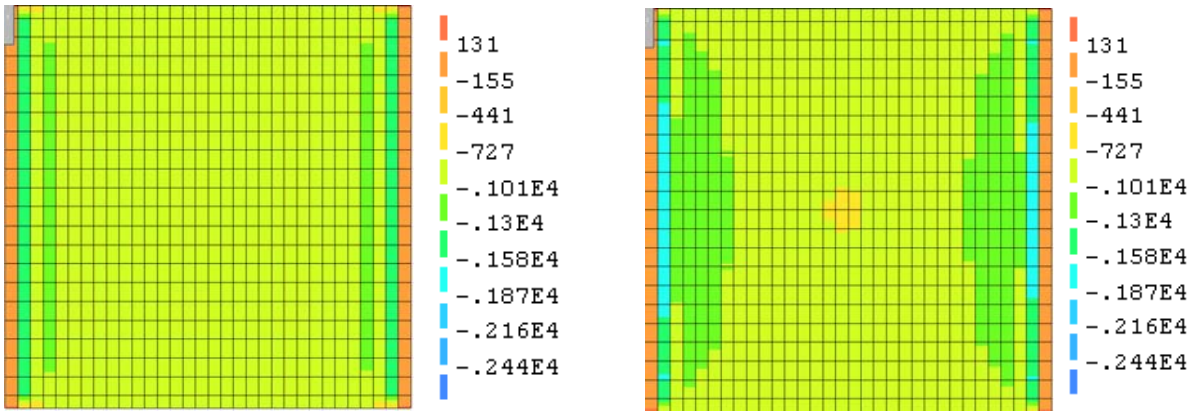

(d) H-ST-FRC-CO

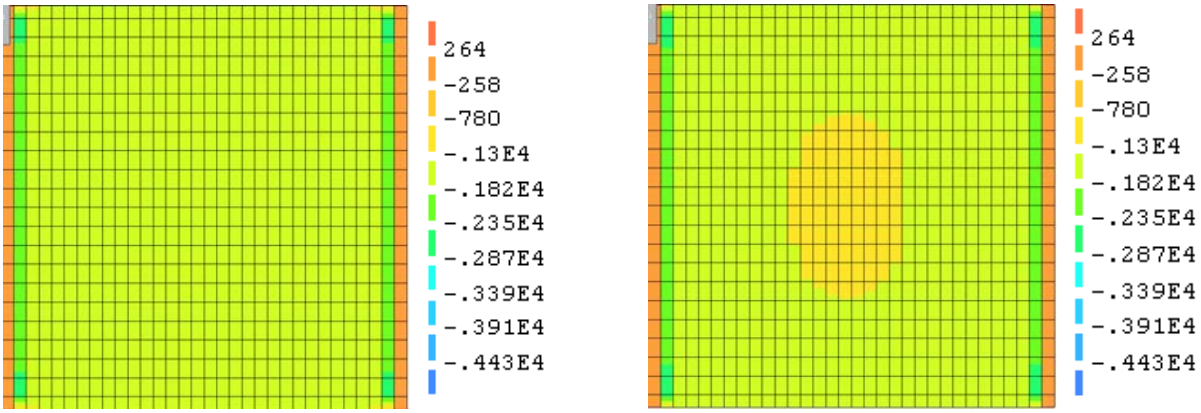

(e) H-CFRPT-ST-NC

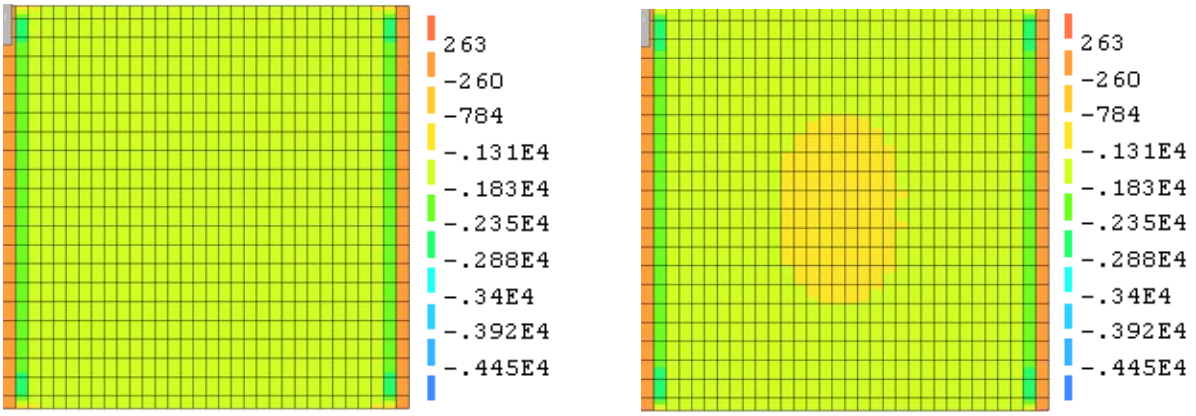

(f) H-CFRPT-ST-FRC

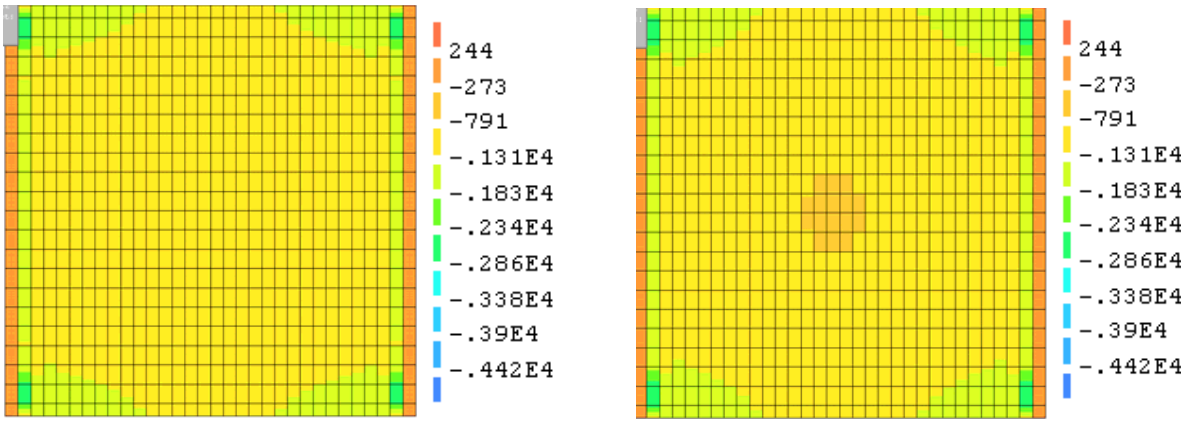

(g) H-CFRPT-ST-NC-CO

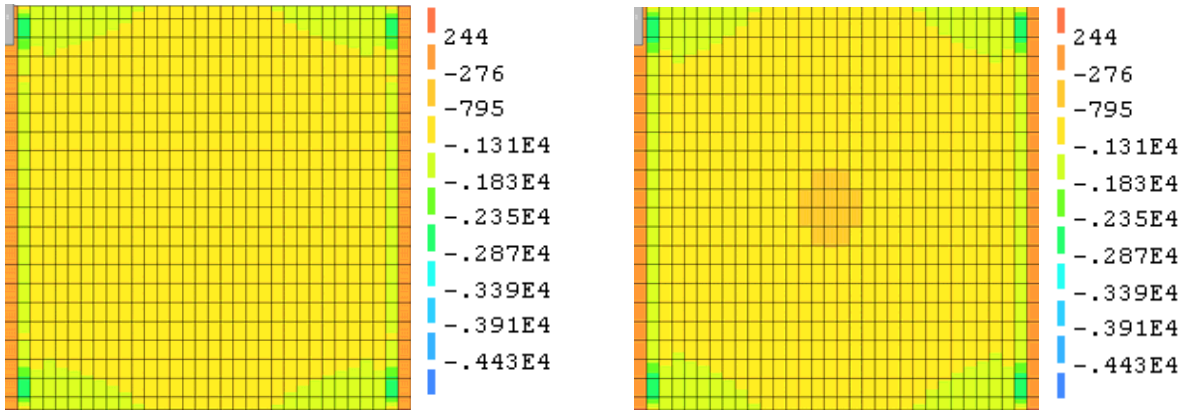

(h) H-CFRPT-ST-FRC-CO

Figure 6-29 Normal Stress Variations on Concrete under Combined Loading at Phase II

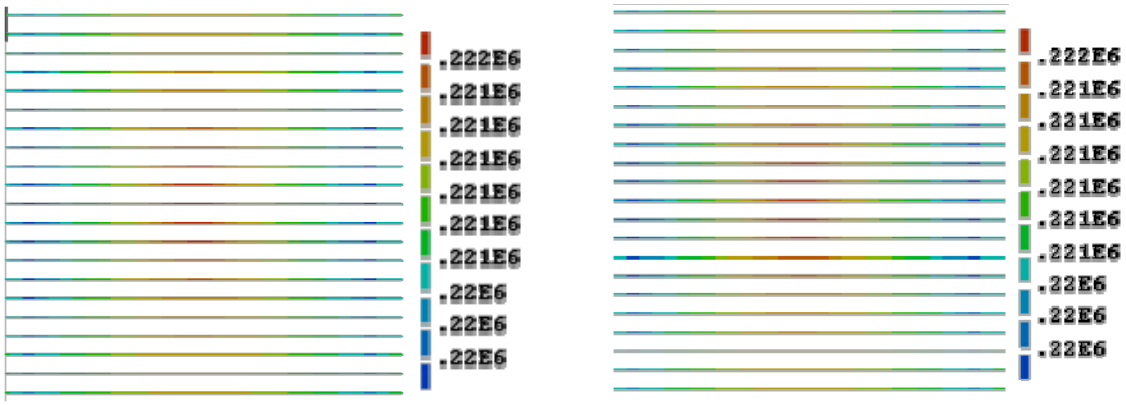

(a) H-ST-NC

(b) H-ST-FRC

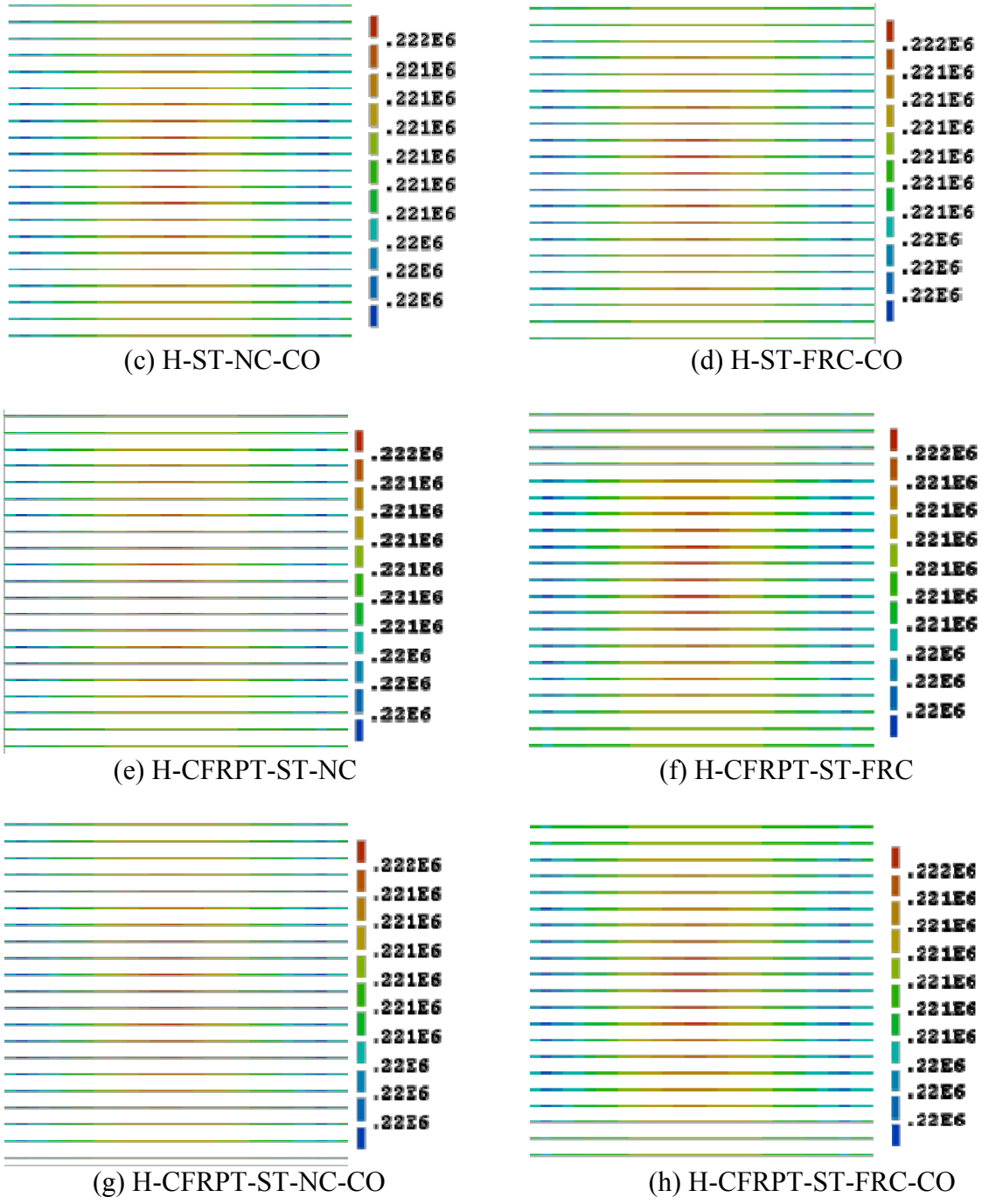

(c) H-ST-NC-CO (d) H-ST-FRC-CO

(e) H-CFRPT-ST-NC (f) H-CFRPT-ST-FRC

(g) H-CFRPT-ST-NC-CO (h) H-CFRPT-ST-FRC-CO

Figure 6-30 Principal Tensile Stress Variations on Tendons under Combined Loading at Phase II

6.3.3 Simulation of Deck Behavior with CIP Reinforcement Modifications

This section presents results of FE simulation of the deck behavior when proposed modifications are made to the CIP topping reinforcement to reduce the occurrence of transverse reflective cracks at panel joint locations. As discussed in the Chapter 4 field investigations, the occurrence of transverse reflective cracks showed a consistent trend. Most reflective cracks were observed within the bridge girder positive moment regions, while a relatively smaller number of reflective

cracks were observed in the negative moment regions (i.e., over the pier locations). In most cases, the CIP topping in this region is more heavily reinforced due to negative moment requirements. This structural reinforcement also helps to restrain shrinkage of the CIP topping concrete resulting in mitigation of stress concentrations at the panel joint locations. Based on this observation, 2D FE simulation was carried out to investigate the effect of increased amounts of reinforcement in the CIP topping to restrain the shrinkage of the CIP topping concrete. Configuration of the A4709 bridge (located in Mexico, MO) as shown in Figure 6-31 is again used in this analysis. FE simulation was conducted on two FE models having different amounts of CIP topping reinforcement within the positive moment and negative moment regions according to Figure 6-31. For the sake of emphasizing the effects of increased reinforcement on the shrinkage, only one-dimensional behavior in the bridge longitudinal direction (along traffic direction) was considered excluding the other factors such as loading conditions or 3-dimensional configurations.

6.3.3.1 FE Model Configuration

A local section of the bridge deck shown in Figure 6-31 was considered in the FE model consisting of three SIP panels along the traffic direction and one layer of SIP panel along the transverse direction. Figure 6-32 illustrates the configuration of the FE model. Note that the figure exaggerates the local area at the joints in order to show clearly the detailed configuration of the FE model because fine mesh in the FE model makes it otherwise difficult to visualize. As shown in the top figure, both ends of model were assumed as a fixed boundary condition. Shrinkage of concrete was modeled using methodology described in ACI 209 (1982), which was adopted in DIANA as a built-in option, with respect to time variations from 1 day to 15 years.

The four-node quadrilateral isoparametric plane stress element (Q8MEM) was used for modeling the SIP panel and CIP topping concrete, while both top and bottom longitudinal reinforcements in the CIP topping were modeled as embedded bar elements specified by DIANA assuming perfect bond.

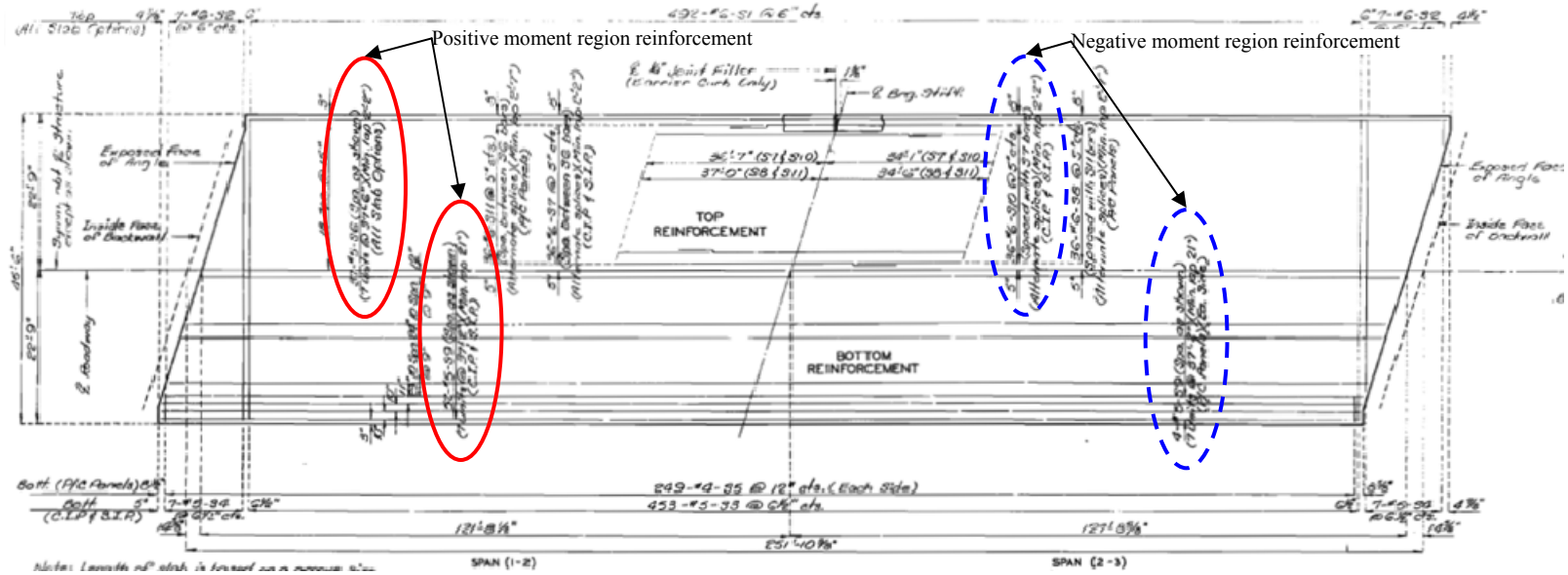

Figure 6-31 CIP Deck Reinforcement Detail of Bridge A4709 (Mexico, MO)

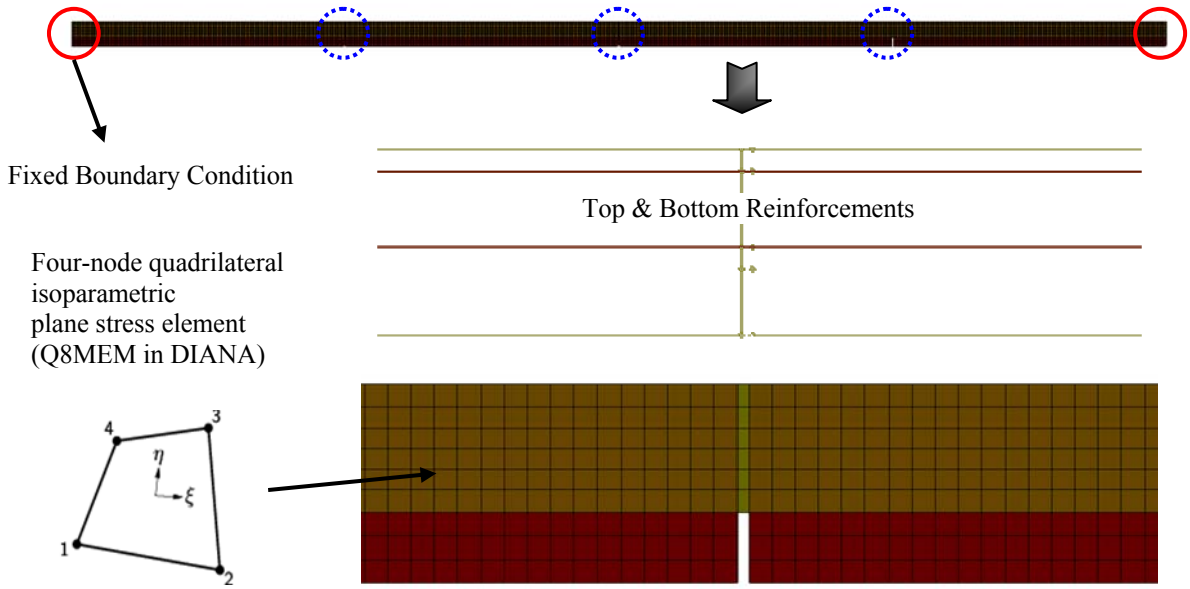

Figure 6-32 FE Models for Slab Deck with Modified CIP Reinforcement

6.3.3.2 Results and Discussion

Von Mises stresses and crack patterns at representative times are summarized in Table 6-7. No shrinkage cracks are observed in either of the FE models at the period of 3 months, however, differences can be seen in the stress variations at this time. For the model with the positive moment reinforcement condition, different amounts of reinforcement tend to induce more stress participation from the bottom reinforcement due to the larger amount of bottom reinforcement. The model with the negative moment reinforcement condition, shows similar stress participation by both top and bottom reinforcement due to similar amounts of both reinforcement. Moreover, discontinuity at the panel joints induces a stress concentration at the bottom of the CIP topping concrete in both models. This phenomenon is observed in all analytical results regardless of time. Shrinkage cracks are observed in the model with the positive moment reinforcement condition in three years at the joint location, while no cracks are observed in the model with the negative moment reinforcement condition. Crack patterns at this time are highlighted in Figure 6-33. As shown in the figure, cracks in the top portion of the CIP concrete are wider than cracks in the bottom portion resulting in stress relief on the top portion of the concrete. These crack patterns remain the same until fifteen years with increasing crack width. In contrast, the model with the negative moment reinforcement condition finally shows shrinkage cracks at fifteen years. These crack patterns are also highlighted in Figure 6-34. As opposed to the crack patterns in the model with the positive moment reinforcement condition, cracks at the bottom portion of the CIP concrete are wider than those at the top portion. Crack widths of this model are very small, however, compared to those of the positive moment reinforcement condition model.

Although simplified assumptions of FE models cannot reflect all features occurring in real structures, this analysis provides insight to the beneficial effects of enhanced reinforcement in CIP topping deck as well as the mechanism of crack propagation. From this analysis, it can be

found that increased CIP topping reinforcement can at least retard the shrinkage cracking and change the mechanism of crack propagation.

Table 6-7 Von Mises Stress Variations and Crack Patterns of Slab Deck with Modified CIP Reinforcement

Period	Positive Moment Region Reinforcement	Negative Moment Region Reinforcement
3 month	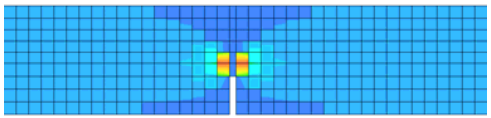 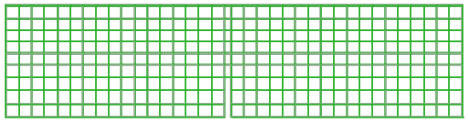	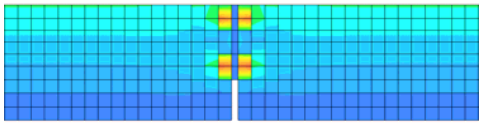 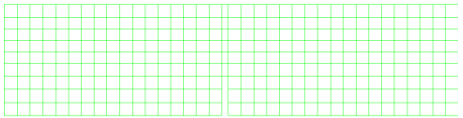
3 year	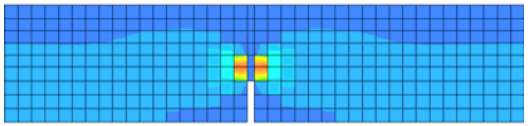 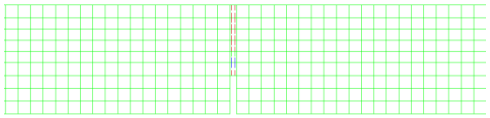	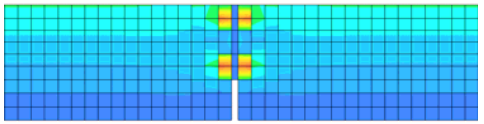 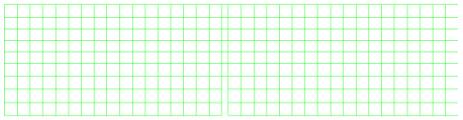
15 year	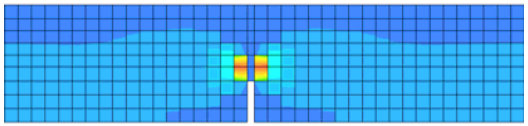 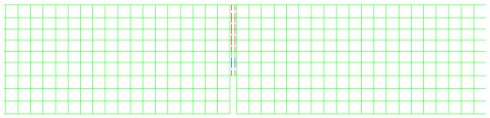	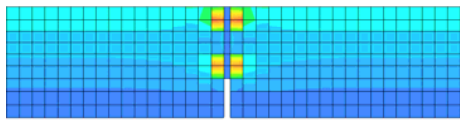 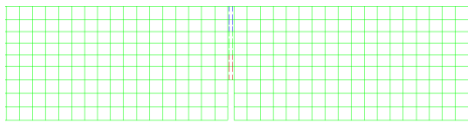

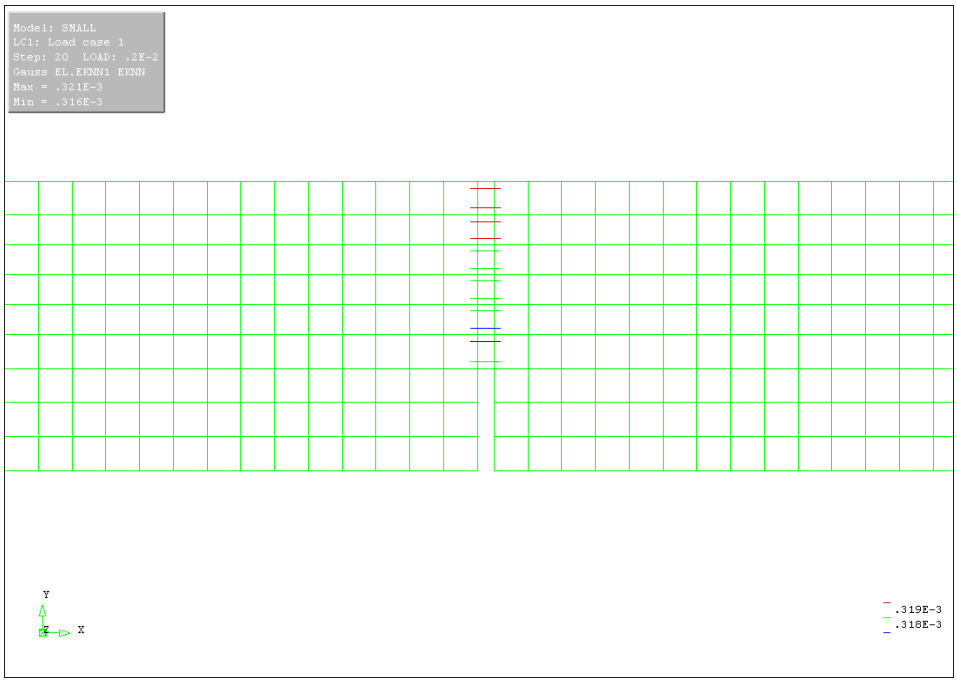

Figure 6-33 Crack Patterns on FE Models with Positive Moment Region Reinforcement at 3 Years

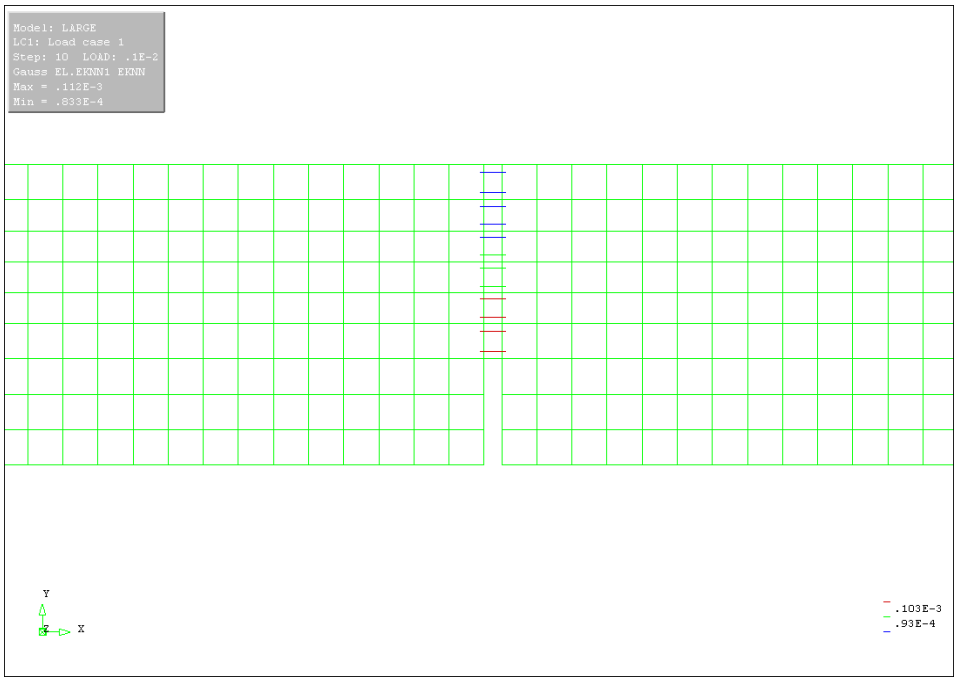

Figure 6-34 Crack Patterns on FE Models Having Negative Moment Region Reinforcement at 15 Years

6.4 Summary

FE analysis results presented in this chapter provide valuable information about identifying the spalling problems and examining the proposed SIP-CIP deck system modifications. The following key observations are made from the results of the FE simulations.

- Preliminary FE analysis indicated that corrosion cracks could not propagate from the locations of reinforcements to side surfaces regardless of number of reinforcements and boundary conditions. This analysis evoked examination of other causes of spalling problems in the SIP panel.
- Distance between adjacent reinforcement was examined to investigate the effects on spalling by rearranging the U1 lifting bar according to MoDOT specifications (2004). When this bar was located between the first and second tendon with 2 in. spacing between reinforcements, a bridging crack was observed at the final stage between the first tendon and U1 bar triggering the spalling of the edge concrete. No crack propagation was observed in the case of the FE model with the U1 bar between the second and third tendons with 2.25 in spacing between reinforcements. The significance of the bridging crack is a key finding of this analysis, because corrosion of temperature reinforcement oriented perpendicular to the tendon direction can induce cracks along the temperature reinforcement playing a similar role as the bridging crack. Thus, it can be concluded that the bridging crack is a primary agency for corrosion-induced spalling problem in the panel.
- Increasing amounts of side cover showed beneficial effects on mitigating the spalling problem by mitigating crack propagation to the side surface of the panel regardless of reinforcement arrangement.
- Loss of edge tendons did not significantly affect the serviceability of SIP panel in terms of structural performance.
- FE simulation of the Chapter 5 unit panel test specimens showed consistency in overall behavior for the panels with combinations of steel or CFRP edge tendons and normal concrete or FRC. In contrast, the Chapter 5 test results were sensitive to the use of different materials. This might be caused by different material properties adopted in the FE models or mechanical assumptions made in the FE model such as perfect bond between concrete and reinforcements. In spite of the small discrepancy in overall behavior, FE analysis also provided detailed information about local behavior of each component as well as the failure mechanism. Similar with test results, failure was governed by concrete crushing on top of the panel. Even at failure, the stress in all tendons was less than the yield stress.
- Results of FE simulation showed that as the corrosion level of steel tendons was increased, the capacity of the panels decreased under the same loading configuration as the Chapter 5 unit panel test set-up. However, when these panels were modeled as a composite section under real service loading states, FE simulations results showed that there were no significant differences in stress variations on tendons, while concrete was more responsible to carry the subjected load due to stress redistribution.
- Serviceability of the composite system was examined by incorporating the proposed panels to the composite section. As observed in stress variations on tendons and concrete, concrete properties were found to be more influential in the serviceability of the composite system, similar to the results of unit panel analysis.
- Enhanced reinforcement in the CIP topping deck increased the resistivity for shrinkage cracks. It delayed the time of occurrence of shrinkage cracks with smaller crack widths as

well as changed the mechanism of crack propagation.

7 REPAIR

7.1 Introduction

Findings from the Chapter 4 field investigations and the Chapter 6 simulations were used to determine the nature and mechanism of spalling observed in partial-depth PPC bridge decks. Based on these findings, this chapter discusses repair options specific to this type of bridge deck construction based on MoDOT specifications and the spalling problems observed.

Physical evidence discussed in Chapter 4 suggests that transverse cracking in the CIP topping at the panel joint locations and corrosion of panel reinforcement play a key role in spalling of the panels. The spalling observed was found to be the result of the penetration of water and chlorides through the transverse reflective cracking in the CIP topping at the panel joints, to the interface between the CIP topping and the SIP panels, then through the SIP panels to the prestressing tendons and other reinforcement located near the panel joints. GPR results indicated that most of the deck deterioration is concentrated near the area of reflective cracking in the CIP topping. Additionally, increased transverse crack control was found to be significant in increasing the concrete integrity and delaying the onset of spalling at the panel joints. Finally, evidence of delamination was found at the interface between the CIP topping and SIP panels, particularly at panel joint locations, despite the roughened SIP panel surface.

Evidence from the Chapter 6 simulations corroborates the Chapter 4 findings in terms of the significance of delamination of the SIP panel-CIP topping interface and corrosion-induced cracking at the SIP panel edges. Based on the typical arrangement of panel reinforcement in the current MoDOT specifications (2004), however, Chapter 6 simulations suggest that other factors need to be present (such as butting of panels) in order to trigger the horizontal crack propagation that leads to spalling.

The Chapter 6 simulations were also significant in that they showed that the loss of edge tendons did not significantly affect the structural performance of the SIP panels under service loads. Accordingly, the repair methodology discussed in this chapter is focused on non-structural repair to mitigate further penetration of water and chlorides to the panels. Section 7.2 discusses the repair of cracks and surface treatment of the CIP topping, while Section 7.3 discusses repair of the SIP panel.

7.2 Repair of CIP topping

7.2.1 Crack Repair

Because of the inherent discontinuity of the partial depth precast panel system discussed in Section 2.1.2, transverse reflective cracks in the CIP topping cannot be avoided (although crack width can be restrained by reinforcement crossing the crack). Repair methods of the CIP topping discussed in this section address ways to repair and seal the transverse reflective cracks at the panel joint locations in order to reduce the penetration of water and ingress of chlorides. Several methods used to repair cracks are described below with considerations specifically related to this study. Delamination at the SIP panel-CIP topping interface is also addressed in this section.

Table 7-1 CIP Topping Crack Repair Options

Type	Epoxy Injection	Routing and Sealing	Near-surface Reinforcing and Pinning	Gravity filling	Drypacking
Corresponding width of crack or slot	As narrow as 0.002 in.	0.2-1.0 in.	Slot that is cut to approximately 0.125 in. wider and deeper than the diameter of the reinforcement to be installed	0.001-0.08 in.	Slot about 1 in. wide and 1 in. deep

7.2.1.1 Epoxy Injection

As shown in Table 7-1, cracks as narrow as 0.002 in. can be repaired by epoxy injection techniques. Ports are established for entry and venting, and epoxy is injected under pressure (ACI 224.1R 2007). This method of crack repair is appropriate for structural crack repair on bridge decks (ACI 503R 1998). Epoxy injection has also been used successfully in repairing delamination within bridge decks, as well as rebonding delaminated bridge deck overlays (Stratton and McCollum 1974, Smith 1992, and Smithson and Whiting 1992).

Epoxy injection requires advanced skill for successful execution, and use of the technique may be influenced by the temperature. Details for the general procedures involved in epoxy injection are provided in ACI 503R (1998), ACI 503.7 (2007) and RAP-1 (ACI 2003). Epoxy materials used for structural repairs should conform to ASTM C 881 Type IV (2002).

A major limitation to this technique is that cracks must be dried before injection of epoxy. Wet cracks can be injected using certain materials that are moisture tolerant and that will cure and bond under moist conditions. All cracks, however, must be cleaned as contaminants can reduce the effectiveness of the repair (Barlow 1993).

7.2.1.2 Routing and Sealing

Crack routing and sealing is an appropriate choice for non-structural repair of cracks of width ranging from 0.2 - 1.0 in. as shown in Table 7-1. Much of the transverse reflective cracking observed at the panel joint locations fall into this category. Using this technique, the crack is essentially treated as a joint. Sealant materials can be epoxies, urethanes, silicones, polysulfide, asphaltic materials, or polymer mortar materials with a high elongation capacity. Surface preparation is critical in this technique, since bond failure can occur at edges of the groove.

This treatment reduces the ability of moisture to reach the reinforcing steel or pass through the concrete. Findings from the Chapter 4 field investigations, including evidence of water staining and deterioration at the panel joint locations, indicates the consequences of moisture penetration through the concrete at the panel joint locations is a critical problem for this deck system. Thus, this treatment would be beneficial in reducing this mode of moisture transmission.

Figure 7-1 Crack Repaired by Routing and Sealing (ACI 345.1R 2006)

7.2.1.3 Near-surface Reinforcing and Pinning

Findings from the Chapter 4 field observations and the Chapter 6 simulations indicate that repairing transverse cracks can be significant in increasing the concrete integrity at the panel joint locations and thus can delay the onset of spalling at the panel joints. Near-surface reinforcing (NSR) is a technique that involves adding reinforcement to an existing concrete structure that is oriented perpendicular to a crack plane in order to provide additional tensile strength. As shown in Figure 7-2, a slot is saw cut across the crack and then cleaned. A reinforcing bar is then placed within the slot that is bonded to the concrete by an epoxy resin. Deformed steel reinforcing bars as well as FRP bars have been used successfully in this application. The reinforcing should be designed to increase the capacity beyond the tensile forces at the crack location (ACI 224.1R 2007).

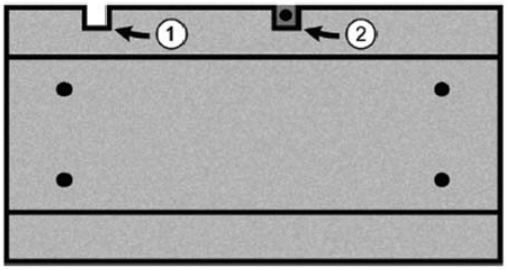

Figure 7-2 Repair Using Near-Surface-Mounted Reinforcing: (1) Sawcut 1/8 to 1/4 in. Larger Than Bar Diameter; and (2) Deformed Bar or FRP Bar Bedded in Epoxy Resin (ACI 224.1R 2007)

7.2.2 Surface Treatment

Various sealers can be used to protect concrete by reducing the permeability of the concrete surface to moisture and chloride ions. Among the many different types of sealing materials, penetrating sealers are useful in reducing chloride ion penetration. Sealing and caulking slow the absorption of deleterious chemicals through cracks or through the concrete surface. This treatment can be used to prevent against deterioration of both concrete and embedded reinforcing steel (ACI 345.1R 2006).

Figure 7-3 Application of Penetrating Concrete Sealer (ACI 345.1R 2006)

7.3 Repair of SIP Panel

As discussed in the Chapter 4 field investigations, spalling conditions of SIP panels revealed corroded prestressing and mild reinforcement, some of which had corroded to the point of rupture. Corrosion of the reinforcement was found to be the result of penetration of water and chlorides through the transverse reflective cracking in the CIP topping at the panel joints, to the interface between the CIP topping and the SIP panels, then through the SIP panels to the embedded reinforcement. The Chapter 6 simulations showed that the loss of edge tendons did not significantly affect the structural performance of the SIP panels under service loads. Thus, nonstructural repair methods for repairing the SIP panel are provided in Section 7.3.1 related to remediation techniques to address the corrosion of prestressing steel. For conditions that are more severe than those in this study that would require flexural strengthening, Section 7.3.2 provides a brief overview of methods for structural repair for reference.

7.3.1 Remediation Techniques for Corrosion of Prestressing Steel

Corrosion activity in embedded prestressing steel strands can be mitigated by various measures discussed in ACI 222R (2001) and ACI 345.1R (2006). Options that are applicable to the system in this study are discussed below.

7.3.1.1 Discrete Patching

In this treatment, the degraded concrete is removed and replaced with an appropriate patch material. The patch material serves as a barrier system that would reduce the ingress of chlorides and thus delay the corrosion process. Certain types of barrier systems can substantially reduce the rate of intrusion of chloride agents and retard the corrosion process. Since the new material would only be provided in areas where the panel concrete is severely degraded, however, this

option would be temporary without other methods to eliminate the source of water and chloride intrusion from the CIP topping (ref. Section 7.2).

7.3.1.2 Cathodic Protection

Cathodic protection can be installed to protect the embedded steel reinforcement from further corrosion. Cathodic protection of concrete bridge decks is discussed in AASHTO-AGC-ARTBA Subcommittee (1992).

7.3.1.3 Electrochemical Chloride Extraction (ECE)

Electrochemical chloride extraction (ECE) has been used successfully to remove chloride from the surface of the reinforcing bars and to improve the alkalinity at the bar surface. Concrete patching follows this treatment.

7.3.1.4 Corrosion Inhibiting Surface Treatment

This treatment involves injecting corrosion-inhibiting treatment directly into cracks to reduce the corrosion rate of the embedded reinforcing bars. This treatment is relatively new and the long-term effectiveness is not yet fully known.

7.3.2 Panel Strengthening

Results from the literature show that externally bonding FRP plates (or sheets) and/or rods can increase deck strength as well as stiffness of aging or deteriorated structures. The advantages to using FRP strengthening systems include reduced labor costs, minimum shutdown time/cost and traffic disruption, and minimal maintenance requirements. From the literature review, it was found that the increase in stiffness and strength varied for the different field applications. In all cases, however, an increase was observed. It was also found that the benefits of such a retrofitting system do not change with time.

Figure 7-4 shows the procedure for applying adhesive to the bottom surface (flexural tension surface) of the bridge deck. Figure 7-5 shows the installation of FRP sheets. Figure 7-6 shows examples of flexural strengthening using FRP sheets and FRP rods.

Figure 7-4 Application of the Adhesive to the Underside of the Deck (Mayo et al., 2000)

Figure 7-5 Installation of CFRP Sheets (Mayo et al., 2000)

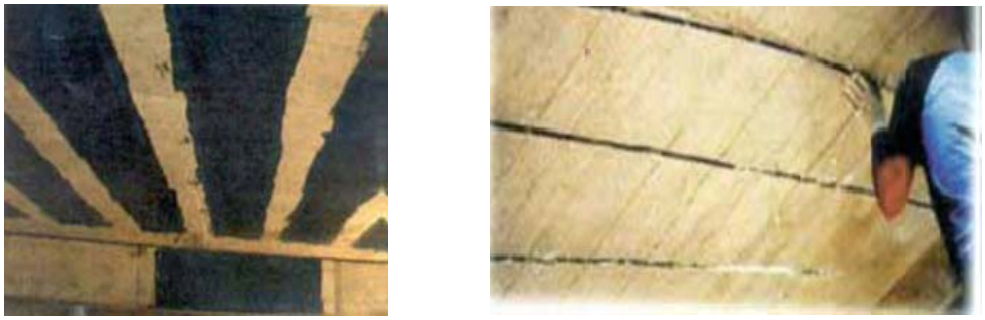

Figure 7-6 Strengthening Schemes: (a) FRP sheets, (b) FRP rods (Alkhrdaji et al., 1999)

7.4 Summary

The Chapter 6 simulations were significant in that they showed that the loss of edge tendons did not significantly affect the structural performance of the SIP panels under service loads. Accordingly, recommendations for repair methods are focused on non-structural repair to mitigate further penetration of water and chlorides to the panels.

Physical evidence discussed in Chapter 4 showed that transverse cracking in the CIP topping at the panel joint locations and corrosion of panel reinforcement play a key role in spalling of the panels. Spalling observed was found be the result of the penetration of water and chlorides through the transverse reflective cracking in the CIP topping at the panel joints, to the interface between the CIP topping and the SIP panels, then through the SIP panels to the prestressing tendons and other reinforcement located near the panel joints. GPR results indicated that most of the deck deterioration is concentrated near the area of reflective cracking in the CIP topping. Routing and sealing techniques reduce the ability of moisture to reach the reinforcing steel or pass through the concrete. Accordingly, this treatment is recommended for transverse reflective cracks at the panel joint locations and is particularly critical in the girder positive moment regions, where relatively lower levels of CIP topping reinforcement are used (compared with negative moment regions).

Increased transverse crack control was found to be significant in increasing the concrete integrity

and delaying the onset of spalling at the panel joints, based on physical observations from the Chapter 4 field investigations as well as the Chapter 6 simulations. Near surface reinforcing and pinning may be considered in locations on bridges where transverse reflective cracks are determined to be very wide and full depth.

Finally, evidence of delamination was found at the interface between the CIP topping and SIP panels, particularly at panel joint locations, despite the roughened SIP panel surface. Delamination at the interface can affect the composite behavior of the bridge deck system. Accordingly, epoxy-injection is recommended for interface delamination regions.

8 SUMMARY OF FINDINGS AND RECOMMENDATIONS

As discussed in Section 1.2, the primary objectives of this project were to investigate the causes for spalling in precast-prestressed panels and propose cost-effective alternative solutions including improved design options for new construction, as well as suggest mitigation methods for existing deteriorated bridge decks. Section 8.1 presents a summary of findings with respect to each of these objectives. Section 8.2 discusses price impact and construction implications of the different systems investigated in this study. Section 8.3 presents recommendations based on the results of this research.

8.1 Summary of Findings

8.1.1 Causes of Spalling

Results of the Questionnaire Survey presented in Chapter 3 indicate that the most prominent deterioration problem reported by the survey respondents in partial-depth PPC bridge decks is transverse (reflective) and longitudinal cracking on the top deck surface. Of the states reporting problems on the bottom deck surface (Missouri, Michigan and Colorado), a common trend is transverse cracking in the CIP topping as well as water seepage at the panel joints. This indicates water progression through the deck slab at the panel joint locations. Most of the reported deterioration problems with the PPC panel system appear to be related to environmental conditions resulting in corrosion of embedded steel rather than structural issues. Missouri panels have the smallest thickness reported (3 in.) and have been in service longer than most other states (35 years). Relative to the other survey respondents, shallow concrete cover associated with the use of a thin panel and small specified minimum edge distance exacerbates the long-term effects of environmental conditions.

Based on the survey responses, the combination of design parameters, age, environmental conditions, and the problems reported in Missouri bridges with partial-depth PPC panels are unique with respect to the other respondents. Thus, field investigations discussed in Chapter 4 were performed to determine the specific cause of deterioration and mechanism of spalling reported in Missouri bridges with partial-depth PPC panels. Findings from the Chapter 4 field investigations indicated that spalling observed in the PPC panels is the result of the penetration of water and chlorides through the transverse reflective cracking in the CIP topping, to the interface between the CIP topping and the PPC panels, then through the PPC panels to the prestressing tendons located near the panel joints. Transverse reflective cracking over the panel joints allows water and chlorides entrance into and, in many cases, through the CIP topping. GPR results confirmed that most deterioration in Bridge A4709 is occurring near the area of reflective cracking in the CIP topping and not in the area of concrete over the middle of the panels. Evidence of delamination at the interface between the CIP topping and PPC panels was also found at panel joint locations.

Chapter 6 simulations of spalling causes showed that corrosion cracks could not propagate from the locations of reinforcements to side surfaces from corrosion of the prestressed tendons only. This analysis evoked examination of other causes of spalling problems in the SIP panel. Further simulations showed that initiation of a bridging crack between adjacent tendons is a primary agency to trigger corrosion-induced spalling of the panel. The significance of the bridging crack is a key finding of this analysis, because corrosion of temperature reinforcement oriented

perpendicular to the tendon direction can induce cracks along the temperature reinforcement playing a similar role as the bridging crack. Additionally, butting of adjacent panels in combination with delamination of the SIP-CIP interface was also shown to contribute to the spalling problem.

8.1.2 Solutions for New Construction

Five systems were selected for evaluation for potential use in new construction as shown in Table 8-1. (Table 8-1 is a subset of proposed systems shown in Table 1-1). As discussed in Section 1.3, systems selected were based on discussions with the MoDOT project Technical Advisory Panel (TAP) members considering cost, feasibility, and practicality of systems. Methods used to evaluate each of the systems are also summarized in Table 8-1. Evaluations of each system are discussed below.

Table 8-1 Systems Evaluated

System	Evaluation Method
1. Increase side cover of prestressing tendons	▪ Durability Experiments (Chapter 5) ▪ Numerical Analysis (Chapter 6)
2. Use enhanced concrete using FRC	▪ Structural Performance - Unit Panel Experiments (Chapter 5) ▪ Durability Experiments (Chapter 5) ▪ Numerical Analysis (Chapter 6)
3. Use corrosion-free concrete using corrosion inhibitor	▪ Durability Experiments (Chapter 5)
4. Enhance the reinforcement in CIP concrete topping	▪ Field Investigations (Chapter 4) ▪ Numerical Analysis (Chapter 6)
6. Substitute 2 epoxy-coated steel or CFRP tendons for 2 steel tendons at each edge	▪ Structural Performance - Unit Panel Experiments (Chapter 5) ▪ Numerical Analysis (Chapter 6)

System 1 - Increase side cover of prestressing tendons

During the Chapter 4 field investigation of the A4709 bridge, measurements at spalled sections showed edge distance to tendon ranged from 1.5 to 2.0 in. (center of tendon to edge of concrete). The durability experiments conducted in Chapter 5 show a distinct relationship between tendon edge distance and level of deterioration. Results indicated that as the edge distance increased, level of concrete deterioration and tendon corrosion rate decreased. Chapter 6 simulations also supported this relationship and indicated that increasing amounts of side cover showed beneficial effects on mitigating the spalling problem by mitigating crack propagation to the side surface of the panel.

System 2 - Use enhanced concrete using FRC

Results from the Chapter 5 durability experiments show little difference in deterioration levels between specimens with FRC and the control specimens with normal concrete. In terms of structural performance, results from the unit panel tests conducted in Chapter 5 show that the static and fatigue performance of panels with FRC is comparable to the control panel with normal concrete. Panels with FRC showed less stiffness degradation than panels with normal concrete. Chapter 6 simulation of the unit panel experiments confirmed the behavior in terms of failure mode. Behavior of the panel within the composite deck system under service load

conditions was examined by incorporating the proposed panels within a model of the composite section. Serviceability of the composite section was also governed by the compressive strength of concrete in the SIP panel similar to FE analysis of the test specimens.

System 3 - Use corrosion-free concrete using corrosion inhibitor

Results from the Chapter 5 durability experiments showed higher levels of deterioration in specimens with corrosion inhibitor compared to the control specimens with normal concrete. No beneficial effects on mitigating the spalling problem were observed.

System 4 - Enhance the reinforcement in CIP topping concrete deck

Physical evidence from the Chapter 4 field investigations confirmed that increased longitudinal CIP reinforcement, which serves as transverse crack control, was found to be significant in increasing the concrete integrity and delaying the onset of spalling at the panel joints. Visual inspection results from the Chapter 4 field investigation of the bottom surface of the A4079 bridge deck indicated an uneven distribution of deterioration in the bridge deck panels. GPR and rebound hammer results indicate that panels located under the area with increased negative moment reinforcement (i.e. girder interior supports) were less deteriorated. Further investigation of Bridges A4067 and A4705 confirmed this relationship. Numerical analysis from Chapter 6 also showed that increased amounts of reinforcement in the CIP topping deck increased the resistivity for shrinkage cracks. Increased amounts were shown to delay the time of occurrence of shrinkage cracks, decrease widths, as well as changed the mechanism of crack propagation.

System 6 - Substitute 2 Epoxy-coated steel or CFRP tendons for 2 steel tendons at each edge

- Epoxy-coated steel edge tendons

  Results from the unit panel specimens conducted in Chapter 5 show that the static and fatigue structural performance under service load conditions of panels with epoxy-coated steel edge tendons is comparable to the panels with steel edge tendons. Similar to the panels with steel edge tendons, panels with epoxy-coated steel edge tendons were able to withstand the prescribed two million cycles without failure. No cracks were observed during the fatigue load cycles and the quasi-static test at each 500,000 cycle increment. When tested to failure, the failure mode for the static and fatigue specimens was the same as that of the control specimens. Panels with epoxy-coated steel edge tendons, however, showed a marked reduction in maximum load, maximum displacement, and ductility as compared to the panels with steel edge tendons (with the exception of static load panels with FRC).

  Panels with epoxy-coated steel edge tendons showed no significant differences between static and fatigue test specimens with respect to cracking and maximum load. Marked reductions in maximum displacement were observed after the panels had been subjected to 2 million cycles. This phenomenon is attributed to the accumulated damage in the fatigue test specimens. Panels with normal concrete showed more stiffness degradation than panels with FRC.

- CFRP edge tendons

  Results from the unit panel specimens conducted in Chapter 5 show that the static and fatigue structural performance under service load conditions of panels with CFRP edge tendons is comparable to the panels with steel edge tendons. Similar to the panels with steel edge

tendons, panels with CFRP edge tendons were able to withstand the prescribed two million cycles without failure. No cracks were observed during the fatigue load cycles and the quasi-static test at each 500,000 cycle increment. When tested to failure, the failure mode for the static and fatigue specimens was the same as that of the control specimens. Panels with CFRP edge tendons, however, showed a marked reduction in maximum load, maximum displacement, and ductility as compared to the panels with steel edge tendons.

Panels with CFRP edge tendons showed marked reduction in maximum load after being subjected to 2 million cycles. Panels with CFRP edge tendons and normal concrete showed a 17% reduction in ultimate capacity, while panels with CFRP tendons and FRC showed a 13% reduction in ultimate capacity. Marked reductions in maximum displacement were also observed after the panels had been subjected to 2 million cycles. This phenomenon is attributed to the accumulated damage in the fatigue test specimens. Panels with normal concrete showed more stiffness degradation than panels with FRC.

Chapter 6 simulation of the unit panel experiments confirmed the behavior in terms of failure mode. Behavior of the panel within the composite deck system under service load conditions was examined by incorporating the proposed panels within a model of the composite section. Serviceability of the composite section was also governed by the compressive strength of concrete in the SIP panel.

8.1.3 Mitigation Methods for Existing Deteriorated Bridge Decks

The Chapter 6 simulations were significant in that they showed that the loss of edge tendons did not significantly affect the structural performance of the SIP panels under service loads. Accordingly, recommendations for repair methods are focused on non-structural repair to mitigate further penetration of water and chlorides to the panels.

Physical evidence discussed in Chapter 4 showed that transverse cracking in the CIP topping at the panel joint locations and corrosion of panel reinforcement play a key role in spalling of the panels. The spalling observed was found be the result of the penetration of water and chlorides through the transverse reflective cracking in the CIP topping at the panel joints, to the interface between the CIP topping and the SIP panels, then through the SIP panels to the prestressing tendons and other reinforcement located near the panel joints. GPR results indicated that most of the deck deterioration is concentrated near the area of reflective cracking in the CIP topping. Routing and sealing techniques reduce the ability of moisture to reach the reinforcing steel or pass through the concrete. Accordingly, this treatment is recommended for transverse reflective cracks at the panel joint locations and is particularly critical at the girder positive moment regions, where relatively lower levels of CIP topping reinforcement are used (compared with negative moment regions).

Increased transverse crack control was found to be significant in increasing the concrete integrity and delaying the onset of spalling at the panel joints, based on physical observations from the Chapter 4 field investigations as well as the Chapter 6 simulations. Near surface reinforcing and pinning may be considered in locations on bridges where transverse reflective cracks are determined to be very wide and full depth.

Finally, evidence of delamination was found at the interface between the CIP topping and SIP panels, particularly at panel joint locations, despite the roughened surface SIP panel surface. Delamination at the interface can affect the composite behavior of the bridge deck system. Accordingly, epoxy-injection is recommended for interface delamination regions.

8.2 Construction Implications

8.2.1 Price Impact

As discussed in Appendix C, unit panels and other test specimens were constructed at Coreslab Structures in Marshall, MO. Price impact information for the different options shown in Table 8-2 is the producer price provided by Coreslab Structures on the basis of dollars per square yard. Price information is estimated only as of August 9, 2010 and may fluctuate depending on experience gained, project location, and market conditions. Epoxy-coated steel strand and CFRP tendon options are based on full runs with these strands in the two outside positions on both sides of the full width panels only. They do not address additional costs that would be incurred for narrow panels if these strands were required on both sides or for less than full runs.

Table 8-2 Unit Panel Price Impact

Option	Cost	Premium	
Standard panel	$60/sy	-	-
Fiber (BASF) additive	$62/sy	$2/sy	3.3%
Corrosion inhibitor (MCI) additive	$63/sy	$3/sy	5.0%
Epoxy-coated steel edge tendons (2 each end)	$68/sy	$8/sy	11.8%
CFRP edge tendons (2 each end)	$118/sy	$58/sy	96.7%

8.2.2 Other Considerations

Based on feedback from Coreslab Structures in Marshall, MO, the use of fibers or corrosion inhibitor would be the easiest options shown in Table 8-2 to implement. The use of corrosion inhibitor, however, would require close coordination between MoDOT, producer, and additive manufacturer to determine correct dosages.

Coreslab Structures expressed that in previous experience with the use of epoxy-coated steel strands, problems occurred during the stressing procedure with cracking of panels. Manufacturing of the panels for this study, however, went more smoothly. No problems occurred in implementing the CFRP tendon option, although it was more complicated since CFRP tendons had to be spliced to a steel strand in order to stress the strand as well as keep the cost of the material down. The use of CFRP tendons may cause scheduling concerns, however. The greatest challenge for either the epoxy-coated steel or CFRP edge tendon option is treatment of odd size panels (skewed partial-width, etc.).

8.3 Recommendations

The following recommendations are made based on the findings of this research:

Existing construction

- Because of the deicing frequency and tactics used by MoDOT, routing and sealing treatment is recommended on a regular basis for transverse reflective cracks at the panel joint locations. This treatment is particularly critical for full-depth transverse cracks and at the girder positive moment regions, where relatively lower levels of CIP topping reinforcement are used (compared with negative moment regions).
- Epoxy-injection is recommended for areas of delamination that are found at the interface between the CIP topping and SIP panels.
- Loose concrete should be removed from spalled panels, and exposed reinforcement should be protected from further deterioration.

New construction

- The specified minimum side edge distance to tendon should be increased from the current minimum of 1.5 in.
- To preempt the development of bridging cracks, panel lifting hooks should not be located between the first and second tendons from edges of panel. Also, temperature reinforcement placed perpendicular to the tendon direction should be epoxy-coated.
- The current specification recommends sealing at the panel joints. Proper sealing at the panel joints should be required.

REFERENCES

ACI, 2003, "Structural Crack Repair by Epoxy Injection (ACI RAP-1)," American Concrete Institute, Farmington Hills, MI, http://www.concrete.org/general/RAP-1.pdf.

ACI Committee 201, 1992 (Reapproved 1997), "Guide for Making a Condition Survey of Concrete in Service (ACI 201.1R)," American Concrete Institute, Farmington Hills, MI, 16 pp.

ACI Committee 209, 1982, "Prediction of Creep, Shrinkage and Temperature Effects in Concrete Structures," Designing for Creep and Shrinkage in Concrete Structures, A Tribute to Adrian Pauw, SP-76, American Concrete Institute, Farmington Hills, MI, pp. 193-300.

ACI Committee 222, 2001, "Protection of Metals in Concrete Against Corrosion (ACI 222R)," American Concrete Institute, Farmington Hills, MI, 41 pp.

ACI Committee 222, 2001, "Corrosion of Prestressing Steels (ACI 222.2R)," American Concrete Institute, Farmington Hills, MI, 43 pp.

ACI Committee 222, 2003, "Design and Construction Practices to Mitigate Corrosion of Reinforcement in Concrete Structures (ACI 222.3R)," American Concrete Institute, Farmington Hills, MI, 29 pp.

ACI Committee 224, 2007, "Causes, Evaluation, and Repair of Cracks in Concrete Structures (ACI 224.1R)," American Concrete Institute, Farmington Hills, MI, 22 pp.

ACI Committee 345, 2006, "Guide for Maintenance of Concrete Bridge Members (ACI 345.1R-06)," American Concrete Institute, Farmington Hills, MI, 20 pp.

ACI Committee 440. 2004, "Prestressing Concrete Structures with FRP Tendons (ACI 440.4R),"American Concrete Institute, Farmington Hills, MI, 35 pp.

ACI Committee 503, 1993 (Reapproved 1998), "Use of Epoxy Compounds with Concrete (ACI 503R-98)," American Concrete Institute, Farmington Hills, MI, 28 pp.

ACI Committee 503, 2007, "Specification for Crack Repair by Epoxy Injection (ACI 503.7-07)," American Concrete Institute, Farmington Hills, MI, 7 pp.

ACI Committee 544, 2009, "Report Fiber Reinforced Concrete (ACI 544.1R),".American Concrete Institute, Farmington Hills, MI, 35 pp.

ACI Committee 549, 2004, "Report on Thin Reinforced Cementitious Products (ACI 549.2R),".American Concrete Institute, Farmington Hills, MI, 35 pp.

Abendroth, R.E., Pratanata, H., and Singh, B.A., 1991, "Composite Precast Prestressed Concrete Bridge Slabs," Iowa Department of Transportation Report, Project No. HieHR-301.

Ahmed, S.F.U., Maalej, M., and Mihashi, H., 2007, "Cover Cracking of Reinforced Concrete Beams," ACI Materials Journal, ACI, V. 104, No. 2, pp. 153-161.

American Association of State Highway and Transportation Officials, 1998, "AASHTO LRFD bridge design specifications: customary U.S. unit," American Association of State Highway and Transportation Officials, Washington D.C., 2 ed.

Amey, S. L., Johnson, D. A., Miltenberger M. A., and Farzam, H., (1998), "Temperature Dependence of Compressive Strength of Conversion Inhibited High Alumina Cement Concrete," ACI Structural Journal, ACI, V. 95, No. 1, pp. 27-36.

ASTM A 882, 2004, "Standard Specification for Filled Epoxy-Coated Seven-Wire Prestressing Steel Strand," ASTM, West Conshohocken, PA, 5 pp.

ASTM C 881, 2002, "Specification for Epoxy-Resin-Base Bonding Systems for Concrete," ASTM, West Conshohocken, PA, 6 pp.

ASTM C 1218, 1999, "Standard Test Method for Water-Soluble Chloride in Mortar and Concrete," ASTM, West Conshohocken, PA, 3 pp.

ASTM G 109, 2007, "Standard Test Method for Determining Effects of Chemical Admixtures on Corrosion of Embedded Steel Reinforcement in Concrete Exposed to Chloride Environments," ASTM, West Conshohocken, PA, 6 pp.

Badie, S.S., Baishya, M.C., and Tadros, M.K., 1998, "NUDECK- An efficient and economical precast prestressed bridge deck system," PCI Journal, V. 43, No. 5, pp. 56-74.

Bakis, C.E., Bhat, B.B., Schokker, A.J., and Boothby, T.E., 2001, "Flexure of Concrete Beams Prestressed with FRP Tendons," Proceedings of the Fifth International Symposium on Fiber Reinforced Polymer Reinforcement for Concrete Structures (FRPRCS-5), Cambridge, London, pp. 689-697.

Barlow, P. B., 1993, "Epoxy Injection of Cracked Slabs," Concrete Construction, Apr., 4 pp., ftp://imgs.ebuild.com/woc/C930253.pdf.

Bazant, Z.P., 1979, "Physical model for steel corrosion in concrete sea structures–applications," Journal of Structural Division, ASCE, V. 105, No. 6, pp. 1155–1166.

Bazant, Z.P., 1979, "Blunt Crack Band Propagation in Finite Element Analysis," Journal of the Engineering Mechanics Division, ASCE, V. 105, No. EM2.

Bazant, Z.P., 1984, "Size Effect in Blunt Fracture: Concrete, Rock, Metal," Journal of the Engineering Mechanics Division, ASCE, V. 110, No. 4, pp. 518-535.

Bazant, Z.P., and Oh, B.H., 1983, "Crack Band Theory for Fracture of Concrete," Materials and Structure, RILEM, V.16, No. 94.

Biswas, M., 1986, "Precast Bridge Deck Design Systems," PCI Journal, V. 31, No.2, pp. 40-94.

Biswas, M., Osegueda, R.A., and Noel, J.S., 1984, "Scale-model tests for full-depth precast concrete panel-decked composite bridge span," Transportation Research Record 950, No. 1, Transportation Research Board, Washington D.C., pp. 163-173.

Bohner, E. and Muller, H.S., 2006, "Modeling of reinforcement corrosion- Investigations on the influence of shrinkage and creep on the development of concrete cracking in the early propagation stage of reinforcement corrosion," *Materials and Corrosion*, V. 57, No. 12, pp. 940-944.

Bowen, J.D, Mufti, A., and Dick, K., 2006 "Combining Steel Free Deck Technology with Partial Depth Precast Concrete Panels," 1st International Structural Specialty Conference, Calgary, Alberta, Canada, pp. 1-10.

Brearley, L.M., and Johnston, D.W., 1990, "Pull-Out Bond Tests of Epoxy-Coated Prestressing Strand," Journal of Structural Engineering, ASCE, V. 116, No. 8, pp. 2236-2252.

Broomfield, J.,P., 2007,"Corrosion of Steel in Concrete: Understanding, Investigation and Repair (2nd Edition),", Taylor & Francis, 277 pp.

Cady, P. D., and Renton, J.B., 1976, "Durability of Steel-Formed and Sealed Bridge Decks," Transportation Research Record 613, TRB, National Research Council, Washington, D.C. pp. 14-20.

Canin, 2007, "Corrosion analyzing instrument for the measurement of corrosion potential and electrical resistivity," Proceq SA, Schwerzenbach.

Chen, D., and Mahadevan, S. 2008, "Chloride-induced reinforcement corrosion and concrete cracking simulation," Cement and Concrete Composites, V. 30, pp. 227-238.

Cheng, T.T.H., and Johnston, D.W., 1985, "Incidence Assessment of Transverse Cracking in Concrete Bridge Decks: Construction and Material Considerations," Report FHWA/NC/85-002, Vol. 1, North Carolina State University, Raleigh, 232 pp.

Coronelli, D. and Gambarova, P., 2004, "Structural Assessment of Corroded Reinforced Concrete Beams: Modeling Guidelines," Journal of Structural Engineering, ASCE, V. 130, No. 5, pp. 1214-1224.

Cousins, T. E., Johnston, D. W., and Zia, P., 1986, "Bond of epoxy coated prestressing strand," Final Report FHWA/NC/87-005, Center for Transportation Engineering Studies, Department of Civil Engineering, North Carolina State University, Raleigh, NC.

Cousins, T. E., Johnston, D.W., and Zia, P., 1990, "Transfer Length and Development. Length of Epoxy Coated and Uncoated Prestressing Strand," PCI Journal, V. 35, No. 4, pp. 92-103.

Cousins, T. E., Francis, L.H., Stallings, J.M., and Gopu, V., 1993, "Spacing and Concrete Cover Requirements for Epoxy-Coated Prestressing Strand in Unconfined Sections," PCI Journal, V. 38, No. 5, pp. 76-84.

Currier, J., 1995, "Deformation of Prestressed Concrete Beams with FRP Tendons," MS thesis, Department of Civil and Architectural Engineering, University of Wyoming, Laramie, WY, 112 pp.

Dagher, H.J. and Kulendran, S., 1992, "Finite Element Modeling of Corrosion Damage in Concrete Structures," ACI Structural Journal, ACI, V. 89, No. 6, pp. 699-708.

Dakhil, F.H., Cady, P.D., and Carrier, R.E., 1975," Cracking of Concrete as Related to Reinforcement," Journal of the American Concrete Institute, V. 72, No. 8, pp. 421–428.

Dolan, C. W., 1990, "Developments in Non-Metallic Prestressing Tendons," PCI Journal, V. 35, No. 5, pp. 80-88.

Dorsten, V., Hunt, F., and Preston, H., 1984, "Epoxy-coated seven-wire strand for prestressed concrete," PCI Journal, V. 29, No. 4, pp. 120-129.

Du, Y.G., Chan, A.H.C., and Clark, L.A., 2006, "Finite element analysis of the effects of radial expansion of corroded reinforcement," Computers and Structures, V. 84, pp. 917-929.

Dunker, K.F., and Rabbat, B.G., 1992, "Performance of prestressed concrete highway bridges in the United States- The first 40 years," PCI Journal, V. 37, No. 3, pp. 48-64.

Ehsani, M. R., Saadatmanesh, H., and Nelson, C. T., 1997, "Transfer and Flexural Bond Performance of Aramid and Carbon FRP Tendons," PCI Journal, V. 42, No. 1, pp. 76-86

El Maaddawy, T. and Soudki, K., 2007, "A model for Prediction of Time from Corrosion Initiation to Corrosion Cracking," Cement and Concrete Composites, V. 29, pp. 168-175.

Fagundo, F.E., Tabatabal, H., Soongswang, K. Richardson, J.M., and Callis, E.G., 1985, "Precast Panel Composite Bridge Decks," Concrete International, V. 7, No.5, pp. 59-65.

Frost, S.L., 2006, "Effect of Stay-in-Place Metal Forms on Performance of Concrete Bridge Deck," Thesis, Department of Civil and Environmental Engineering, Brigham Young University.

Geophysical Survey System, Inc., 2007, "Bridge assessment module: Radan 6.25 users manual MN 43-172 Rev C. Salem," New Hampshire: Geophysical System Survey Inc.

Goldberg, D., 1987, "Precast Prestressed Concrete Bridge Deck Panels," PCI Journal, V. 32, No. 2, pp 26-45.

Grace N.F., Abdel-Sayed G., 1998, "Behavior of Externally Draped CFRP Tendons in Prestressed Concrete Bridges," PCI Journal, V. 43, No. 5, pp. 88-101.

Grace, N.F., Hanson, J., and Messih H., 2004, "Inspection and Deterioration of Bridge Decks Constructed Using Stay-in-Place Metal Forms and Epoxy-Coated Reinforcement," Department of Civil Engineering, Lawrence Technological University, Southfield, MI, Report No. RC-1455, 359 pp.

Hamid, A., 2004, "A TEM Study of the Oxide Scale Development in Ni-Cr Alloys," Anti-Corrosion Methods and Materials, Vol. 51, Isse. 3, pp. 216 – 222.

Hansen, E. J., and Saouma, V. E., 1999, "Numerical Simulation of Reinforced Concrete Deterioration: Part II—Steel Corrosion and Concrete Cracking," ACI Materials Journal, ACI, V. 96, No. 3, pp. 331-338.

Hastak, M., Halpin, D., and Hong, T., 2004, "Constructability, Maintainability, and Operability of Fiber Reinforced Polymer (FRP) Bridge Deck Panels," Joint Transportation Research Program (JTRP), JTRP Research Report SPR-2778, Purdue University, West Lafayette, IN.

Hieber, D.G., Wacker, J.M., Eberhard, M.O., and Stanton, J.F., 2005, "State-of-the-Art Report on Precast Concrete Systems for Rapid Construction of Bridges," Washington State Transportation Center (TRAC), Report No. WA-RD 594.1, 112 pp.

Issa, M.A., Idriss, A., Kaspar, I.I., and Khayyat, S.Y., 1995, "Full depth precast and precast, prestressed concrete bridge deck panels," PCI Journal, V. 40, No. 1, pp. 59-80.

Jang, B.S., and Oh, B.H., 2010, "Effects of Non-uniform Corrosion on the Cracking and Service Life of Reinforced Concrete Structures," Cement and Concrete Research, V. 40, No.9, pp. 1441-1450.

Klingner, R.E. and Bieschke, L.A., 1988, "Effects of Transverse Panel Strand Extensions on the Behavior of Precast Prestressed Panel Bridges," PCI Journal, V. 33, No. 1, pp. 68-88.

Lee, H. S., Kage, T., Noguchi, T., and Tomosawa, F., 1999, "The Evaluation of Flexural Strength of RC beams Damaged by Rebar Corrosion," Proceedings, 8th International Conference on Durable Building Materials and Components, National Research Council, Ottawa, Ontario, Canada, 31, pp. 320–330.

Liang M.T, Lin L.H, Liang C.H., 2002, "Service Life Prediction of Existing Reinforced Concrete Bridges Exposed to Chloride Environment," Journal of Infrastructure Systems, Volume 8, No.3, pp. 76-85.

Liu, Y. and Weyers, R., 1998, "Modeling the Time-to-corrosion Cracking in Chloride Contaminated Reinforced Concrete Structures," ACI Materials Journal, V. 95, No. 6, pp. 675–681.

Lu, Z., Boothby, T.E., Bakis, C.E., and Nanni, A., 2000, "Transfer and Development Length of FRP Prestressing Tendons," PCI Journal, V. 45, No. 2, pp. 84-95.

Maierhofer, Christiane, 2003. "Nondestructive evaluation of concrete infrastructure with ground penetrating radar." Journal of Materials in Civil Engineering, ASCE, V. 15, No. 3, May/June.

Matsui, S., Soda, N., Terada, K., and Manabe, H., 1994, "Application of channel-shaped PC precast slabs on steel bridges," Proceedings, Fourth International Conference on Short and Medium Span Bridges, Halifax, Nova Scotia, pp. 699-709.

Missouri Department of Transportation (MoDOT), 2004, "2004 Missouri Standard Specification Book for Highway Construction," Missouri Department of Transportation, Jefferson City, MO.

Molina, F.J., Alonso, C., and Andrade, C., 1993, "Cover Cracking as a Function of Rebar Corrosion: Part 2- Numerical Model," Materials and Structure, RILEM, V.26, pp. 532-548.

Morinaga, S., 1988. "Prediction of Service Lives of Reinforced Concrete Buildings Based on Rate of Corrosion of Reinforcing Steel," Report No. 23, Shimizu Corp, Japan, 82 pp.

Nanni, A., and Tanigaki, M., 1992, "Pretensioned Prestressed Concrete Members with Bonded Fiber Reinforced Plastic Tendons: Development and Flexural Bond Length (Static)," ACI Structural Journal, V. 89, No. 4, pp. 433-441.

Ngo, D., and Scordelis, A.C., 1967, "Finite Element Analysis of Reinforced Concrete Beams," Proceedings, ACI Journal, V. 3, No. 64, pp. 152-163.

Noghabai, K., 1999, "Discrete versus smeared versus element-embedded crack models on ring problem," Journal of Engineering Mechanics, ASCE, V. 125, No. 3, pp. 307-315.

Noghabai, K., 1999, "FE-Modelling of cover splitting due to corrosion by use of inner softening band," Materials and Structure, RILEM, V.32, No. 7, pp. 486-491.

PCA, 1970, "Durability of Concrete Bridge Decks: A Cooperative Study," Final Report, Portland Cement Association (PCA), Skokie, IL.

PCI-NER, 2001, "Precast Deck Panel Guidelines," Report Number PCINER-01-PDPG, Precast/Prestressed Concrete Institute New England Region, 13 pp.

Perfetti, G.R., Johnston, D.W., and Bingham, W.L., 1985, "Incidence Assessment of Transverse Cracking in Concrete Bridge Decks: Structural Considerations," Report HWA/NC/88002, Vol. 2, North Carolina State University, Raleigh, 201 pp.

Ralls, M.L., 2005, "The Future is Now Successes in Bridge Construction," TRB 2005 Annual Meeting, Session 628 Highways for Life.

Rashid, Y.R., 1968, "Analysis of Prestressed Concrete Pressure Vessels," *Nuclear Engineering and Design*, V. 7, No. 4, pp. 334-344.

Richard, B., Ragueneau, F., Cremona C., Adelaide, L., and Tailhan, J.L., 2010, "A three-dimensional steel/concrete interface model including corrosion effects," Engineering Fracture Mechanics, V. 77, No.6, pp. 951-973.

Ross Bryan Associates, Inc., 1988, "Recommended Practice for Precast Prestressed Concrete Composite Bridge Deck Panels," PCI Journal, V. 33, No. 2, pp. 67-109

Saetta, A. V., 2005, "Deterioration of Reinforced Concrete Structures due to Chemical–Physical Phenomena: Model-Based Simulation," Journal of Materials in Civil Engineering, ASCE, V. 17, No. 3, pp. 313-319.

Slavis, C., 1982, "Precast Concrete Deck Modules for Bridge Deck Reconstruction," Transportation Research Record 871, Transportation Research Board, Washington D.C., pp. 30-33.

Smith, B. J., 1992, "Epoxy Injection of Bridge Deck Delaminations," Transportation Research Record 1533, Transportation Research Board, National Research Council, pp. 10-18.

Smith J.L., Virmani Y.P., 2000,"Materials and Methods for Corrosion Control of Reinforced and Prestressed Concrete Structures in New Construction." FHWA Report No. 00-081, Federal Highway Administration, Virginia, 82 pp.

Smithson, L. D., and Whiting, J. E., 1992, "Rebonding Delaminated Bridge Deck Overlays," Concrete Repair Digest, V. 3, No. 3, June-July, pp. 100-101.

Sohanghpurwala, A.A, 2006, "Manual on Service Life of Corrosion-Damaged Reinforced Concrete Bridge Superstructure Elements." NCHRP Report 558, National Cooperative Highway Research Program, Washington D.C., 72 pp.

Sprinkel, M. M., 1985, "Prefabricated Bridge Elements and Systems," National Cooperative Highway Research Program, Synthesis of Highway Practice, Washington D.C., 81 pp.

State Highway Departments of California, Illinois, Kansas, Michigan, Minnesota, Missouri, New Jersey, Ohio, Texas, and Virginia; the Bureau of Public Roads; and Portland Cement

Association, 1970, “Durability of Concrete Bridge Decks—A Cooperative Study,” Final Report, 35 pp.

Stratton, F. W., and McCollum, B. F., 1974, “Repair of Hollow or Softened Areas in Bridge Decks by Rebonding with Injected Epoxy Resin or Other Polymers,” Report No. KF-72-5, State Highway Commission of Kansas, July, 104 pp.

Tadros, M.K., and Baishya, M.C., 1998, “Rapid replacement of bridge decks,” National Cooperative Highway Research Program, NCHRP Report 407, Washington D.C., 51 pp.

Tamer, A., E., and Khaled, A., S., 2003, “Effectiveness of Impressed Current Technique to Simulate Corrosion of Steel Reinforcement in Concrete,” J. Mat. in Civ. Engrg., Volume 15, Issue 1, pp. 41-47.

Val, D.V., Chernin, L., and Stewart, M.G., 2009, “Experimental and Numerical Investigation of Corrosion-Induced Cover Cracking in Reinforced Concrete Structures,” Journal of Structural Engineering, ASCE, V. 135, No. 4, pp. 376-385.

Wenzlick, J.D., 2005, “Follow up Report on the Performance of Bridge Decks Using Precast Prestressed Panels in Missouri,” Missouri Department of Transportation, Report No. RI05-024

Wenzlick, J.D., 2008, “Inspection of deterioration of precast prestressed panels on bridges in Missouri,” Missouri Department of Transportation, Report No. RI05-024B.

Wieberg, K., 2010, “Investigation of Spalling in Bridge Decks with Partial-Depth Precast Concrete Panel Systems,” Thesis, Civil Engineering Department, Missouri University of Science and Technology.

Yamane, T., Tadros, M.K., Badie, S.S., and Baishya, M.C., 1998, “Full Depth Precast, Prestressed Concrete Bridge Deck System,” PCI Journal, V. 43, No. 3, pp. 50-66.

Zhou, K., Martin-Perez, B., and Lounis, Z., 2005, “Finite Element Analysis of Corrosion-Induced Cracking, Spalling and Delamination of RC Bridge Deck,” Proceedings, 1st Canadian Conference on Effective Design of Structures, McMaster University Hamilton, Ontario, Canada, July 10-13.

APPENDIX A

QUESTIONNAIRE SURVEY AND RESULTS

TABLE OF CONTENTS

LIST OF FIGURES

LIST OF TABLES

A.1 INTRODUCTION

This appendix provides additional information and results from the questionnaire survey distributed to 52 different state transportation agencies described in Chapter 3. Twenty-nine of the fifty-two agencies responded. Among the agencies responding, thirteen reported no or minimal use of precast-prestressed bridge deck panels (full or partial-depth). Results from the sixteen states that reported using precast-prestressed panels are fully described in this appendix. Comments from the agencies reporting non-usage of this system are also included.

A.2 METHODOLOGY OF QUESTIONNAIRE SURVEY

A.2.1 Cover letter

The cover letter included with the questionnaire survey form is shown below.

Dear Sir or Madam:

The Missouri University of Science and Technology, under the Missouri Department of Transportation (MoDOT), is conducting a project investigation entitled "**Spalling Solution of Precast-Prestressed Bridge Deck Panels.**" The objectives of this research project are to investigate the problems and develop a cost-effective mitigation solution to the current concrete deterioration problems found in the existing partial-depth precast-prestressed concrete panels, as well as review improved design options for new construction for the panels that are currently used by the Missouri Department of Transportation.

MoDOT has been using the partial-depth precast paneling system since the early 1970's. Since then several bridge decks have been inspected and found to have rusted embedded steel reinforcement and concrete spalling issues in deck panels. MoDOT has contracted a research project with Missouri University of Science and Technology to investigate the cause and development of solutions including alternate design options for these panels.

The enclosed questionnaire is intended to generate ideas about the main cause(s) of the panel deterioration and gather ideas about ways to mitigate it. In addition, this questionnaire is aimed at compiling a list of important issues and parameters that need to be considered for possibly developing new design specifications for MoDOT.

We realize that you may receive many inquiries like this and that they take up a lot of your time. We, therefore, sincerely appreciate your efforts in sharing your department's experience with others who can benefit from it. At the completion of this project and with approval of MoDOT, a copy of research project report will be shared with you.

Sincerely,

Abdeldjelil Belarbi, Ph.D., P.E.
Principal Investigator

Lesley H. Sneed, Ph.D., P.E.
Co-Principal Investigator

A.2.2 Questionnaire survey form

A total number of twenty questions were included in the survey form. The questionnaire survey is shown below.

Questionnaire Survey

Bridge Research Program

Sponsored by

The Missouri Department of Transportation

SPALLING SOLUTION OF PRECAST-PRESTRESSED CONCRETE BRIDGE DECK PANELS

Conducted by

Missouri University of Science and Technology (Missouri S&T)

Please return this survey to:
Abdeldjelil Belarbi, PhD, PE
Distinguished Professor
Missouri University of Science and Technology
323 Butler-Carlton Hall
1401 North Pine Street
Rolla, MO 65409-1050
Email: belarbi@mst.edu
Fax: (573) 202-2117

PURPOSE OF THE QUESTIONNAIRE

This research is sponsored by Missouri Department of Transportation (MoDOT) and is being conducted by Missouri University of Science and Technology (Missouri S&T). The purpose of this survey is to collect objective data with regard to spalling problems observed in the soffit of the precast-prestressed concrete bridge deck panels and to request information about field data and/or research studies related to this issue. Your input will assist in the development of a detailed report and research summary that will compile the research findings and provide directions for future application and design approach.

GENERAL INFORMATION

Organization: _____

Respondent's name: _____

Position/Title: _____

Address: _____

Tel: _____ Fax: _____ E-mail: _____

PART I: DOCUMENTS REQUESTED

1. If possible, please provide us with a copy of design guidelines and specifications for construction of precast-prestressed concrete bridge deck panels in use by your organization.
2. Please complete the survey on the following pages. If it is more convenient, please call us at (573) 341-4478 to discuss this questionnaire.

PART II: BRIDGE DECK SYSTEMS

1. Has your DOT ever used a precast-prestressed paneling system for bridge decks? ☐ Yes ☐ No

   (If no, please go to question 2. If yes, please proceed to question 3.)

2. If your agency has never used the precast-prestressed concrete deck panels, why? Have you ever considered the use of this system? (Please skip to question 20.)

_____

_____

_____

_____

3. Which precast-prestressed concrete deck panel is primarily used in your state?

	Percentage of Panels
☐ Full-Depth Precast Panel	_____ %
☐ Partial-Depth Precast Panel	_____ %

4. What are the dimensions of the precast concrete bridge deck panels used?

_____

5. When did your DOT first start to use precast concrete panels as bridge deck? How old are the bridges that have these components? _____

6. What type of reinforcement has been used in the concrete deck panels?

   ☐ Mild reinforcement ☐ Epoxy coated reinforcing steel ☐ Prestressing reinforcement
   ☐ Fiber reinforced polymer (FRP) reinforcing bars ☐ Other: _____

7. What is the specified 28-day compressive strength of concrete for the precast bridge deck panels?
☐ ≤ 4000 psi ☐ 6000 psi ☐ 8000 psi ☐ 10,000 psi Other: _____

8. Has your DOT updated design guidelines for these deck systems? If so, please describe the main changes and the reasons for the changes. _____

_____

_____

_____

PART IIA: PARTIAL-DEPTH PANELS

9. What is the specified compressive strength of concrete for the cast-in-place (CIP) concrete topping slab? ☐ ≤ 3500 psi ☐ 4000 psi ☐ 5000 psi ☐ Other: _____

10. What are the types and lengths of the curing process for the cast-in-place (CIP) concrete?

Procedures:	Duration:	
☐ Moist curing method	_____	Days
☐ Liquid membrane curing compound method	_____	Days
☐ Waterproof cover method	_____	Days
☐ Other: _____	_____	Days

11. How are panel joints constructed?
☐ Compressible filler ☐ None ☐ Other: _____

_____

PART IIB: FULL-DEPTH PANELS

12. How are panel joints constructed?
☐ Compressible filler ☐ None ☐ Other: _____

_____

PART III: PROBLEMS OBSERVED IN PRECAST CONCRETE DECK PANELS

13. Please indicate which of the following problems (if any) have been observed with these systems.

☐ Transverse cracks over the topping concrete at the location of joints
☐ Longitudinal cracks in CIP concrete topping along the girder line
☐ Cracks in the bottom side of panels
☐ Seepage at the joints
☐ Efflorescence in deck panels
☐ Rust stains of deck panels along the direction of prestressed tendons
☐ Concrete spalling at the joints
☐ Corrosion of reinforcement at the joints
☐ None
☐ Other: _____

_____

14. What, if any, attempts have been made to mitigate these problems?

☐ Linseed oil
☐ Epoxy injection
☐ Total deck surface treatment
☐ Shotcrete
☐ Deck crack pouring
☐ Chip seal
☐ Deck replacement
☐ None
☐ Other: _____

15. How frequently are deicing procedures typically used, and what is the typical deicing solution material makeup?

Deicing Solution:	Frequency:	
☐ Conventional road salt	_____	Per/year
☐ Chloride salts	_____	Per/year
☐ Organic products	_____	Per/year
☐ Nitrogen products	_____	Per/year
☐ Abrasives	_____	Per/year
☐ Other: _____	_____	Per/year
☐ None	Never	

16. How frequently are the deck joints (either panel to panel in the case of full-depth precast panels or contraction joints in concrete CIP topping) maintained, and what are the maintenance tactics?

Tactic:	Frequency:	
☐ Hot pour sealing	_____	Per/year
☐ Silicone sealing	_____	Per/year
☐ Polytite sealing	_____	Per/year
☐ Other: _____	_____	Per/year
☐ None	Never	Per/year

17. Which type of girder is used to support the precast concrete deck panel?

	Percentage of girders:	
☐ Steel girders	_____	
☐ Prestressed concrete girders	_____	%
	_____	%

PART IV: MITIGATIONS & NEWLY-DEVELOPED TECHNOLOGIES

18. If your DOT has experienced any of the above mentioned problems, do you have specific mitigation or repair methods to resolve them? If available please list below.

☐ Yes ☐ No Please explain: _____

19. Does your DOT have specific guidelines for the repair of deteriorated precast concrete deck panels? ☐ Yes ☐ No

20. Would your agency be willing to share any report related to the repair/mitigation of spalling and corrosion-related issues in your concrete bridge system? ☐ Yes ☐ No

A.3 SURVEY RESULTS

This section presents the results of questionnaire survey with respect to each question.

A.3.1 Part II: Bridge deck system

A.3.1.1 Questions 1 & 2: Usage of a precast-prestressed paneling system

Table A-1 lists the 16 responding state agencies that reported use of precast-prestressed paneling systems. Table A-2 lists the 13 responding state agencies that reported non-usage of this system and includes corresponding comments received by those agencies.

Table A-1 State Agencies Reporting Use of Precast-Prestressed Paneling Systems

No.	State
1	Alaska
2	Arkansas
3	Colorado
4	Florida
5	Georgia
6	Hawaii
7	Iowa
8	Kansas
9	Kentucky
10	Michigan
11	Minnesota
12	Missouri
13	Nebraska
14	Oklahoma
15	Tennessee
16	Texas

Table A-2 State Agencies Reporting Non-Usage of Precast-Prestressed Paneling Systems and Related Comments

No.	State	Comments
1	Delaware	We have considered it in a couple of instances but found alternative solutions.
2	Idaho	Generally our contractors are not acquainted with deck panels. We have heard that there can be issues with workmanship and (partial-depth) grout strip (camber strip) with contractors who are not familiar with this approach.
3	Louisiana	In Louisiana, even though we have a detail for P/C P/S Concrete Bridge Deck Panels under Optional Span Detail, this type of deck is seldom used. A very high percentage of our deck are SIP or wood formwork in place. If the Empirical Design method is used, P/S P/C Concrete Bridge Deck Panels are not used.
4	Maine	We have used some partial-depth precast deck panels. However, their uses have been limited because it is difficult for bridge maintenance inspectors to look at the cast in place portion of deck over time. I am not aware of any spalling problems with these deck panels.
5	Maryland	We have only used once for a temporary measure. The panels are no longer in service. We don't use because the end ride surface isn't as good as a cast-in-place deck.
6	Montana	Not cost effective without need for rapid construction.
7	New Mexico	We have only used precast deck panels. Have yet to use prestressed panels but hope to in the near future.
8	North Dakota	We tried in 1978 and contractor had difficulty installing and ended up with bad ride. Program was discontinued.- was a one time research project.
9	Oregon	Your questionnaire seems to be geared towards those agencies that have a history of precast deck panels. Oregon does not have any significant history with precast deck panels. Therefore, we do not have any specifications for deck panels or any standardized repair procedures. For this reason, I would like to just mention a few things about our direction rather than send you a mostly blank questionnaire. We are in the early stages of our own research. We are looking at precast concrete deck panels (possibly prestressed) as a way to improve abrasion resistance. At this point we are still working on optimizing a concrete mix to meet the objective of improved abrasion resistance. Should we be able to show significant improvement in abrasion resistance, we then intend to place precast panels on a trial bridge. Oregon's interest is focused on full-depth panels. We are not considering partial-depth panels. We have not settled on the compressive strength we intend to require, but are expecting to fall somewhere between 6,000 and 8,000 psi. We will likely use prestressing strand and black steel in our precast deck panels. We are interested in evaluating FRP reinforcing bars for some applications, but are not considering them in precast panels. We are also evaluating various curing options, but are likely to settle on a combination of steam curing and liquid curing compound.
10	Pennsylvania	No comment
11	South Dakota	There has not been much interest from our local contractors to utilize them and not many critical sites where formwork construction time or removal are a big issue. We have also had concern over reflective cracking at panel joints/edges through topping slab.
12	Vermont	We do have a section in our prestress specifications that covers the production of them. It could possibly be the designers in our structures section are not aware of the systems or familiar enough with them. They may also be concerned of reflective cracking at the joints.
13	Wyoming	We have considered the system only. We have not chose to utilize them at this time.

A.3.1.2 Question 3: Type of precast-prestressed concrete deck panel

Table A-3 Type of PPC Panels

No.	State	Percentage of Panels	
		Full-Depth	Partial-Depth
1	Alaska	33	66
2	Arkansas	100	0
3	Colorado	95	5
4	Florida		
5	Georgia	100	0
6	Hawaii	100	0
7	Iowa	83.33	16.67
8	Kansas	100	0
9	Kentucky	100	0
10	Michigan	100	
11	Minnesota	100	0
12	Missouri	90	10
13	Nebraska	0	100
14	Oklahoma	100	
15	Tennessee	100	0
16	Texas	100	0

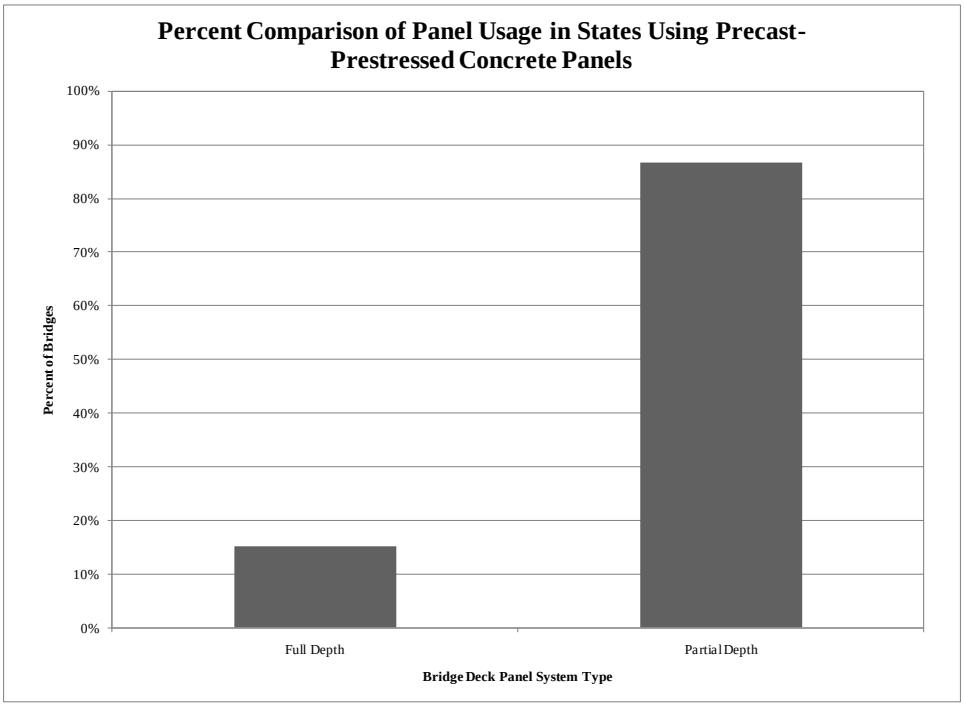

Figure A-1 Survey Results of Question 3

A.3.1.3 Question 4: Panel Dimensions

Table A-4 Thickness of Panels

No.	State	Panel Thickness (in.)
1	Alaska	8
2	Arkansas	No response
3	Colorado	No response
4	Florida	No response
5	Georgia	6
6	Hawaii	3.5
7	Iowa	3.5
8	Kansas	3
9	Kentucky	No response
10	Michigan	No response
11	Minnesota	3.5
12	Missouri	3
13	Nebraska	No response
14	Oklahoma	4
15	Tennessee	3.5
16	Texas	4

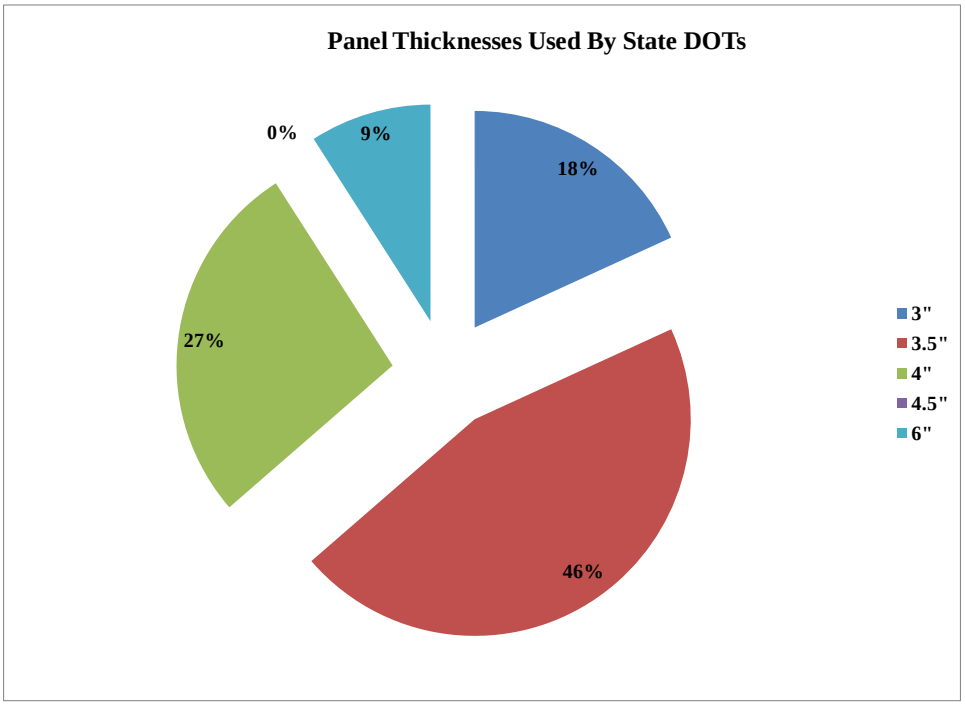

Figure A-2 Survey Results of Question 4

A.3.1.4 Question 5: Panel Age

Table A-5 Age of Panels

No.	State	Age (year)
1	Alaska	20
2	Arkansas	0
3	Colorado	16
4	Florida	40
5	Georgia	28
6	Hawaii	14
7	Iowa	25
8	Kansas	20
9	Kentucky	10
10	Michigan	NA
11	Minnesota	8
12	Missouri	35
13	Nebraska	5
14	Oklahoma	15
15	Tennessee	33
16	Texas	25

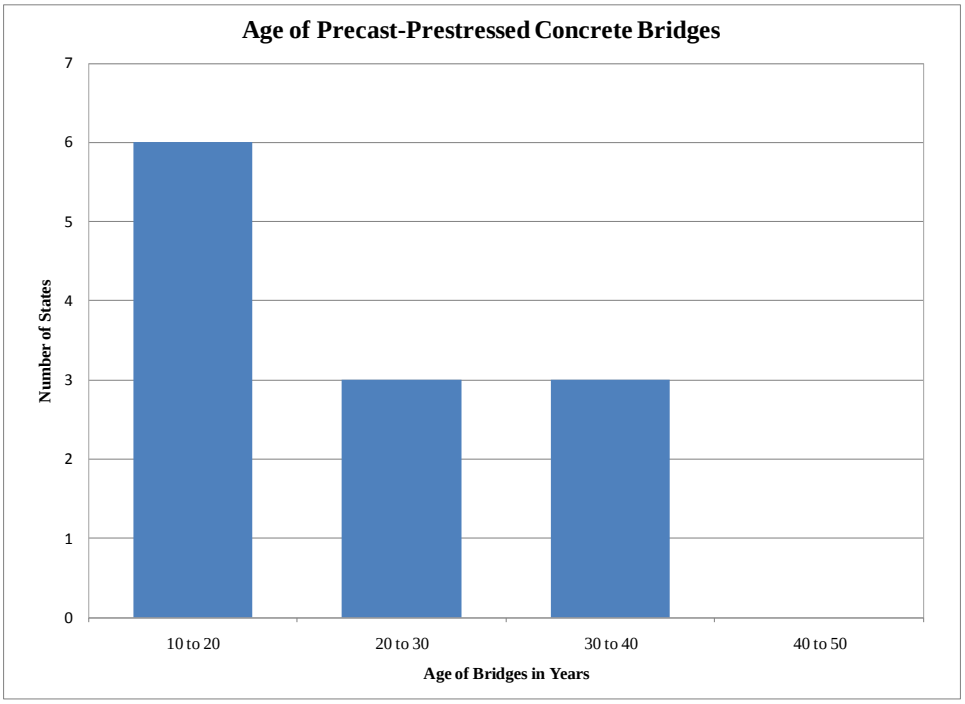

Figure A-3 Survey Results of Question 5

A.3.1.5 Question 6: Reinforcement Type

Table A-6 Types of Panel Reinforcement

No.	State	Mild Reinforcement	Epoxy Coated Reinforcing Steel	Prestressing Reinforcement	FRP Reinforcing Bars
1	Alaska	O	O		
2	Arkansas		O		
3	Colorado	O			O
4	Florida	O			
5	Georgia	O			O
6	Hawaii	O			O
7	Iowa	O	O		O
8	Kansas	O	O		
9	Kentucky	O	O		
10	Michigan		O		
11	Minnesota	O	O	O	
12	Missouri	O			
13	Nebraska	O	O		
14	Oklahoma	O		O	
15	Tennessee	O			
16	Texas	O			

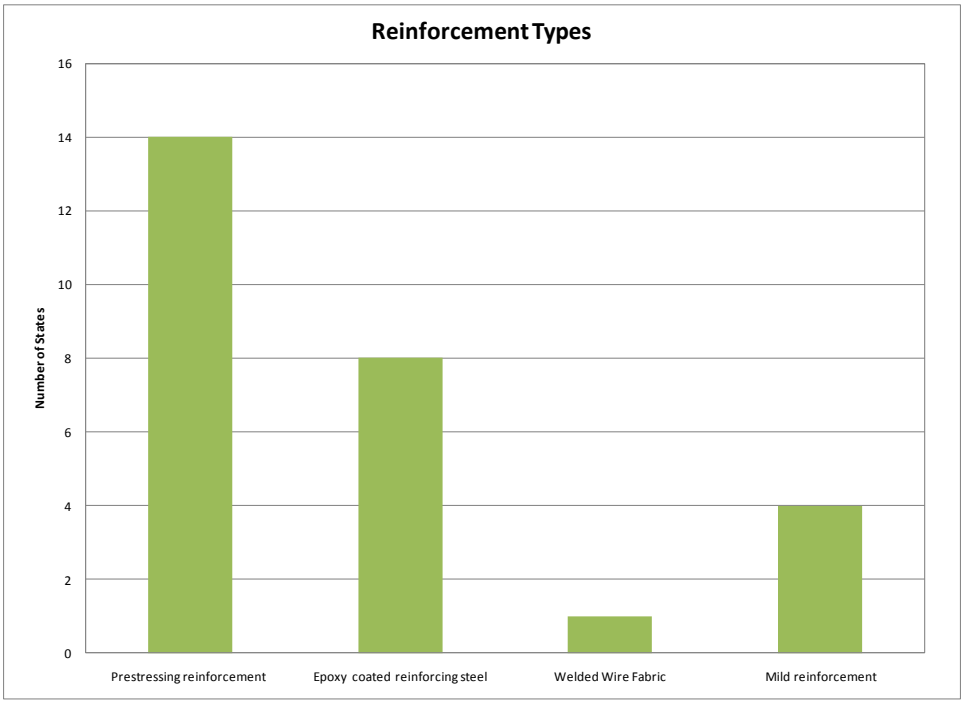

Figure A-4 Survey Results of Question 6

A.3.1.6 Question 7: Specified Compressive Strength of Precast Panel

Table A-7 Specified Compressive Strength of Panel

No.	State	≤ 4,000 psi	≤ 6,000 psi	≤ 8,000 psi	≤ 10,000 psi
1	Alaska		6,000		
2	Arkansas		5,800		
3	Colorado		5,000		
4	Florida				
5	Georgia		5,000		
6	Hawaii		6,000		
7	Iowa				10,000
8	Kansas	4,000			
9	Kentucky				
10	Michigan	4,000			
11	Minnesota		6,000		
12	Missouri		6,000		
13	Nebraska			8,000	
14	Oklahoma		5,000		
15	Tennessee	4,000			
16	Texas		5,000		

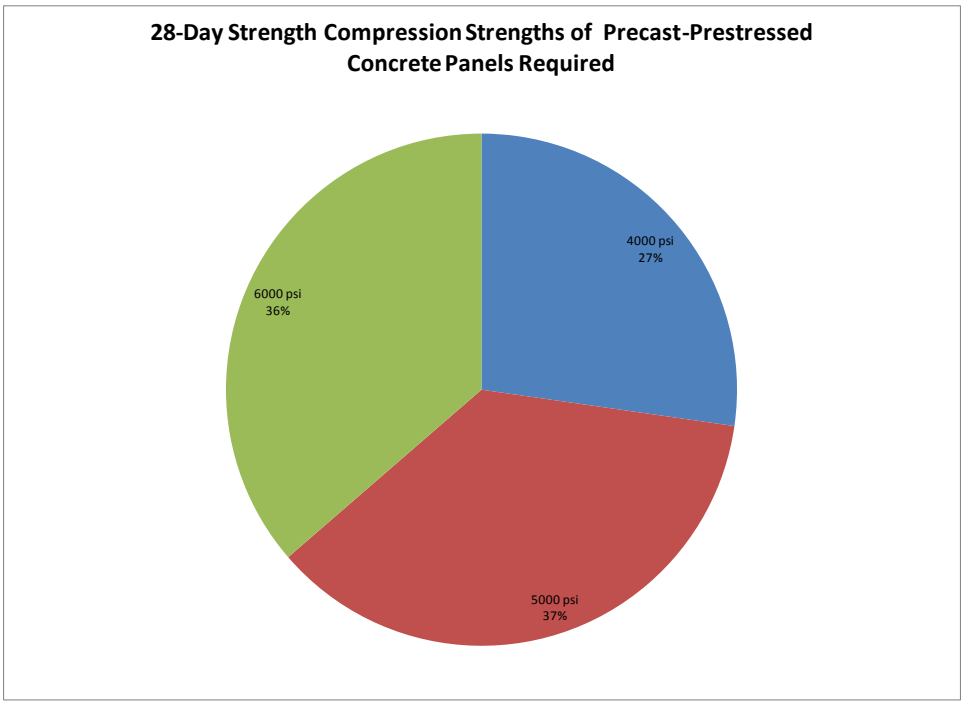

Figure A-5 Survey Results of Question 7

A.3.1.7 Question 8: Design Guidelines

Table A-8 Updated Design Guidelines

No.	State	Yes	No	Comments
1	Alaska	O		Full-depth, precast deck planks (sometimes prestressed) were originally used to replace worn glue-lam timber decks at remote locations. These deck planks are not stressed longitudinally and were intended as a more durable version of the older timber deck system
2	Arkansas		O	
3	Colorado		O	
4	Florida		O	
5	Georgia	O		(Used partial-depth panels a lot in time period 1980-1995; however, the contractors stopped using them) Took them out of specifications
6	Hawaii		O	
7	Iowa	O		Set 28 day strength of panels to 10000 psi
8	Kansas	O		LRFD Loads
9	Kentucky		O	
10	Michigan		O	
11	Minnesota	O		We used information from MoDOT
12	Missouri	O		Panel thickness reduced from 3.5" to 3" to increase top concrete thickness from 5" to 5.5" to reduce reflective cracking at the joints where panels meet. Concrete strength rose from 5000 psi to 6000 psi in order to provide corrosion protection to the strands. Min. joint filler increased 3/4" to 1" to permit better consolidation and firm bearing
13	Nebraska		O	
14	Oklahoma		O	
15	Tennessee	O		We updated standard for the support system during panel placement and deck pours. Previously, the bituminous strips supporting panels were placed on beam flanges. This becomes unwieldy when correcting for camber and grade differences. We now require support outside the flanges as shown
16	Texas		O	

A.3.1.8 Question 9: Concrete Strength of CIP Topping Concrete

Table A-9 Compressive Strength of Concrete for CIP Topping Concrete

No.	State	≤ 3,500 psi	≤ 4,000 psi	≤ 5,000 psi	Other
1	Alaska				5,800
2	Arkansas			5,000	
3	Colorado				
4	Florida	3,500			
5	Georgia		4,000		
6	Hawaii	3,500			
7	Iowa		4,000		
8	Kansas			5,000	
9	Kentucky		4,000		
10	Michigan		4,000		
11	Minnesota		4,000		
12	Missouri				
13	Nebraska		4,000		
14	Oklahoma		4,000		
15	Tennessee		4,000		
16	Texas				5,800

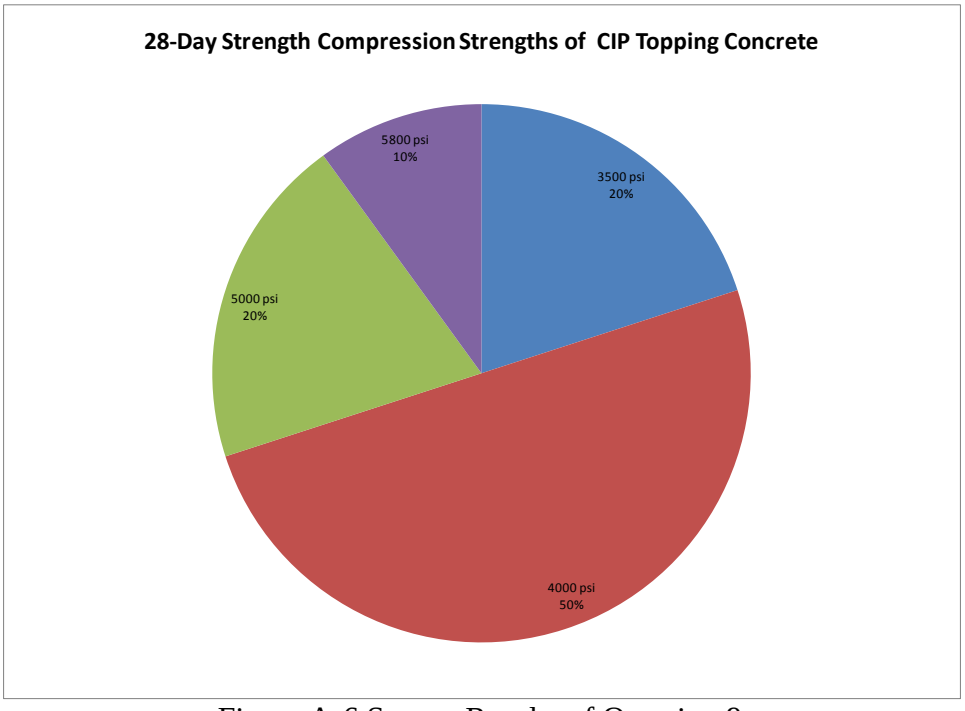

Figure A-6 Survey Results of Question 9

A.3.1.9 Question 10: Curing

Table A-10 Types and Lengths of Curing for CIP Topping Concrete

No.	State	Moist Curing	Liquid Membrane Curing Compound	Waterproof Cover	Others
1	Alaska				No response
2	Arkansas	14 days			
3	Colorado		O	O	
4	Florida				No response
5	Georgia	5 days		5 days	
6	Hawaii	7 days	7 days		
7	Iowa			4 days	
8	Kansas	7 days			
9	Kentucky	O			
10	Michigan	7 days			
11	Minnesota	7 days			
12	Missouri	7 days	9 days		
13	Nebraska				No response
14	Oklahoma	7 days			
15	Tennessee	5 days	O		
16	Texas	8 days		10 days	

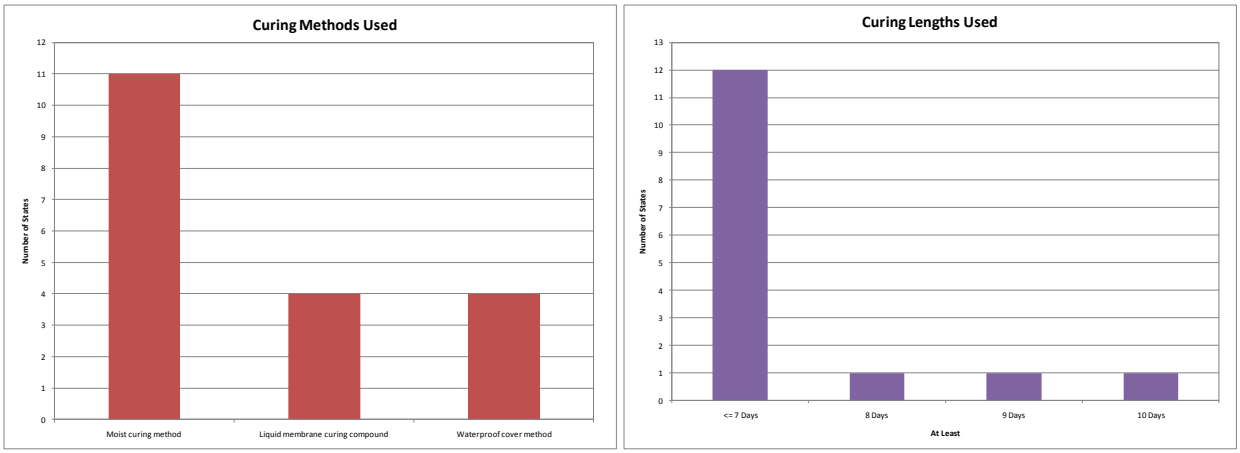

Figure A-7 Survey Results of Question 10

A.3.1.10 Questions 11 & 12: Construction of Deck Joint

Table A-11 Panel Joints of Partial-Depth Panels

No.	State	Compressive Filler	CIP Concrete	Tight Fit	Butt Joints	None
1	Alaska					O
2	Arkansas					O
3	Colorado					O
4	Florida					O
5	Georgia					O
6	Hawaii	O*				
7	Iowa		O			
8	Kansas	O				
9	Kentucky					O
10	Michigan					O
11	Minnesota			O		
12	Missouri	O				
13	Nebraska					O
14	Oklahoma					O
15	Tennessee				O**	
16	Texas					O

*Edges of panels are beveled to slightly above the bottom with compressible filler placed to seal the joint prior to placement of topping.
**Transverse cracking is inevitable as wet concrete will shrink differentially than beams or in this case, beams and deck panels. If decks are placed full depth, cracks occur every 4 ft, with panels, every 8 ft.

Table A-12 Panel Joints of Full-Depth Panels

No.	State	Compressive Filler	CIP Concrete	Grouted to Female Joints
1	Alaska	O		
2	Arkansas			
3	Colorado			O
4	Florida			
5	Georgia			
6	Hawaii			
7	Iowa		O	
8	Kansas			
9	Kentucky			
10	Michigan			
11	Minnesota			
12	Missouri			
13	Nebraska	O		
14	Oklahoma			
15	Tennessee			
16	Texas			

A.3.2 Part III: Problems observed in precast concrete deck panels

A.3.2.1 Question 13: Observed problems

Table A-13 Problem Description

No.	Observed Problems
1	Transverse cracks in CIP
2	Longitudinal cracks in CIP
3	Cracks in the bottom side of panels
4	Seepage at the Joints
5	Efflorescence at the joints
6	Rust stains of deck panels along tendons
7	Concrete spalling at the joints
8	Corrosion of Reinforcement

Table A-14 Observed Problems in Precast Concrete Deck System

No.	State	1	2	3	4	5	6	7	8
1	Alaska				O				
2	Arkansas								
3	Colorado	O		O	O	O			
4	Florida		O						
5	Georgia								
6	Hawaii								
7	Iowa								
8	Kansas	O	O						
9	Kentucky								
10	Michigan	O	O	O	O				
11	Minnesota	O	O						
12	Missouri	O	O	O	O		O	O	O
13	Nebraska								
14	Oklahoma	O							
15	Tennessee								
16	Texas	O	O						
Sum		***7***	***6***	***3***	***4***	***1***	***1***	***1***	***1***

A.3.2.2 Question 14: Mitigation methods

Table A-15 Description of Mitigation Methods

No.	Observed Problems
1	Polymer overlay
2	Epoxy injection
3	Deck replacement
4	Deck crack pouring
5	Chip seal
6	HMWMA
7	Water-proofing membrane w/asphalt overlay
8	Concrete sealer
9	Total deck surface treatment
10	Linseed oil

Table A-16 Mitigation Methods for Observed Problems

No.	State	1	2	3	4	5	6	7	8	9	10
1	Alaska							O			
2	Arkansas										
3	Colorado		O		O					O	
4	Florida		O	O							
5	Georgia										
6	Hawaii										
7	Iowa										
8	Kansas	O									
9	Kentucky										
10	Michigan										
11	Minnesota				O						
12	Missouri			O		O			O	O	O
13	Nebraska										
14	Oklahoma						O				
15	Tennessee										
16	Texas				O	O					
Sum		***1***	***2***	***2***	***3***	***2***	***1***	***1***	***1***	***2***	***1***

A.3.2.3 Question 15: Deicing procedure

Table A-17 Frequency of Deicing Procedures and Materials (per year)

No.	State	Conventional Road salt	Chloride salts	Brine solution	Abrasives	Magnetism Chloride	None
1	Alaska						O
2	Arkansas						O
3	Colorado				1		
4	Florida						O
5	Georgia	1				1	
6	Hawaii						O
7	Iowa	varies	O				
8	Kansas	10	40				
9	Kentucky	15	15				
10	Michigan	O					
11	Minnesota	20	20				
12	Missouri	30					
13	Nebraska		O				
14	Oklahoma	2	10				
15	Tennessee	10		15			
16	Texas	varies					

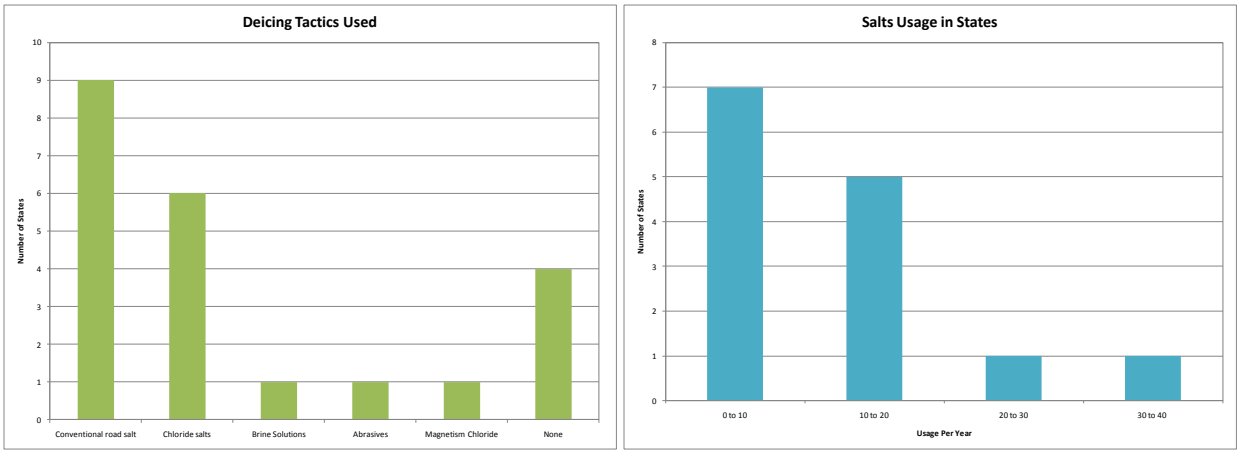

Figure A-8 Survey Results of Question 15

A.3.2.4 Question 16: Maintenance of deck joints

Table A-18 Period of Maintenance of Deck Joints and Materials (years)

No.	State	Silicon sealing	Hot pour sealing	Methacrylate resin treatment	None
1	Alaska	5			
2	Arkansas				O
3	Colorado			O	
4	Florida				O
5	Georgia	0.1			
6	Hawaii				O
7	Iowa		O		
8	Kansas				O
9	Kentucky				O
10	Michigan				O
11	Minnesota	2-3			
12	Missouri		O		
13	Nebraska				O
14	Oklahoma	At construction			
15	Tennessee				O
16	Texas				O

A.3.2.5 Question 17: Girder types

Table A-19 Types of Girders Supporting Precast Concrete Deck Panels (%)

No.	State	Steel Girders	Prestressed Concrete Girders	Other
1	Alaska	100		
2	Arkansas	100		
3	Colorado	10	90	
4	Florida		100	
5	Georgia		100	
6	Hawaii		100	
7	Iowa	20	80	
8	Kansas	5	10	85
9	Kentucky	100		
10	Michigan		100	
11	Minnesota		100	
12	Missouri	40	60	
13	Nebraska	100		
14	Oklahoma	50	50	
15	Tennessee	30	50	20
16	Texas	5	95	

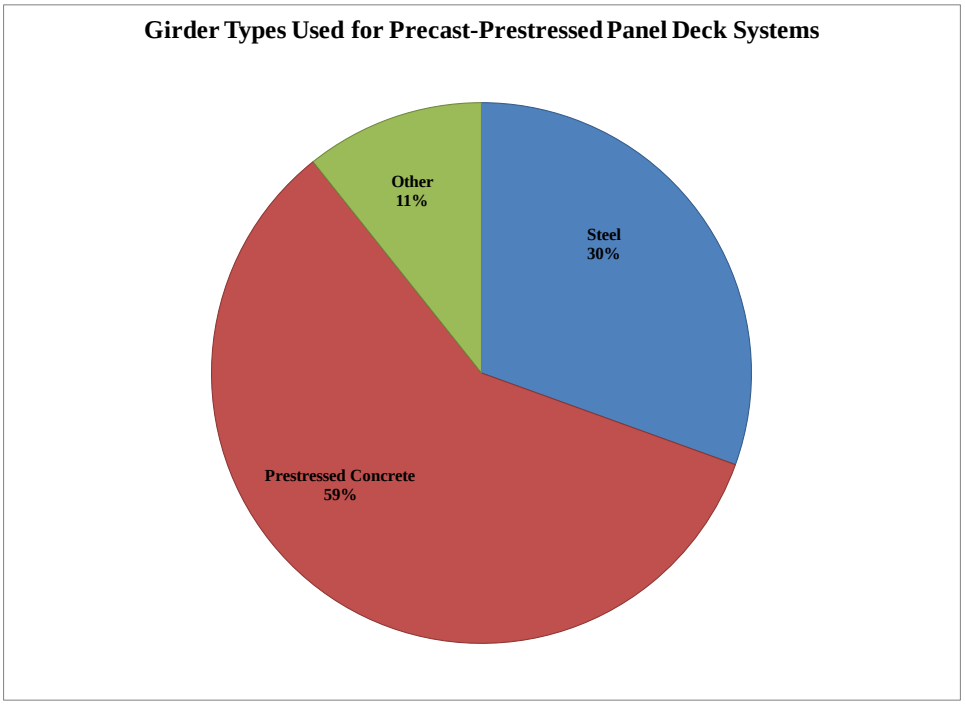

Figure A-9 Survey Results of Question 17

APPENDIX B

FIELD INVESTIGATIONS

TABLE OF CONTENTS

LIST OF FIGURES

LIST OF TABLES

B.1 INTRODUCTION

This appendix provides data obtained during the field investigation of Bridge A4709 described in Chapter 4.

B.2 CONTENTS

Tables B-1 and B-2 present the half-cell potential and resistivity data from Bridge A4709 respectively. Table B-3 presents calibrated rebound hammer compressive strength values from panels on Bridge A4709. Table B-4 summarizes core depth, reinforcement encountered, bottom surface type, chloride ion content, and carbonation depth data from cores taken from Bridge A4709. Figure B-1 show visual inspection data observed from the bottom surface of the bridge deck, respectively including efflorescence, water staining, spalling, and discoloration line locations. Figure B-2 shows visual inspection data observed from the top surface of the bridge deck, including crack maps and drain locations. Photos of cores taken from Bridge A4709 are shown in Figure B-3.

Table B-1 Half-cell Potential Data from Bridge A4709

Panel	Potential Difference (mV)*	Tendon Description	Corrosion
D23-22	-583	Fully exposed and fractured	probable
	-524	Fully exposed and fractured	probable
	-538	Fully exposed and fractured	probable
	-497	Fully exposed and fractured	probable
	-514	Fully exposed and fractured	probable
	-454	Partially exposed	probable
	-460	Partially exposed	probable
	-388	Partially exposed	probable
	-365	Partially exposed	probable
D22-23	-600	Partially exposed	probable
	-635	Partially exposed	probable
	-479	Partially exposed	probable
	-300	Partially exposed	probable
D23-24	-445	Fully exposed, not fractured	probable
	-362	Fully exposed, not fractured	probable
	-383	Fully exposed, not fractured	probable
	-320	Fully exposed, not fractured	probable
	-560	Fully exposed, not fractured	probable
	-517	Fully exposed, not fractured	probable
	-570	Fully exposed, not fractured	probable
	-675	Fully exposed, not fractured	probable
D24-23	-395	Partially exposed	probable
	-407	Partially exposed	probable
	-376	Partially exposed	probable
	-320	Partially exposed	probable
D23-24	-445	Partially exposed	probable
	-410	Partially exposed	probable
	-420	Partially exposed	probable
	-400	Partially exposed	probable
	-436	Partially exposed	probable

*Potential difference levels less than -500 mV correspond to corrosion levels producing visible evidence of corrosion; -350 to -500 mV corresponds to a 95% chance of corrosion; -200 to -350 corresponds to a 50% chance of corrosion; and more than -200 corresponds to 5% chance of reinforcement being corroded

Table B-2 Resistivity Data from Bridge A4709

Panel	Resistivity (kΩcm)	Current %	Reliable*	Corrosion Probability
A24-25	47	100	yes	unlikely
A24-25	35	90	yes	unlikely
A24-25	99	20	no	-
A24-25	23	100	yes	unlikely
A24-25	13	100	yes	unlikely
A24-25	77	42	no	-
A23-24	55	50	yes	unlikely
A23-24	30	100	yes	unlikely
A23-24	56	100	yes	unlikely
A23-24	63	100	yes	unlikely
A23-24	51	100	yes	unlikely
A22-23	38	36	no	-
A22-23	42	61	yes	unlikely
A22-23	34	100	yes	unlikely
A22-23	18	100	yes	unlikely
A22-23	62	48	no	-
B24-25	0	-	-	-
B23-24	0	-	-	-
B22-23	0	-	-	-
C24-25	29	100	yes	unlikely
C24-25	47	60	yes	unlikely
C24-25	99	47	no	-
C23-24	77	41	no	-
C23-24	49	81	yes	unlikely
C23-24	21	78	yes	unlikely
C23-24	39	52	yes	unlikely
C23-24	46	48	no	-
C23-24	95	42	no	-
C23-24	87	28	no	-
C23-24	50	51	yes	unlikely
C23-24	59	55	yes	unlikely
C22-23	51	64	yes	unlikely
D24-25	99	100	yes	unlikely
D24-25	99	72	yes	unlikely
D24-25	99	98	yes	unlikely
D24-25	99	100	yes	unlikely
D24-25	75	100	yes	unlikely
D24-25	56	100	yes	unlikely
D24-25	16	100	yes	unlikely

D24-25	36	79	yes	unlikely
D24-25	36	60	yes	unlikely
D24-25	38	65	yes	unlikely
D24-25	26	89	yes	unlikely
D24-25	53	42	no	-
D23-24	21	61	yes	unlikely
D23-24	68	50	yes	unlikely
D23-24	99	38	no	-
D23-24	18	61	yes	unlikely
D22-23	41	44	no	-
D22-23	33	100	yes	unlikely
D22-23	21	100	yes	unlikely
D22-23	10	100	yes	possible
D22-23	14	76	yes	unlikely
D22-23	23	100	yes	unlikely
D22-23	16	100	yes	unlikely
D12-13	64	66	yes	unlikely
D12-13	85	66	yes	unlikely
D12-13	99	76	yes	unlikely
D12-13	53	82	yes	unlikely
D12-13	99	48	no	-
D12-13	99	20	no	-
D12-13	99	32	no	-
D12-13	99	10	no	-
D12-13	99	27	no	-
D12-13	99	20	no	-
D12-13	99	42	no	-
D12-13	99	45	no	-
C11-12	99	60	yes	unlikely
C11-12	99	80	yes	unlikely
C11-12	99	68	yes	unlikely
C11-12	99	100	yes	unlikely
C11-12	51	100	yes	unlikely
C11-12	55	75	yes	unlikely
C11-12	37	-	no	-
C11-12	84	-	no	-
C12-13	0	-	-	-
C13-14	0	-	-	-
B13-14	0	-	-	-
B12-13	0	-	-	-
B11-12	0	-	-	-

A11-12	55	95	yes	unlikely
A11-12	99	32	no	-
A11-12	30	100	yes	unlikely
A11-12	54	100	yes	unlikely
A11-12	66	100	yes	unlikely
A11-12	52	100	yes	unlikely
A11-12	29	100	yes	unlikely
A12-13	99	10	no	-
A12-13	99	18	no	-
A13-14	99	12	no	-
A13-14	99	10	no	-

* A reading with a current percentage between 50% and 100% indicates a reliable reading, between 20% and 50% indicates the value is not exact and any readings below 20% indicate a very poor connection between the four-prong probe and the concrete of interest (IAEA 2002).

Table B-3 Rebound Hammer Compressive Strength Values for Each Panel from Bridge A4709

Panel Number	Average compressive strength calibrated with panel results (psi)[1]
A23-A24	6350
D24-D25[3]	7520
D23-D24[3]	7590
B25-B26	7650
C26-C27[3]	7810
C24-C25[3]	7930
A26-A27	7970
C23-C24[3]	8020
A25-A26	8150
B26-B27	8120
A24-A25	7630
B24-B25	8170
B23-B24	8200
D25-D26[3]	8350
A11-A12	8420
C13-C14	8420
C25-C26[3]	8450
B13-B14	8610
A13-A14	8310
C12-C13[2]	8590
B12-B13	8640
A12-A13	8640
C14-C15	8780
B14-B15	8830
D14-D15	8870
D13-D14	9210
D12-D13[2]	9260

[1]Values reported are the average of 10 readings
[2] Panels with one cracked and/or spalled edge
[3] Panels with two cracked and/or spalled edges

Table B-4 Summary of Core Data from Bridge A4709

Core ID	Depth of core (in.)	Depth of reinforcement encountered (in.)	Bottom surface of core	Sampling Depths (in.)	lb Cl- /yd^3	Corrosion Possibility	Carbonation Depth (mm)
C-1	4.5	4.5	broken	3	0.332	Not Likely	1 mm
C-2	5.5	None	smooth	3	0.224	Not Likely	1 mm or less
				4	1.445	Possible	
C-3	6.125	None	smooth	3	2.610	Possible	1 mm
				4	2.614	Possible	
				5	1.377	Possible	
C-4	3.125	3.125	broken	2	0.643	Not Likely	less than 1 mm
C-5	6.5	None	broken	3	0.257	Not Likely	less than 1 mm
				4	0.363	Not Likely	
				5	0.115	Not Likely	
C-6	6.625	3.875	broken	3	0.263	Not Likely	1-2 mm
				4	0.100	Not Likely	
				5	0.252	Not Likely	
C-7	6.5	4.75	smooth	3	0.279	Not Likely	1- 2 mm
				4	0.181	Not Likely	
				5	0.268	Not Likely	
C-8	6.375	4.5	smooth	3	0.221	Not Likely	1 mm, 11 mm at large void
				4	0.183	Not Likely	
				5	0.212	Not Likely	
C-9	7	6.875	broken	3	0.189	Not Likely	1 mm, 11 mm in crack
				4	0.328	Not Likely	
				5	0.230	Not Likely	
C-10	7.125	4.25	broken	3	6.532	Possible	less than 1 mm
				4	5.393	Possible	
				5	6.051	Possible	

Figure B-1 Visual Inspection Data from the Bottom Surface of the Bridge Deck – Bridge

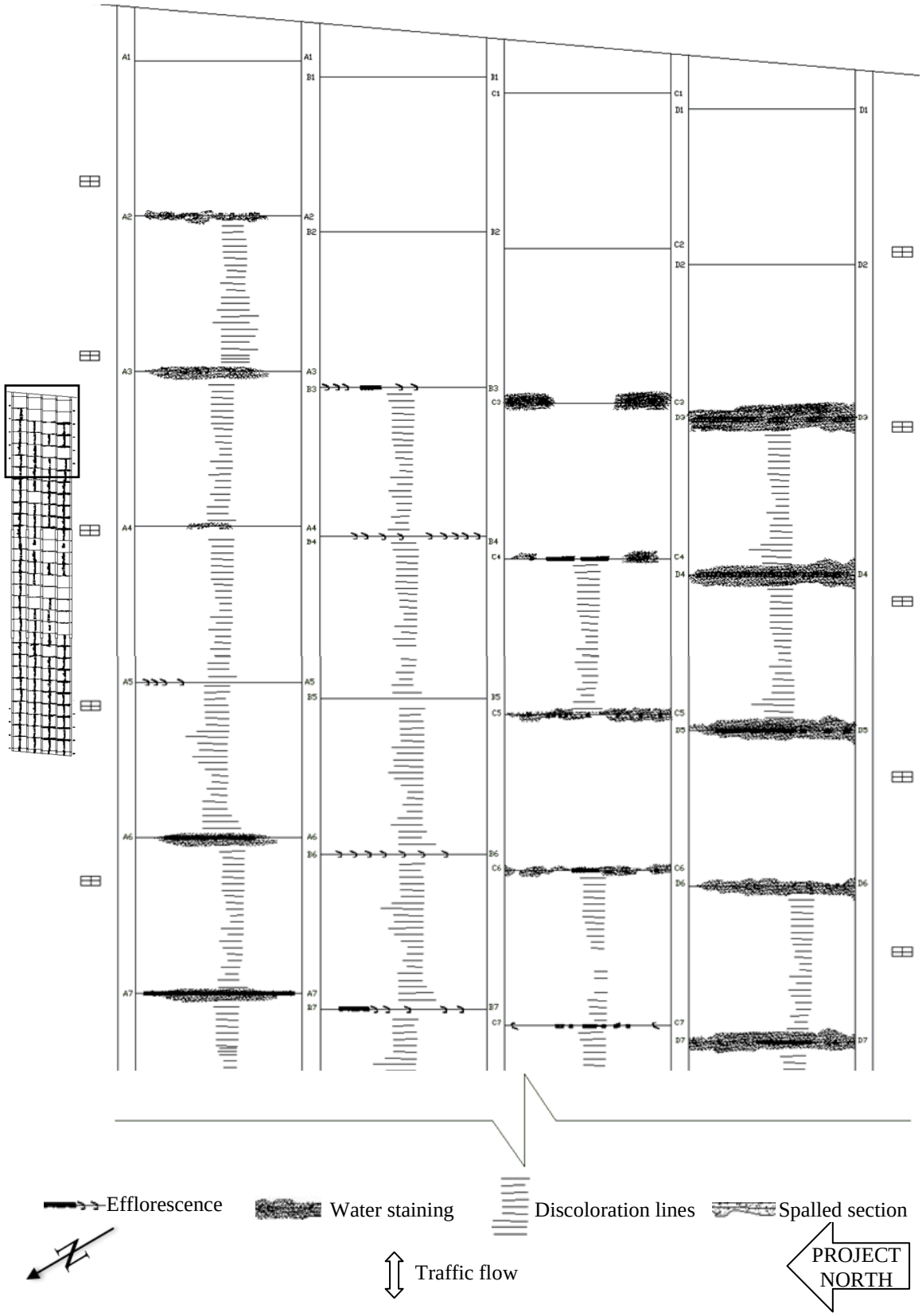

Figure B-1 Visual Inspection Data from the Bottom Surface of the Bridge Deck – Bridge A4709 (Cont.)

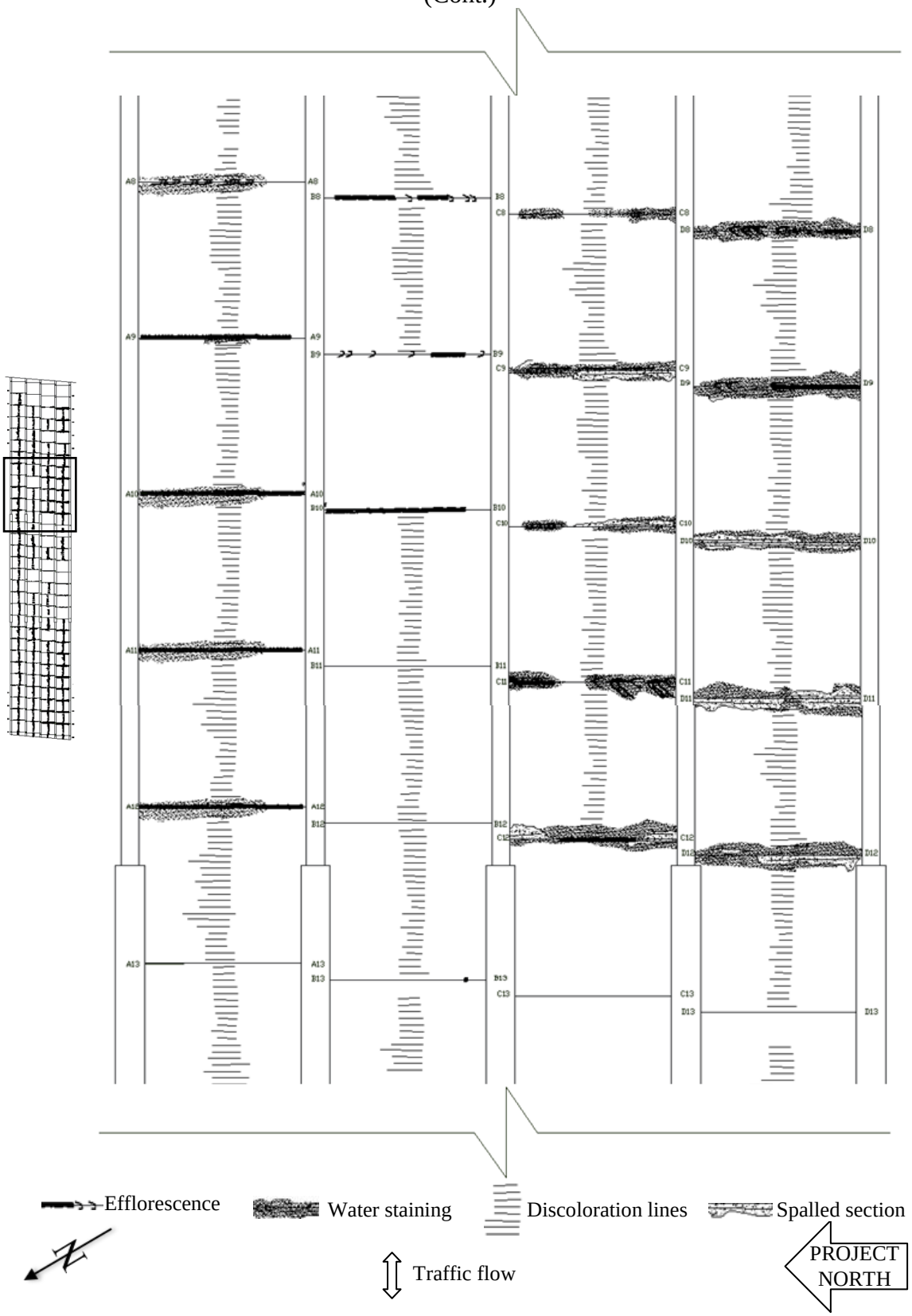

Figure B-1 Visual Inspection Data from the Bottom Surface of the Bridge Deck – Bridge A4709 (Cont.)

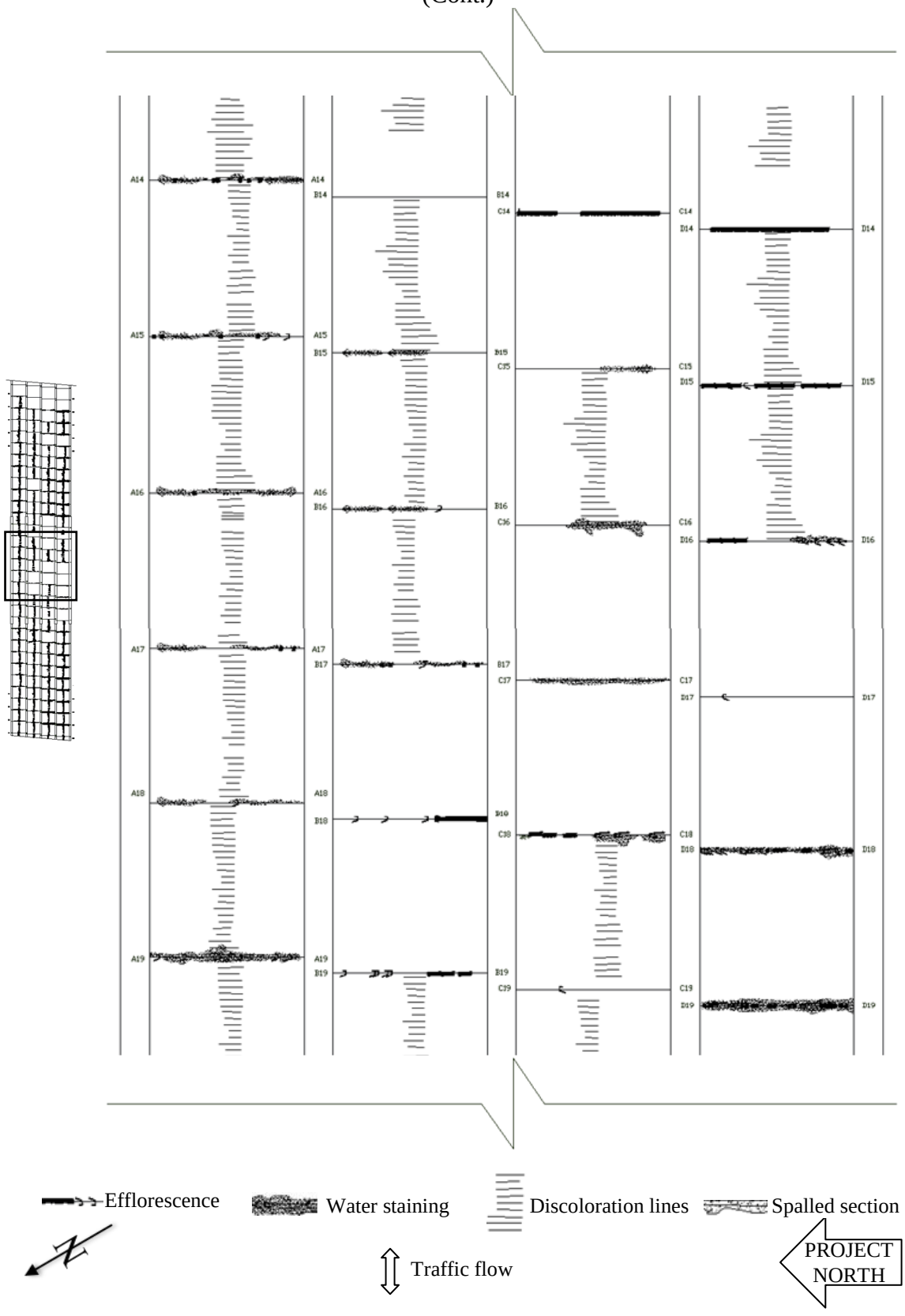

Figure B-1 Visual Inspection Data from the Bottom Surface of the Bridge Deck – Bridge A4709 (Cont.)

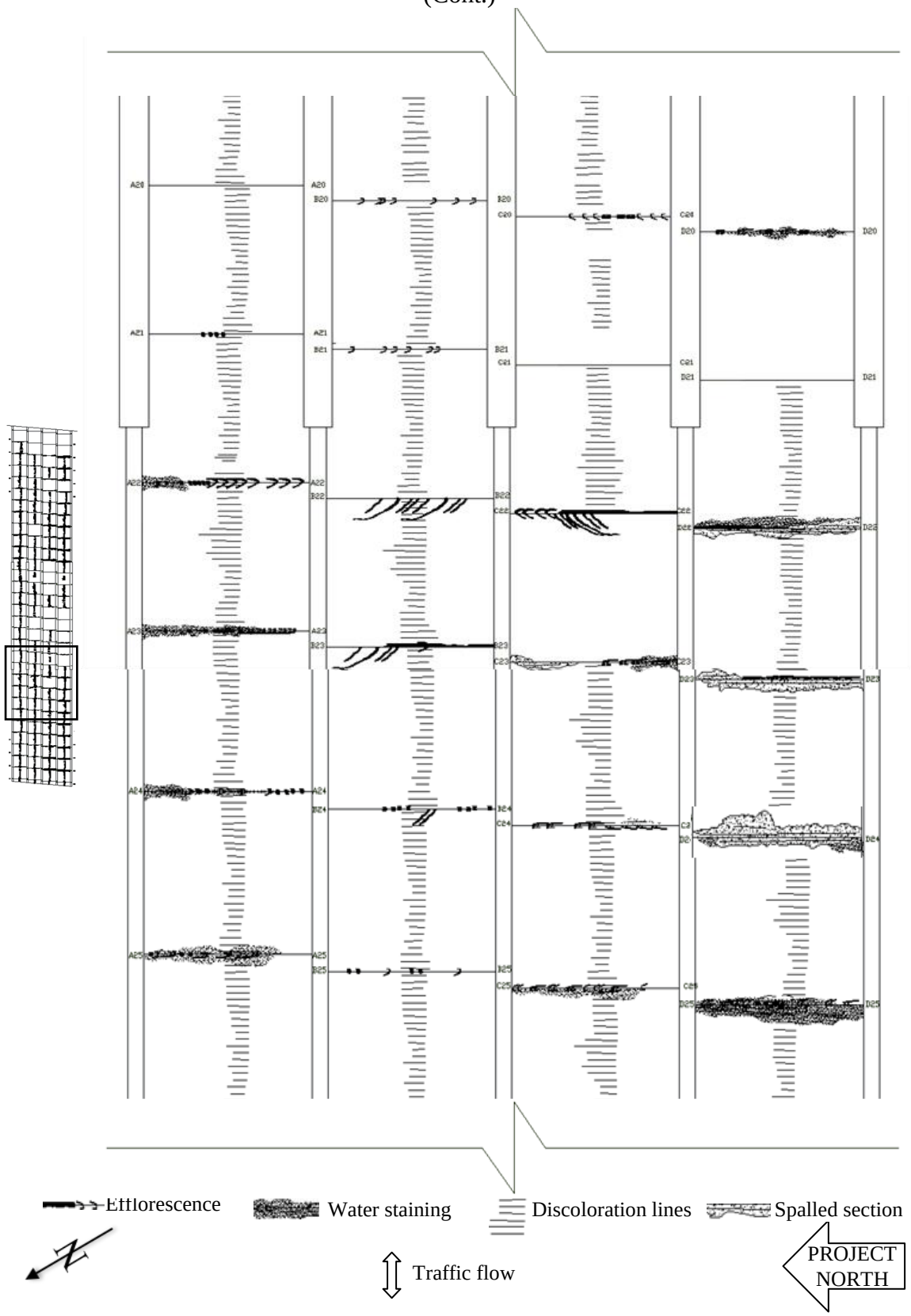

Figure B-1 Visual Inspection Data from the Bottom Surface of the Bridge Deck – Bridge A4709 (Cont.)

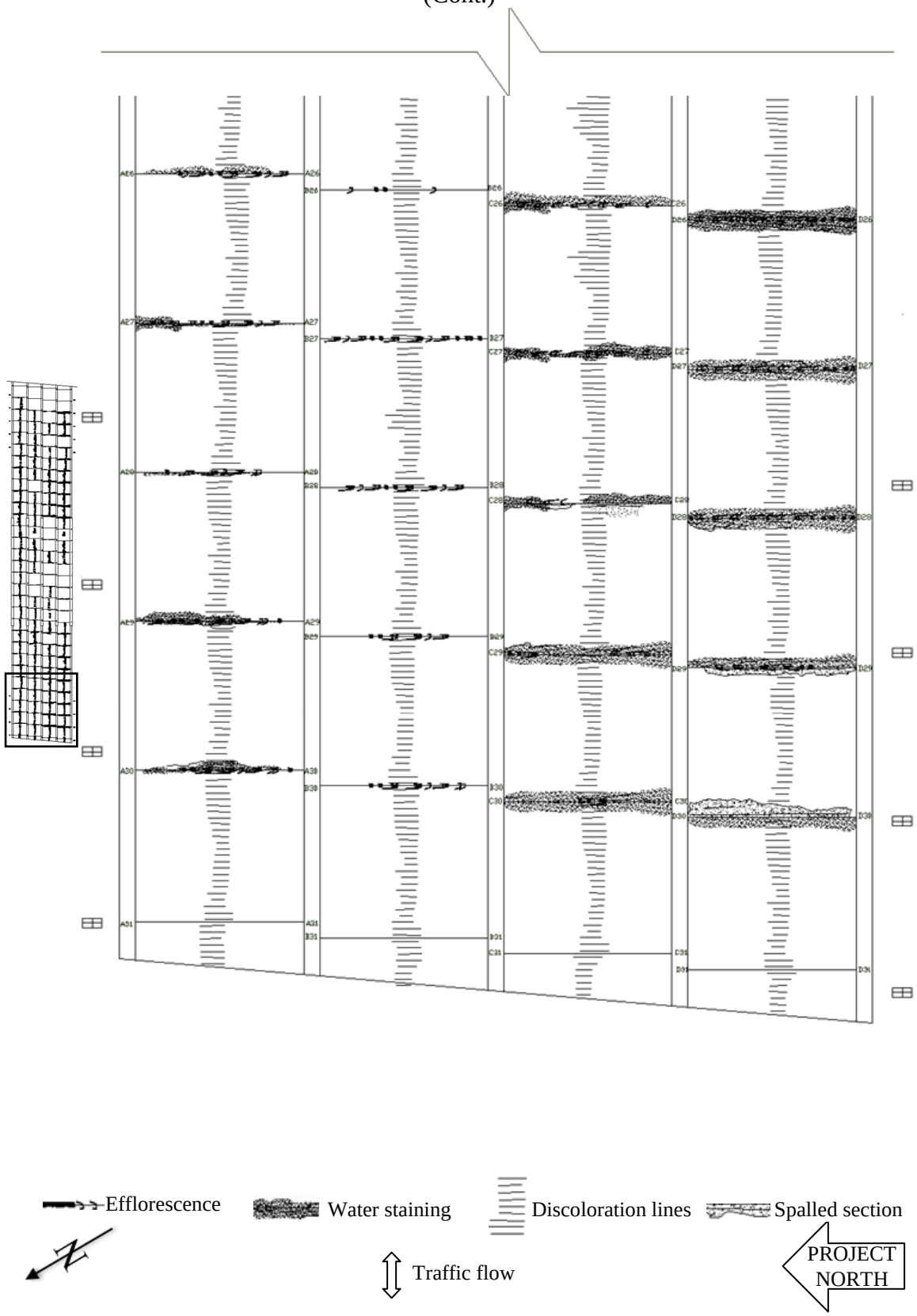

Figure B-2 Visual Inspection Data from the Top Surface of the Bridge Deck - Crack Map and Drain Locations – Bridge A4709A4709

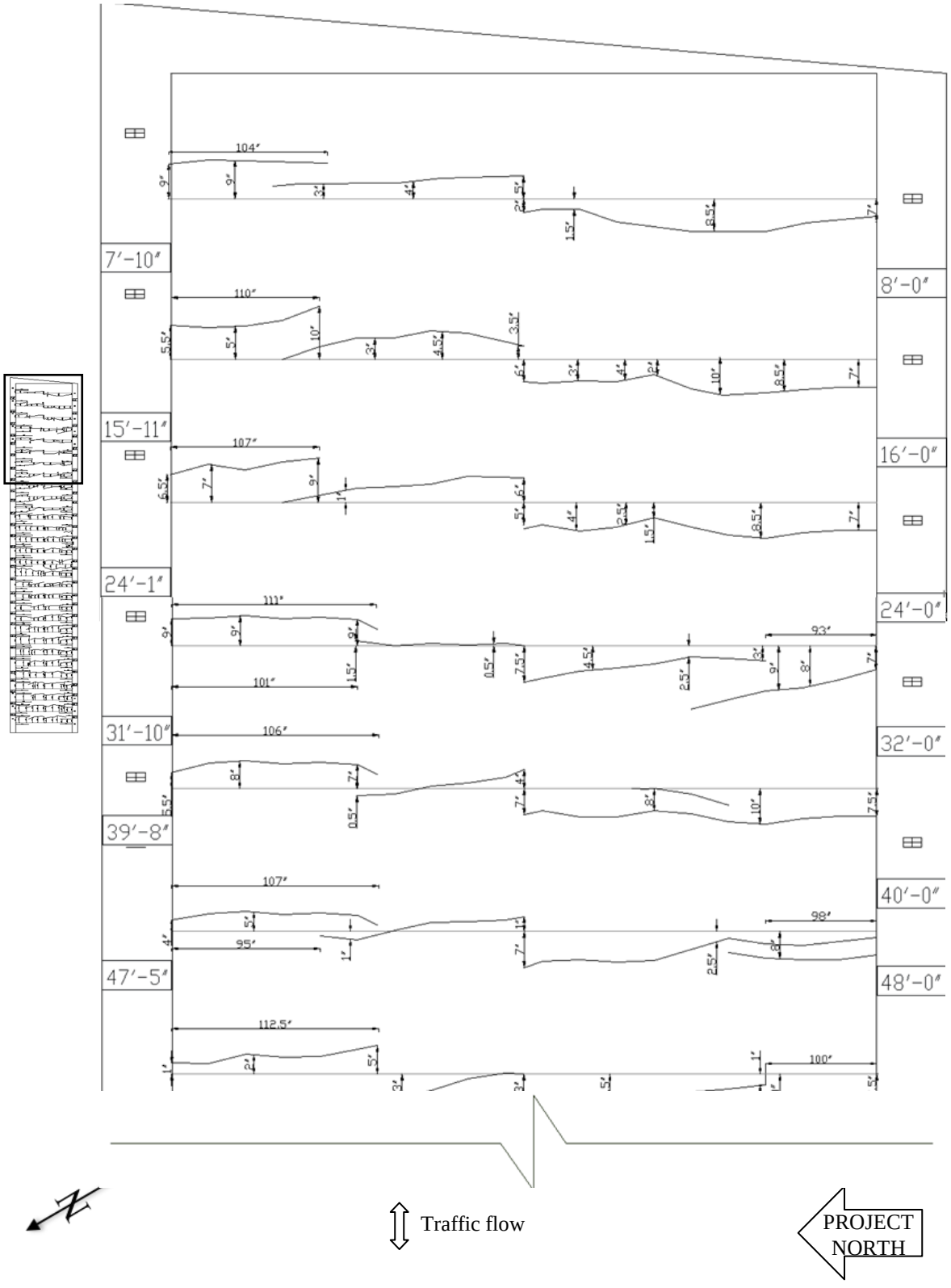

Figure B-2 Visual Inspection Data from the Top Surface of the Bridge Deck - Crack Map and Drain Locations – Bridge A4709 (Cont.)

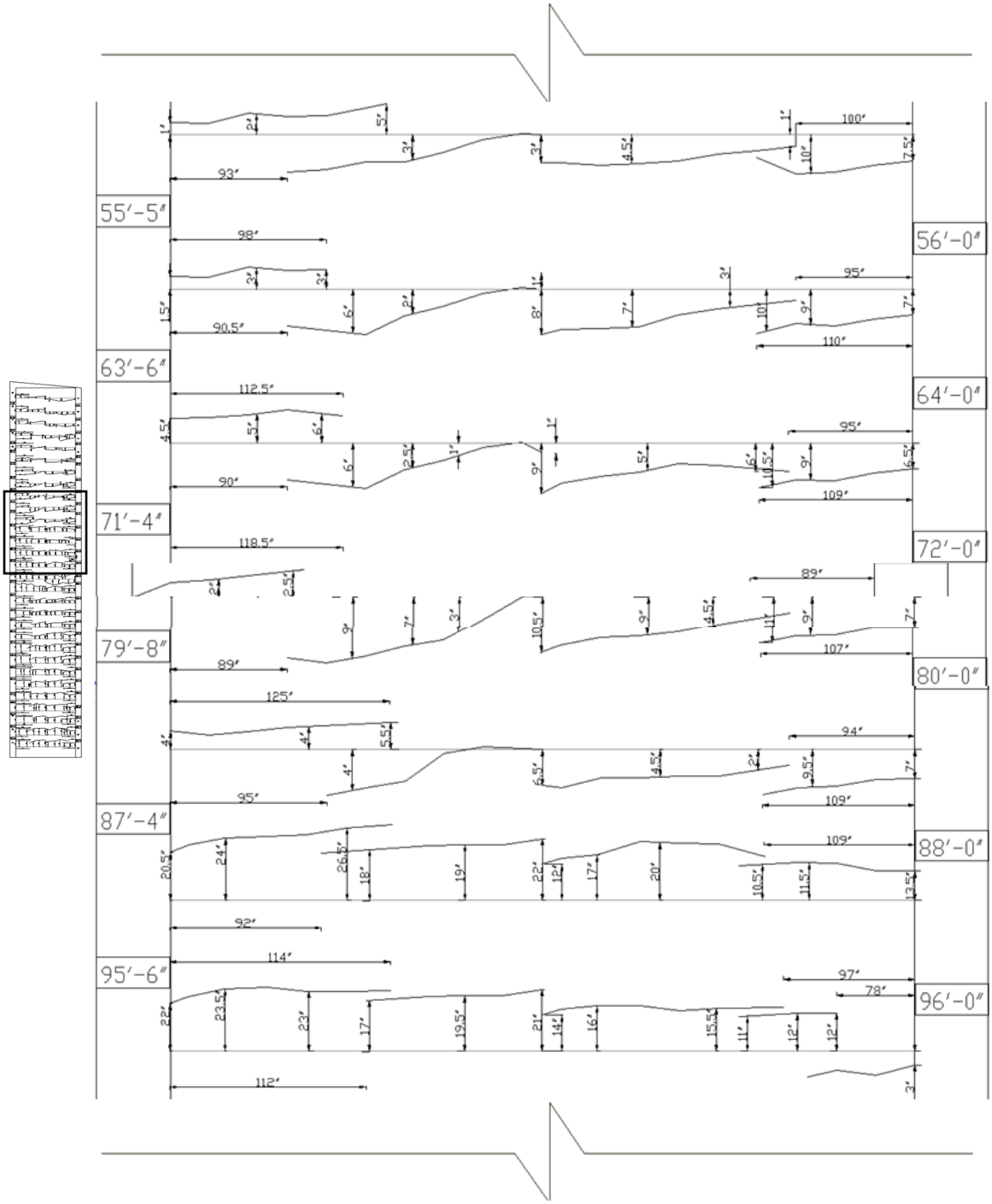

Figure B-2 Visual Inspection Data from the Top Surface of the Bridge Deck - Crack Map and Drain Locations – Bridge A4709 (Cont.)

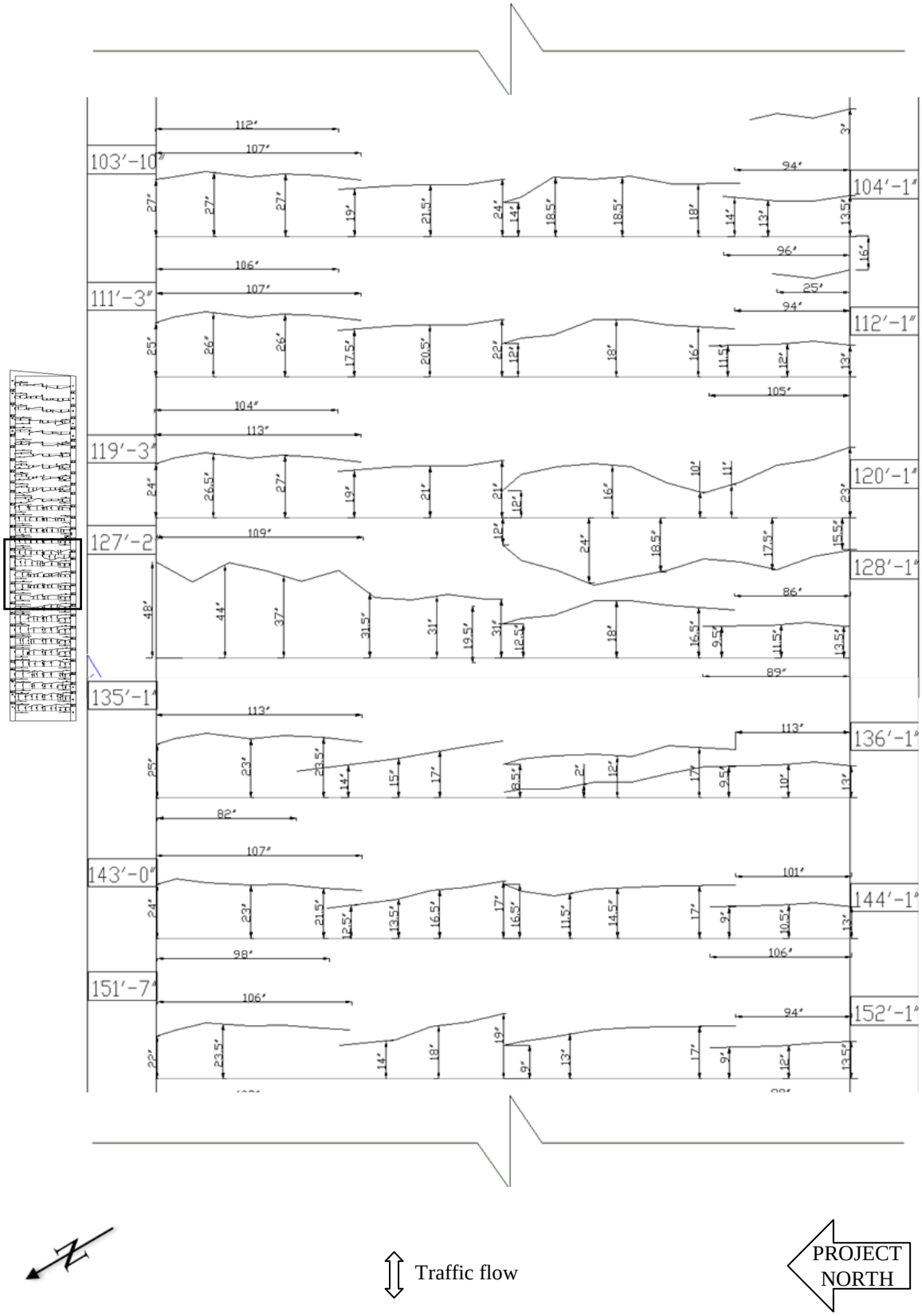

Figure B-2 Visual Inspection Data from the Top Surface of the Bridge Deck - Crack Map and Drain Locations – Bridge A4709 (Cont.)

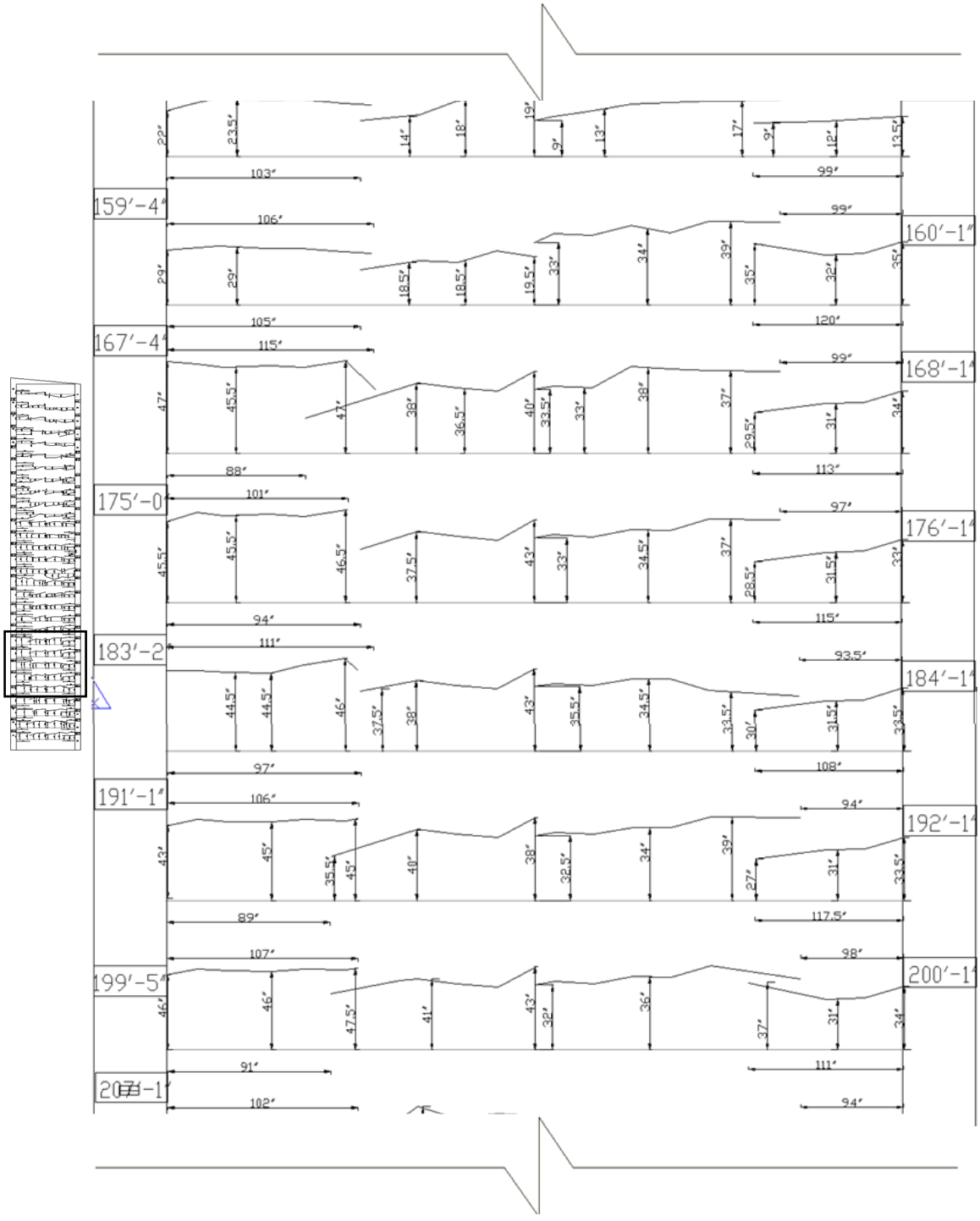

Figure B-2 Visual Inspection Data from the Top Surface of the Bridge Deck - Crack Map and Drain Locations – Bridge A4709 (Cont.)

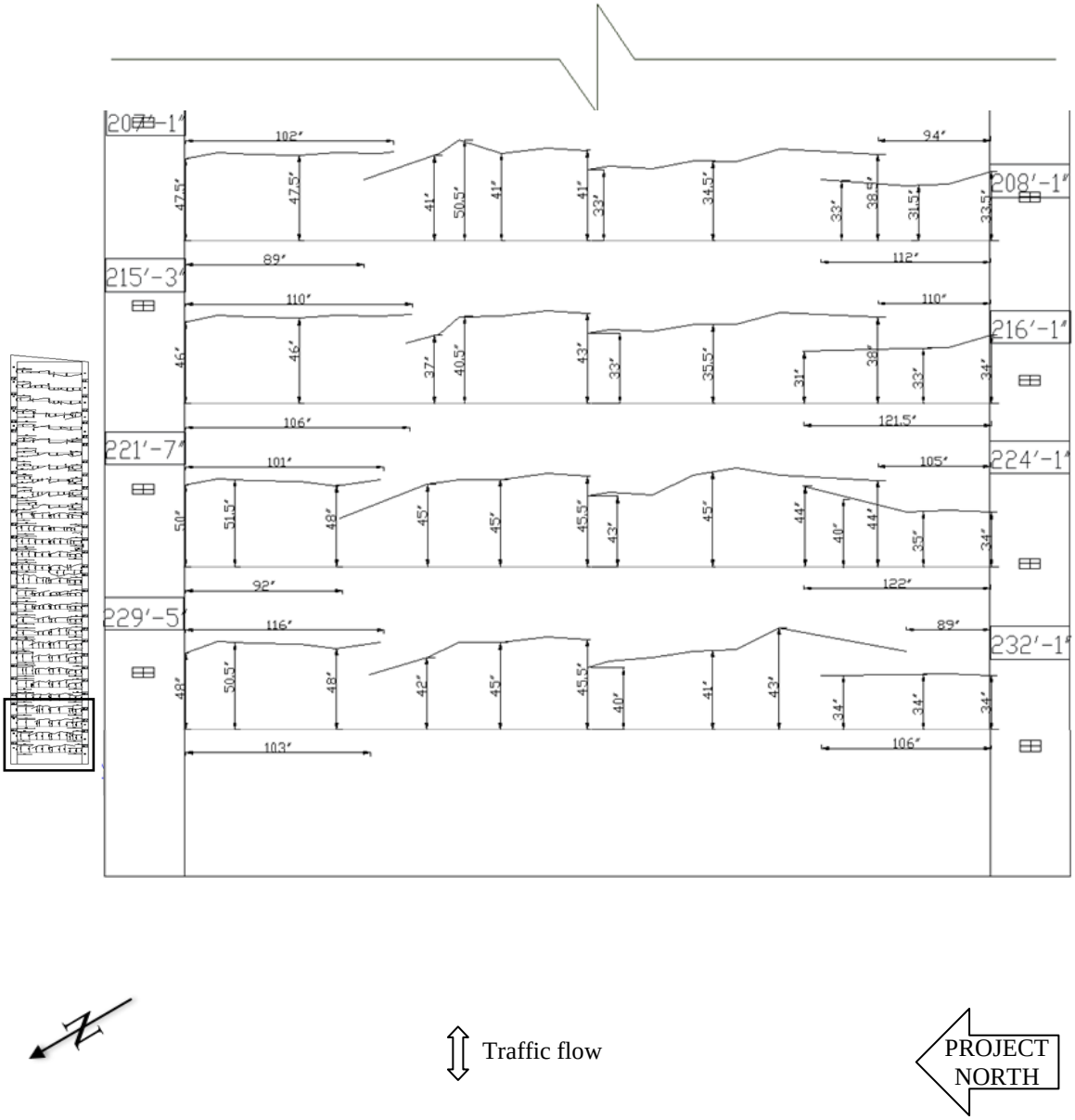

Figure B-3 Photos of Cores Including Lengths and Bottom Type from Bridge A4709

Core C-1: 4.5” long (broken)

Core C-2: 5.5” long (smooth)

Core C-3: 6.125” long (smooth)

Core C-4: 6.125” long (smooth)

Core C-5: 6.5” long (broken)

Core C-6: 6.625” long (broken)

Figure B-3 Photos of Cores Including Lengths and Bottom Type from Bridge A4709 (Cont.)

Core C-7: 6.5” long (smooth)

Core C-8: 6.375” long (smooth)

Core C-9: 7” long (broken)

Core C-10: 7.125” long (broken)

APPENDIX C

EXPERIMENTS

TABLE OF CONTENTS

LIST OF FIGURES

LIST OF TABLES

C.1 INTRODUCTION

This appendix provides information about the experiments discussed in Chapter 5 including mechanical properties of materials used and test specimen construction (Section C.2), test setup (Section C.3), and individual test specimen results (Sections C.4 and C.5).

C.2 TEST SPECIMENS

C.2.1 Specimen Materials

Specified and as-built material properties of the specimens tested in this study are discussed in the following sections. Concrete is discussed in Section C.2.1.1, and reinforcement is discussed in Section C.2.1.2

C.2.1.1 Concrete

The concrete mixtures used in the specimen construction were provided by Coreslab Structures in Marshall, MO. The concrete mixture designs selected for this study were based on Coreslab Structure's standard concrete mixture design that is used to construct precast slab panels provided to MoDOT in accordance with current MoDOT specifications for this type of construction. This concrete mixture is referred to herein as "normal concrete." The aggregates used in the concrete mixture were from aggregates local to the region. The specified compressive strength of the standard concrete mixture at 28 days is 6000 psi.

Variations of the standard concrete mixture were used in this study to examine various test parameters, as explained in Section 5.1. Six different types of concrete were used which include the addition of fibers and varying levels of corrosion inhibitor and NaCl: normal concrete, normal concrete with NaCl, normal concrete with corrosion inhibitor, normal concrete with both NaCl and MCI corrosion inhibitor, normal concrete with fibers, and normal concrete with fibers and NaCl. Fibers were type Master Fiber F 70 (fibrillated micro synthetic fiber) from Master Builders. Corrosion inhibitor was MCI from Cortec Corporation. NaCL solution was provided by Master Builders. The concrete mixture proportions are given in Table C-1.

Ten 4x8 in. cylinders were cast for each different type of concrete to examine the evolution of the concrete compressive strengths. For each type of concrete, compressive strength was tested in uniaxial compression with three 4x8 in. cylinders (unless noted otherwise) seven and 28 days after the concrete was cast, as well as on the day unit panels were tested. Cylinders were capped with sulfur caps prior to testing. Additional cylinders were tested for compressive strength by Coreslab Structures to determine the compressive strength after one day for the purpose of form removal. The compression cylinders were tested in a 600-kip Forney® testing machine in the Civil Engineering Materials Laboratory at Missouri S&T. The loading rate for the compressive strength tests was 565 lb/sec. Flexural beams (6x6x24 in.) were also tested on the same date in the Civil Engineering Materials Laboratory at Missouri S&T. Flexural beams were tested in a 600-kip Forney® at a rate of 30 lbs/sec. All loading rates were within the limits prescribed in ASTM C293 (2008).

Mechanical properties of concrete and the date at which each property was tested are presented in Table C- 2.

C.2.1.2 Reinforcement

Three types of prestressed reinforcement were used in the experiments to examine various test parameters, as explained in Section 5.1. Steel strand was 3/8 in. diameter, 7-wire, Grade 270 low-relaxation conforming to ASTM A 416 (2010). Epoxy-coated strand was 3/8 in. diameter, 7-wire, Grade 270 low-relaxation grit-impregnated conforming to ASTM A 882 (2010). Epoxy-coated strand was type Flo-Bond manufactured by Sumiden Wire Products Corporation. Carbon fiber reinforced polymer (CFRP) tendons were No. 3 reinforcing bar. CFRP tendons were type Aslan 200 manufactured by Hughes Bros.

Other types of reinforcement used in the experiments include reinforcing bars, used as shrinkage and temperature reinforcement, and fibers. Reinforcing bars were No. 3 epoxy-coated reinforcing bar. Fibers were type Master Fiber F 70 (fibrillated micro synthetic fiber) from Master Builders as discussed in Section C.2.1.

All reinforcement of a given type used to construct the test specimens on a given day came from a single producer and from a single heat of material.

Yield and breaking strengths of the steel strand were determined in accordance with ASTM A 370 (2010) with uniaxial tension tests from samples that were from the same heat as the strand used in fabricating the specimens. Tension tests were conducted in a 200 kip 4-pole MTS®880 testing machine under displacement control. The testing machine had a precision of 10 lbs and 0.0001 in. Coupons were tested at a single continuous loading rate of 1,930 lbs/min. Figure C- 1 shows typical load-strain relationships obtained from the tensile coupons for each of the steel strand types used in the specimens. Prestressed reinforcement material properties, including measured and reported by the manufacturer, are shown in Table C- 3. Measured values represent the average of three tensile coupons tested for each strand.

C.2.2 Specimen Construction

Construction of the specimens by a precast concrete manufacturer, including the use of local materials and standard concrete mixtures, was decided so that the specimens tested would be representative of components used in service. This decision was based on feedback from the MoDOT project TAP members.

Two general types of test specimens were used in the experiments in this study: corrosion specimens and unit panel specimens. The test specimens were constructed at Coreslab Structures precast concrete plant in Marshall, MO on two separate dates. All of the corrosion specimens and four of the unit panels were cast on December 29, 2009. The remaining eight unit panels were cast on March 12, 2010. All specimens were transported to the High Bay Structures Laboratory at Missouri S&T within seven days of casting, where they were stored until they were tested. Specimens were stored in conditioned space. Construction of the unit panel specimens is described in Section C.2.2.1, and construction of the durability specimens is described in Section C.2.2.2.

C.2.2.1 Unit Panel Specimens

Twelve unit panels of six types were constructed comprised of the following prestressed reinforcement types (2 panels each): steel strand with normal concrete, steel strand with normal

concrete and fibers, steel and epoxy-coated steel strand with normal concrete, steel and epoxy-coated steel strand with normal concrete and fibers, steel strand and CFRP bars with normal concrete, steel strand and CFRP bars with normal concrete and fibers. The rational for the different panel types is explained in Section 5.2.1.

Four unit panel specimens were cast at Coreslab Structures in Marshall, MO on December 29, 2009 along with the corrosion specimens (see Section C.3.1). The first four unit panels consisted of panels with steel strand only. The remaining eight unit panel specimens were cast together at the same facility on March 12, 2010. The remaining eight panels included epoxy-coated steel strand and CFRP tendons. Figure C-5 shows the prestressed reinforcement in the casting bed prior to concrete placement.

Tendons were prestressed in the prestressing beds prior to the application of strain gages. This was in an attempt to ensure the bond between the strain gage and tendon would remain intact during the fabrication process. All strain gages were installed the day prior to casting the specimens. Figure C-6 shows the strain gages applied to the prestressed reinforcement. Strain gage types and locations are discussed in Section C.3.1.1.

Prestressing steel strands were pretensioned to achieve jacking force of 17.2 kips. The force in the tendon was measured with the jack, and the measured elongation was compared to the theoretical elongation. Standard prestressing anchorages were used for the uncoated and epoxy-coated prestressing strand. For the epoxy-coated strand, the epoxy was removed before anchoring the strand. For the CFRP tendons, a specialized splice system designed by Hughes Bros. was used to splice the two CFRP tendons to a single 0.6 in. diameter strand on the one end, and to two epoxy-coated strands on the other end. Figure C-7 shows the splice system anchorage system and set-up.

The formwork was blown out with an air compressor immediately before casting the concrete. Care was taken not to disturb the integrity of the strain gages during concrete placement. Concrete was batched on site at the Coreslab Structures precast plant and was placed and consolidated using normal procedures. Concrete was moist-cured using wet burlap applied to the top surface of each specimen. For both cast dates, four project representatives were present at the precast plant to observe the concrete placement.

C.2.2.2 Durability Specimens

Durability specimens were constructed at Coreslab structures in Marshall, MO on December 29, 2009. Two types of corrosion specimens were constructed, non-prestressed corrosion specimens and prestressed corrosion specimens, as explained in Section 5.3.2.

Custom new wood formwork was designed and constructed by Coreslab Structures to form the non-prestressed corrosions specimens. The reinforcement was placed within the specimen forms and supported with plastic-tipped steel chairs. Prior to placing the reinforcement, the weight of the reinforcement was measured to facilitate the gravimetric study based on the loss of steel weight due to corrosion. Figure C-3 shows the formwork and reinforcement prior to casting.The prestressed corrosion specimens were constructed in the same casting bed used for the casting of full-size unit panels by adding block-outs to achieve the dimensions required. Figure C-4 shows

the formwork prior to casting. Prestressing steel strands were pretensioned to achieve jacking force of 17.2 kips. The force in the tendon was measured with the jack, and the measured elongation was compared to the theoretical elongation. Standard prestressing anchorages were used for the uncoated and epoxy-coated prestressing strand.

The formwork was blown out with an air compressor immediately before casting the concrete. Concrete was batched on site at the Coreslab Structures precast plant and was placed and consolidated using normal procedures. Concrete was moist-cured using wet burlap applied to the top surface of each specimen. Four project representatives were present at the precast plant to observe the concrete placement.

C.3 TEST SETUP

C.3.1 Unit Panel Specimens

C.3.1.1 Instrumentation

C.3.1.1.1 Strain Gages

Uniaxial electrical resistance strain gages (Vishay Micro-Measurements Type EA-06-125BT-120/LE) were attached to the tendons at locations selected to study the variation of longitudinal tensile strains along the length of the reinforcement. Tendons were pretentioned prior to gage installation. Uniaxial electrical resistance strain gages (Tokyo Sokki Kenkyujo Co., Ltd. TML Type PL-60-11) were attached to the top and bottom surface of the concrete to study the longitudinal strain in the extreme tension and compression fibers. Concrete surface strain gage locations were selected such that they would correspond to locations where tendon strain gages were located to study the strain distribution at that section. Because the unit panel specimens were pretensioned, precompression strain was not accounted for in concrete surface gage measurements. Locations of all strain gages are shown in Figure C-8. All strain gages were installed per the manufacturer's recommendations.

C.3.2 Durability Specimens

C.3.2.1 Corrosion initiation specimens

Figure C-110 shows the dimensions and specimen numbers for the 27 specimens included in the corrosion initiation test. The test specimens were subjected to wet/dry cycles during a test period of six months. Two main measurements were conducted at different time intervals. The half-cell potential test was performed according to ASTM C876 (1991) every two weeks during the test period using a Canin Corrosion Analyzing Instrument manufactured by Proceq. Figure C-111 shows a typical half-cell potential measurement. In addition, visual inspection was also conducted every two weeks together with half-cell potential test to observe the deterioration levels of concrete. The chloride content test was performed every two months. Two month testing was performed by MoDOT. Four and six month testing was performed by Missouri S&T according to ASTM C1218 (1999) using the Rapid Chloride Test (RCT) instrument. Finally, a gravimetric study was conducted according to ASTM G1-03 after six months. Cleaning, preparing, and evaluating of corrosion specimens followed this recommendation. Based on ASTM G1-03, rust on the corroded steel tendons was removed by scrubbing with a nonmetallic bristle brush. Cleaned steel tendons were placed into a muriatic acid solution for further cleaning

as shown in Figure C-112. The weights of steel tendons were measured before concrete casting and after testing.

C.3.2.1 Accelerated corrosion specimens
Figure C-113 shows the dimensions and specimen numbers for the 18 specimens included in the accelerated corrosion test. The specimens were subjected to 0.4 mA electrical current for six months. Weekly visual inspection was conducted to observe and record deterioration during the test period. A gravimetric study was also performed to measure the steel loss due to the accelerated corrosion process. Steel tendon losses were used to estimate the corrosion rate.

C.4 UNIT PANEL EXPERIMENT RESULTS

The experimental results and behavior of each unit panel specimen are described in the sections that follow. Specimens subjected to monotonic static loading are presented in Sections C.4.1 through C.4.6. Specimens subjected to fatigue loading are presented in Sections C.4.7 through C.4.11.

C.4.1 Panel ST-NC-SL

C.4.1.1 Failure and Cracking Behavior
Panel ST-NC-SL was tested to failure on 3/05/10, 65 days after the concrete was cast. Flexural cracks first developed on the extreme tension face, which increased in length and number with increasing applied load. Cracks were first observed on the side face at an applied load of 16.94 kips and displacement of 0.8 inch. The initial cracks started to appear at locations near the edge of the spreader beam location. As the applied displacement (and corresponding applied load) was increased, additional flexural cracks appeared and existing cracks propagated upward. The panel failed by concrete crushing as the failure crack penetrated the flexural compression zone completely at the location of the spreader beam. As a result of the loss of load carrying capacity associated with the destruction of the flexural compression zone, the applied load dropped to 16.94 kips. The maximum load and corresponding displacement were 22.08 kips and 2.14 in., respectively. Upon attempt to maintain and increase the load level, further deformation was imposed on the specimen. Thus the failure load for Panel ST-NC-SL corresponds to an applied load of 22.08 kips. Figure C-9 shows the post-failure state of the panel after the spreader beam was removed.

C.4.1.2 Load-displacement
Figure C- 10 shows the measured displacement along the length the panel length at Grids E, E', and F for various load levels, including cracking and maximum loads (13.92 kips and 22.08 kips, respectively). The cracking load was determined based on the change in behavior in the load displacement relationship from Figure C- 11, as well as the change in load-strain relationship discussed in Section C.4.1.3. Note that the cracking load determined in this manner is slightly lower than the load corresponding to when flexural cracks were first observed as discussed in Section C.4.1.1. Displacements measured at Grids E, E', and F are similar (within 4%) at each load level with the exception of the failure load, where the displacement measured at Grid E was slightly higher (5%) than Grids E' and F. Figure C- 11 shows the applied load-displacement response for all locations.

Figure C-12 shows the measured displacements along width of panel at Grids 1, 2, and 3. At each load level, displacements measured at different locations along the width of the panel were similar (within 10%), which indicates that the load applied by the actuator was uniformly distributed along width at the panel midspan by the spreader beam.

C.4.1.3 Load-strain

Figure C-13 shows the applied load-tendon strain relationship. Note that the relationship shown does not account for the effects of precompression (ref. Section C.3.1.1.1). In the figure, compression strain is shown as negative while tension strain is shown as positive. Tendon strains measured at all locations are negligible for applied load less than 13.92 kips. For applied load greater than 13.92 kips tensile strains measured in the tendons along midspan (-2 locations in the figure) increase linearly with increasing applied load, indicated that the neutral axis is shifting upwards and that the section has cracked. At quarter span (1- and -3 locations in the figure), the tendon strains are almost zero during the entire test. This change in behavior at this load level is consistent with the change in behavior of the load-displacement relationship described in Section C.4.1.2.

Figure C-14 shows the applied load-concrete surface strain relationship. Note that the relationship shown does not account for the effects of precompression (ref. Section C.3.1.1.1). (Also note that gage E-B-3 was not working and was not plotted in the figure.) The load-strain relationship for the concrete surface at midspan (-2 locations in Figure C-14) has a bilinear behavior, with a greater slope when the applied load is less than the cracking load and a lesser slope when load is greater than the cracking load. At quarter span (-1 and -3 locations), the the surface strains increase linearly until the maximum load is achieved. Concrete surface gages along Grid 2 on the bottom surface of the panel stopped working after flexural cracks occurred at the gage location; thus measured strain in these locations is reported only until the respective gage stopped working.

The strain distribution within the section at various locations is shown in Figure C-15. Note that the relationship shown does not account for the effects of precompression (ref. Section C.3.1.1.1). For each location, Figure C-15 shows strains measured on the top and bottom concrete surfaces and the corresponding strain measured in the tendon at different load levels, including cracking and failure loads (13.92 kips and 22.08 kips, respectively). Concrete surface gages along Grid 2 on the bottom surface of the panel stopped working after flexural cracks occurred at the gage location; thus, measured strain in these locations is reported only until the respective gage stopped working.

C.4.2 Panel ST-FRC-SL

C.4.2.1 Failure and Cracking Behavior

Panel ST-FRC-SL was tested to failure on 3/19/10, 79 days after the concrete was cast. Flexural cracks first developed on the extreme tension face, which increased in length and number with increasing applied load. Cracks were first observed on the side face at an applied load of 17.07 kips and displacement of 0.8 in. The initial cracks started to appear at locations near the edge of the spreader beam location. As the applied load was increased, additional flexural cracks

appeared and existing cracks propagated upward. Failure occurred as the failure crack penetrated the flexural compression zone completely at the location of the spreader beam. As a result of the loss of load carrying capacity associated with the destruction of the flexural compression zone, the applied load dropped to 9.64 kips. Upon attempt to maintain and increase the load level, further deformation was imposed on the specimen. The maximum load of 20.25 kips was not able to be recovered; thus the failure load for Panel ST-FRC-SL corresponds to an applied load of 20.25 kips with a corresponding displacement of 1.65 in. Figure C-16 shows the post-failure state of the panel after the spreader beam was removed. The failure crack was located near the east side of the spreader beam on the top surface of the panel and extended the entire width of the panel.

During the test, cracks were marked on the side faces of the panel at discrete load increments until the failure load was achieved. Figure C-17shows the progression of cracking from an applied load of 17.07 kips (shortly after first observed flexural cracking occurred) to the maximum load of 20.25 kips.

C.4.2.2 Load-displacement

Figure C-18 shows the measured displacement along the length the panel length at Grids E, E', and F for various load levels, including cracking and maximum loads (13.79 kips and 20.25 kips, respectively). The cracking load was determined based on the change in behavior in the load displacement relationship from Figure C-18, as well as the change in load-strain relationship discussed in Section C.4.2.3. Note that the cracking load determined in this manner is slightly lower than the load corresponding to when flexural cracks were first observed as discussed in Section C.4.2. Displacements measured at Grids E, E', and F are similar (within 5%) at each load level. Figure C-19 shows the applied load-displacement response for all locations.

Figure C-20 shows the measured displacements along width of panel at Grids 1, 2, and 3. At each load level, displacements measured at different locations along the width of the panel were similar (within 10%), which indicates that the load applied by the actuator was uniformly distributed along width at the panel midspan by the spreader beam.

C.4.2.3 Load-strain

Figure C-21 shows the applied load-tendon strain relationship. Note that the relationship shown does not account for the effects of precompression (ref. Section C.3.1.1.1). In the figure, compression strain is shown as negative while tension strain is shown as positive. Tendon strains measured at all locations are negligible for applied load less than 13.79 kips. For applied load greater than 13.79 kips tensile strains measured in the tendons along Grid 2 increase linearly with increasing applied load, indicated that the neutral axis is shifting upwards and that the section has cracked. This change in behavior at this load level is consistent with the change in behavior of the load-displacement relationship described in Section C.4.2.2.

Figure C-22 shows the applied load-concrete surface strain relationship. Note that the relationship shown does not account for the effects of precompression (ref. Section C.3.1.1.1). (Also note that gage A-T-3 was not working and was not plotted in the figure.) Concrete surface gages along Grid 2 on the bottom surface of the panel stopped working after flexural cracks

occurred at the gage location; thus measured strain in these locations is reported only until the respective gage stopped working.

The strain distribution within the section at various locations is shown in Figure C-23. Note that the relationship shown does not account for the effects of precompression (ref. Section C.3.1.1.1). For each location, Figure C-23 shows strains measured on the top and bottom concrete surfaces and the corresponding strain measured in the tendon at different load levels, including cracking and failure loads (13.79 kips and 20.25 kips, respectively). Concrete surface gages along Grid 2 on the bottom surface of the panel stopped working after flexural cracks occurred at the gage location; thus, measured strain in these locations is reported only until the respective gage stopped working.

C.4.3 Panel ECST-NC-SL

C.4.3.1 Failure and Cracking Behavior

Panel ECST-NC-SL was tested to failure on 4/08/10, 28 days after the concrete was cast. Flexural cracks first developed on the extreme tension face, which increased in length and number with increasing applied load. Cracks were first observed on the side face at an applied load of 17.00 kips and displacement of 0.7 in. The initial cracks started to appear at locations near the edge of the spreader beam location. As the applied displacement (and corresponding applied load) was increased, additional flexural cracks appeared and existing cracks propagated upward. Additional longitudinal splitting cracks were evident on the panel side surfaces as shown in Figure C-24. Failure occurred as the failure crack penetrated the flexural compression zone completely at the location of the spreader beam. As a result of the loss of load carrying capacity associated with the destruction of the flexural compression zone, the applied load dropped to 8.2 kips. Upon attempt to maintain and increase the load level, further deformation was imposed on the specimen. The deformation of the panel increased, but the maximum load of 18.50 kips was not able to be recovered; thus the failure load for Panel ECST-NC-SL corresponds to an applied load of 18.50 kips with a corresponding displacement of 1.05 in. Figure C-24 shows the post-failure state of the panel after the spreader beam was removed.

During the test, cracks were marked on the side faces of the panel at discrete load increments until the failure load was achieved. Figure C-25 shows the progression of cracking from an applied load of 17.00 kips (shortly after first observed flexural cracking occurred) to the maximum load of 18.50 kips.

C.4.3.2 Load-displacement

Figure C-26 shows the measured displacement along the length the panel length at Grids E, E', and F for various load levels, including cracking and maximum loads (14.19 kips and 18.49 kips, respectively). The cracking load was determined based on the change in behavior in the load displacement relationship from Figure C-26, as well as the change in load-strain relationship discussed in Section C.4.3.3. Note that the cracking load determined in this manner is slightly lower than the load corresponding to when flexural cracks were first observed as discussed in Section C.4.3.1. Displacements measured at Grids E, E', and F are similar (within 5%) at each load level. Figure C-27 shows the applied load-displacement response for all locations.

Figure C-28 shows the measured displacements along width of panel at Grids 1, 2, and 3. At each load level, displacements measured at different locations along the width of the panel at Grids 2 and 3 were similar (within 10%), which indicates that the load applied by the actuator was uniformly distributed along width at the panel midspan by the spreader beam. At Grid 1, the displacement measured at Grid F larger than at Grid E by 17% at the maximum load.

C.4.3.3 Load-strain

Figure C-29 shows the applied load-tendon strain relationship. Note that the relationship shown does not account for the effects of precompression (ref. Section C.3.1.1.1). In the figure, compression strain is shown as negative while tension strain is shown as positive. Tendon strains measured at all locations are negligible for applied load less than 14.19 kips. For applied load greater than 14.19 kips tensile strains measured in the tendons along Grid 2 increase linearly with increasing applied load, indicated that the neutral axis is shifting upwards and that the section has cracked. This change in behavior at this load level is consistent with the change in behavior of the load-displacement relationship described in Section C.4.3.2.

Figure C-30 shows the applied load-concrete surface strain relationship. Note that the relationship shown does not account for the effects of precompression (ref. Section C.3.1.1.1). Concrete surface gage A-B-2 along Grid 2 on the bottom surface of the panel stopped working after flexural cracks occurred at the gage location; thus measured strain in this location is reported only until the respective gage stopped working.

The strain distribution within the section at various locations is shown in Figure C-31. Note that the relationship shown does not account for the effects of precompression (ref. Section C.3.1.1.1). For each location, Figure C-31 shows strains measured on the top and bottom concrete surfaces and the corresponding strain measured in the tendon at different load levels, including cracking and failure loads (14.19 kips and 18.49 kips, respectively). Concrete surface gage A-B-2 along Grid 2 on the bottom surface of the panel stopped working after flexural cracks occurred at the gage location; thus measured strain in this location is reported only until the respective gage stopped working.

C.4.4 Panel ECST-FRC-SL

C.4.4.1 Failure and Cracking Behavior

Panel ECST-FRC-SL was tested to failure on 4/12/10, 32 days after the concrete was cast. Flexural cracks first developed on the extreme tension face, which increased in length and number with increasing applied load. Cracks were first observed on the side face at an applied load of 15.80 kips and applied displacement of 0.5 in. The initial cracks started to appear at locations near the edge of the spreader beam location. As the applied displacement (and corresponding applied load) was increased, additional flexural cracks appeared and existing cracks propagated upward. Failure occurred as the failure crack penetrated the flexural compression zone completely at the location of the spreader beam. As a result of the loss of load carrying capacity associated with the destruction of the flexural compression zone, the applied load dropped to 16.70 kips. Upon attempt to maintain and increase the load level, further deformation was imposed on the specimen. The maximum load of 21.20 kips was not able to be recovered; thus the failure load for Panel ECST-FRC-SL corresponds to an applied load of 21.20

kips with a corresponding displacement of 1.70 in Figure C-32 shows the post-failure state of the panel after the spreader beam was removed.

During the test, cracks were marked on the side faces of the panel at discrete load increments until the failure load was achieved. Figure C-33 shows the progression of cracking from an applied load of 15.80 kips (shortly after first observed flexural cracking occurred) to the maximum load of 20.20 kips.

C.4.4.2 Load-displacement

Figure C-34 shows the measured displacement along the length the panel length at Grids E, E', and F for various load levels, including cracking and maximum loads (14.25 kips and 21.20 kips, respectively). The cracking load was determined based on the change in behavior in the load displacement relationship from Figure C-34 as well as the change in load-strain relationship discussed in Section C4.4.3. Note that the cracking load determined in this manner is slightly lower than the load corresponding to when flexural cracks were first observed as discussed in Section C.4.4.1. Displacements measured at Grids E, E', and F are similar (within 5%) at each load level with the exception of the failure load, where the displacement measured at Grid E was slightly higher (10%) than Grids E' and F. Figure C-35 shows the applied load-displacement response for all locations.

Figure C-36 shows the measured displacements along width of panel at Grids 1, 2, and 3. For each load level, displacements measured at different locations along the width of the panel were similar (within 12%), which indicates that the load applied by the actuator was uniformly distributed along width at the panel midspan by the spreader beam.

C.4.4.3 Load-strain

Figure C-37 shows the applied load-tendon strain relationship. Note that the relationship shown does not account for the effects of precompression (ref. Section C.3.1.1.1). (Also note that gages A-2, E-2, and F-3 were not working and were not plotted in the figure.) In the figure, compression strain is shown as negative while tension strain is shown as positive. Tendon strains measured at all locations are negligible for applied load less than 14.25 kips. For applied load greater than 14.25 kips tensile strains measured in the tendons along Grid 2 increase linearly with increasing applied load, indicated that the neutral axis is shifting upwards and that the section has cracked. This change in behavior at this load level is consistent with the change in behavior of the load-displacement relationship described in Section C.4.4.2.

Figure C-38 shows the applied load-concrete surface strain relationship. Note that the relationship shown does not account for the effects of precompression (ref. Section C.3.1.1.1). Concrete surface gages along Grid 2 on the bottom surface of the panel stopped working after flexural cracks occurred at the gage location; thus, measured strain in these locations is reported only until the respective gage stopped working.

The strain distribution within the section at various locations is shown in Figure C-39. Note that the relationship shown does not account for the effects of precompression (ref. Section C.3.1.1.1). For each location, Figure C-39 shows strains measured on the top and bottom concrete surfaces and the corresponding strain measured in the tendon at different load levels,

including cracking and failure loads (14.25 kips and 21.20 kips, respectively). Concrete surface gages along Grid 2 on the bottom surface of the panel stopped working after flexural cracks occurred at the gage location; thus measured strain in these locations is reported only until the respective gage stopped working.

C.4.5 Panel CFRPT-NC-SL

C.4.5.1 Failure and Cracking Behavior

Panel CFRPT-NC-SL was tested to failure on 4/13/10, 33 days after the concrete was cast. Cracks were first observed on the side face at an applied load of 18.8 kips. The initial cracks started to appear at locations near the edge of the spreader beam location. As the applied displacement (and corresponding applied load) was increased, additional flexural cracks appeared and existing cracks propagated upward. Failure occurred as the failure crack penetrated the flexural compression zone completely at the location of the spreader beam. As a result of the loss of load carrying capacity associated with the destruction of the flexural compression zone, the applied load gradually dropped to 15.9 kips. Upon attempt to maintain and increase the load level, further deformation was imposed on the specimen. The maximum load of 21.15 kips was not able to be recovered; thus the failure load for Panel CFRPT-NC-SL corresponds to an applied load of 21.15 kips with a corresponding displacement of 1.38 in. Figure C-40 shows the post-failure state of the panel after the spreader beam was removed.

During the test, cracks were marked on the side faces of the panel at discrete load increments until the failure load was achieved. Figure C-41 shows the progression of cracking from an applied load of 18.45 kips (shortly after first observed flexural cracking occurred) to the maximum load of 21.05 kips.

C.4.5.2 Load-displacement

Figure C-42 shows the measured displacement along the length the panel length at Grids E, E', and F for various load levels, including cracking and maximum loads (14.99 kips and 21.05 kips, respectively). The cracking load was determined based on the change in behavior in the load displacement relationship from Figure C-42, as well as the change in load-strain relationship discussed in Section C.4.5.3. Note that the cracking load determined in this manner is slightly lower than the load corresponding to when flexural cracks were first observed as discussed in Section C.4.5.1. Displacements measured at Grids E, E', and F are similar (within 5%) at each load level. Figure C-43 shows the applied load-displacement response for all locations.

Figure C-44 shows the measured displacements along width of panel at Grids 1, 2, and 3. For each load level, displacements measured at different locations along the width of the panel were similar (within 5%), which indicates that the load applied by the actuator was uniformly distributed along width at the panel midspan by the spreader beam.

C.4.5.3 Load-strain

Figure C-45 shows the applied load-tendon strain relationship. Note that the relationship shown does not account for the effects of precompression (ref. Section C.3.1.1.1). (Also note that gages A-3, B-2, C-3, D-2, E-1, and E-3 were not working and were not plotted in the figure.) In the figure, compression strain is shown as negative while tension strain is shown as positive. Tendon

strains measured at all locations are negligible for applied load less than 14.99 kips. For applied load greater than 14.99 kips, tensile strains measured in the tendons along Grid 2 increase linearly with increasing applied load, indicated that the neutral axis is shifting upwards and that the section has cracked. This change in behavior at this load level is consistent with the change in behavior of the load-displacement relationship described in Section C.4.5.2.

Figure C-46 shows the applied load-concrete surface strain relationship. Note that the relationship shown does not account for the effects of precompression (ref. Section C.3.1.1.1). Concrete surface gages along Grid 2 on the bottom surface of the panel stopped working after flexural cracks occurred at the gage location; thus measured strain in these locations is reported only until the respective gage stopped working.

The strain distribution within the section at various locations is shown in Figure C-47. Note that the relationship shown does not account for the effects of precompression (ref. Section C.3.1.1.1). For each location, Figure C-47 shows strains measured on the top and bottom concrete surfaces and the corresponding strain measured in the tendon at different load levels, including cracking and failure loads (14.99 kips and 21.05 kips, respectively). Concrete surface gages along Grid 2 on the bottom surface of the panel stopped working after flexural cracks occurred at the gage location; thus measured strain in these locations is reported only until the respective gage stopped working.

C.4.6 Panel CFRPT-FRC-SL

C.4.6.1 Failure and Cracking Behavior

Panel CFRPT-FRC-SL was tested to failure on 4/19/10, 39 days after the concrete was cast. Cracks were first observed on the side face at an applied load of 16.72 kips and displacement of 0.7 in. The initial cracks started to appear at locations near the edge of the spreader beam location. As the applied displacement (and corresponding applied load) was increased, additional flexural cracks appeared and existing cracks propagated upward. Failure occurred as the failure crack penetrated the flexural compression zone completely at the location of the spreader beam. As a result of the loss of load carrying capacity associated with the destruction of the flexural compression zone, the applied load dropped to 17.3 kips. Upon attempt to maintain and increase the load level, further deformation was imposed on the specimen. The maximum load of 20.70 kips was not able to be recovered; thus the failure load for Panel CFRPT-FRC-SL corresponds to an applied load of 20.70 kips and corresponding displacement of 1.75 in. Figure C-48 shows the post-failure state of the panel after the spreader beam was removed.

During the test, cracks were marked on the side faces of the panel at discrete load increments until the failure load was achieved. Figure C-49 shows the progression of cracking from an applied load of 16.72 kips (shortly after first observed flexural cracking occurred) to the maximum load of 20.70 kips.

C.4.6.2 Load-displacement

Figure C-50 shows the measured displacement along the length the panel length at Grids E, E', and F for various load levels, including cracking and maximum loads (14.06 kips and 20.70 kips, respectively). The cracking load was determined based on the change in behavior in the load

displacement relationship from Figure C-50, as well as the change in load-strain relationship discussed in Section C.4.6.3. Note that the cracking load determined in this manner is slightly lower than the load corresponding to when flexural cracks were first observed as discussed in Section C.4.6.1. Displacements measured at Grids E, E', and F are similar (within 5%) at each load level. Figure C-51 shows the applied load-displacement response for all locations.

Figure C-52 shows the measured displacements along width of panel at Grids 1, 2, and 3. At each load level, displacements measured at different locations along the width of the panel were similar (within 5%), which indicates that the load applied by the actuator was uniformly distributed along width at the panel midspan by the spreader beam.

C.4.6.3 Load-strain

Figure C-53 shows the applied load-tendon strain relationship. Note that the relationship shown does not account for the effects of precompression (ref. Section C.3.1.1.1). (Also note that gage E-2 was not working and was not plotted in the figure.) In the figure, compression strain is shown as negative while tension strain is shown as positive. Tendon strains measured at all locations are negligible for applied load less than 14.06 kips. For applied load greater than 14.06 kips, tensile strains measured in the tendons along Grid 2 increase linearly with increasing applied load, indicated that the neutral axis is shifting upwards and that the section has cracked. This change in behavior at this load level is consistent with the change in behavior of the load-displacement relationship described in Section C.4.6.2.

Figure C-54 shows the applied load-concrete surface strain relationship. Note that the relationship shown does not account for the effects of precompression (ref. Section C.3.1.1.1). Concrete surface gages along Grid 2 on the bottom surface of the panel stopped working after flexural cracks occurred at the gage location; thus measured strain in these locations is reported only until the respective gage stopped working.

The strain distribution within the section at various locations is shown in Figure C-55. Note that the relationship shown does not account for the effects of precompression (ref. Section C.3.1.1.1). For each location, Figure C-55 shows strains measured on the top and bottom concrete surfaces and the corresponding strain measured in the tendon at different load levels, including cracking and failure loads (14.06 kips and 20.70 kips, respectively). Concrete surface gages along Grid 2 on the bottom surface of the panel stopped working after flexural cracks occurred at the gage location; thus measured strain in these locations is reported only until the respective gage stopped working.

C.4.7 Panel ST-NC-FL

C.4.7.1 Failure and Cracking Behavior

Panel ST-NC-FL was tested under fatigue loading during the period between 5/26/10 and 6/14/10. The panel was subjected to two million cycles with the loading protocol described in Section 5.2.3.3. The panel was subjected to post-fatigue quasi-static load test until failure on 6/14/10, 148 days after the concrete was cast. No flexural cracks were observed during the cyclic loading process since the loading was within elastic range. In the post-fatigue static load test, flexural cracks first developed on the extreme tension face, which increased in length and

numbers with increasing applied load. Cracks were first observed on the side face at an applied load of 18.77 kips and displacement of 1 in. The initial cracks started to appear at locations near the edge of the spreader beam location. As the applied load was increased, additional flexural cracks appeared and existing cracks propagated upward. At the final load stage the panel failed by concrete crushing. Failure occurred as the crack penetrated the flexural compression zone completely at the location of the spreader beam. As a result of the loss of load carrying capacity associated with the destruction of the flexural compression zone, the applied load dropped to 18.33 kips. The maximum load and corresponding displacement was 22.10 kips and 1.76 in., respectively. Upon attempt to regain the load level, further deformation was imposed on the specimen. The maximum load of 22.1 kips was not able to be recovered; thus the failure load for Panel ST-NC-FL corresponds to an applied load of 22.1 kips. Figure C-56 shows the post-failure state of the panel after the spreader beam was removed.

During the test, cracks were marked on the side faces of the panel at discrete load increments until the failure load was achieved. Figure C-57 shows the progression of cracking from an applied load of 18.77 kips (shortly after first observed flexural cracking occurred) to the maximum load of 22.1 kips.

C.4.7.2 Load-displacement

The stiffness degradation of the panel was studied by performing a quasi-static load test up to 0.25 inch after each 500,000 cycles. Panel ST-NC-FL was not subjected to the first two quasi-static load tests (0 cycles and 500,000 cycles). Figure C-58 shows the results of the quasi-static load tests at 1,000,000, 1,500,000, and 2,000,000 cycles at all locations. In Figure C-58, the stiffness degradation was observed to have the same rate in the cycles between 1,000,000 and 1,500,000 and in the cycles between 1,500,000 and 2,000,000. In addition, the stiffness degradation can be observed by the decreased maximum displacement, which affects the overall ductility. Figure C-59 shows the measured displacement along the panel length at Grids E, E', and F for various load levels, including cracking and maximum loads (13.98 kips and 22.1 kips, respectively). As discussed in the static load test results sections, the cracking load was determined based on the change in behavior of the load-displacement relationship from Figure C-59 as well as the change in load-strain relationship discussed in Section C.4.1.3. Note that the cracking load determined in this manner is lower than the load corresponding to when side cracks were first observed as discussed in Section C.4.1.1. Displacements measured at Grids E, E', and F are similar (within 3%) at each load level with the exception of the failure load. Figure C-60 shows the applied load-displacement response for all locations.

C.4.7.3 Load-strain

Figure C-61 shows the applied load-tendon strain relationship. In the figure, compression strain is shown as negative while tension strain is shown as positive. Tendon strains measured at all locations are negligible for applied load less than 13.98 kips. For applied load greater than 13.98 kips, tendon strains measured along Grid 2 increased linearly with increasing applied load, indicating that the neutral axis is shifting upwards and that the section has cracked. This change in behavior at this load level is consistent with the change in behavior of the load-displacement relationship described in Section C.4.7.2.

Figure C-62 shows the applied load-concrete surface strain relationship. Concrete surface gages along Grid 2 on the bottom surface of the panel stopped working after flexural cracks occurred at the gage location; thus measured strain in this location is reported only until the respective gage stopped working.

The strain distribution within the section at various locations is shown in Figure C-63. For each location, Figure C-63 shows strains measured on the top and bottom concrete surfaces and the corresponding strain measured in the tendon at different load levels, including cracking and failure loads (13.98 kips and 22.1 kips, respectively). Concrete surface gages along Grid 2 on the bottom surface of the panel stopped working after flexural cracks occurred at the gage location; thus measured strain in this location is reported only until the respective gage stopped working.

Figure C-64 shows the strain distribution within the section at various locations. For each location, Figure C-64 shows strains measured on the top and bottom concrete surfaces and the corresponding strain measured in the tendon at the maximum load for different number of cycles. The maximum load ranged between 8 kips and 12 kips. The measured strains in all locations are reported only for the working gages at the maximum load level.

C.4.8 Panel ST-FRC-FL

C.4.8.1 Failure and Cracking Behavior

Panel ST-FRC-FL was tested under fatigue loading during the period between 7/8/10 and 7/15/10. The panel was subjected to two million cycles with the loading protocol described in Section 5.2.3.3. The panel was subjected to a post-fatigue quasi-static load test until failure immediately after two million load cycles. The static load test was conducted on 7/16/10, 190 days after the concrete was cast. No flexural cracks were observed during the cyclic loading process since the loading was within elastic range. In the post fatigue static load test, flexural cracks first developed on the extreme tension face, which increased in length and number with increasing applied load. Cracks were first observed on the side face at an applied load of 15.33 kips and displacement of 0.45 in. The initial cracks started to appear at locations near the edge of the spreader beam location. As the applied load was increased, additional flexural cracks appeared and existing cracks propagated upward. As observed in the static load test, at the final load stage the panel failed by concrete crushing by means failure occurred as the crack penetrated the flexural compression zone completely at the location of the spreader beam. As a result of the loss of load carrying capacity associated with the destruction of the flexural compression zone, the applied load dropped to 17.18 kips. The maximum load and corresponding displacement was 20.7 kips and 1.63 in., respectively. Upon attempt to maintain and increase the load level, further deformation was imposed on the specimen. The maximum load of 20.7 kips was not able to be recovered; thus the failure load for Panel ST-FRC-FL corresponds to an applied load of 20.7 kips. Figure C-65 shows the post-failure state of the panel after the spreader beam was removed.

During the post fatigue static load test, cracks were marked on the side faces of the panel at discrete load increments until the failure load was achieved. Figure C-66 shows the progression

of cracking from an applied load of 15.33 kips (shortly after first observed flexural cracking occurred) to the maximum load of 20.7 kips.

C.4.8.2 Load-displacement

The stiffness degradation of the panel was studied by performing a quasi-static load test up to 0.25 inch after each 500,000 cycles. Panel ST-FRC-FL was subjected to a total of five quasi-static load tests before the cyclic loading began and after each 500,000 cycles (0, 500,000, 1,000,000, 1,500,000, and 2,000,000 cycles). Figure C-67 shows the applied load and displacement relationships for the quasi-static load tests at all locations. The figure shows major stiffness degradation in the cycles between 0 and 500,000 and the cycles between 1,500,000 and 2,000,000 cycles. At the final load stage, the stiffness degradation was observed by the decreased maximum displacement, which affects the overall ductility. Figure C-68 shows the measured displacement along the panel length at Grids E, E', and F for various load levels, including cracking and maximum loads (14 kips and 20.7 kips, respectively). As discussed in the static load test section, the cracking load was determined based on the change in behavior of the load-displacement relationship from Figure C-68 as well as the change in load-strain relationship discussed in Section C.4.8.3. Note that the cracking load determined in this manner is slightly lower than the load corresponding to when flexural cracks were first observed as discussed in Section C.4.8.1. Displacements measured at Grids E, E', and F are similar (within 3.5%) at each load level with the exception of the failure load. Figure C-69 shows the applied load-displacement response for all locations.

C.4.8.3 Load-strain

Figure C-70 shows the applied load-tendon strain relationship at the final load stage. In the figure, compression strain is shown as negative while tension strain is shown as positive. Tendon strains measured at all locations are negligible for applied load less than 14.0 kips. For applied load greater than 14.0 kips tensile strains measured in the tendons along Grid 2 increase linearly with increasing applied load, indicating that the neutral axis is shifting upwards and that the section has cracked. This change in behavior at this load level is consistent with the change in behavior of the load-displacement relationship described in Section C.4.8.2. The response of the applied load-tendon strain shows the insignificant effects of two million cycles on the panel behavior.

Figure C-71 shows the applied load-concrete surface strain relationship at the final load stage. Concrete surface gages along Grid 2 on the bottom surface of the panel stopped working after flexural cracks occurred at the gage location; thus measured strain in this location is reported only until the respective gage stopped working.

The strain distribution within the section at various locations at the final loading stage is shown in Figure C-72. For each location, Figure C-72 show strains measured on the top and bottom concrete surfaces and the corresponding strain measured in the tendon at different load levels, including cracking and failure loads (14.0 kips and 20.7 kips, respectively). Concrete surface gages along Grid 2 on the bottom surface of the panel stopped working after flexural cracks occurred at the gage location; thus, measured strain in this location is reported only until the respective gage stopped working.

Figure C-73 shows the strain distribution within the section at various locations. For each location, Figure C-73 shows strains measured on the top and bottom concrete surfaces and the corresponding strain measured in the tendon at the maximum load for different number of cycles. The maximum load after each 500,000 cycles ranged between 8 kips and 12 kips. The measured strains in all locations are reported only for the working gages at the maximum load level.

C.4.9 Panel ECST-NC-FL

C.4.9.1 Failure and Cracking Behavior

Panel ST-NC-FL was tested under fatigue loading on the period between 6/28/10 and 7/7/10. The panel was subjected to two million cycles with the loading protocol described in Section 5.2.3.3. The panel was subjected to static load test until failure immediately after two million load cycles. The static load test was conducted on 7/7/10, 118 days after the concrete was cast. No flexural cracks were observed during the cyclic loading process since the loading was within elastic range. In the post fatigue static load test, flexural cracks first developed on the extreme tension face, which increased in length and number with increasing applied load. Cracks were first observed on the side face at an applied load of 17.18 kips and displacement of 0.65 in. The initial cracks started to appear at locations near the edge of the spreader beam location. As the applied load was increased, additional flexural cracks appeared and existing cracks propagated upward. As observed in the static load test, at the final load stage the panel failed by concrete crushing by means failure occurred as the crack penetrated the flexural compression zone completely at the location of the spreader beam. As a result of the loss of load carrying capacity associated with the destruction of the flexural compression zone, the applied load dropped suddenly to 10.35 kips. The maximum load and corresponding displacement was 19.0 kips and 1.12 in., respectively. Upon attempt to maintain and increase the load level, further deformation was imposed on the specimen. No decrease in the displacement was observed. The maximum load of 19 kips was not able to be recovered; thus the failure load for Panel ST-NC-FL corresponds to an applied load of 19 kips. Figure C-74 shows the post-failure state of the panel after the spreader beam was removed.

During the test, cracks were marked on the side faces of the panel at discrete load increments until the failure load was achieved. Figure C-75 shows the progression of cracking from an applied load of 17.18 kips (shortly after first observed flexural cracking occurred) to the maximum load of 19.00 kips.

C.4.9.2 Load-displacement

The stiffness degradation of the panel was studied by performing a quasi-static load test up to 0.25 inch after each 500,000 cycles. Panel ST-NC-FL was subjected to a total of five quasi-static load tests (0, 500,000, 1,000,000, 1,500,000, and 2,000,000 cycles). Figure C-76 shows the applied load and displacement results of the quasi-static load tests at all locations. The figure shows main stiffness degradation in the cycles between 0 and 500,000 and the cycles between 1,500,000 and 2,000,000 cycles. In addition, the stiffness degradation was observed by the decreased maximum displacement, which affects the overall ductility. Figure C-77 shows the measured displacement along the panel length at Grids E, E', and F for various load levels, including cracking and maximum loads (15.5 kips and 19.0 kips, respectively). As discussed in the static load test section, the cracking load was determined based on the change in behavior of

the load- displacement relationship from Figure C-77, as well as the change in load-strain relationship discussed in Section C.4.9.3. Note that the cracking load determined in this manner is slightly lower than the load corresponding to when flexural cracks were first observed as discussed in Section C.4.9.1. Displacements measured at Grids E, E', and F are similar (within 3.5%) at each load level with the exception of the failure load. Figure C-78 shows the applied load-displacement response for all locations.

C.4.9.3 Load-strain

Figure C-79 shows the applied load-tendon strain relationship. In the figure, compression strain is shown as negative while tension strain is shown as positive. Tendon strains measured at all locations are negligible for applied load less than 15.5 kips. For applied load greater than 15.5 kips tensile strains measured in the tendons along Grid 2 increase linearly with increasing applied load, indicating that the neutral axis is shifting upwards and that the section has cracked. This change in behavior at this load level is consistent with the change in behavior of the load-displacement relationship described in Section C.4.9.2. The response of the applied load-tendon strain shows the insignificant effects of two million cycles on the panel behavior.

Figure C-80 shows the applied load-concrete surface strain relationship. Concrete surface gages along Grid 2 on the bottom surface of the panel stopped working after flexural cracks occurred at the gage location; thus measured strain in this location is reported only until the respective gage stopped working.

The strain distribution within the section at various locations at the final loading stage is shown in Figure C-81. For each location, in Figure C-81 shows strains measured on the top and bottom concrete surfaces and the corresponding strain measured in the tendon at different load levels, including cracking and failure loads (15.5 kips and 19.0 kips, respectively). Concrete surface gage along Grid 2 on the bottom surface of the panel stopped working after flexural cracks occurred at the gage location; thus measured strain in this location is reported only until the respective gage stopped working.

Figure C-82 shows the strain distribution within the section at various locations. For each location, Figure C-82 shows strains measured on the top and bottom concrete surfaces and the corresponding strain measured in the tendon at the maximum load for different number of cycles. The maximum load after each 500,000 cycles ranged between 8 kips and 12 kips. The measured strains in all locations are reported only for the working gages at the maximum load level.

C.4.10 Panel ECST-FRC-FL

C.4.10.1 Failure and Cracking Behavior

Panel ECST-FRC-FL was tested under fatigue loading during the period between 7/28/10 and 8/4/10. No flexural cracks were observed during the cyclic loading process since the loading was within elastic range. The panel was subjected to static load test until failure immediately after two million load cycles. The static load test was conducted on 8/4/10, 143 days after the concrete was cast. No flexural cracks were observed during the cyclic loading process since the loading was within elastic range. In the post fatigue static load test, flexural cracks first developed on the extreme tension face, which increased in length and number with increasing applied load.

Cracks were first observed on the side face at an applied load of 15.71 kips and displacement of 0.50 in. The initial cracks started to appear at locations near the edge of the spreader beam location. As the applied load was increased, additional flexural cracks appeared and existing cracks propagated upward. As observed in the static load test, at the final load stage the panel failed by concrete crushing by means failure occurred as the crack penetrated the flexural compression zone completely at the location of the spreader beam. As a result of the loss of load carrying capacity associated with the destruction of the flexural compression zone, the applied load dropped suddenly to 11.15 kips. The maximum load and corresponding displacement was 19.49 kips and 1.40 in., respectively. Upon attempt to maintain and increase the load level, further deformation was imposed on the specimen. The maximum load of 19.49 kips was not able to be recovered; thus the failure load for Panel ECST-FRC-FL corresponds to an applied load of 19.49 kips. Figure C-83 shows the post-failure state of the panel after the spreader beam was removed.

During the test, cracks were marked on the side faces of the panel at discrete load increments until the failure load was achieved. Figure C-84 shows the progression of cracking from an applied load of 15.71 kips (shortly after first observed flexural cracking occurred) to the maximum load of 19.49 kips.

C.4.10.2 Load-displacement

The stiffness degradation of the panel was studied by performing a quasi-static load test up to 0.25 inch after each 500,000 cycles. Panel ST-NC-FL was subjected to a total of five quasi-static load tests (0, 500,000, 1,000,000, 1,500,000, and 2,000,000 cycles). Figure C-85 shows the applied load and displacement results of the quasi-static load tests at all locations. The figure shows main stiffness degradation in the cycles between 0 and 500,000 and the cycles between 1,500,000 and 2,000,000 cycles. In addition, the stiffness degradation was observed by the decreased maximum displacement, which affects the overall ductility. Figure C-86 shows the measured displacement along the panel length at Grids E, E', and F for various load levels, including cracking and maximum loads (13.25 kips and 19.49 kips, respectively). As discussed in the static load test section, the cracking load was determined based on the change in behavior of the load- displacement relationship from Figure C-86, as well as the change in load-strain relationship discussed in Section C.4.1.3. Note that the cracking load determined in this manner is slightly lower than the load corresponding to when flexural cracks were first observed as discussed in Section C.4.1.1. Displacements measured at Grids E, E', and F are similar (within 3%) at each load level with the exception of the failure load. Figure C-87 shows the applied load-displacement response for all locations.

C.4.10.3 Load-strain

Figure C-88 shows the applied load-tendon strain relationship. In the figure, compression strain is shown as negative while tension strain is shown as positive. Tendon strains measured at all locations are negligible for applied load less than 13.25 kips. For applied load greater than 13.25 kips tensile strains measured in the tendons along Grid 2 increase linearly with increasing applied load, indicating that the neutral axis is shifting upwards and that the section has cracked. This change in behavior at this load level is consistent with the change in behavior of the load-displacement relationship described in Section C.4.3.2. The response of the applied load-tendon strain shows the insignificant effects of two million cycles on the panel behavior.

Figure C-89 shows the applied load-concrete surface strain relationship. Concrete surface gages along Grid 2 on the bottom surface of the panel stopped working after flexural cracks occurred at the gage location; thus measured strain in this location is reported only until the respective gage stopped working.

The strain distribution within the section at various locations at the final loading stage is shown in Figure C-90. For each location, Figure C-90 shows strains measured on the top and bottom concrete surfaces and the corresponding strain measured in the tendon at different load levels, including cracking and failure loads (13.25 kips and 19.49 kips, respectively). Concrete surface gage along Grid 2 on the bottom surface of the panel stopped working after flexural cracks occurred at the gage location; thus measured strain in this location is reported only until the respective gage stopped working.

Figure C-91 shows the strain distribution within the section at various locations. For each location, Figure C-91 shows strains measured on the top and bottom concrete surfaces and the corresponding strain measured in the tendon at the maximum load for different number of cycles. The maximum load after each 500,000 cycles ranged between 8 kips and 12 kips. The measured strains in all locations are reported only for the working gages at the maximum load level.

C.4.11 Panel CFRPT-NC-FL

C.4.11.1 Failure and Cracking Behavior

Panel CFRPT-NC-FL was tested under fatigue loading on the period between 6/16/10 and 6/23/10. The panel was subjected to two million cycles with the loading protocol described in Section 5.2.3.3. The panel was subjected to static load test until failure immediately after two million load cycles. The static load test was conducted on 6/25/10, 106 days after the concrete was cast. No flexural cracks were observed during the cyclic loading process since the loading was within elastic range. In the post fatigue static load test, flexural cracks first developed on the extreme tension face, which increased in length and number with increasing applied load. Cracks were first observed on the side face at an applied load of 16.38 kips and displacement of 0.70 in. The initial cracks started to appear at locations near the edge of the spreader beam location. As the applied load was increased, additional flexural cracks appeared and existing cracks propagated upward. As observed in the static load test, at the final load stage the panel failed by concrete crushing by means failure occurred as the crack penetrated the flexural compression zone completely at the location of the spreader beam. As a result of the loss of load carrying capacity associated with the destruction of the flexural compression zone, the applied load dropped to 14.95 kips. The maximum load and corresponding displacement was 17.49 kips and 1.02 in., respectively. Upon attempt to maintain and increase the load level, further deformation was imposed on the specimen. No significant displacement increase was observed. The maximum load of 17.49 kips was not able to be recovered; thus the failure load for Panel CFRPT-NC-FL corresponds to an applied load of 17.49 kips. Figure C-92 shows the post-failure state of the panel after the spreader beam was removed.

During the post fatigue static load test, cracks were marked on the side faces of the panel at discrete load increments until the failure load was achieved. Figure C-93 shows the progression

of cracking from an applied load of 16.38 kips (shortly after first observed flexural cracking occurred) to the maximum load of 17.49 kips.

C.4.11.2 Load-displacement

The stiffness degradation of the panel was studied by performing a quasi-static load test up to 0.25 inch after each 500,000 cycles. Panel CFRPT-NC-FL was subjected to a total of five quasi-static load test before the cyclic loading and after each 500,000 cycles (0, 500,000, 1,000,000, 1,500,000, and 2,000,000 cycles). Figure C-94 shows the applied load and displacement results of the quasi-static load tests at all locations. The figure shows major stiffness degradation in the cycles between 0 and 500,000 and the cycles between 1,500,000 and 2,000,000 cycles. In addition, the stiffness degradation was observed by the decreased maximum displacement, which affects the overall ductility. Figure C-95 shows the measured displacement along the panel length at Grids E, E', and F for various load levels, including cracking and maximum loads (13.7 kips and 17.49 kips, respectively). As discussed in the static load test section, the cracking load was determined based on the change in behavior of the load- displacement relationship from Figure C-95, as well as the change in load-strain relationship discussed in Section C.4.11.3. Note that the cracking load determined in this manner is slightly lower than the load corresponding to when flexural cracks were first observed as discussed in Section C.4.11.1. Displacements measured at Grids E, E', and F are similar (within 3.5%) at each load level with the exception of the failure load. Figure C-96 shows the applied load-displacement response for all locations.

C.4.11.3 Load-strain

Figure C-97 shows the applied load-tendon strain relationship at the final load stage. In the figure, compression strain is shown as negative while tension strain is shown as positive. Tendon strains measured at all locations are negligible for applied load less than 13.7 kips. For applied load greater than 13.7 kips tensile strains measured in the tendons along Grid 2 increase linearly with increasing applied load, indicating that the neutral axis is shifting upwards and that the section has cracked. This change in behavior at this load level is consistent with the change in behavior of the load-displacement relationship described in Section C.4.11.3. The response of the applied load-tendon strain shows the insignificant effects of two million cycles on the panel behavior.

Figure C-98 shows the applied load-concrete surface strain relationship at the final load stage. Concrete surface gages along Grid 2 on the bottom surface of the panel stopped working after flexural cracks occurred at the gage location; thus, measured strain in this location is reported only until the respective gage stopped working.

The strain distribution within the section at various locations at the final loading stage is shown in Figure C-99. For each location, Figure C-99 shows strains measured on the top and bottom concrete surfaces and the corresponding strain measured in the tendon at different load levels, including cracking and failure loads (13.7 kips and 17.49 kips, respectively). Concrete surface gages along Grid 2 on the bottom surface of the panel stopped working after flexural cracks occurred at the gage location; thus measured strain in this location is reported only until the respective gage stopped working.

Figure C-100 shows the strain distribution within the section at various locations. For each location, Figure C-100 shows strains measured on the top and bottom concrete surfaces and the corresponding strain measured in the tendon at the maximum load for different number of cycles. The maximum load after each 500,000 cycles ranged between 8 kips and 12 kips. The measured strains in all locations are reported only for the working gages at the maximum load level.

C.4.12 Panel CFRPT-FRC-FL

C.4.12.1 Failure and Cracking Behavior

Panel CFRPT-NC-FL was tested under fatigue loading on the period between 7/20/10 and 7/26/10. The panel was subjected to two million cycles with the loading protocol described in Section 5.2.3.3. The panel was subjected to static load test until failure immediately after two million load cycles. The static load test was conducted on 7/26/10, 134 days after the concrete was cast. No Flexural cracks observed during the cyclic loading process due to the elastic loading range. In the post fatigue static load test, flexural cracks first developed on the extreme tension face, which increased in length and number with increasing applied load. Cracks were first observed on the side face at an applied load of 15.14 kips and displacement of 0.60 in. The initial cracks started to appear at locations near the edge of the spreader beam location. As the applied load was increased, additional flexural cracks appeared and existing cracks propagated upward. As observed in the static load test, at the final load stage the panel failed by concrete crushing by means failure occurred as the crack penetrated the flexural compression zone completely at the location of the spreader beam. As a result of the loss of load carrying capacity associated with the destruction of the flexural compression zone, the applied load dropped to 11.24 kips. The maximum load and corresponding displacement was 17.95 kips and 1.33 in., respectively. Upon attempt to maintain and increase the load level, further deformation was imposed on the specimen. No significant displacement increase was observed. The maximum load of 17.95 kips was not able to be recovered; thus the failure load for Panel CFRPT-FRC-FL corresponds to an applied load of 17.95 kips. Figure C-101 shows the post-failure state of the panel after the spreader beam was removed.

During the post fatigue static load test, cracks were marked on the side faces of the panel at discrete load increments until the failure load was achieved. Figure C-102 shows the progression of cracking from an applied load of 16.38 kips (shortly after first observed flexural cracking occurred) to the maximum load of 17.49 kips.

C.4.12.2 Load-displacement

The stiffness degradation of the panel was studied by performing quasi-static load test up to 0.25 inch after each 500,000 cycles. Panel CFRPT-FRC-FL was subjected to five quasi-static load test before the cyclic loading and after each 500,000 cycles (0, 500,000, 1,000,000, 1,500,000, and 2,000,000 cycles). Figure C-103 shows the applied load and displacement results of the quasi static at all locations. The figure shows major stiffness degradation in the cycles between 0 and 500,000 and the cycles between 1,500,000 and 2,000,000 cycles. In addition, the stiffness degradation was observed by the decreased maximum displacement, which affects the overall ductility. Figure C-104 shows the measured displacement along the panel length at Grids E, E', and F for various load levels, including cracking and maximum loads (13 kips and 17.95 kips, respectively). As discussed in the static load test section, the cracking load was determined based

on the change in behavior of the load- displacement relationship from Figure C-104, as well as the change in load-strain relationship discussed in Section C.4.12.3. Note that the cracking load determined in this manner is slightly lower than the load corresponding to when flexural cracks were first observed as discussed in Section C.4.12.1. Displacements measured at Grids E, E', and F are similar (within 3 %) at each load level with the exception of the failure load. Figure C-105 shows the applied load-displacement response for all locations.

C.4.12.3 Load-strain

Figure C-106 shows the applied load-tendon strain relationship. In the figure, compression strain is shown as negative while tension strain is shown as positive. Tendon strains measured at all locations are negligible for applied load less than 13 kips. For applied load greater than 13 kips tensile strains measured in the tendons along Grid 2 increase linearly with increasing applied load, indicating that the neutral axis is shifting upwards and that the section has cracked. This change in behavior at this load level is consistent with the change in behavior of the load-displacement relationship described in Section C.4.12.2.

Figure C-107 shows the applied load-concrete surface strain relationship. Concrete surface gages along Grid 2 on the bottom surface of the panel stopped working after flexural cracks occurred at the gage location; thus measured strain in this location is reported only until the respective gage stopped working.

The strain distribution within the section at various locations is shown in Figure C-108. For each location, Figure C-108 shows strains measured on the top and bottom concrete surfaces and the corresponding strain measured in the tendon at different load levels, including cracking and failure loads (13 kips and 17.95 kips, respectively). Concrete surface gages along Grid 2 on the bottom surface of the panel stopped working after flexural cracks occurred at the gage location; thus measured strain in this location is reported only until the respective gage stopped working.

Figure C-109 shows the strain distribution within the section at various locations. For each location, Figure C-109 shows strains measured on the top and bottom concrete surfaces and the corresponding strain measured in the tendon at the maximum load for different number of cycles. The maximum load ranged between 8 kips and 12 kips. The measured strains in all locations are reported only for the working gages at the maximum load level.

C.5 DURABILITY EXPERIMENT RESULTS

C.5.1 Corrosion initiation test

C.5.1.1 Visual inspection

The corrosion initiation test was conducted in the Missouri S&T Civil Engineering Materials Laboratory from 1/27/2010 to 8/3/2010. Test specimens were subjected to wet/dry cycles during the test period. Test specimens were submerged in 5% NaCl solution for 4 days then were dried in oven at 104ºF for 3 days. Table C-4, Table C-5, and Table C-6 show the concrete deterioration observed with respect to different edge distance. Efflorescence was observed in all specimens regardless of geometrical and material properties. Rust was observed on most of specimens with 1.5 in. edge distance, while two specimens for each specimen group with 2.5 in. and 3.5 in. edge

distances showed rust. Cracking was observed in three specimens with 1.5 in. edge distance, while only one specimen in each specimen group with 2.5 in. and 3.5 in. edge distances showed cracking. All cracks were observed on the surfaces of the specimens only; cracks did not appear to have propagated from the tendon location. In other words, the cracks appeared to be superficial cracks and not corrosion-induced cracks. Thus, it was concluded that the corrosion of the embedded tendons was not enough to cause corrosion-induced cracks.

C.5.1.2 Half-cell potential

Table C-7, Table C-8, and Table C-9 show half-cell potential data collected every two weeks during the test period. The values in the tables can be compared to limiting values reported in ASTM C876-91. Accordingly, corrosion probability is higher than 90% when potential value is higher than -350 mV. Values within the range of -200mV to -350mV indicate a 50% probability of corrosion. For values lower than -200mV, probability is less than 5%. Figure C-114 shows the relationship between potential and time duration for each of the different concrete materials. Figure C-115 shows the relationship between potential and time duration for specimens with different edge distance. Although there are some fluctuations in the data, decreasing edge distance tended to increase the probability of corrosion. From both Figure C-114 and Figure C-115, it can be seen that specimens with corrosion inhibitor tended to have the highest probability of corrosion.

C.5.1.3 Chloride content analysis

Figure C-116 shows the chloride contents at different depths for specimens of the same material but different edge distances, while Figure C-117 shows the chloride contents at different depths for specimens with the same edge distances and different concrete materials. Concrete samples were taken from three locations: 0.5 in. from the surface, mid-depth between surface and steel location, and at the steel location. Although it is somewhat difficult to distinguish the effects of material and edge distance due to the scatter of the data, general observations can be made. Specimens with corrosion inhibitor tended to have the greatest chloride ingress. Specimens with 3.5 in. edge distance tended to show the lowest chloride ingress.

C.5.2 Accelerated corrosion test

C.5.2.1 Visual inspection

Accelerated corrosion test specimens were tested for a six month time duration from 1/29/2010 to 7/8/2010. Table C-10 shows the steel tendons retrieved at the end of test. Corrosion length was measured at both ends of the specimen, and longer length was taken as the corrosion length for the corresponding specimen.

C.5.2.2 Gravimetric study

Steel tendons were retrieved from all test specimens to measure the steel loss after 4,400 hours. The initial weight of the steel tendons was determined on the day the specimens were constructed (12/29/2009). Steel loss, as well as recorded time to corrosion cracking and spalling, is reported in Table C-11. Concrete with fibers showed the longest time for corrosion cracking, while concrete with corrosion inhibitor showed the shortest time. Steel mass loss data were used to estimate the corrosion rate (described in the main body of the report).

Table C- 1 Concrete Mixture Materials and Proportions

Normal concrete, Normal concrete + fibers (12/29/09 Concrete Batch)

	Normal concrete		Normal concrete + fibers	
	Specified	Actual	Specified	Actual
Cement[1] (lbs/cy)	751	748	751	748
Course aggregate[2] (lbs/cy)	1573	1571	1570	1569
Sand[3] (lbs/cy)	1289	1288	1290	1291
Water (lbs/cy)	187	188	185	185
HRWR[6] (oz)	85	86	80	80
Air Entraining Admixture[5] (oz)	37	37	35	35
Fiber[6] (bags/cy)	-	-	1	1
Corrosion inhibitor[7]	-	-	-	-
NaCl[8]	-	-	-	-
Water–cement ratio (w/c)	0.34	0.31	0.34	0.34

Normal concrete, Normal concrete + fibers (3/12/10 Concrete Batch)

	Normal concrete		Normal concrete + fibers	
	Specified	Actual	Specified	Actual
Cement[1] (lbs/cy)	751	751	751	752
Course aggregate[2] (lbs/cy)	1549	1591	1549	1595
Sand[3] (lbs/cy)	1235	1287	1235	1289
Water (lbs/cy)	268	166	268	173
HRWR[6] (oz)	72.02	70.67	72.02	70.67
Air Entraining Admixture[5] (oz)	32	32	32	32
Fiber (bags/cy)	-	-	1.5	1
Corrosion inhibitor[7]	-	-	-	-
NaCl[8]	-	-	-	-
Water–cement ratio (w/c)	0.3656	.321	0.3656	.365

Normal concrete + 3% NaCl, Normal concrete + fibers + 3% NaCl

	Normal concrete + 3% NaCl		Normal concrete + fibers + 3% NaCl	
	Specified	Actual	Specified	Actual
Cement[1] (lbs/cy)	751	750	751	750
Course aggregate[2] (lbs/cy)	1577	1573	1582	1578
Sand[3] (lbs/cy)	1293	1287	1293	1282
Water (lbs/cy)	190	190	190	191
HRWR[6] (oz)	79	81	80	82
Air Entraining Admixture[5] (oz)	35	36	32	32
Fiber (bags/cy)	-	-	1	1
Corrosion inhibitor[7]	-	-	-	-
NaCl[8] (lbs/cy)	22.5	22.5	22.5	22.5
Water–cement ratio (w/c)	0.34	0.34	0.34	0.34

Table C-1 Concrete Mixture Materials and Proportions (Cont.)

Normal concrete + corrosion inhibitor, Normal concrete + corrosion inhibitor + 3% NaCl

	Normal concrete + corrosion inhibitor		Normal concrete + corrosion inhibitor + 3% NaCl	
	Specified	Actual	Specified	Actual
Cement[1] (lbs/cy)	751	748	751	748
Course aggregate[2] (lbs/cy)	1579	1573	1574	1568
Sand[3] (lbs/cy)	1295	1287	1290	1287
Water (lbs/cy)	191	192	187	187
HRWR[6] (oz/cy)	81	83	79	82
Air Entraining Admixture[5] (oz/cy)	37	36	30	31
Fiber (bags/cy)	-	-	-	-
Corrosion inhibitor (oz/cy)[7]	2	3	1	4
NaCl[8] (lbs/cy)	-	-	22.5	22.5
Water–cement ratio (w/c)	0.34	0.34	0.34	0.34

Notes:
1. Cement is ASTM C-150 Type 3 (Ashgrove)
2. Coarse aggregate is ASTM C-33 (Limestone)
3. Fine aggregate is ASTM C-33 (Kaw sand)
4. HRWR is ASTM C-494 (Glenium 7700)
5. Air Entraining Admixture is ASTM C-260 (MB VR standard)
6. Fibers are ASTM C-1116 (Master fiber F70)
7. Corrosion inhibitor is MCI (Cortec Corporation)
8. NaCl is 3% of cement

Table C- 2 Measured Hardened Concrete Properties – Unit Panel Specimens

	ST-NC		ST-FRC		ECT-NC		ECT-FRC		CFRP-NC		CFRP-FRC	
	-SL	-FL	-SL	-FL	-SL	-FL	-SL	-FL	-SL	-FL	-SL	-FL
28-day concrete compr. strength (psi)	6000	6000	6160	6160	5640	5640	7060	7060	5640	5640	7060	5640
Concrete compr. strength at test date (psi)	6360	6380	5580	7710	5900	6200	6460	7600	7000	6040	6390	6080
Modulus of rupture (psi)	600	-	-	855	-	765	-	745	620	-	585	-

Table C- 3 Prestressed Reinforcement Material Properties

	Yield Strength (lbs)		Breaking Strength (lbs)		Elongation (%)	
	Measured	Mill Certification	Measured	Mill Certification	Measured	Mill Certification
Steel strand, 3/8 inch diameter 7-wire Grade 270 ASTM A 416	21450	21,904	23,320	24,404	7.8	7.5
Steel strand, 3/8 inch diameter 7-wire Grade 270 ASTM A 416	22130	21,904	23750	24,404	7.4	7.5
Epoxy-coated steel strand, 3/8 inch diameter 7-wire Grade 270 ASTM A 882	23205	22,438	24,647	24,352	5.1	4.7
CFRP	-	-	-	40,447	-	1.92

Table C- 4 Visual Inspection for Corrosion Initiation Specimens with 1.5 in. Edge Distance

Specimen Designation	Concrete Deterioration		
	Efflorescence	Rust	Cracking
SP1-NC-1		None observed	None observed
SP1-NC-2			None observed
SP1-NC-3		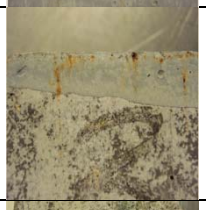	None observed
SP1-CI-1			
SP1-CI-2			
SP1-CI-3		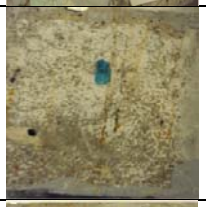	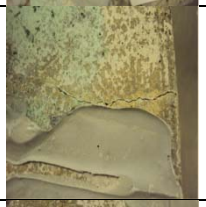
SP1-FRC-1		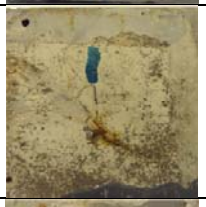	
SP1-FRC-2		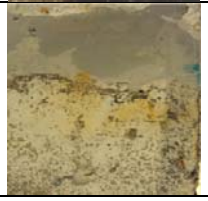	

SP1-FRC-3		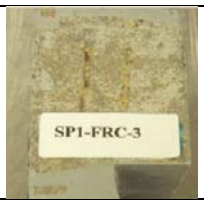						

Table C- 5 Visual Inspection for Corrosion Initiation Specimens with 2.5 in. Edge Distance

Specimen Designation	Concrete Deterioration		
	Efflorescence	Rust	Cracking
SP2-NC-5	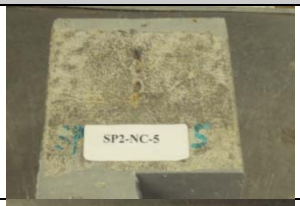	None observed	None observed
SP2-NC-6	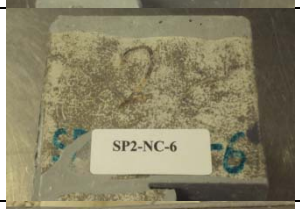	None observed	None observed
SP2-NC-7		None observed	None observed
SP2-CI-5		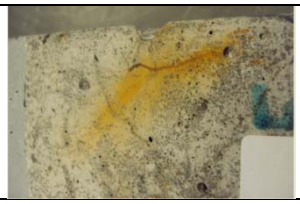	None observed
SP2-CI-6		None observed	None observed
SP2-CI-7			
SP2-FRC-5	None observed	None observed	None observed
SP2-FRC-6		None observed	None observed
SP2-FRC-7		None observed	None observed

Table C- 6 Visual Inspection for Corrosion Initiation Specimens with 3.5 in. Edge Distance

Specimen Designation	Concrete Deterioration		
	Efflorescence	Rust	Cracking
SP3-NC-9		None observed	None observed
SP3-NC-10		None observed	None observed
SP3-NC-11		None observed	None observed
SP3-CI-9			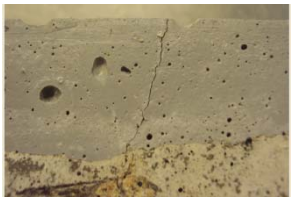
SP3-CI-10			None observed

SP3-CI-11		None observed	None observed
SP3-FRC-9		None observed	None observed
SP3-FRC-10		None observed	None observed
SP3-FRC-11		None observed	None observed

Table C- 7 Half-cell Potential and Resistivity after Two Months

Specimen Label	2 Months specimens - Period and Measurements							
	2 Weeks		4 Weeks		6 Weeks		8 Weeks	
	Potential (mV)	Resistivity (KΩ.cm)	Potential (mV)	Resistivity (KΩ.cm)	Potential (mV)	Resistivity (KΩ.cm)	Potential (mV)	Resistivity (KΩ.cm)
SP1-NC-1	-238.5	5.8	-299.0	19.0	-248.0	13.0	-291.5	14.0
SP1-NC-2	-269.0	5.0	-273.5	11.0	-313.0	11.0	-307.0	17.0
SP1-NC-3	-249.5	12.0	-294.5	36.0	-397.5	11.0	-363.5	19.0
SP1-CI-1	-243.0	14.0	-229.0	19.0	-227.0	8.6	-235.5	17.0
SP1-CI-2	-242.5	7.0	-339.0	14.0	-363.5	14.0	-395.0	20.0
SP1-CI-3	-241.5	10.0	-255.0	12.0	-306.0	11.0	-390.0	17.0
SP1-FRC-1	-344.0	9.0	-369.5	8.5	-356.5	8.1	-350.5	15.0
SP1-FRC-2	-337.5	9.0	-306.5	5.8	-357.5	6.5	-382.5	18.0
SP1-FRC-3	-249.5	7.1	-250.5	9.1	-237.0	7.3	-226.5	15.0
SP2-NC-5	-235.5	17.0	-243.0	16.0	-232.5	29.0	-218.5	32.0
SP2-NC-6	-231.0	15.0	-220.0	12.0	-232.0	14.0	-278.5	28.0
SP2-NC-7	-214.0	13.0	-208.5	18.0	-230.5	19.0	-264.5	33.0
SP2-CI-5	-219.5	10.0	-216.5	12.0	-196.0	11.0	-240.0	19.0
SP2-CI-6	-312.5	21.0	-337.5	18.0	-327.0	16.0	-271.0	25.0
SP2-CI-7	-212.0	18.0	-335.0	13.0	-315.5	15.0	-344.5	23.0
SP2-FRC-5	-255.5	10.0	-328.0	14.0	-321.5	11.0	-318.5	21.0
SP2-FRC-6	-221.5	12.0	-211.0	15.0	-337.0	12.0	-343.0	21.0
SP2-FRC-7	-243.5	15.0	-238.0	15.0	-216.5	14.0	-216.0	26.0
SP3-NC-9	-229.0	18.0	-360.5	23.0	-353.0	25.0	-360.5	37.0
SP3-NC-10	-223.0	16.0	-215.0	20.0	-188.0	28.0	-173.5	45.0
SP3-NC-11	-235.0	15.0	-322.0	18.0	-352.5	23.0	-386.5	35.0
SP3-CI-9	-242.5	20.0	-333.5	17.0	-419.5	24.0	-463.0	29.0
SP3-CI-10	-244.5	15.0	-259.5	18.0	-275.5	25.0	-300.0	30.0
SP3-CI-11	-198.0	17.0	-196.5	20.0	-181.0	20.0	-213.5	32.0
SP3-FRC-9	-215.5	12.0	-218.5	16.0	-244.5	27.0	-303.5	27.0
SP3-FRC-10	-226.0	15.0	-226.5	21.0	-242.0	19.0	-277.0	29.0
SP3-FRC-11	-212.0	15.0	-234.5	18.0	-269.0	19.0	-349.0	29.0

Table C- 8 Half-cell Potential and Resistivity after Four Months

Specimen Label	4 Months specimens - Period and Measurements							
	2 Weeks		4 Weeks		6 Weeks		8 Weeks	
	Potential (mV)	Resistivity (KΩ.cm)	Potential (mV)	Resistivity (KΩ.cm)	Potential (mV)	Resistivity (KΩ.cm)	Potential (mV)	Resistivity (KΩ.cm)
SP1-NC-1	-372.0	31.0	-385.5	34.0	-399.5	19.0	-400.0	54.0
SP1-NC-2	-410.5	14.0	-443.5	11.0	-448.5	13.0	-410.5	20.0
SP1-NC-3	-354.0	15.0	-412.0	11.0	-412.5	9.0	-417.0	16.0
SP1-CI-1	-410.5	9.3	-429.0	12.0	-446.0	9.7	-466.5	14.0
SP1-CI-2	-417.0	6.4	-446.5	5.8	-448.5	5.5	-455.0	9.5
SP1-CI-3	-427.0	6.4	-449.0	6.7	-471.0	8.3	-491.5	12.0
SP1-FRC-1	-385.0	6.3	-390.0	6.6	-420.0	8.0	-398.5	13.0
SP1-FRC-2	-388.5	11.0	-411.0	9.1	-402.5	9.8	-385.0	22.0
SP1-FRC-3	-252.5	10.0	-259.5	10.0	-364.0	11.0	-231.0	17.0
SP2-NC-5	-367.0	17.0	-402.0	16.0	-456.5	20.0	-456.0	29.0
SP2-NC-6	-334.0	19.0	-373.0	17.0	-384.0	21.0	-337.5	31.0
SP2-NC-7	-312.5	14.0	-388.5	14.0	-465.5	16.0	-461.0	24.0
SP2-CI-5	-379.0	19.0	-413.5	16.0	-461.0	22.0	-437.5	30.0
SP2-CI-6	-407.0	14.0	-442.0	12.0	-464.0	14.0	-460.0	19.0
SP2-CI-7	-372.5	12.0	-431.0	11.0	-439.0	12.0	-435.0	17.0
SP2-FRC-5	-352.0	14.0	-350.5	15.0	-381.5	16.0	-400.0	21.0
SP2-FRC-6	-372.0	11.0	-388.5	11.0	-450.0	13.0	-405.5	19.0
SP2-FRC-7	-257.5	13.0	-260.5	12.0	-335.0	15.0	-176.0	21.0
SP3-NC-9	-412.0	18.0	-412.5	22.0	-426.0	22.0	-429.0	33.0
SP3-NC-10	-199.5	27.0	-191.0	23.0	-204.5	24.0	-160.5	44.0
SP3-NC-11	-399.5	24.0	-423.5	18.0	-426.0	25.0	-332.0	27.0
SP3-CI-9	-523.5	17.0	-471.0	15.0	-530.0	19.0	-486.0	24.0
SP3-CI-10	-396.0	20.0	-445.5	18.0	-482.0	20.0	-378.5	30.0
SP3-CI-11	-279.0	19.0	-331.0	19.0	-402.5	23.0	-388.5	37.0
SP3-FRC-9	-356.5	19.0	-351.5	15.0	-352.5	20.0	-368.5	35.0
SP3-FRC-10	-288.0	18.0	-367.5	15.0	-416.0	18.0	-429.0	27.0
SP3-FRC-11	-422.5	20.0	-432.0	18.0	-427.5	20.0	-388.0	31.0

Table C- 9 Half-cell Potential and Resistivity after Six Months

Specimen Label	6 Months specimens - Period and Measurements							
	2 Weeks		4 Weeks		6 Weeks		8 Weeks	
	Potential (mV)	Resistivity (KΩ.cm)	Potential (mV)	Resistivity (KΩ.cm)	Potential (mV)	Resistivity (KΩ.cm)	Potential (mV)	Resistivity (KΩ.cm)
SP1-NC-1	-416.0	19.0	-391.0	20.0	-422.5	18.0	-372.0	54.0
SP1-NC-2	-242.5	8.2	-358.5	10.0	-356.0	11.0	-410.5	20.0
SP1-NC-3	-307.5	10.0	-463.0	13.0	-419.5	12.0	-354.0	11.0
SP1-CI-1	-482.5	12.0	-484.5	11.0	-401.5	10.0	-410.5	14.0
SP1-CI-2	-438.0	4.8	-467.5	3.0	-433.5	5.0	-417.0	8.5
SP1-CI-3	-450.5	12.0	-462.5	11.0	-425.5	12.0	-427.0	12.0
SP1-FRC-1	-361.0	8.0	-455.0	7.0	-469.0	9.0	-385.0	13.0
SP1-FRC-2	-391.5	9.3	-373.5	8.0	-473.0	10.0	-388.5	22.0
SP1-FRC-3	-363.5	14.0	-375.0	13.0	-393.5	15.0	-252.5	17.0
SP2-NC-5	-261.0	21.0	-461.0	20.0	-452.5	21.0	-367.0	29.0
SP2-NC-6	-345.5	17.0	-359.0	16.0	-379.5	15.0	-334.0	31.0
SP2-NC-7	-502.0	13.0	-463.5	12.0	-451.0	11.0	-312.5	24.0
SP2-CI-5	-434.0	21.0	-435.5	20.0	-449.0	18.0	-379.0	30.0
SP2-CI-6	-453.0	11.0	-455.0	12.0	-467.5	13.0	-407.0	19.0
SP2-CI-7	-449.0	13.0	-450.0	11.0	-358.5	10.0	-372.5	17.0
SP2-FRC-5	-435.0	13.0	-444.0	13.0	-467.5	14.0	-352.0	21.0
SP2-FRC-6	-445.0	13.0	-417.0	12.0	-431.0	10.0	-372.0	19.0
SP2-FRC-7	-444.0	13.0	-430.0	10.0	-424.0	9.0	-257.5	21.0
SP3-NC-9	-373.5	17.0	-359.0	15.0	-374.0	18.0	-412.0	33.0
SP3-NC-10	-223.5	18.0	-243.0	19.0	-270.5	17.0	-199.5	44.0
SP3-NC-11	-477.5	21.0	-463.0	20.0	-484.5	18.0	-399.5	27.0
SP3-CI-9	-466.0	17.0	-428.5	18.0	-417.5	17.0	-523.5	24.0
SP3-CI-10	-303.0	20.0	-486.5	19.0	-441.5	21.0	-396.0	30.0
SP3-CI-11	-281.5	28.0	-432.0	26.0	-263.0	25.0	-279.0	37.0
SP3-FRC-9	-380.5	16.0	-386.5	14.0	-392.5	15.0	-356.5	35.0
SP3-FRC-10	-446.0	12.0	-473.5	10.0	-442.0	9.0	-288.0	27.0
SP3-FRC-11	-159.0	17.0	-398.0	15.0	-391.5	16.0	-422.5	31.0

Table C- 10 Visual Inspection for Retrieved Steel Tendons

Specimen Designation	Steel Tendon Deterioration		
	Bottom end	Top end	Overall
SP1-NC-13			
SP1-NC-14		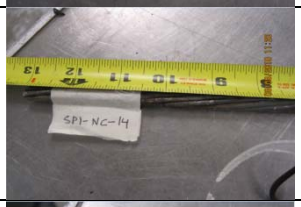	X
SP1-CI-13			
SP1-CI-14			
SP1-FRC-13			
SP1-FRC-14			
SP2-NC-17			
SP2-NC-18			

SP2-CI-17			
SP2-CI-18			
SP2-FRC-17			
SP2-FRC-18			
SP3-NC-21			
SP3-NC-22			
SP3-CI-21			
SP3-CI-22			

SP3-FRC-21			
SP3-FRC-22			

Table C- 11 Recorded Time for Corrosion Cracking and Spalling and Steel Loss

Specimen ID	Initial mass lb (g)	Crack initiation time (hrs)	Spalling time (hrs)	Final mass lb (g)	Mass loss (g)	Ratio of loss (%)
SP1-NC-13	0.312 (141.5)	2304	4440	0.308 (139.7)	1.80	1.3
SP1-NC-14	0.313 (142)	1344	X	0.308 (139.7)	2.30	1.6
SP1-CI-13	0.309 (140.2)	2304	X	0.306 (138.8)	1.40	1.0
SP1-CI-14	0.309 (140.2)	768	4440	0.297 (134.7)	5.50	3.9
SP1-FRC-13	0.312 (141.5)	1344	4440	0.306 (138.8)	2.70	1.9
SP1-FRC-14	0.31 (140.6)	2976	X	0.305 (138.3)	2.30	1.6
SP2-NC-17	0.31(140.6)	3000	X	0.304 (137.9)	2.70	1.9
SP2-NC-18	0.308 (139.7)	No cracks	X	0.302 (137)	2.70	1.9
SP2-CI-17	0.309 (140.2)	1608	X	0.302 (137)	3.20	2.3
SP2-CI-18	0.31(140.6)	No cracks	X	0.309 (140.2)	0.40	0.3
SP2-FRC-17	0.309 (140.2)	2304	X	0.298 (135.2)	5.00	3.6
SP2-FRC-18	0.308 (139.7)	No cracks	X	0.295 (133.8)	5.90	4.2
SP3-NC-21	0.308 (139.7)	3000	X	0.306 (138.6)	0.90	0.6
SP3-NC-22	0.313 (142)	No cracks	X	0.31 (140.6)	1.40	1
SP3-CI-21	0.313 (142)	No cracks	X	0.312 (141.5)	0.50	0.4
SP3-CI-22	0.308 (139.7)	No cracks	X	0.306 (138.8)	0.90	0.6
SP3-FRC-21	0.314 (142.4)	No cracks	X	0.31 (140.6)	1.80	1.3
SP3-FRC-22	0.311 (141.4)	No cracks	X	0.303 (137.4)	3.70	2.6

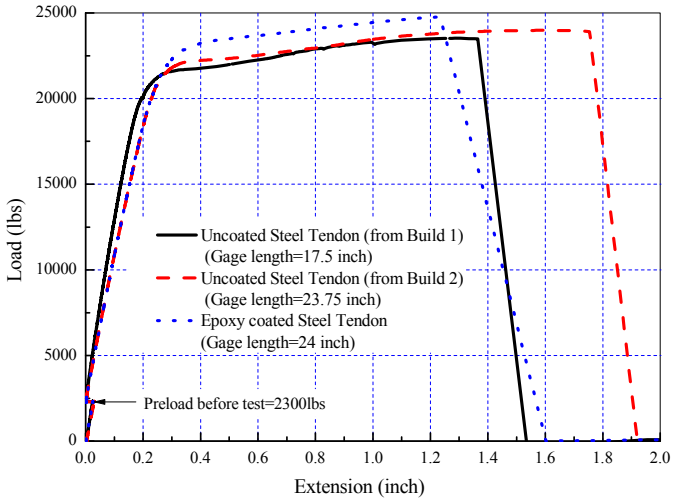

Load-extension relationship for tested tendons

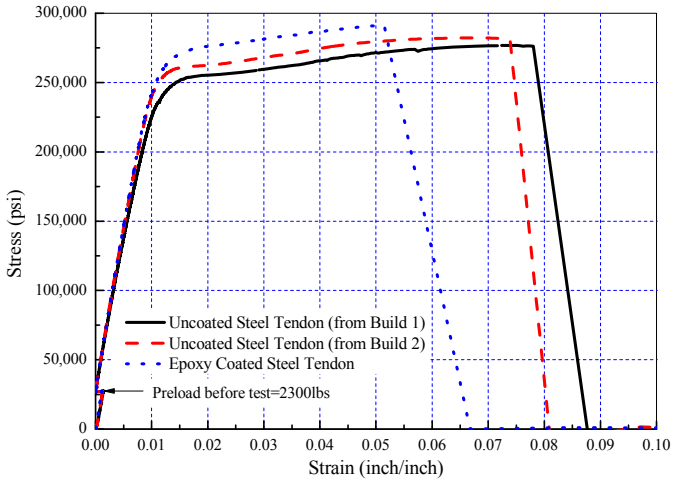

Stress-strain relationship for tested tendons

Note: Epoxy coated steel tendon failed at grips

Figure C- 1 Prestressed Reinforcing Strand Stress-Strain Relationships

Figure C- 2 Non-Prestressed Corrosion Specimen - Formwork and Reinforcement

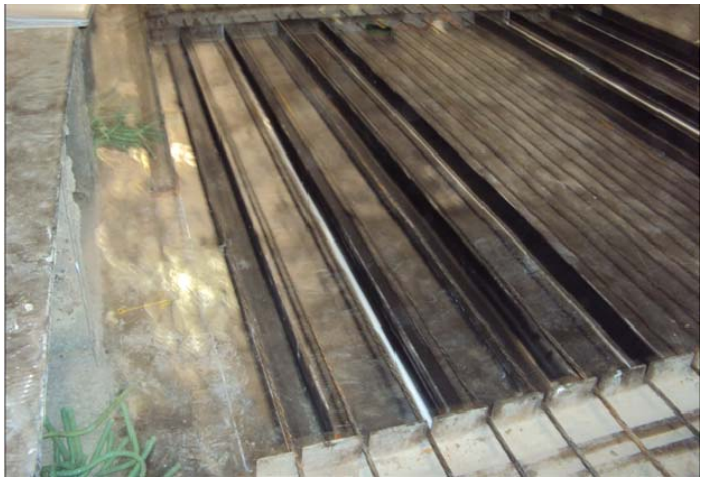

Figure C- 3 Blockouts Provided to Construct Prestressed Corrosion Specimens

Figure C- 4 Prestressed Panel Casting Bed

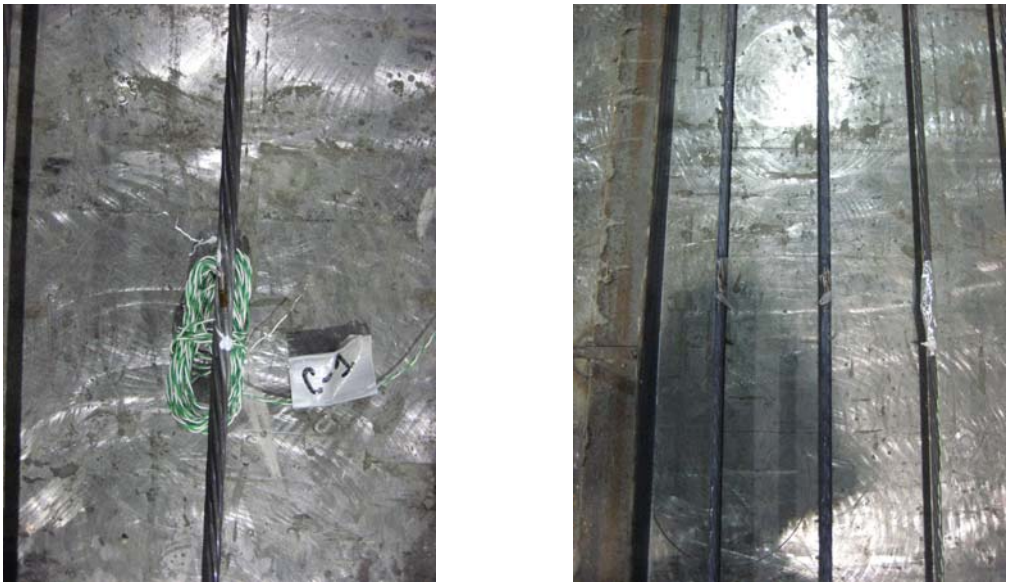

(a) (b)

Figure C- 5 Strain Gages Applied to Prestressed Reinforcement: (a) Steel Strand, (b) Epoxy-Coated Steel Strand

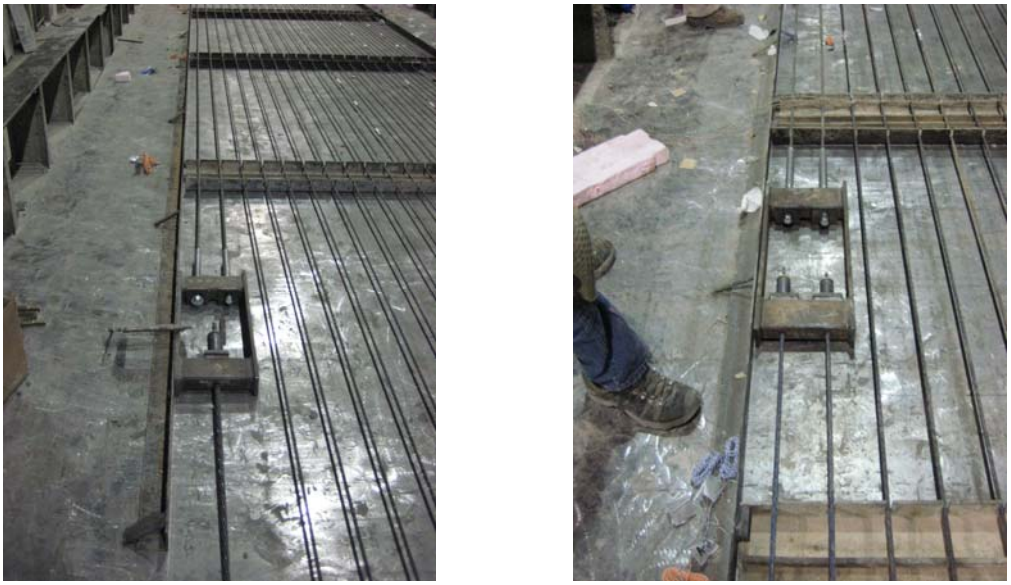

(a) (b)

Figure C- 6 CFRP Prestressed Bar Anchorage Splice: (a) CRFP to 0.6 in. Steel Strand, (b) CRFP to Epoxy-Coated Steel Strand

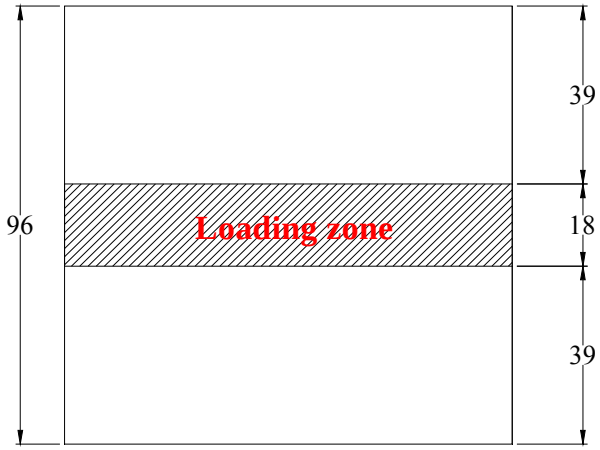

Note: dimensions are in inches

Figure C- 7 Plan View of Panel Loading Zone

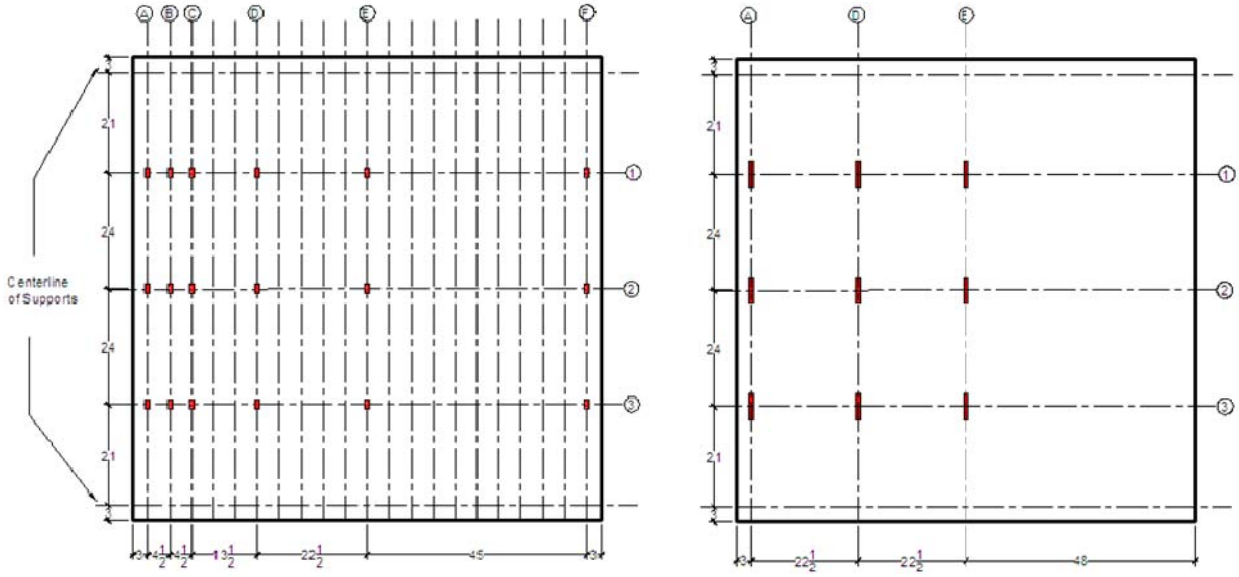

Tendon Strain Gage Layout

Concrete Surface Strain Gage Layout

Note: dimensions are in inches

Figure C- 8 Strain Gage Layout

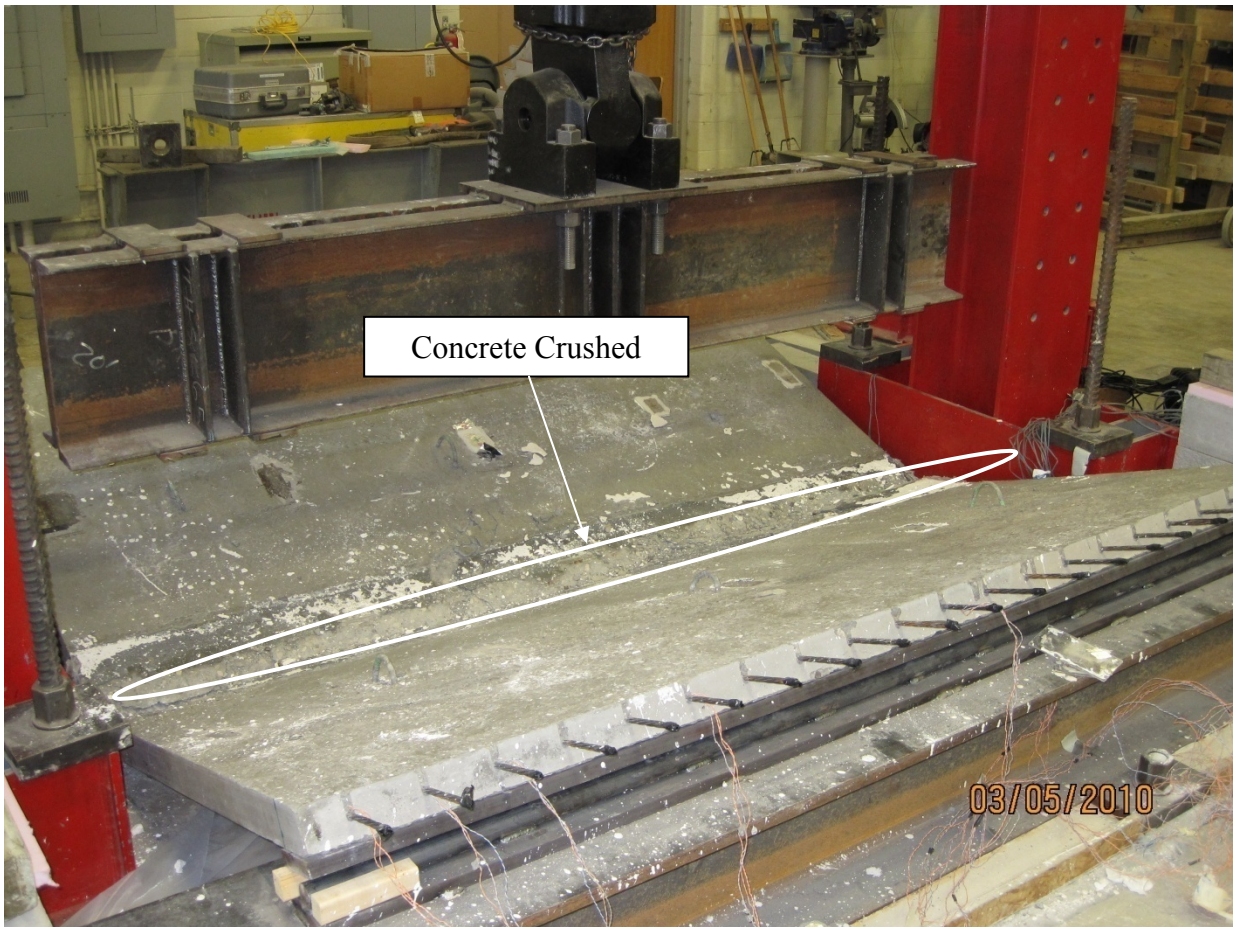

Figure C- 9 Flexural Failure at Midspan by Concrete Crushing of Panel ST-NC-SL

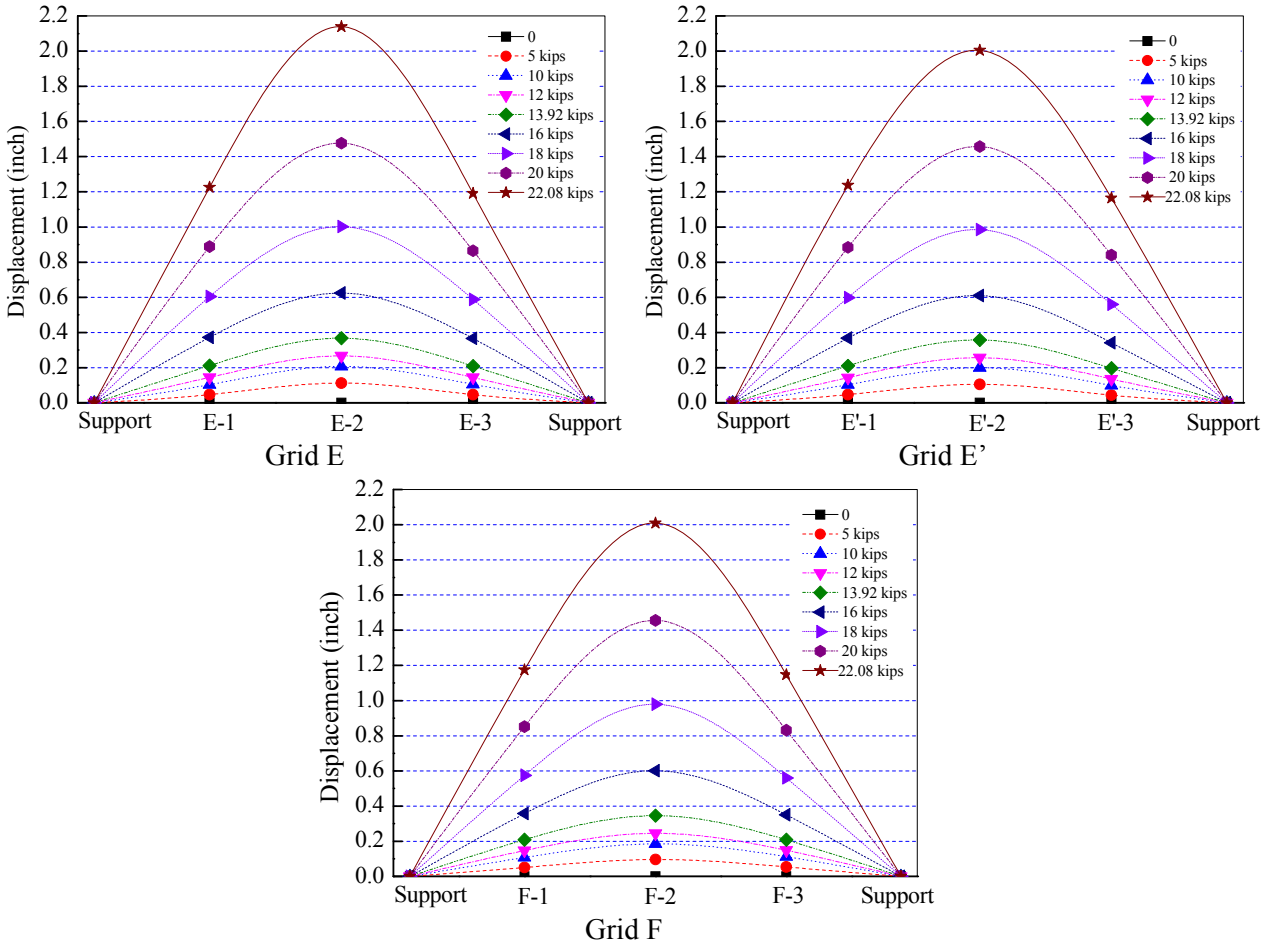

Figure C- 10 Panel ST-NC-SL: Measured Displacement Along Panel Length

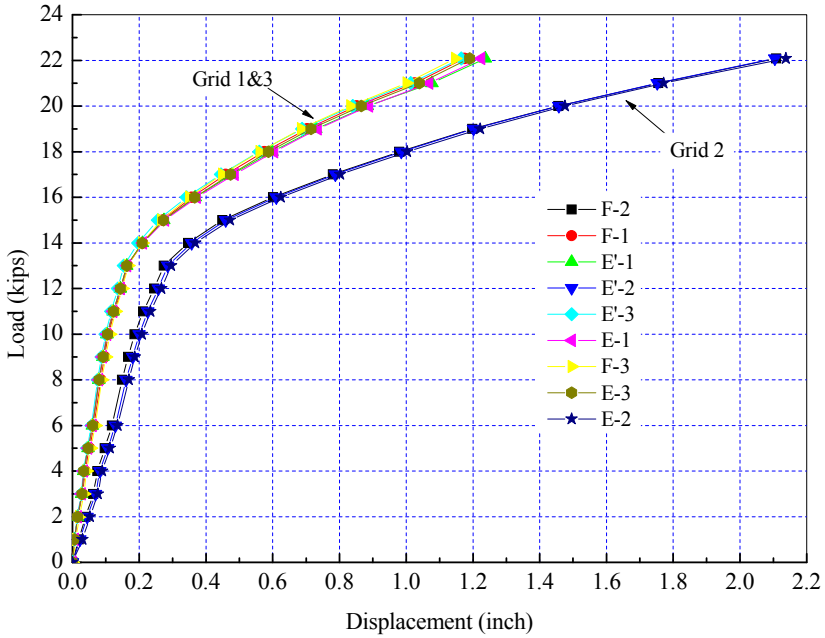

Figure C- 11 Panel ST-NC-SL: Applied Load-Displacement Relationship

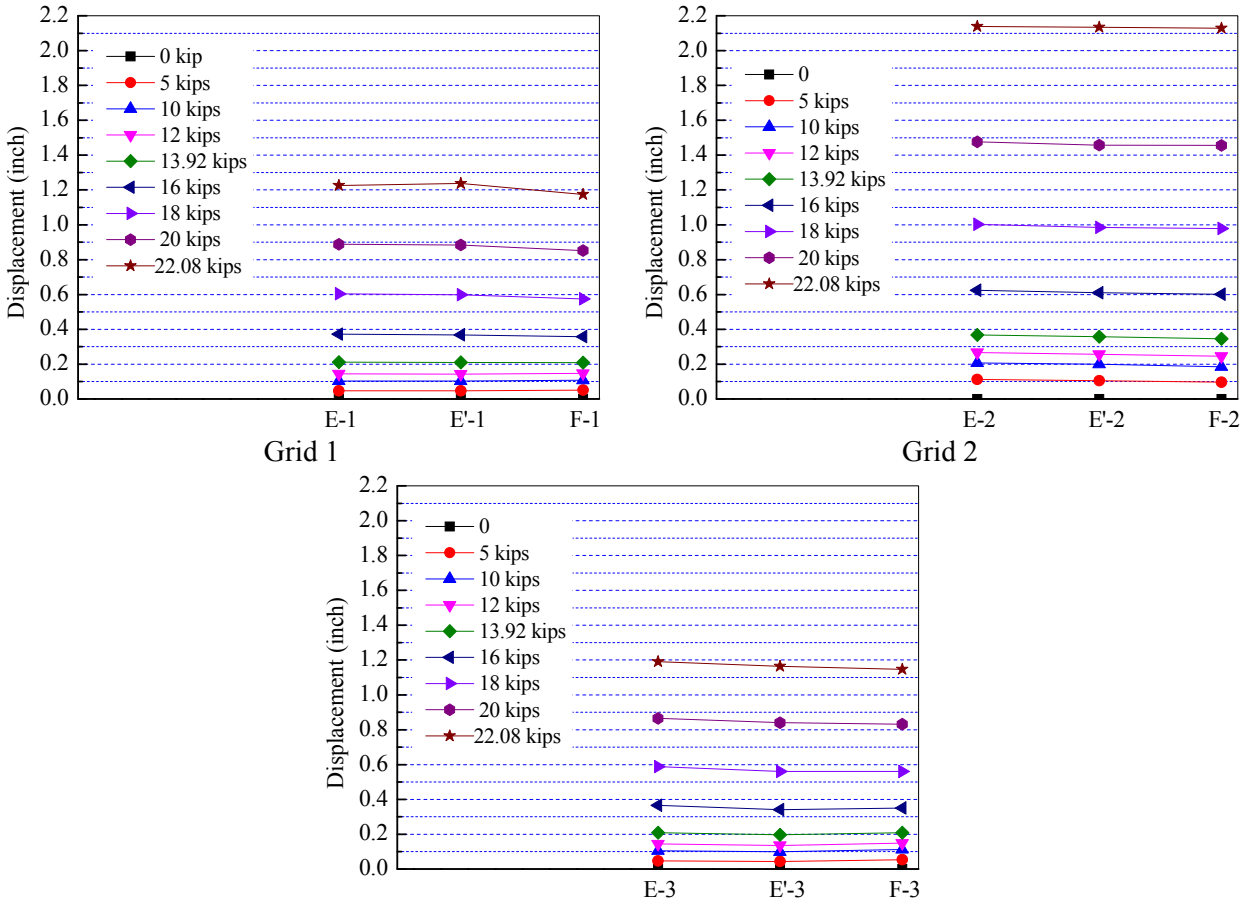

Figure C- 12 Panel ST-NC-SL: Measured Displacement Along Panel Width

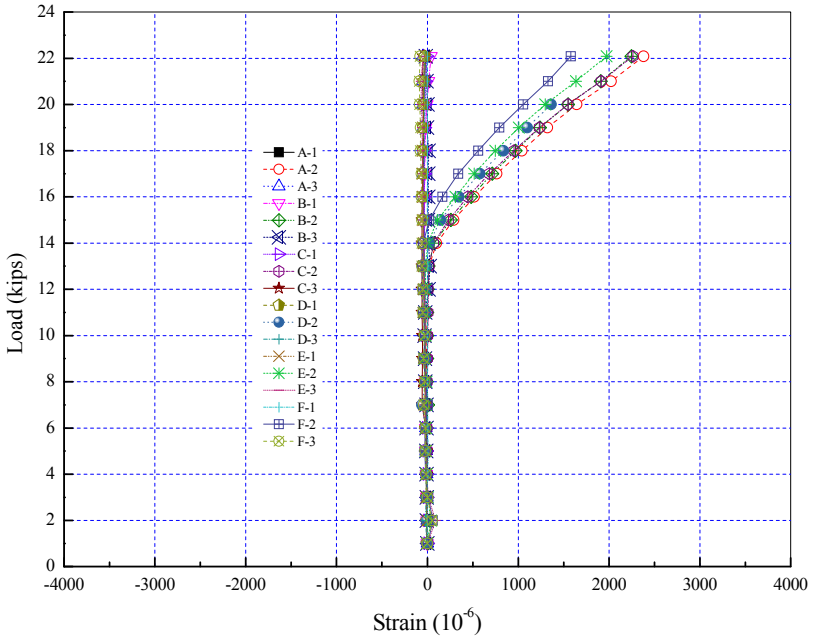

Figure C- 13 Panel ST-NC-SL: Applied Load-Tendon Strain Relationship

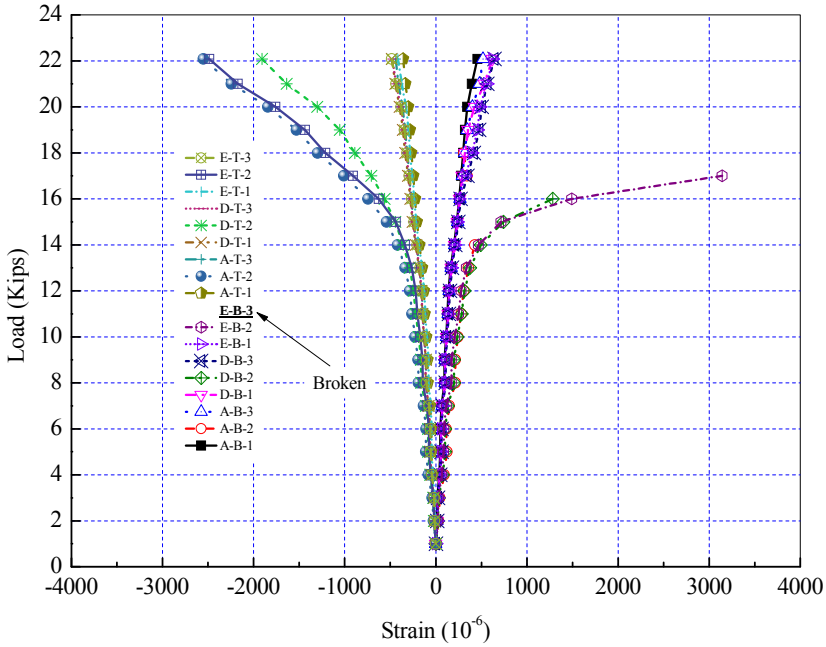

Figure C- 14 Panel ST-NC-SL: Applied Load-Concrete Surface Strain Relationship

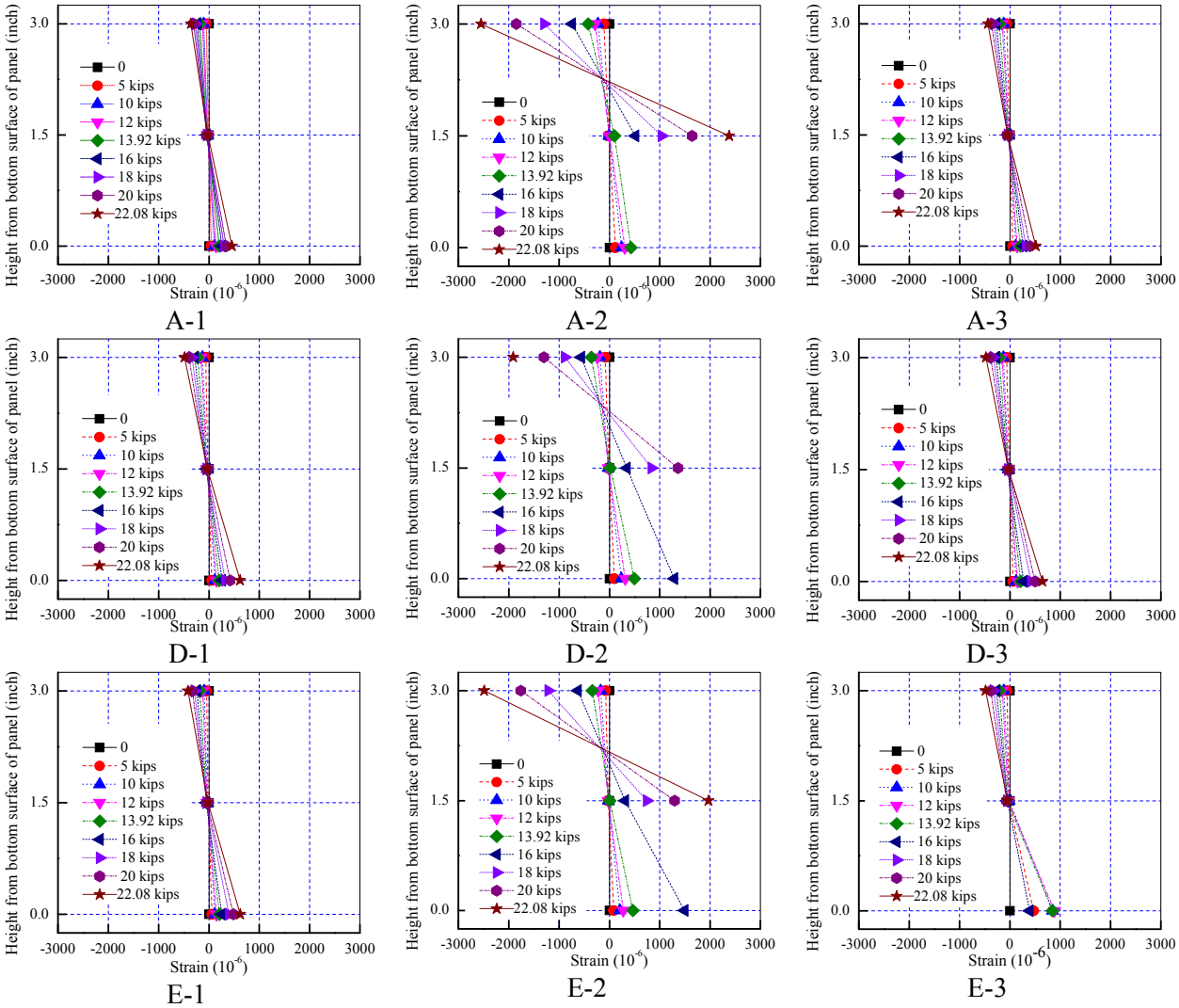

Figure C- 15 Panel ST-NC-SL: Measured Strain Distribution

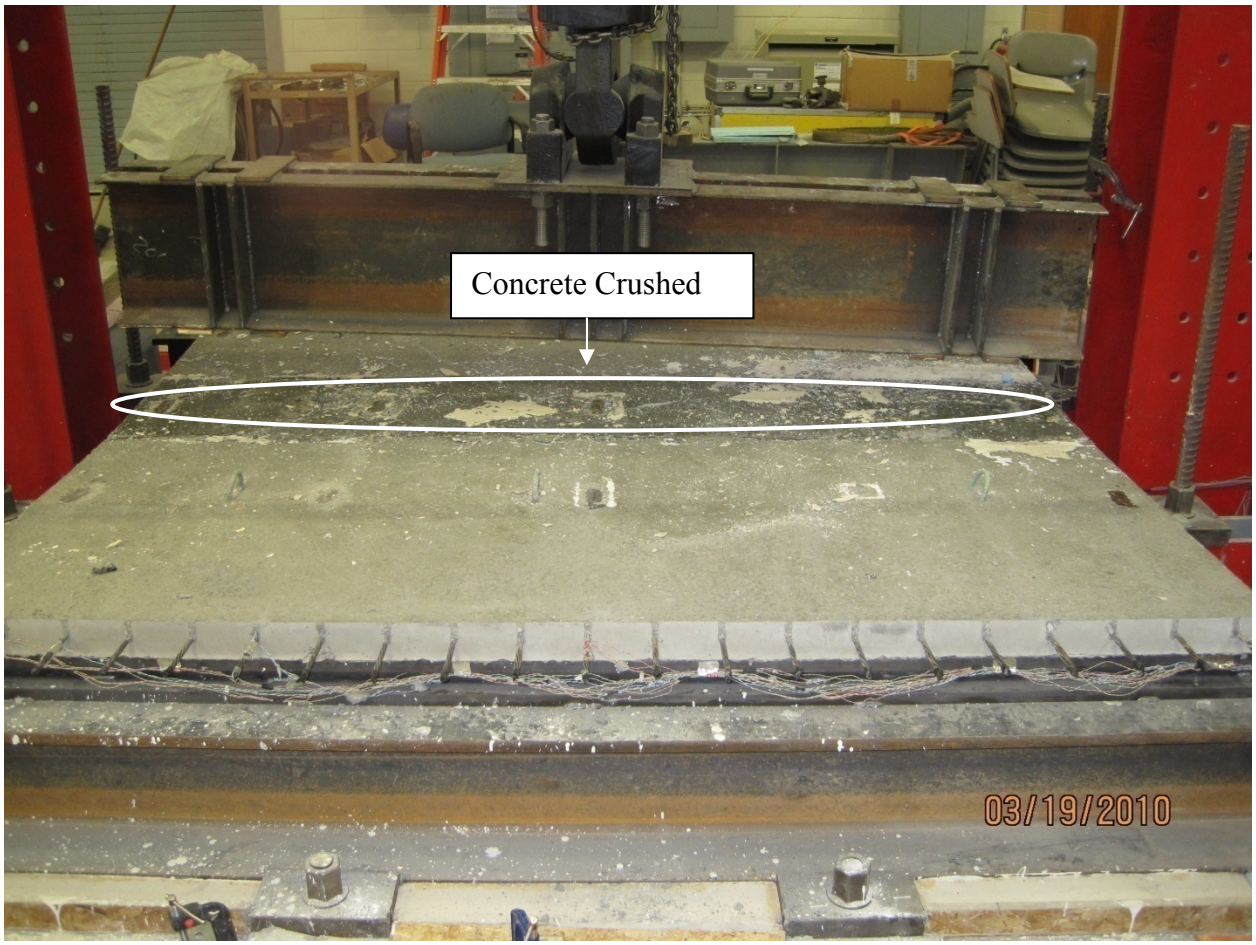

Figure C- 16 Flexural Failure at Midspan by Concrete Crushing of Panel ST-FRC-SL

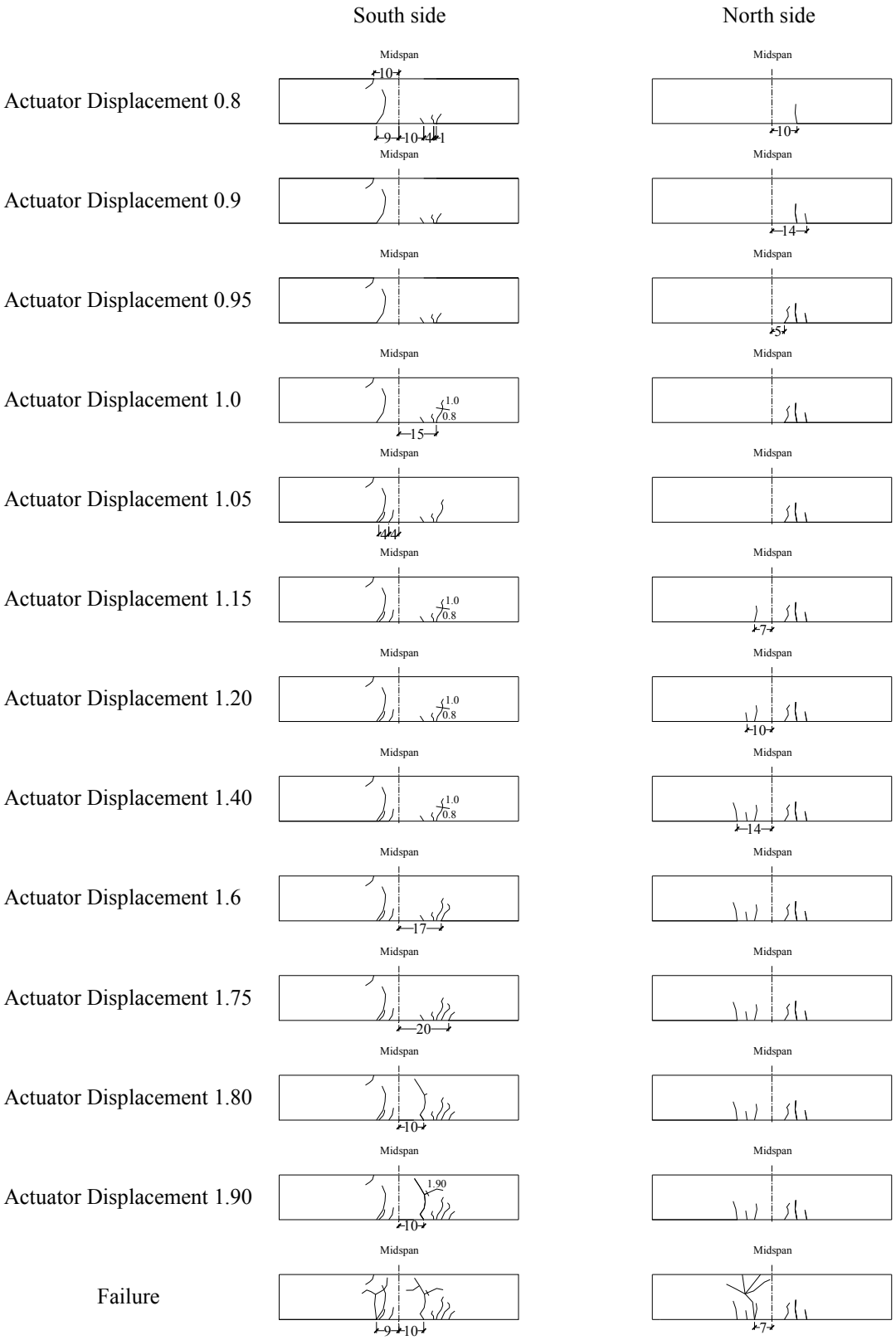

Figure C- 17 Panel ST-FRC-SL: Propagation of Cracking

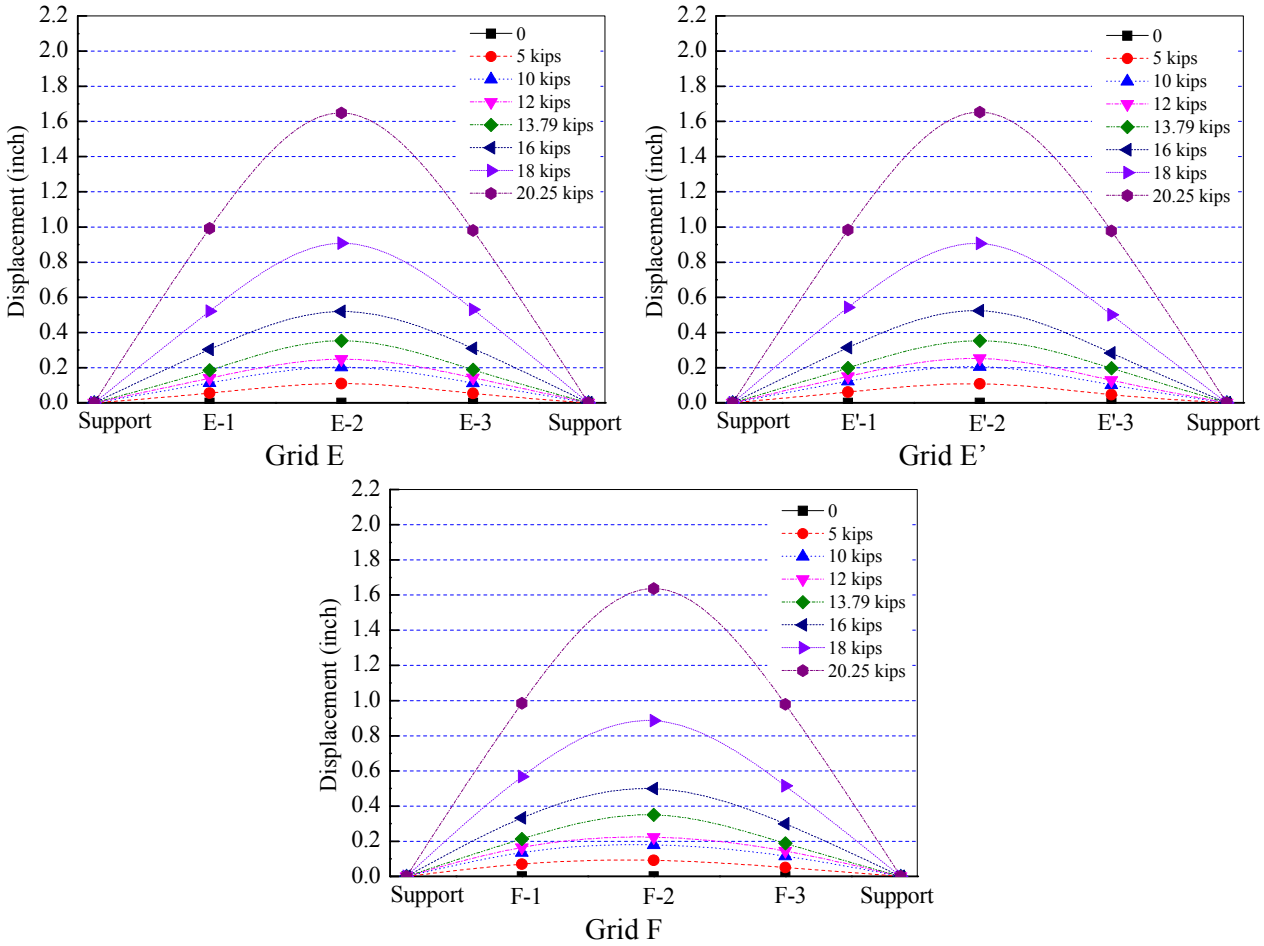

Figure C- 18 Panel ST-FRC-SL: Measured Displacement Along Panel Length

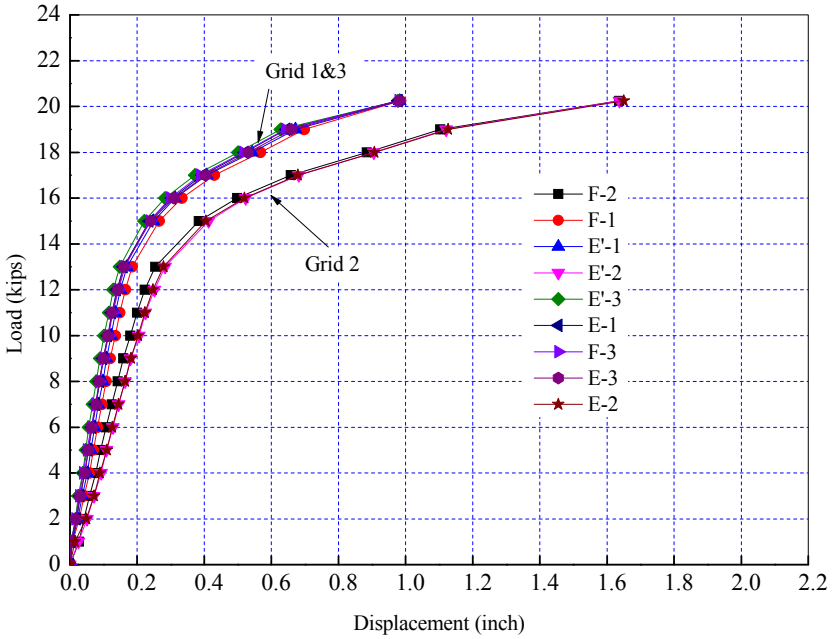

Figure C- 19 Panel ST-FRC-SL: Applied Load-Displacement Relationship

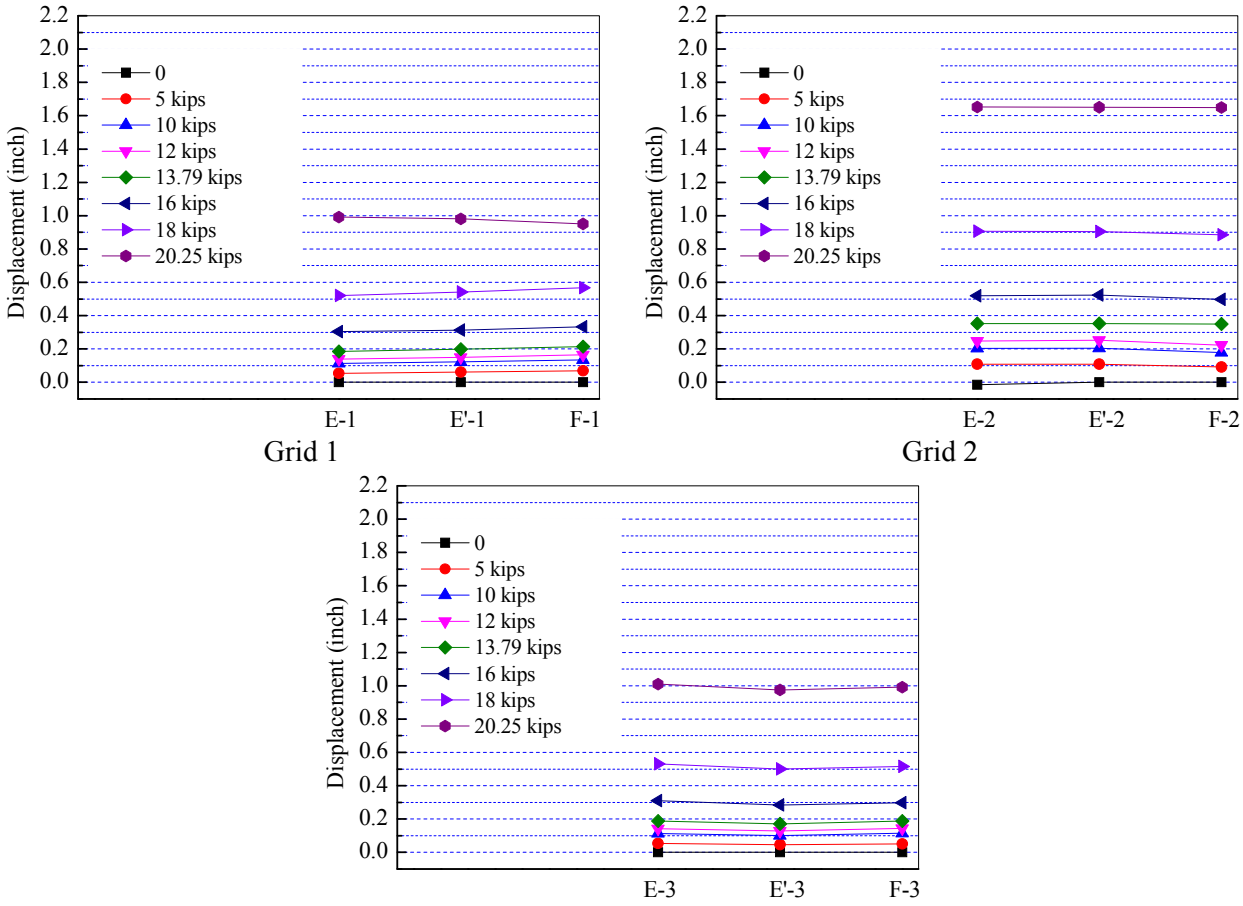

Figure C- 20 Panel ST-FRC-SL: Measured Displacement Along Panel Width

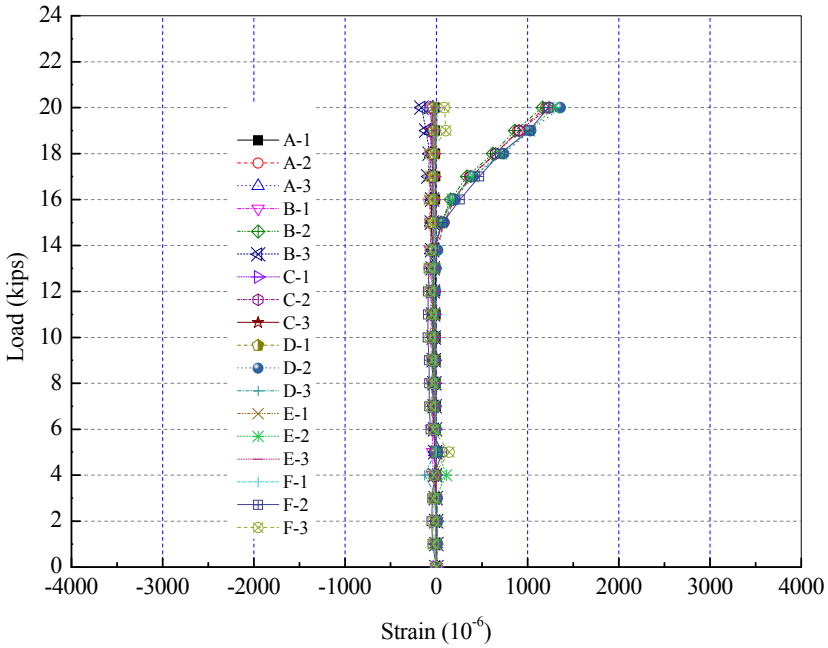

Figure C- 21 Panel ST-FRC-SL: Applied Load-Tendon Strain Relationship

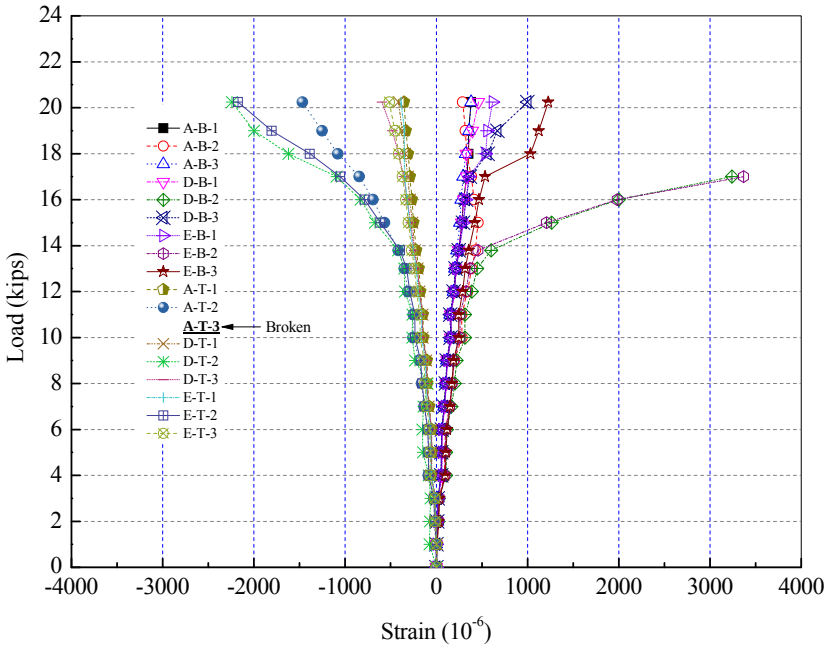

Figure C- 22 Panel ST-FRC-SL: Applied Load-Concrete Surface Strain Relationship

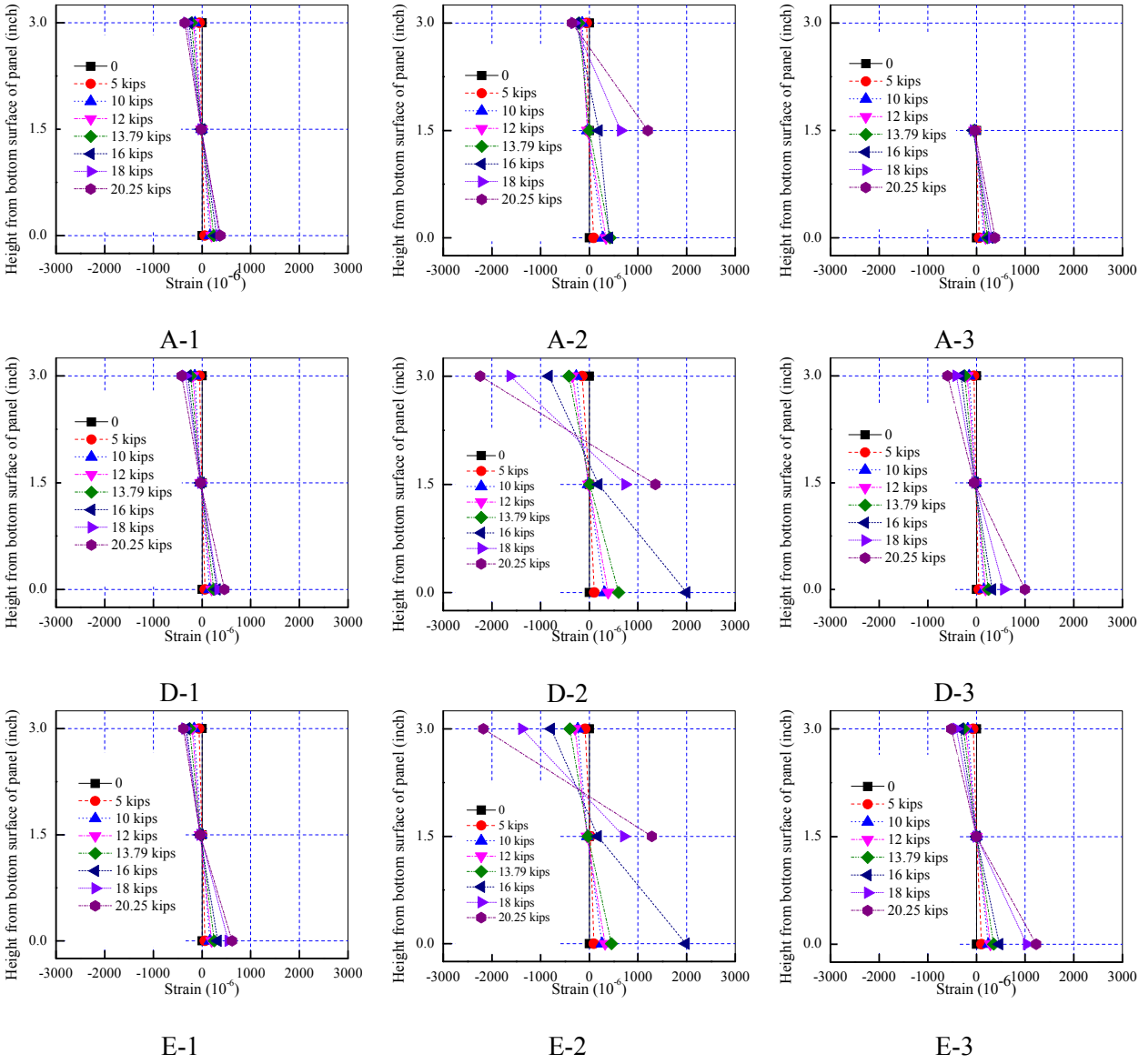

Figure C- 23 Panel ST-FRC-SL: Measured Strain Distribution

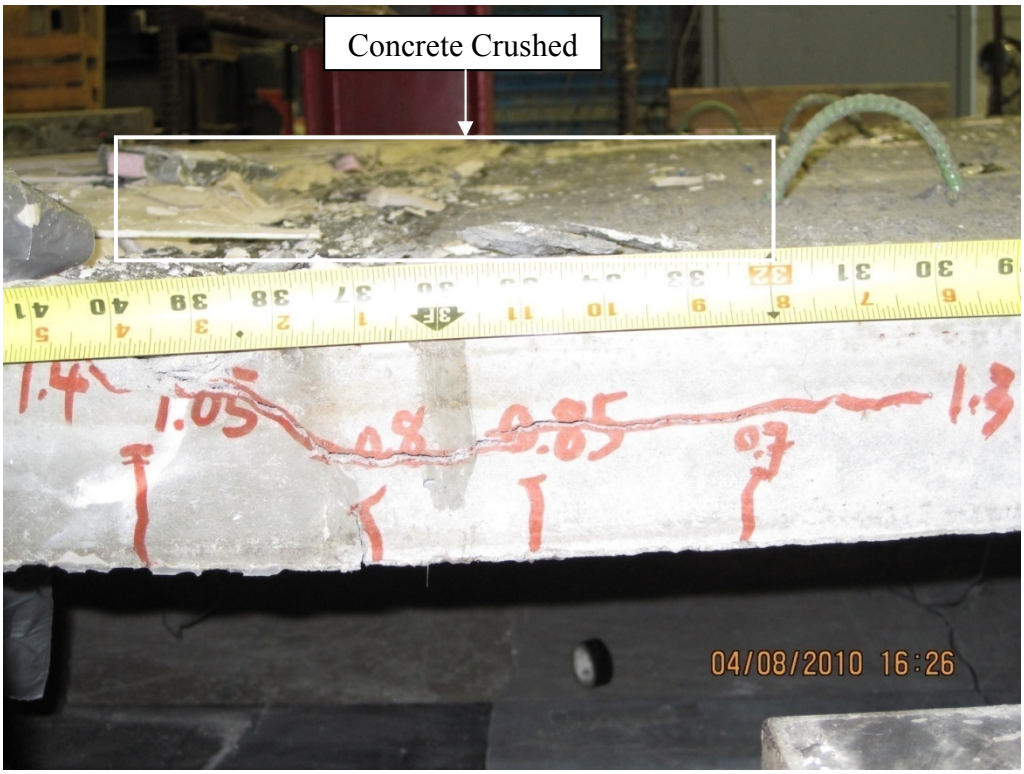

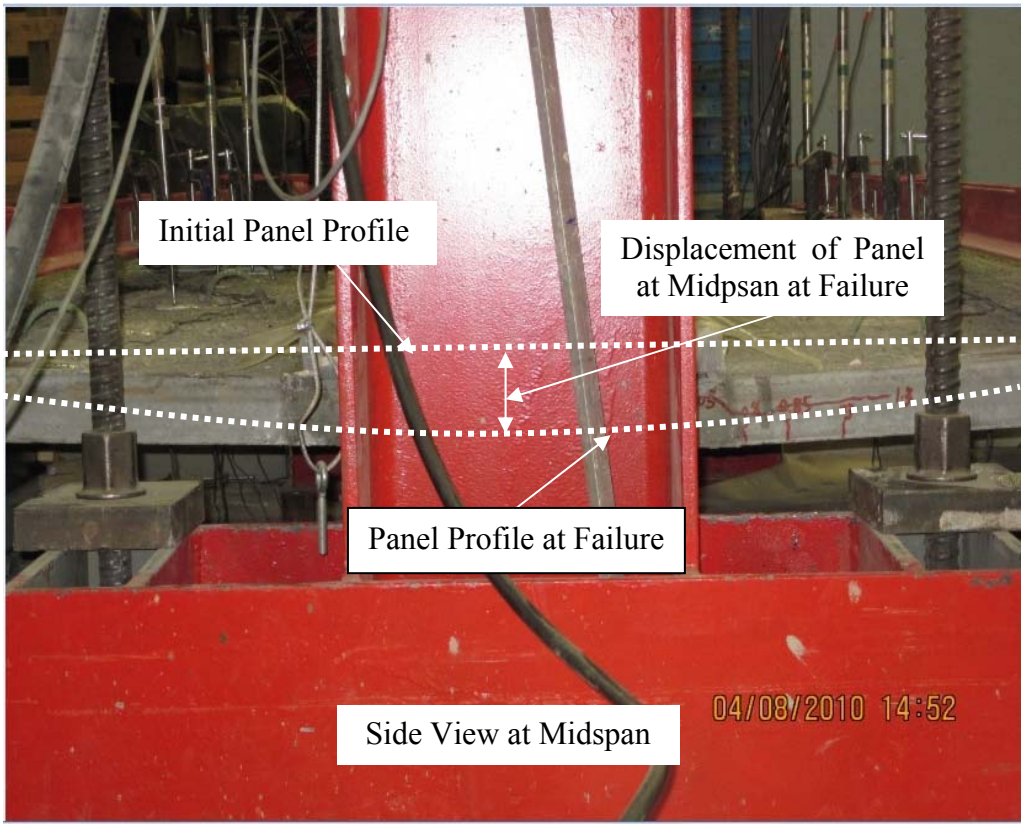

Figure C- 24 Flexural Failure at Midspan by Concrete Crushing of Panel ECST-NC-SL

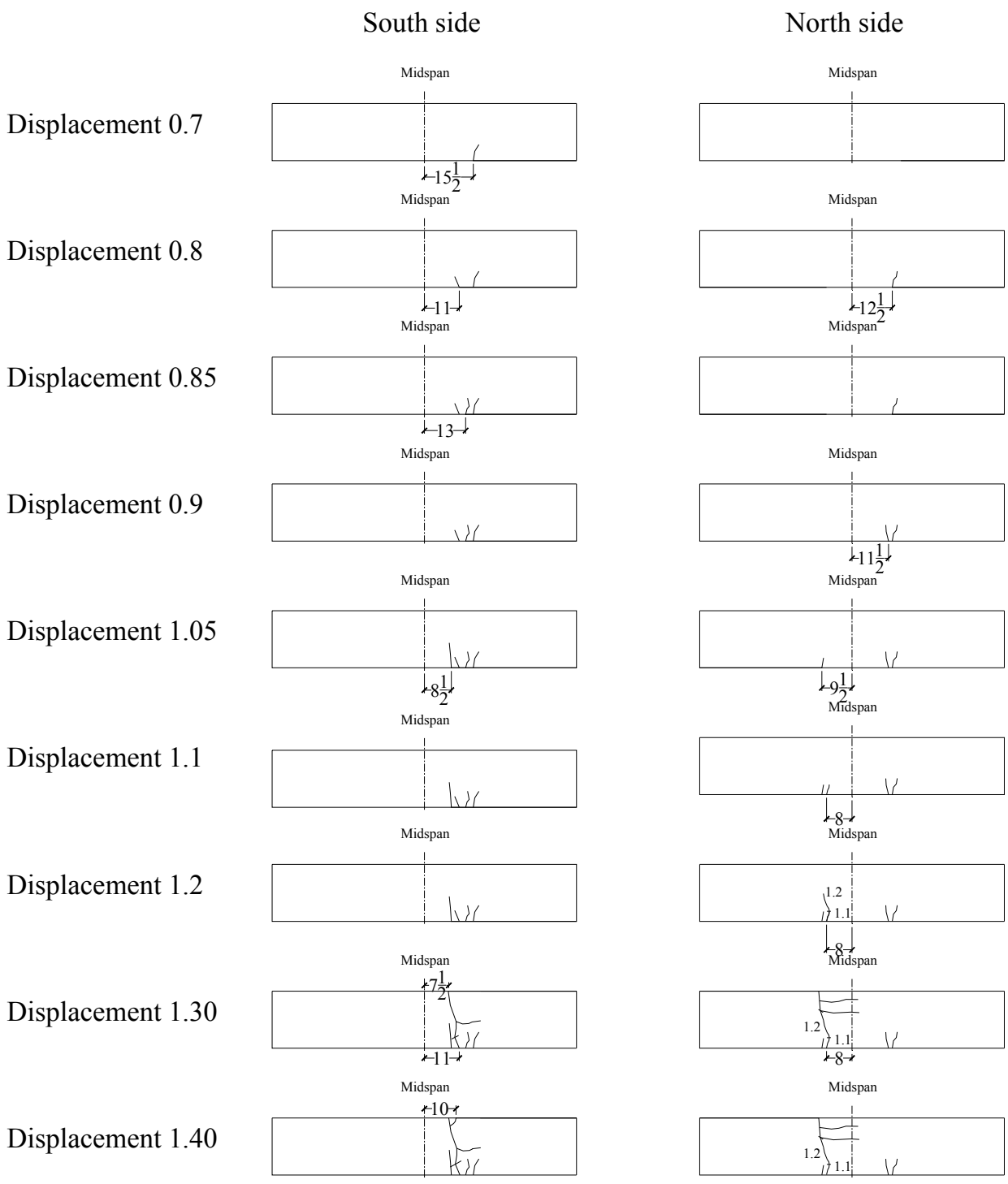

Figure C- 25 Panel ECST-NC-SL: Propagation of Cracking

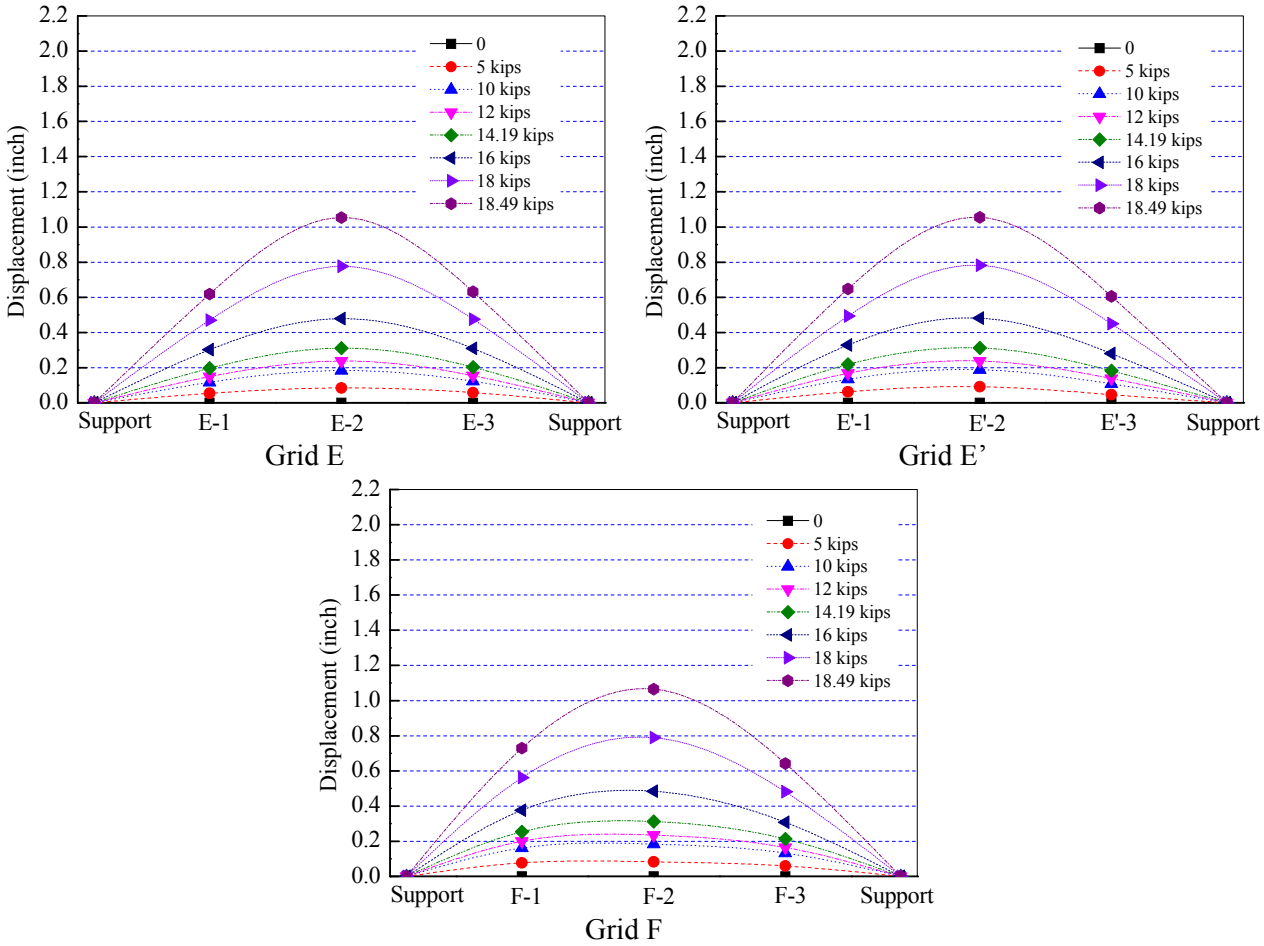

Figure C- 26 Panel ECST-NC-SL: Measured Displacement Along Panel Length

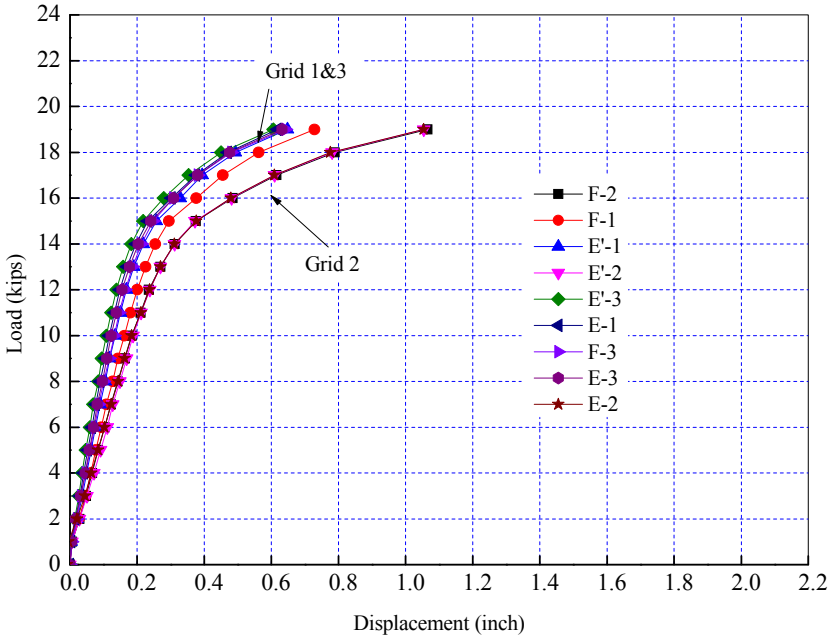

Figure C- 27 Panel ECST-NC-SL: Applied Load-Displacement Relationship

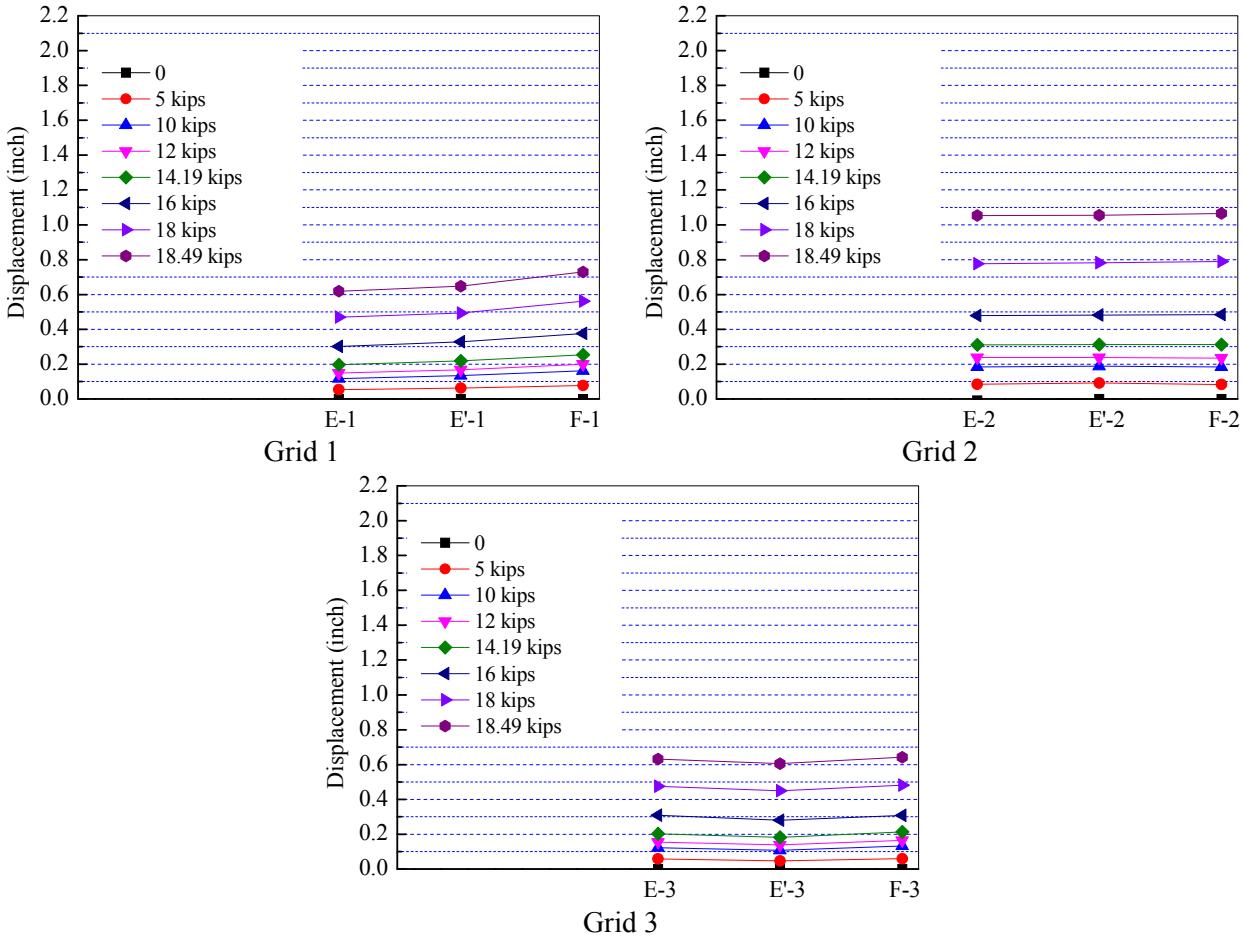

Figure C- 28 Panel ECST-NC-SL: Measured Displacement Along Panel Width

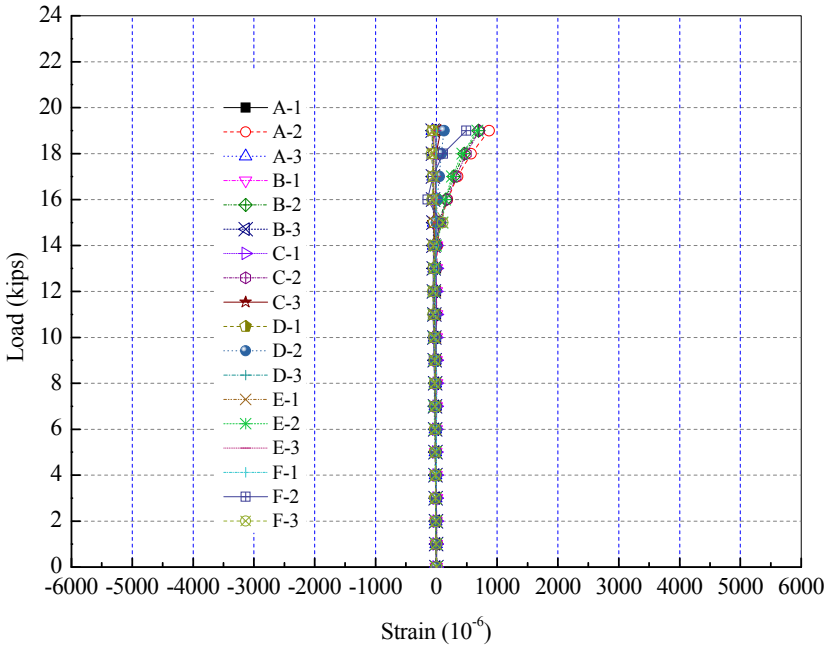

Figure C- 29 Panel ECST-NC-SL: Applied Load-Tendon Strain Relationship

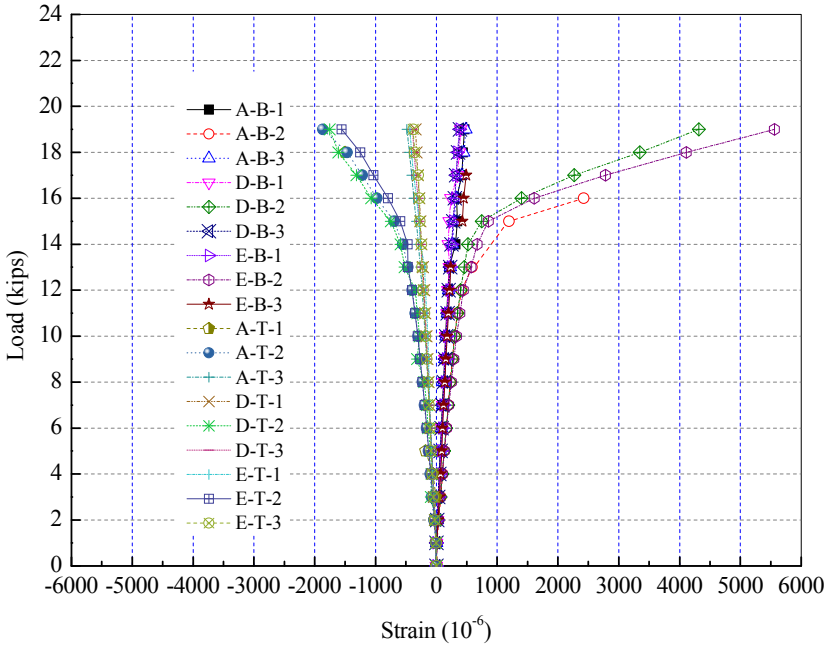

Figure C- 30 Panel ECST-NC-SL: Applied Load-Concrete Surface Strain Relationship

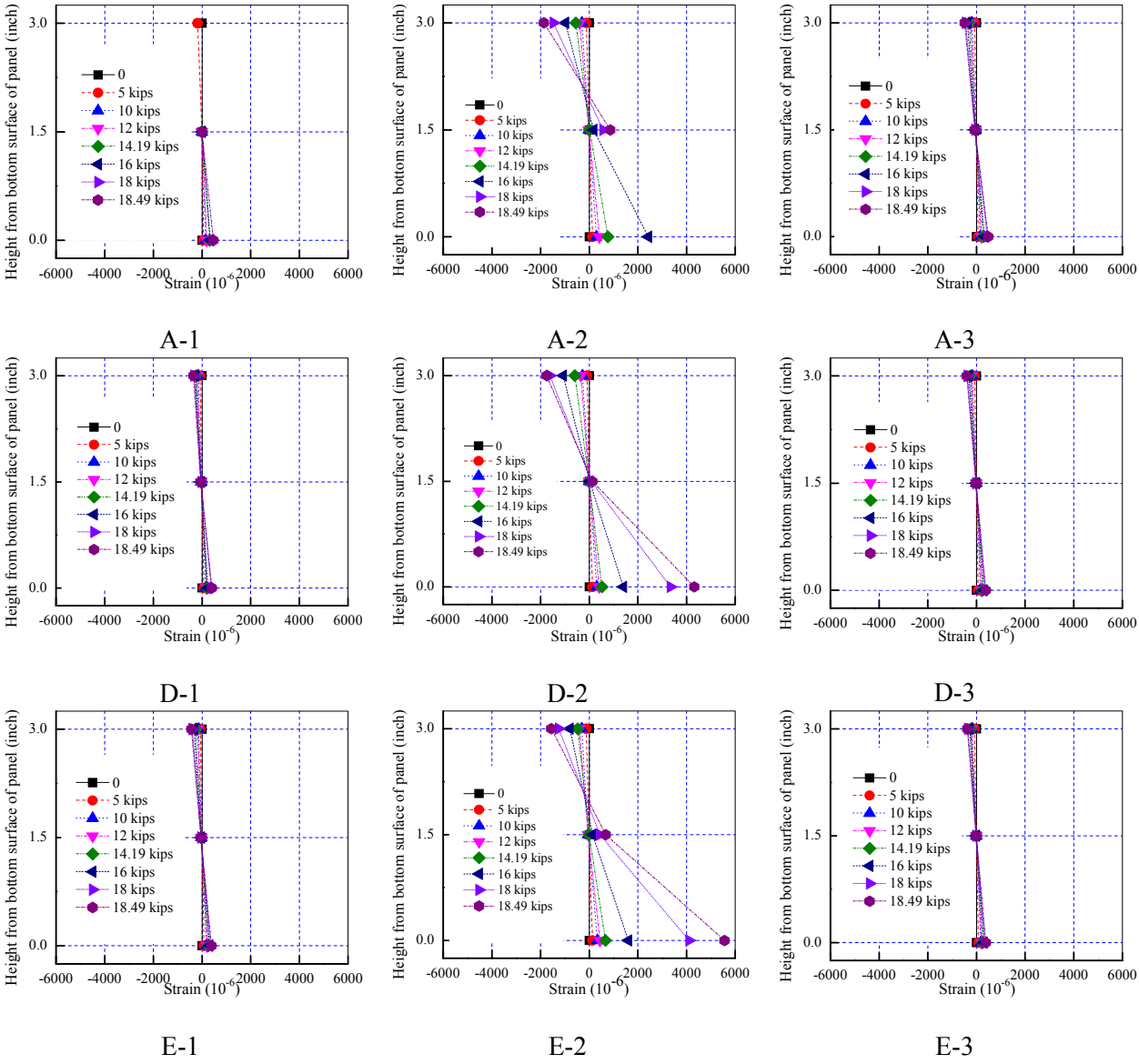

Figure C- 31 Panel ECST-NC-SL: Measured Strain Distribution

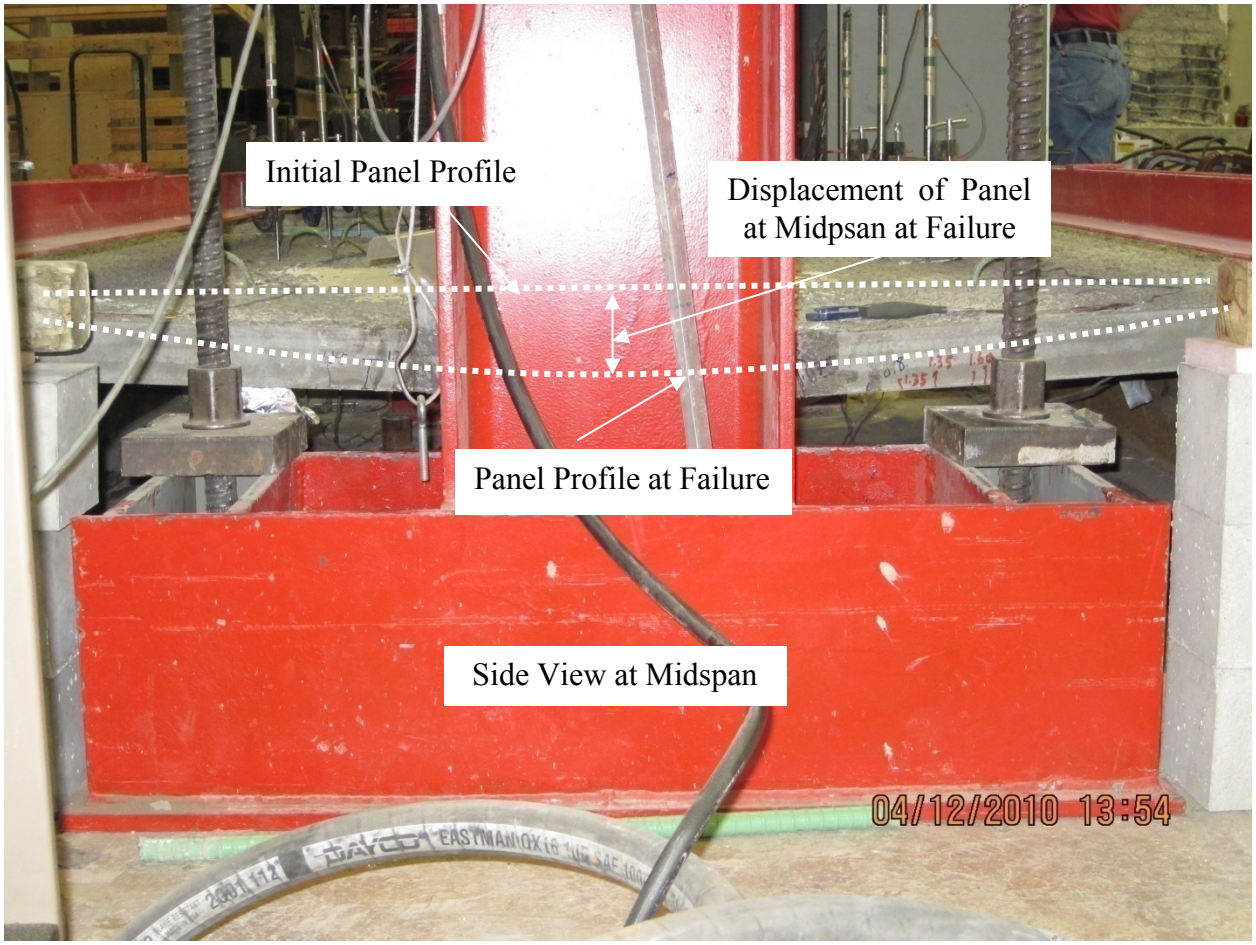

Figure C- 32 Flexural Failure at Midspan by Concrete Crushing of Panel ECST-FRC-SL

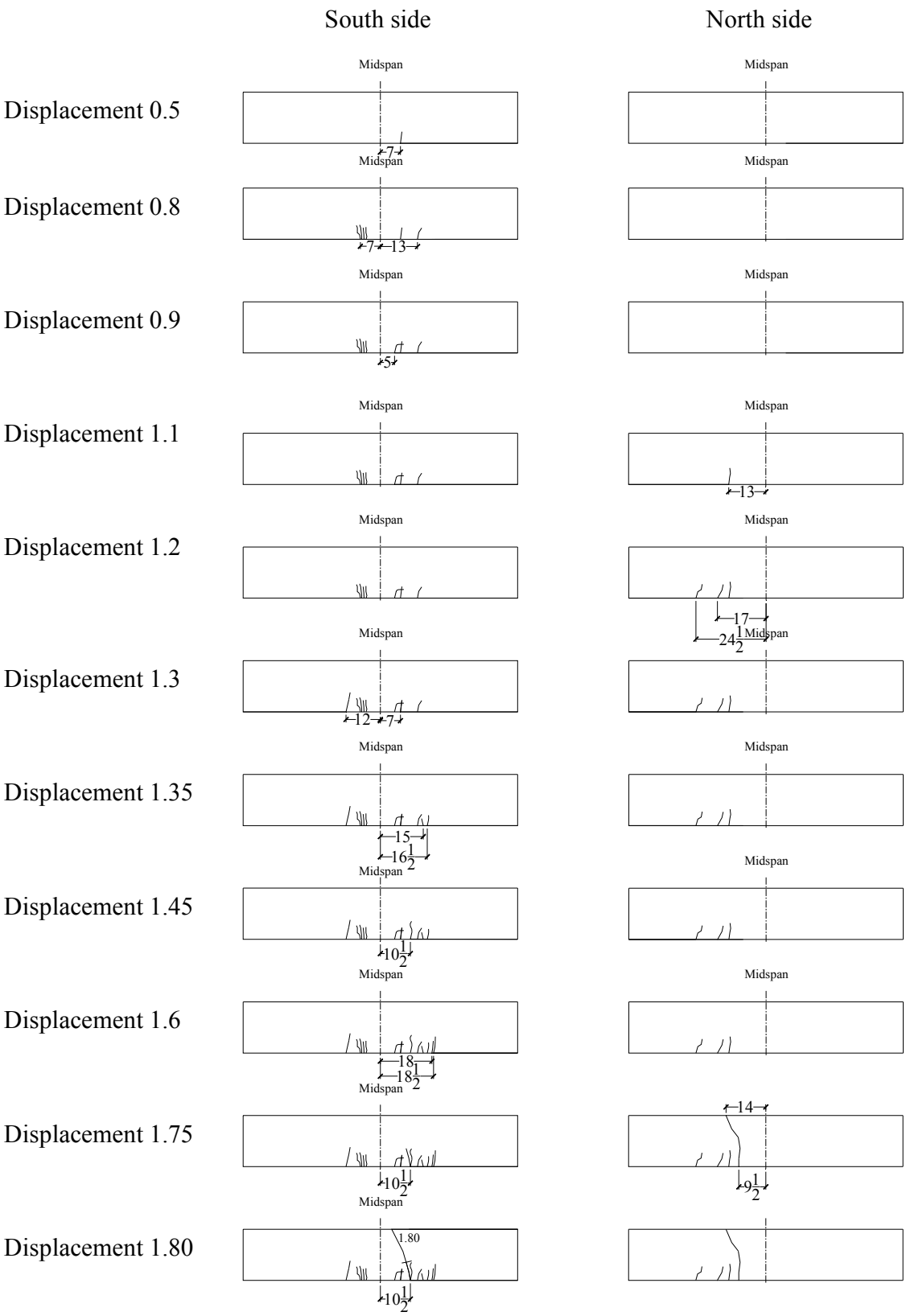

Figure C- 33 Panel ECST-FRC-SL: Propagation of Cracking

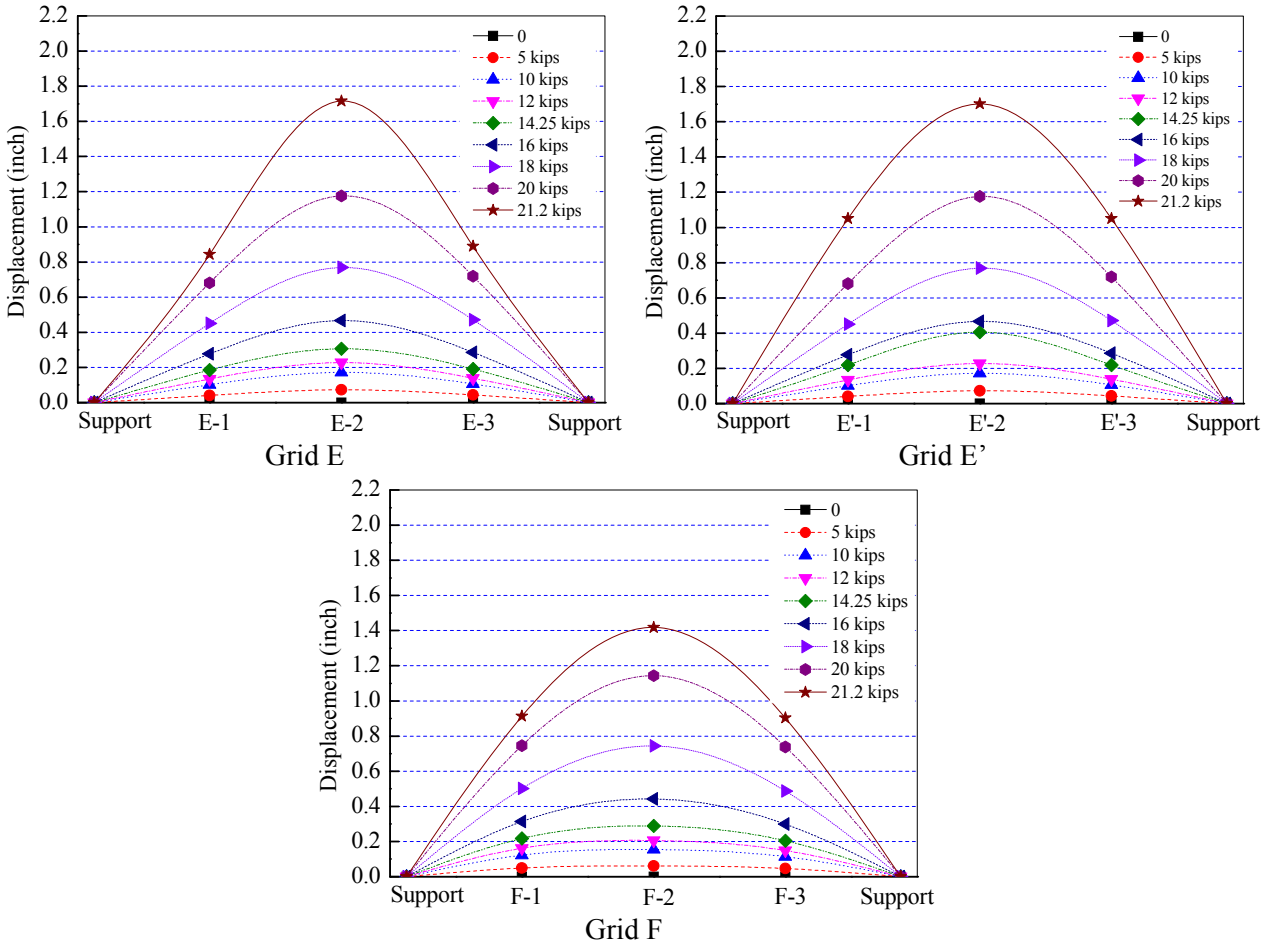

Figure C- 34 Panel ECST-FRC-SL: Measured Displacement Along Panel Length

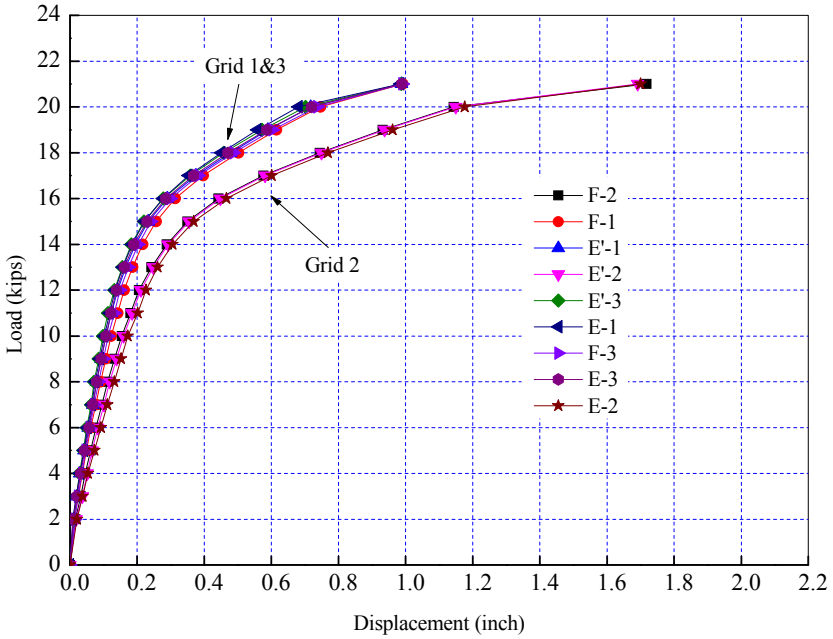

Figure C- 35 Panel ECST-FRC-SL: Applied Load-Displacement Relationship

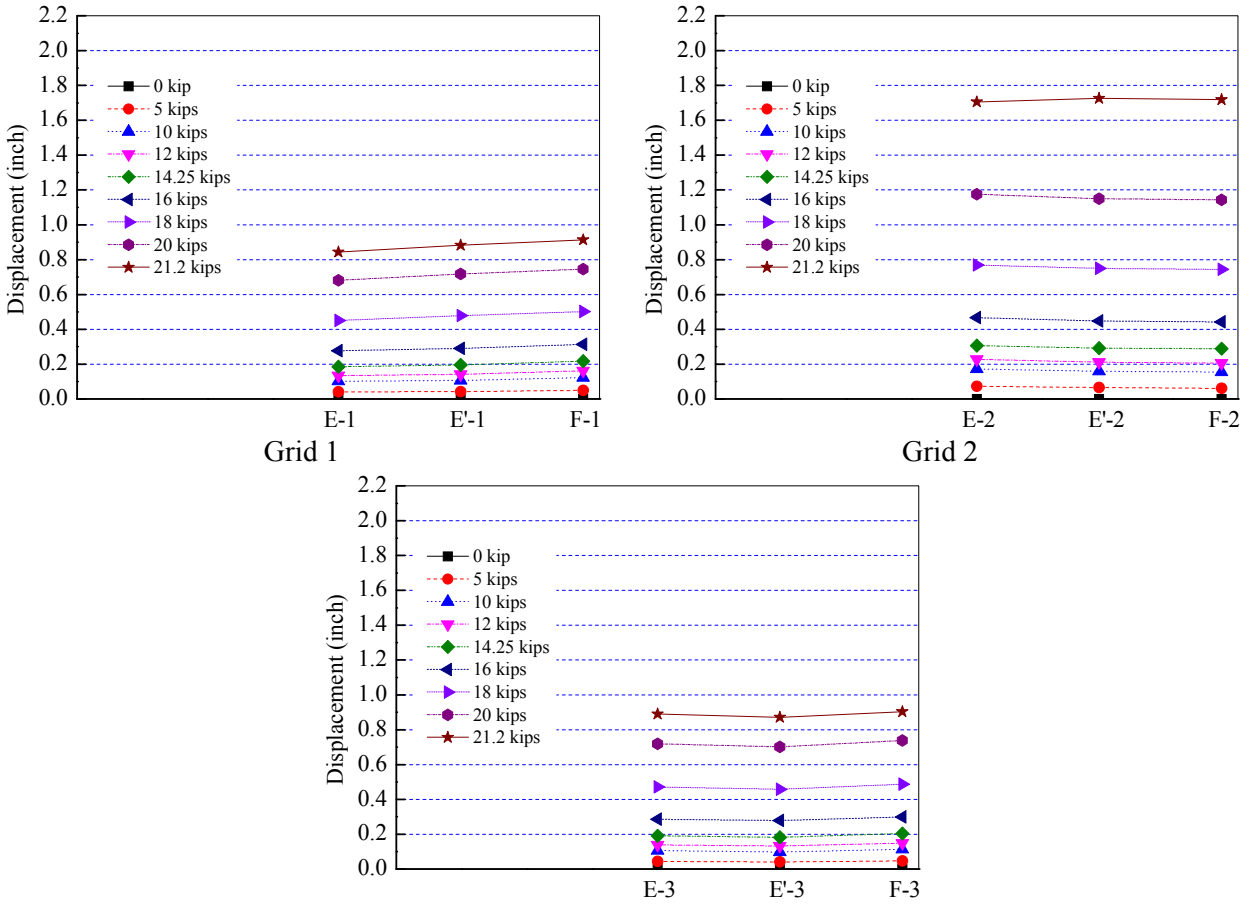

Figure C- 36 Panel ECST-FRC-SL: Measured Displacement Along Panel Width

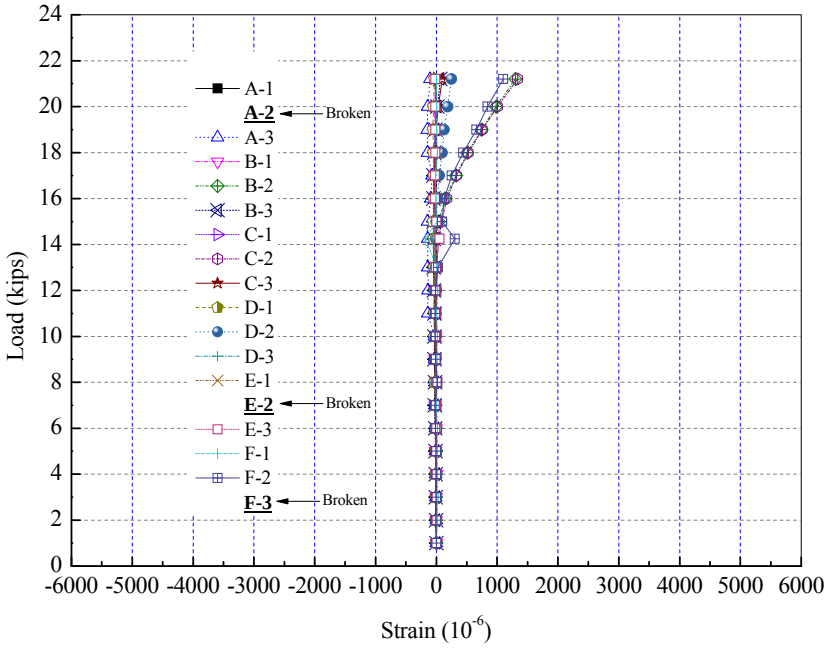

Figure C- 37 Panel ECST-FRC-SL: Applied Load-Tendon Strain Relationship

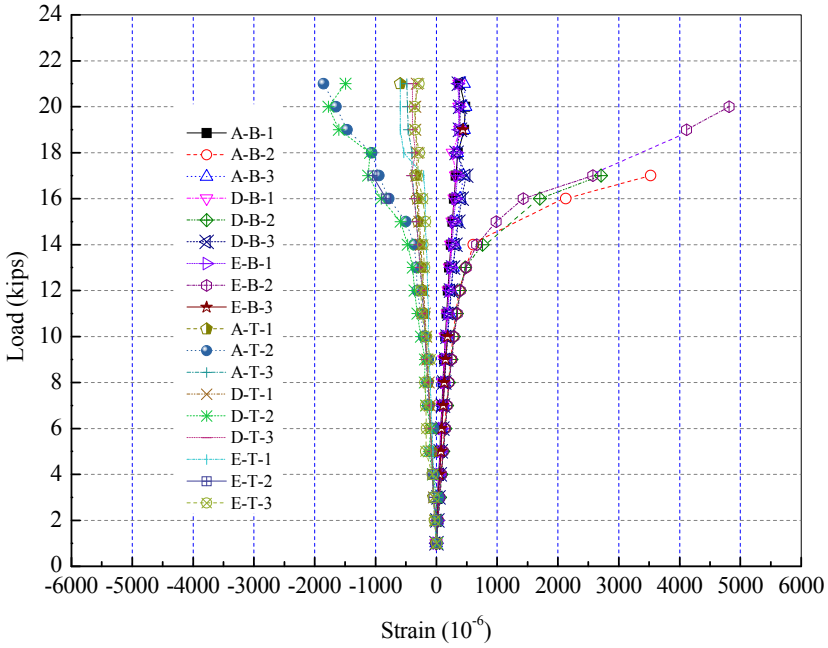

Figure C- 38 Panel ECST-FRC-SL: Applied Load-Concrete Surface Strain Relationship

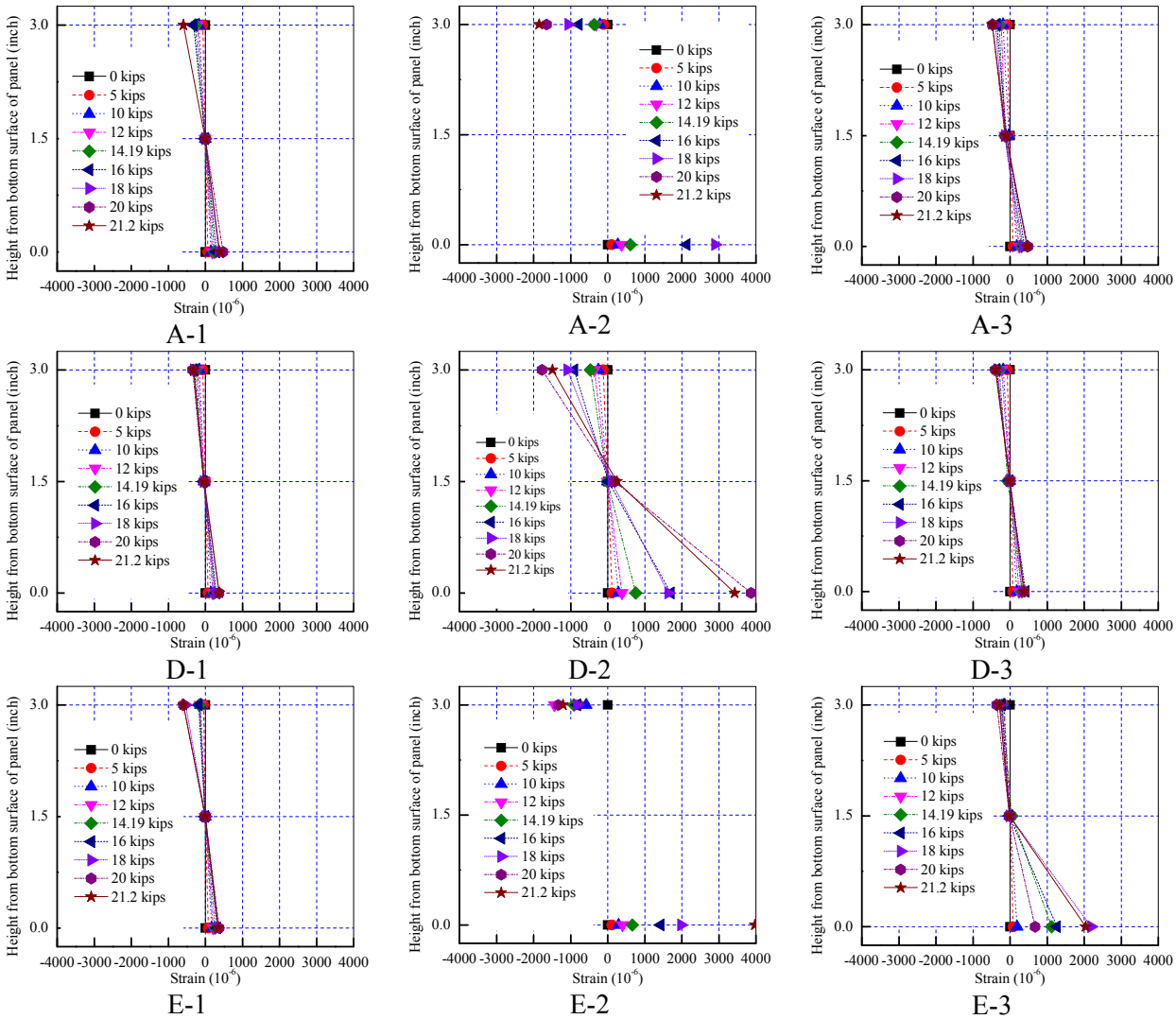

Figure C- 39 Panel ECST-FRC-SL: Measured Strain Distribution

Figure C- 40 Flexural Failure at Midspan by Concrete Crushing of Panel CFRPT-NC-SL

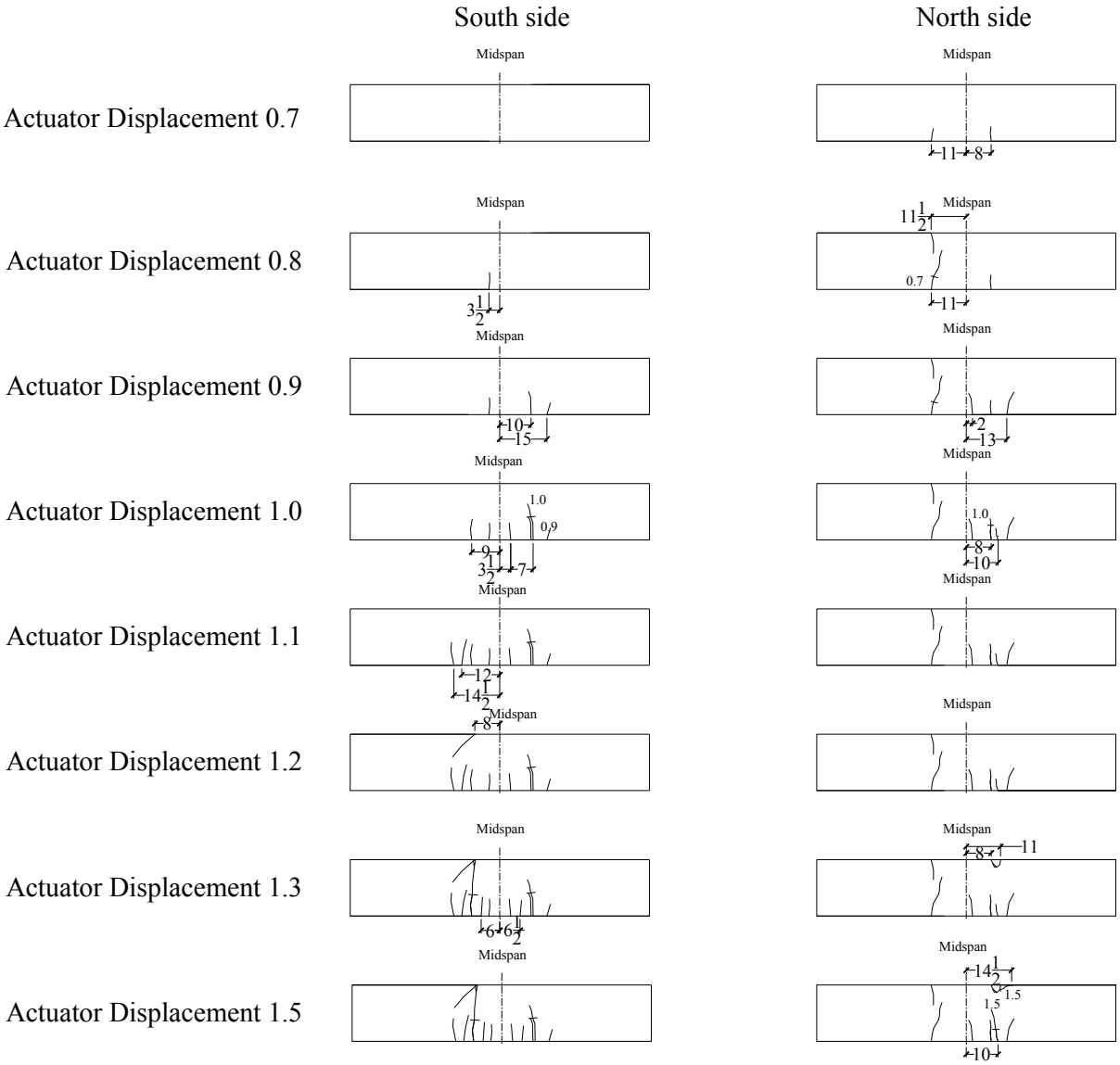

Figure C- 41 Panel CFRPT-NC-SL: Propagation of Cracking

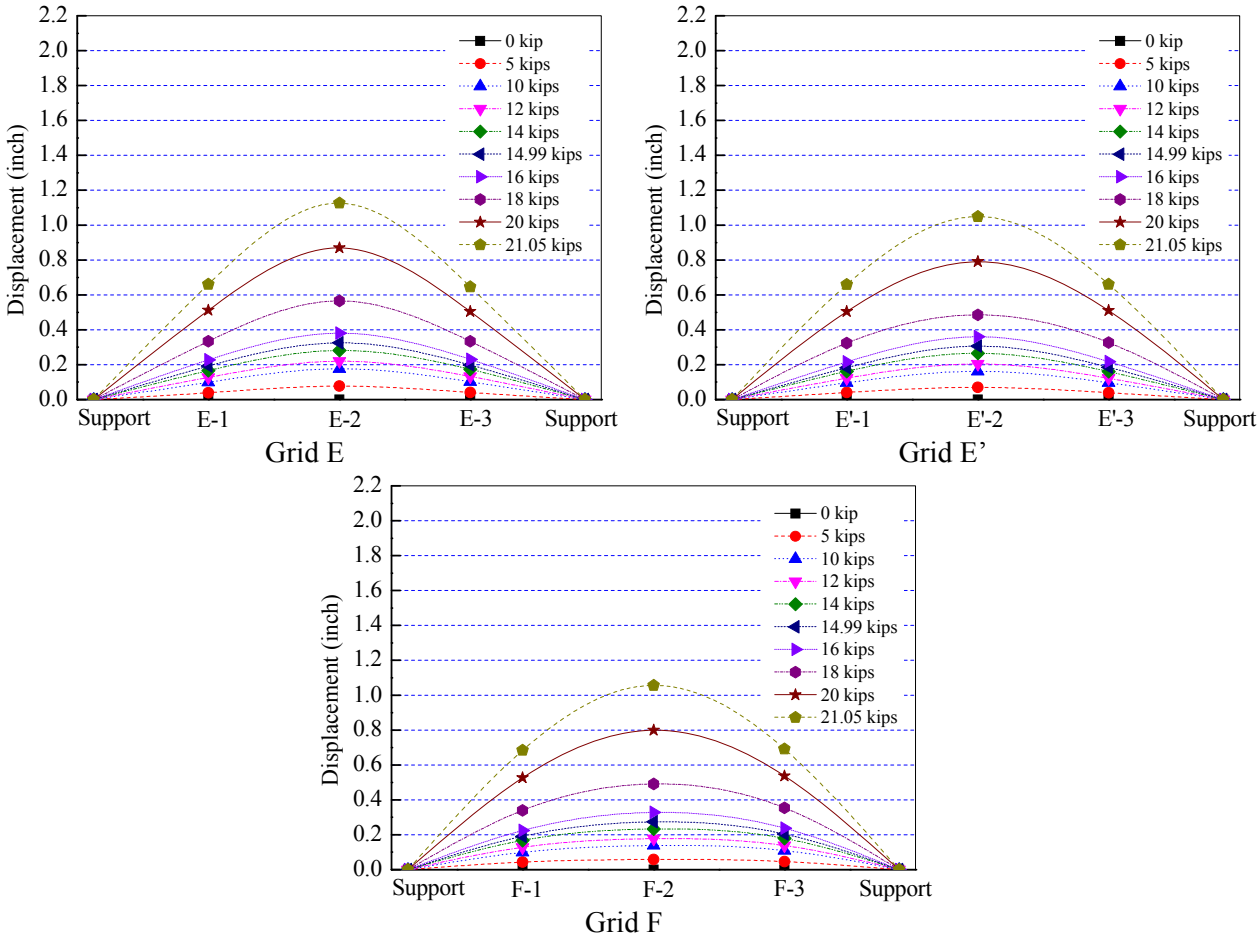

Figure C- 42 Panel CFRPT-NC-SL: Measured Displacement Along Panel Length

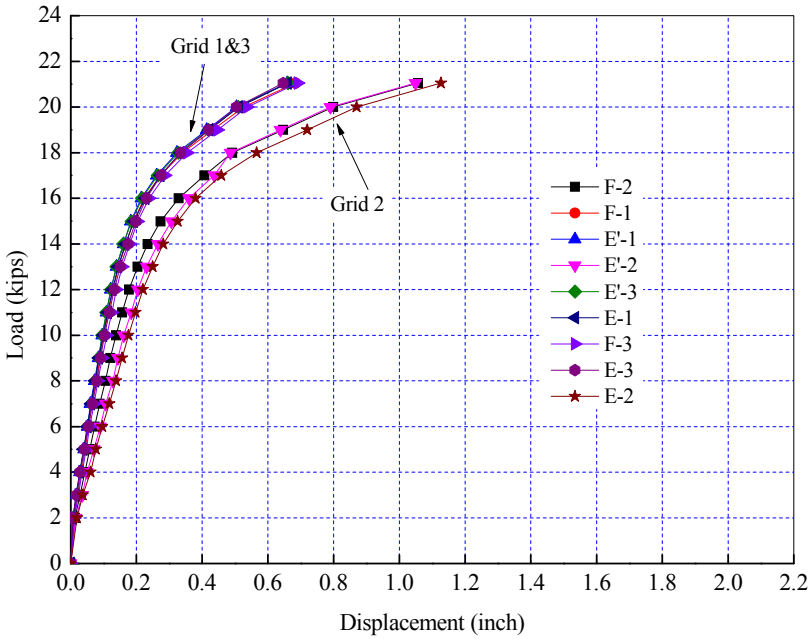

Figure C- 43 Panel CFRPT-NC-SL: Applied Load-Displacement Relationship

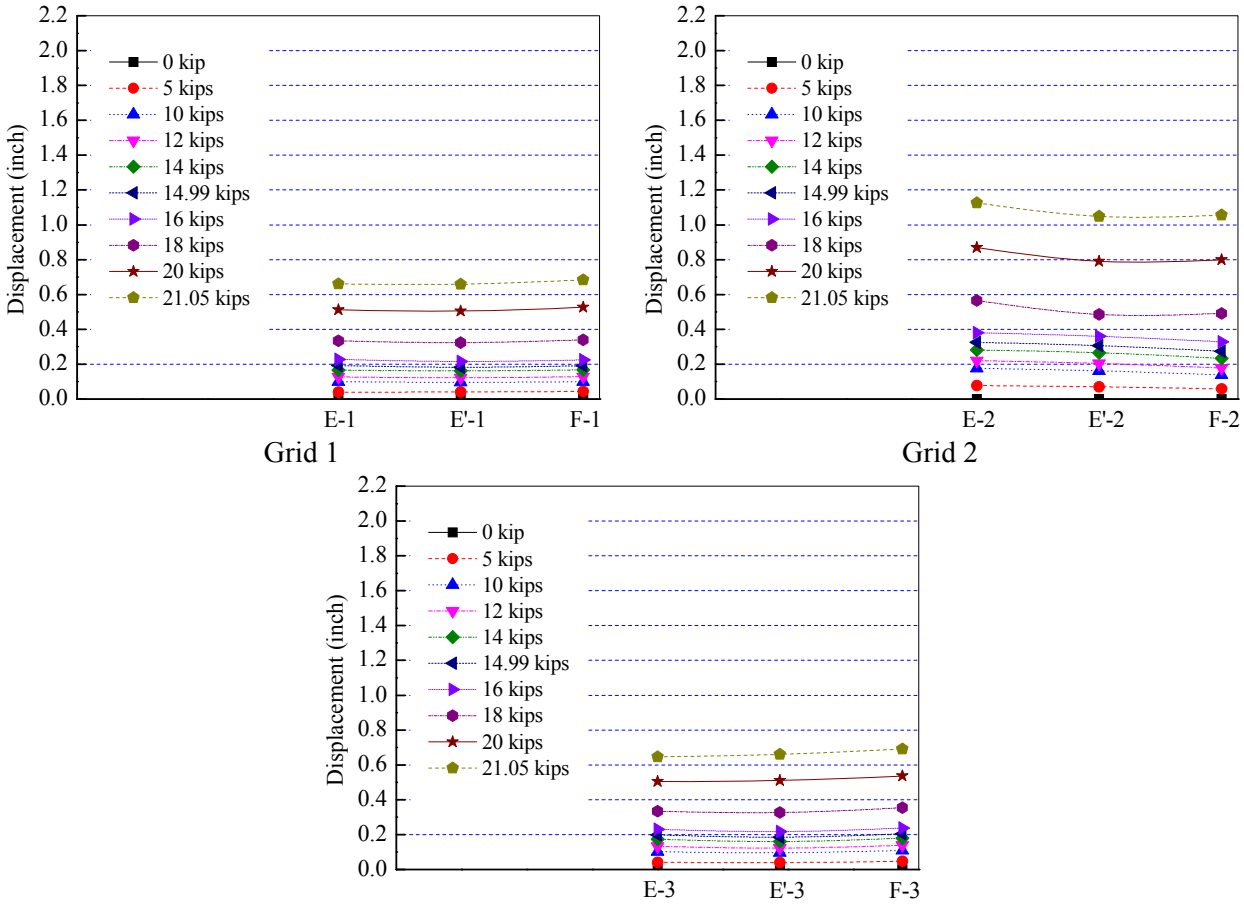

Figure C- 44 Panel CFRPT-NC-SL: Measured Displacement Along Panel Width

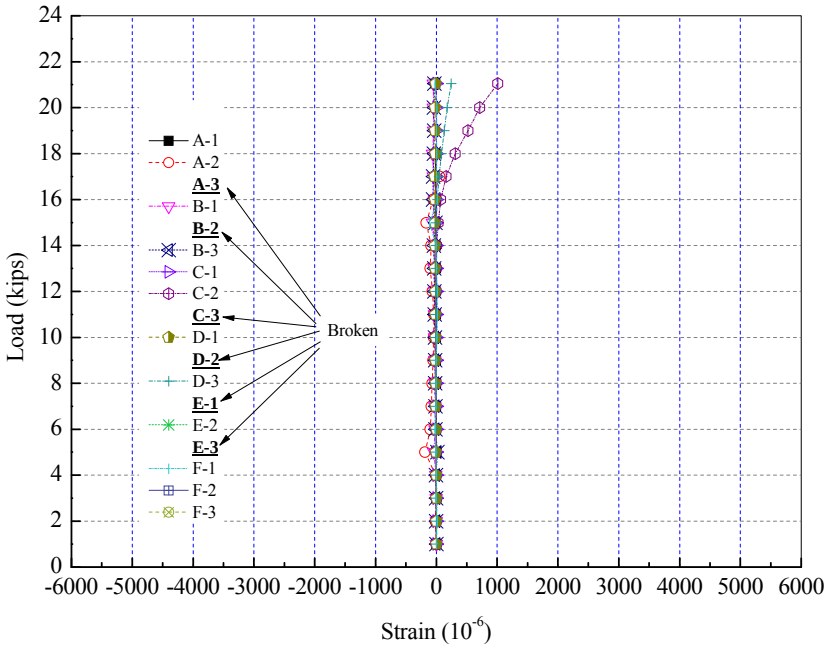

Figure C- 45 Panel CFRPT-NC-SL: Applied Load-Tendon Strain Relationship

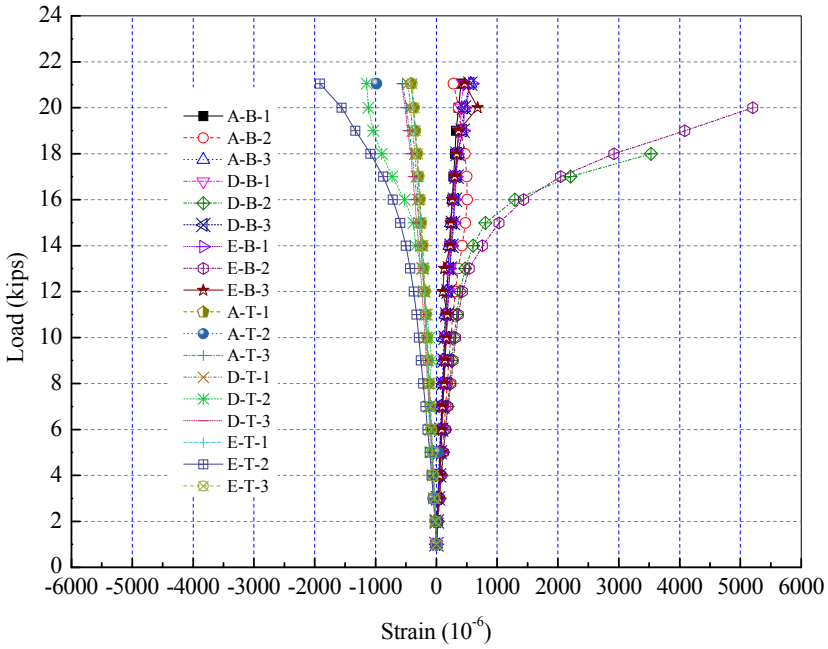

Figure C- 46 Panel CFRPT-NC-SL: Applied Load-Concrete Surface Strain Relationship

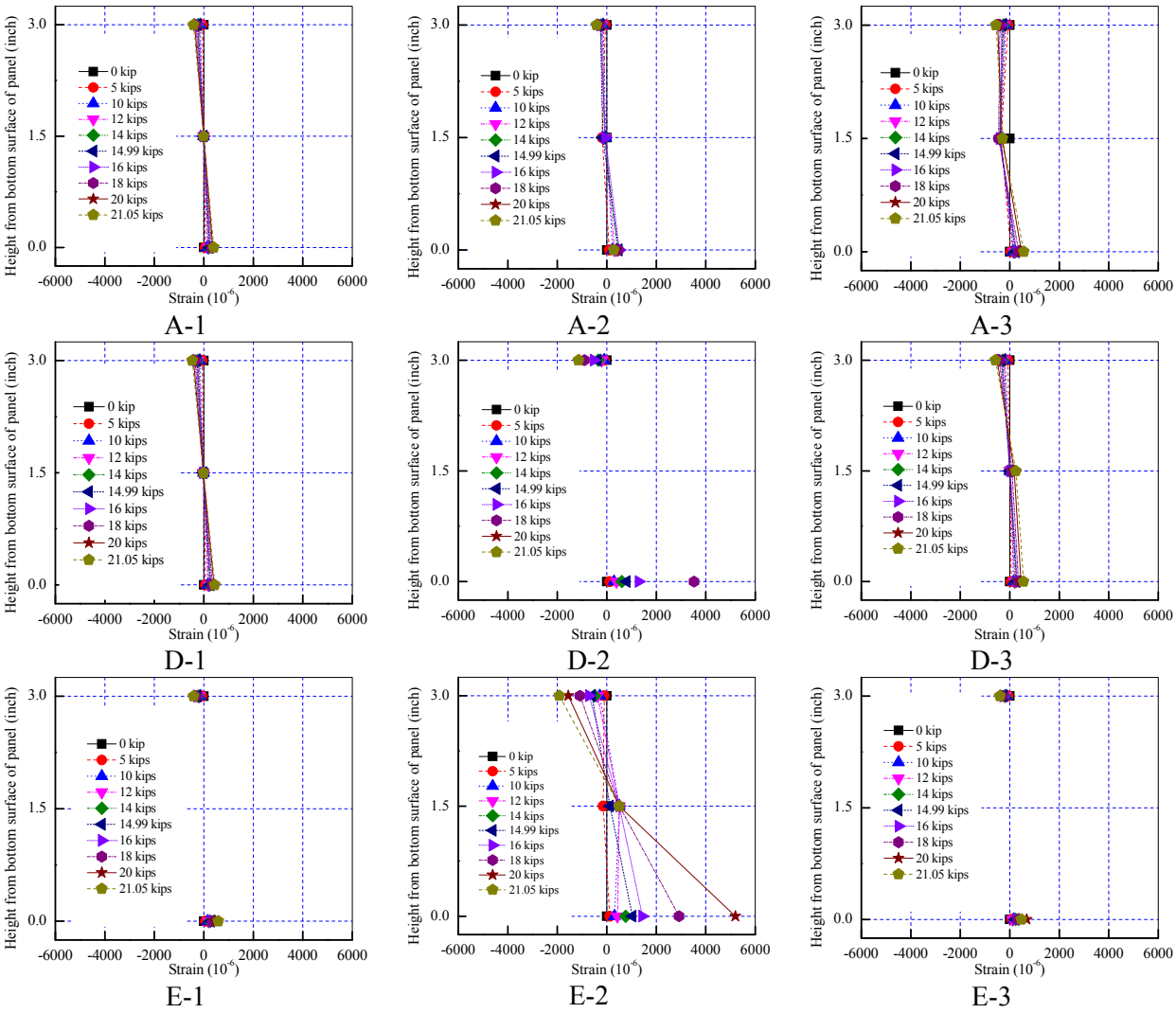

Figure C- 47 Panel CFRT-NC-SL: Measured Strain Distribution

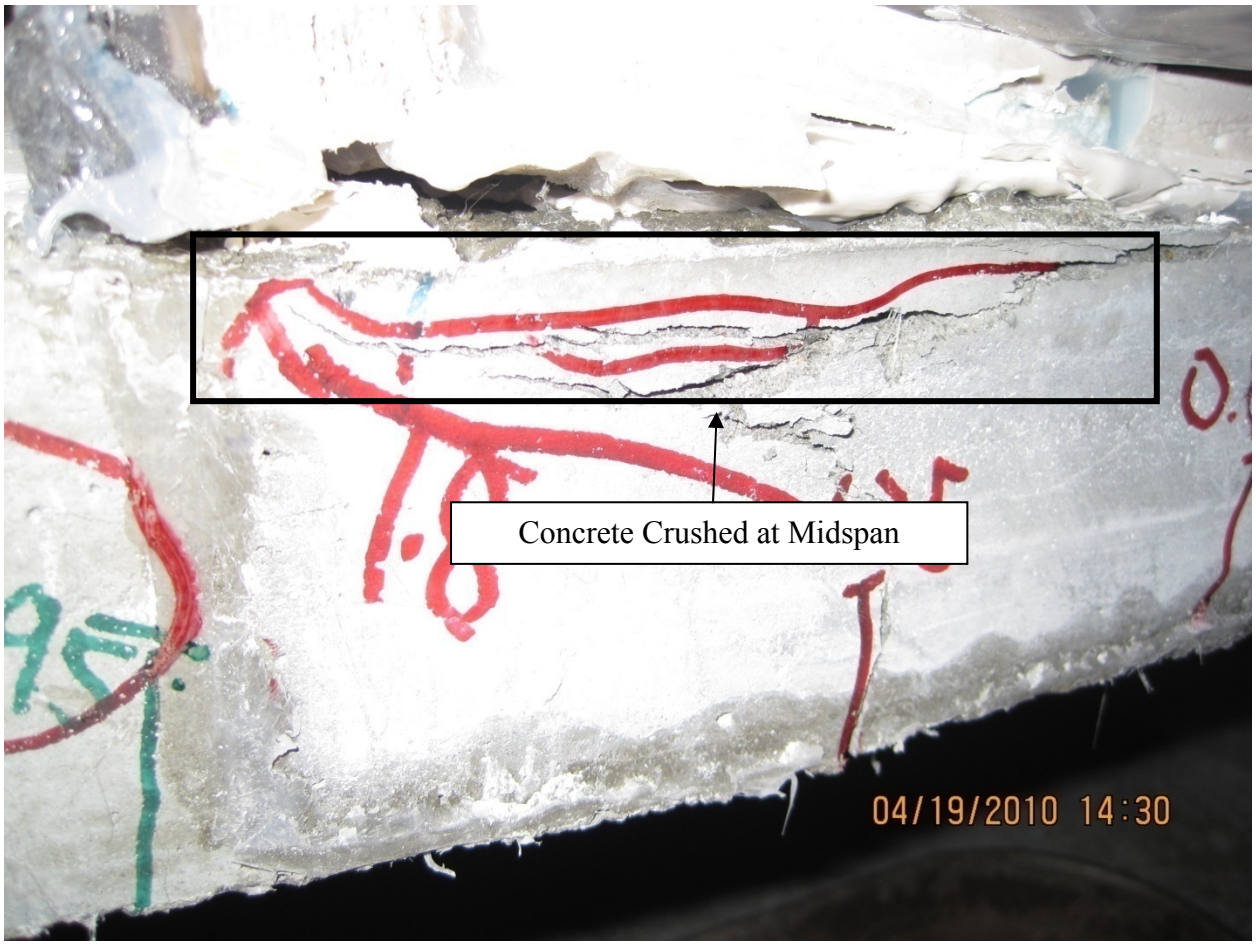

Figure C- 48 Flexural Failure at Midspan by Concrete Crushing of Panel CFRPT-FRC-SL

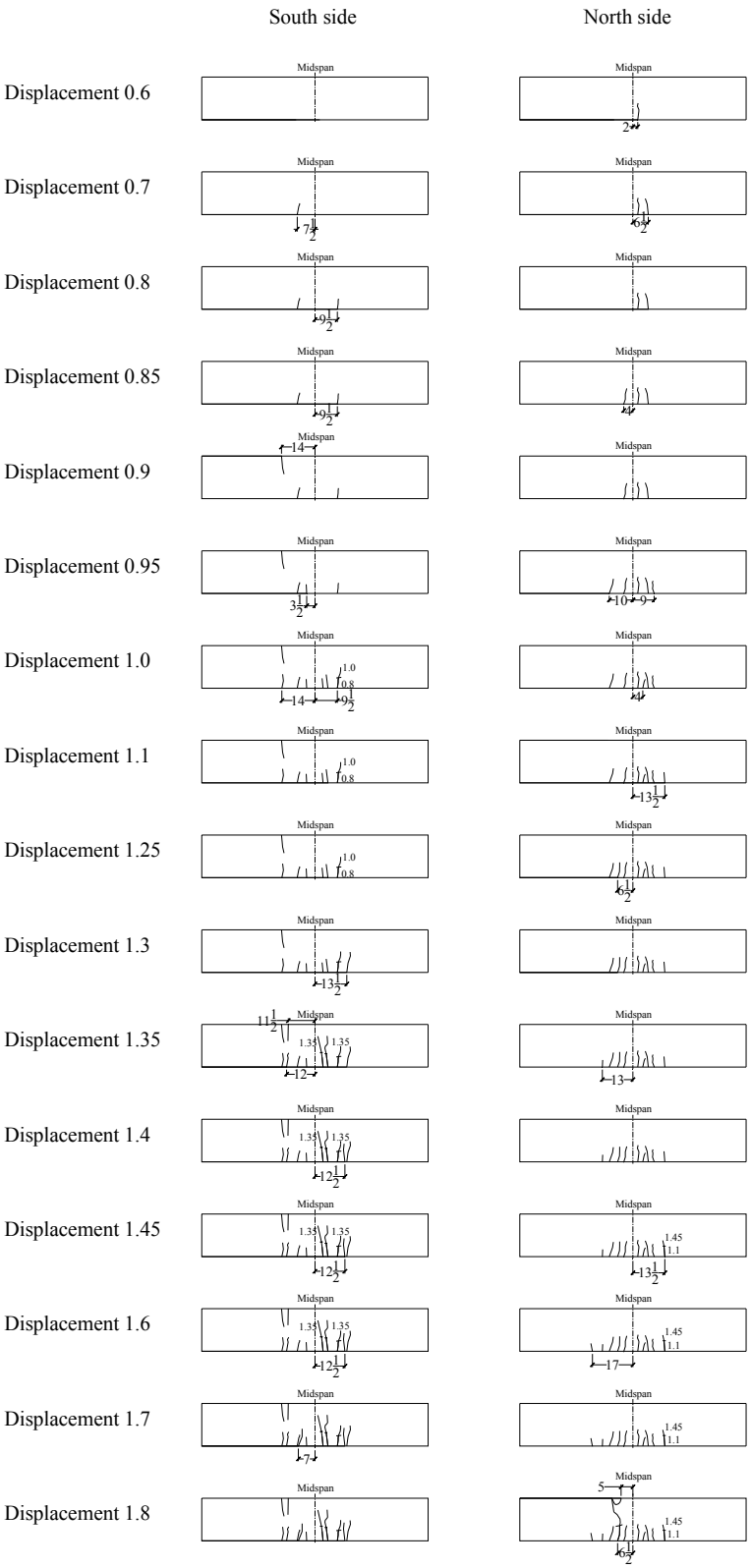

Figure C- 49 Panel CFRPT-FRC-SL: Propagation of Cracking

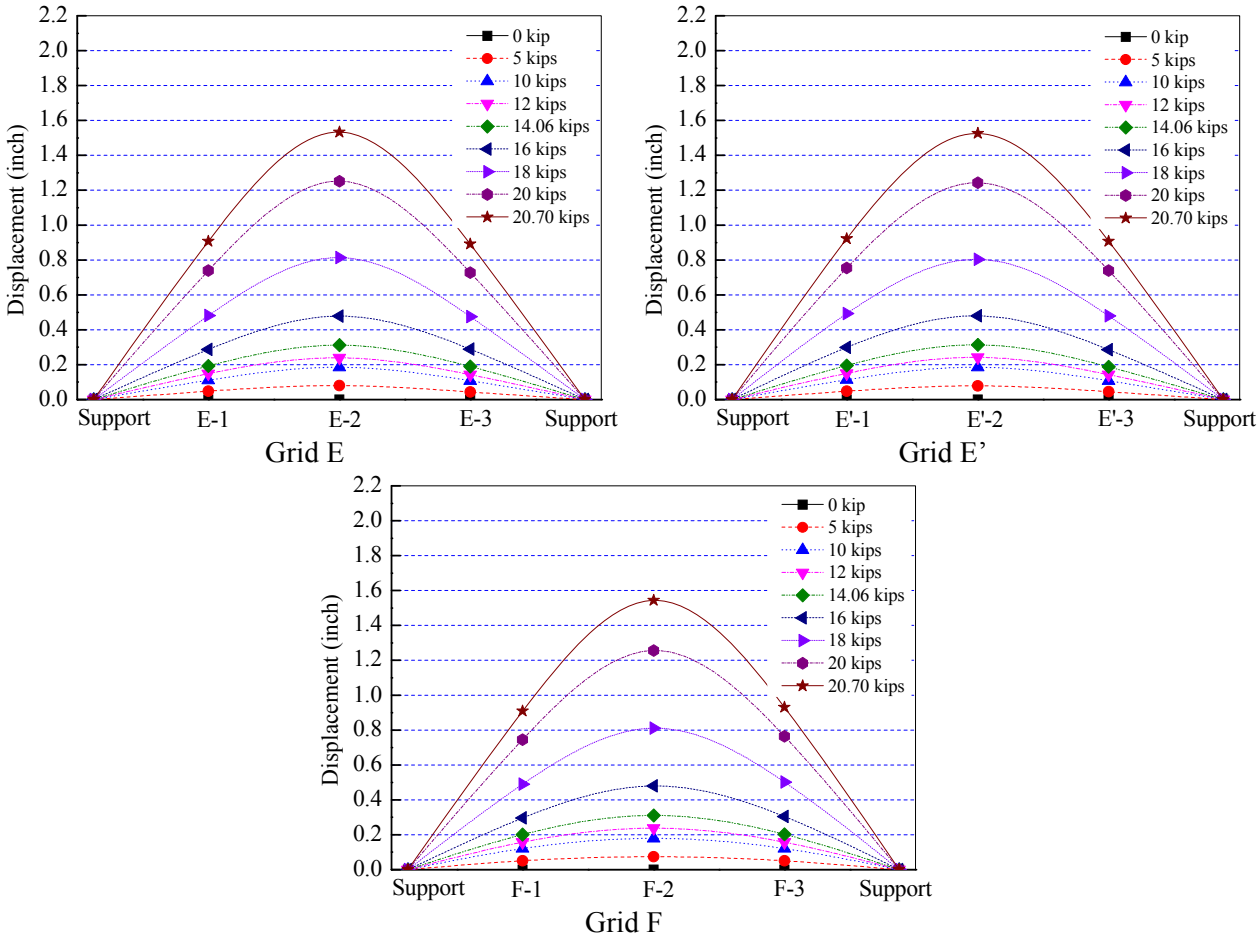

Figure C- 50 Panel CFRT-FRC-SL: Measured Displacement Along Panel Length

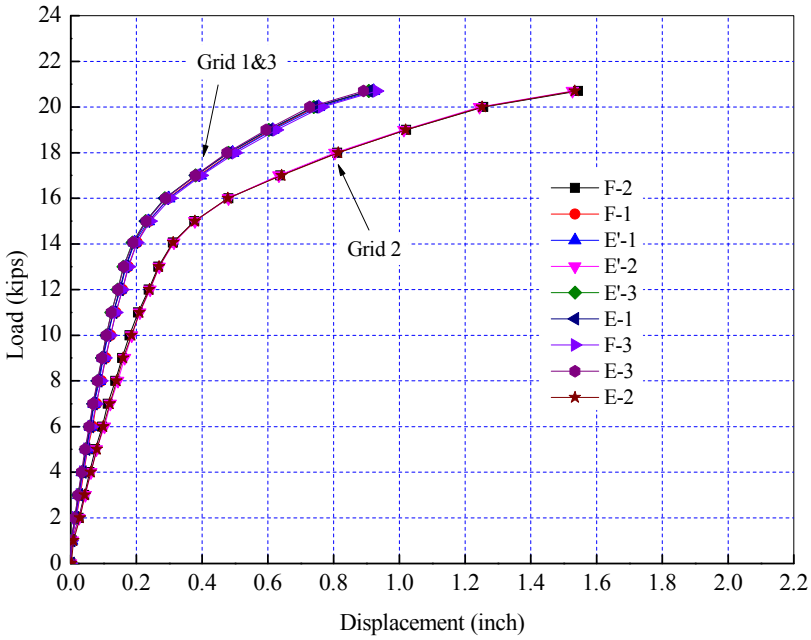

Figure C- 51 Panel CFRP-FRC-SL: Applied Load-Displacement Relationship

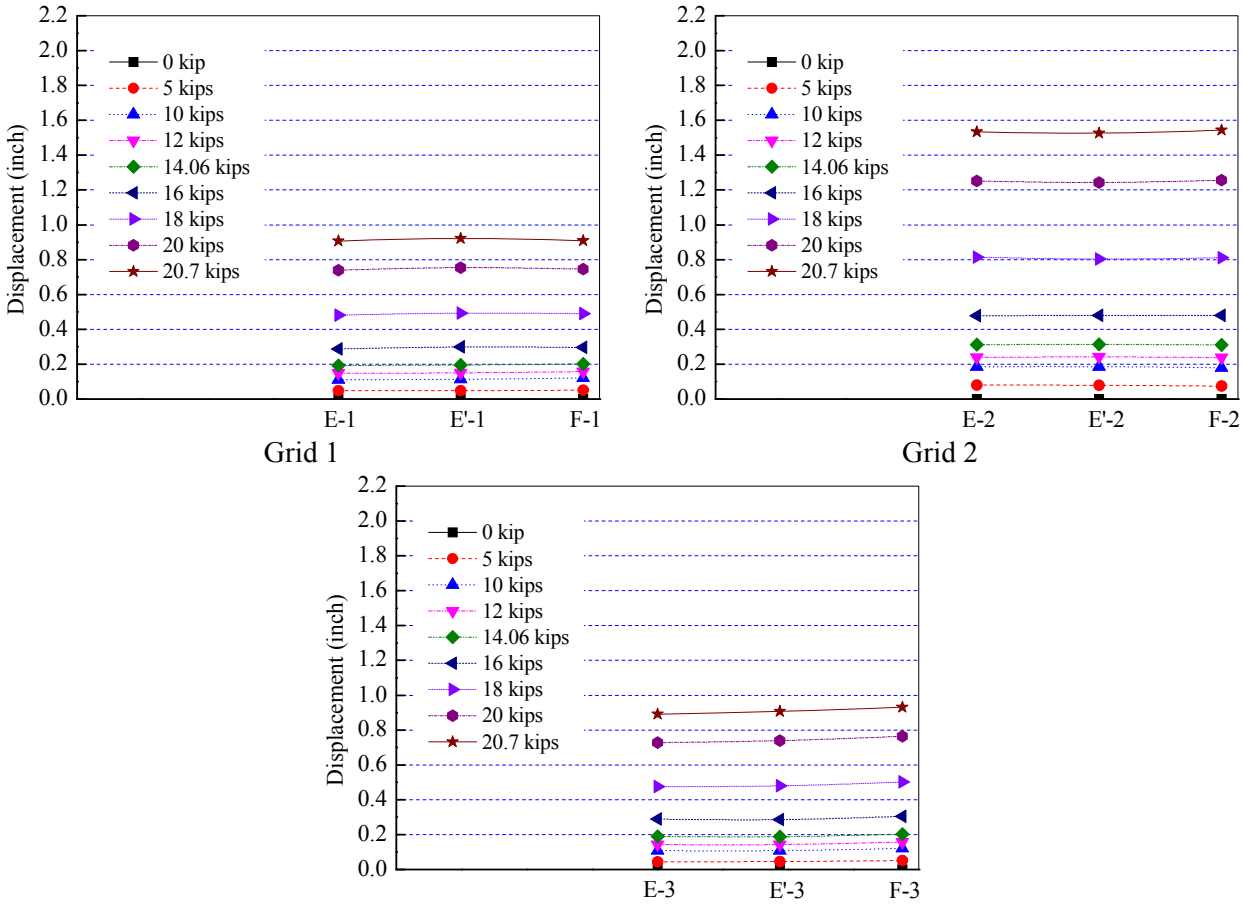

Figure C- 52 Panel CFRPT-FRC-SL: Measured Displacement Along Panel Width

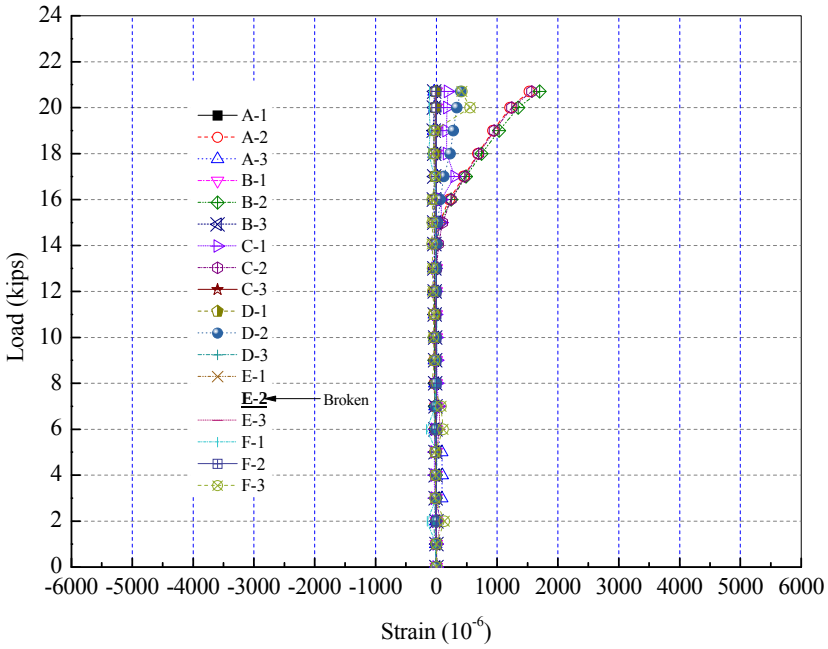

Figure C- 53 Panel CFRPT-FRC-SL: Applied Load-Tendon Strain Relationship

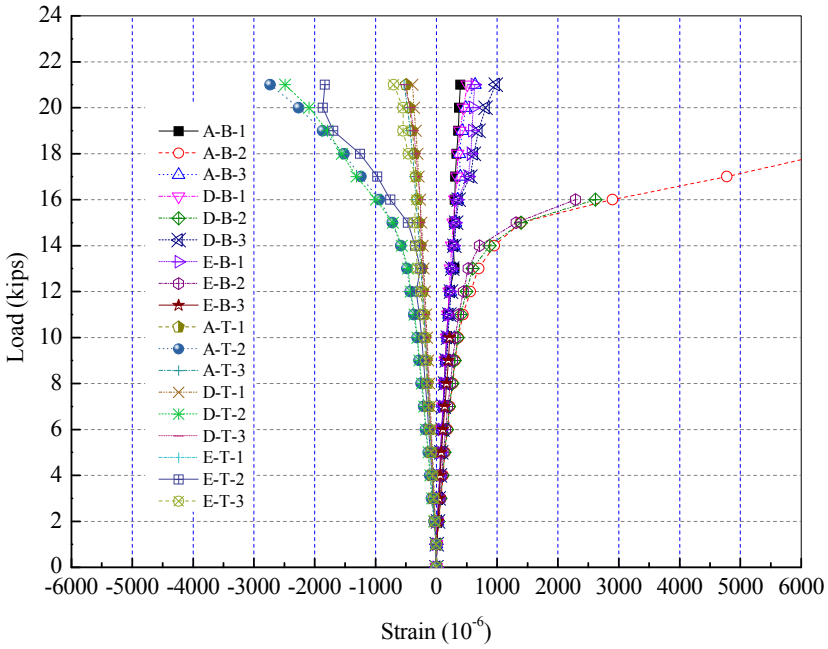

Figure C- 54 Panel CFRPT-FRC-SL: Applied Load-Concrete Surface Strain Relationship

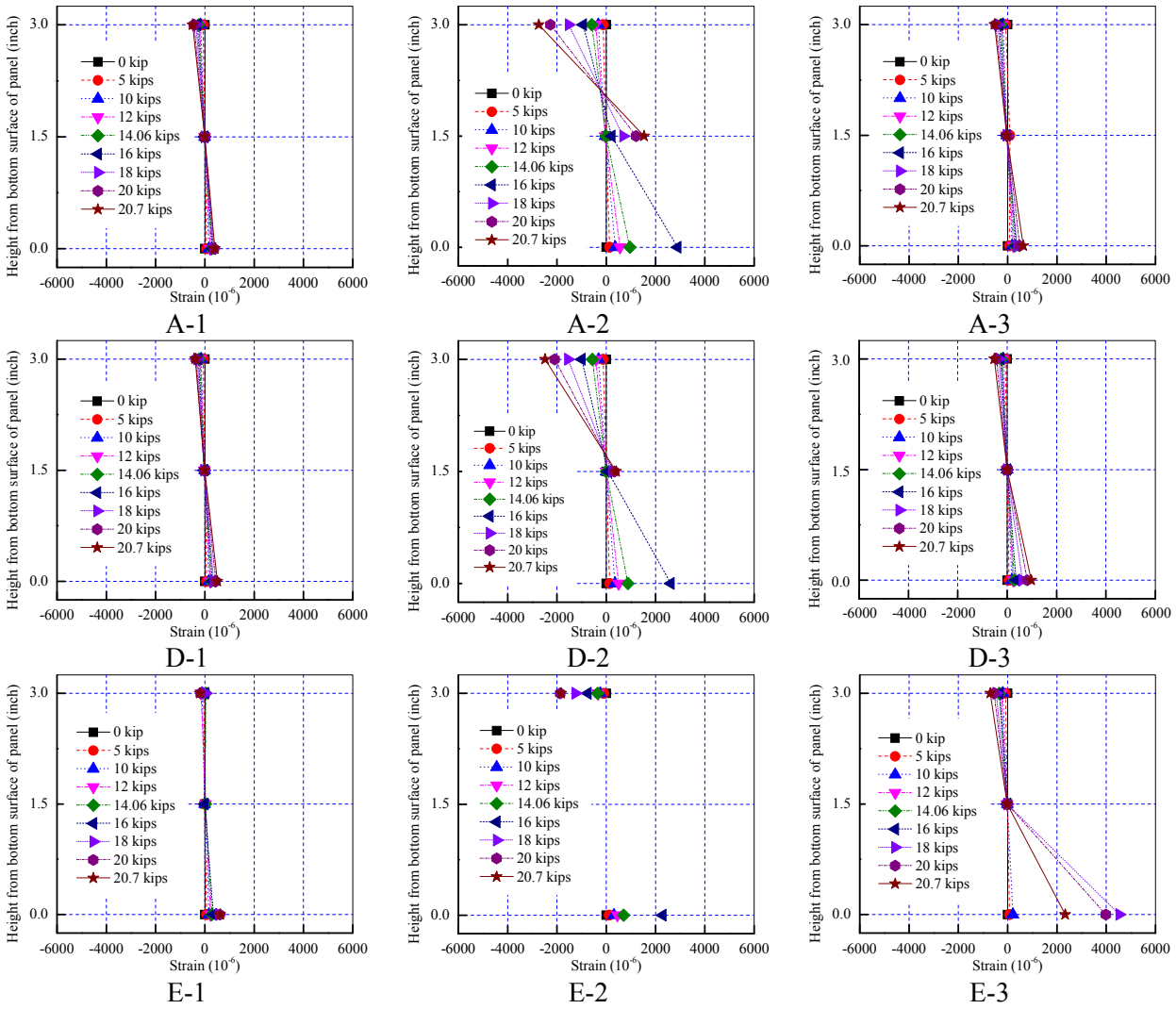

Figure C- 55 Panel CFRPT-FRC-SL: Measured Strain Distribution

Figure C- 56 Flexural Failure at Midspan by Concrete Crushing of Panel ST-NC-FL

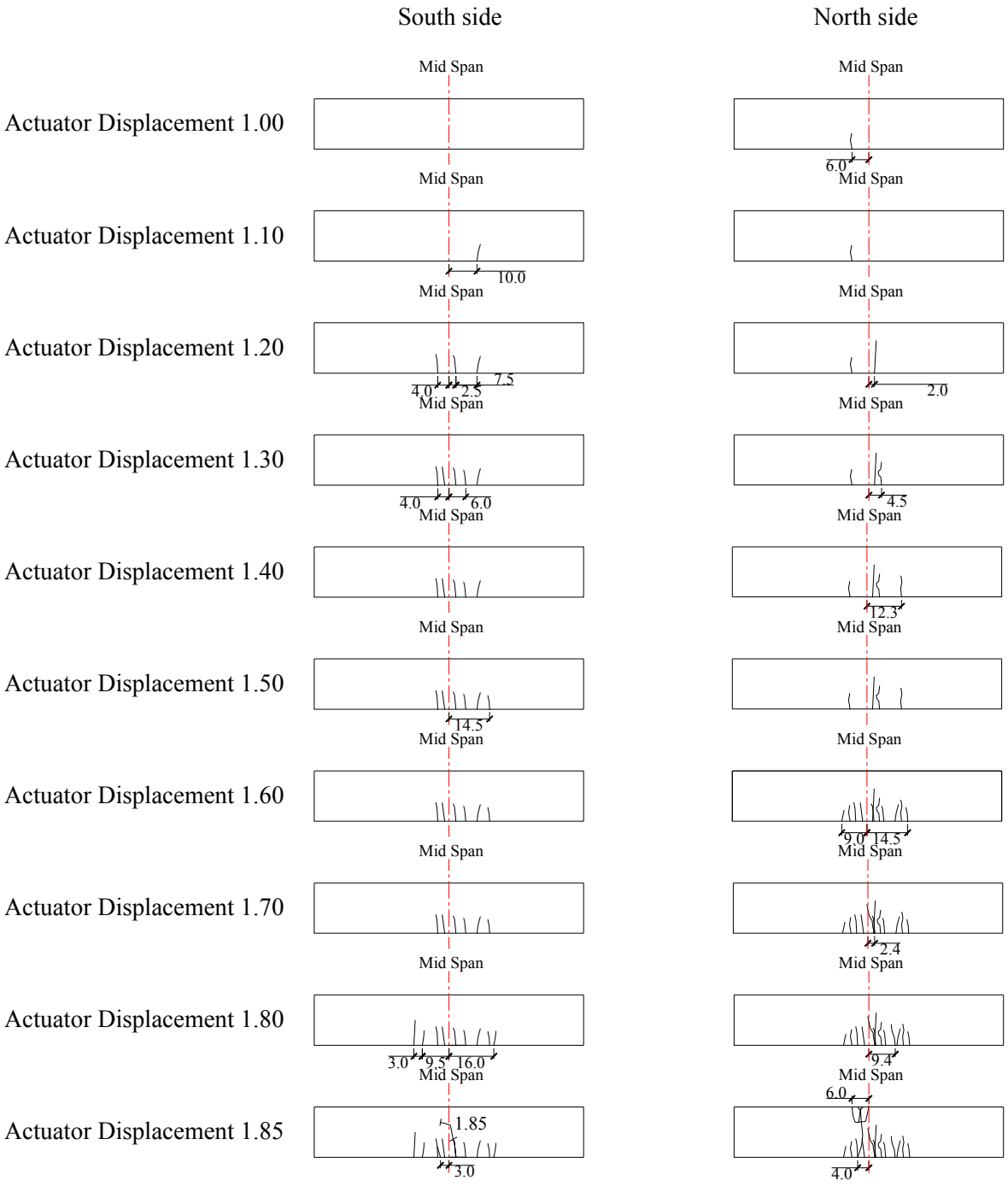

Figure C- 57 Panel ST-NC-FL: Propagation of Cracking

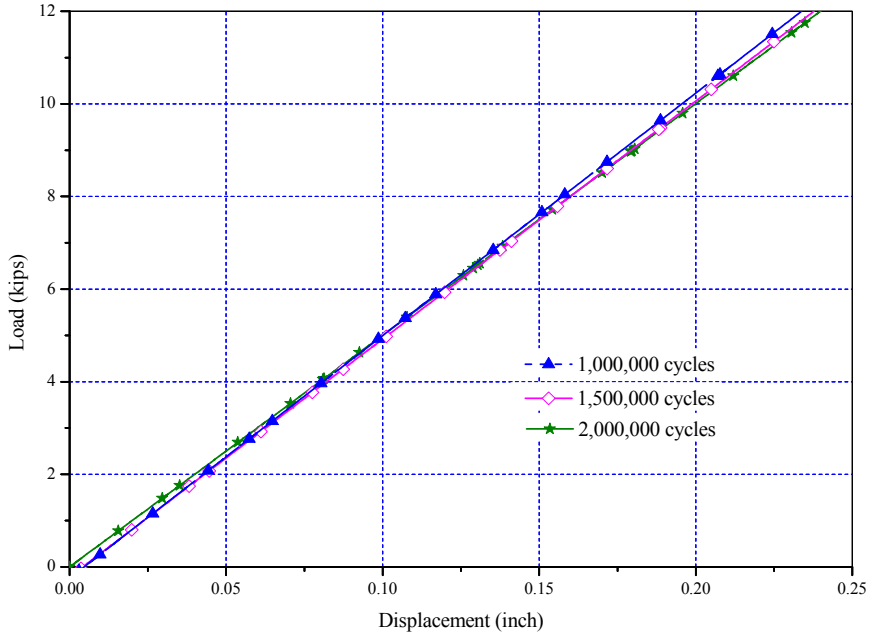

Figure C- 58 Panel ST-NC-FL: Applied Load-Displacement Relationships of the Quasi-Static Load Tests

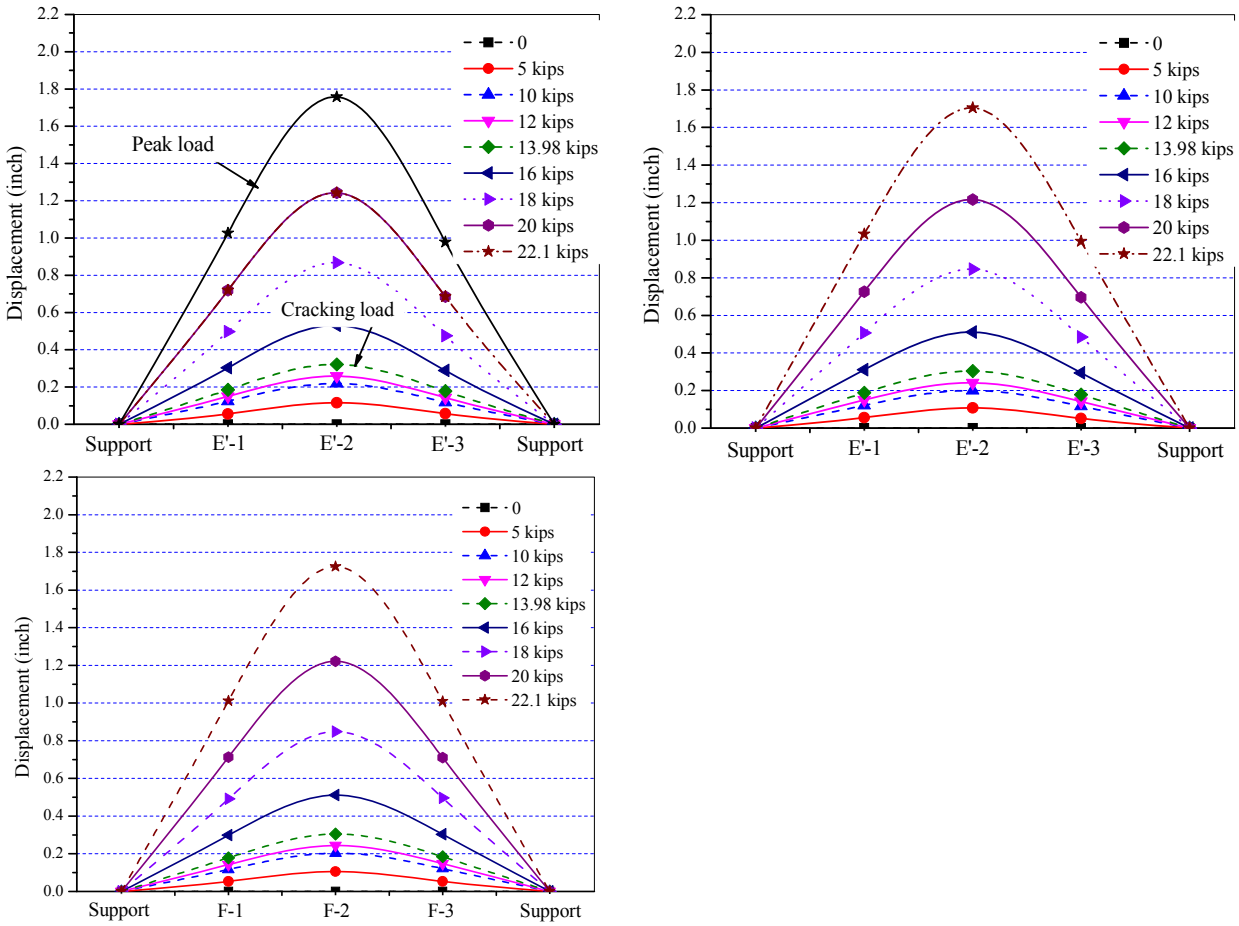

Figure C- 59 Panel ST-NC-FL: Measured Displacement Along Panel Length

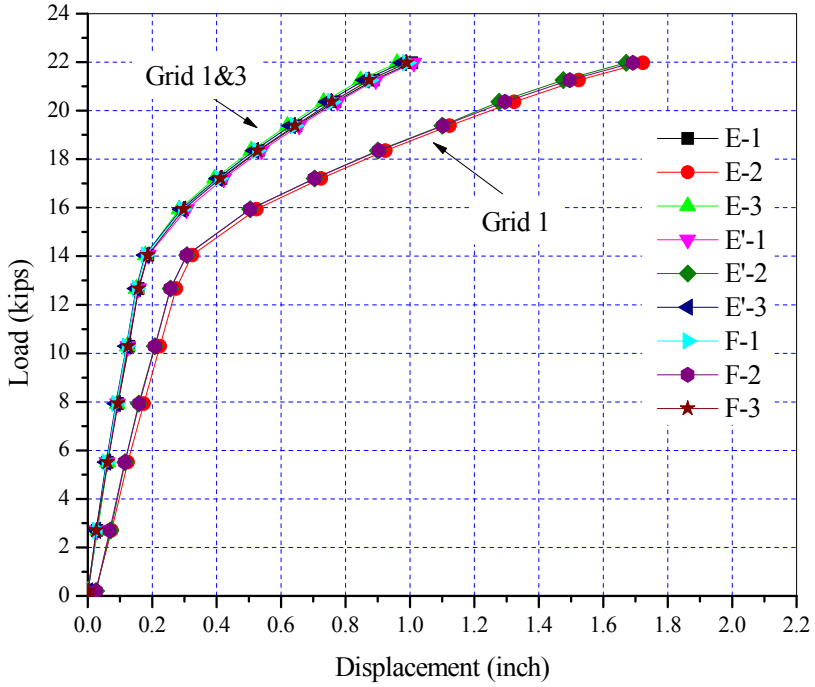

Figure C- 60 Panel ST-NC-FL: Applied Load-Displacement Relationship

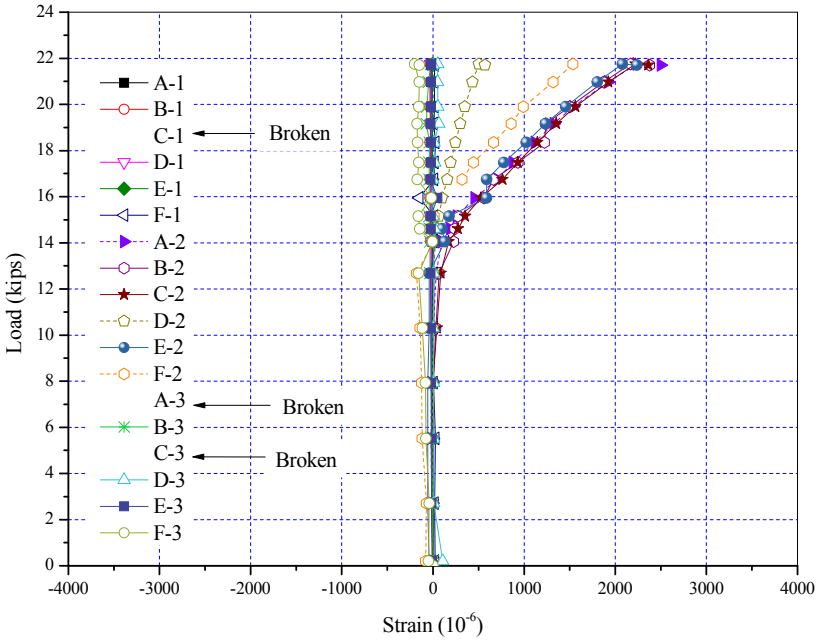

Figure C- 61 Panel ST-NC-FL: Applied Load-Tendon Strain Relationship

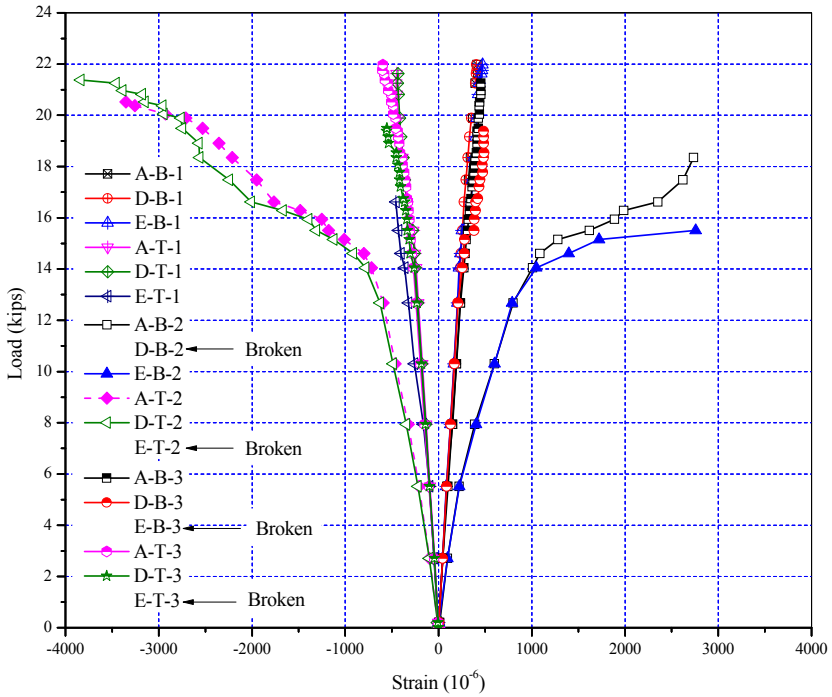

Figure C- 62 Panel ST-NC-FL: Applied Load-Concrete Surface Strain Relationship

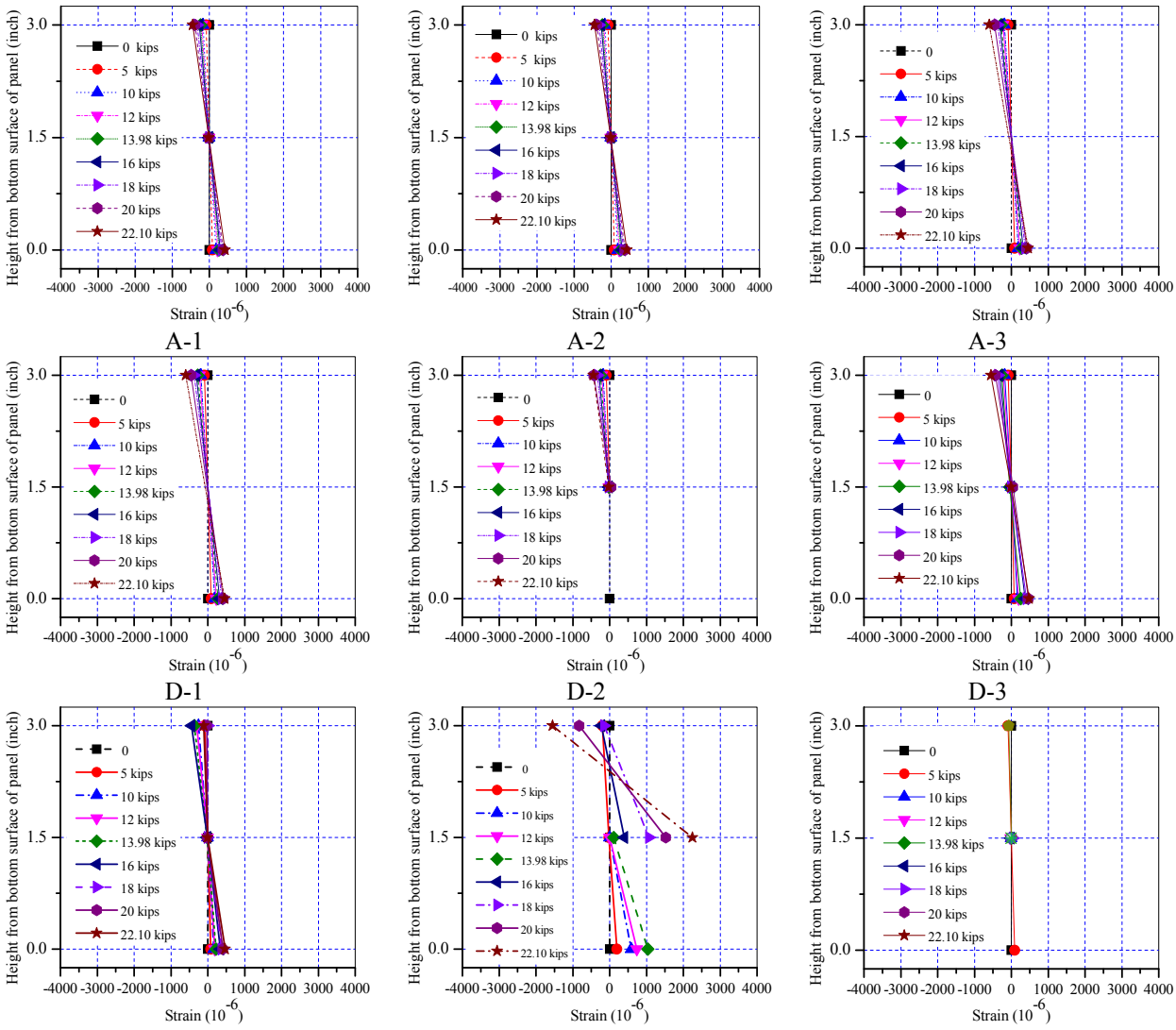

Figure C- 63 Panel ST-NC-FL: Measured Strain Distribution, Post-Fatigue Quasi-Static Test

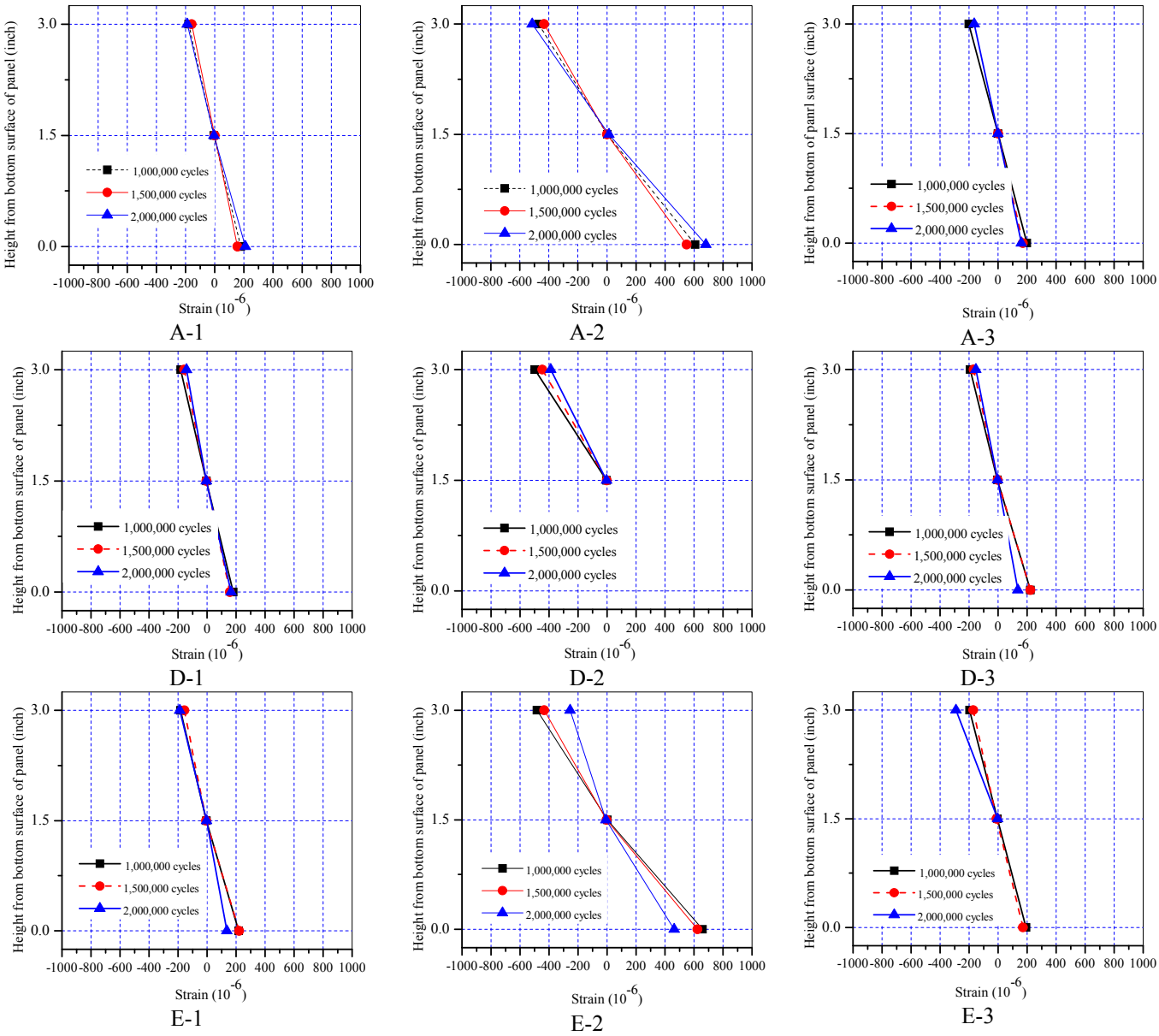

Figure C- 64 Panel ST-NC-FL: Measured Strain Distribution at Various Cycles

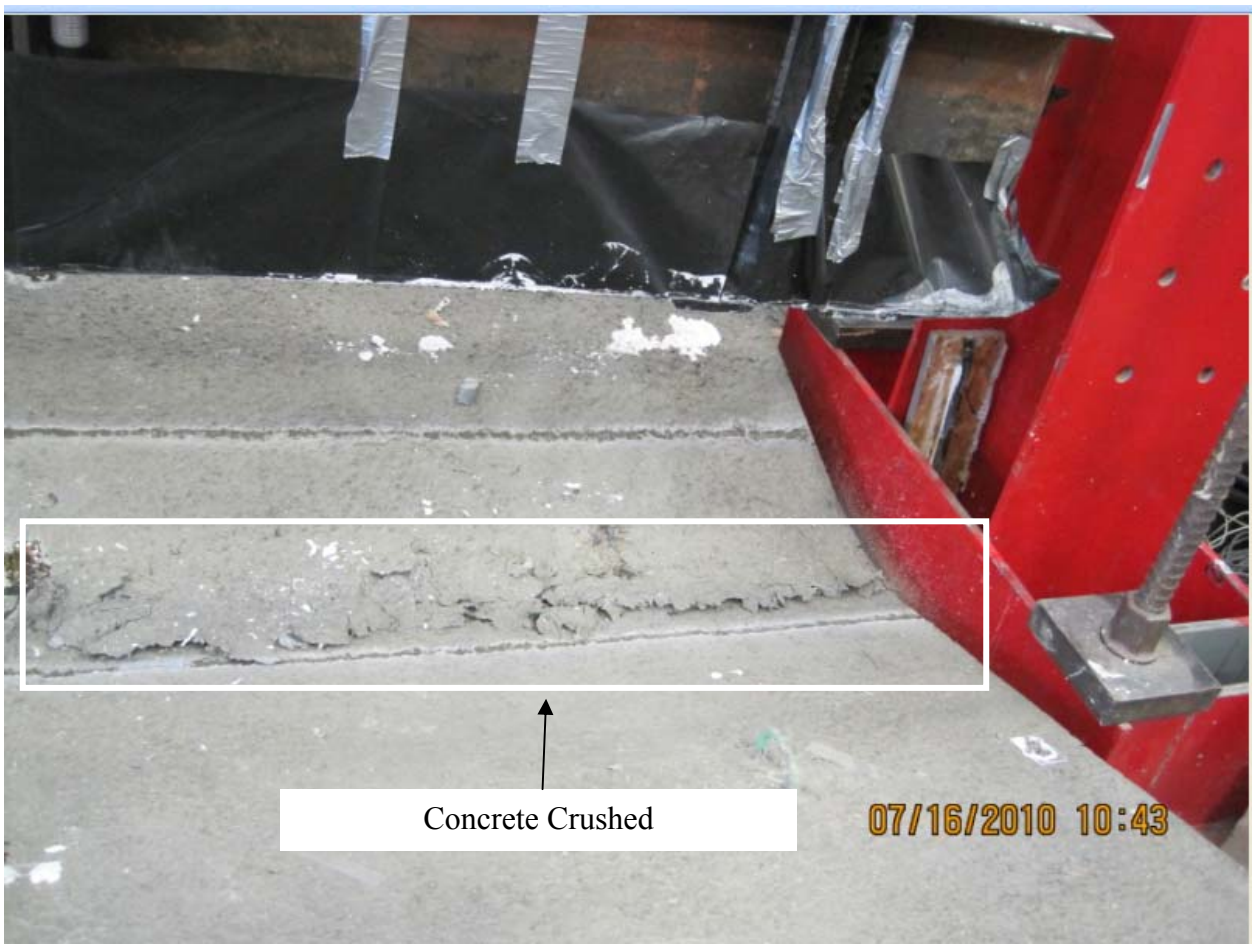

Figure C- 65 Flexural Failure at Midspan by Concrete Crushing of Panel ST-FRC-FL

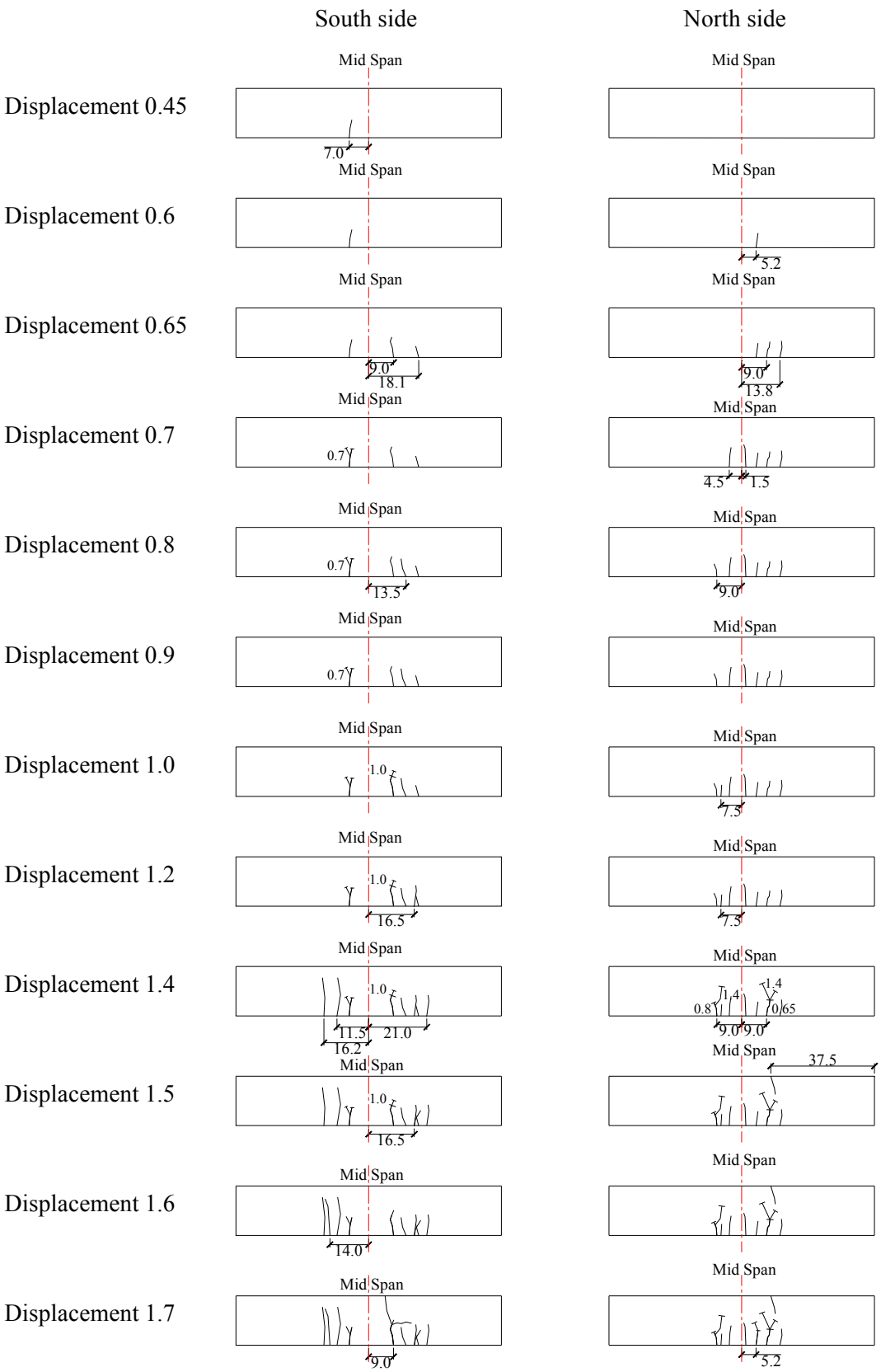

Figure C- 66 Panel ST-FRC-FL: Propagation of Cracking

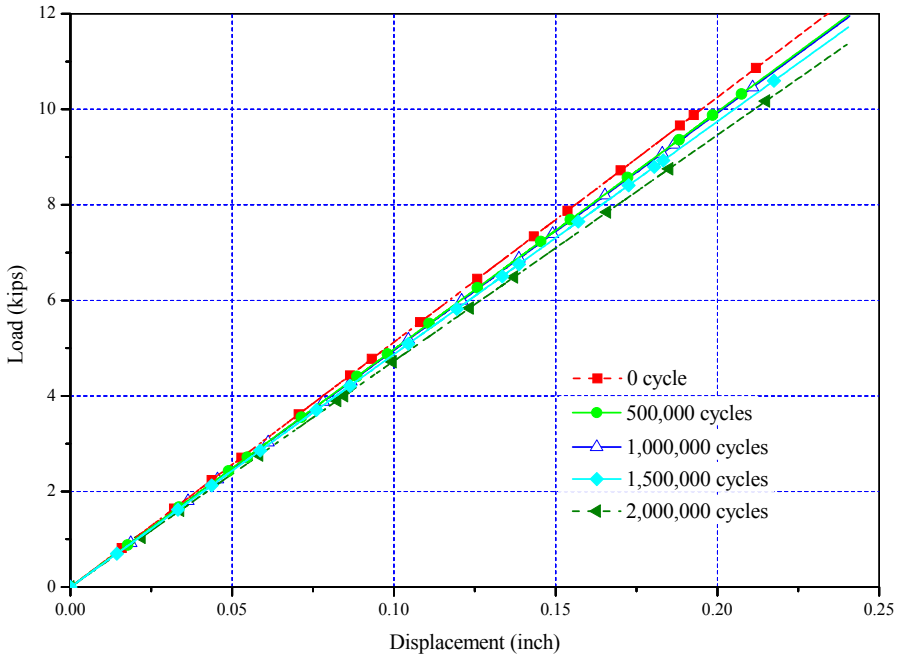

Figure C- 67 Panel ST-FRC-FL: Applied Load-Displacement Relationships of the Quasi-Static Load Tests

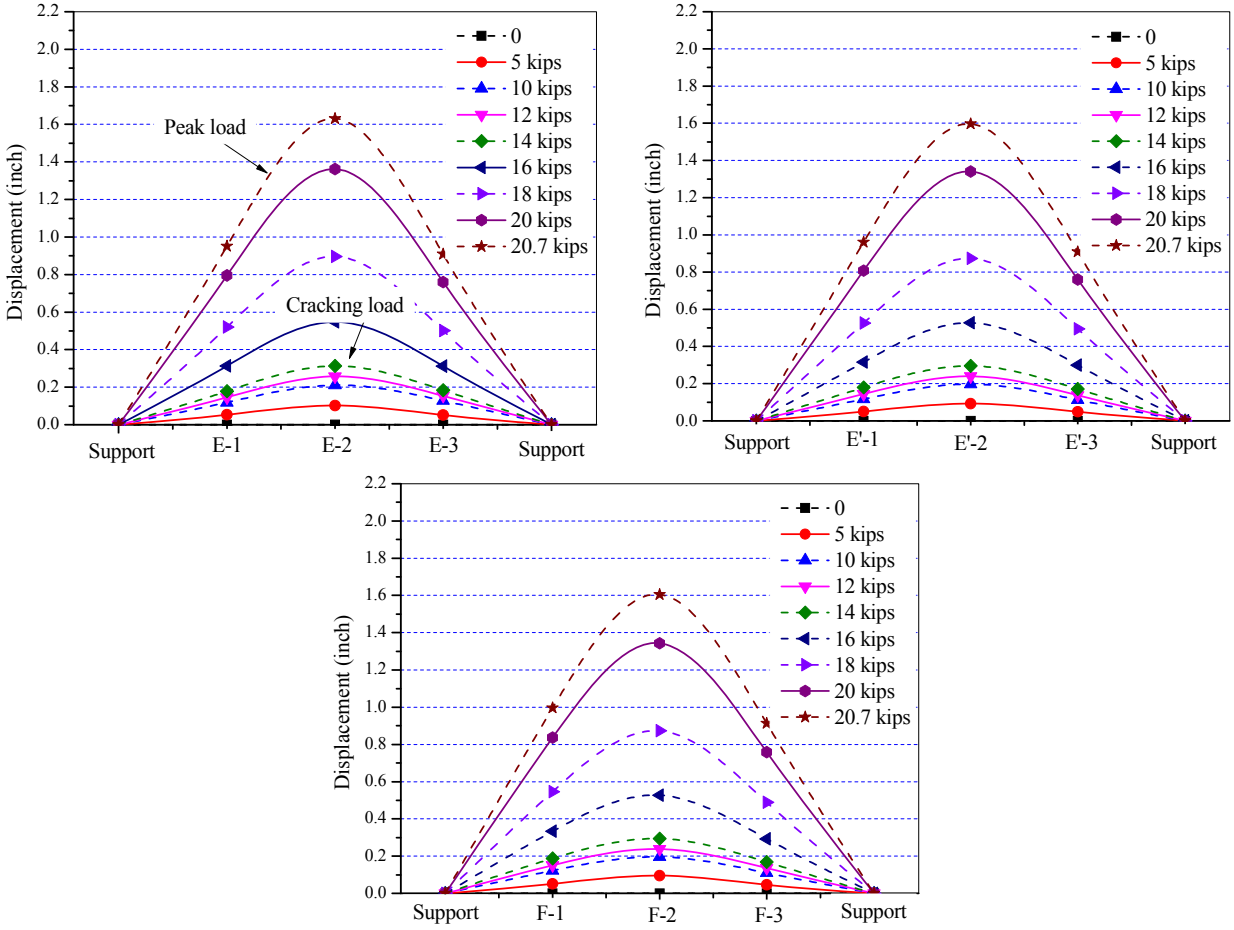

Figure C- 68 Panel ST-FRC-FL: Measured Displacement Along Panel Length

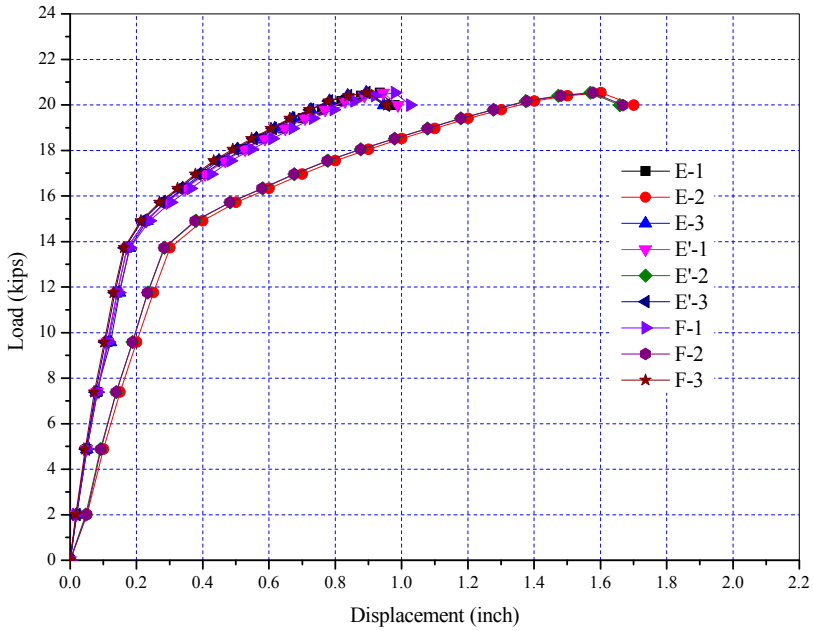

Figure C- 69 Panel ST-FRC-FL: Applied Load-Displacement Relationship

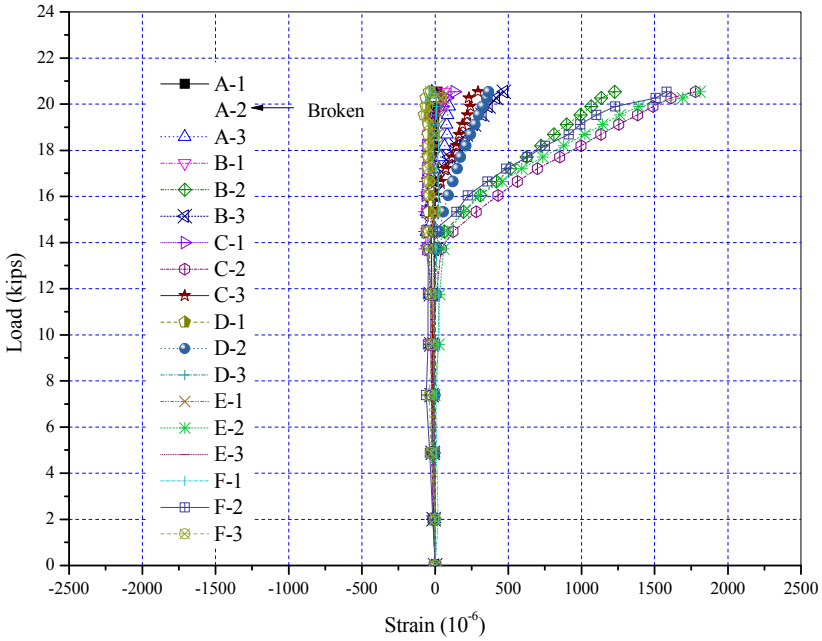

Figure C- 70 Panel ST-FRC-FL: Applied Load-Tendon Strain Relationship

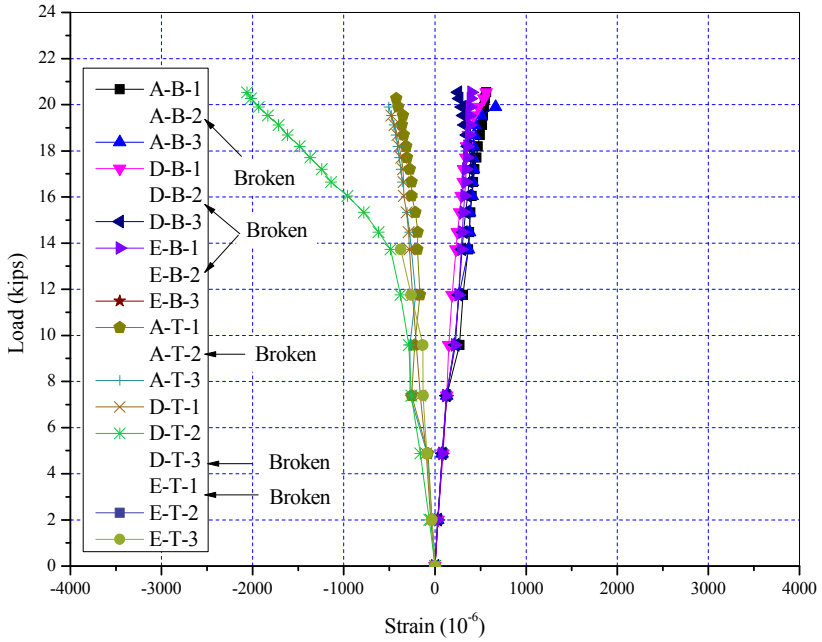

Figure C- 71 Panel ST-FRC-FL: Applied Load-Concrete Surface Strain Relationship

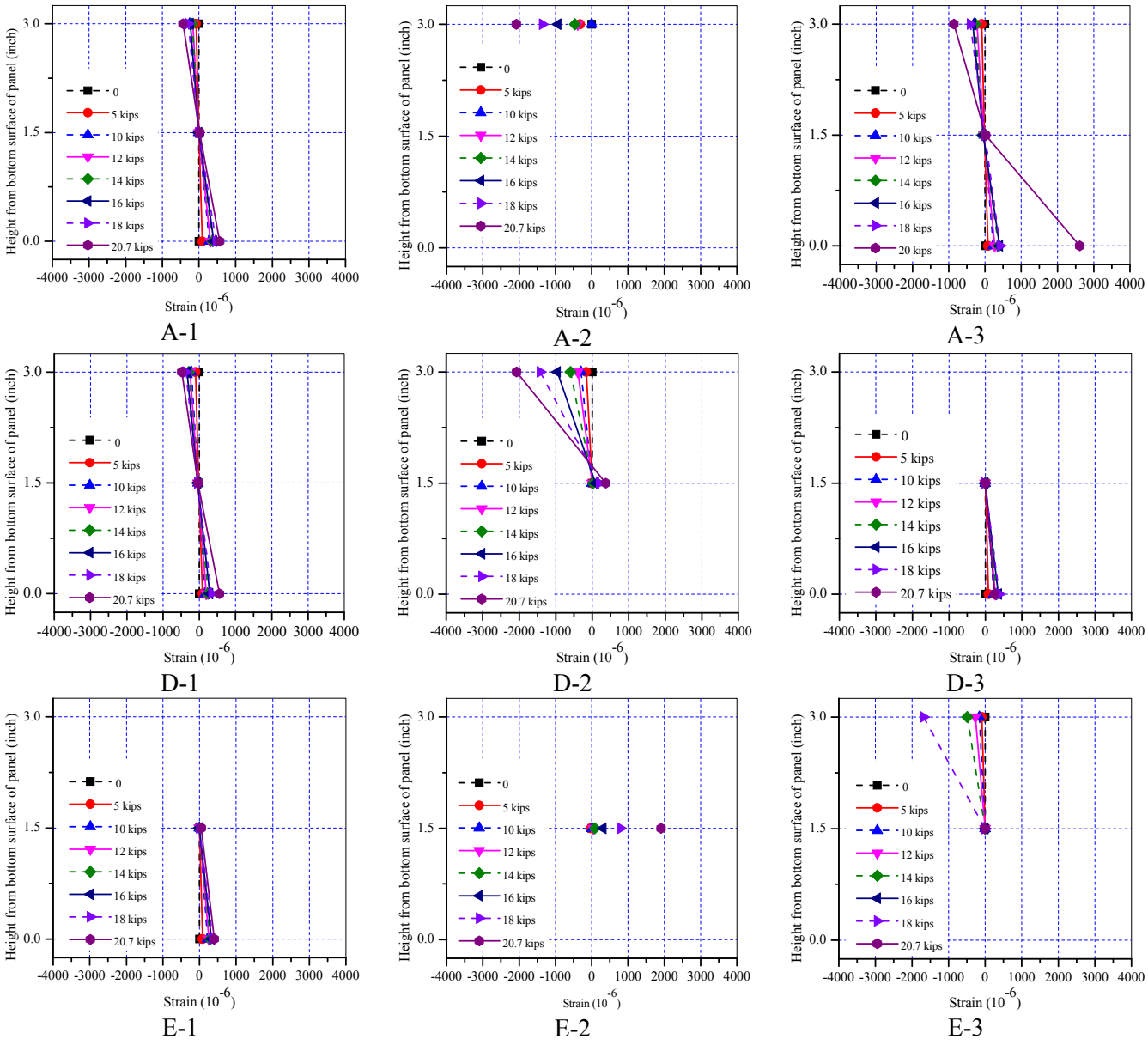

Figure C- 72 Panel ST-FRC-FL: Measured Strain Distribution, Post-Fatigue Quasi-Static Test

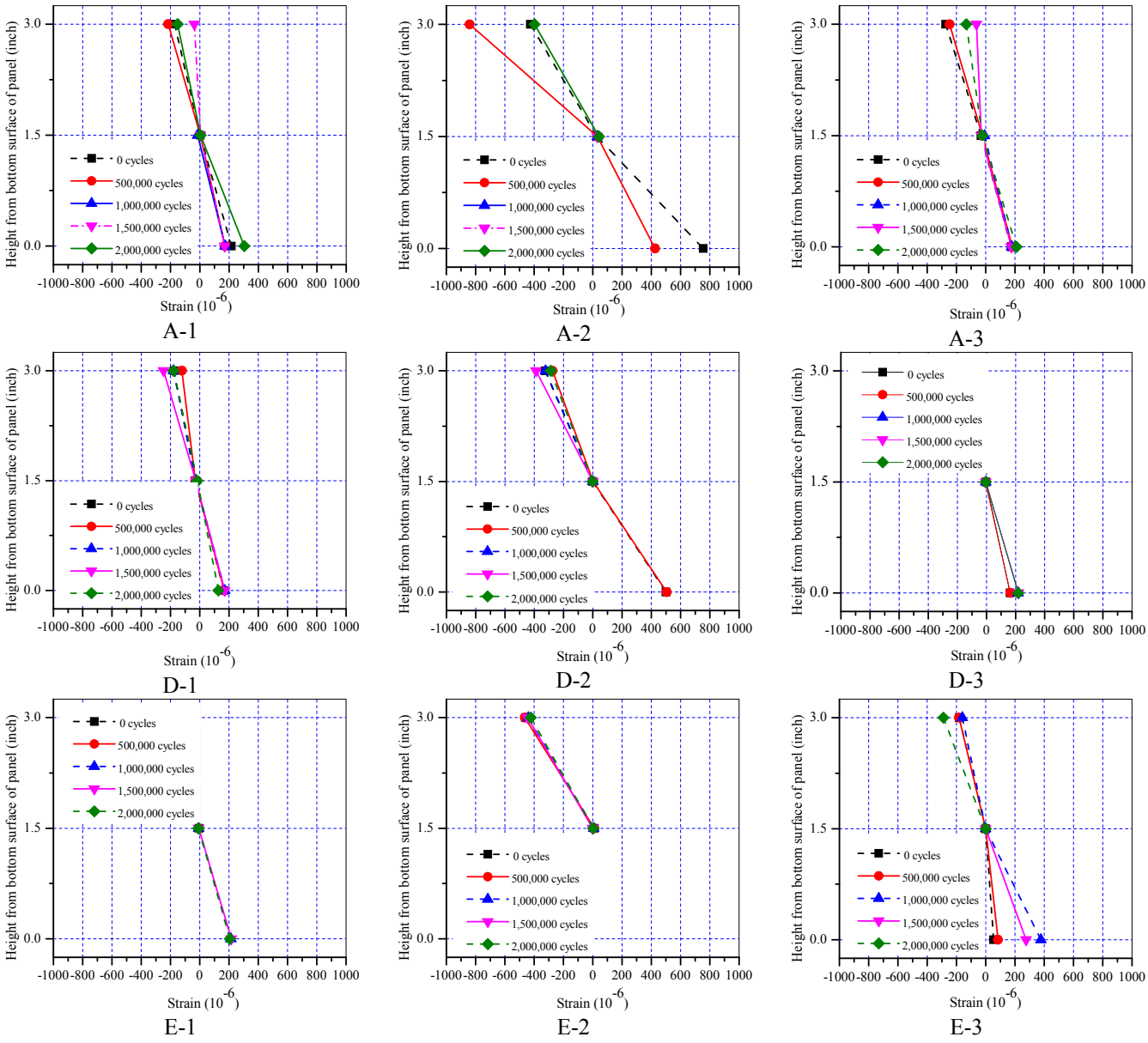

Figure C- 73 Panel ST-FRC-FL: Measured Strain Distribution at Various Cycles

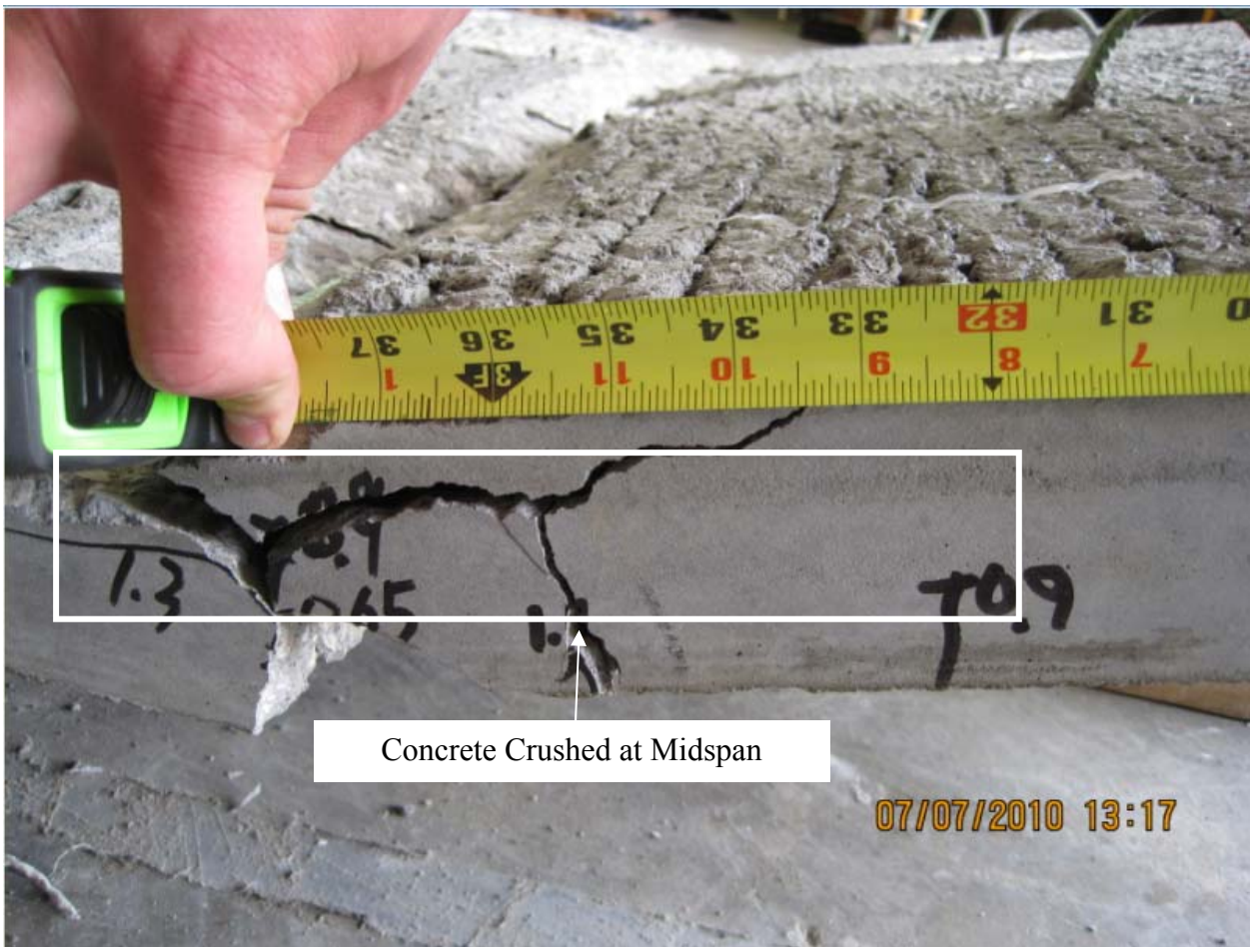

Figure C- 74 Flexural Failure at Midspan by Concrete Crushing of Panel ECST-NC-FL

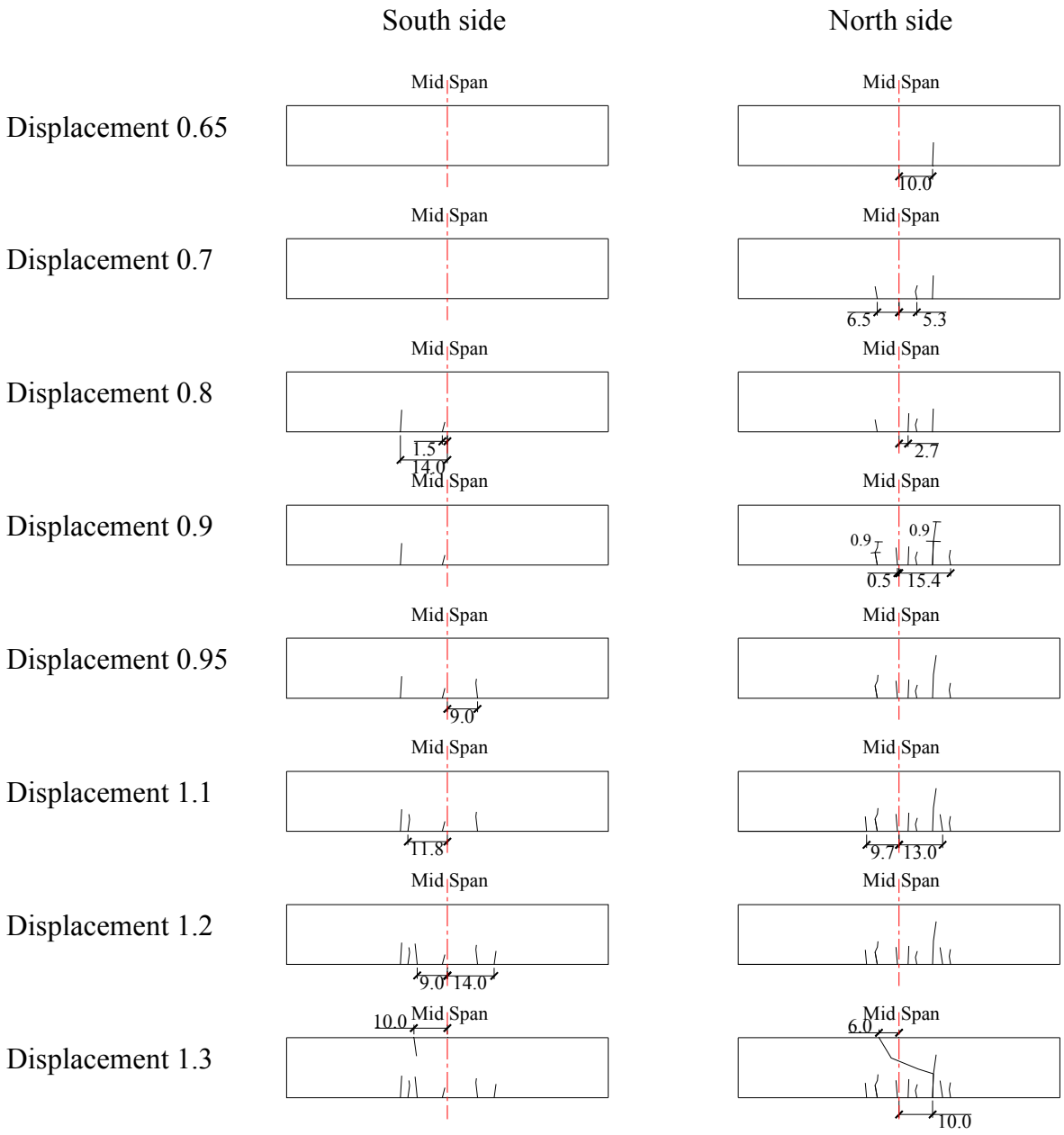

Figure C- 75 Panel ECST-NC-FL: Propagation of Cracking

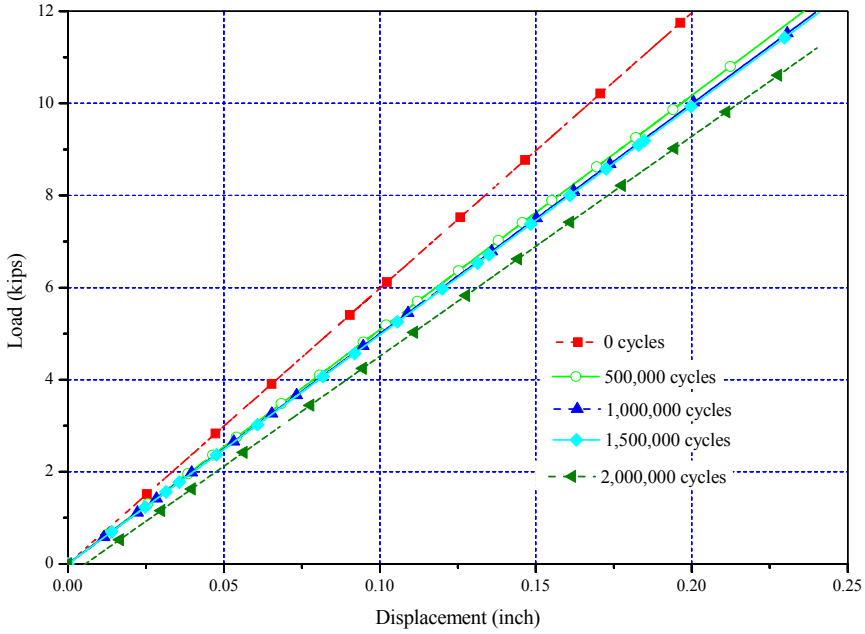

Figure C- 76 Panel ECST-NC-FL: Applied Load-Displacement Relationships of the Quasi-Static Load Tests

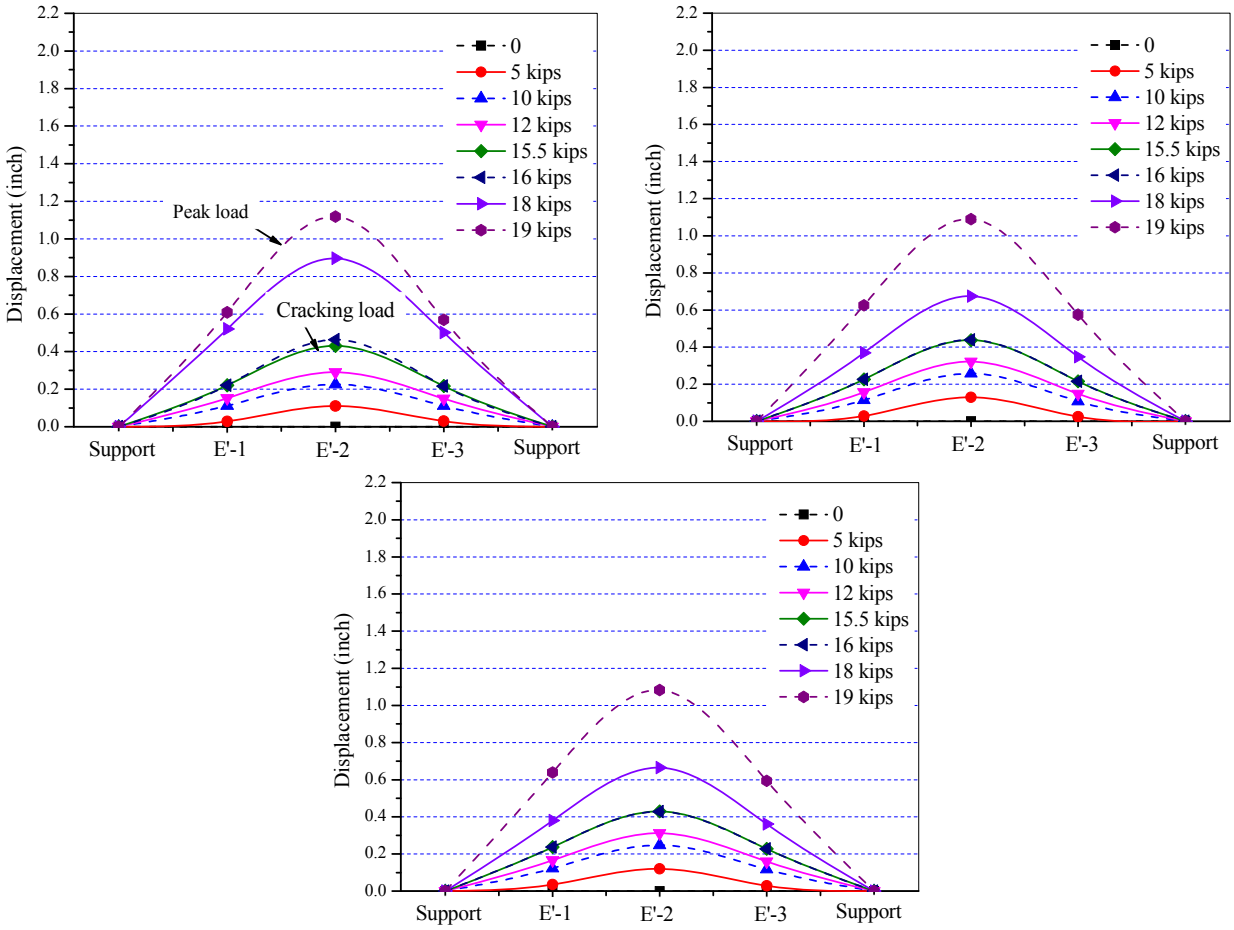

Figure C- 77 Panel ECST-NC-FL: Measured Displacement Along Panel Length

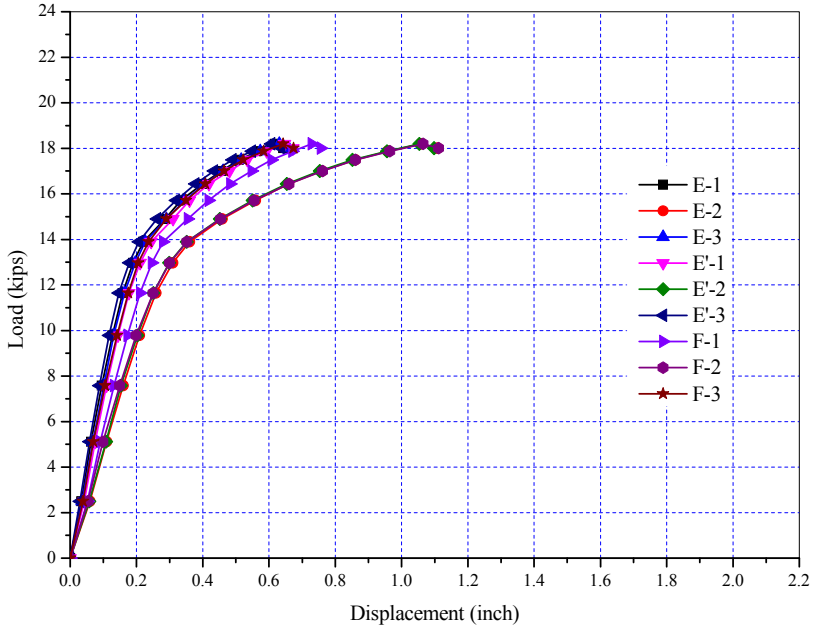

Figure C- 78 Panel ECST-NC-FL: Applied Load-Displacement Relationship

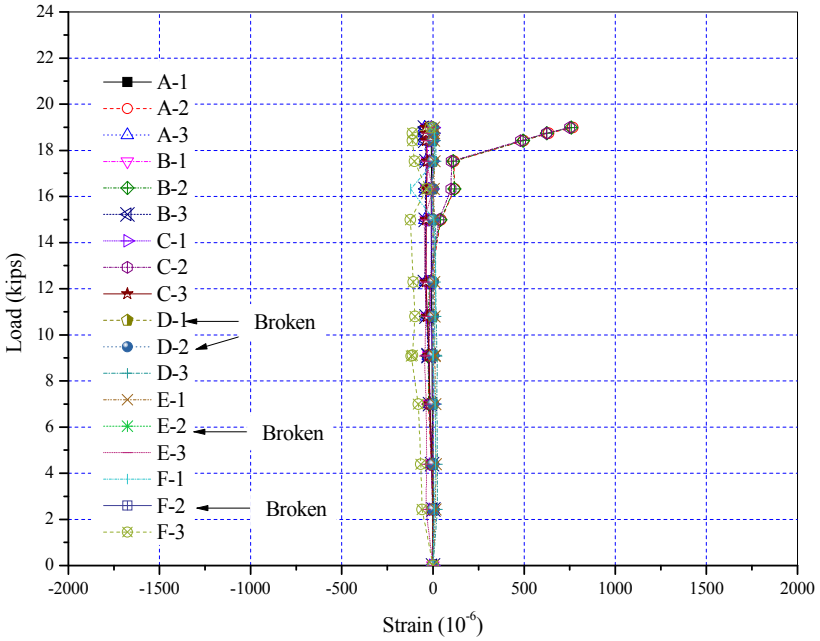

Figure C- 79 Panel ECST-NC-FL: Applied Load-Tendon Strain Relationship

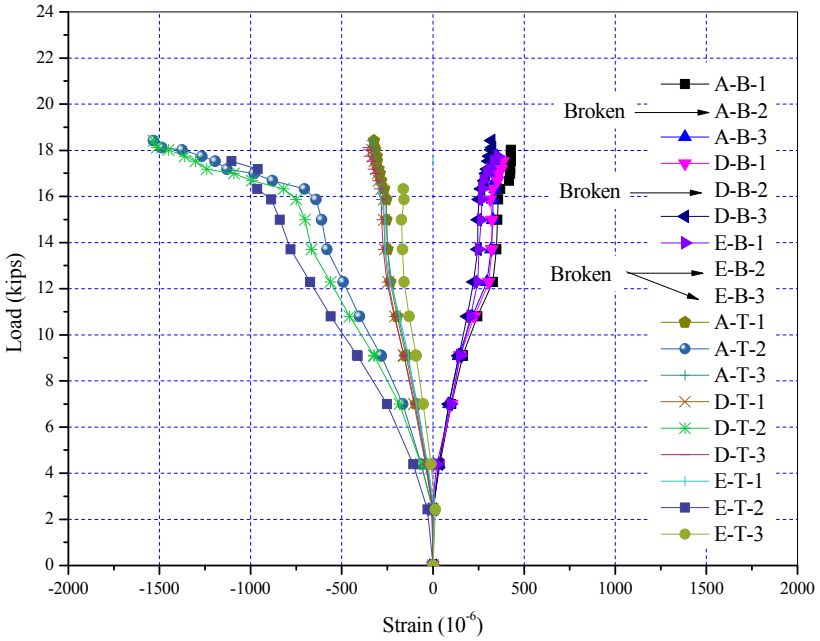

Figure C- 80 Panel ECST-NC-FL: Applied Load-Concrete Surface Strain Relationship

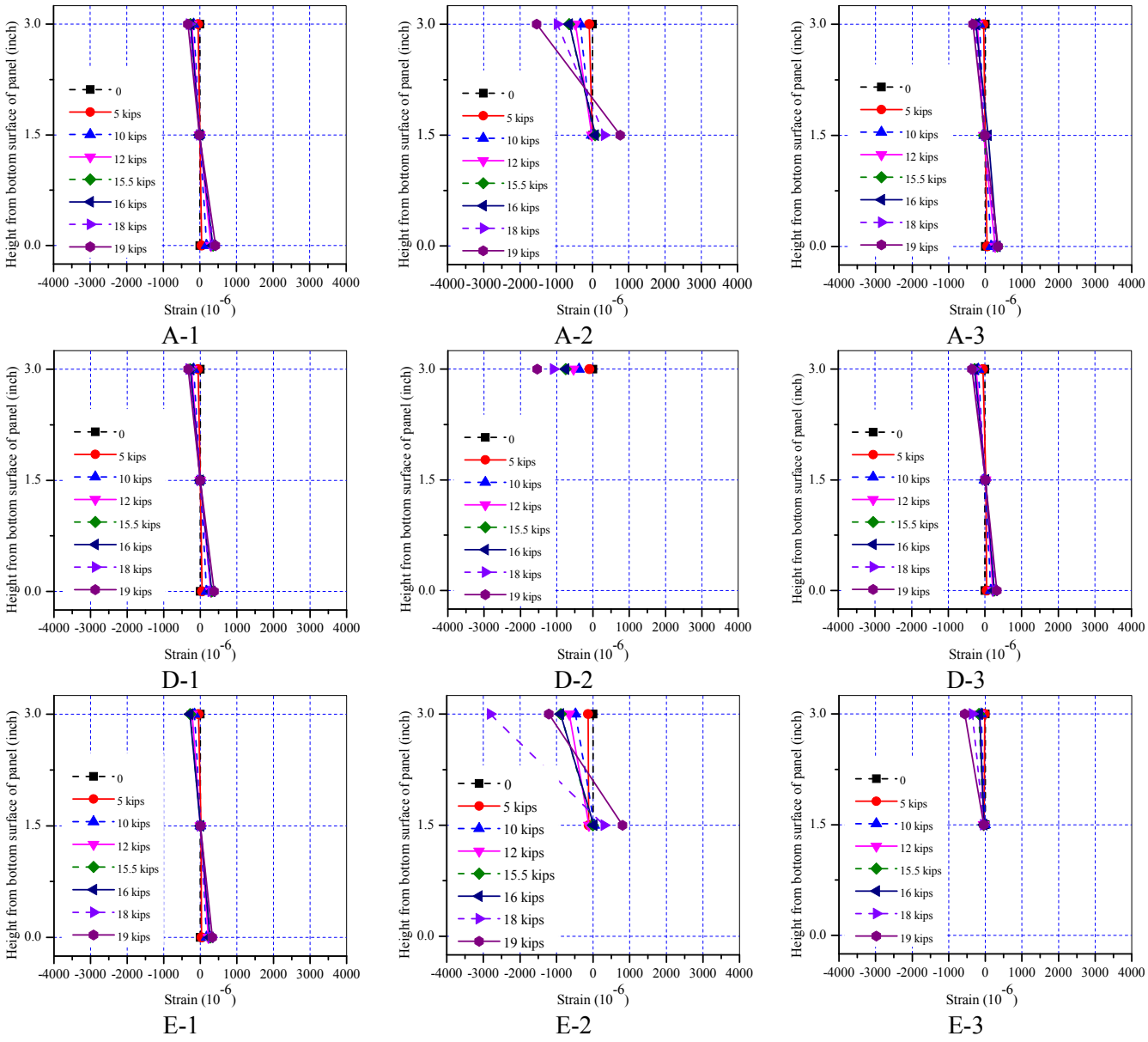

Figure C- 81 Panel ECST-NC-FL: Measured Strain Distribution, Post-Fatigue Quasi-Static Test

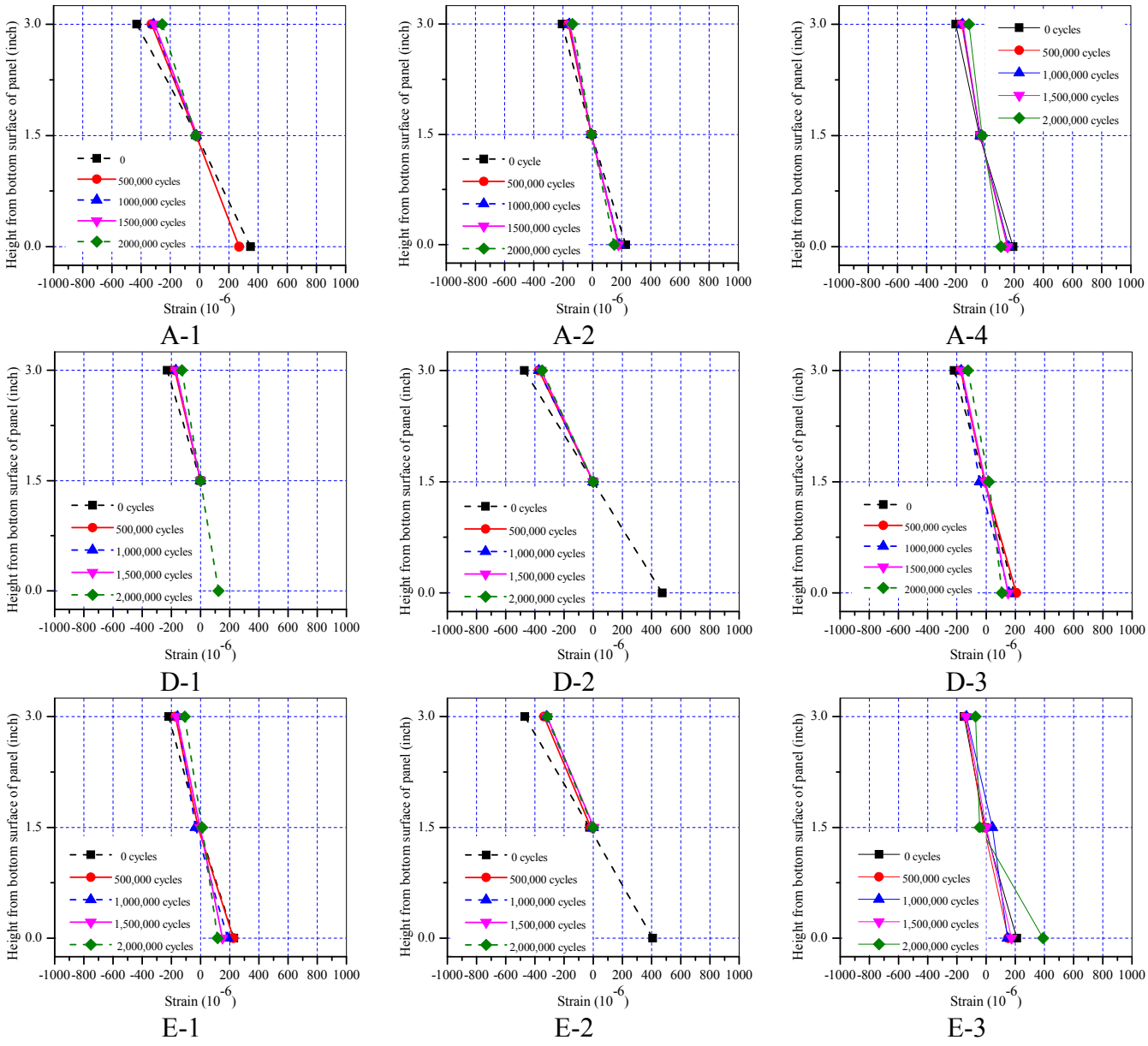

Figure C- 82 Panel ECST-NC-FL: Measured Strain Distribution at Various Cycles

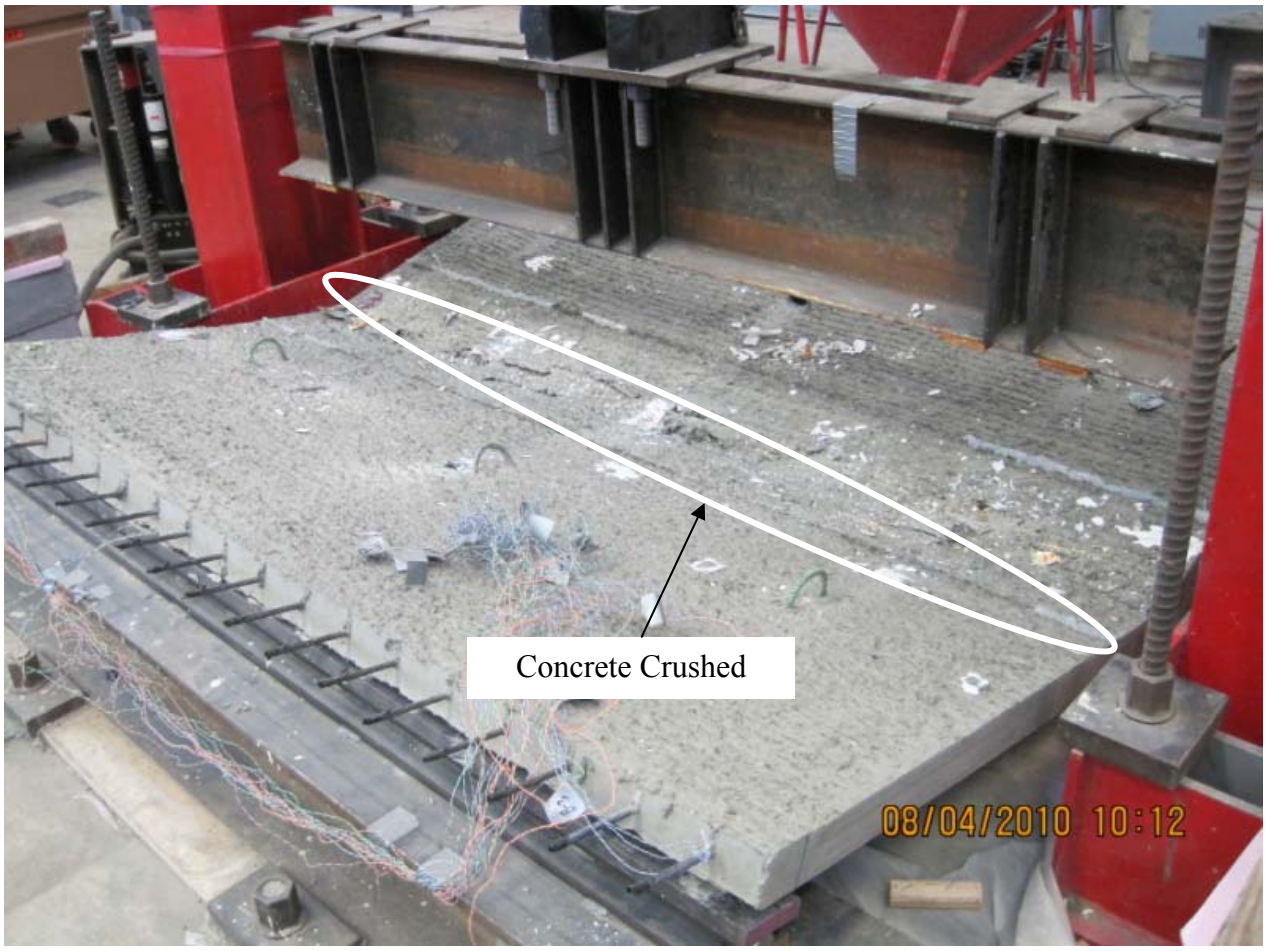

Figure C- 83 Flexural Failure at Midspan by Concrete Crushing of Panel ECST-FRC-FL

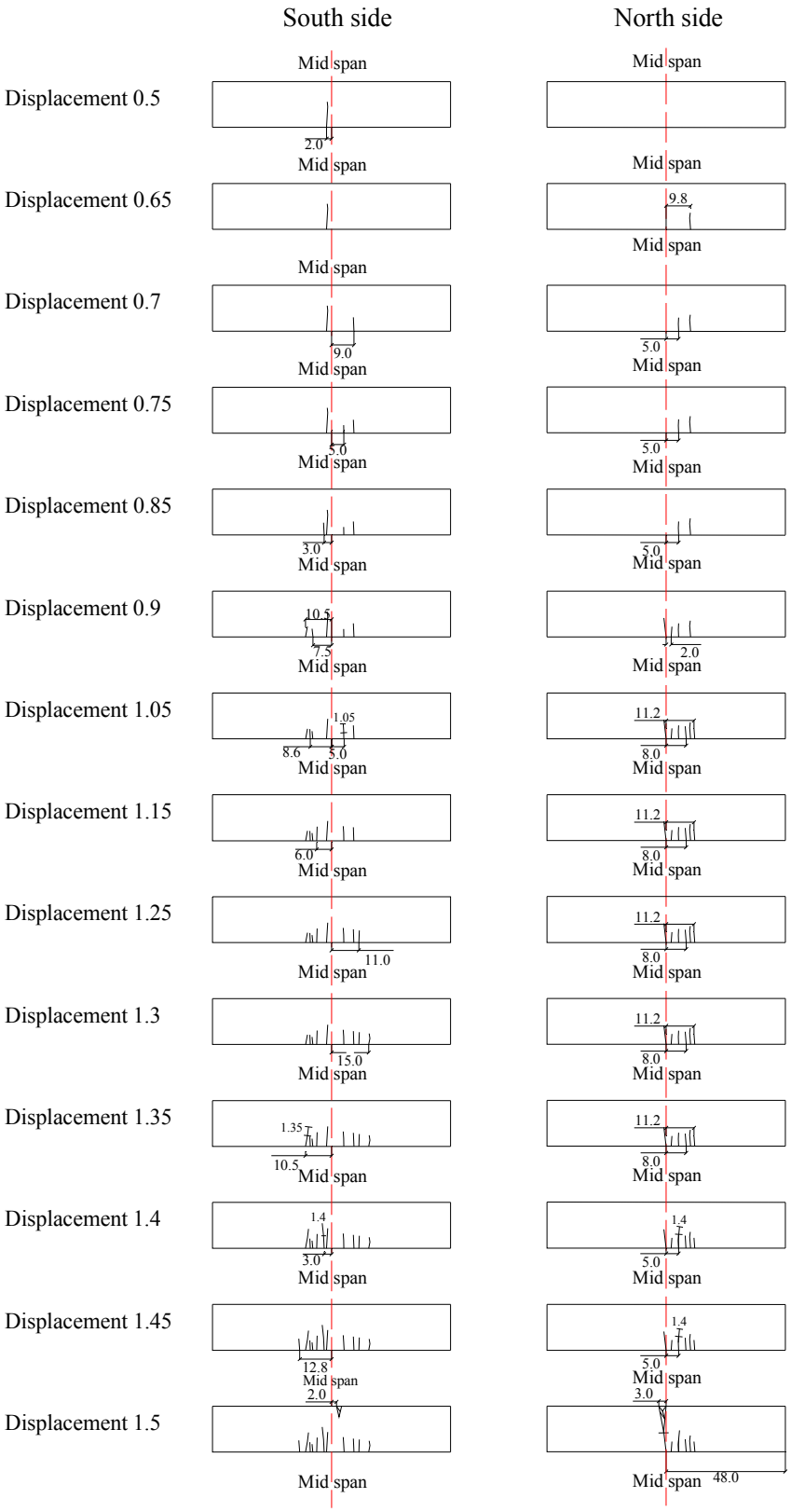

Figure C- 84 Panel ECST-FRC-FL: Propagation of Cracking

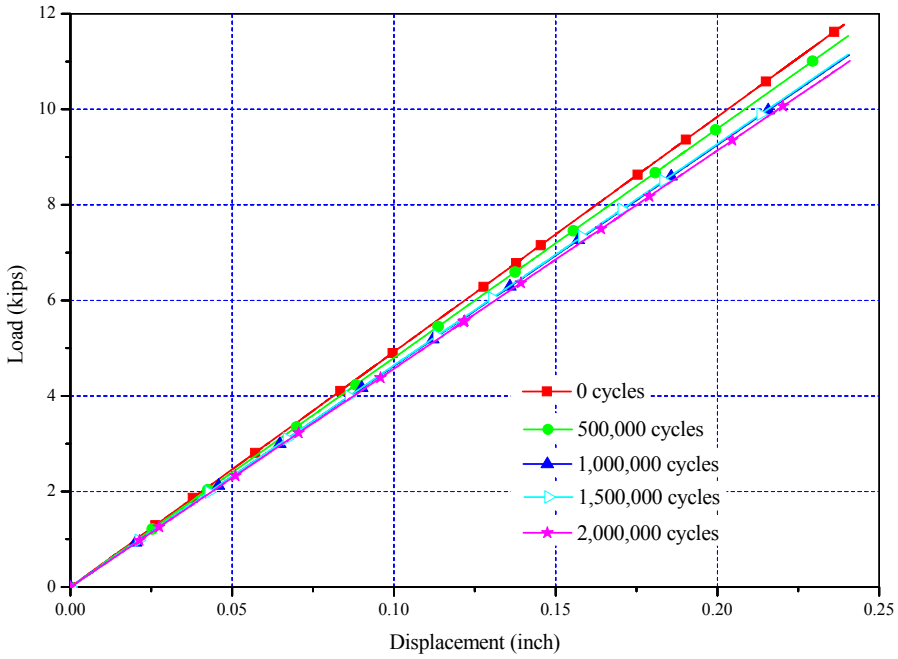

Figure C- 85 Panel ECST-FRC-FL: Applied Load-Displacement Relationships of the Quasi-Static Load Tests

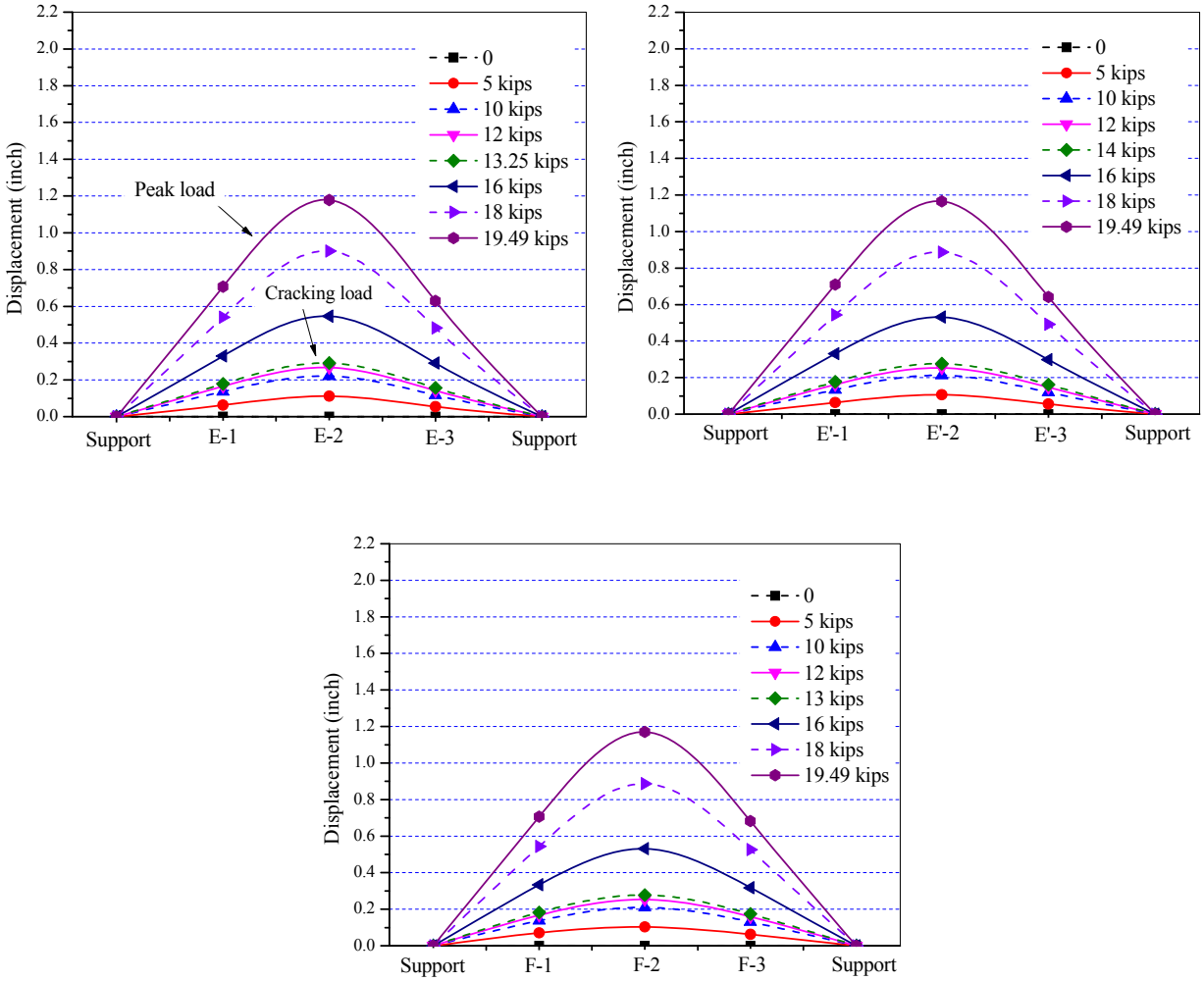

Figure C- 86 Panel ECST-FRC-FL: Measured Displacement Along Panel Length

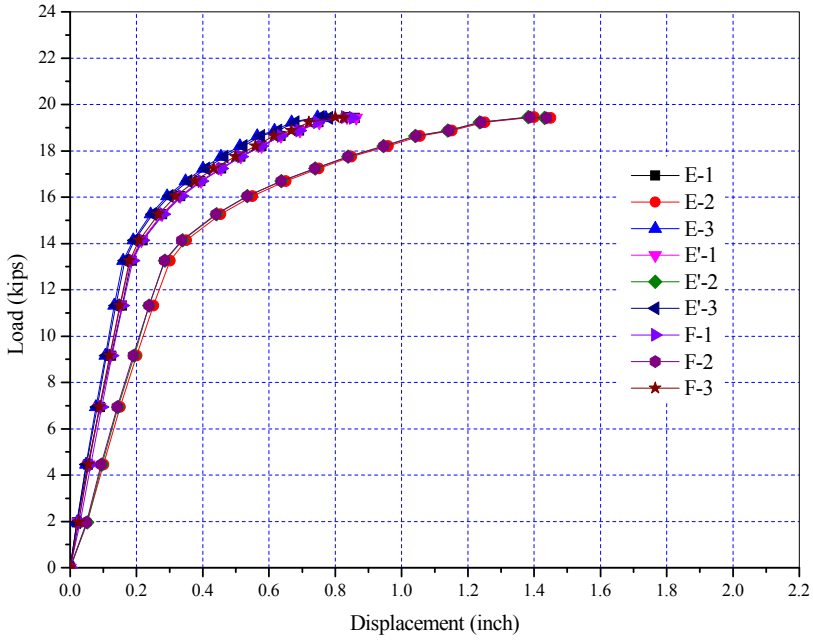

Figure C- 87 Panel ECST-FRC-FL: Applied Load-Displacement Relationship

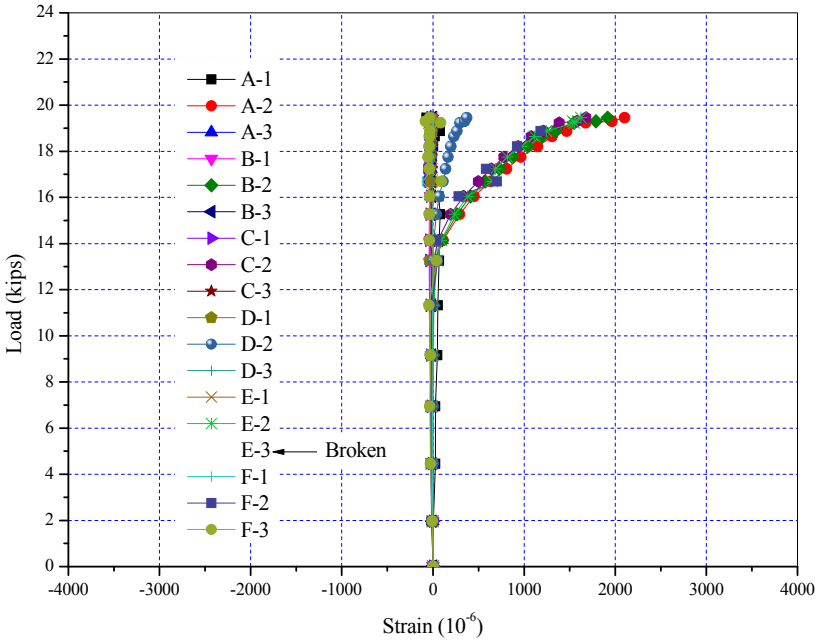

Figure C- 88 Panel ECST-FRC-FL: Applied Load-Tendon Strain Relationship

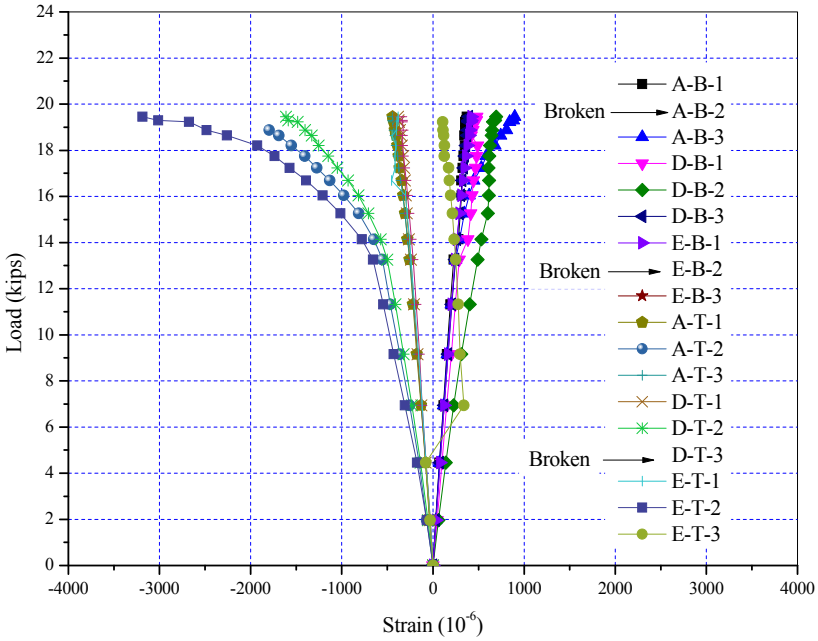

Figure C- 89 Panel ECST-FRC-FL: Applied Load-Concrete Surface Strain Relationship

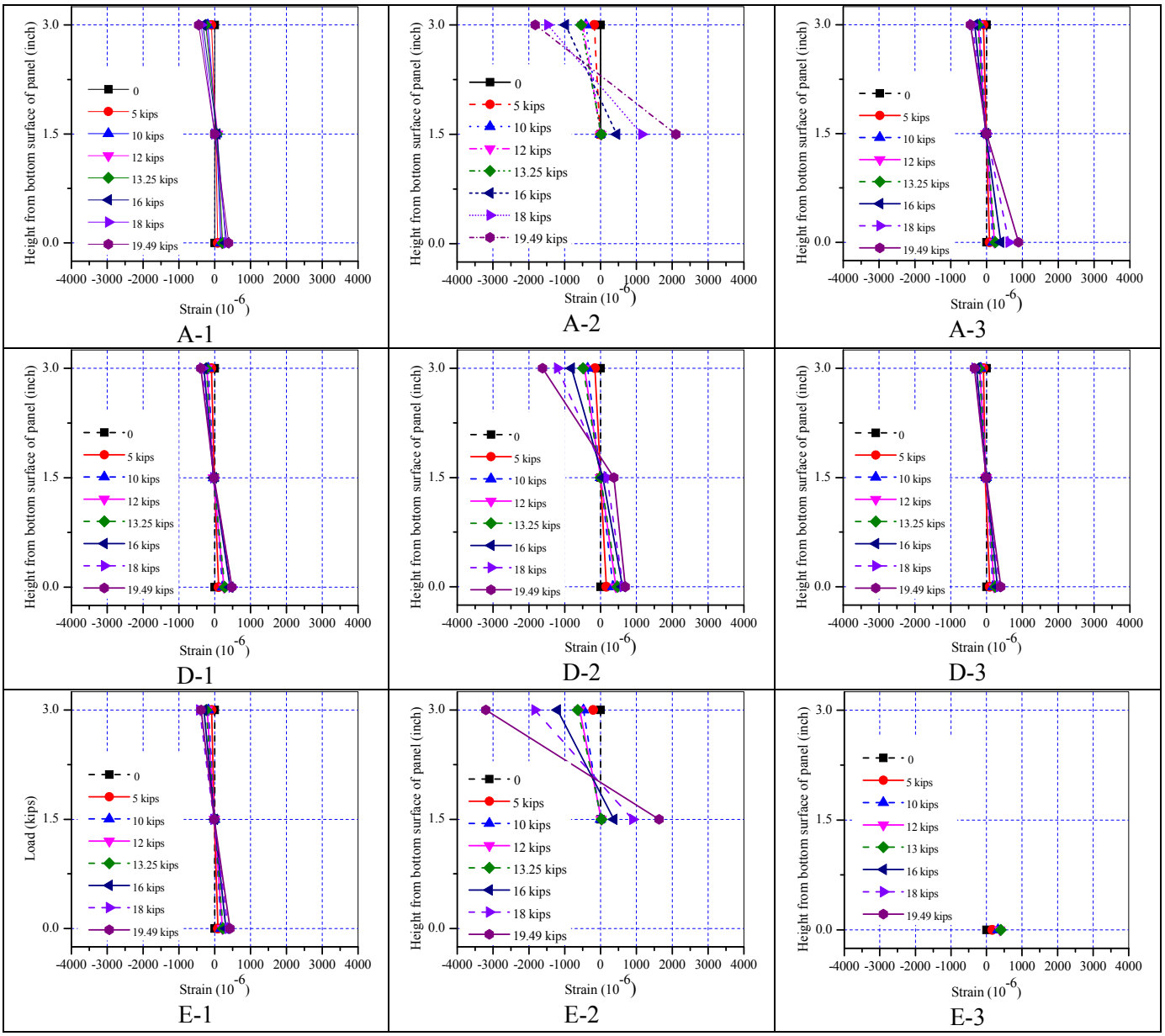

Figure C- 90 Panel ECST-FRC-FL: Measured Strain Distribution, Post-Fatigue Quasi-Static Test

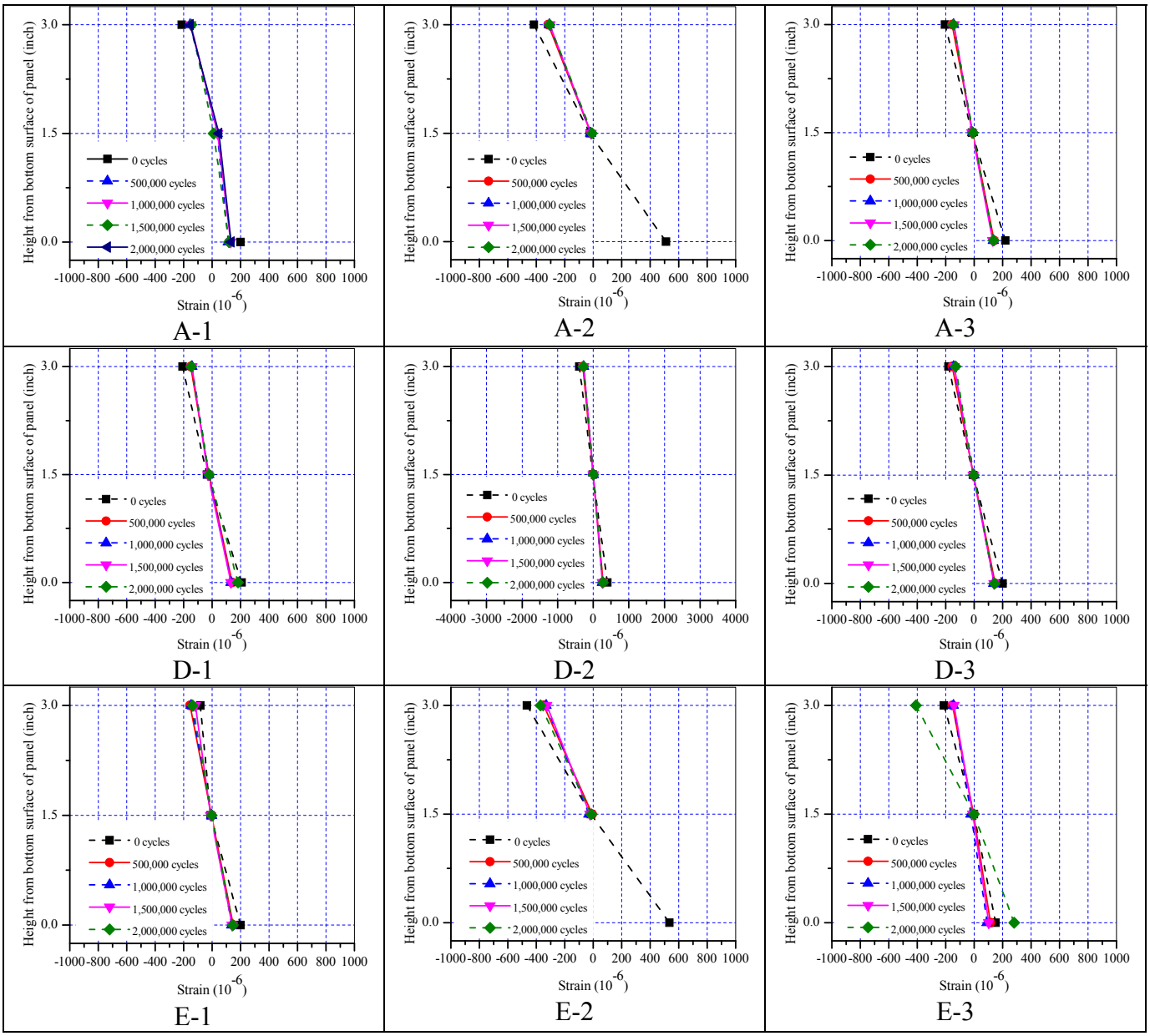

Figure C- 91 Panel ECST-FRC-FL: Measured Strain Distribution at Various Cycles

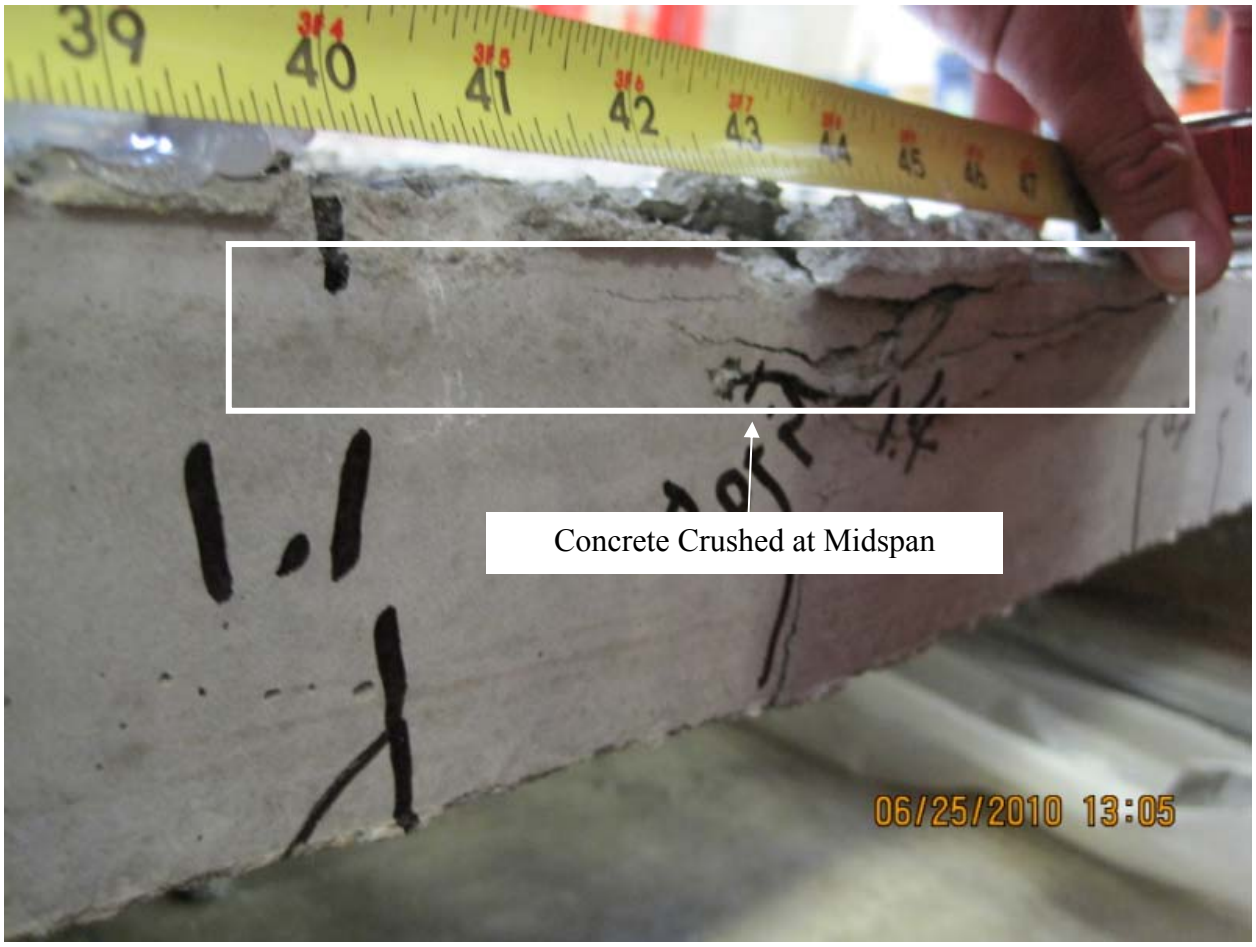

Figure C- 92 Flexural Failure at Midspan by Concrete Crushing of Panel CFRPT-NC-FL

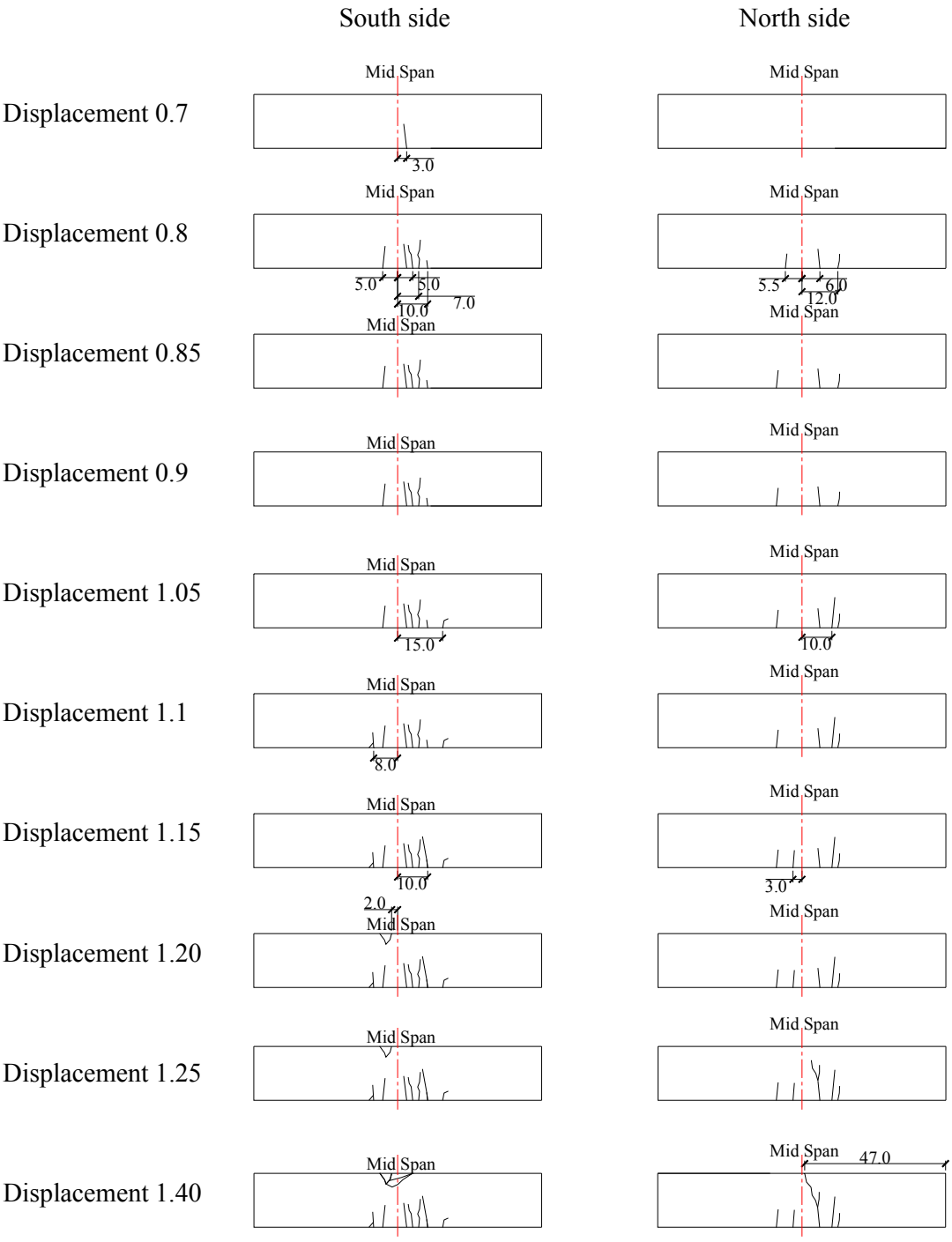

Figure C- 93 Panel CFRPT-NC-FL: Propagation of Cracking

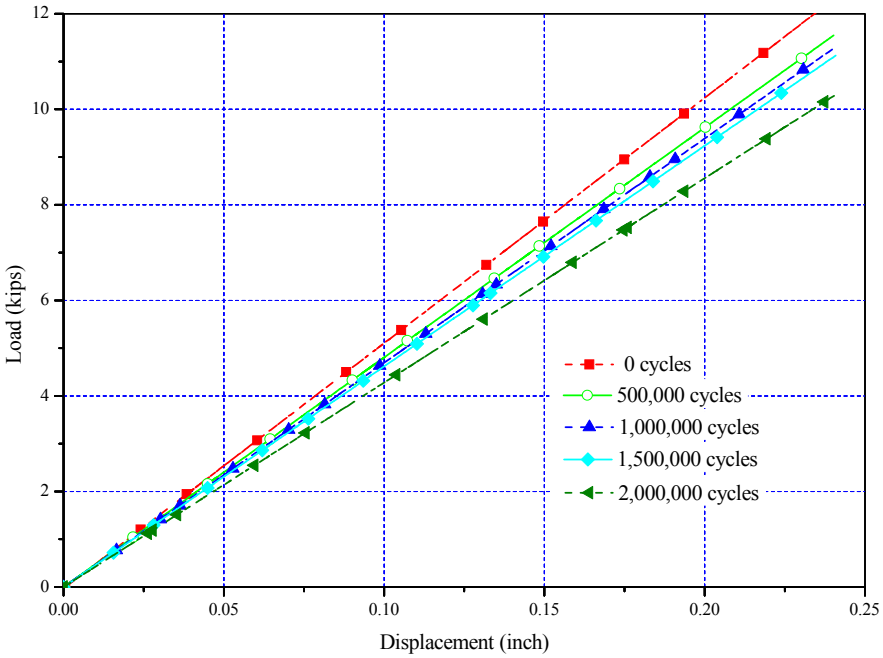

Figure C- 94 Panel CFRPT-NC-FL: Applied Load-Displacement Relationships of the Quasi-Static Load Tests

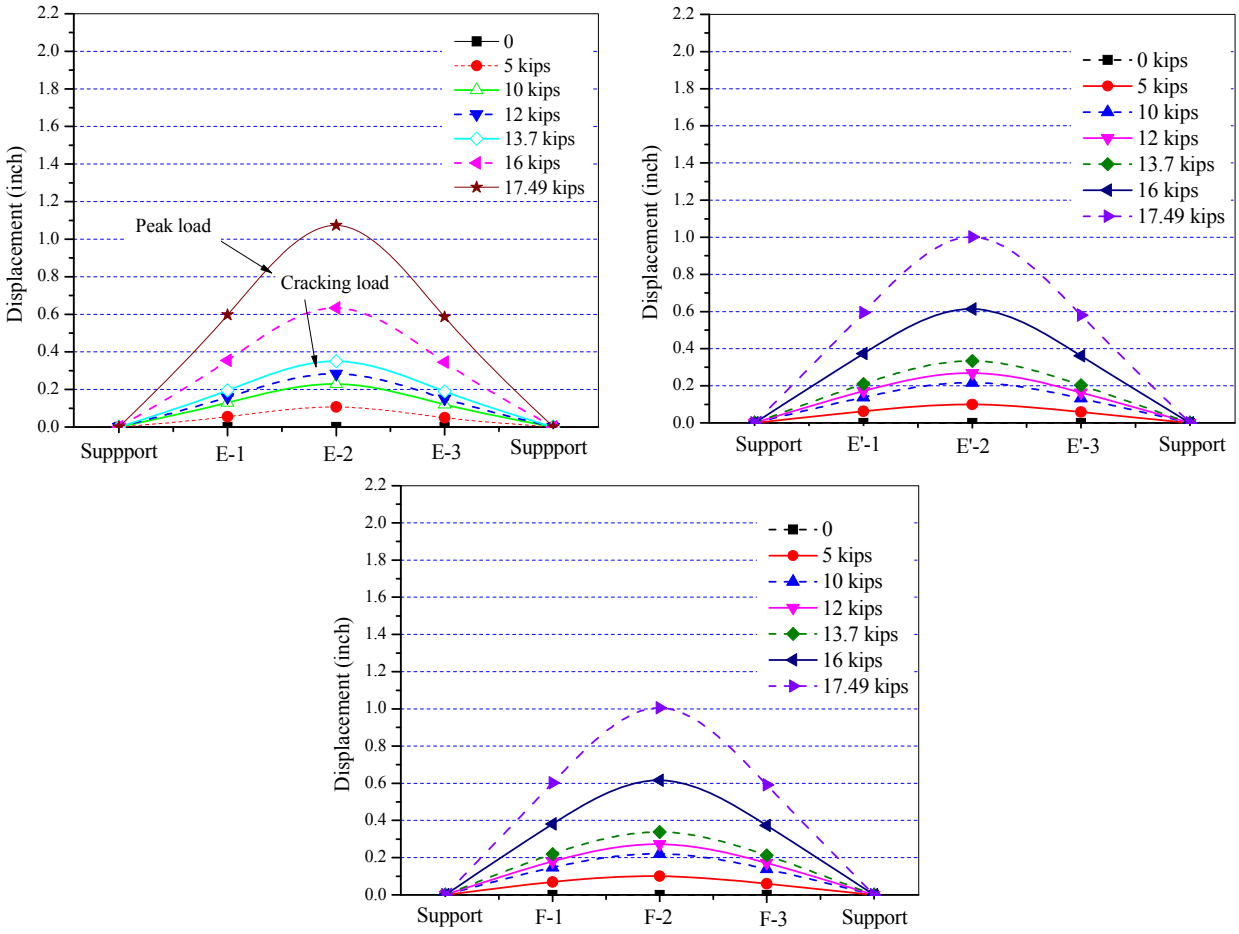

Figure C- 95 Panel CFRPT-NC-FL: Measured Displacement Along Panel Length

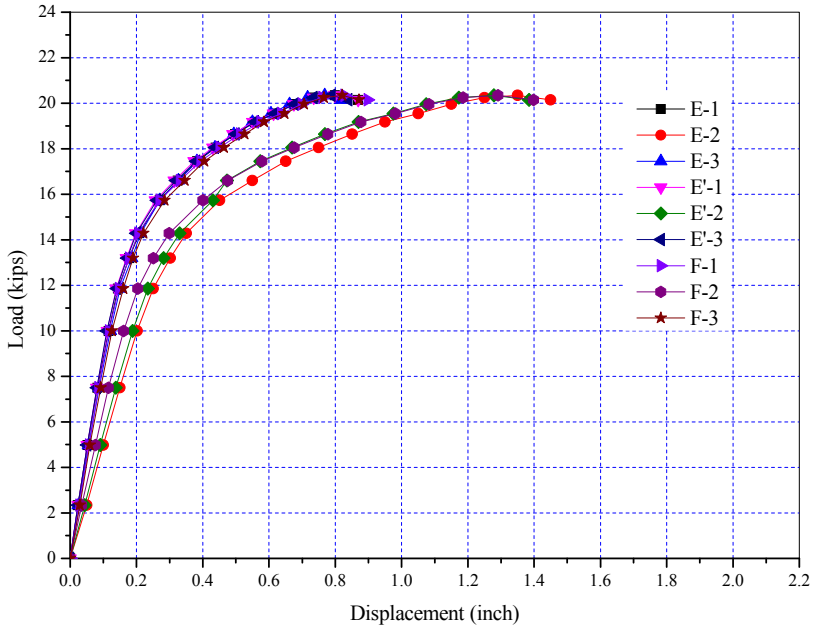

Figure C- 96 Panel CFRPT-NC-FL: Applied Load-Displacement Relationship

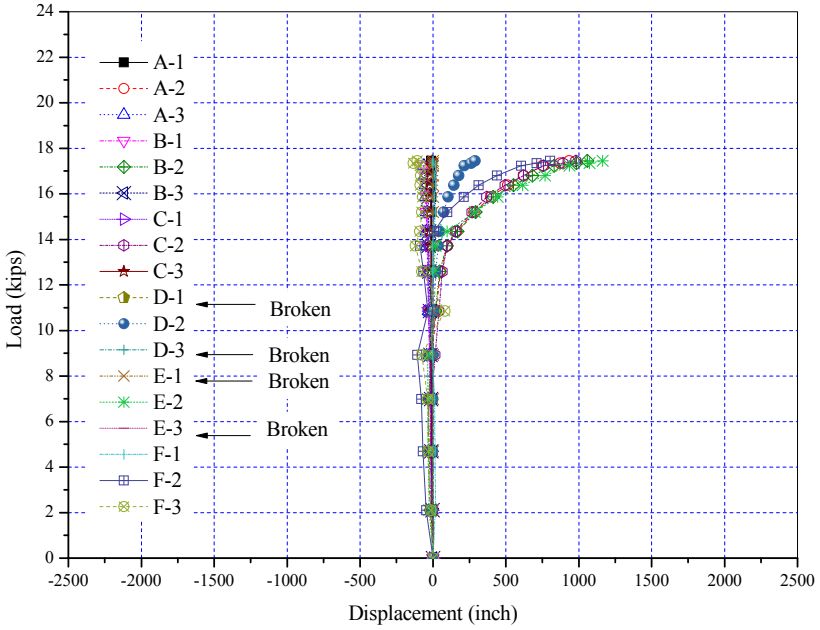

Figure C- 97 Panel CFRPT-NC-FL: Applied Load-Tendon Strain Relationship

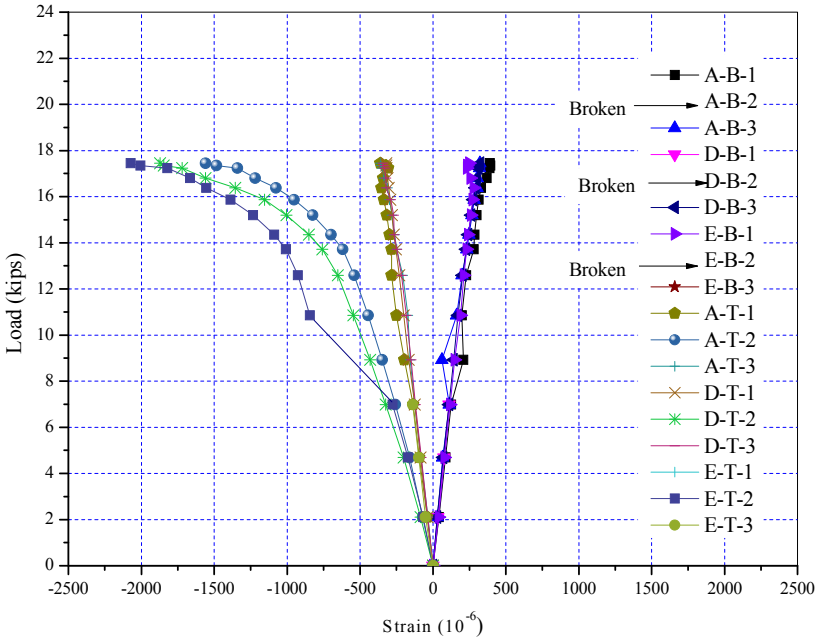

Figure C- 98 Panel CFRPT-NC-FL: Applied Load-Concrete Surface Strain Relationship

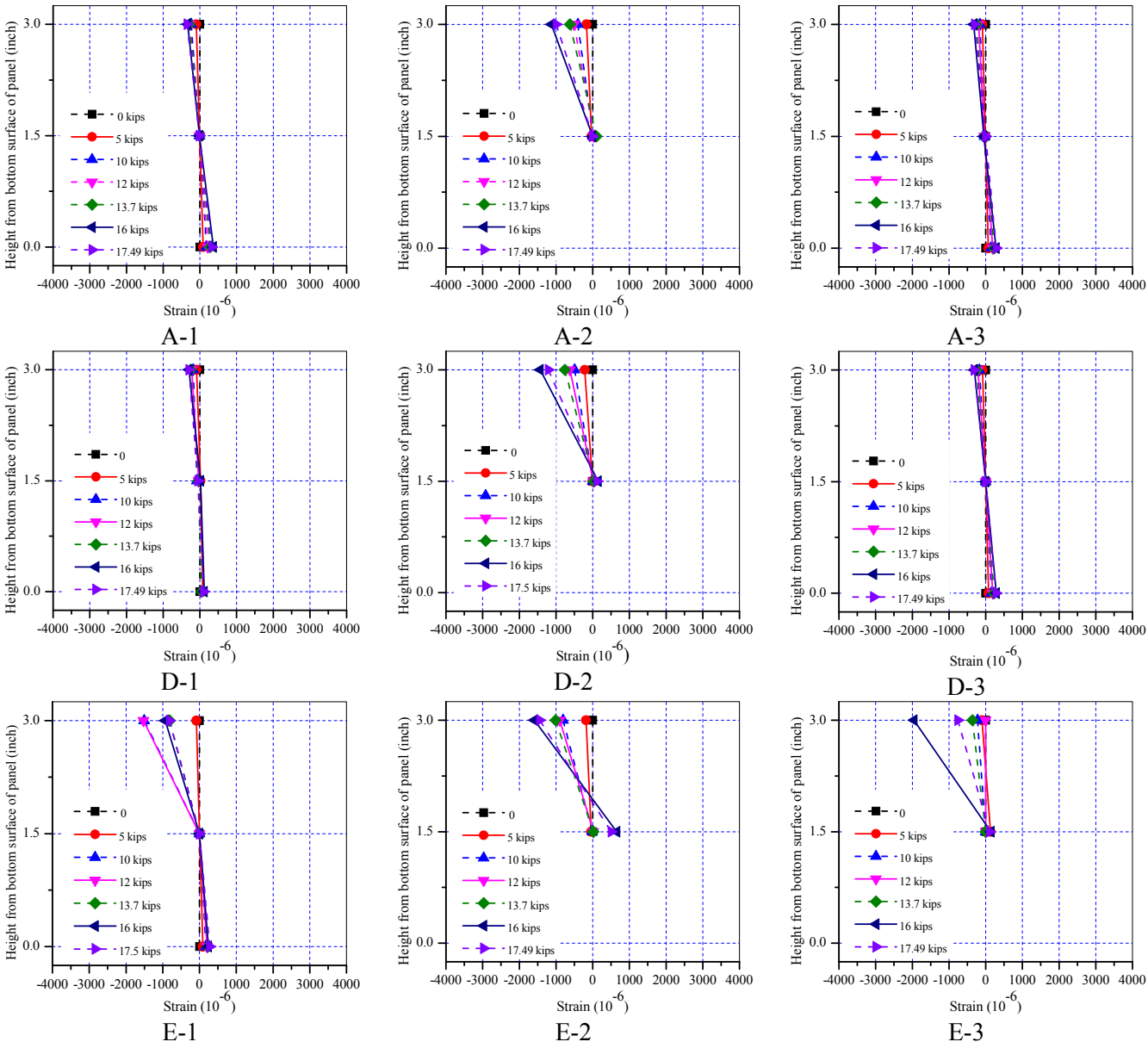

Figure C- 99 Panel CFRPT-NC-FL: Measured Strain Distribution, Post-Fatigue Quasi-Static Test

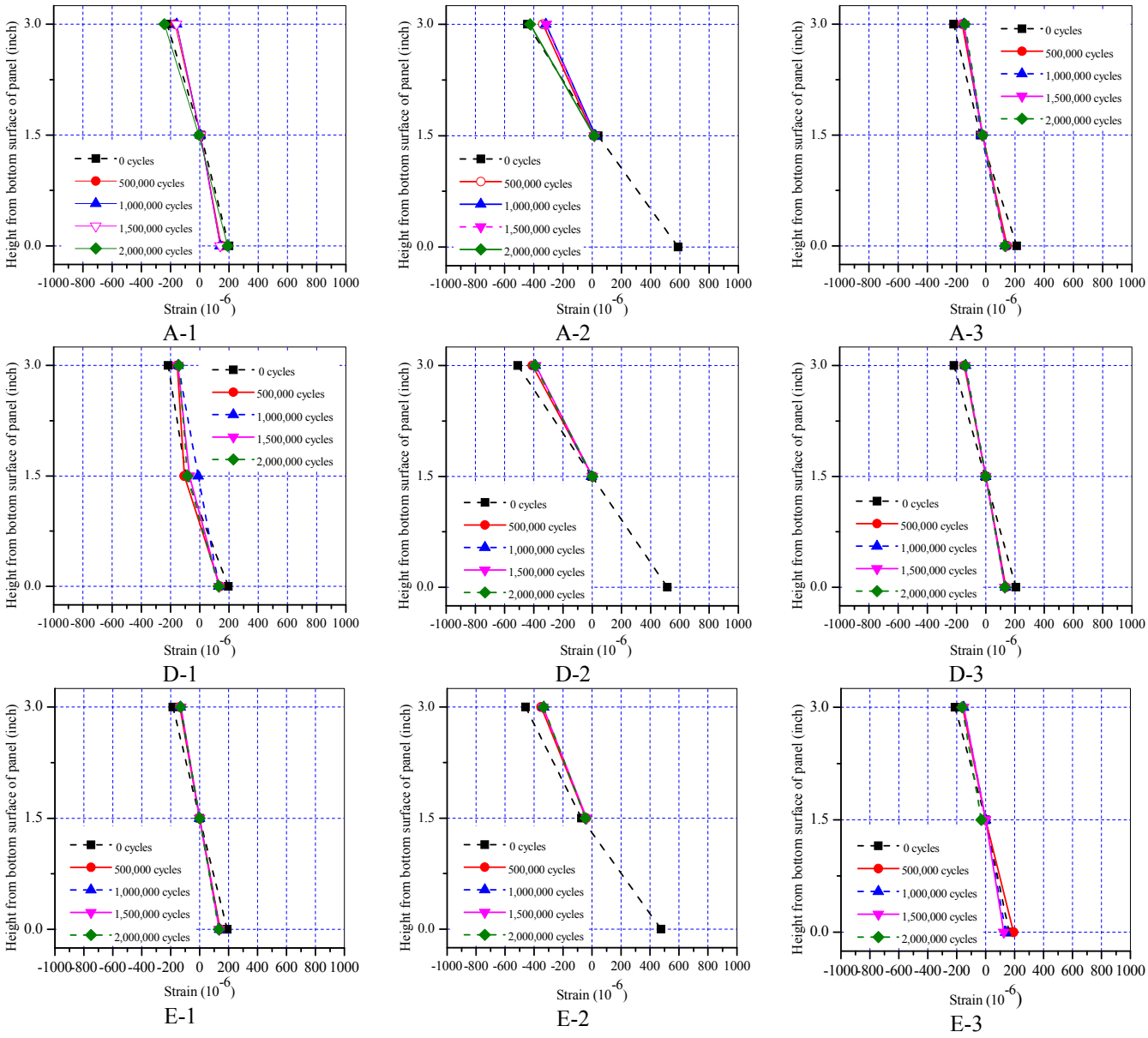

Figure C- 100 Panel CFRPT-NC-FL: Measured Strain Distribution at Various Cycles

Figure C- 101 Flexural Failure at Midspan by Concrete Crushing of Panel CFRPT-FRC-FL

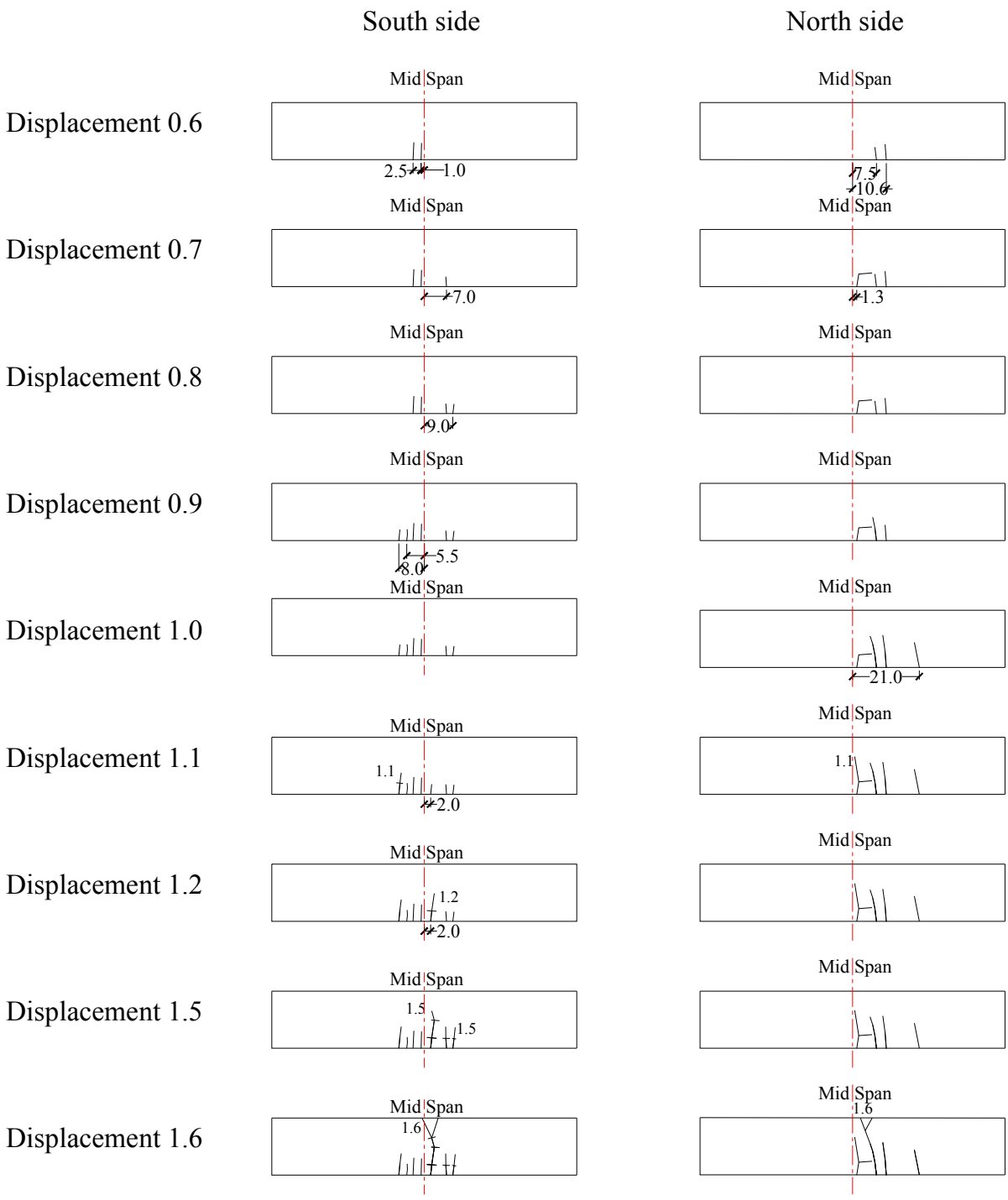

Figure C- 102 Panel CFRPT-FRC-FL: Propagation of Cracking

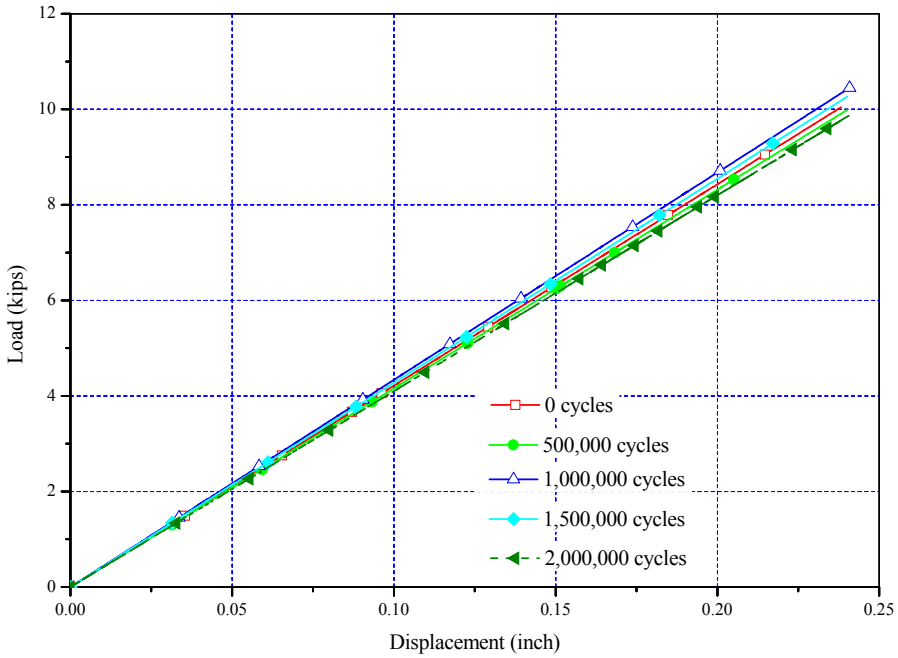

Figure C- 103 Panel CFRPT-FRC-FL: Applied Load-Displacement Relationships of the Quasi-Static Load Tests

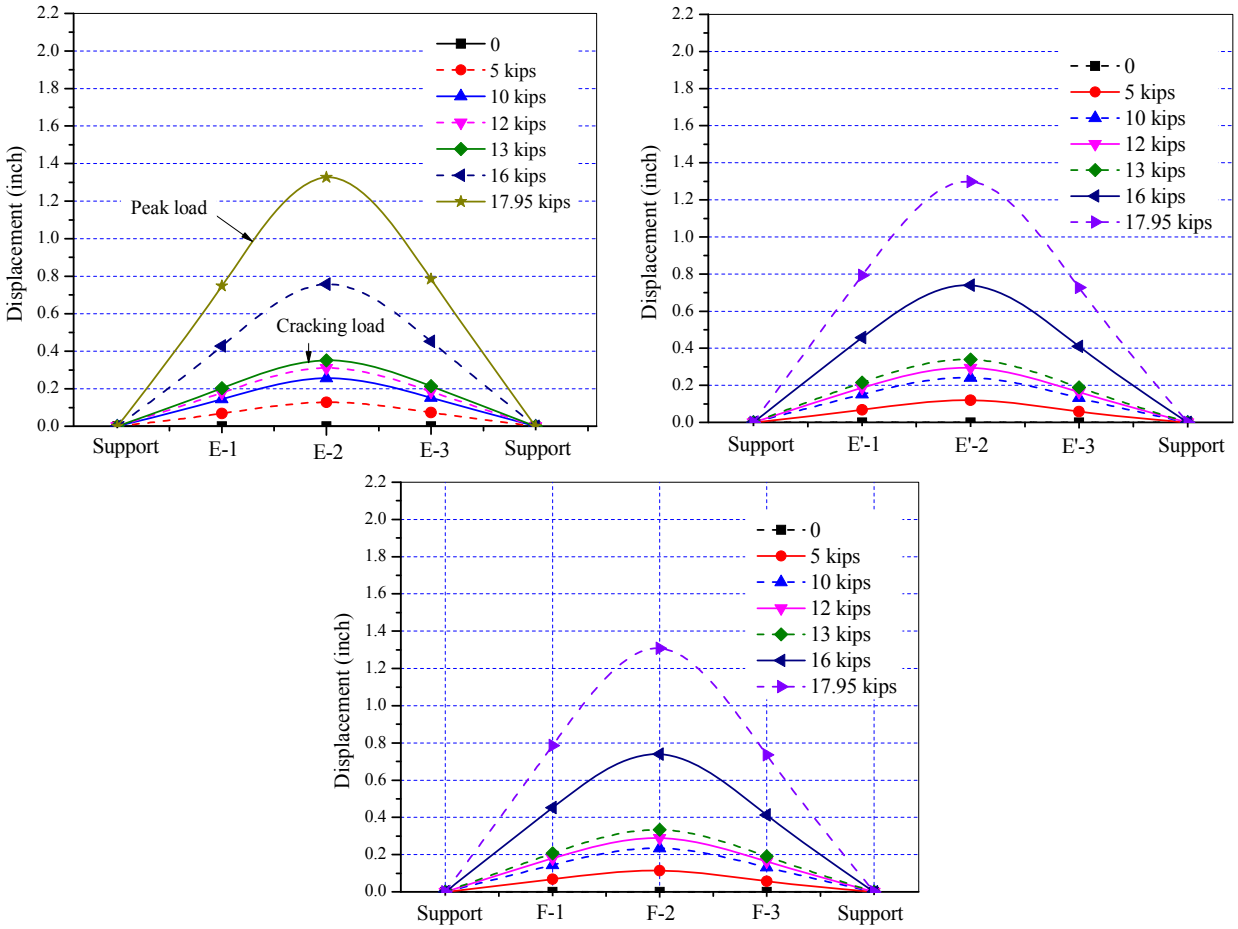

Figure C- 104 Panel CFRPT-FRC-FL: Measured Displacement Along Panel Length

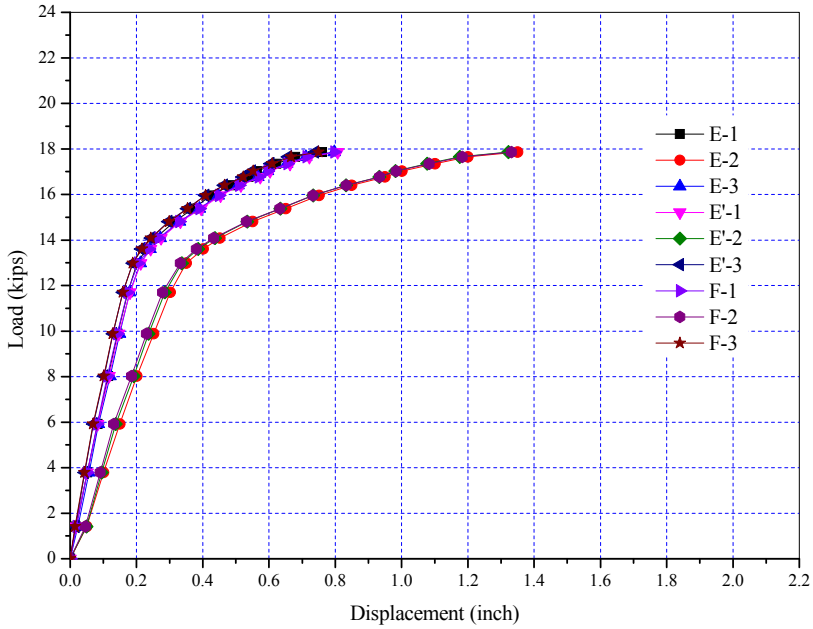

Figure C- 105 Panel CFRPT-FRC-FL: Applied load-displacement relationship

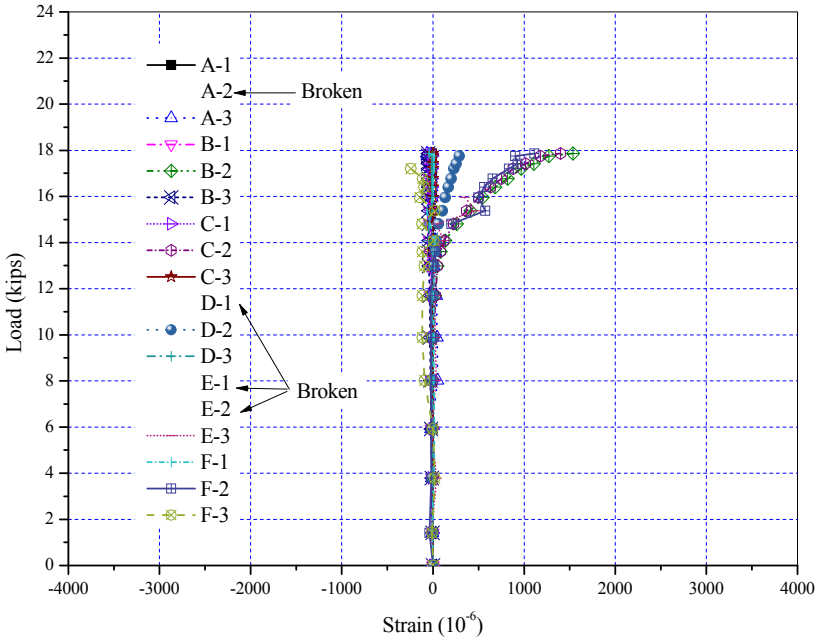

Figure C- 106 Panel CFRPT-FRC-FL: Applied Load-Tendon Strain Relationship

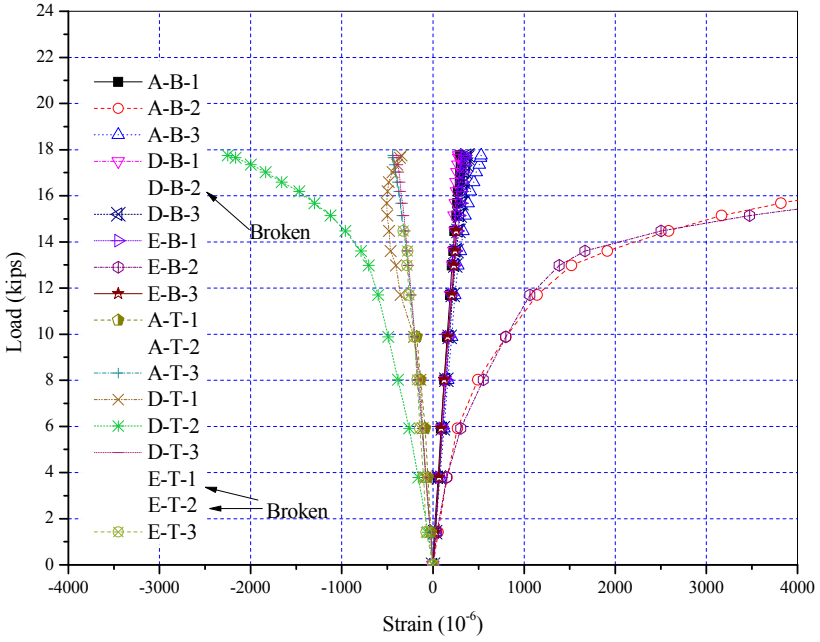

Figure C- 107 Panel CFRPT-FRC-FL: Applied Load-Concrete Surface Strain Relationship

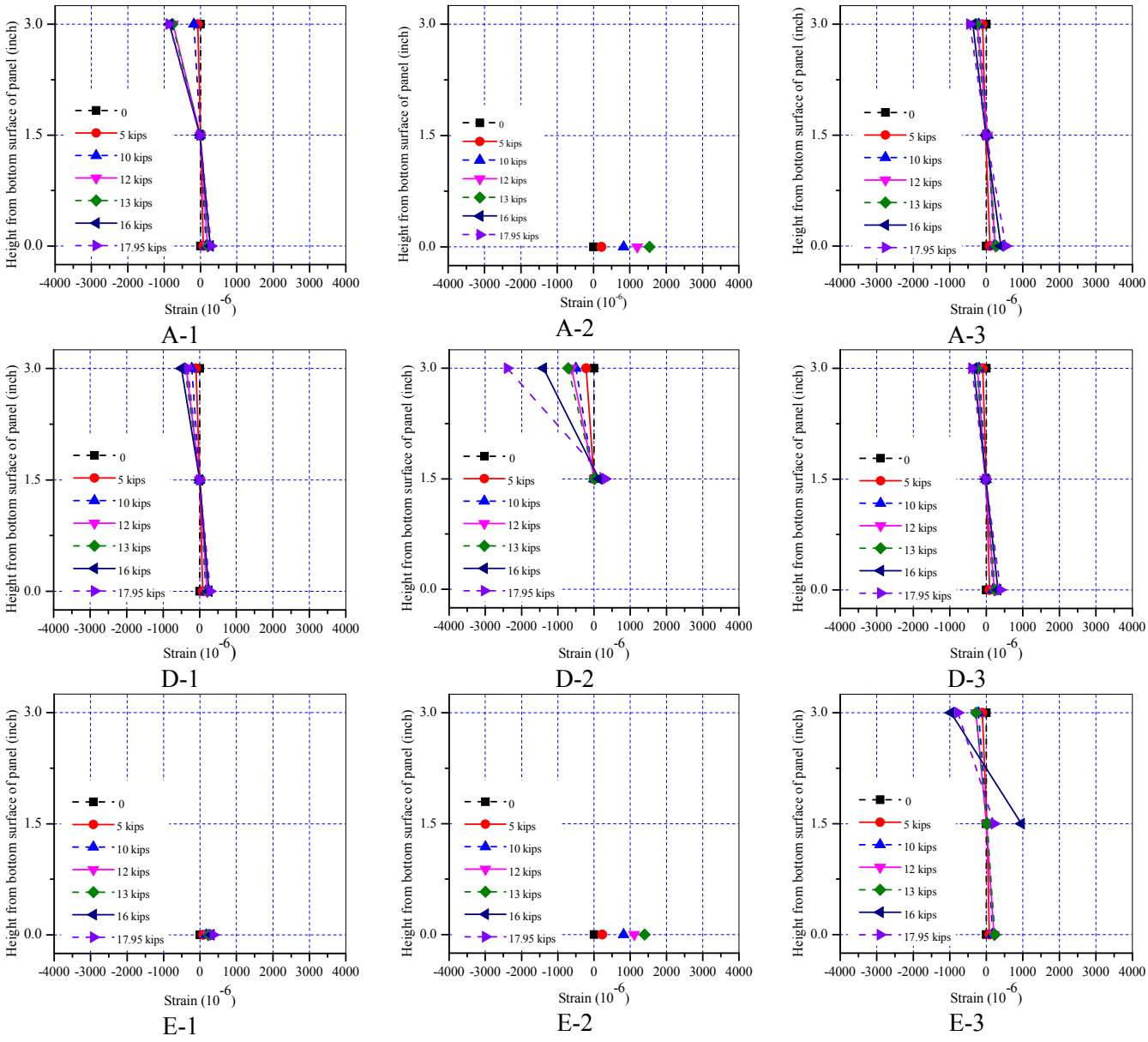

Figure C- 108 Panel CFRPT-FRC-FL: Measured Strain Distribution, Post-Fatigue Quasi-Static Test

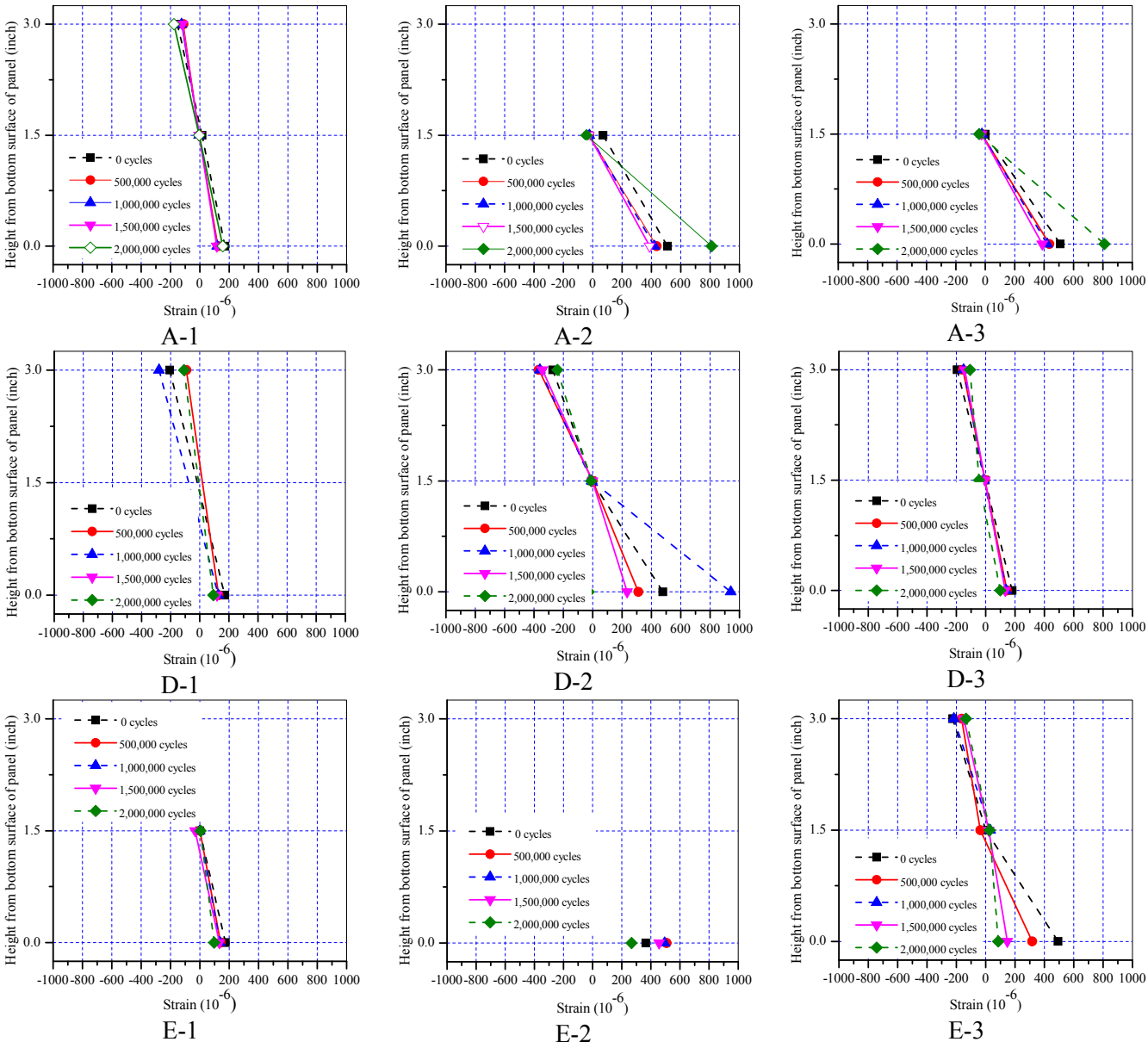

Figure C- 109 Panel CFRPT-FRC-FL: Measured Strain Distribution at Various Cycles

NaCl content (% of cement weight)	Name of specimens	Normal concrete No. of specimens	FRC* No. of specimens	Concrete with CI** No. of specimens	Specimen longitudinal sections	Specimen cross sections
0 %	SP1	3	3	3	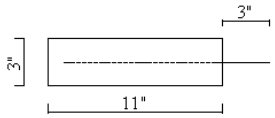	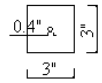
	SP2	3	3	3	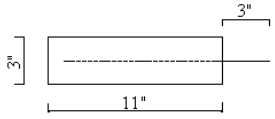	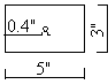
	SP3	3	3	3	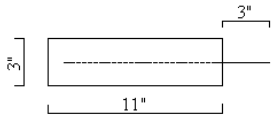	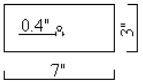
Total number of each concrete type		9	9	9		

* FRC: Fiber Reinforced Concrete
**CI: Corrosion Inhibitor

Figure C- 110 Corrosion Initiation Test Specimen Dimensions

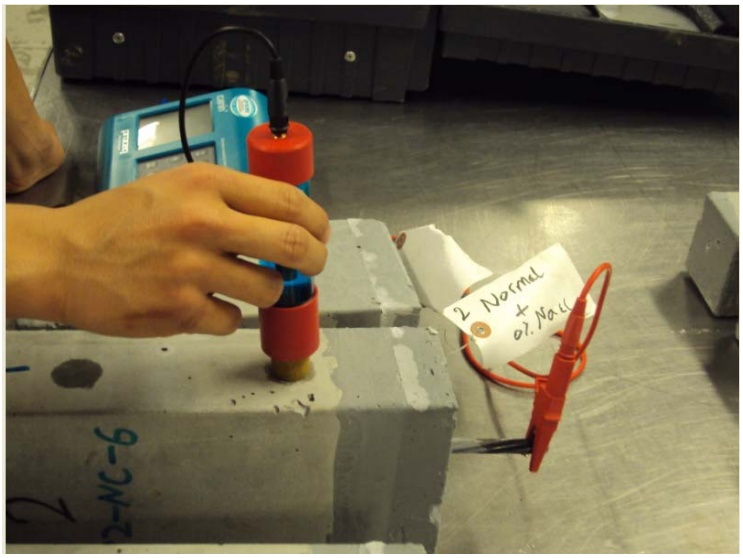

Figure C- 111 Half-cell Potential Measurements

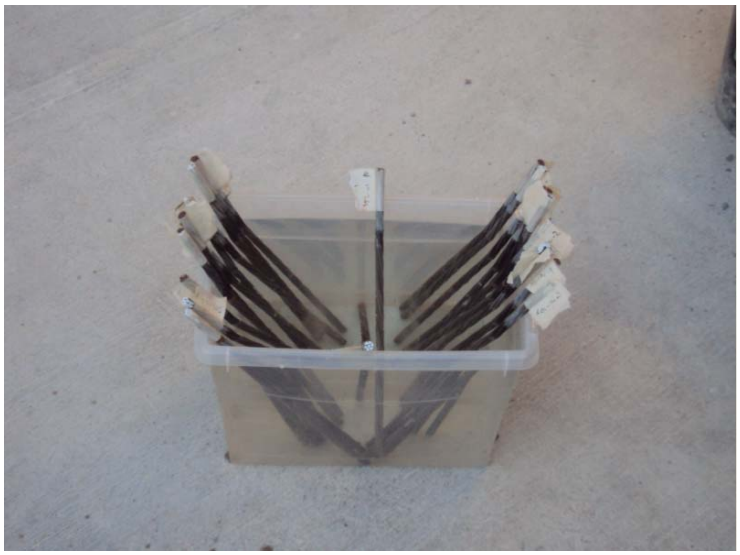

Figure C- 112 Steel Tendons Immersed in Muriatic Acid Solution

NaCl content (% of cement weight)	Name of specimens	Normal concrete No. of specimens	FRC* No. of specimens	Concrete with CI** No. of specimens	Specimen longitudinal sections	Specimen cross sections
3 %	SP1	2	2	2	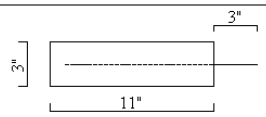	
	SP2	2	2	2	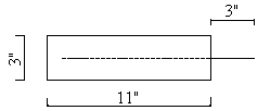	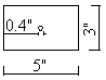
	SP3	2	2	2	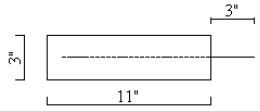	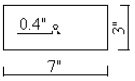
Total number of each concrete type		6	6	6		

* FRC: Fiber Reinforced Concrete
**CI: Corrosion Inhibitor

Figure C- 113 Accelerated Corrosion Test Specimen Dimensions

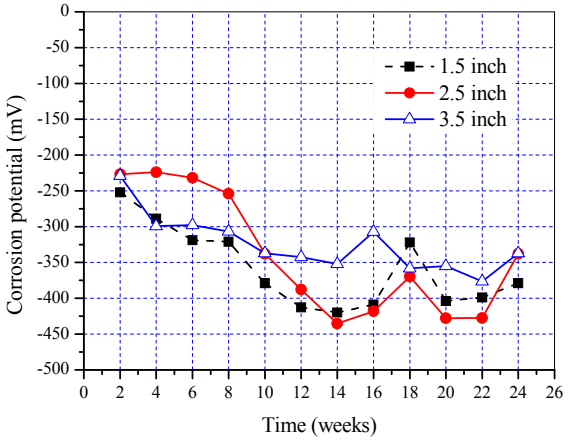

Normal concrete

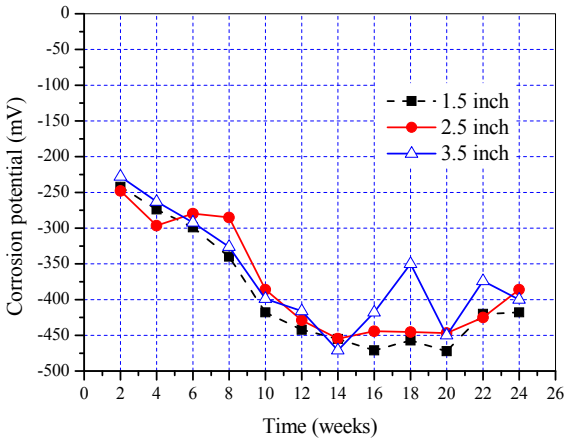

Concrete with corrosion inhibitors

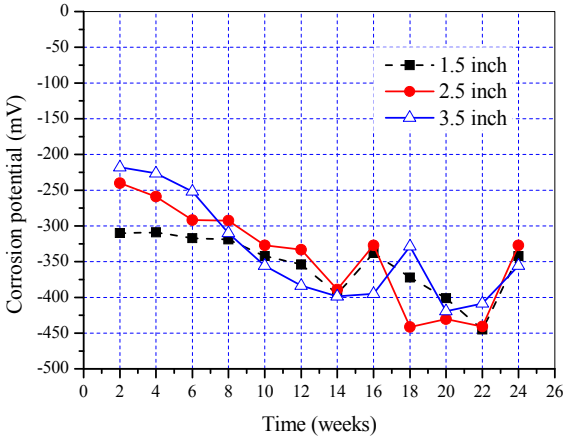

Concrete with fibers

Figure C- 114 Corrosion Potential - Time Relationship for Specimens with Same Concrete Type

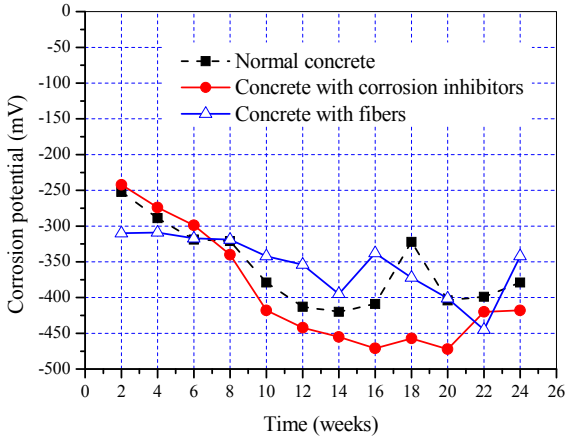

1.5 in. edge distance

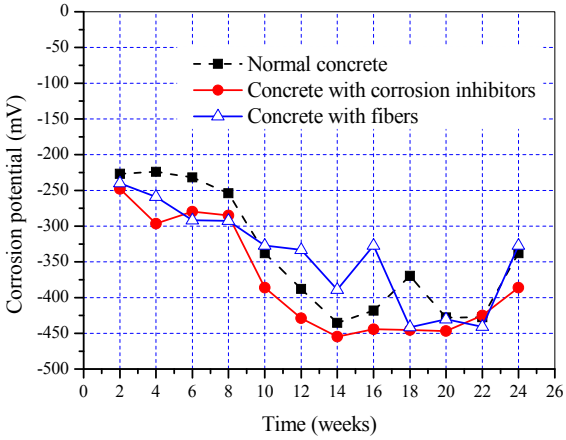

2.5 in. edge distance

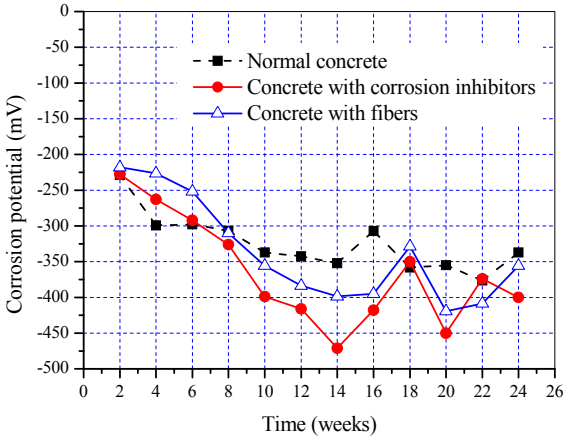

3.5 in. edge distance

Figure C- 115 Corrosion Potential - Time Relationship for Specimens with Same Edge Distance

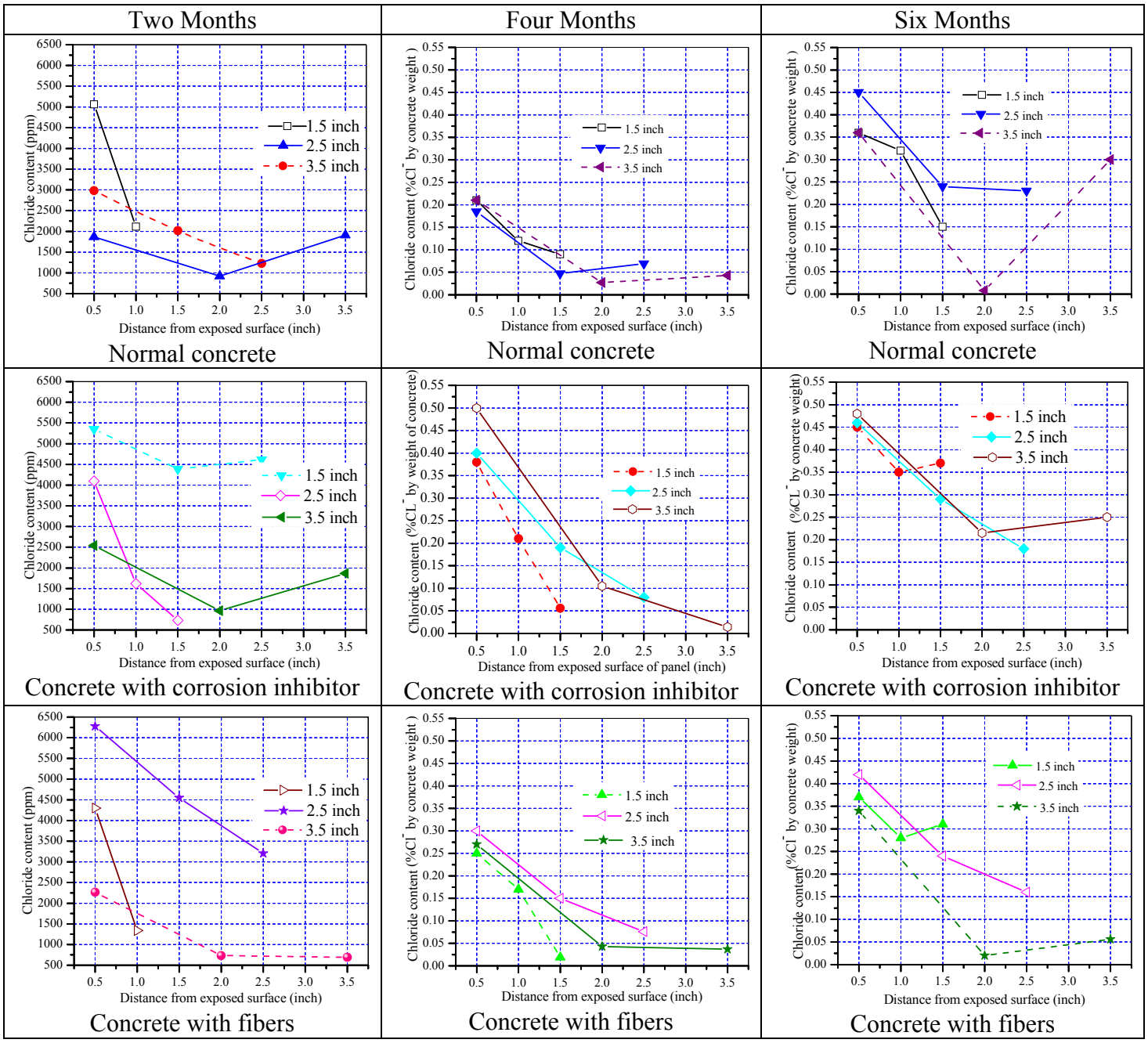

Figure C- 116 Chloride Content Profiles for Specimens with Same Concrete Type

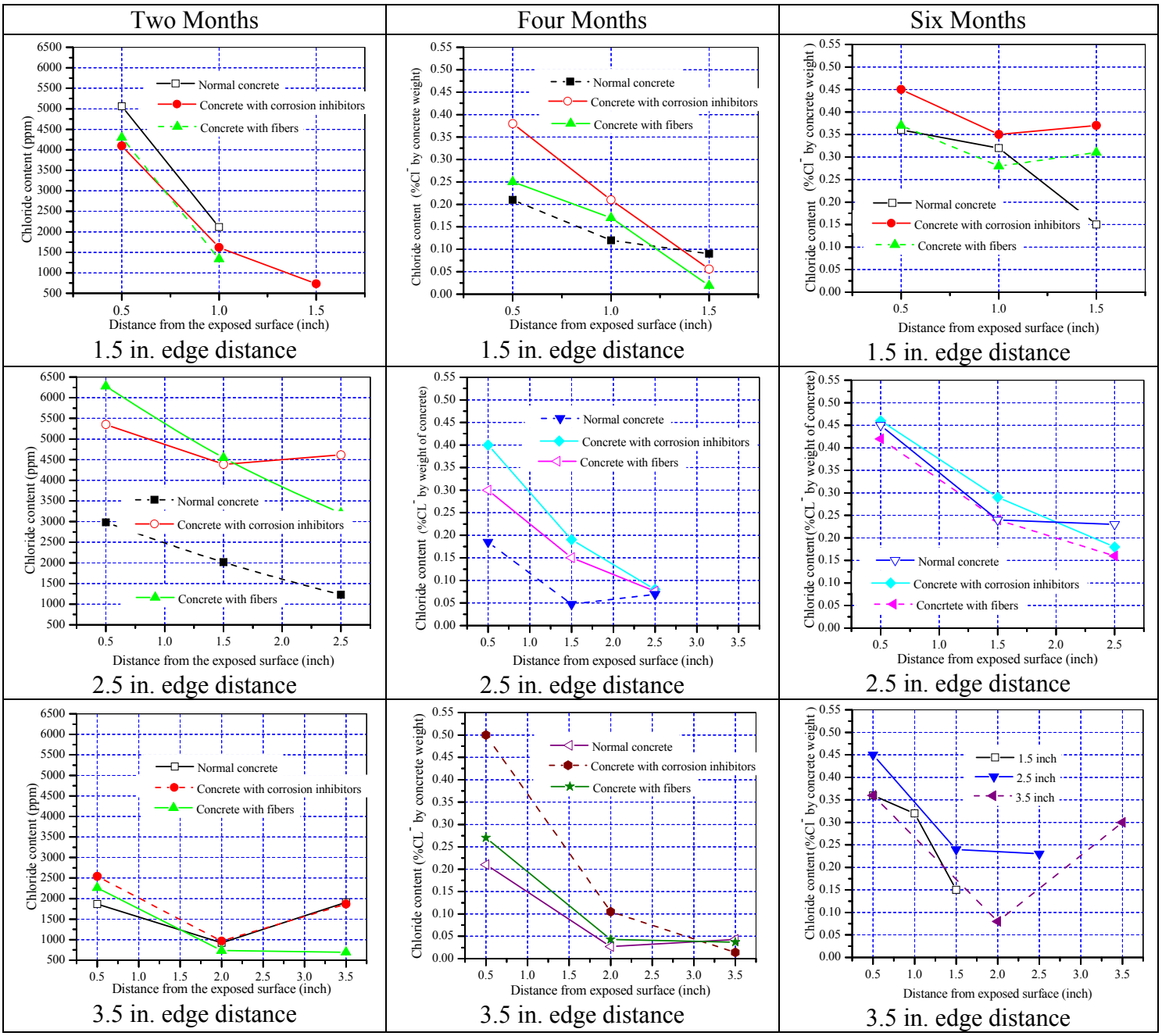

Figure C- 117 Chloride Content Profiles for Specimens with Same Edge Distance

REFERENCES

ASTM A370, 2010. "Standard Test Methods and Definitions for Mechanical Testing of Steel Products," ASTM, West Conshohocken, PA, 47 pp.

ASTM A416, 2010. "Standard Specification for Steel Strand, Uncoated Seven-Wire for Prestressed Concrete," ASTM, West Conshohocken, PA, 5 pp.

ASTM A882, 2010. "Standard Specification for Filled Epoxy-Coated Seven-Wire Prestressing Steel Strand," ASTM, West Conshohocken, PA, 5 pp.

ASTM C1116, 2010. "Standard Specification for Fiber-Reinforced Concrete," ASTM, West Conshohocken, PA, 7 pp.

ASTM C1218, 1999, "Standard Test Method for Water-Soluble Chloride in Mortar and Concrete," ASTM, ASTM, West Conshohocken, PA, 3 pp.

ASTM C150, 2009. "Standard Specification for Portland Cement," ASTM, West Conshohocken, PA, 10 pp.

ASTM C260, 2008. "Standard Specification for Air-Entraining Admixtures for Concrete," ASTM, West Conshohocken, PA, 3 pp.

ASTM C293, 2008. "Standard Test Method for Flexural Strength of Concrete (Using Simple Beam With Center-Point Loading)," ASTM, West Conshohocken, PA, 3 pp.

ASTM C33, 2008. "Standard Specification for Concrete Aggregates," ASTM, West Conshohocken, PA, 11 pp.

ASTM C494, 2010. "Standard Specification for Chemical Admixtures for Concrete," ASTM, West Conshohocken, PA, 10 pp.

ASTM C876, 1991, "Standard Test Method for Half-Cell Potentials of Uncoated Reinforcing Steel in Concrete," ASTM, West Conshohocken, PA, 6 pp.

ASTM G1, 2003, "Standard Practice for Preparing, Cleaning, and Evaluating Corrosion Test Specimens," ASTM, West Conshohocken, PA, 9 pp.

Missouri Department of Transportation (MoDOT), 2004, "2004 Missouri Standard Specification Book for Highway Construction," Missouri Department of Transportation,Jefferson city, MO.

APPENDIX D

NUMERICAL ANALYSES OF SIP PANEL SYSTEMS

TABLE OF CONTENTS

LIST OF FIGURES

D.1 INTRODUCTION

This appendix provides supplemental information and detailed results of the FE simulations summarized in Chapter 6.

D.2 SIMULATION OF SIP PANEL SPALLING

D.2.1 2D FE simulation of reinforcement arrangement effects on corrosion process

Two main FE models were developed according to different locations of the U1 bar as shown in Figure D-1 . Case I represents a critical configuration of reinforcement arrangement that can occur, while Case II represents a typical reinforcement arrangement. Based on these models, side cover was varied from 1.5 in. to 4 in. in both FE models. Crack patterns and Von Mises stress variations for all simulated FE models are presented in this section to compare the effects of the parameters considered.

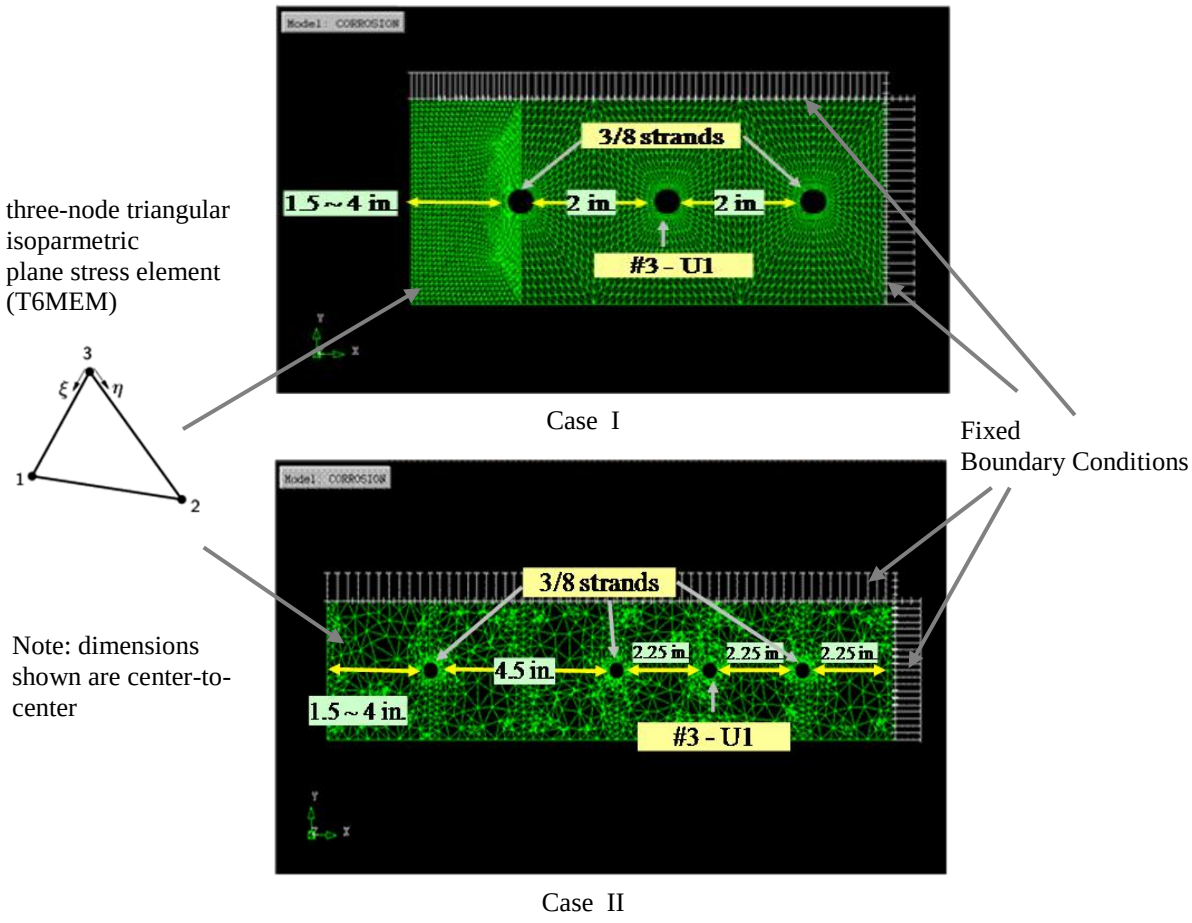

Figure D-1 Two-Dimensional FE Models for Corrosion Process

D.2.1.1 Case I FE analysis results

Crack patterns and corresponding Von Mises stress variations of Case I FE analyses are illustrated from Figure D-2 to Figure D-6. Each figure represents a different side cover, and results are presented with respect to incrementally increasing internal pressures.

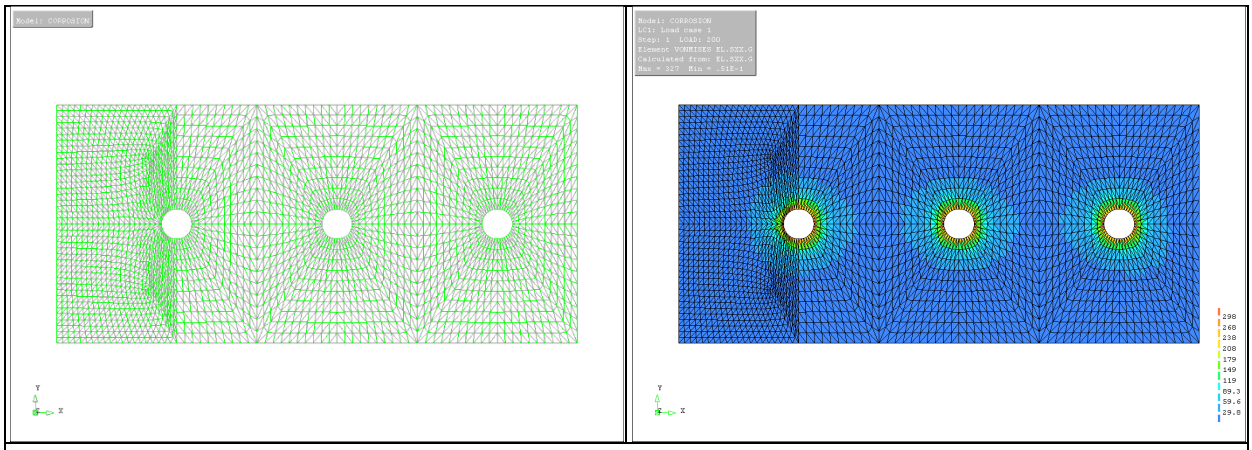

p_{int} = 200 psi

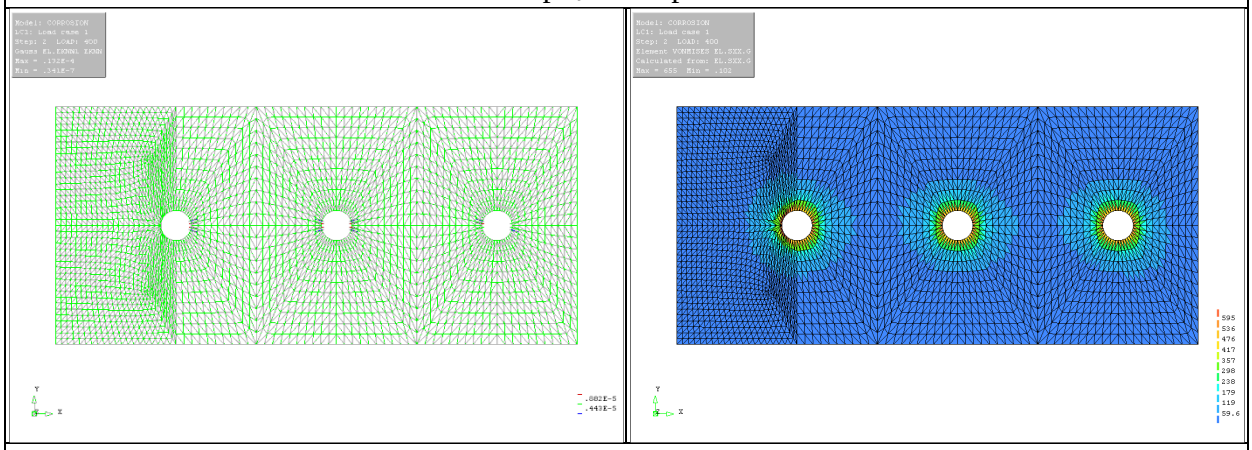

p_{int} = 400 psi

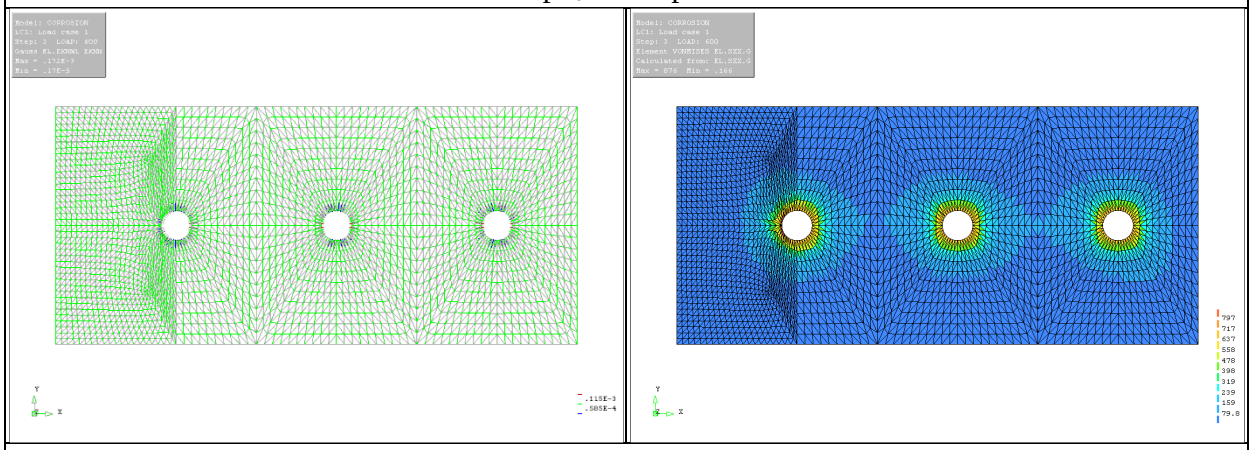

p_{int} = 600 psi

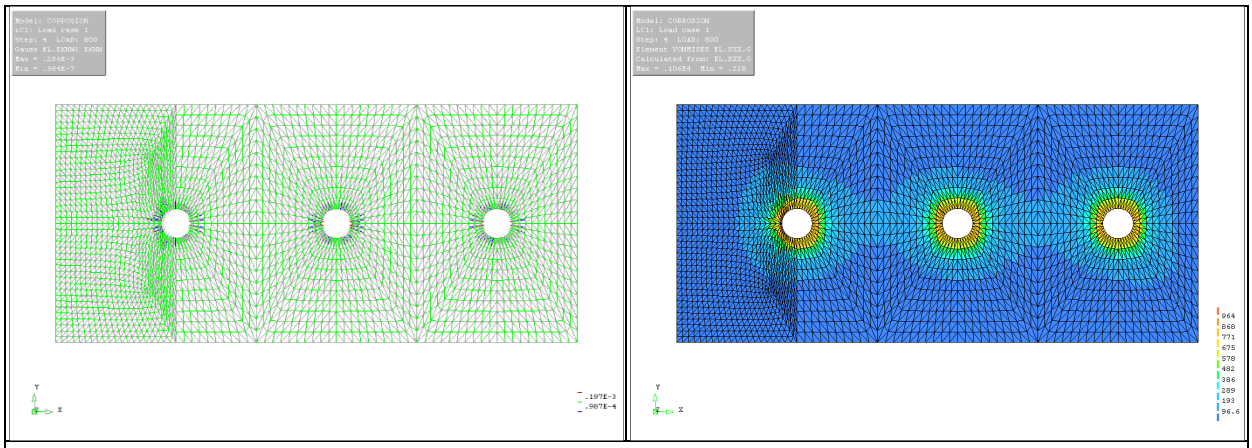

p_{int} = 800 psi

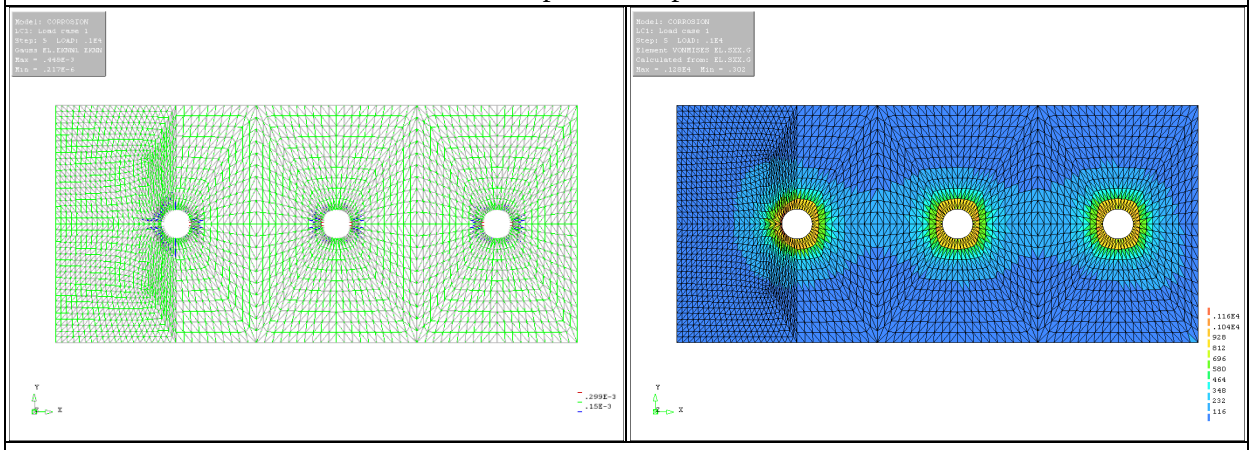

p_{int} = 1,000 psi

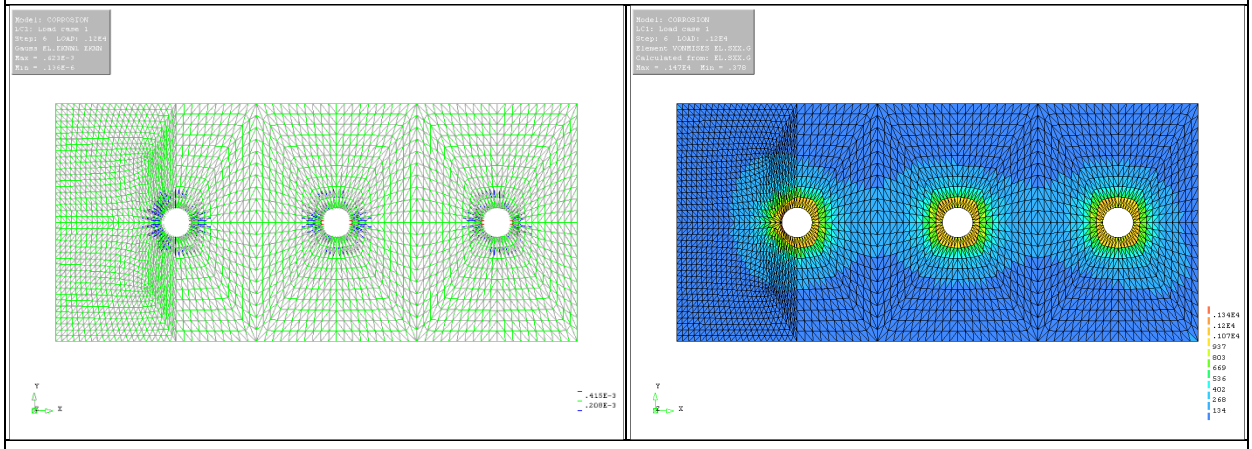

p_{int} = 1,200 psi

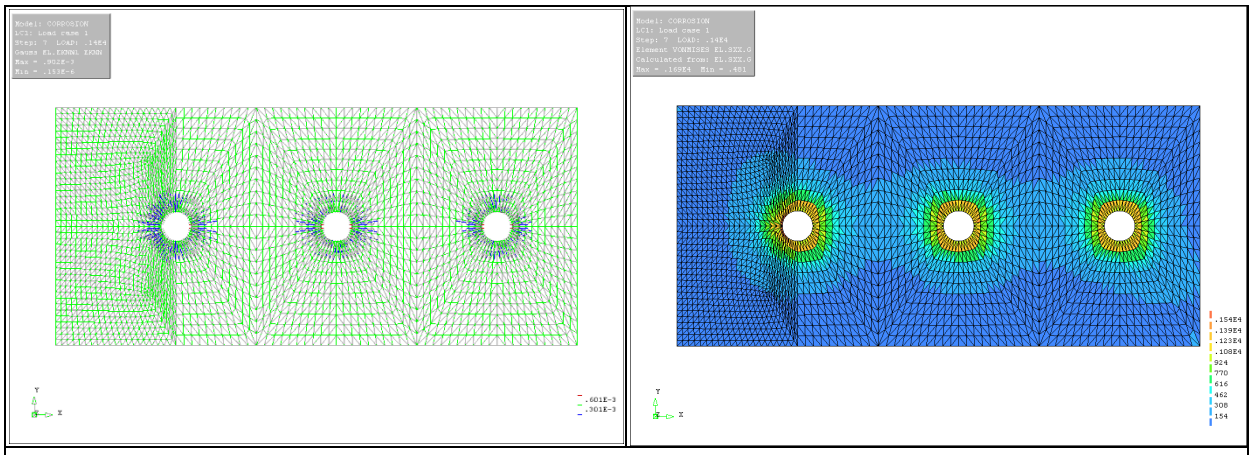

p_{int} = 1,400 psi

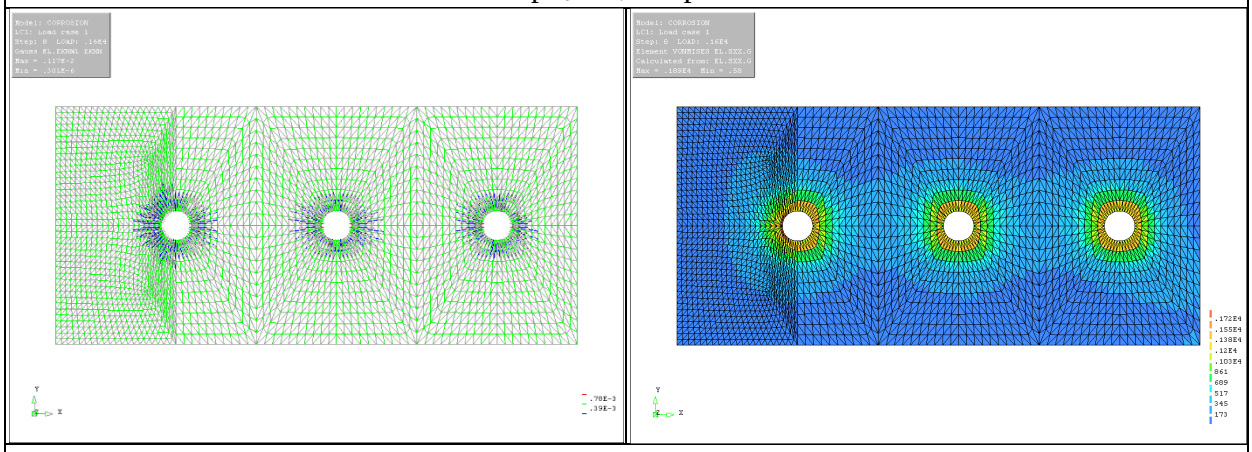

p_{int} = 1,600 psi

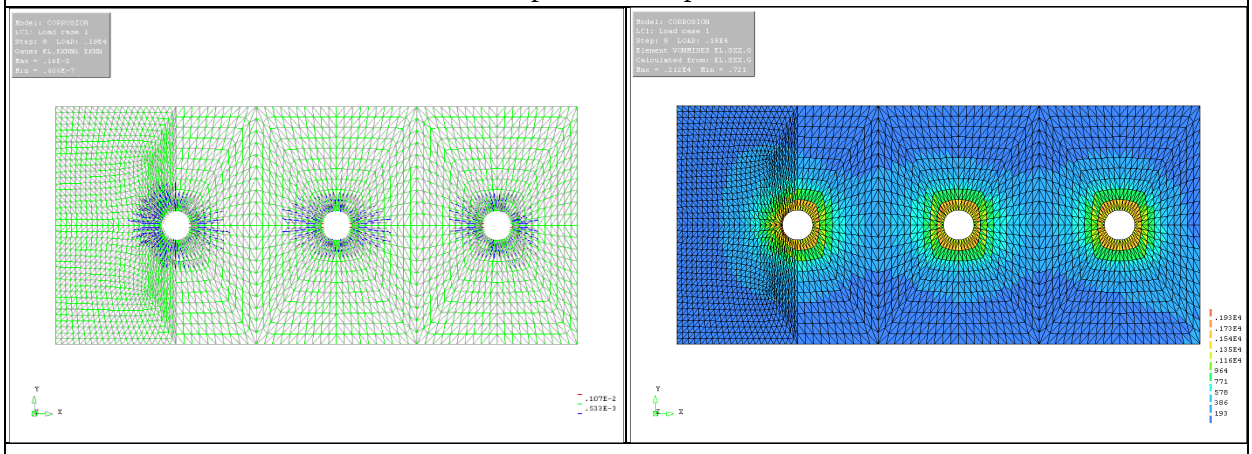

p_{int} = 1,800 psi

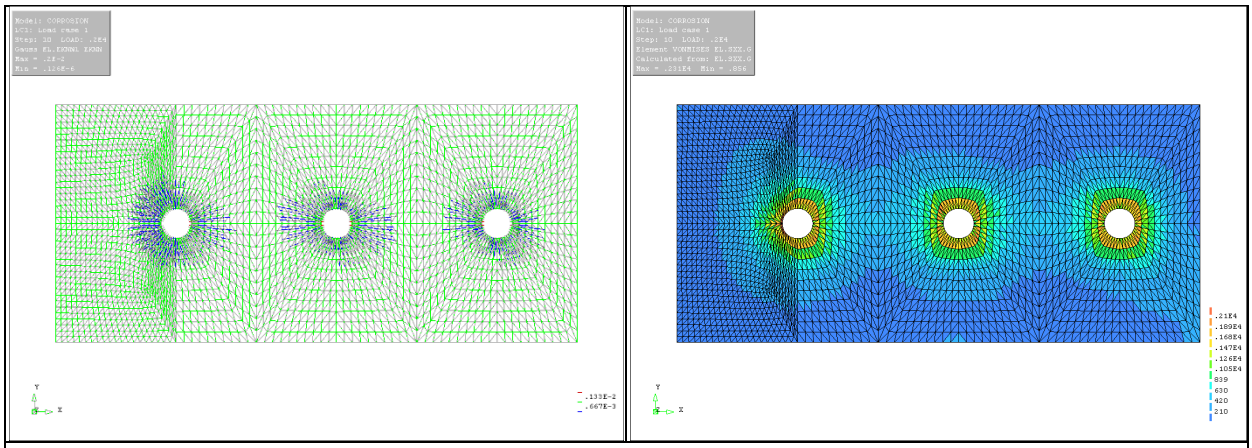

p_{int} = 2,000 psi

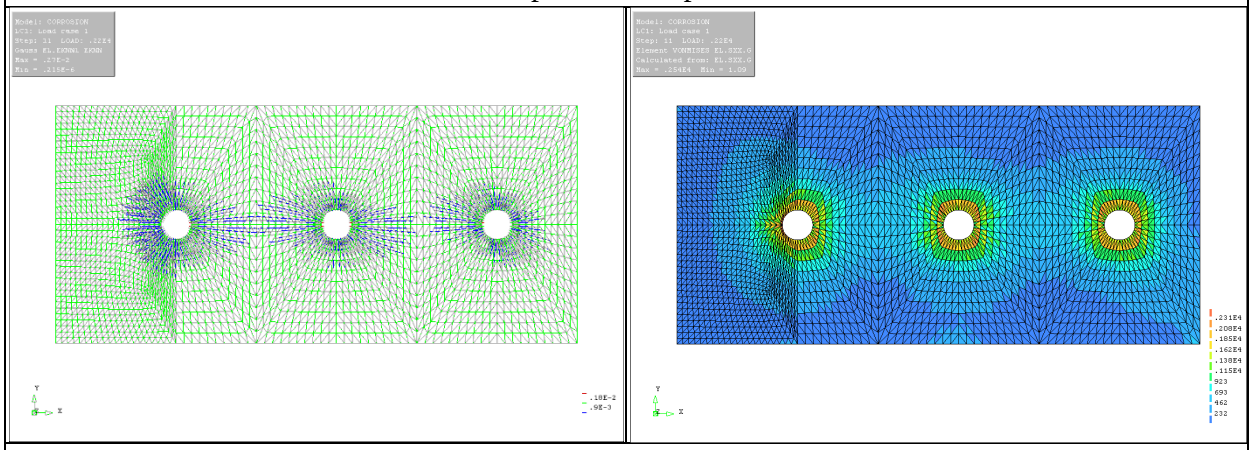

p_{int} = 2,200 psi

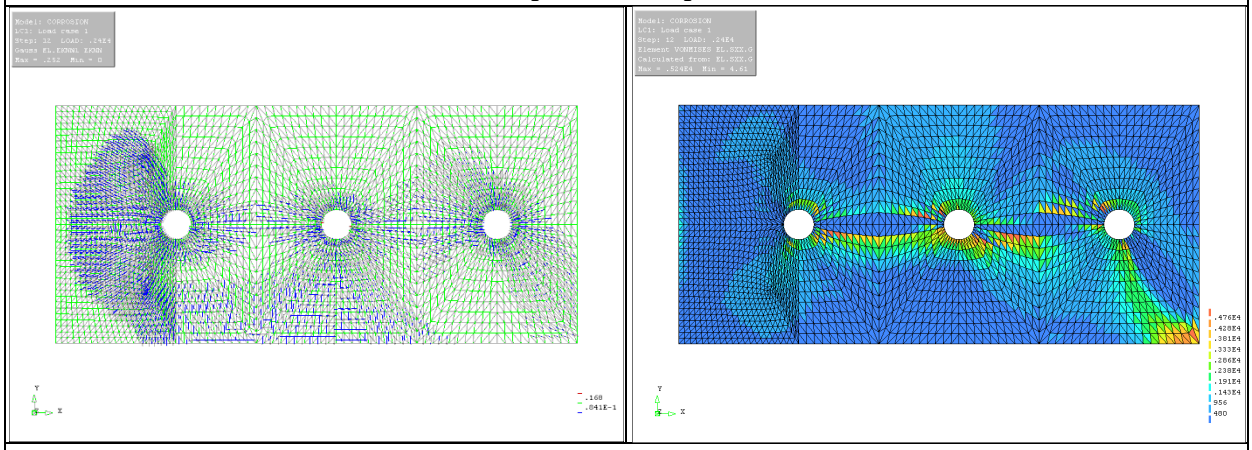

p_{int} = 2,400 psi

Figure D-2 Crack Patterns & Von Mises Stress Variations of Case I FE Model (Cover = 1.5 in.)

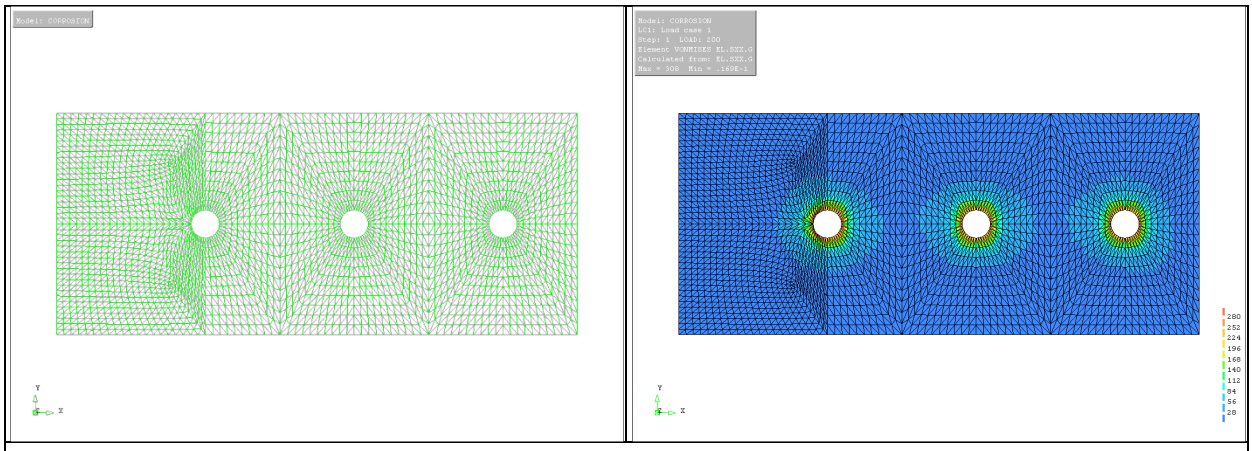

p_{int} = 200 psi

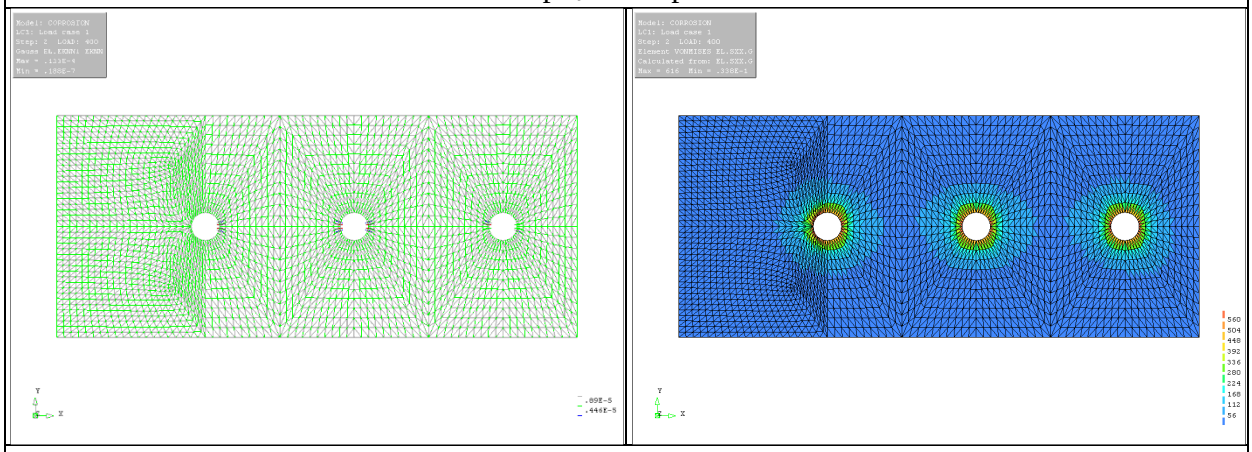

p_{int} = 400 psi

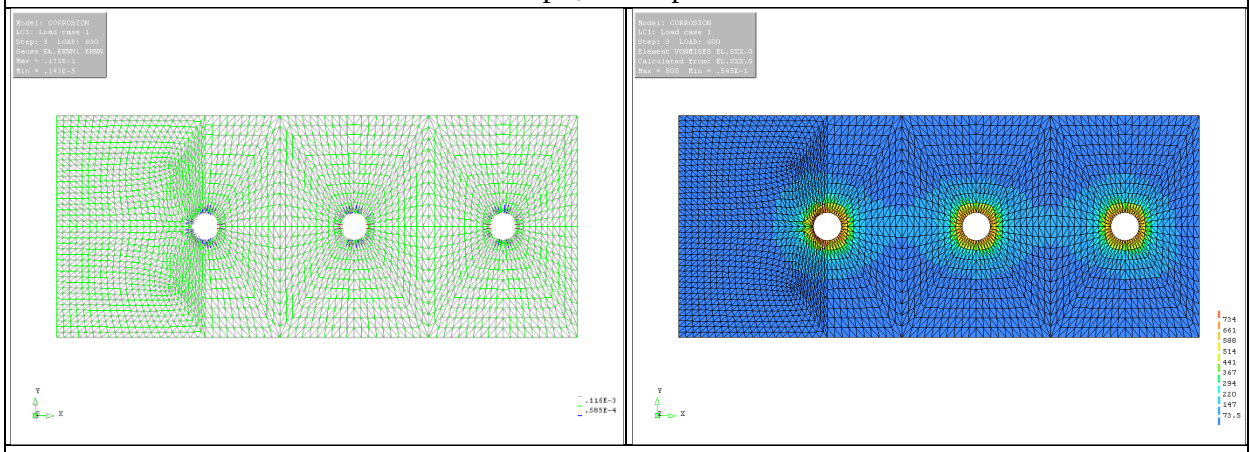

p_{int} = 600 psi

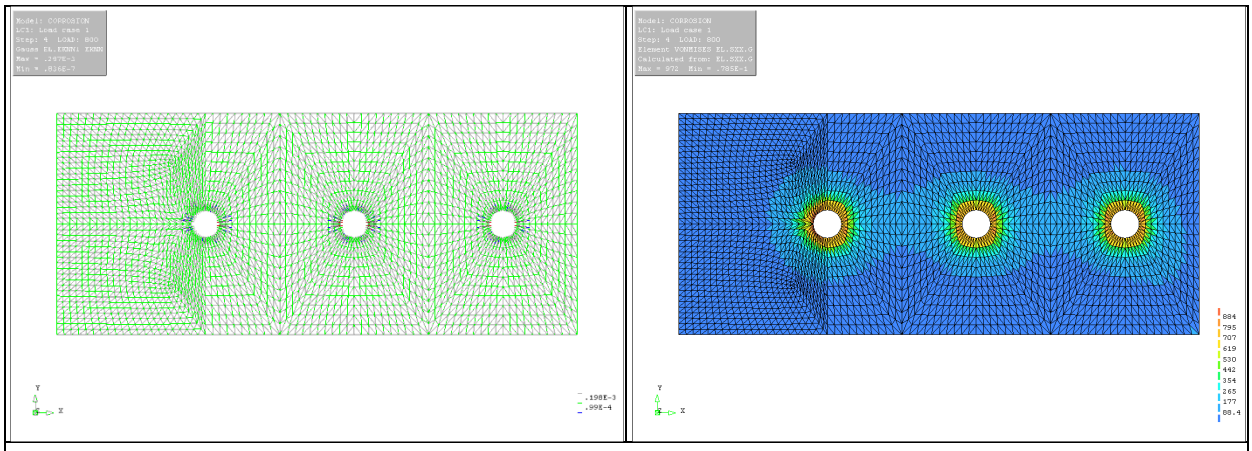

p_{int} = 800 psi

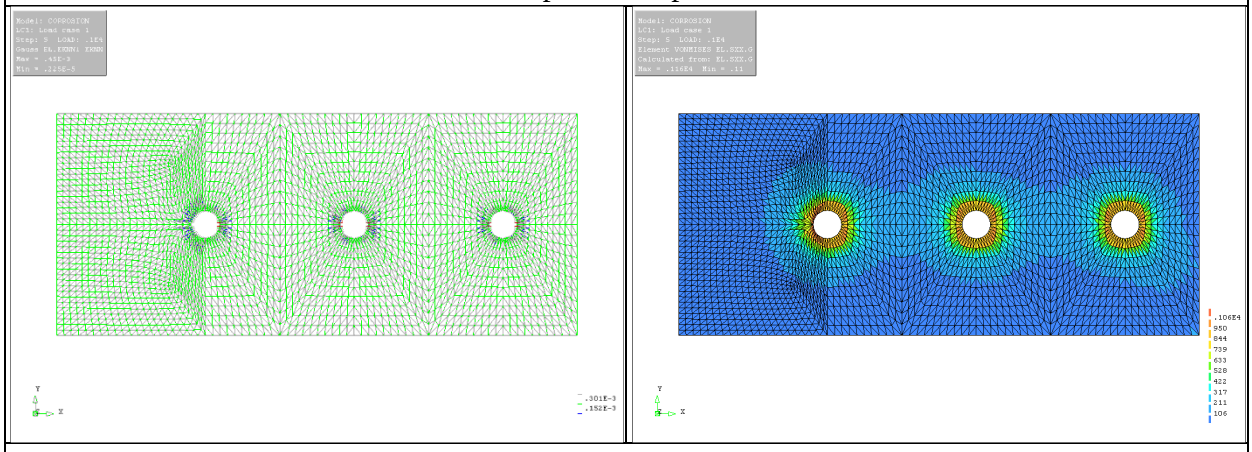

p_{int} = 1,000 psi

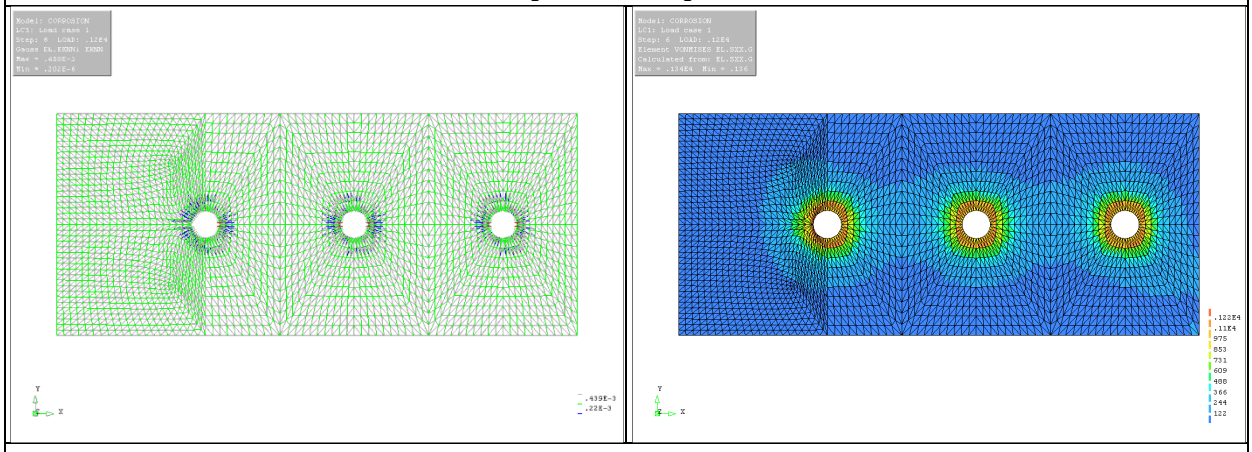

p_{int} = 1,200 psi

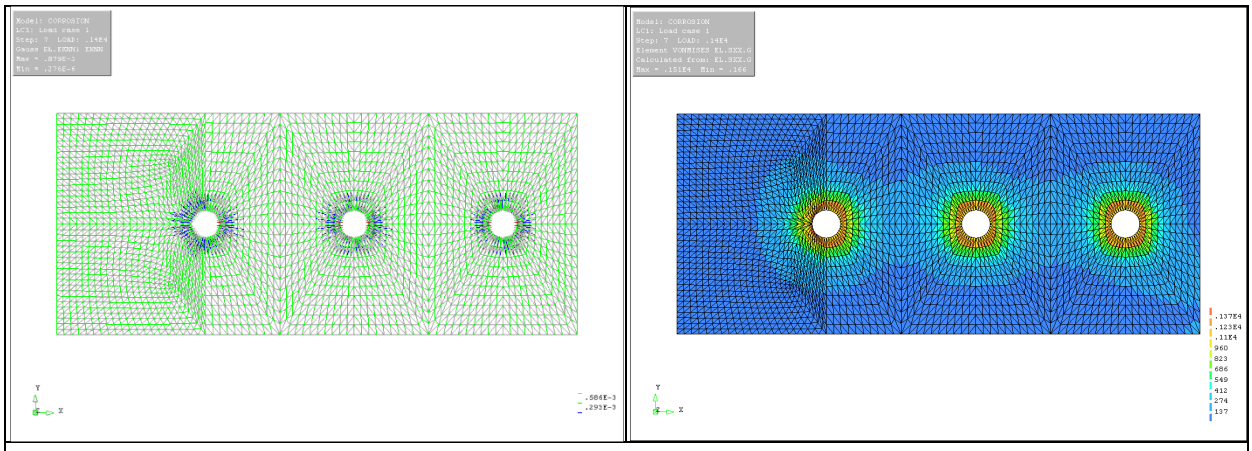

p_{int} = 1,400 psi

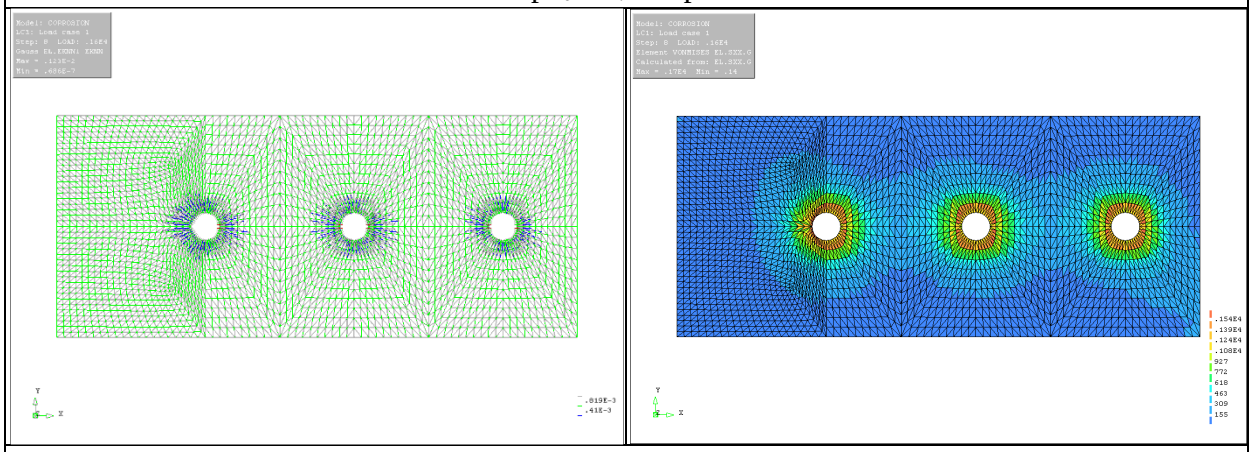

p_{int} = 1,600 psi

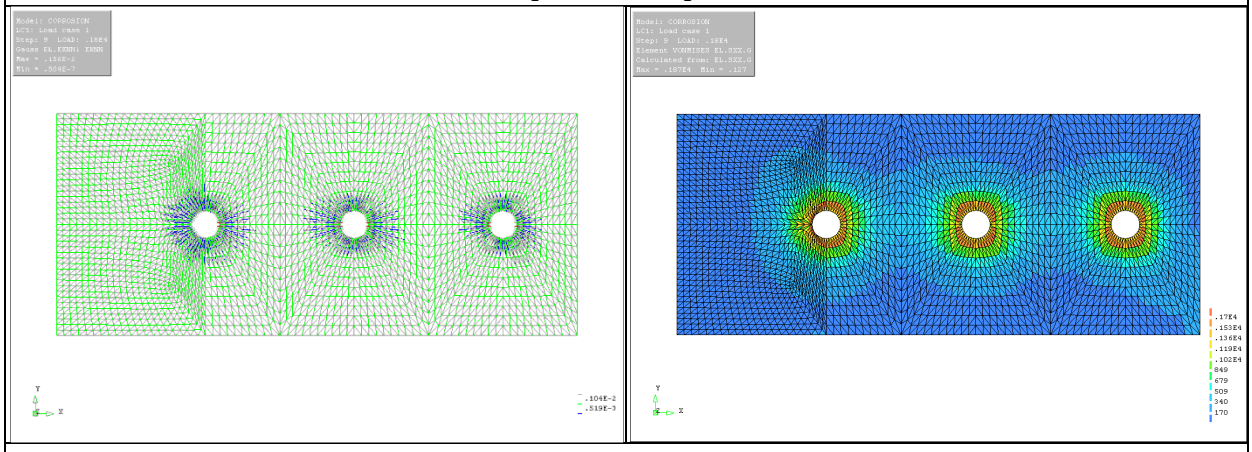

p_{int} = 1,800 psi

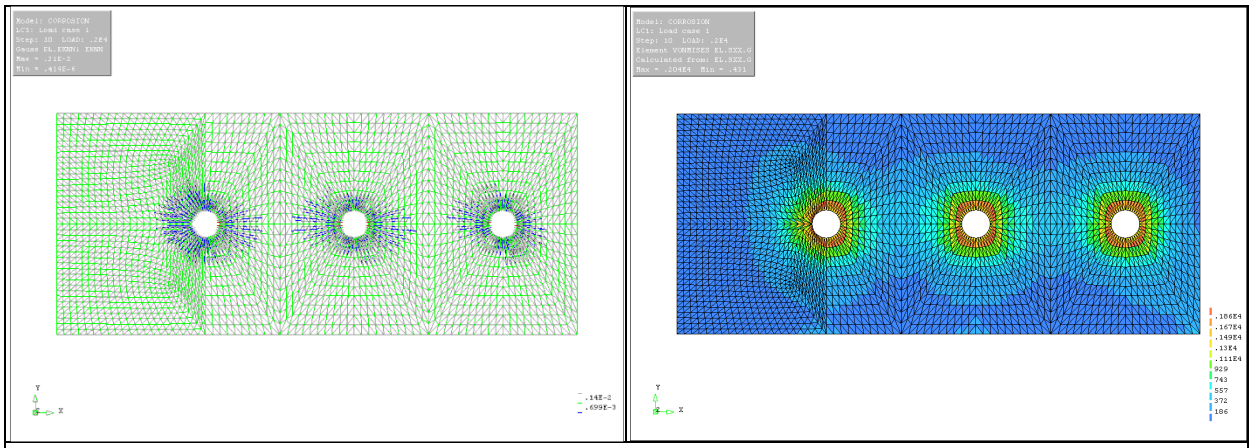

p_{int} = 2,000 psi

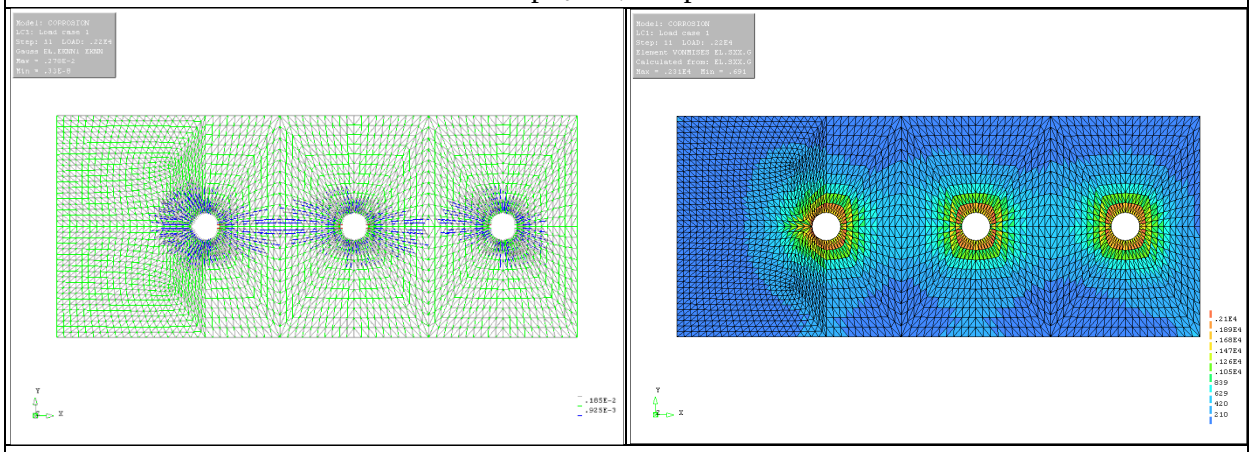

p_{int} = 2,200 psi

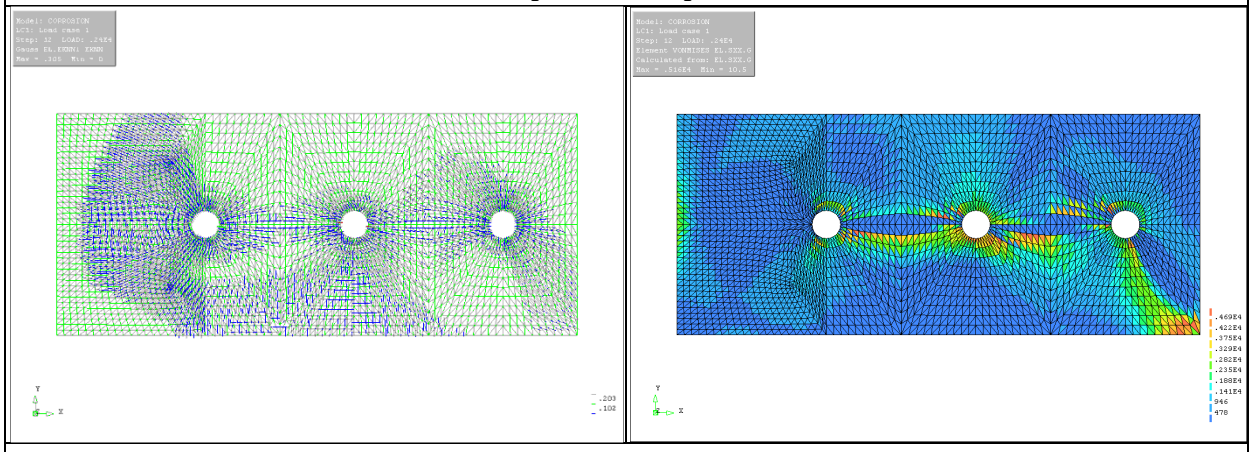

p_{int} = 2,400 psi

Figure D-3 Crack Patterns & Von Mises Stress Variations of Case I FE Model (Cover = 2.0 in.)

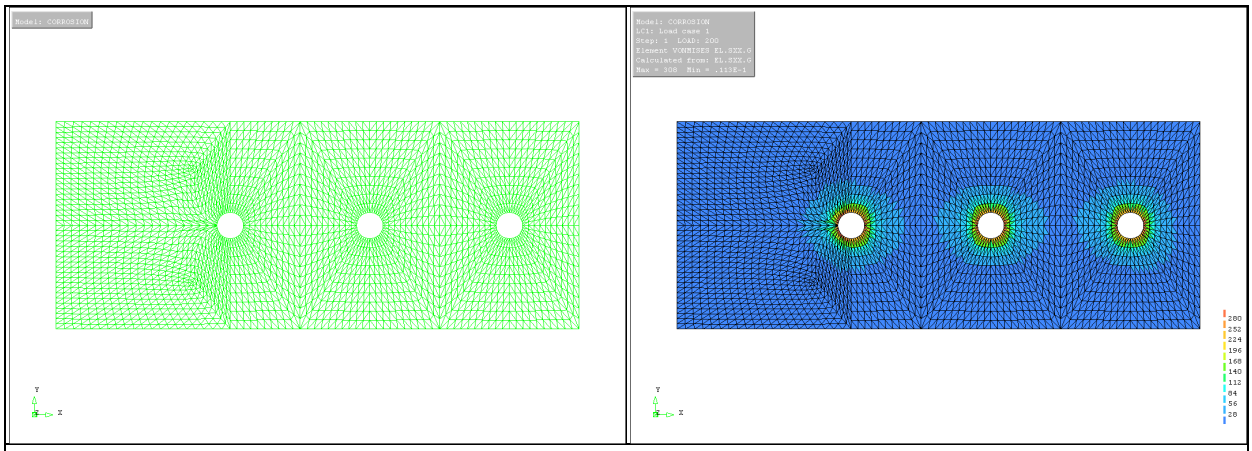

p_{int} = 200 psi

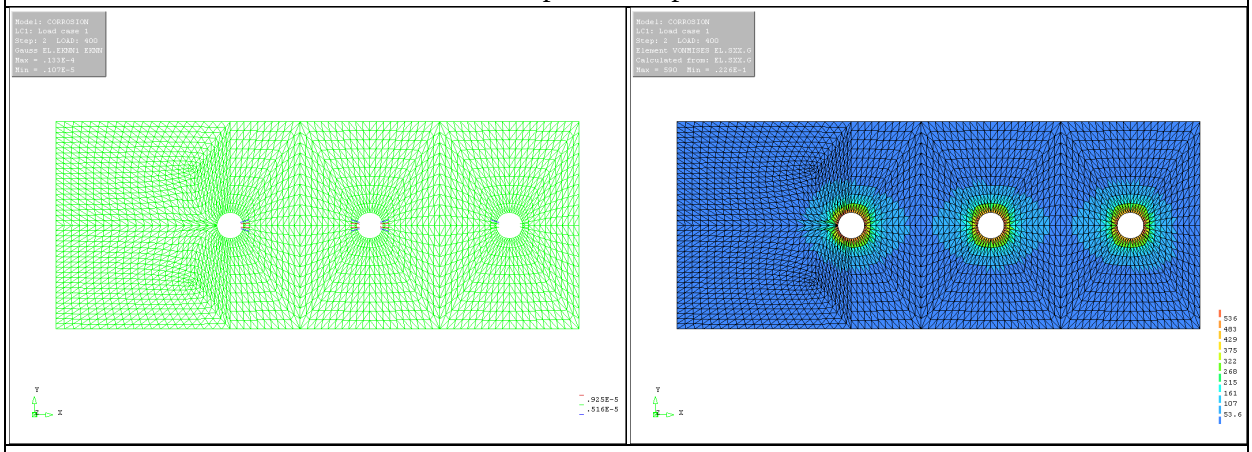

p_{int} = 400 psi

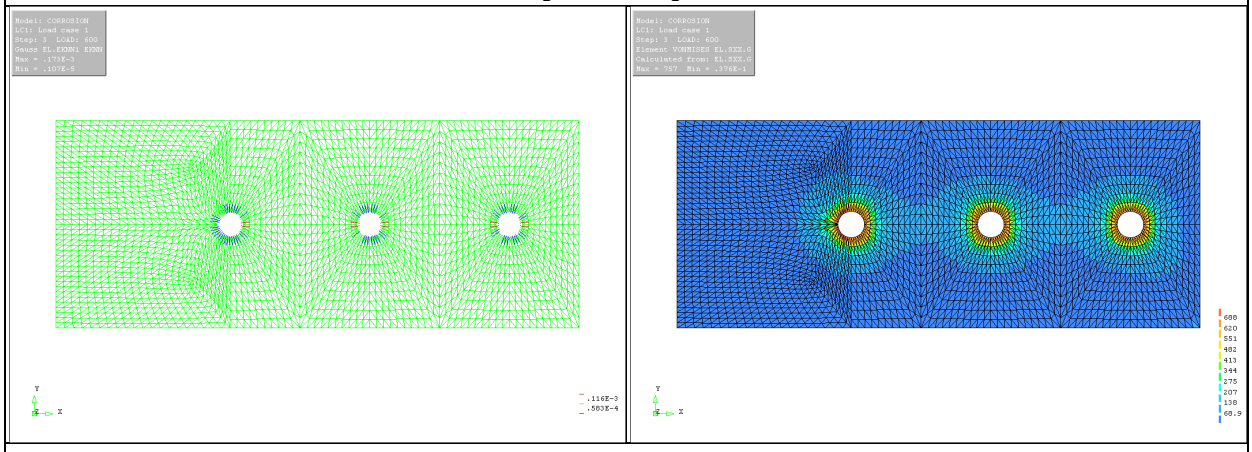

p_{int} = 600 psi

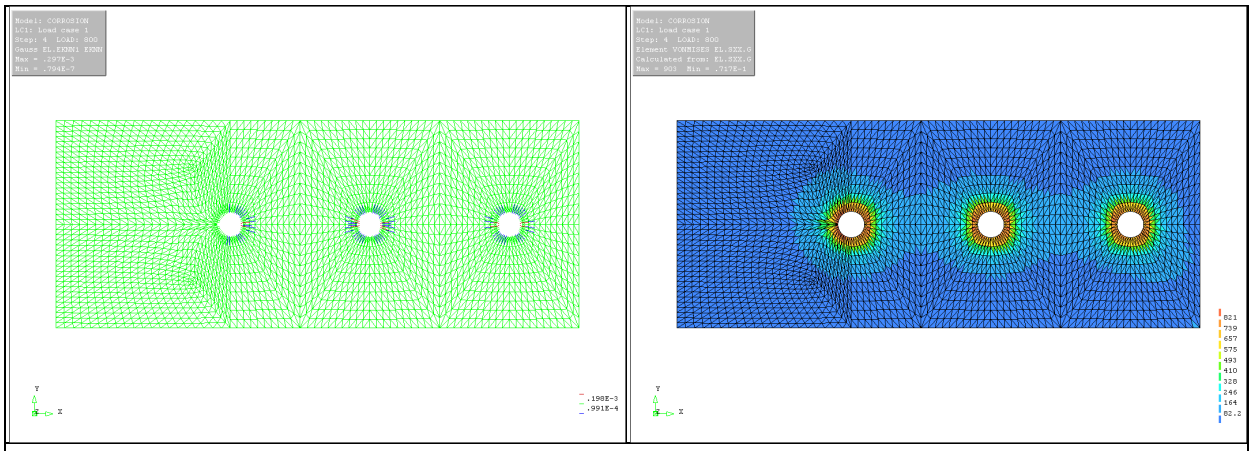

p_{int} = 800 psi

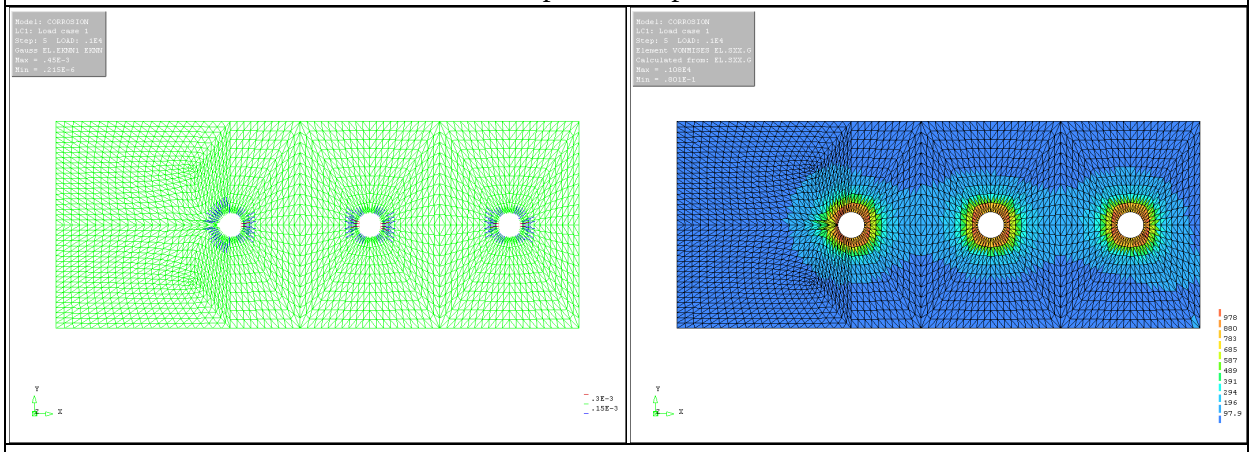

p_{int} = 1,000 psi

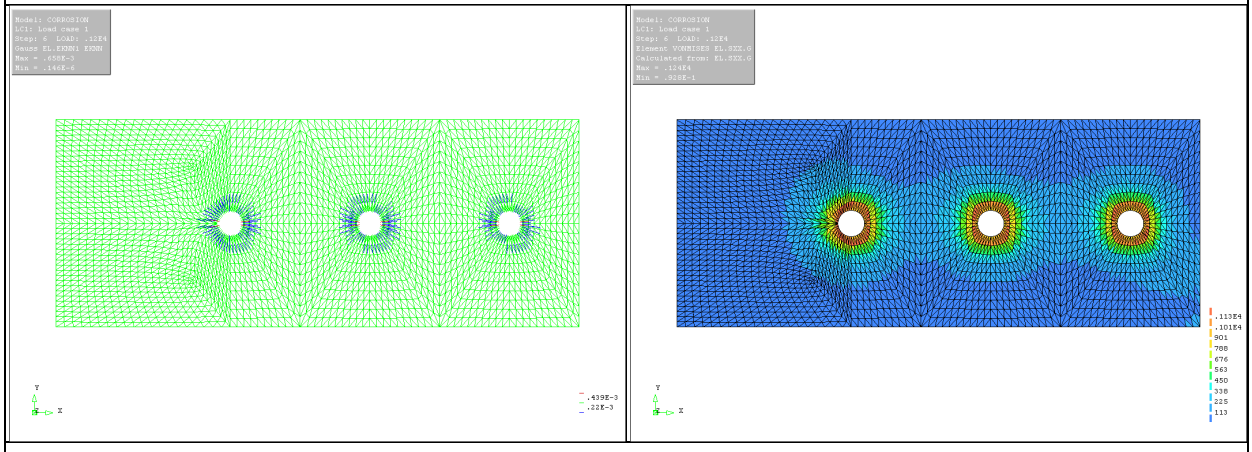

p_{int} = 1,200 psi

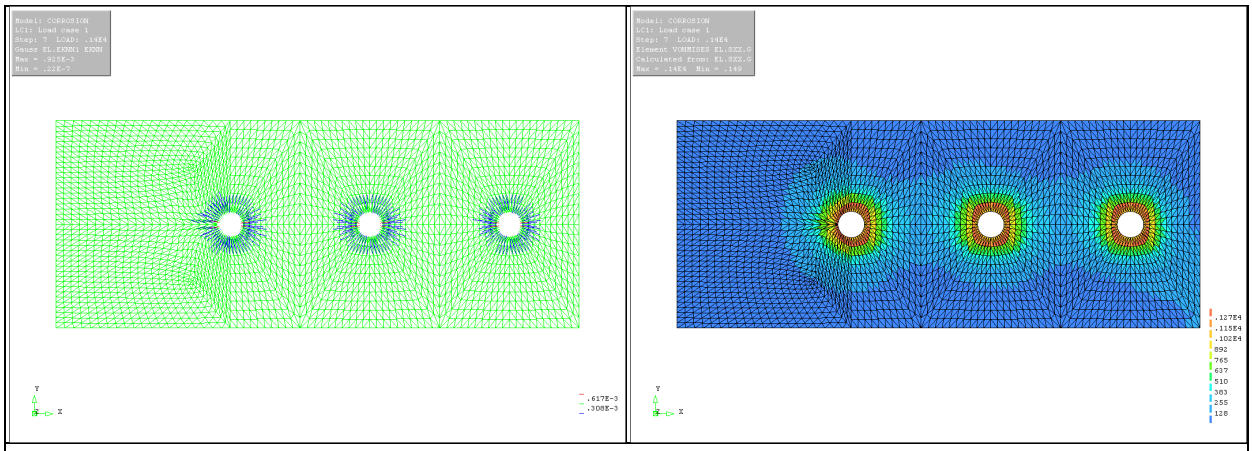

p_{int} = 1,400 psi

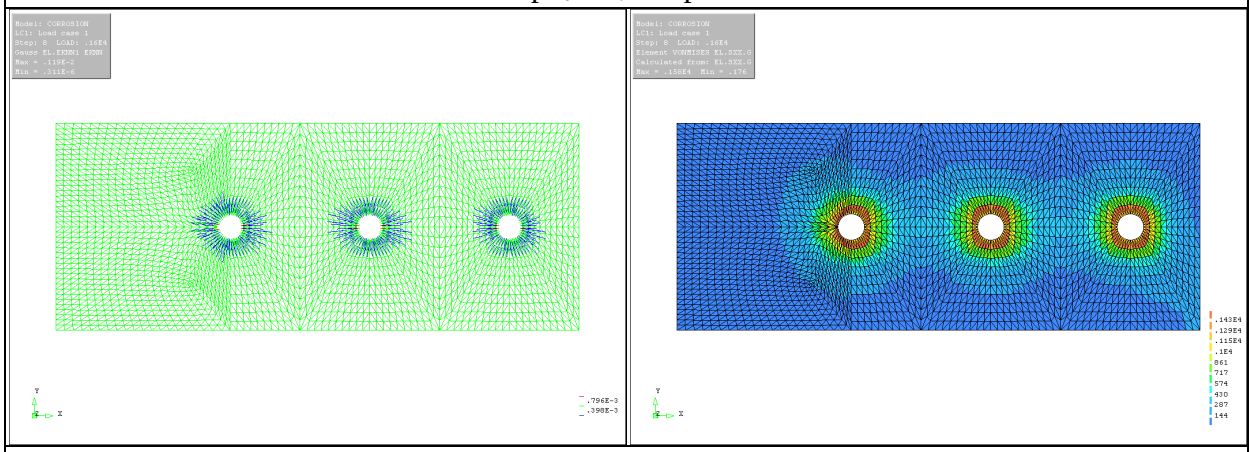

p_{int} = 1,600 psi

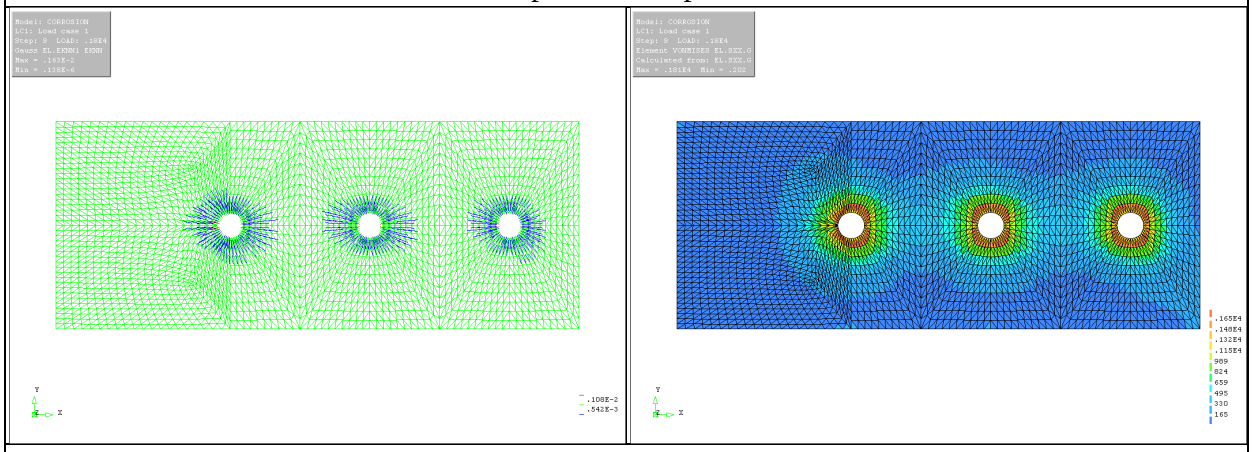

p_{int} = 1,800 psi

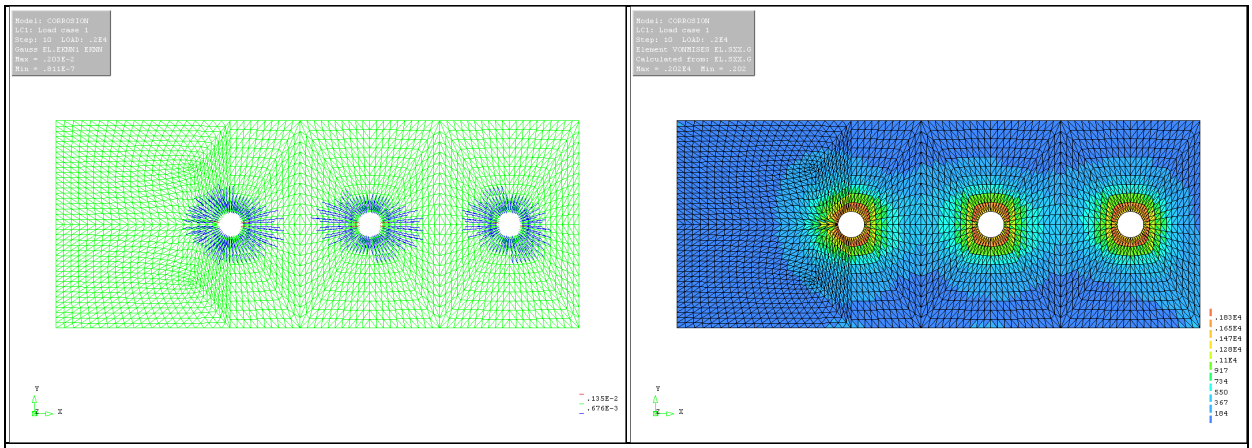

p_{int} = 2,000 psi

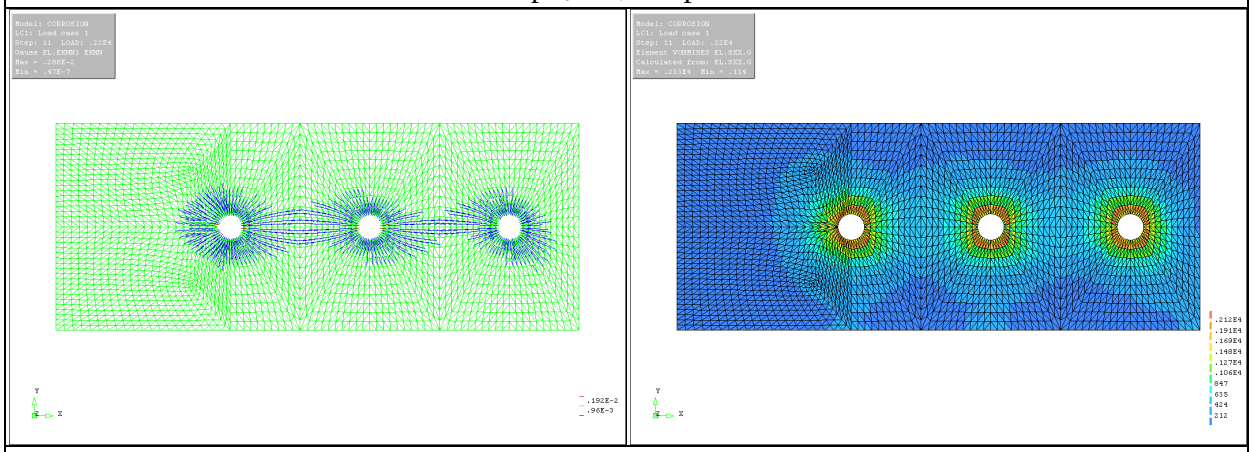

p_{int} = 2,200 psi

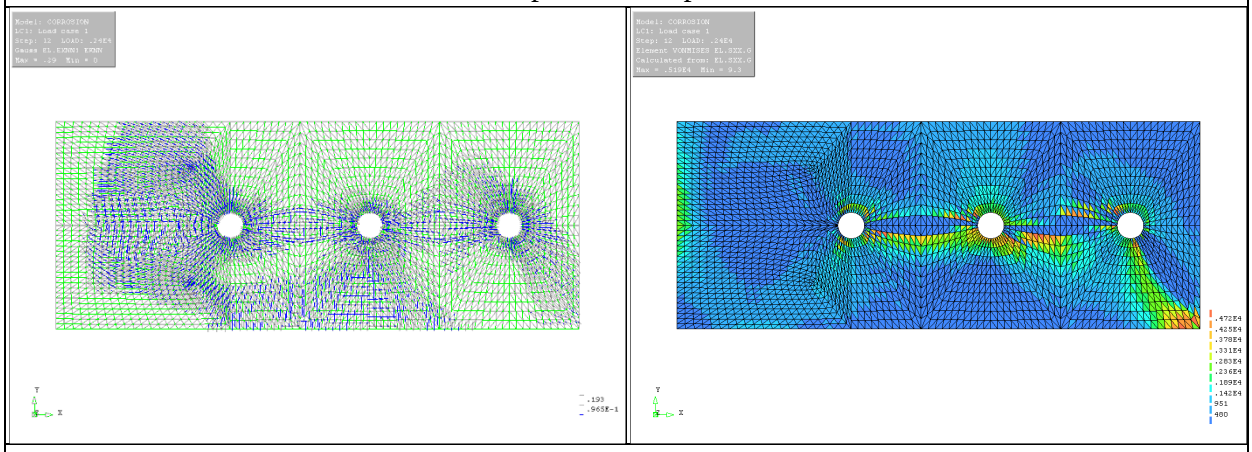

p_{int} = 2,400 psi

Figure D-4 Crack Patterns & Von Mises Stress Variations of Case I FE Model (Cover = 2.5 in.)

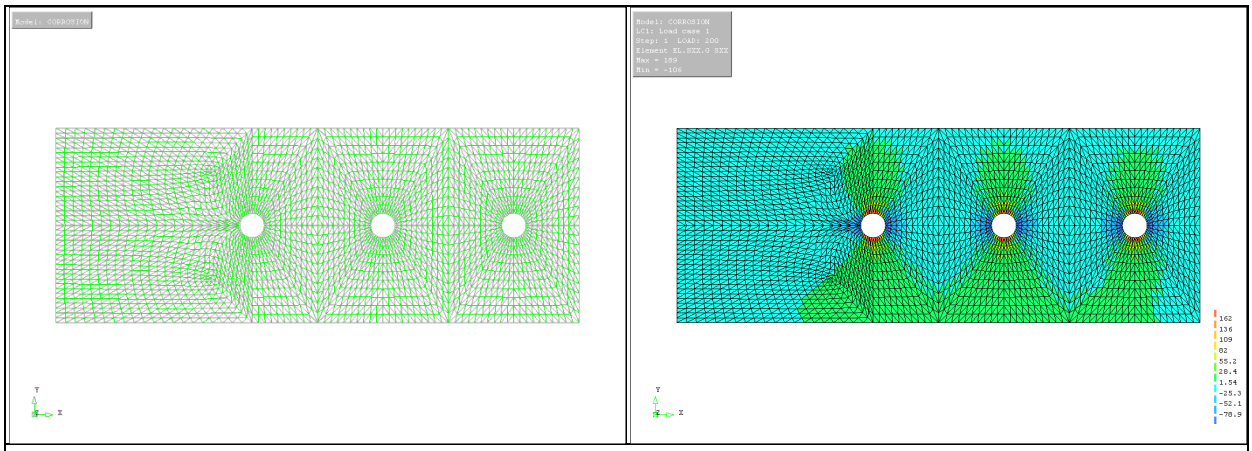

p_{int} = 200 psi

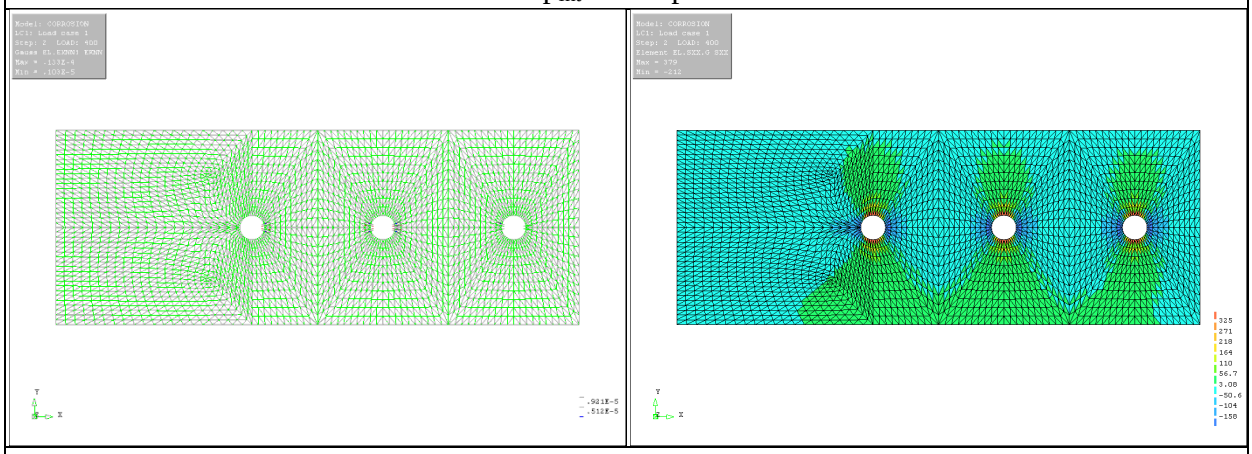

p_{int} = 400 psi

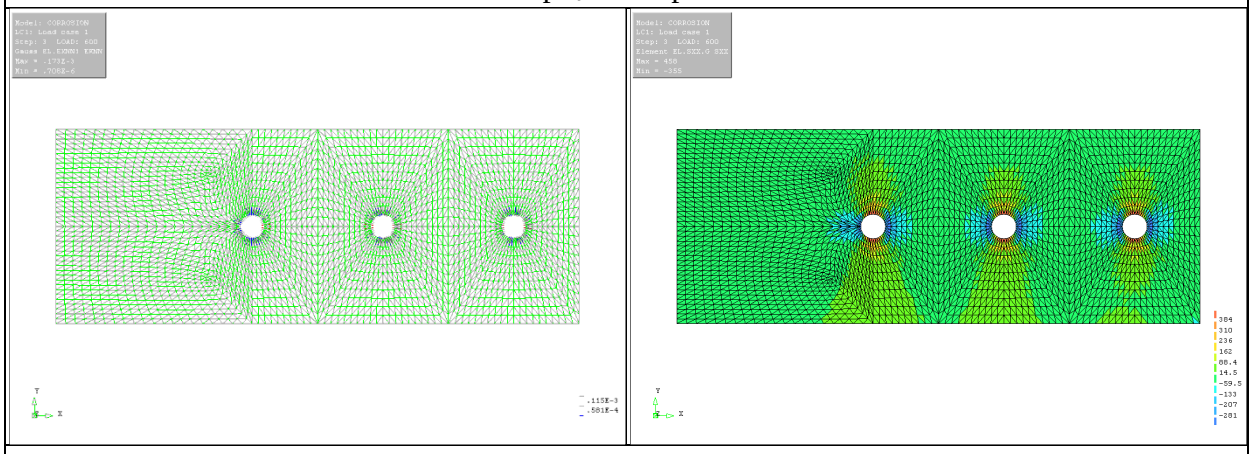

p_{int} = 600 psi

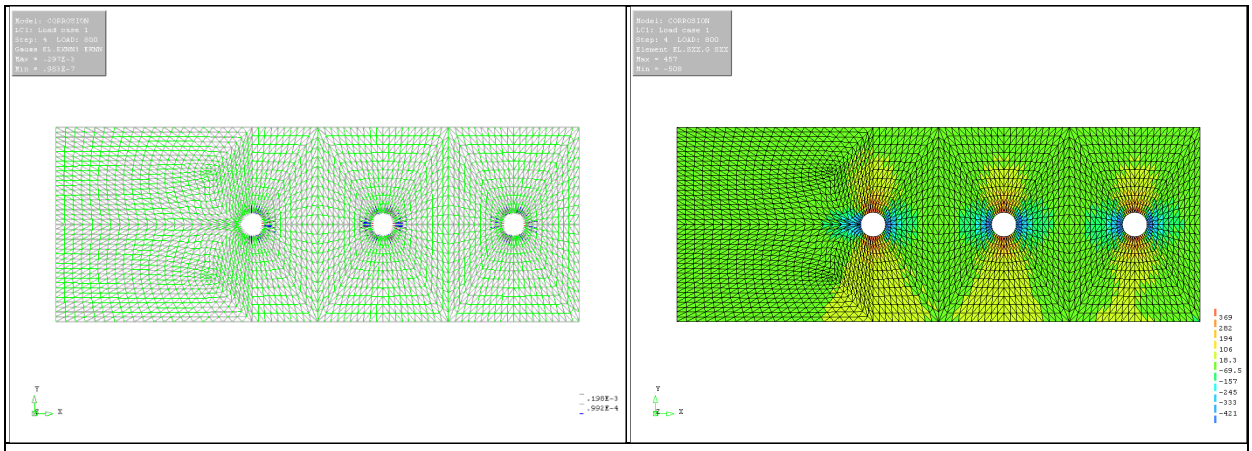

p_{int} = 800 psi

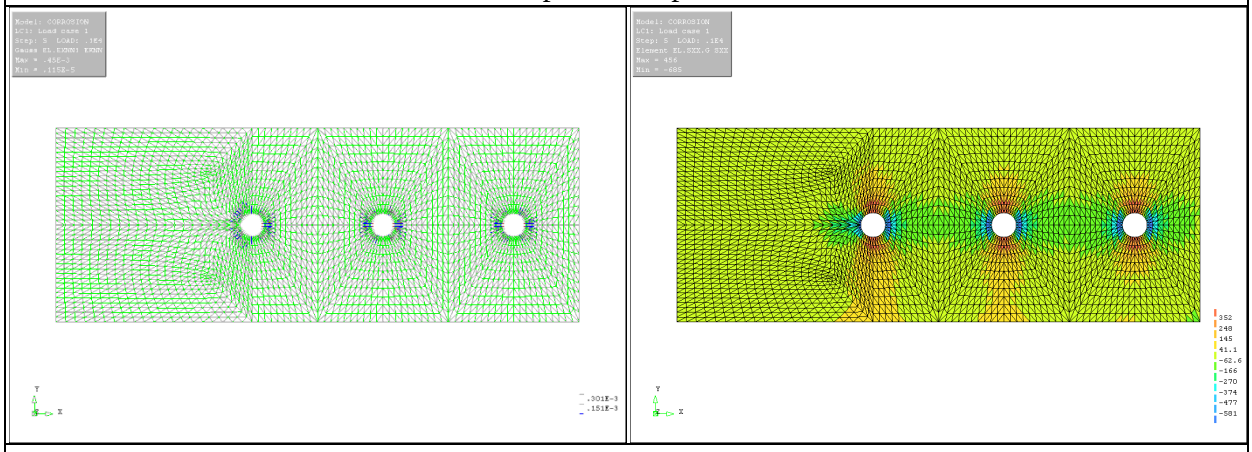

p_{int} = 1,000 psi

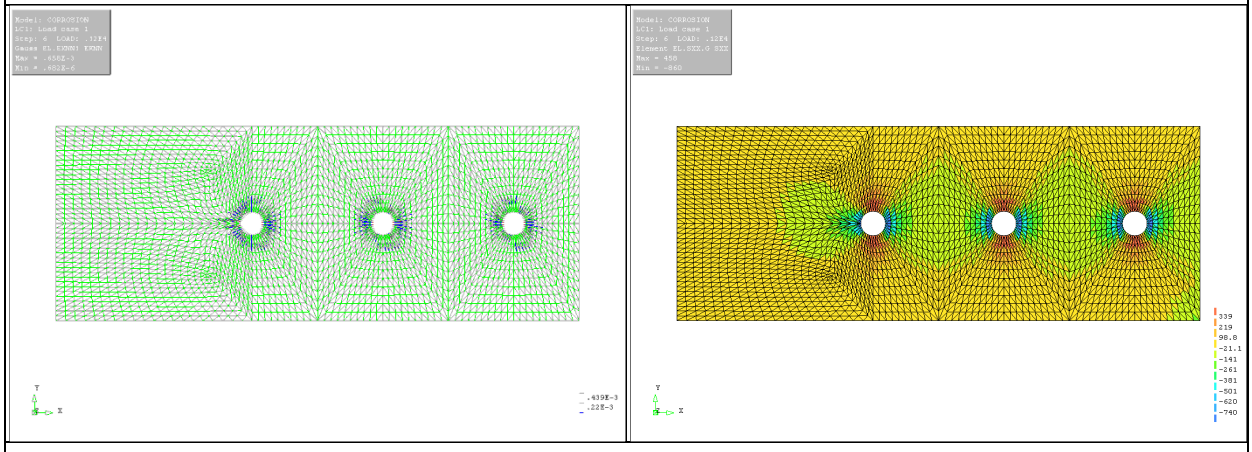

p_{int} = 1,200 psi

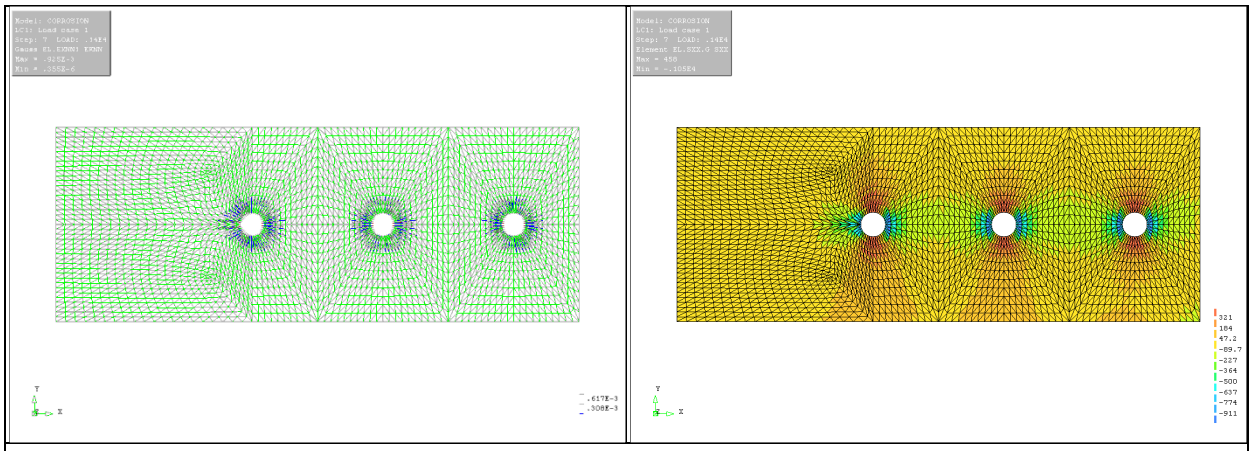

p_{int} = 1,400 psi

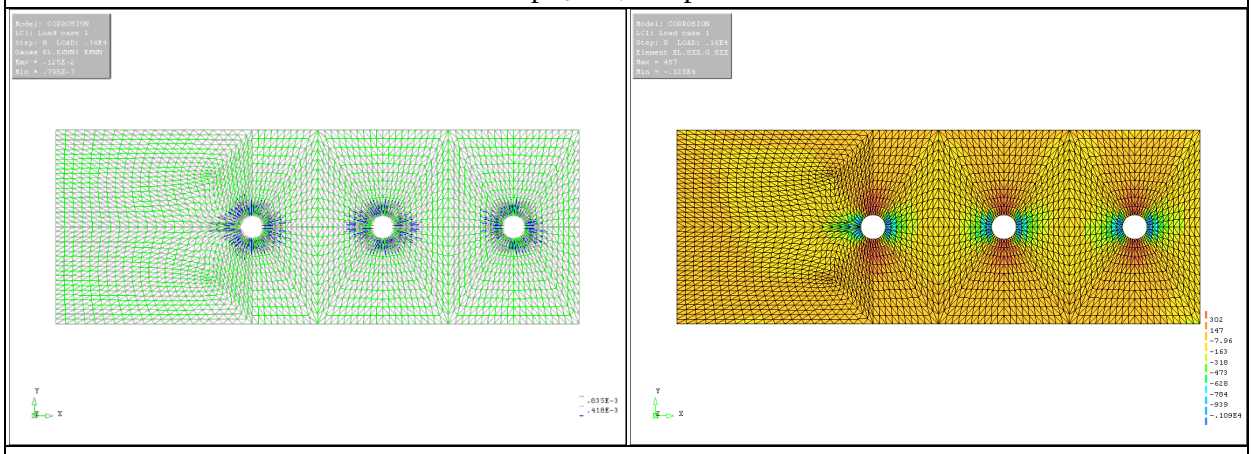

p_{int} = 1,600 psi

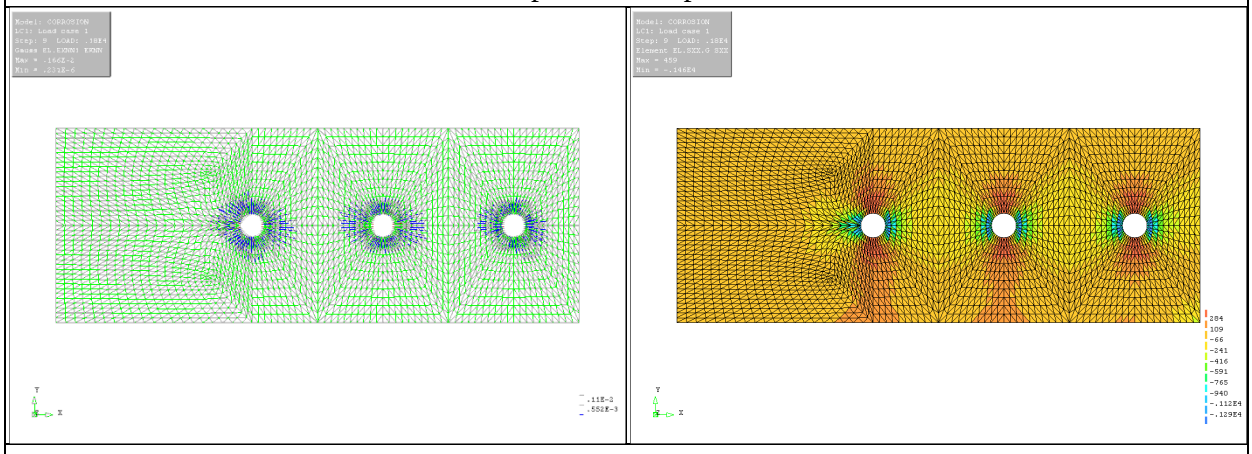

p_{int} = 1,800 psi

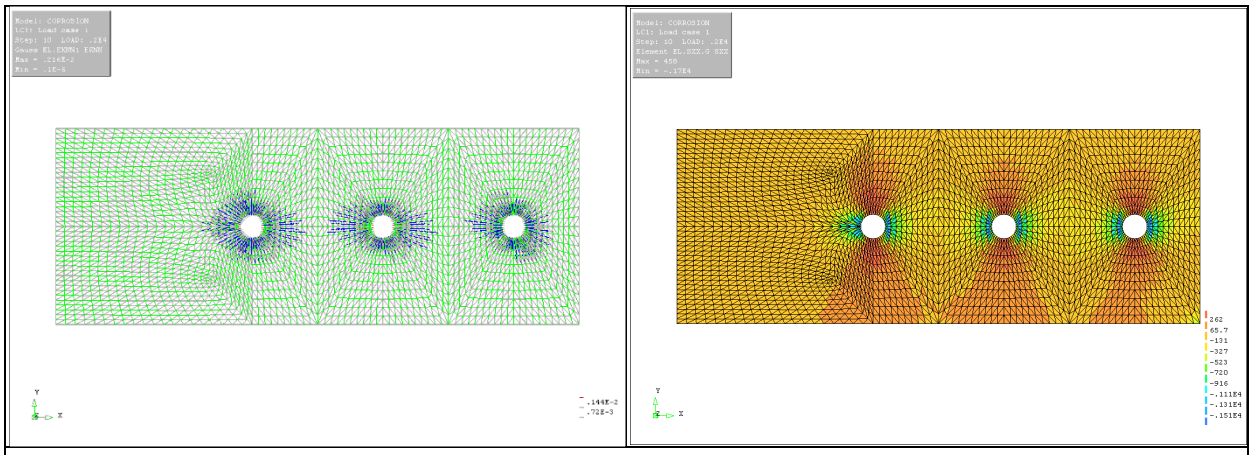

p_{int} = 2,000 psi

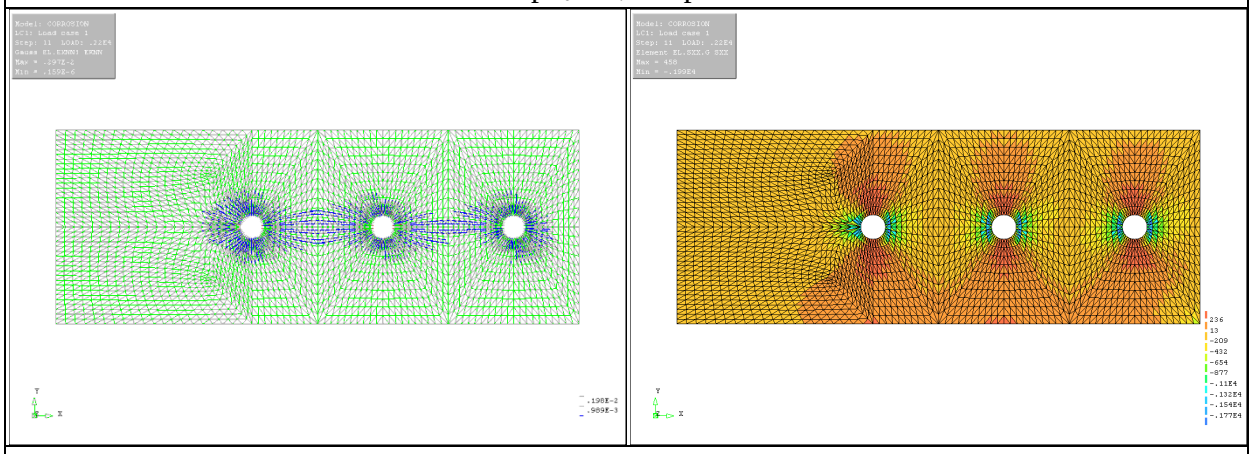

p_{int} = 2,200 psi

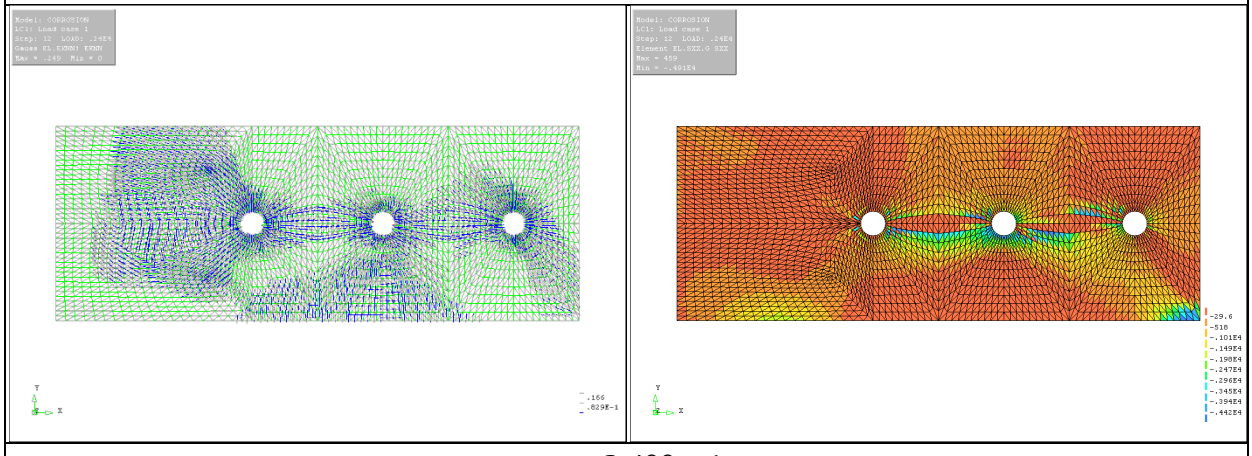

p_{int} = 2,400 psi

Figure D-5 Crack Patterns & Von Mises Stress Variations of Case I FE Model (Cover = 3.0 in.)

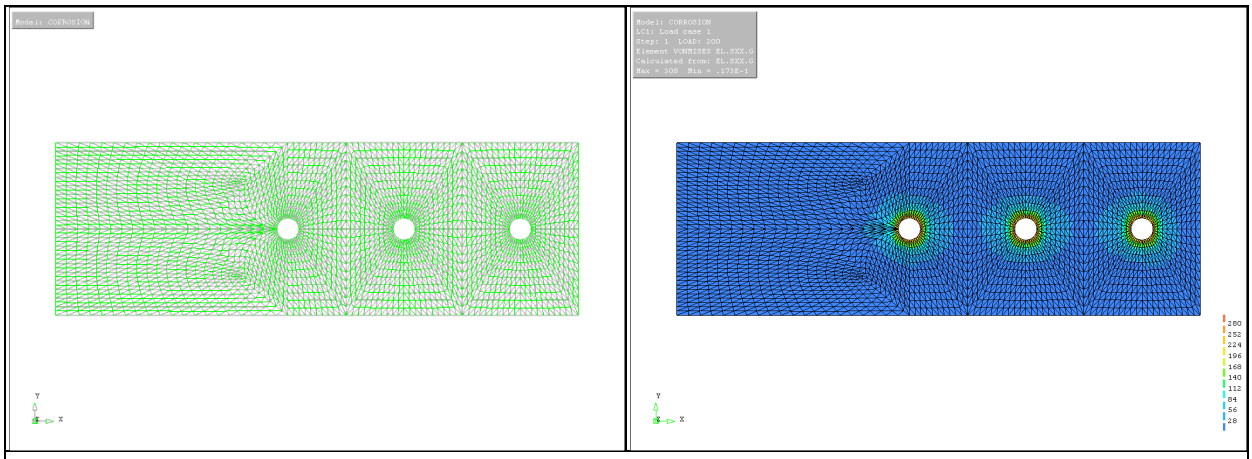

p_{int} = 200 psi

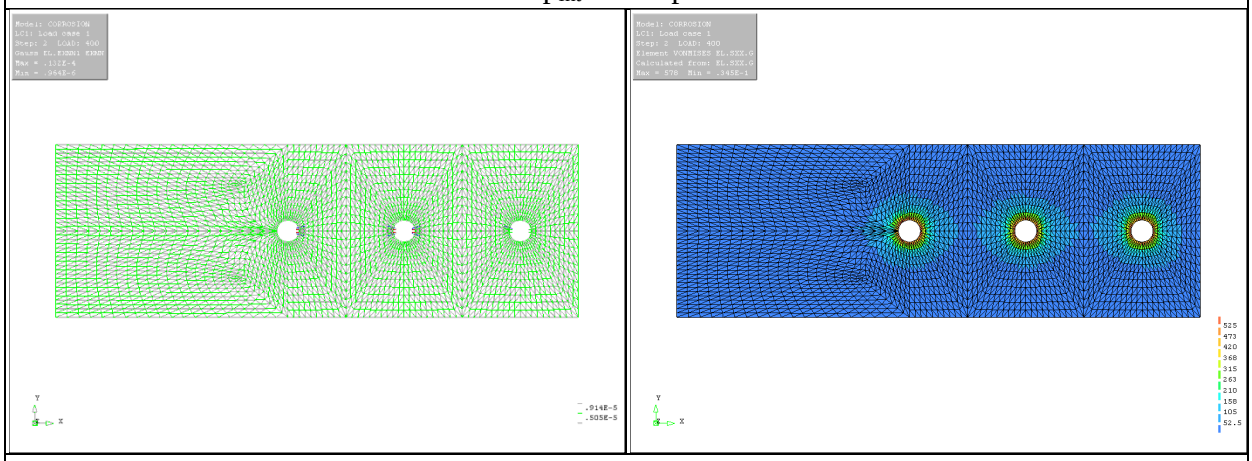

p_{int} = 400 psi

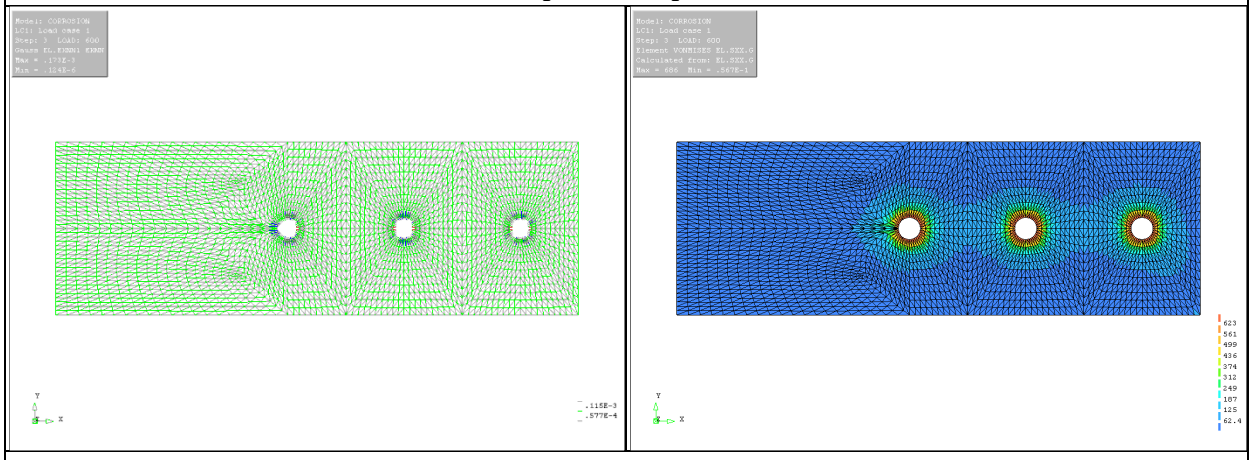

p_{int} = 600 psi

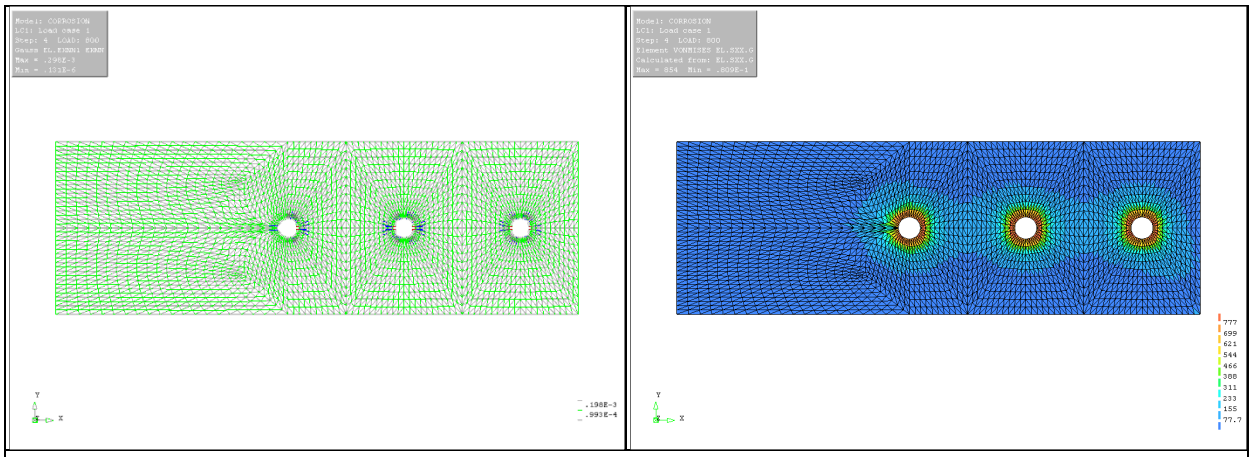

p_{int} = 800 psi

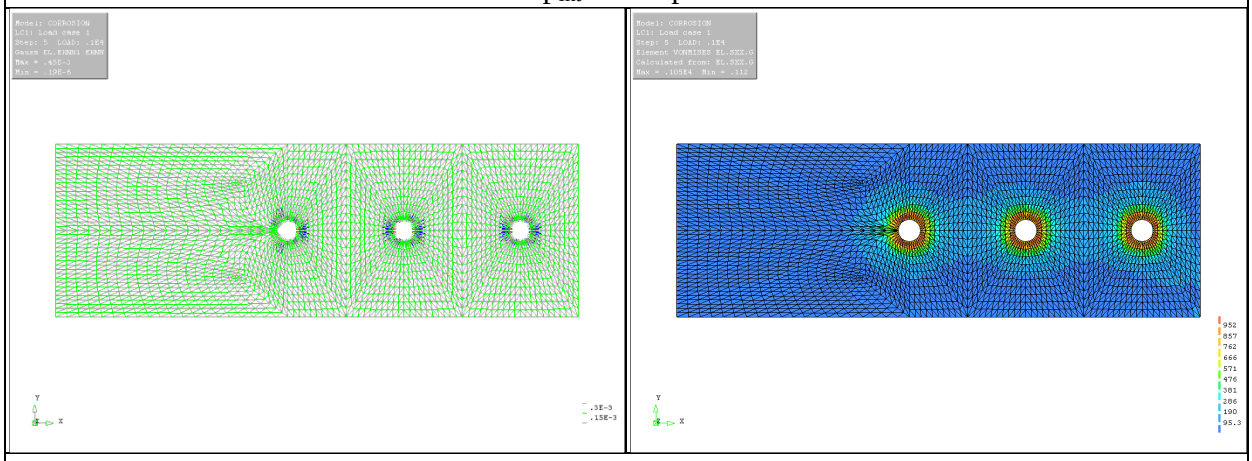

p_{int} = 1,000 psi

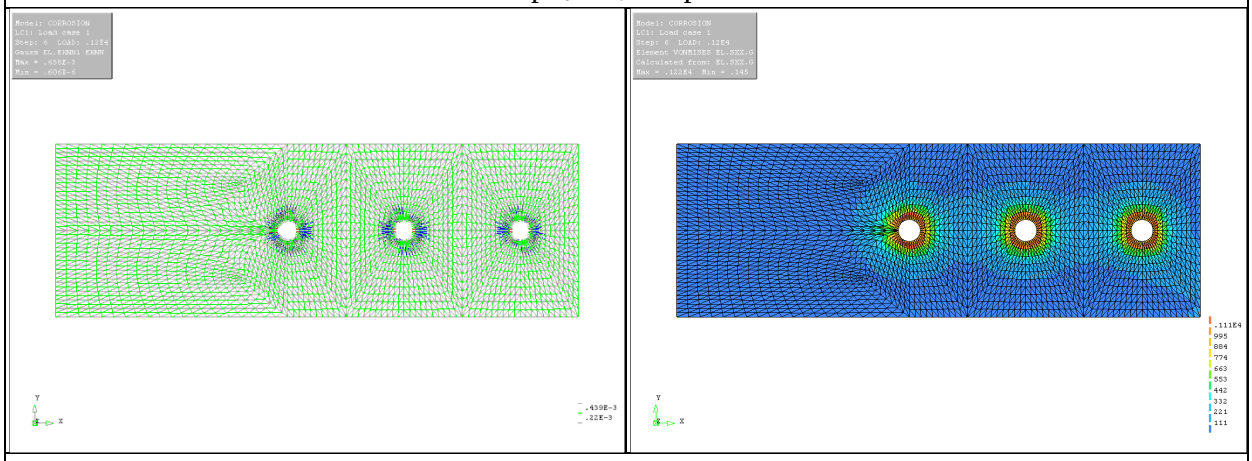

p_{int} = 1,200 psi

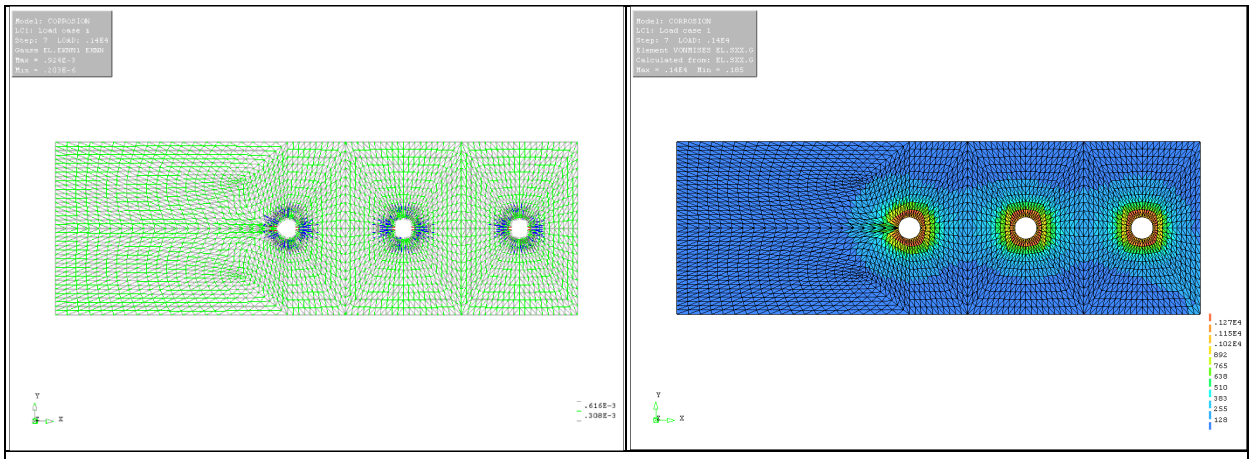

p_{int} = 1,400 psi

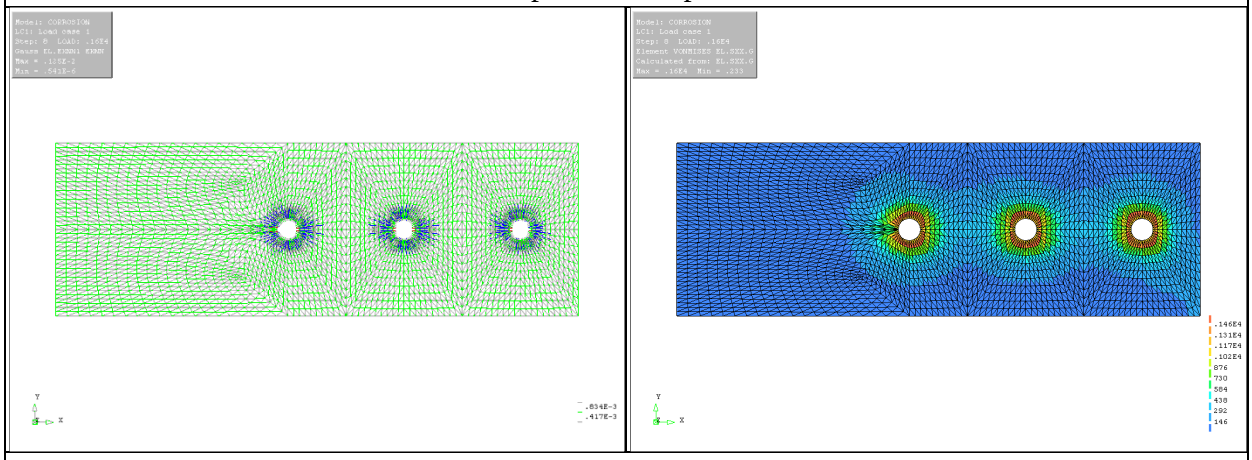

p_{int} = 1,600 psi

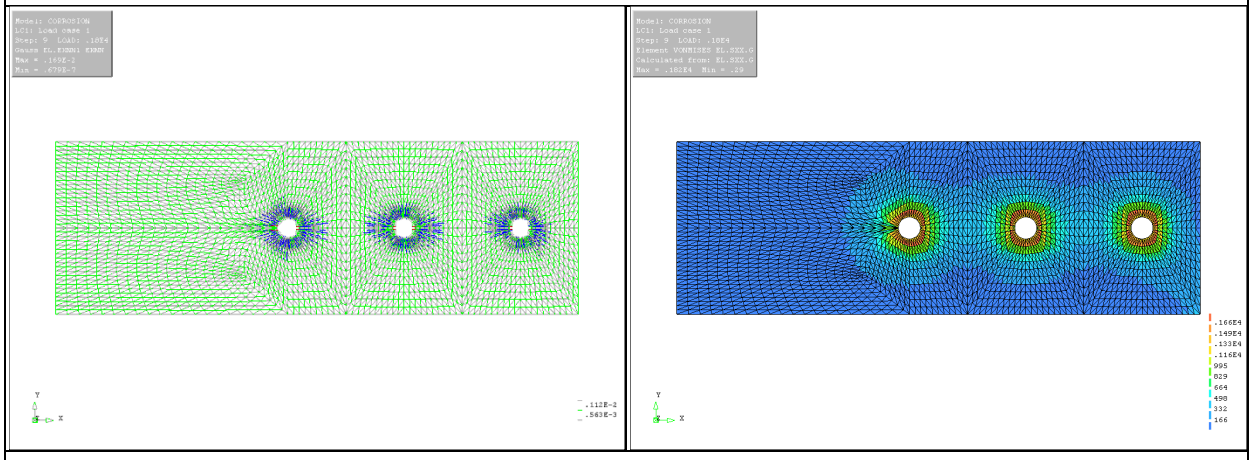

p_{int} = 1,800 psi

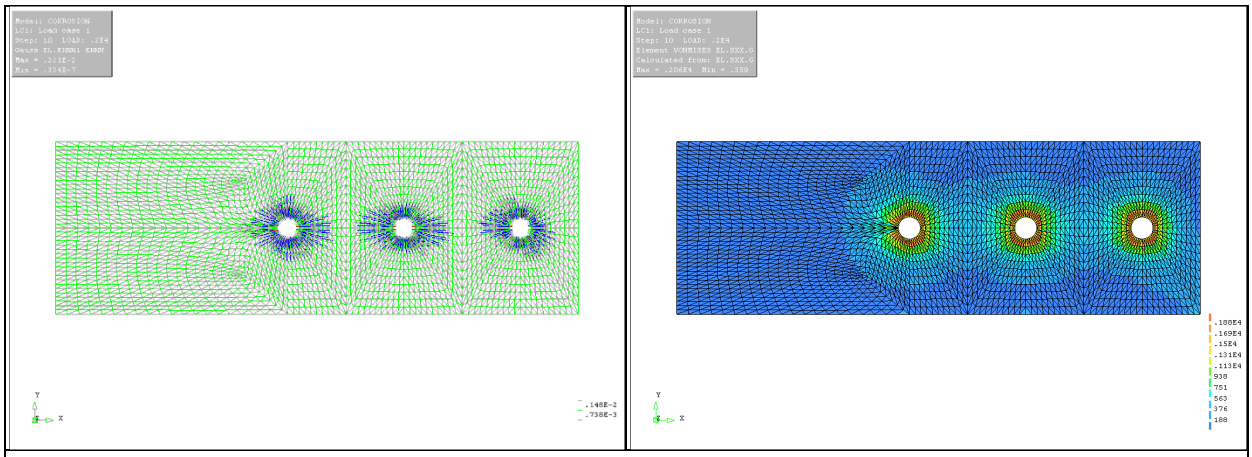

p_{int} = 2,000 psi

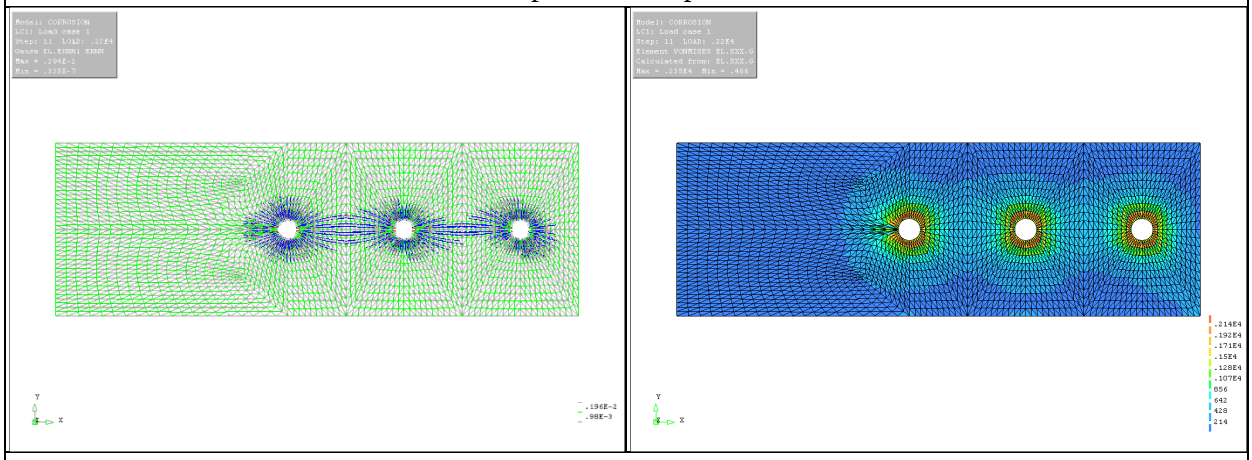

p_{int} = 2,200 psi

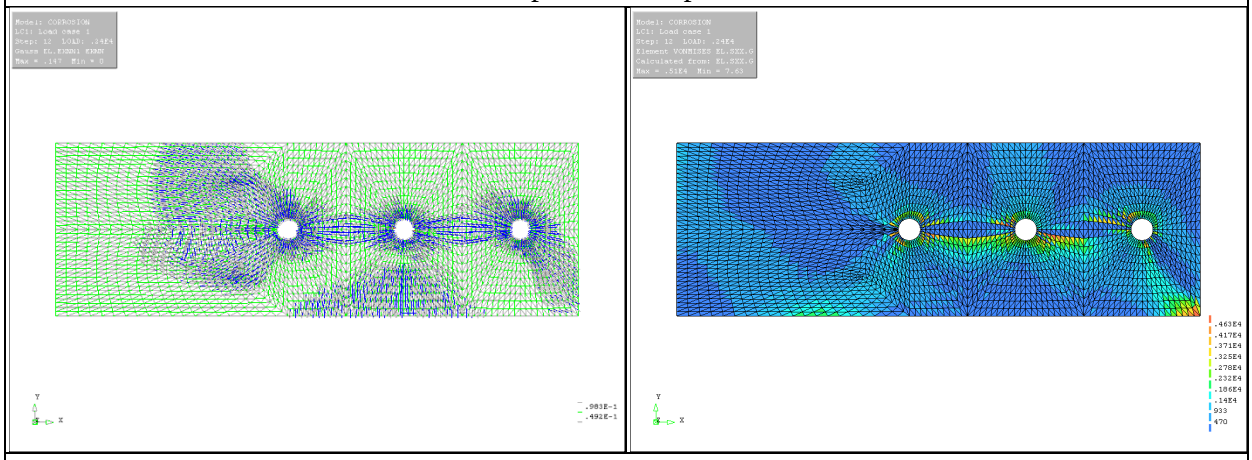

p_{int} = 2,400 psi

Figure D-6 Crack Patterns & Von Mises Stress Variations of Case I FE Model (Cover = 4.0 in.)

D.2.1.2 Case II FE analysis results

Crack patterns and corresponding Von Mises stress variations of Case II FE analyses are illustrated from Figure D-7 to Figure D-11. Each figure represents a different side cover, and results are presented with respect to incrementally increasing internal pressures.

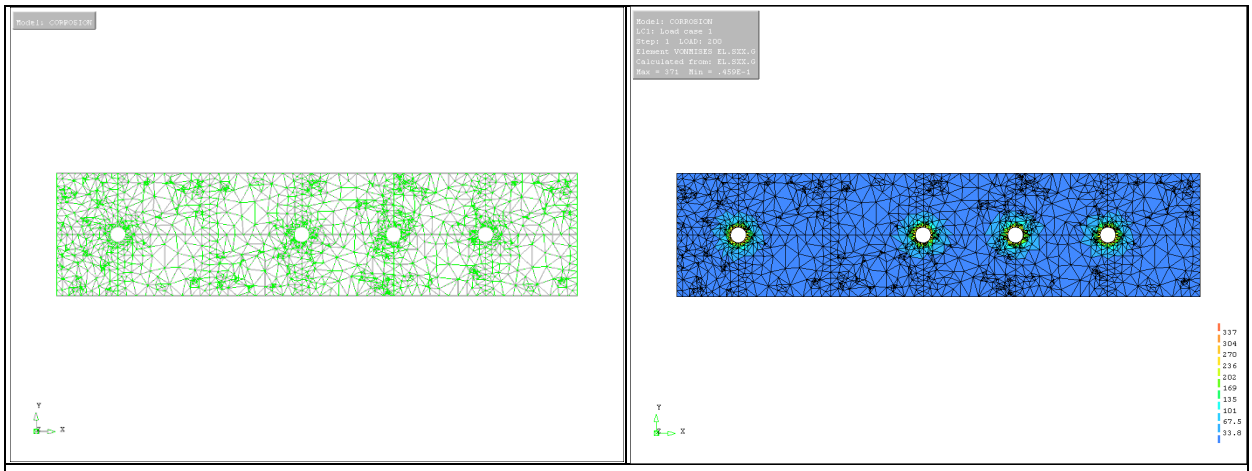

p_{int} = 200 psi

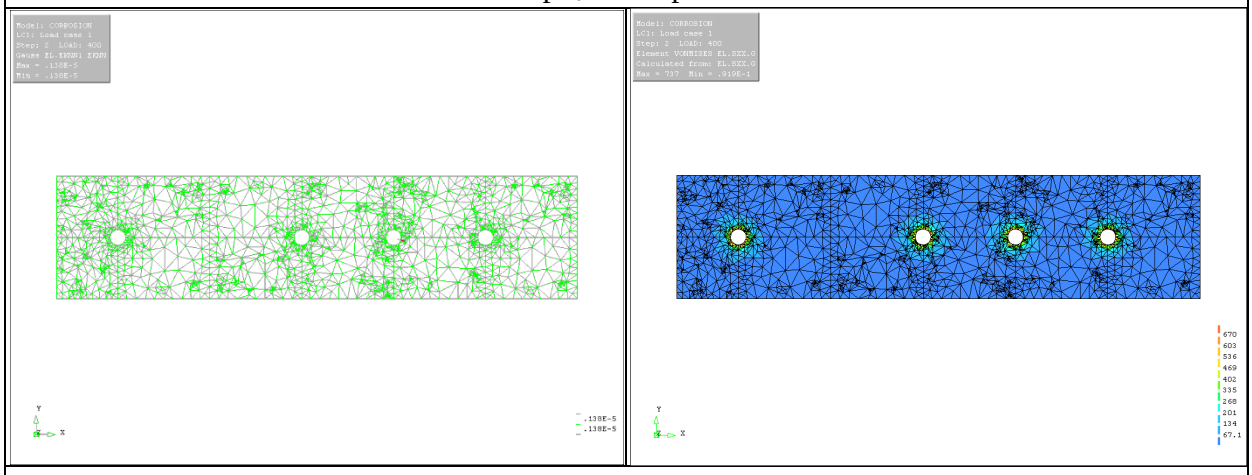

p_{int} = 400 psi

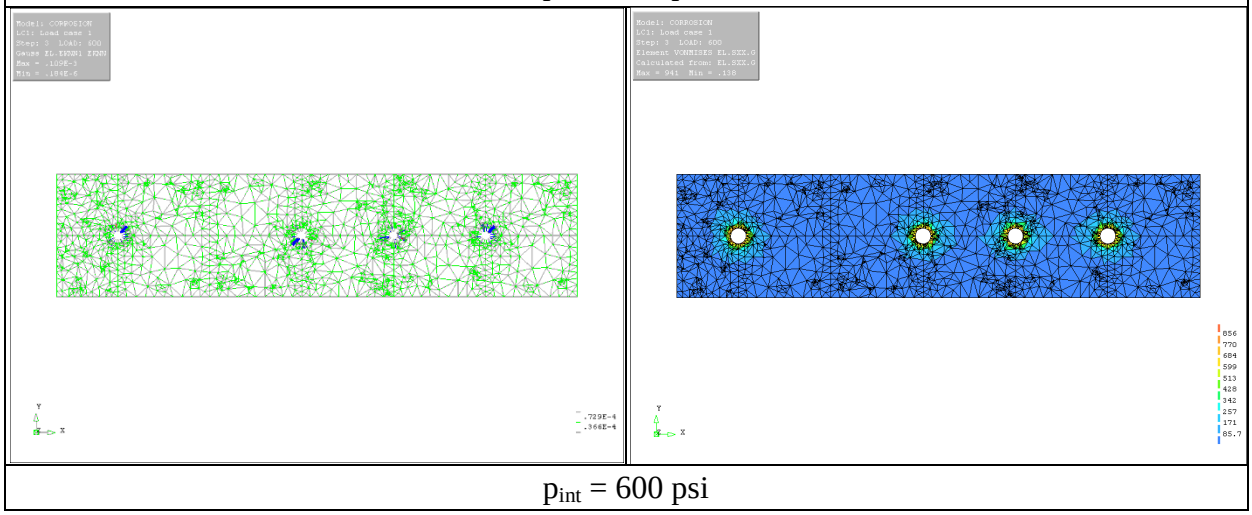

p_{int} = 600 psi

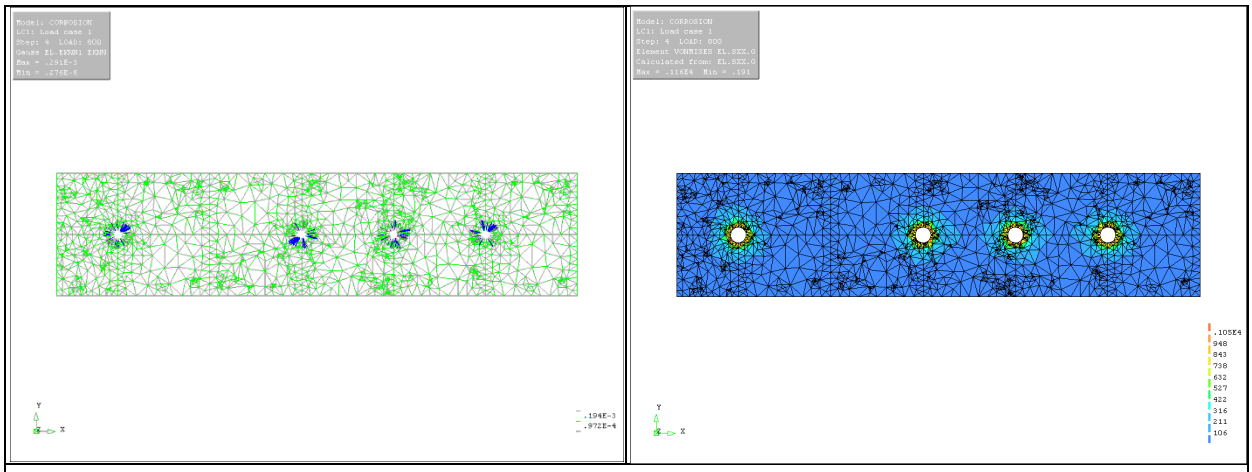

p_{int} = 800 psi

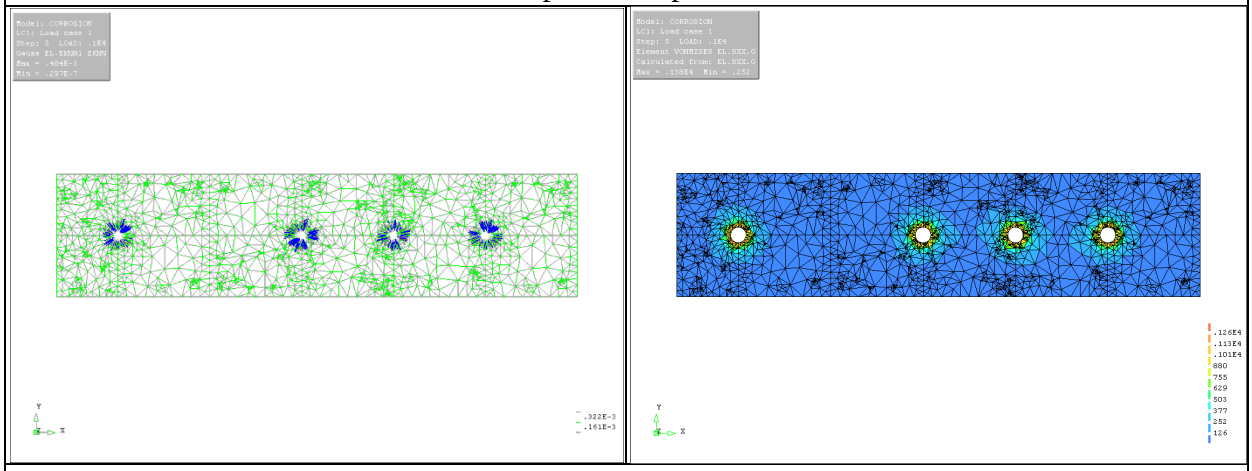

p_{int} = 1,000 psi

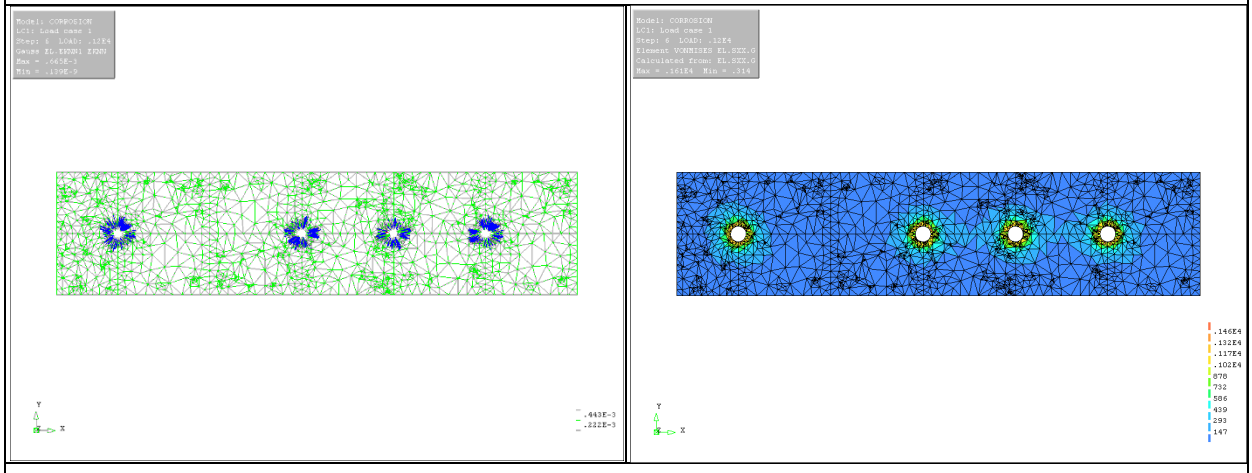

p_{int} = 1,200 psi

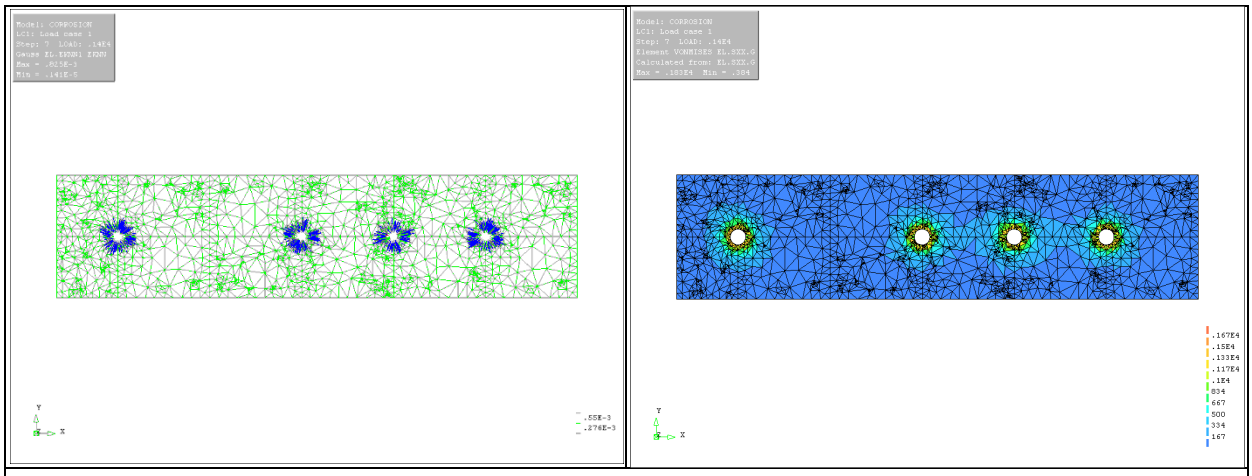

p_{int} = 1,400 psi

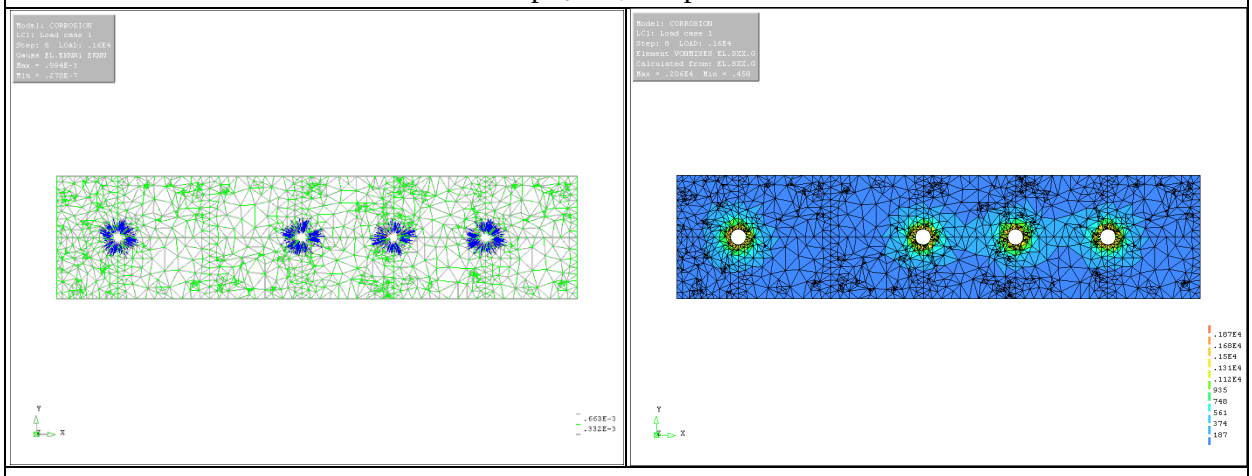

p_{int} = 1,600 psi

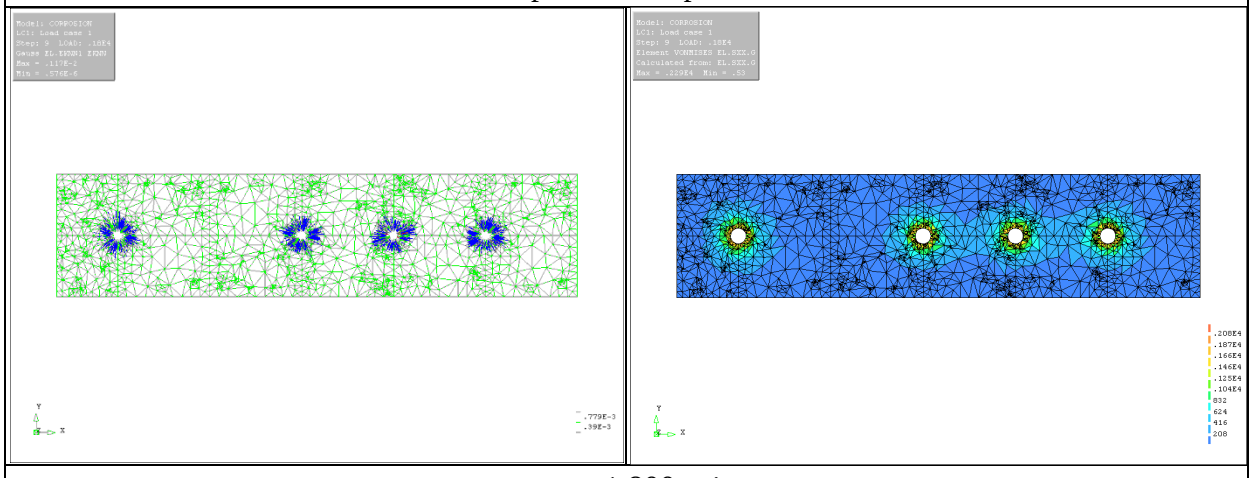

p_{int} = 1,800 psi

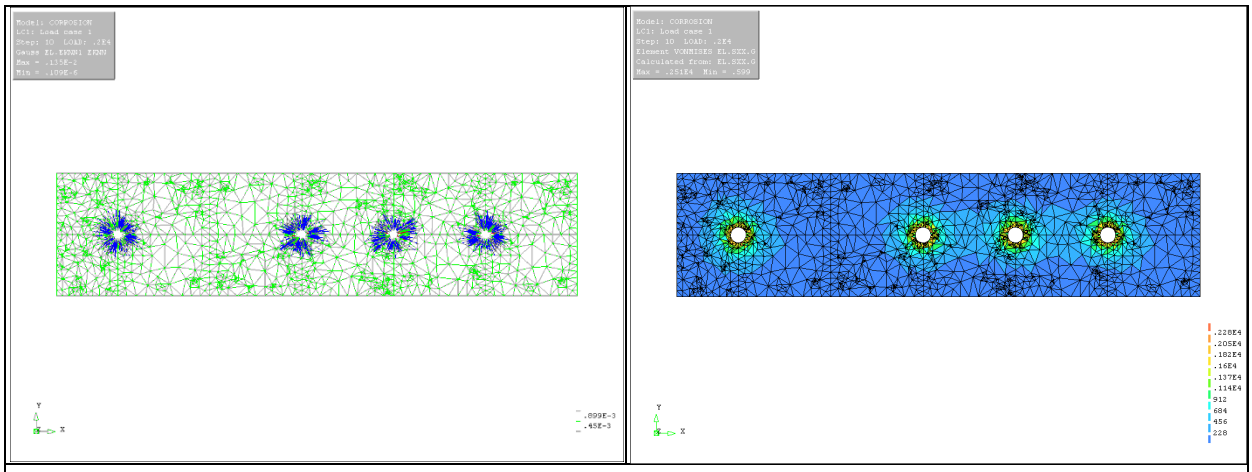

p_{int} = 2,000 psi

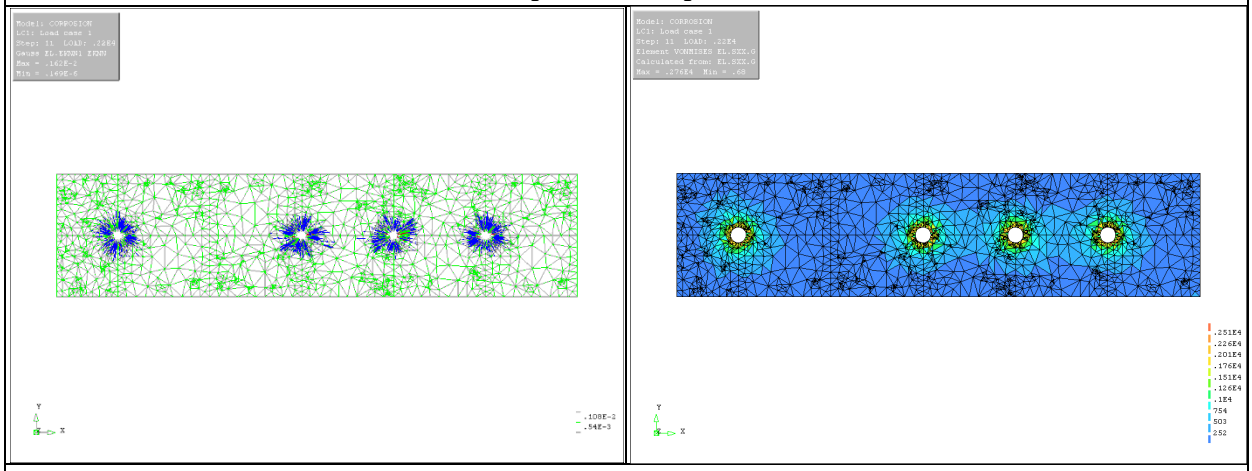

p_{int} = 2,200 psi

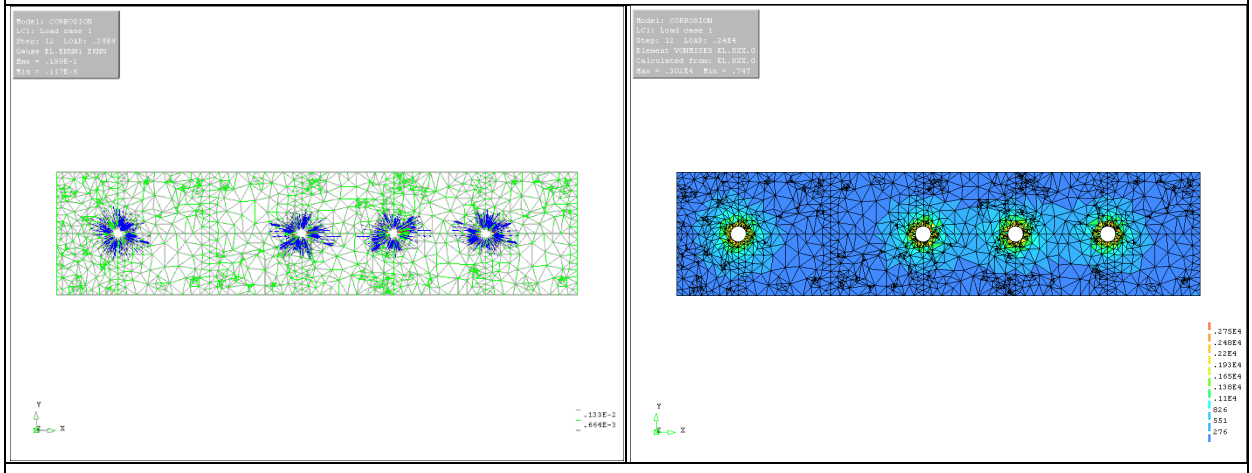

p_{int} = 2,400 psi

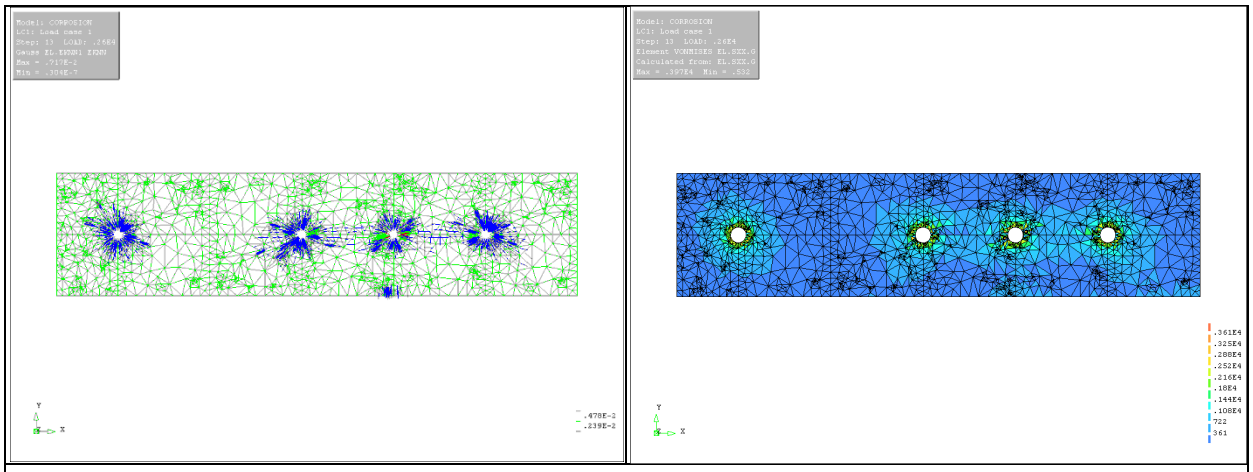

p_{int} = 2,600 psi

Figure D-7 Crack Patterns & Von Mises Stress Variations of Case II FE Model (Cover = 1.5 in.)

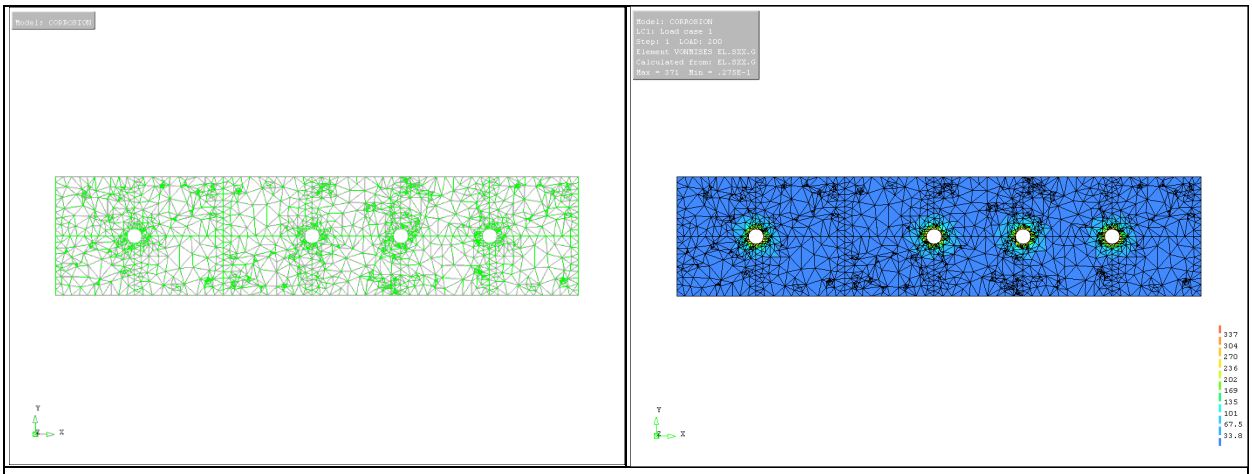

p_{int} = 200 psi

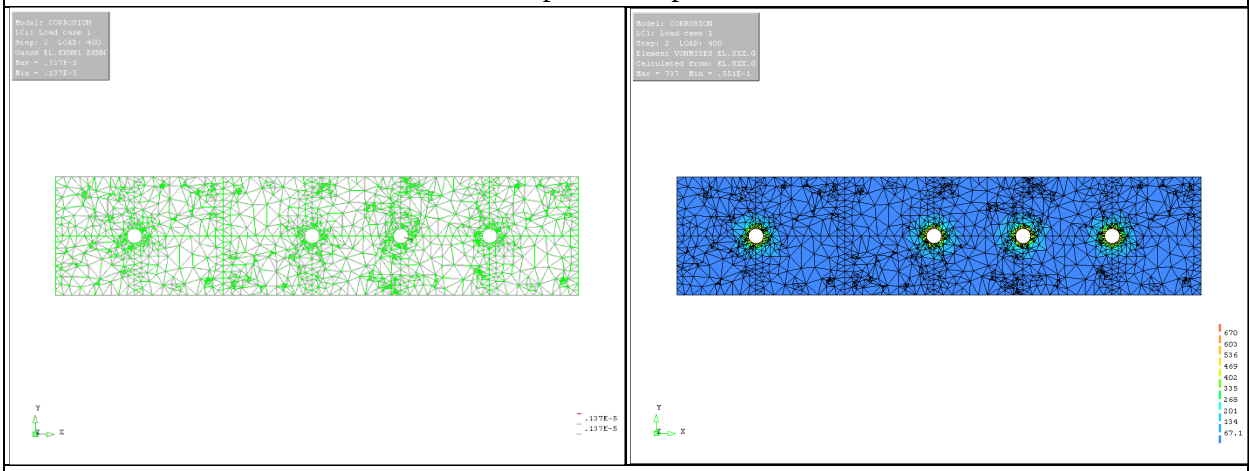

p_{int} = 400 psi

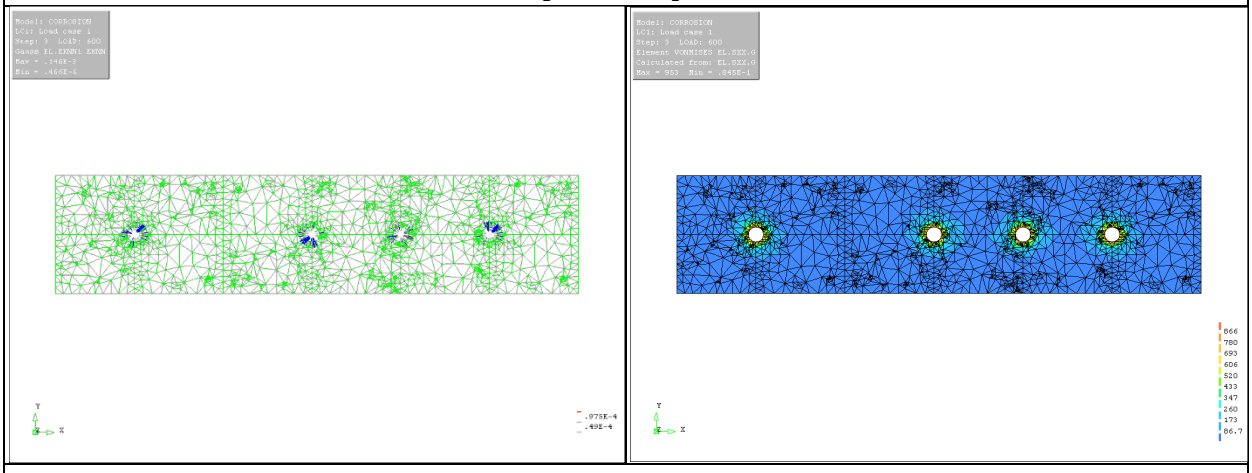

p_{int} = 600 psi

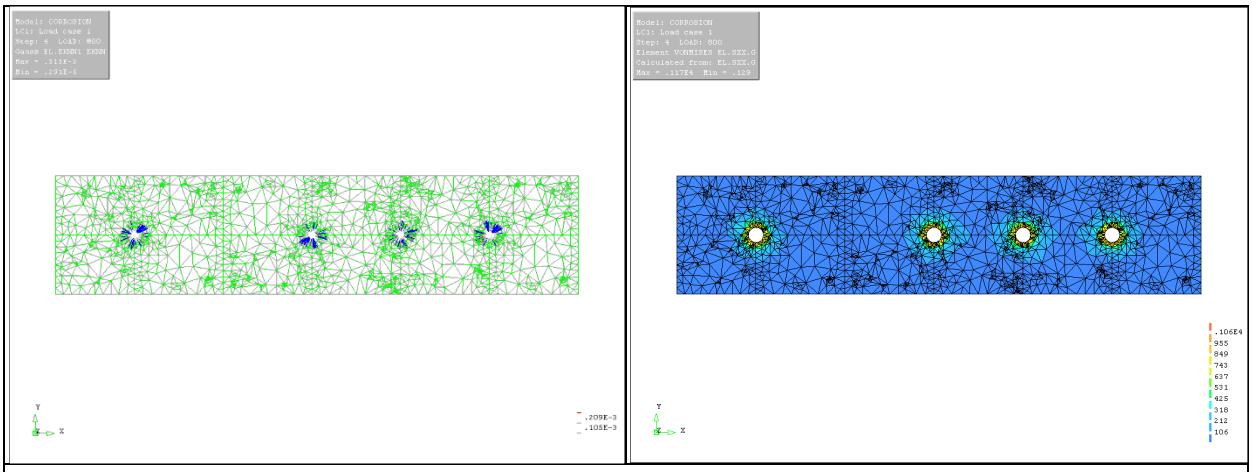

p_{int} = 800 psi

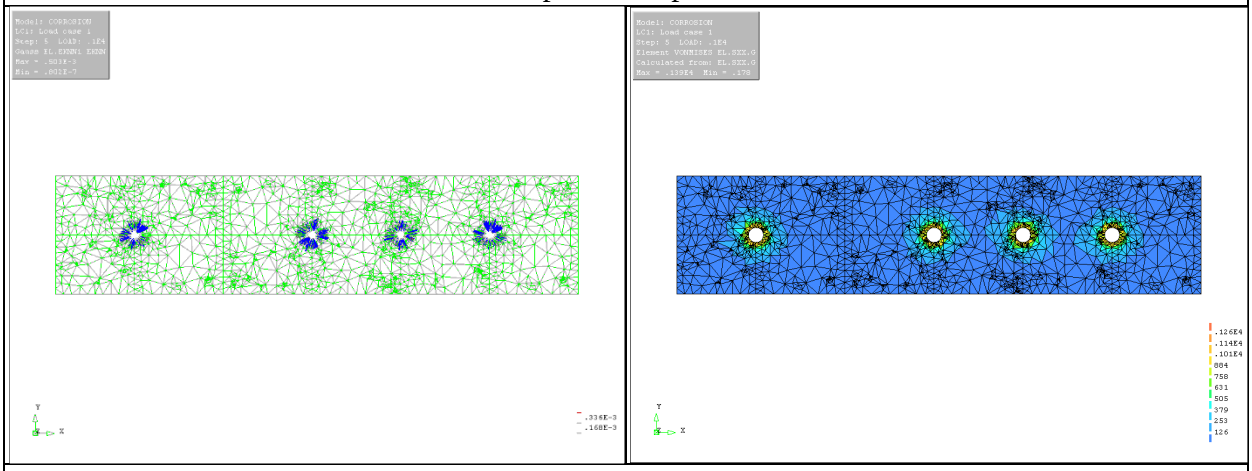

p_{int} = 1,000 psi

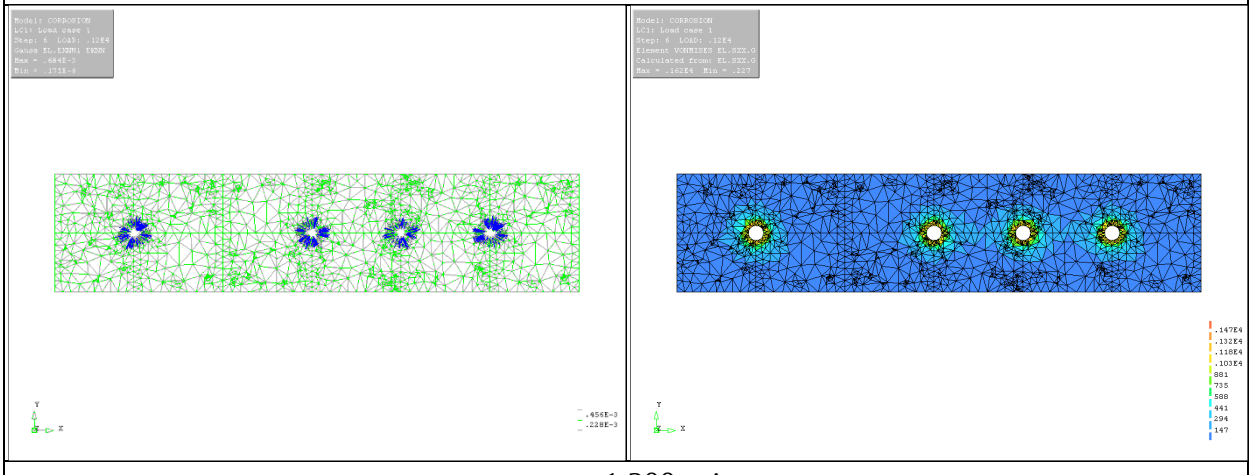

p_{int} = 1,200 psi

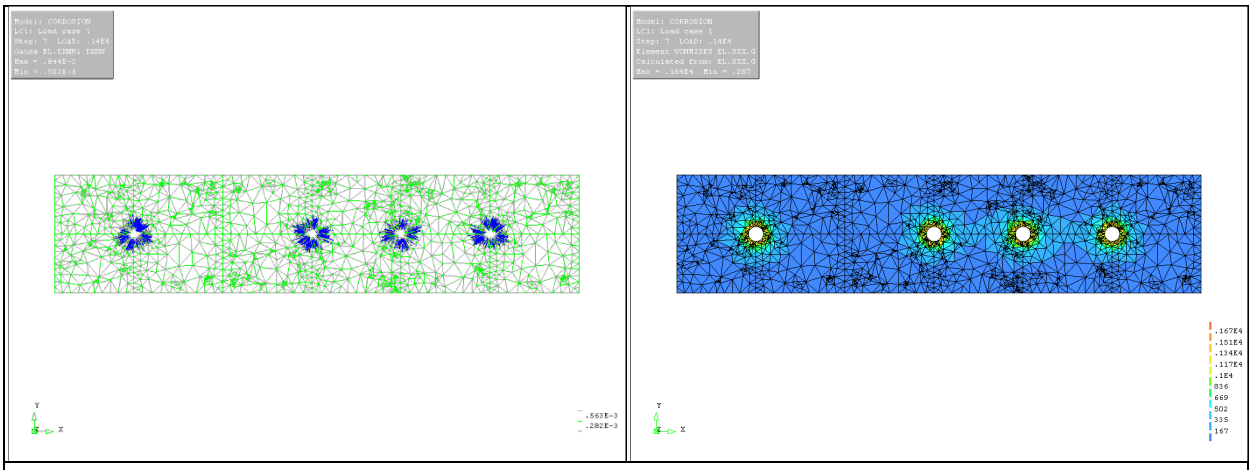

p_{int} = 1,400 psi

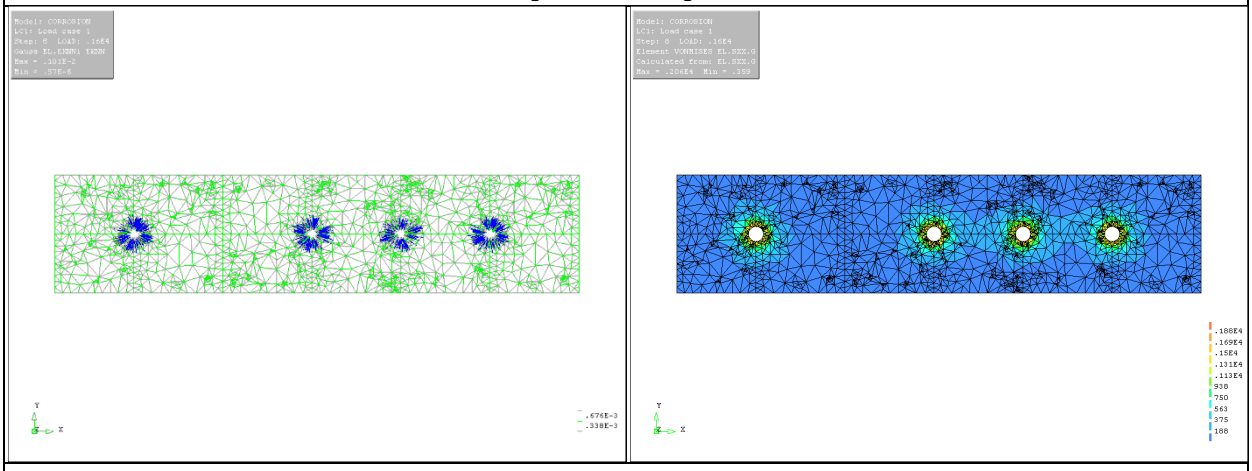

p_{int} = 1,600 psi

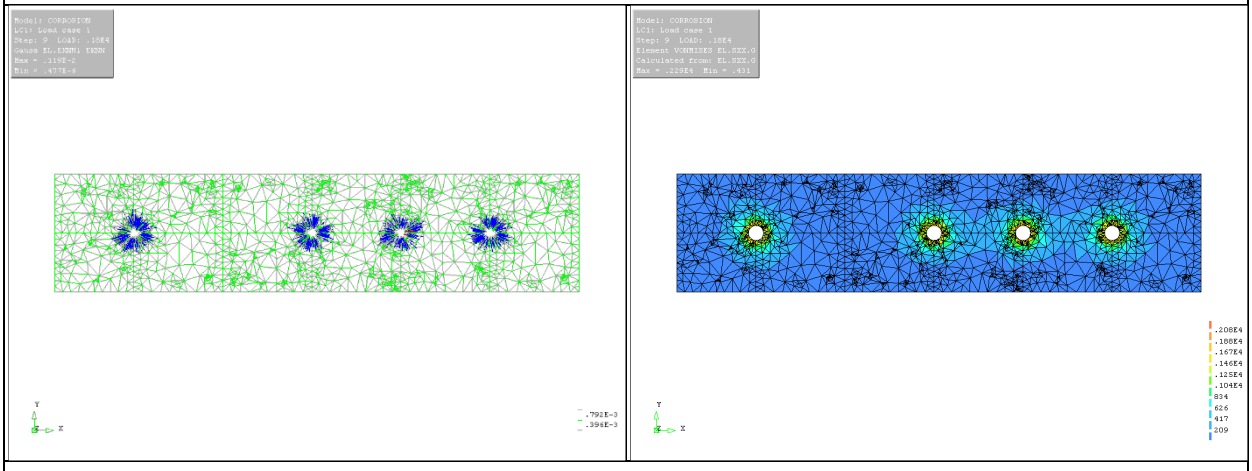

p_{int} = 1,800 psi

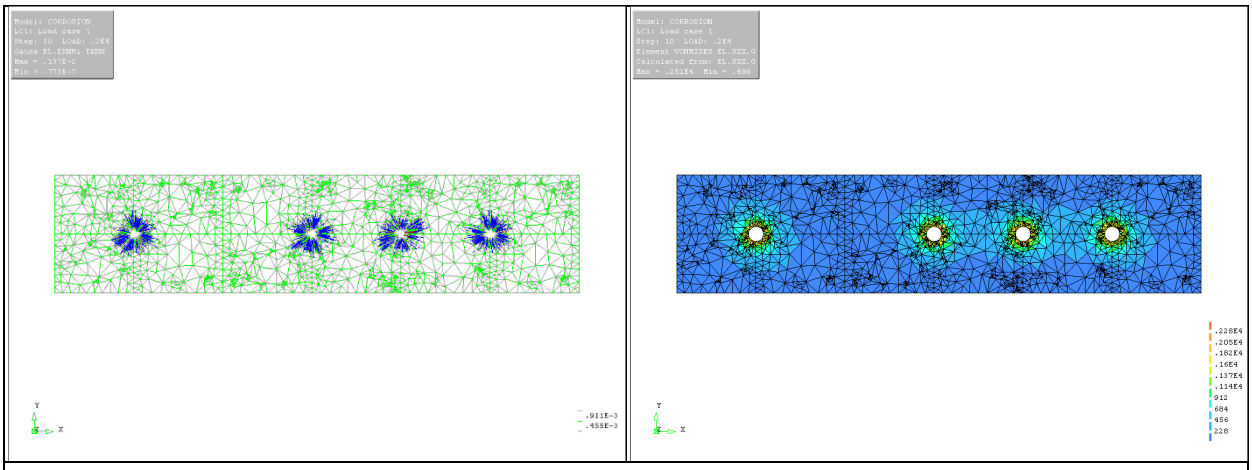

p_{int} = 2,000 psi

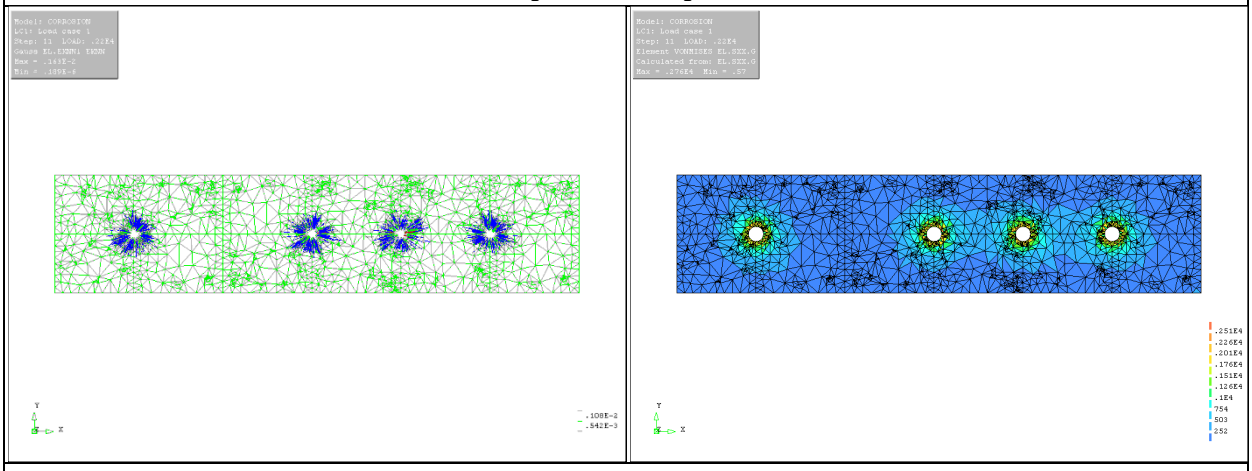

p_{int} = 2,200 psi

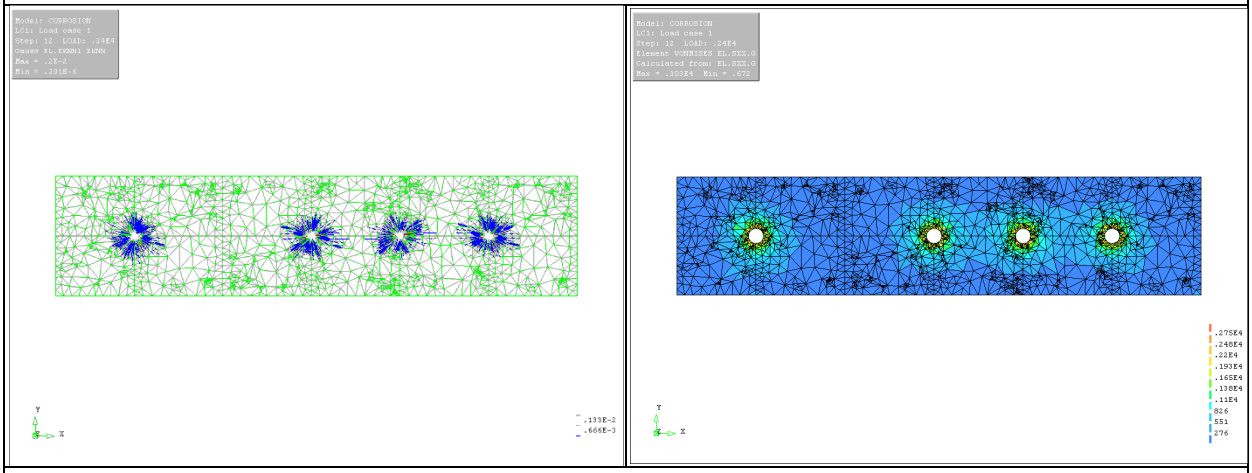

p_{int} = 2,400 psi

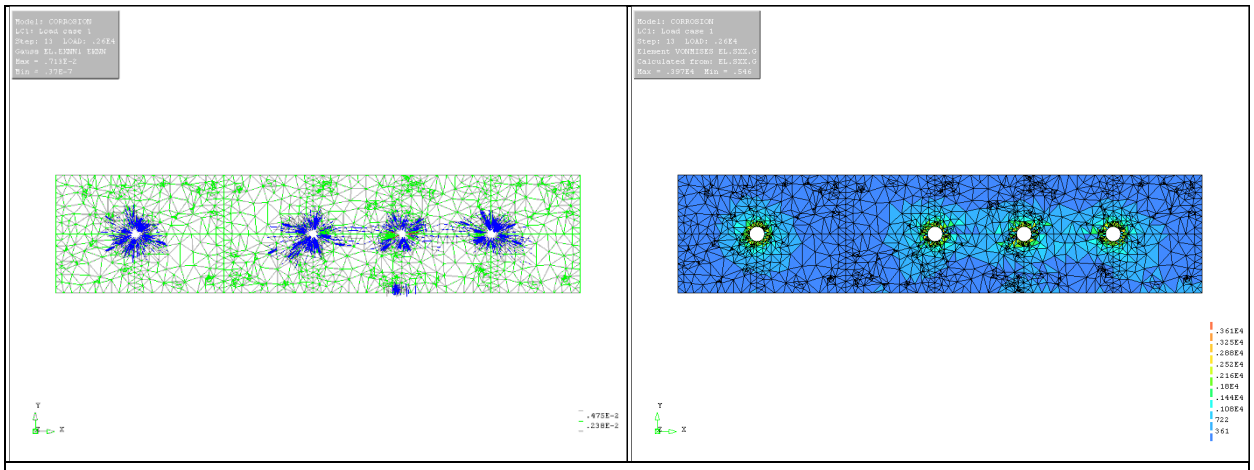

p_{int} = 2,600 psi

Figure D-8 Crack Patterns & Von Mises Stress Variations of Case II FE Model (Cover = 2.0 in.)

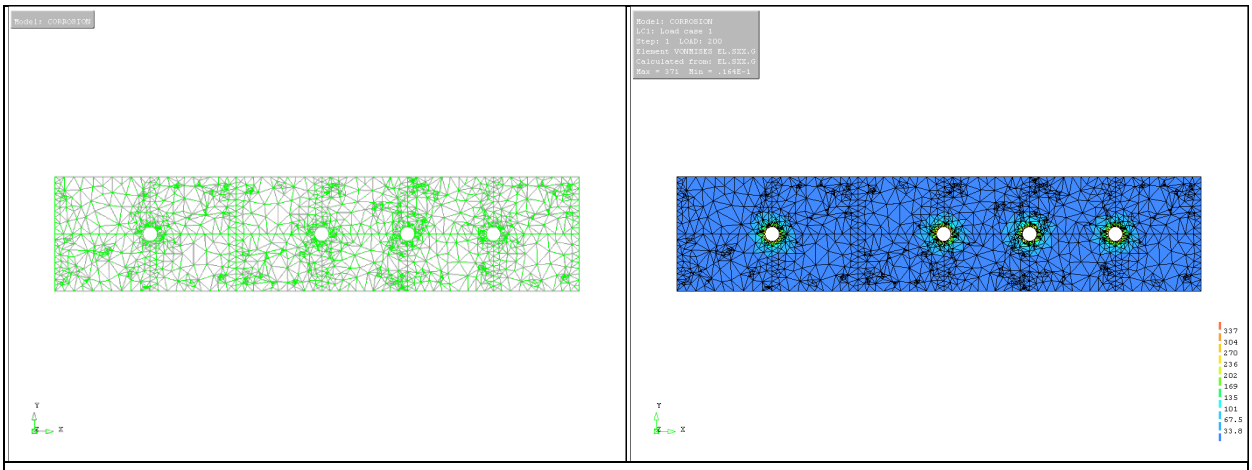

p_{int} = 200 psi

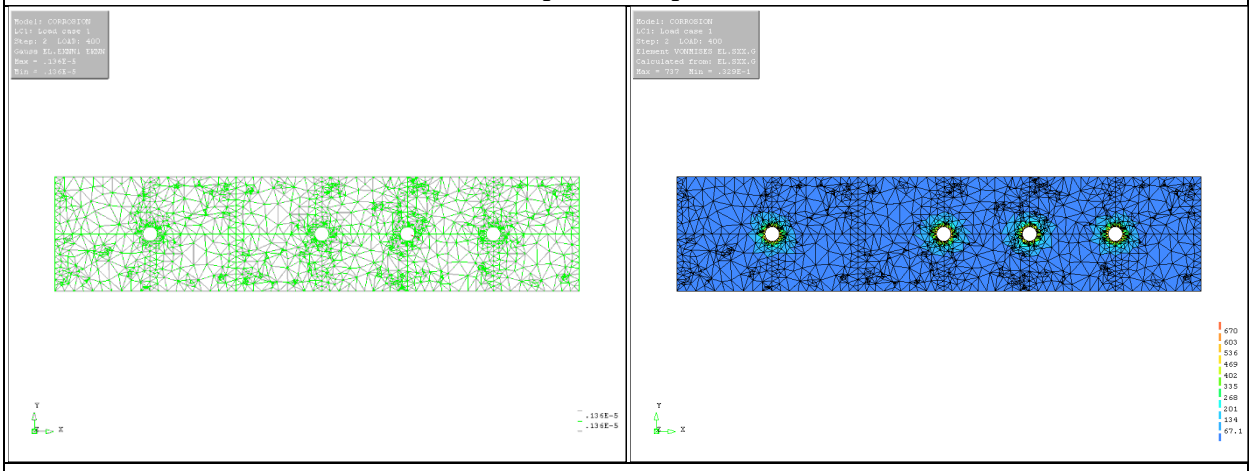

p_{int} = 400 psi

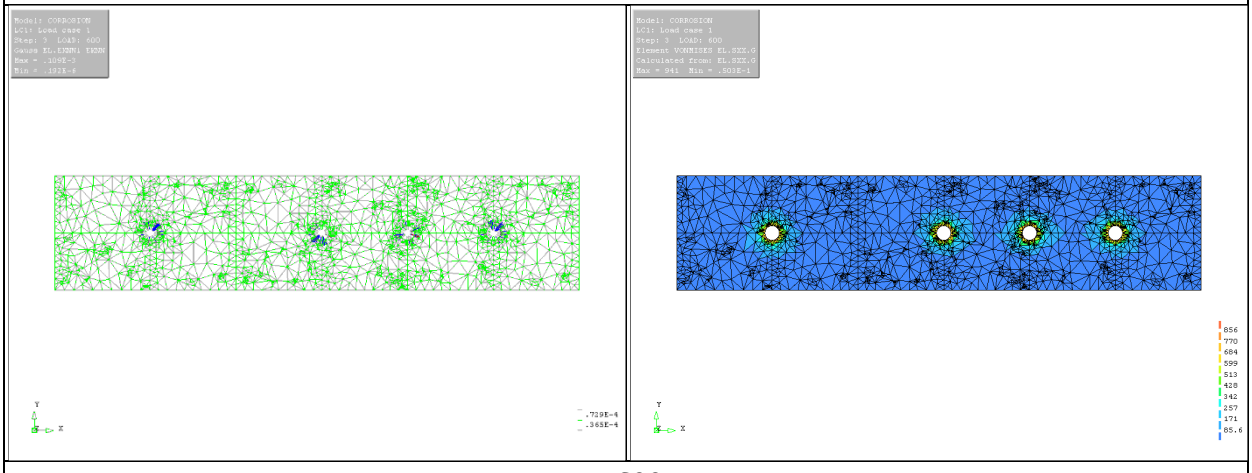

p_{int} = 600 psi

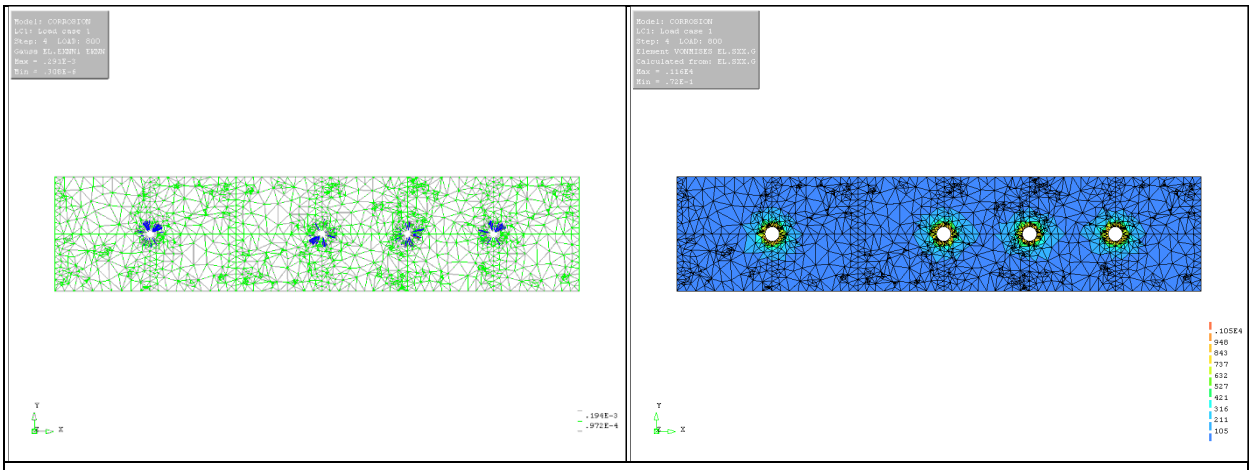

p_{int} = 800 psi

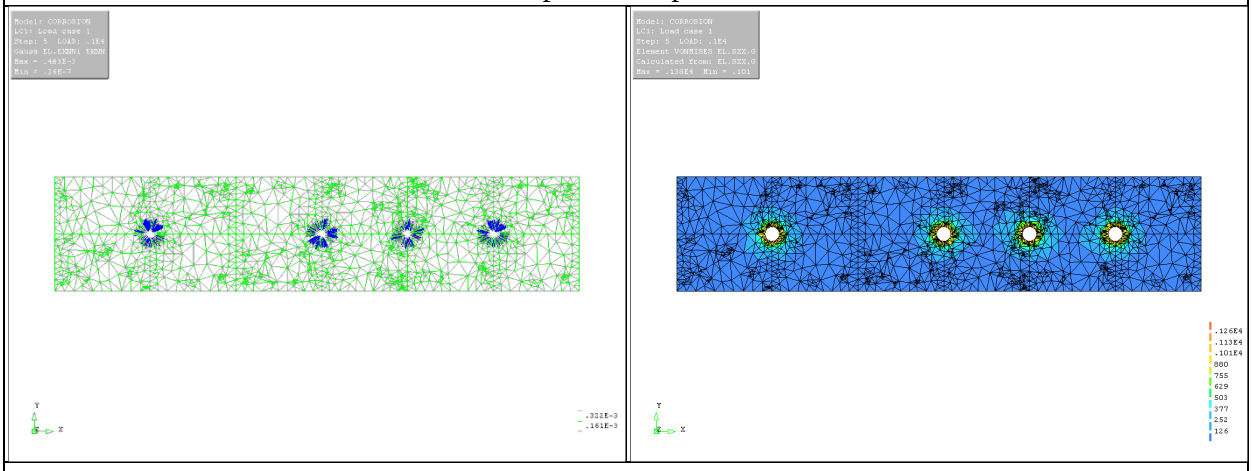

p_{int} = 1,000 psi

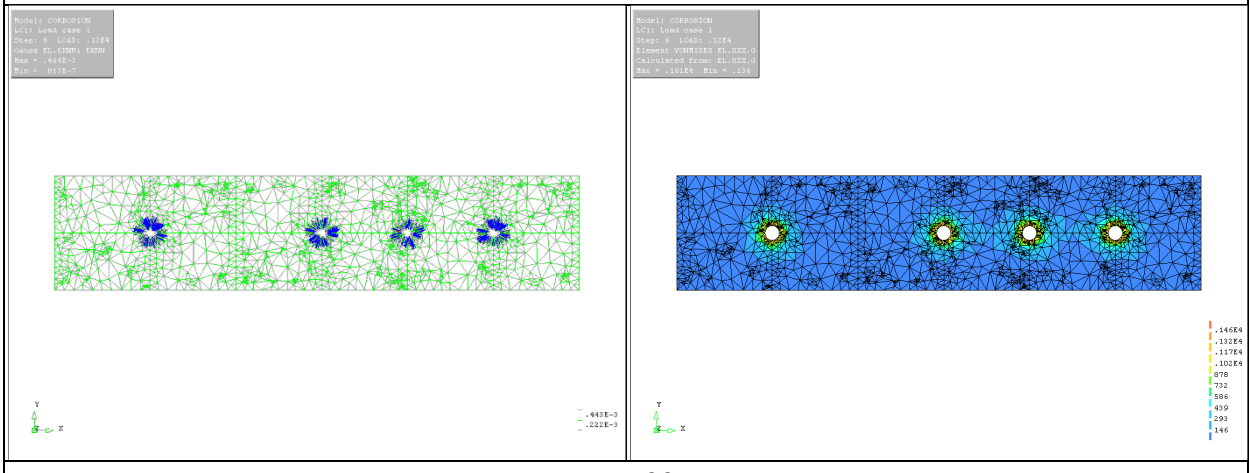

p_{int} = 1,200 psi

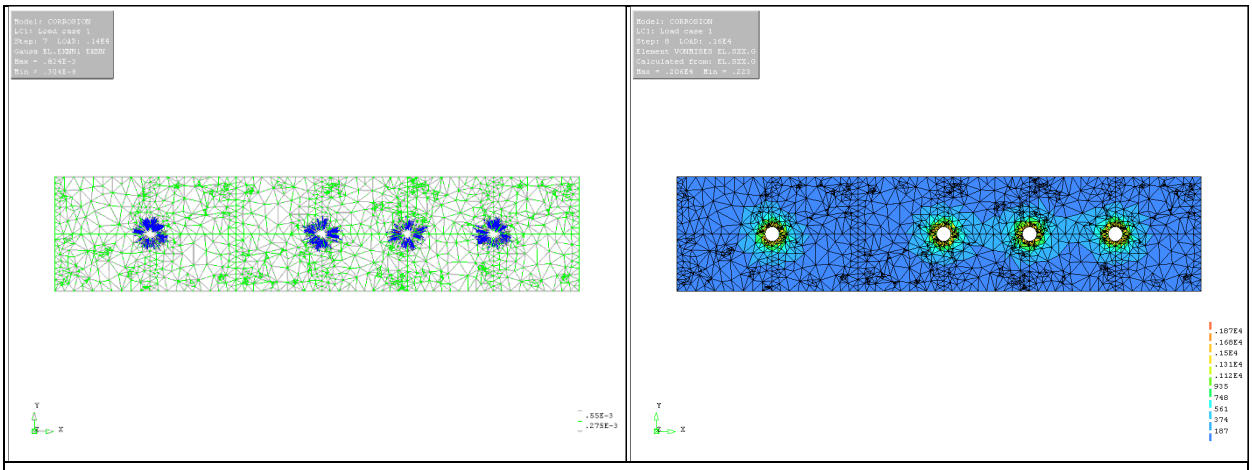

p_{int} = 1,400 psi

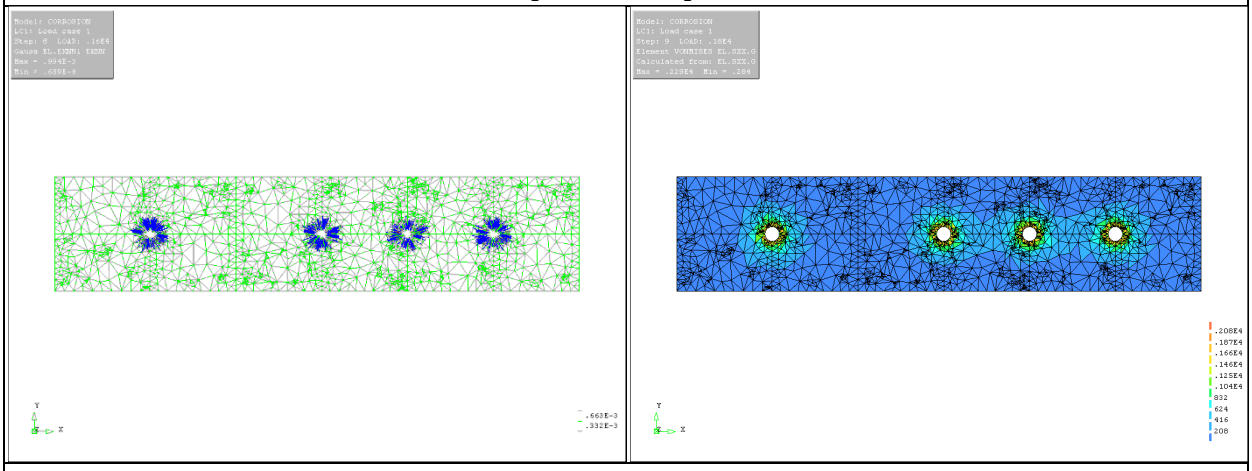

p_{int} = 1,600 psi

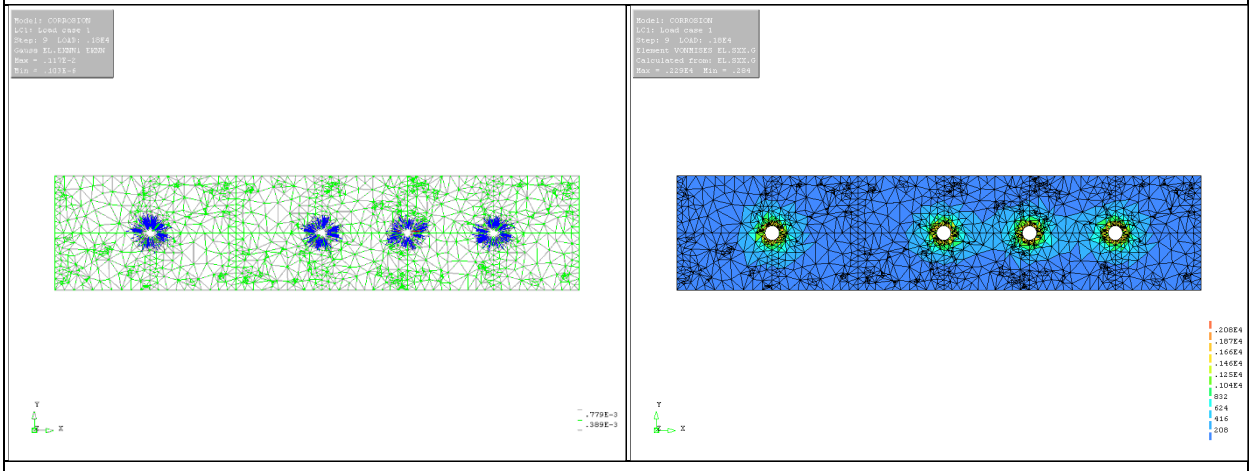

p_{int} = 1,800 psi

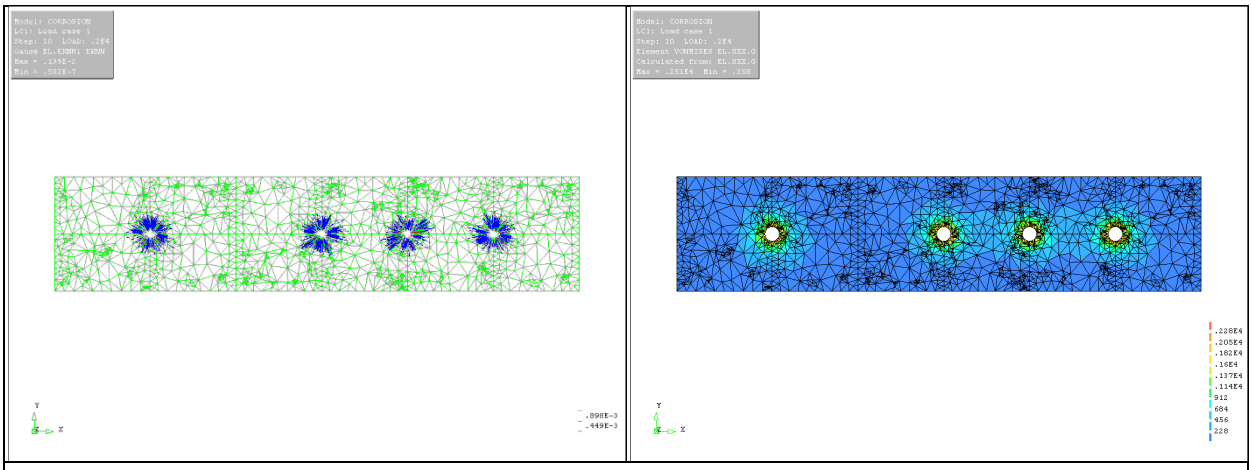

p_{int} = 2,000 psi

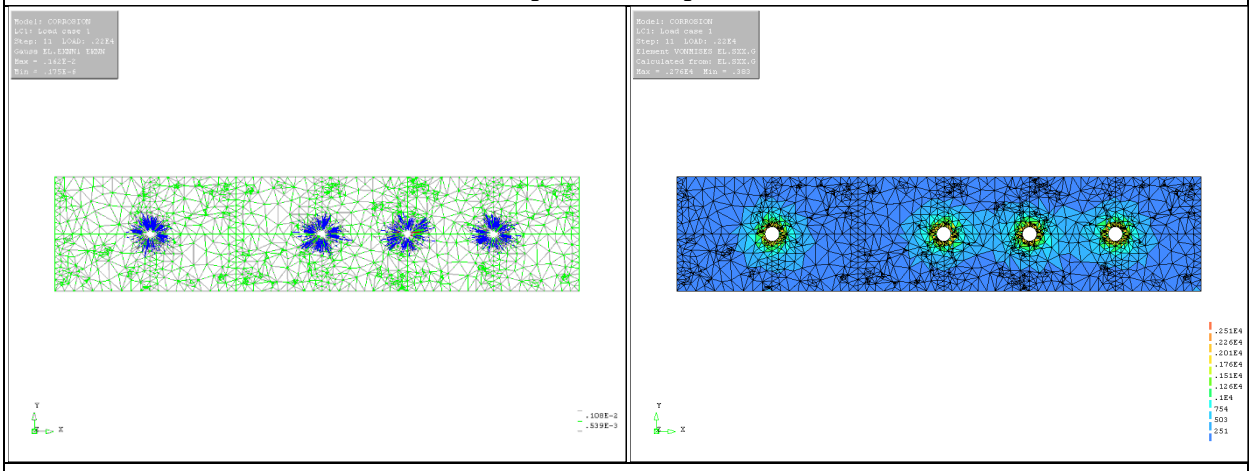

p_{int} = 2,200 psi

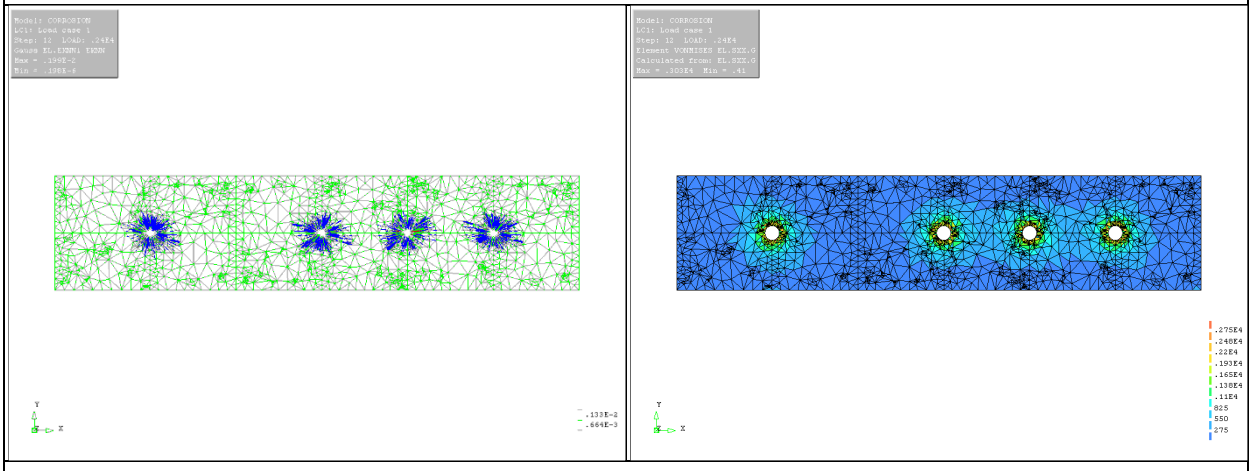

p_{int} = 2,400 psi

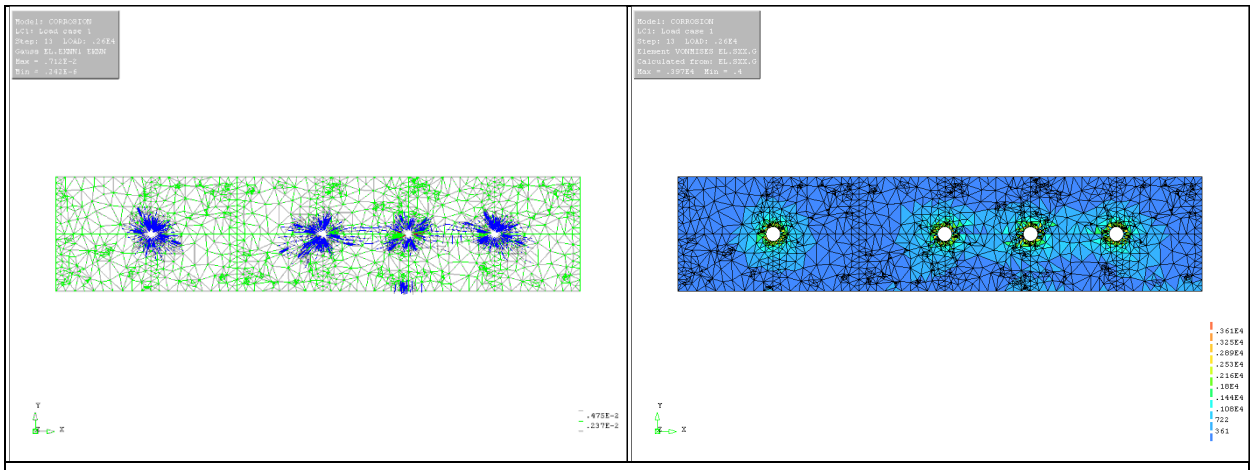

p_{int} = 2,600 psi

Figure D-9 Crack Patterns & Von Mises Stress Variations of Case II FE Model (Cover = 2.5 in.)

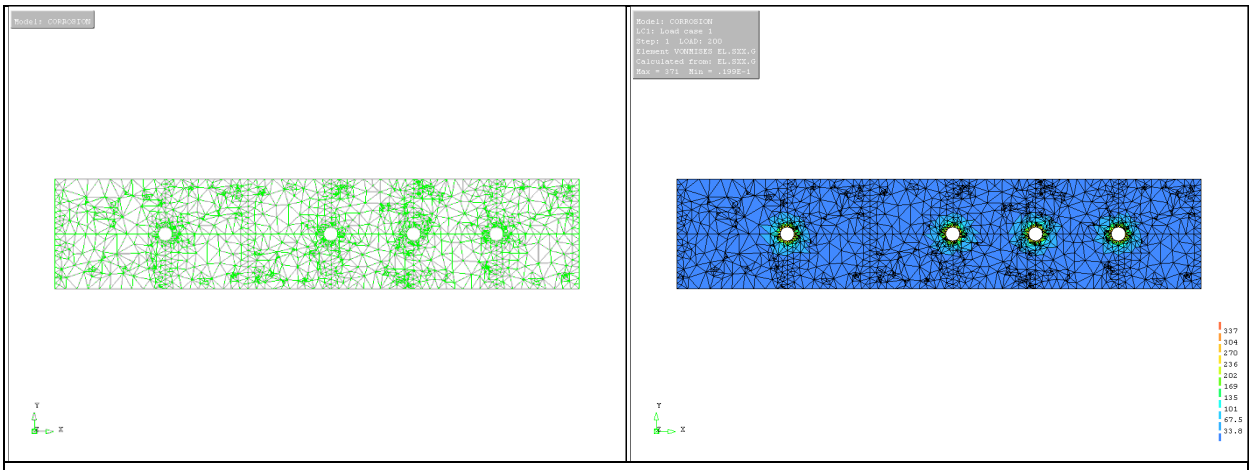

p_{int} = 200 psi

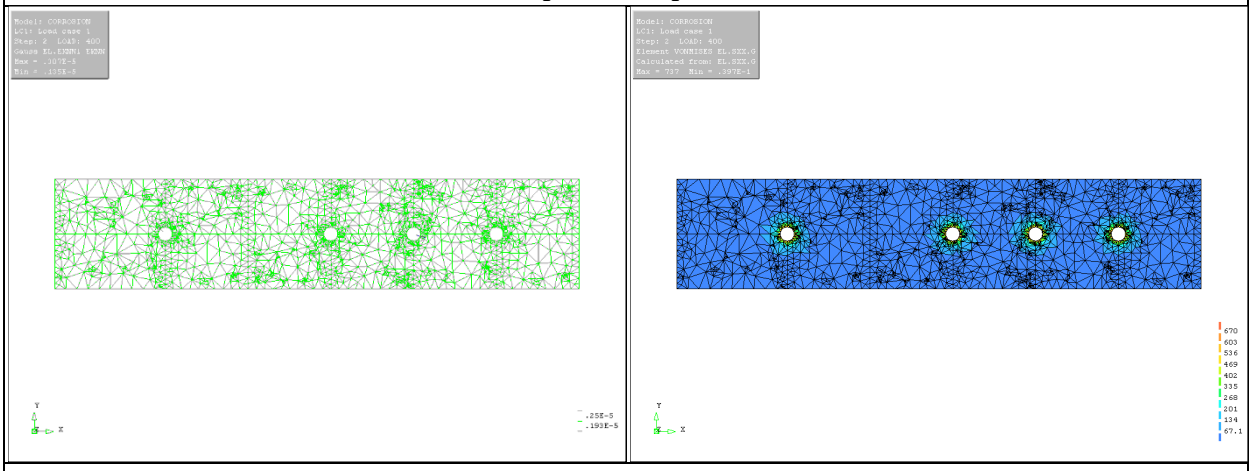

p_{int} = 400 psi

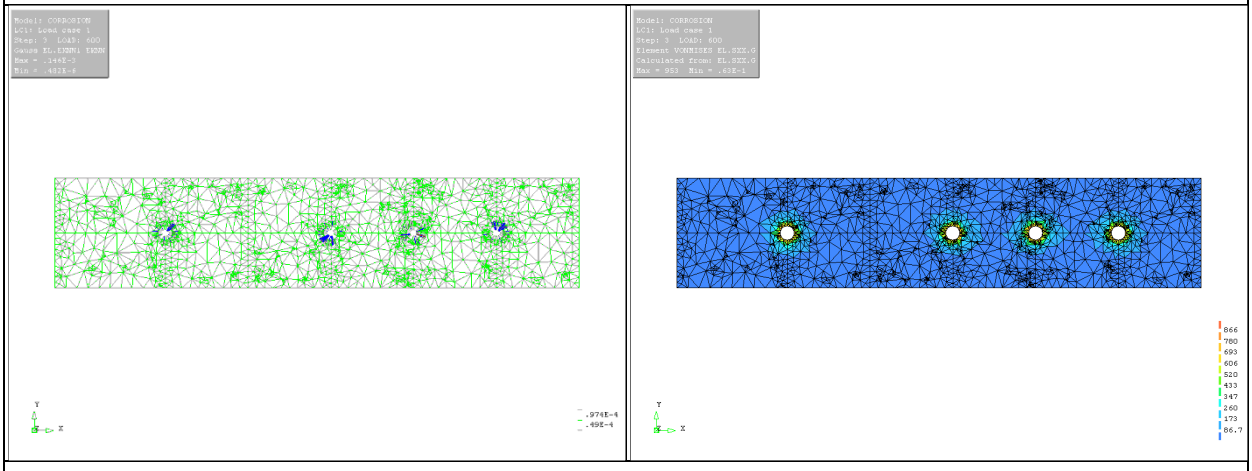

p_{int} = 600 psi

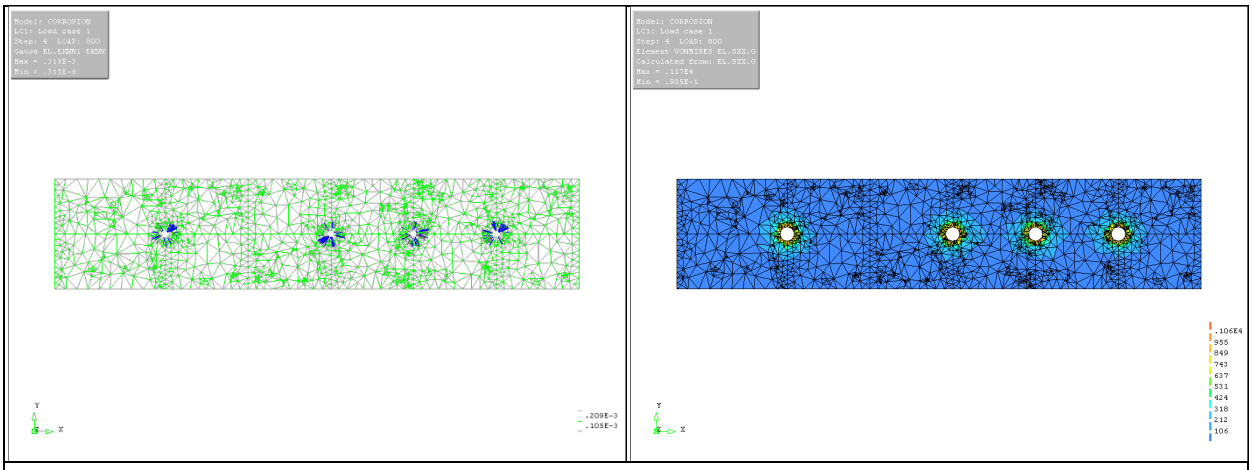

p_{int} = 800 psi

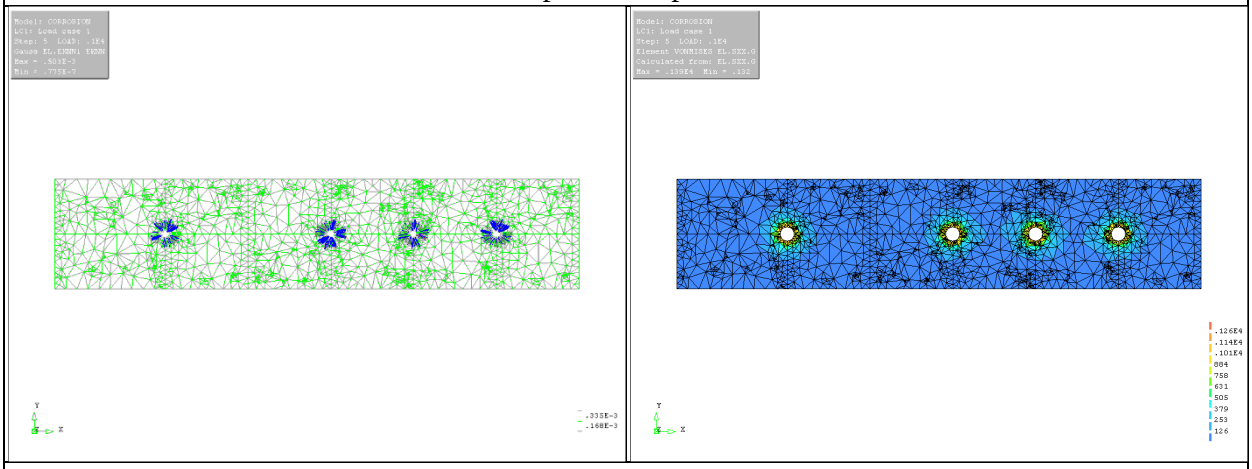

p_{int} = 1,000 psi

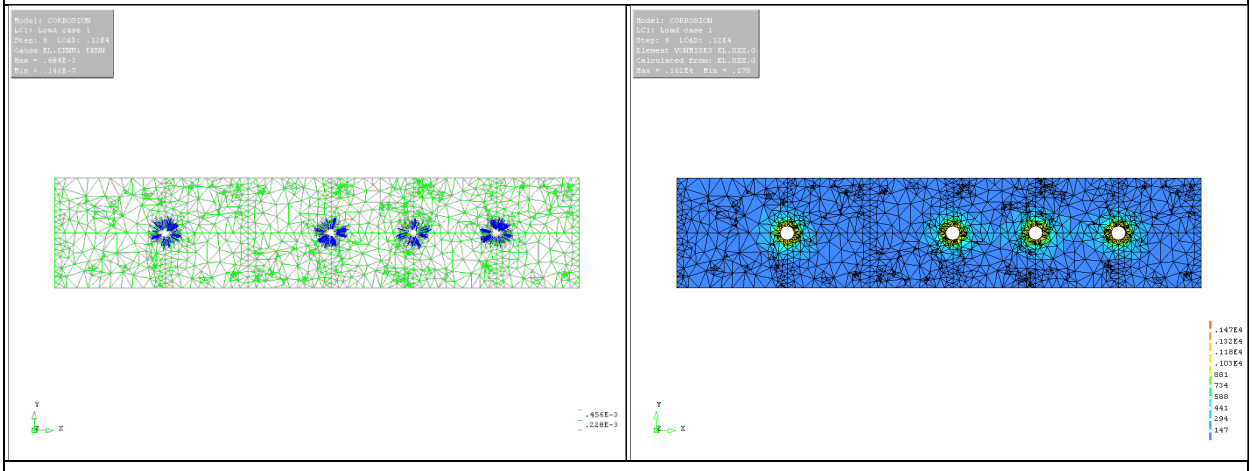

p_{int} = 1,200 psi

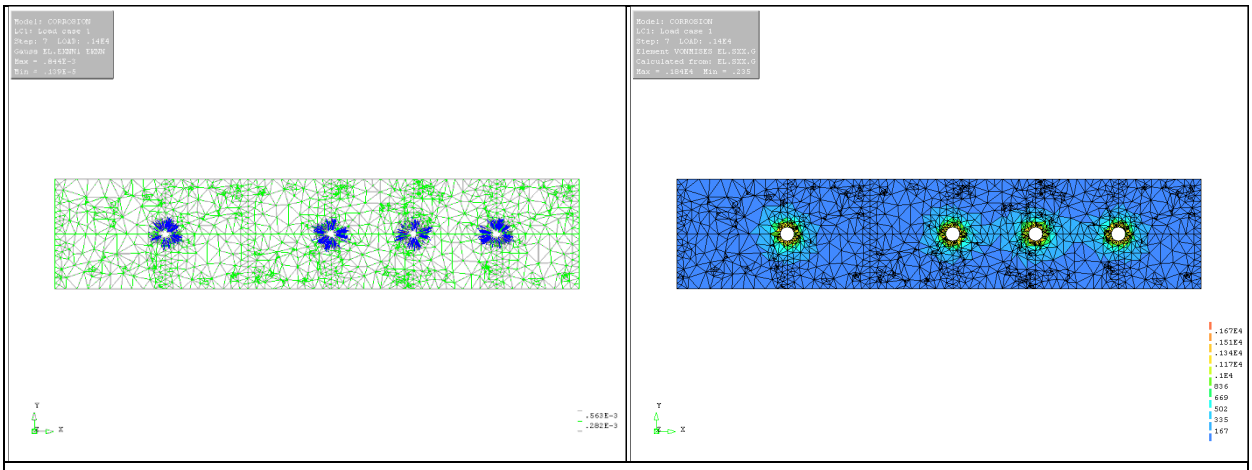

p_{int} = 1,400 psi

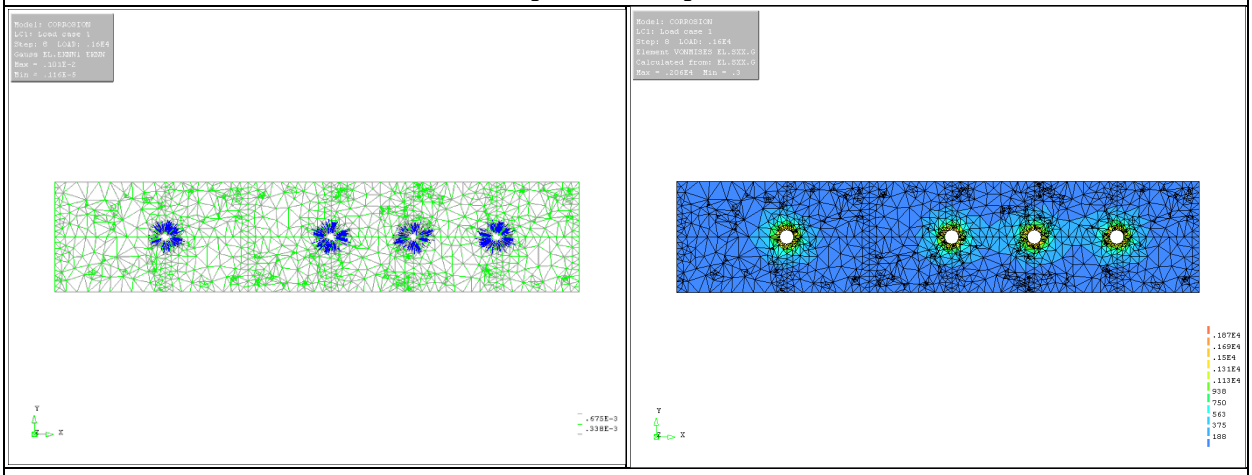

p_{int} = 1,600 psi

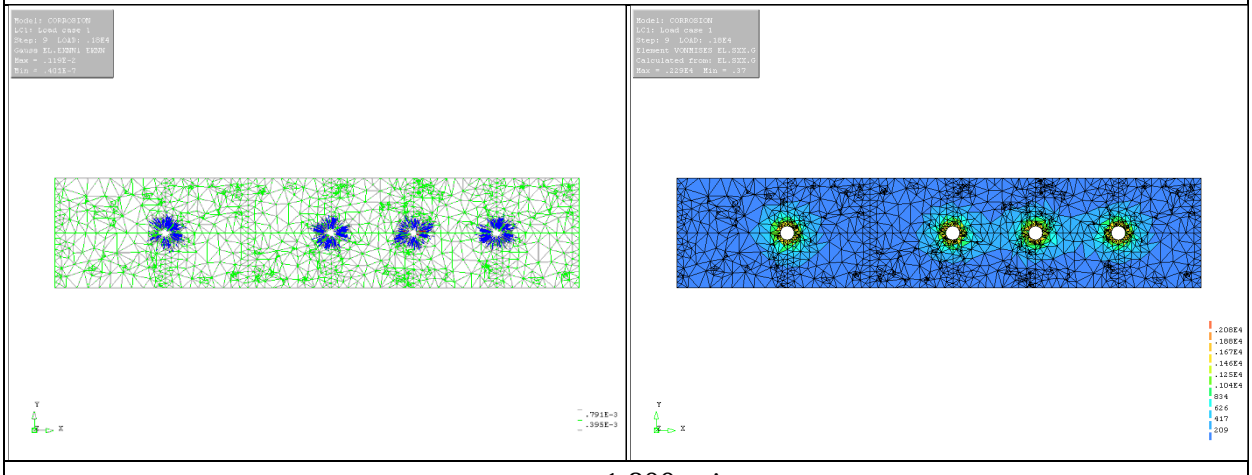

p_{int} = 1,800 psi

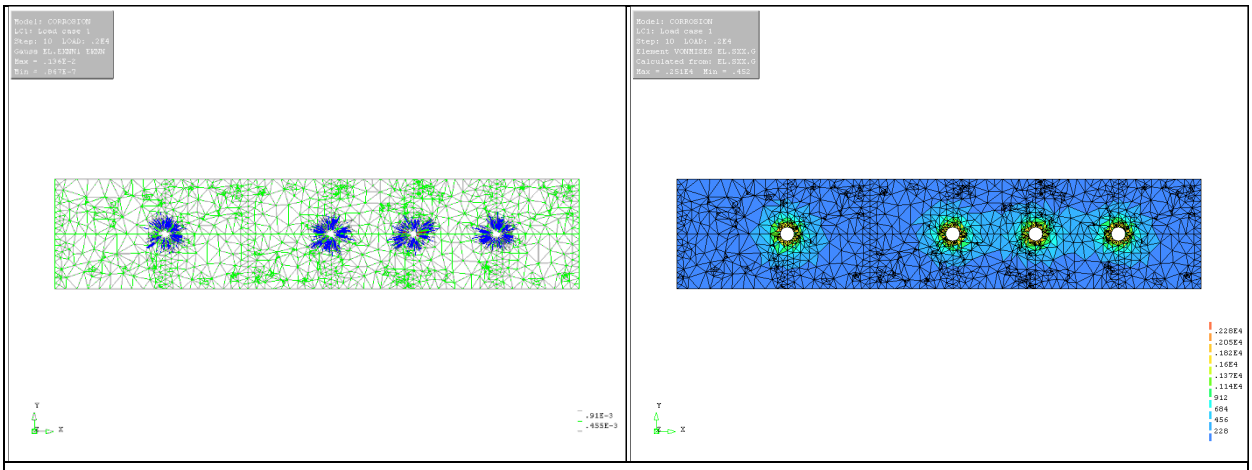

p_{int} = 2,000 psi

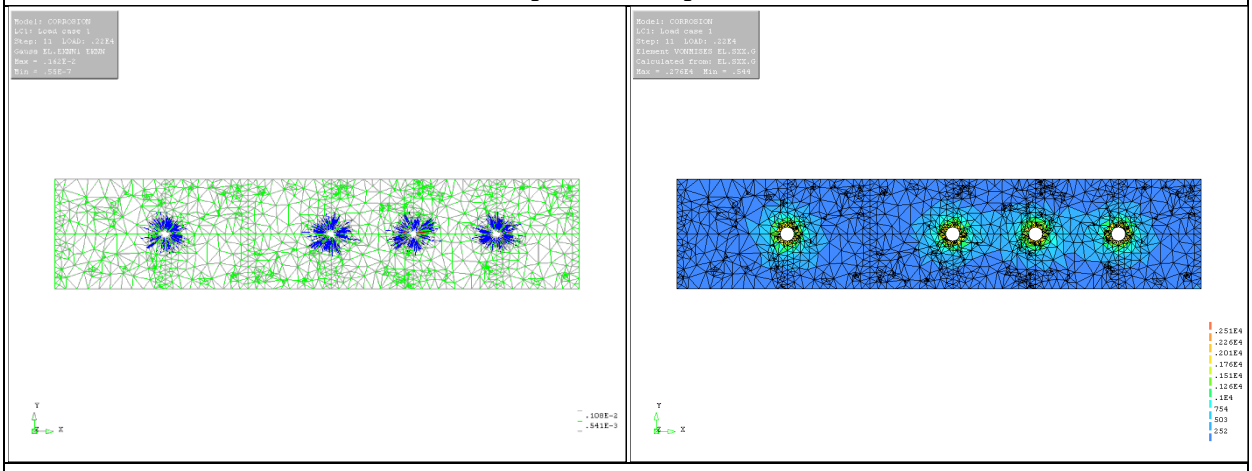

p_{int} = 2,200 psi

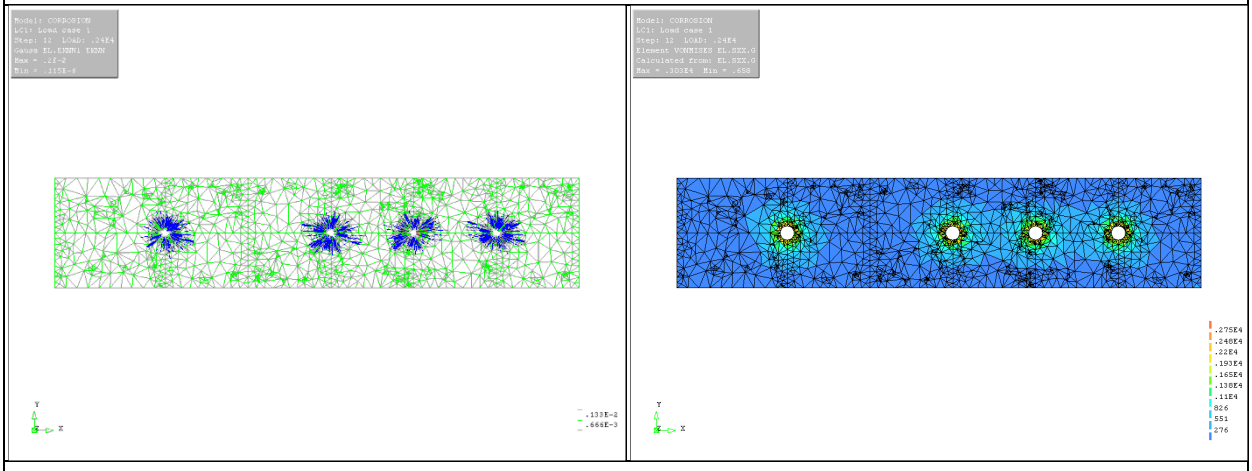

p_{int} = 2,400 psi

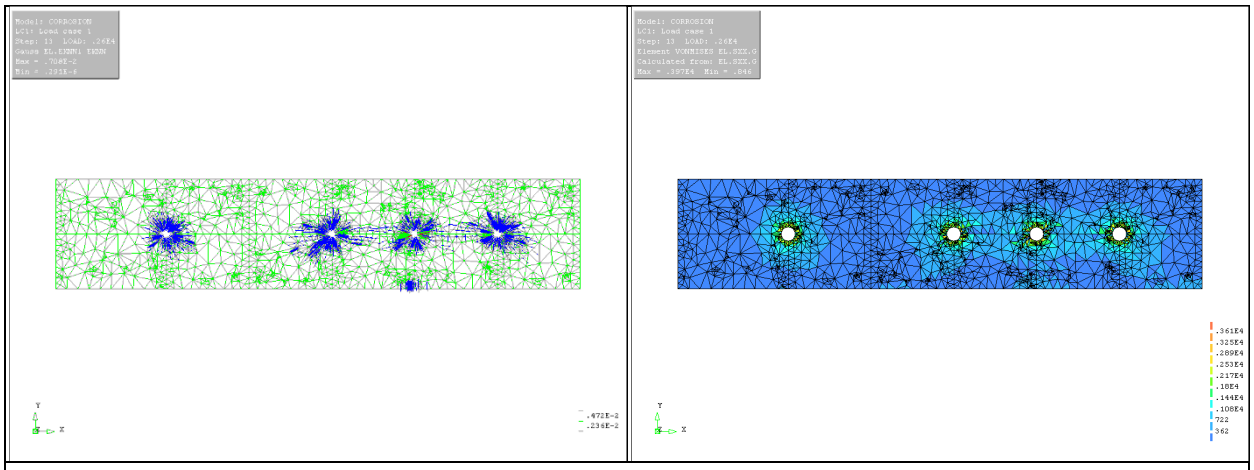

p_{int} = 2,600 psi

Figure D-10 Crack Patterns & Von Mises Stress Variations of Case II FE Model (Cover = 3.0 in.)

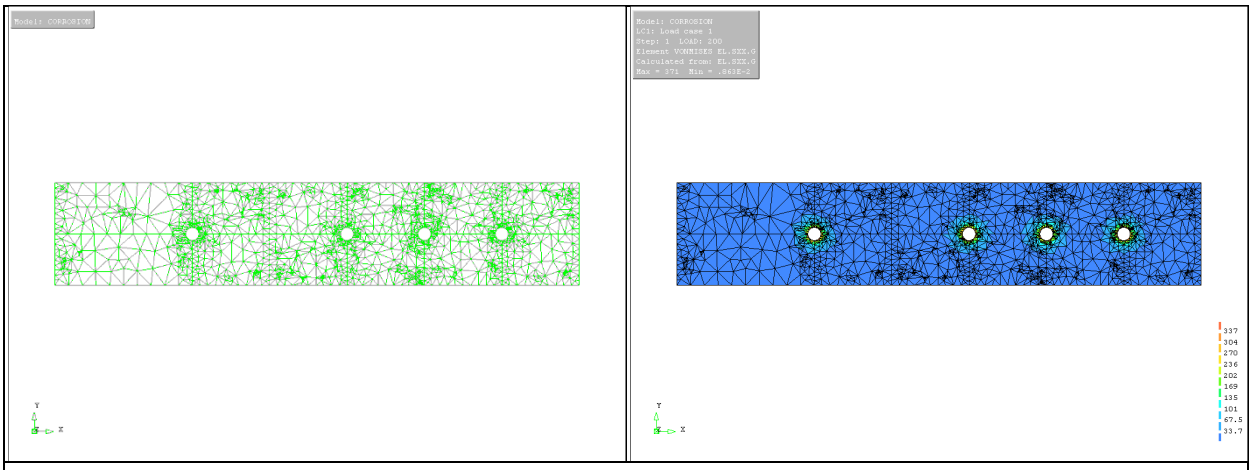

p_{int} = 200 psi

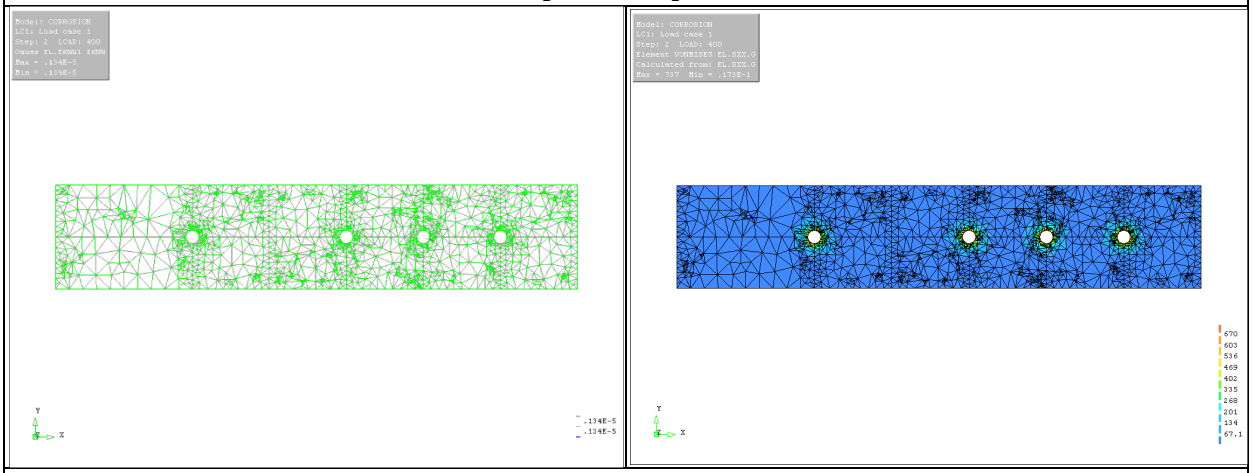

p_{int} = 400 psi

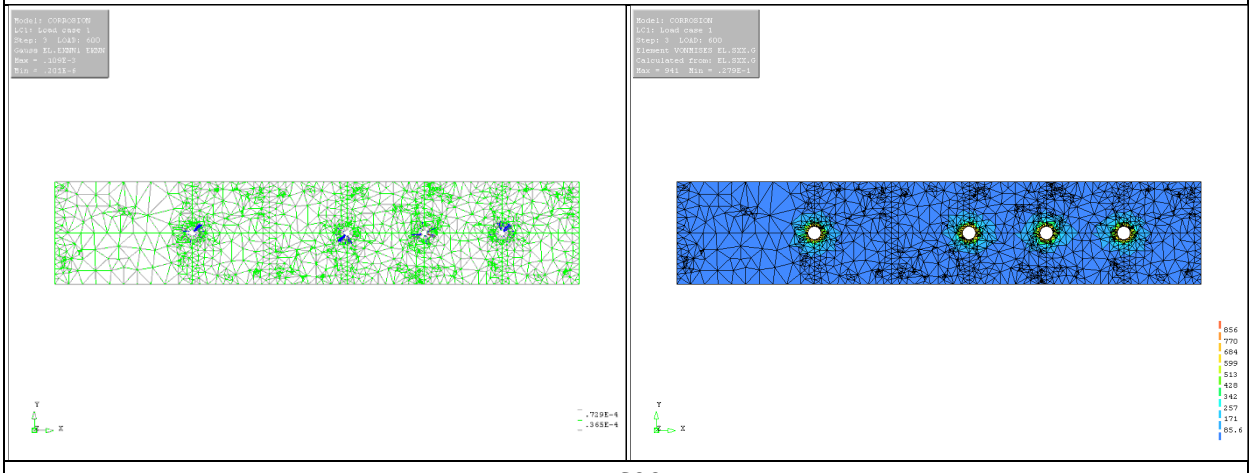

p_{int} = 600 psi

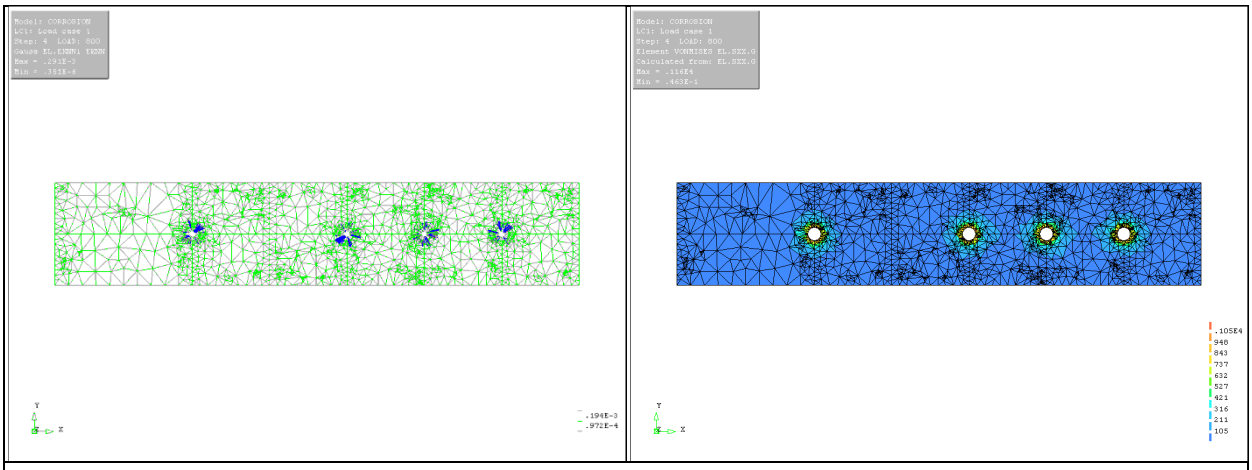

p_{int} = 800 psi

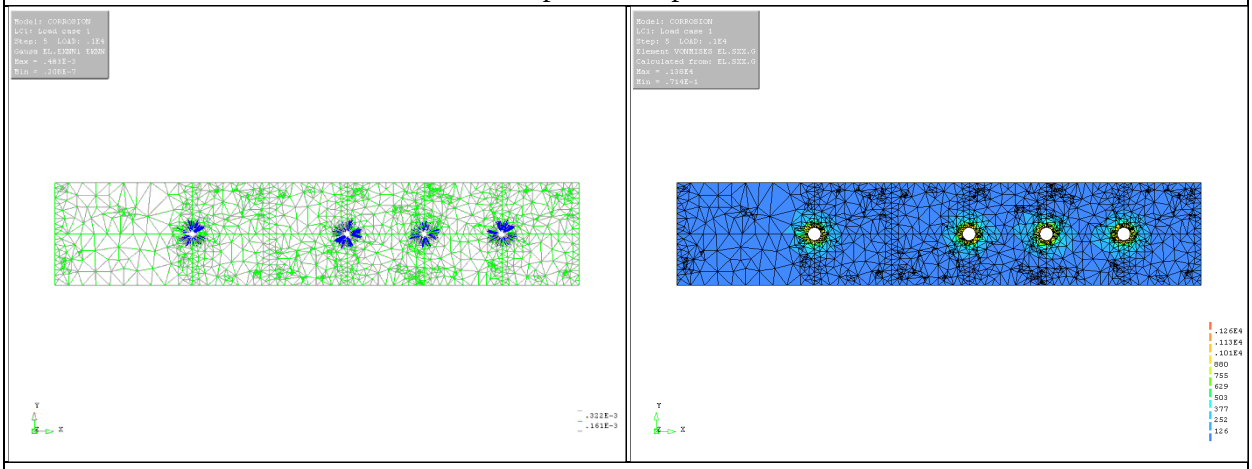

p_{int} = 1,000 psi

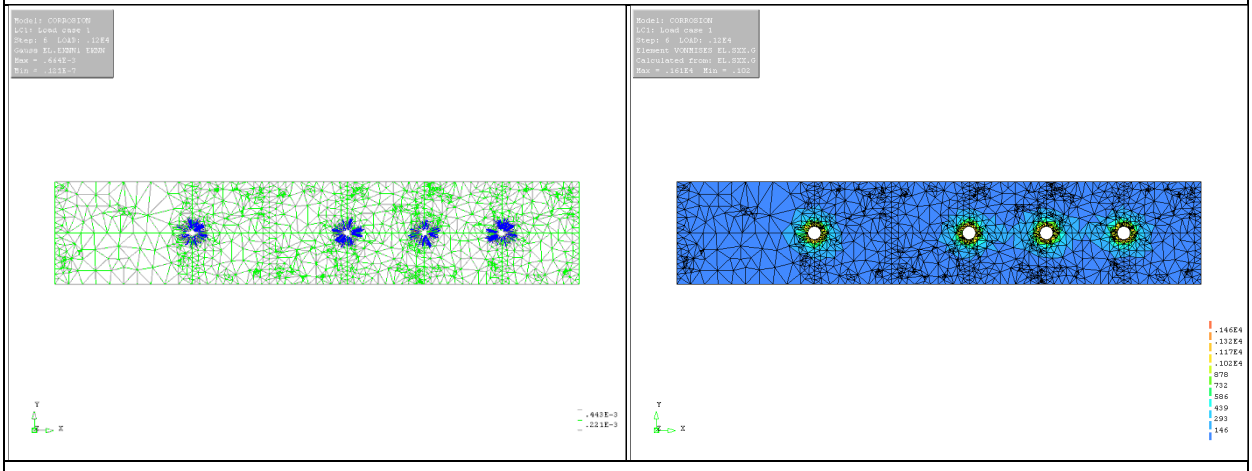

p_{int} = 1,200 psi

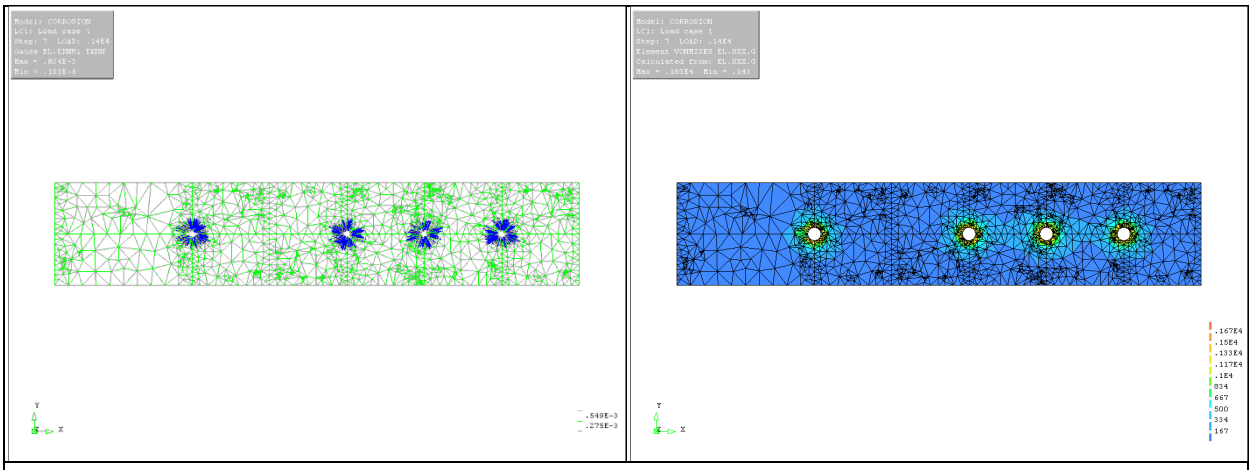

p_{int} = 1,400 psi

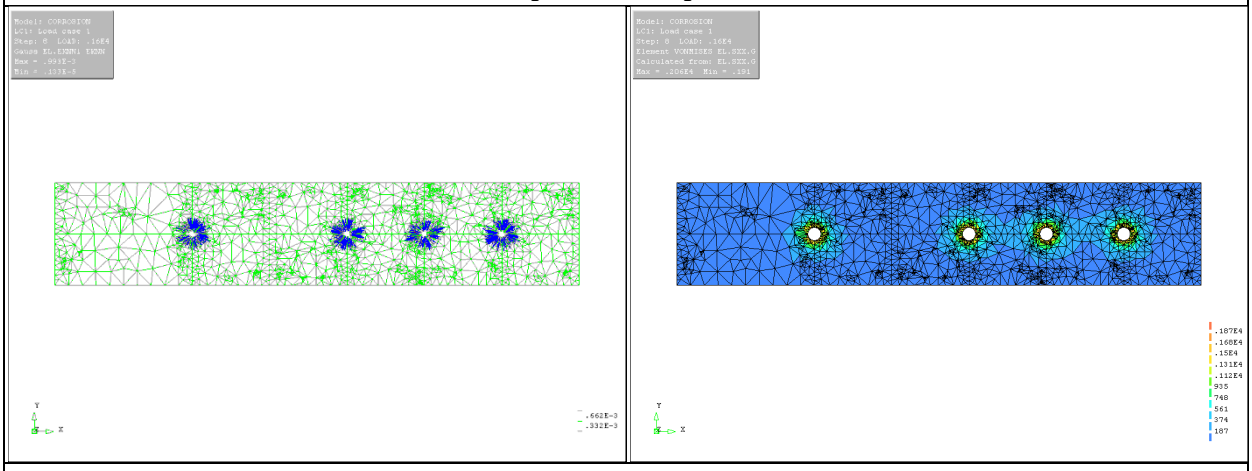

p_{int} = 1,600 psi

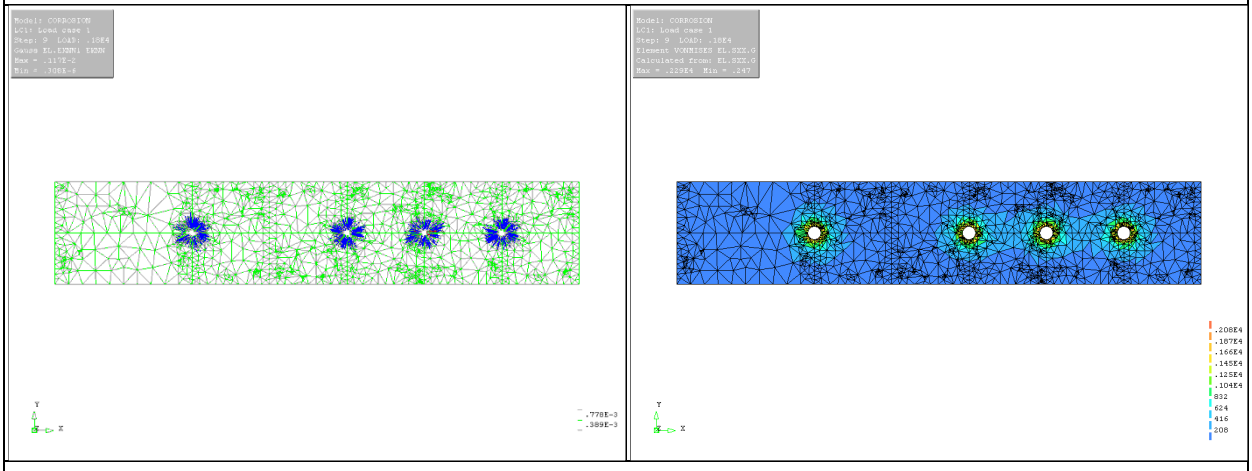

p_{int} = 1,800 psi

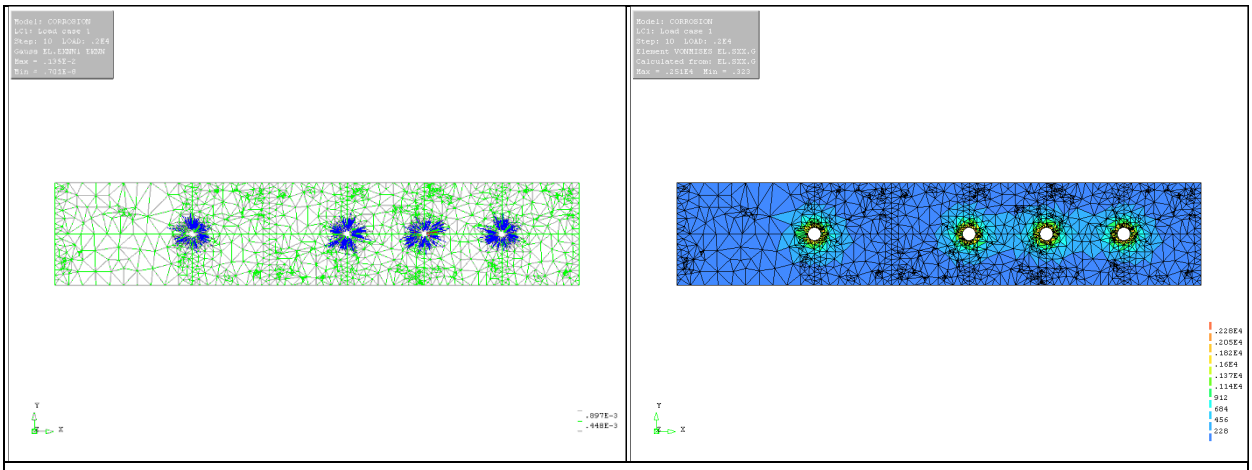

p_{int} = 2,000 psi

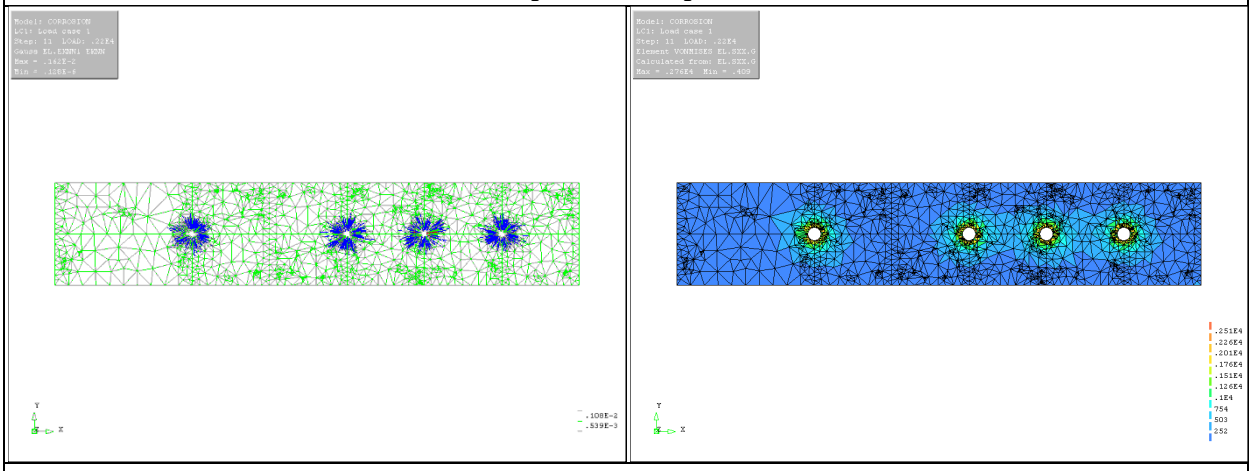

p_{int} = 2,200 psi

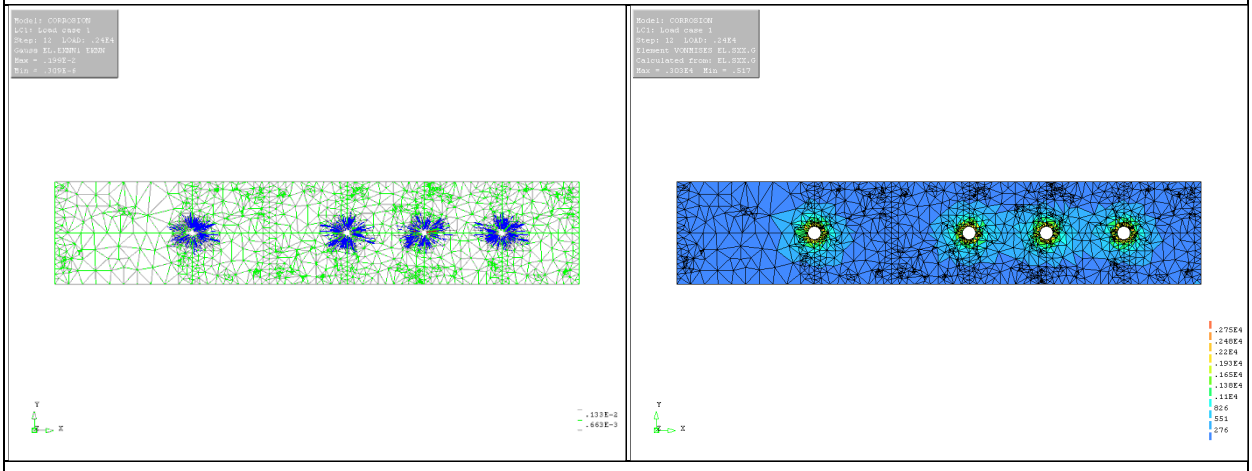

p_{int} = 2,400 psi

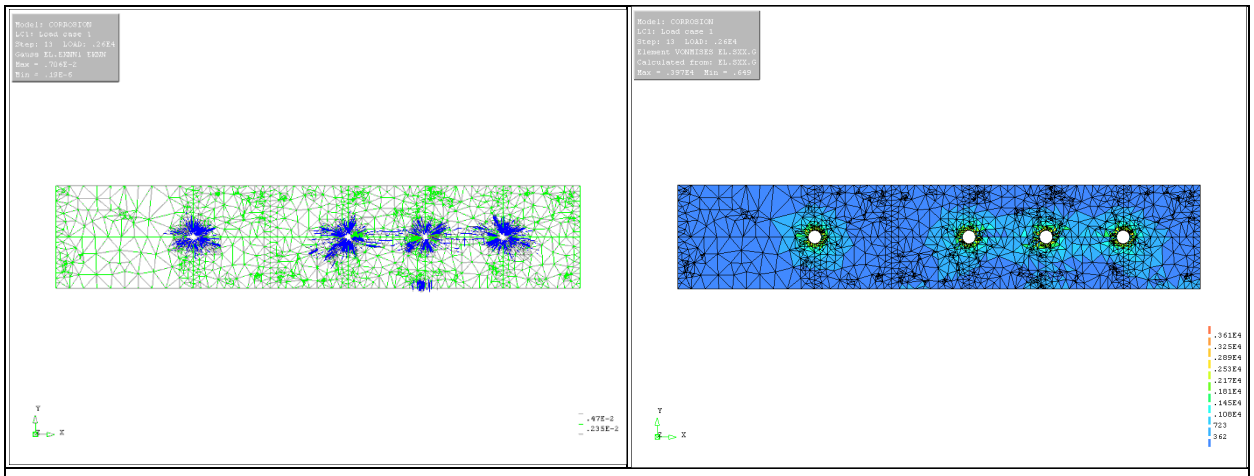

p_{int} = 2,600 psi

Figure D-11 Crack Patterns & Von Mises Stress Variations of Case II FE Model (Cover = 4.0 in.)

D.2.2 2D FE simulation of butting effects

This section presents detailed results of FE analysis performed to model the effects of panel butting. FE simulation was conducted on the Case II FE model in the corrosion analysis with varying configurations of boundary conditions and loading conditions as shown in Figure D-12. Based on results of the Case II FE analysis, 50% of the ultimate internal pressure, 1,300 psi, was applied at each reinforcement location to simulate a small amount of corrosion. Then, impact load induced by butting of the adjacent panel was modeled by incrementally increasing pressure, 200 psi, of varying area on the panel joint side of the panel to account for varying misalignment of the panels. To simulate this sequential loading effect, phased analysis was conducted. Crack patterns and Von Mises stress variations are illustrated from Figure D-13 to Figure D-17 with respect to the parameters considered.

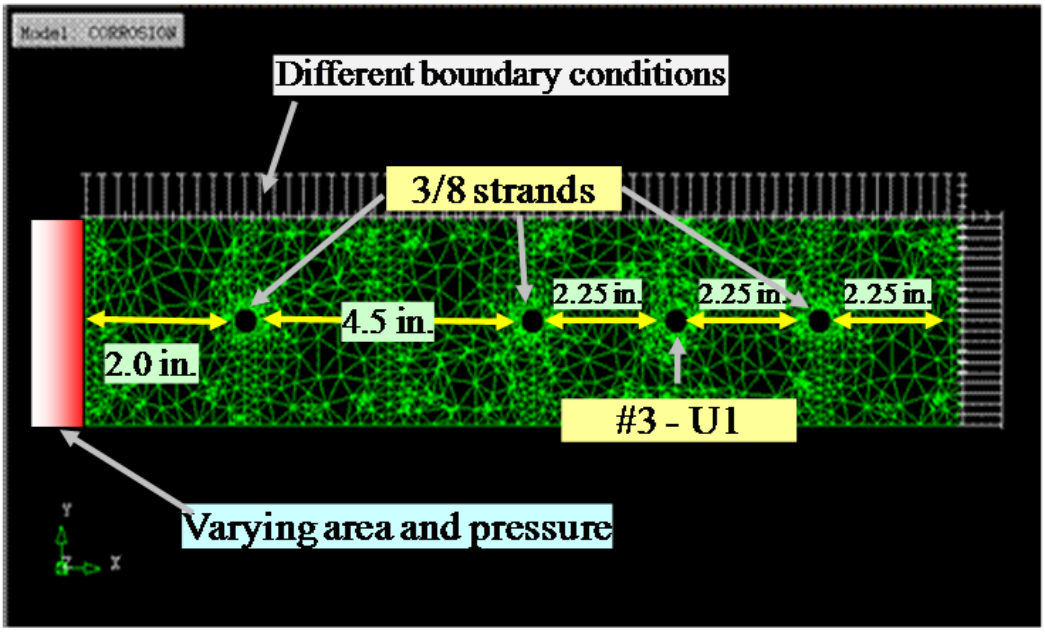

Figure D-12 2D FE Butting Model

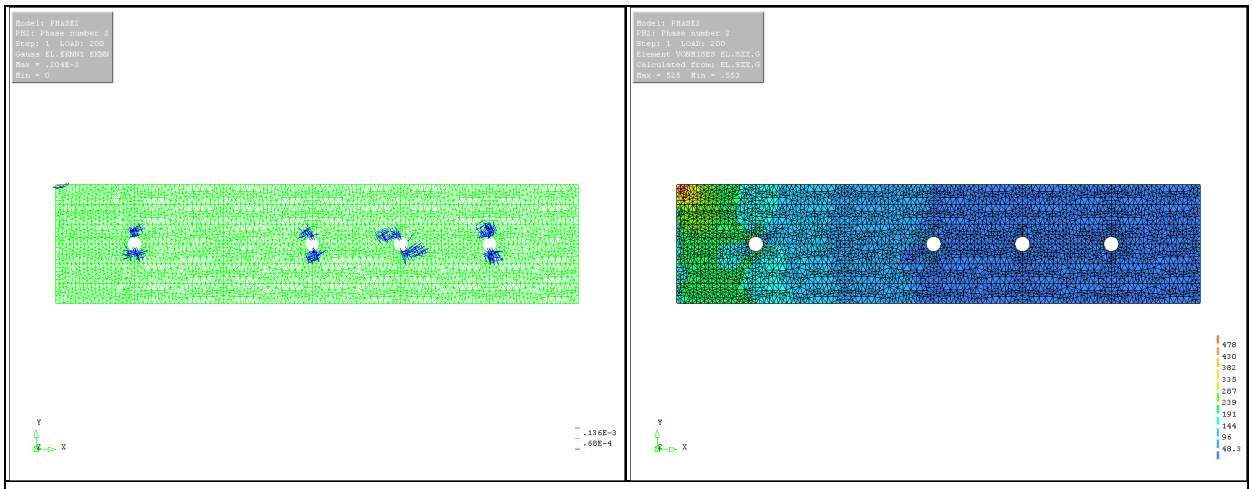

p_{impact} = 200 psi

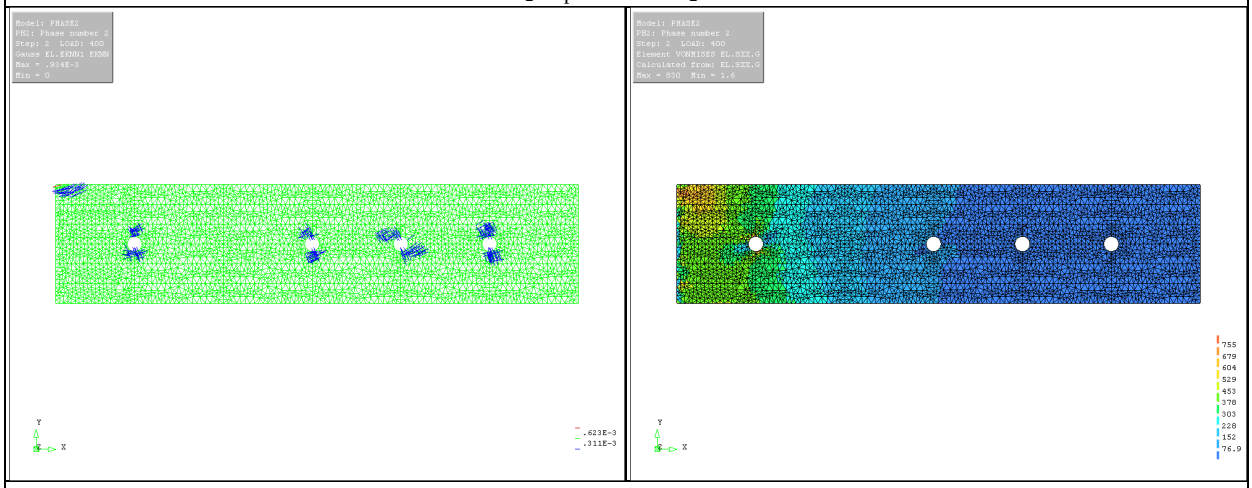

p_{impact} = 400 psi

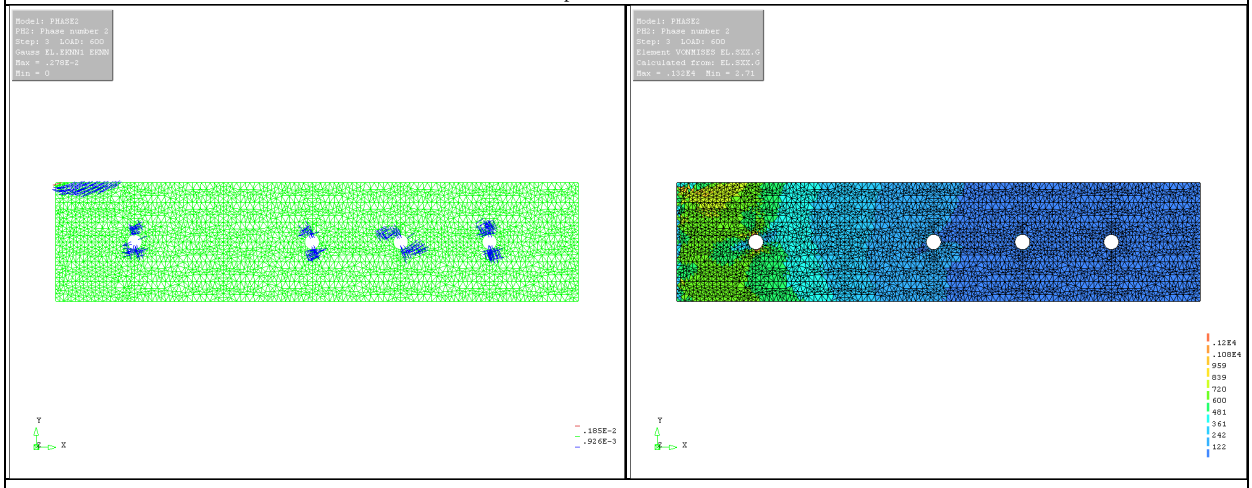

p_{impact} = 600 psi

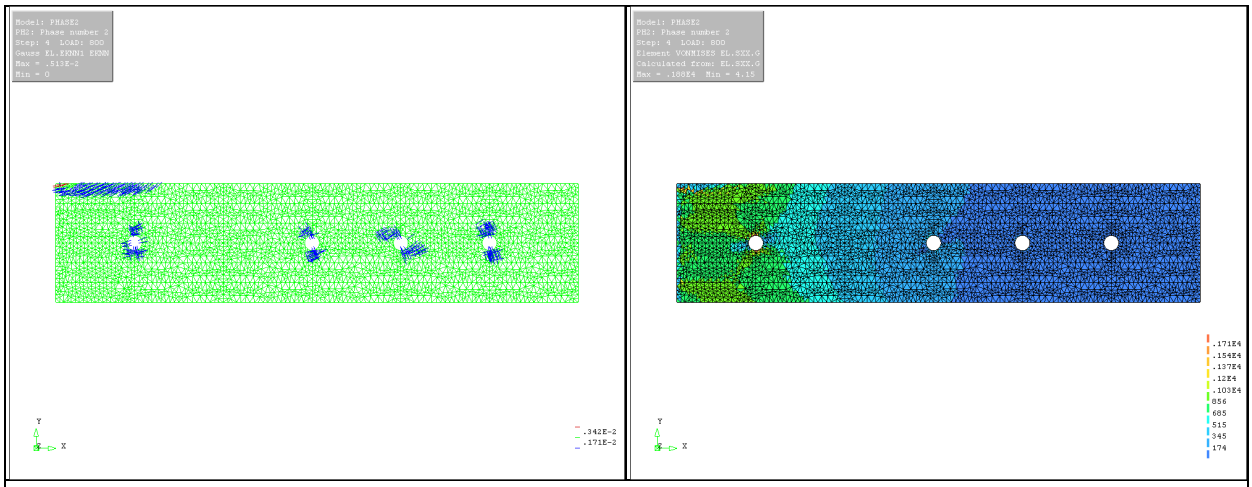

p_{impact} = 800 psi

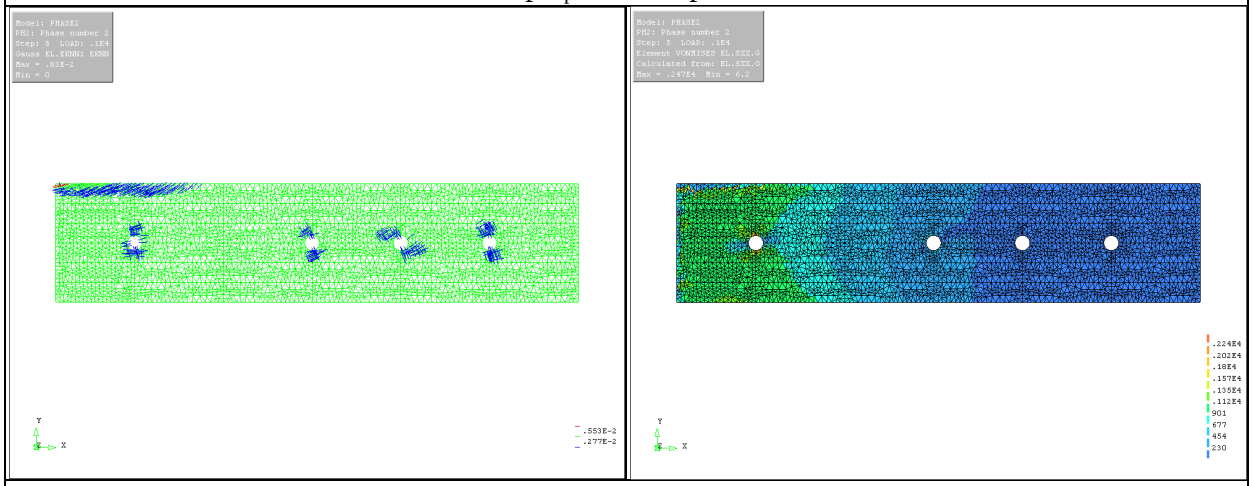

p_{impact} = 1,000 psi

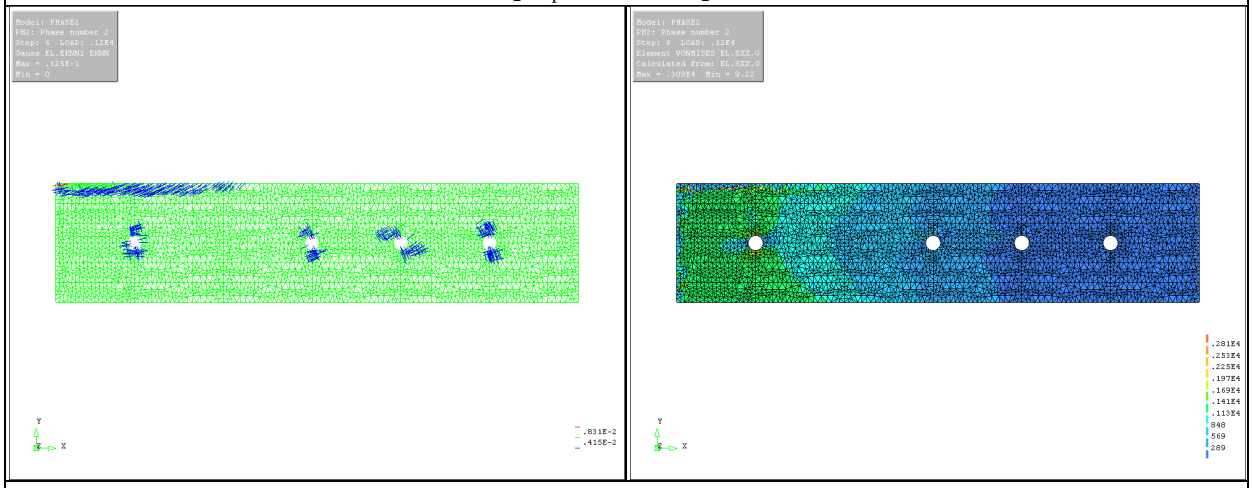

p_{impact} = 1,200 psi

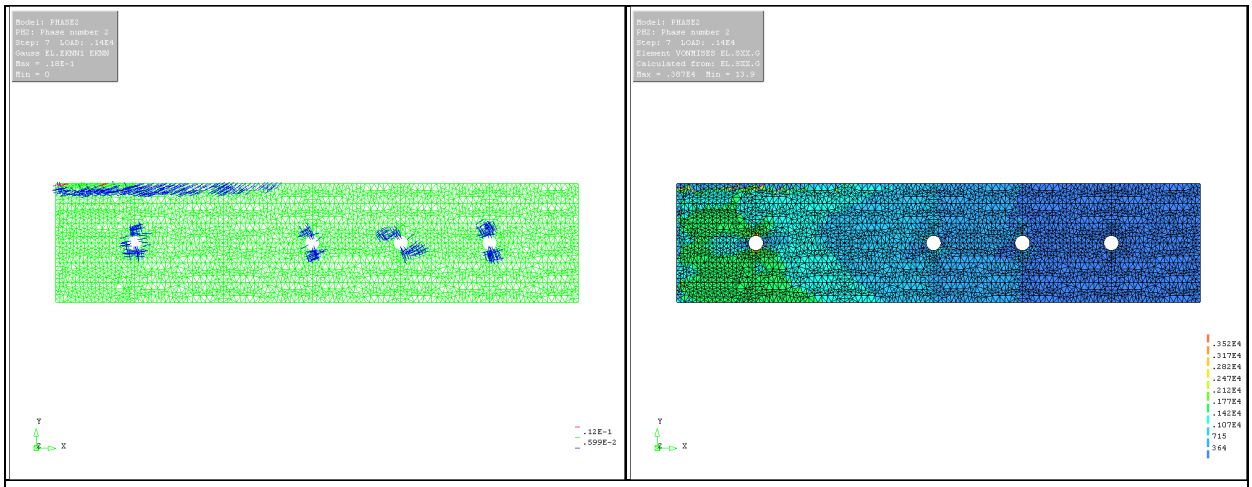

p_{impact} = 1,400 psi

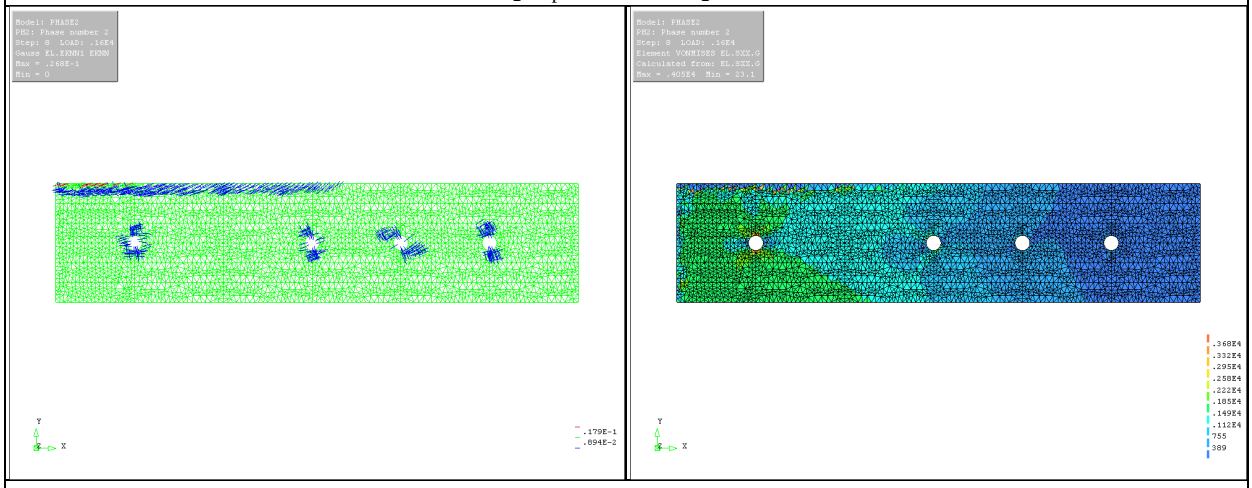

p_{impact} = 1,600 psi

Figure D-13 Crack Patterns & Von Mises Stress Variations of FE Model
(Full Compression + Fixed Boundary Condition)

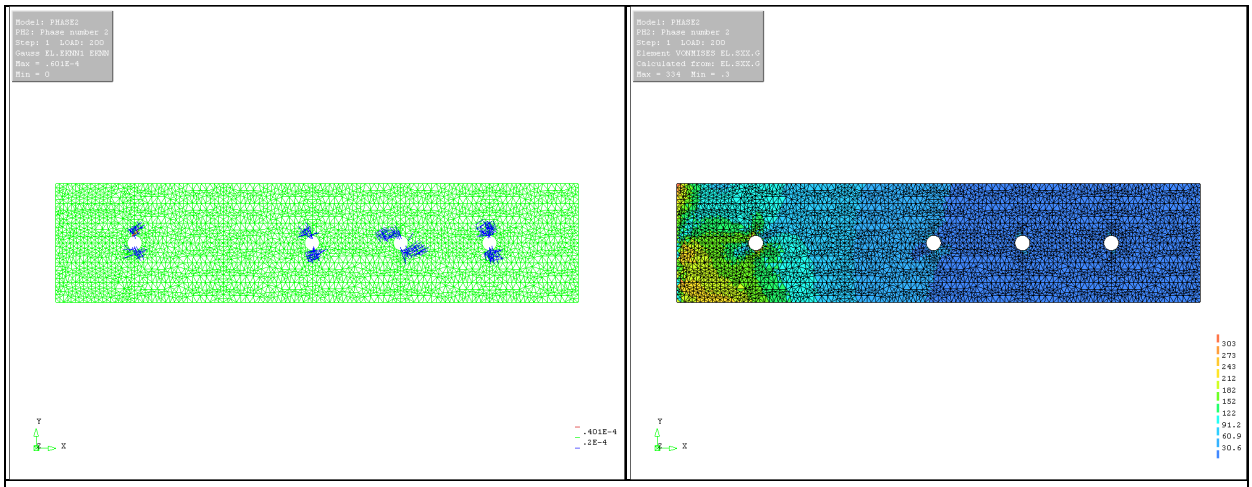

p_{impact} = 200 psi

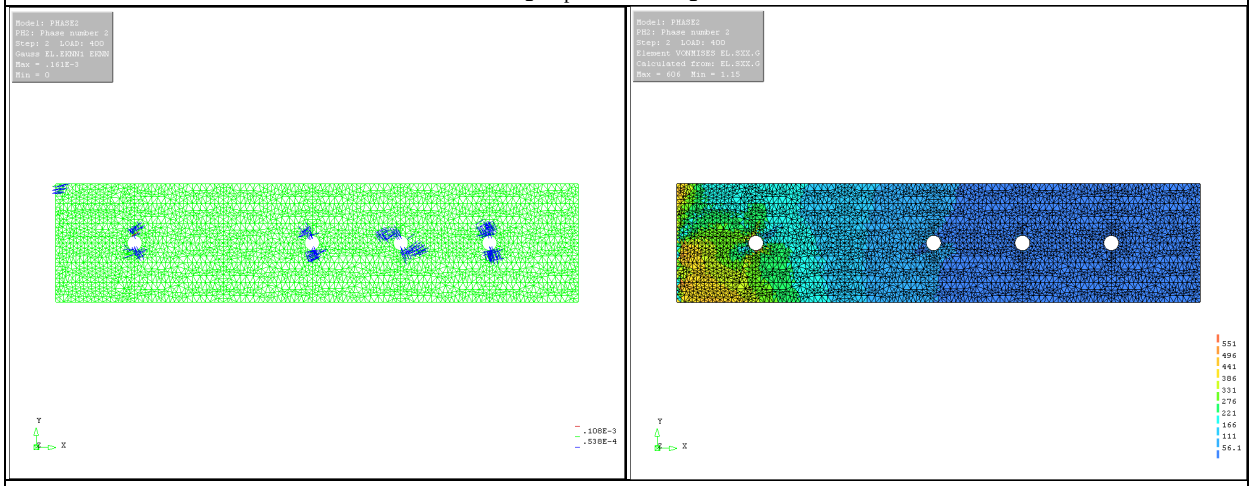

p_{impact} = 400 psi

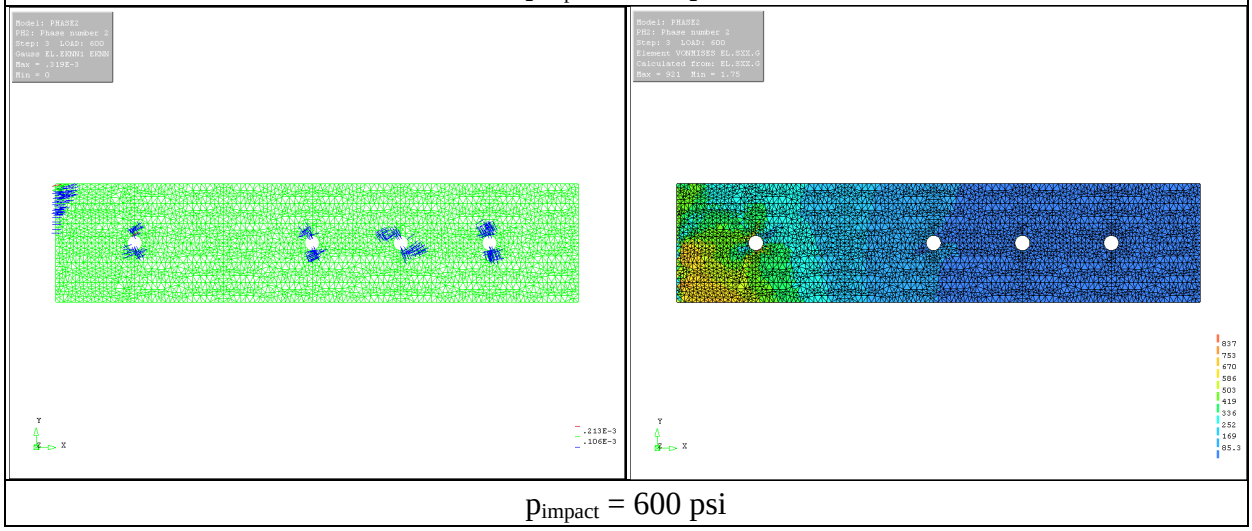

p_{impact} = 600 psi

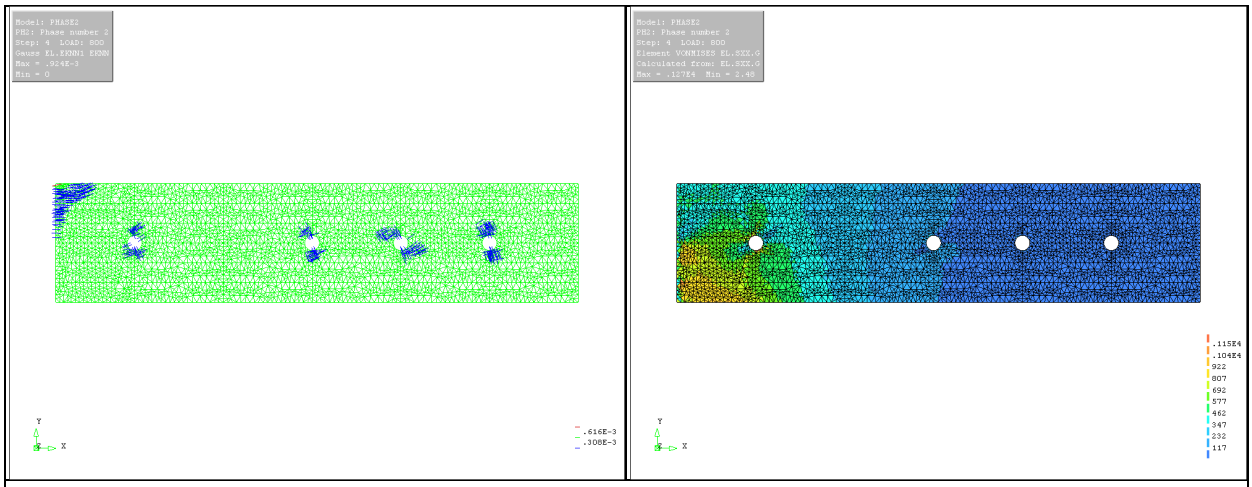

p_{impact} = 800 psi

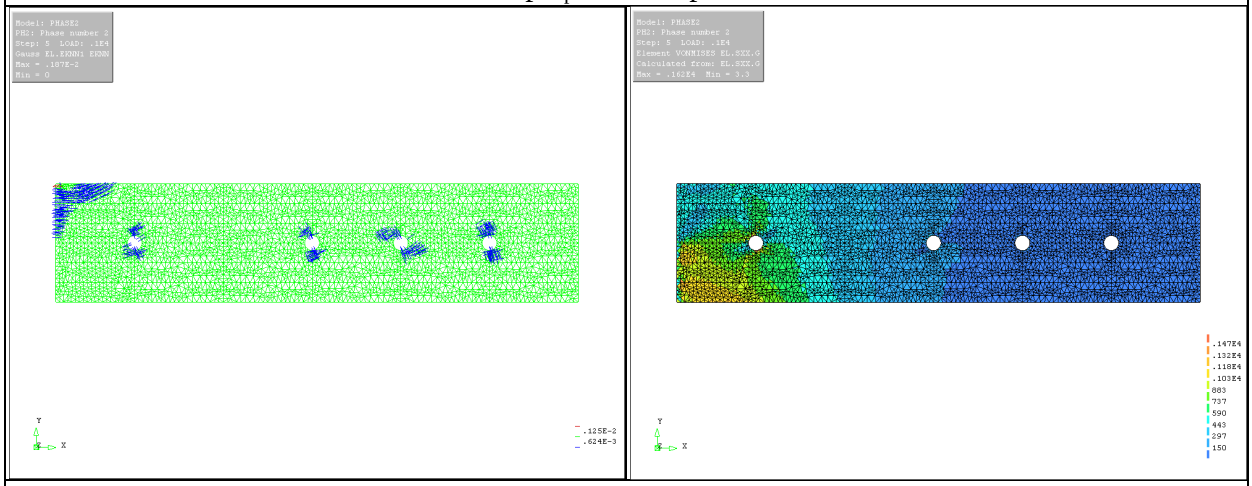

p_{impact} = 1,000 psi

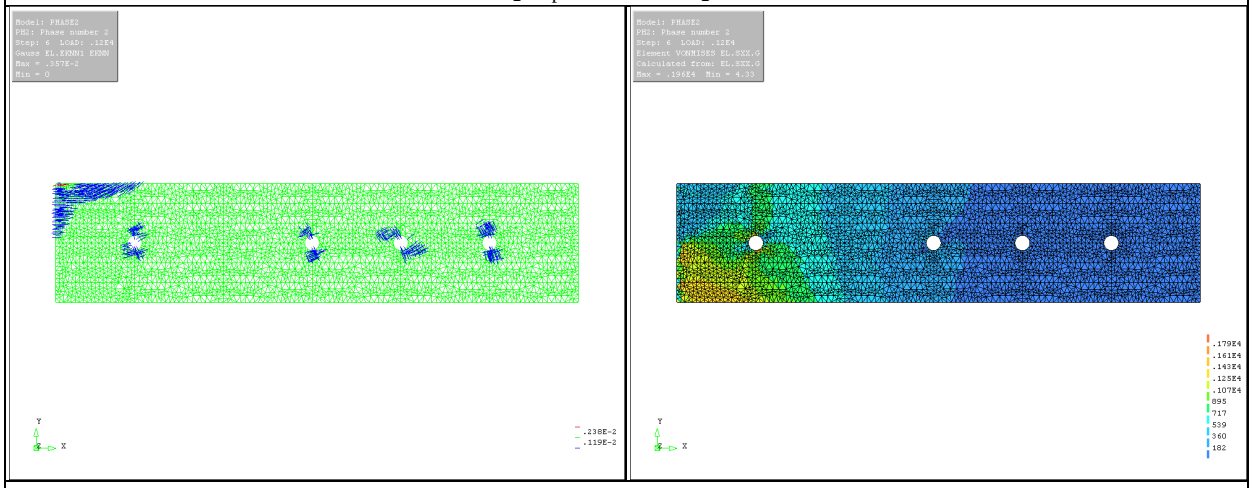

p_{impact} = 1,200 psi

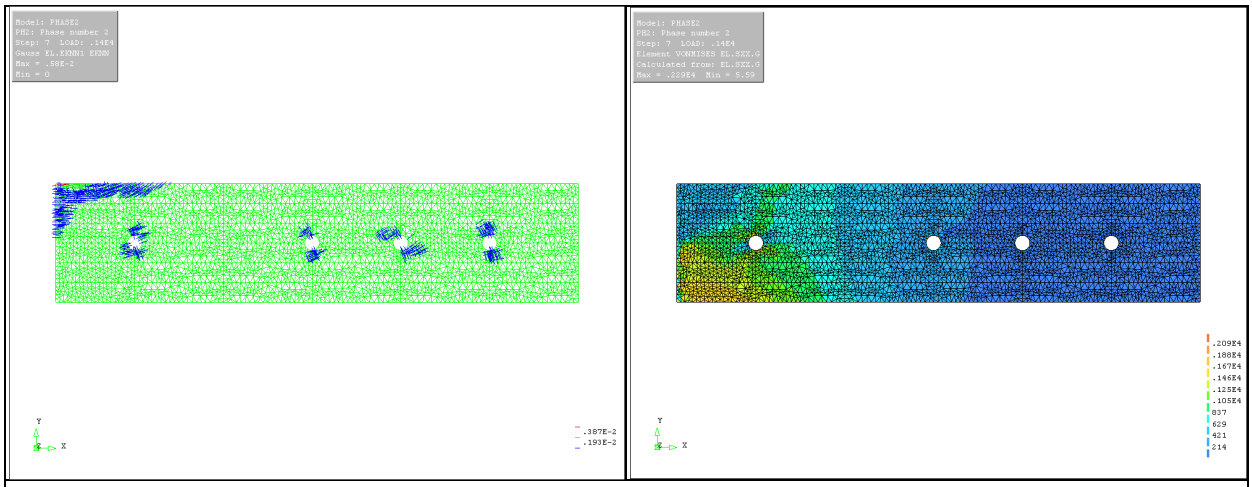

p_{impact} = 1,400 psi

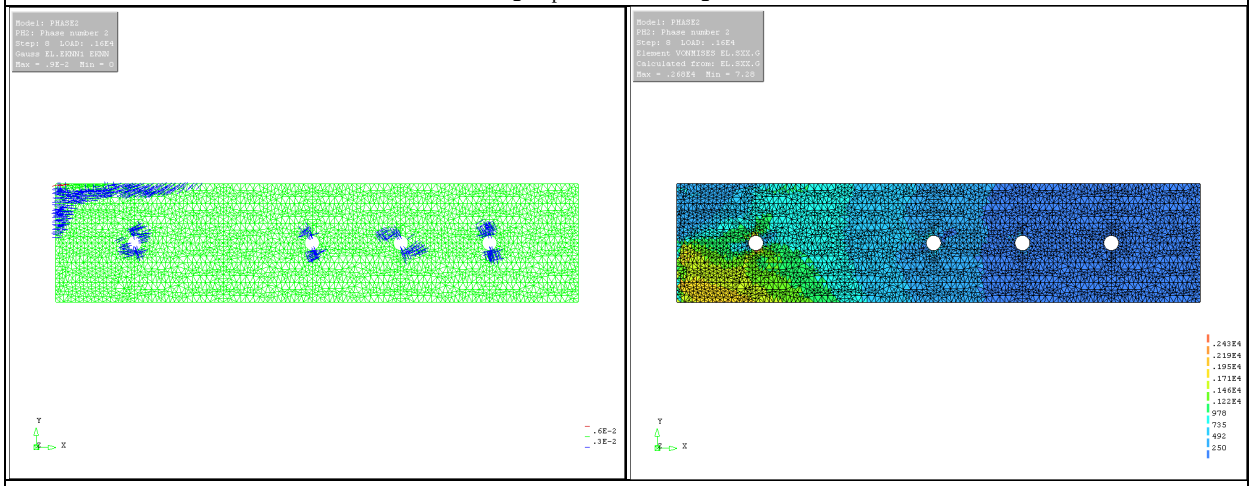

p_{impact} = 1,600 psi

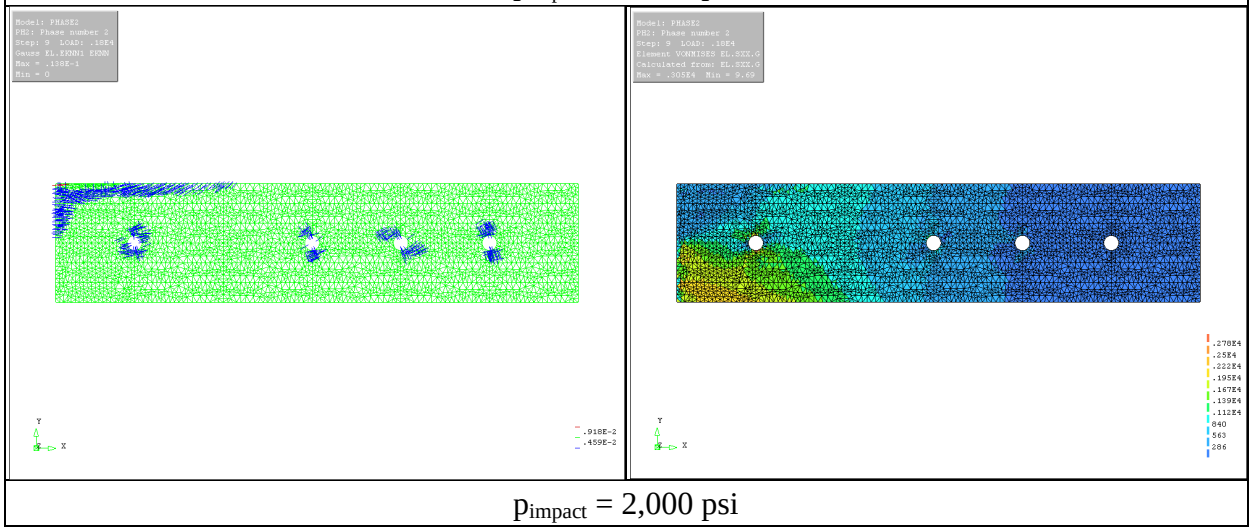

p_{impact} = 2,000 psi

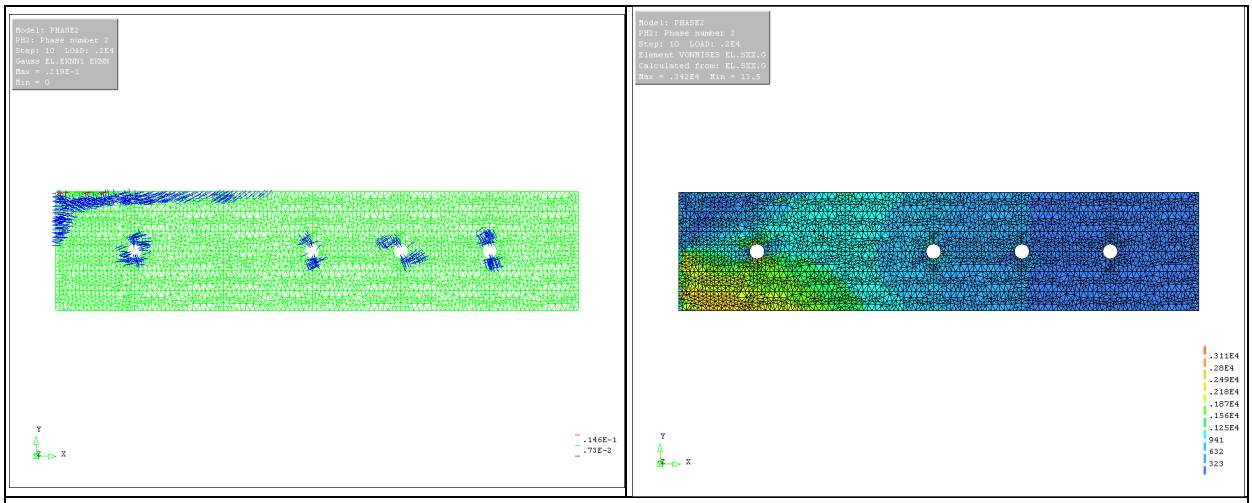

p_{impact} = 2,200 psi

Figure D-14 Crack Patterns & Von Mises Stress Variations of FE Model
(Half Compression + Fixed Boundary Condition)

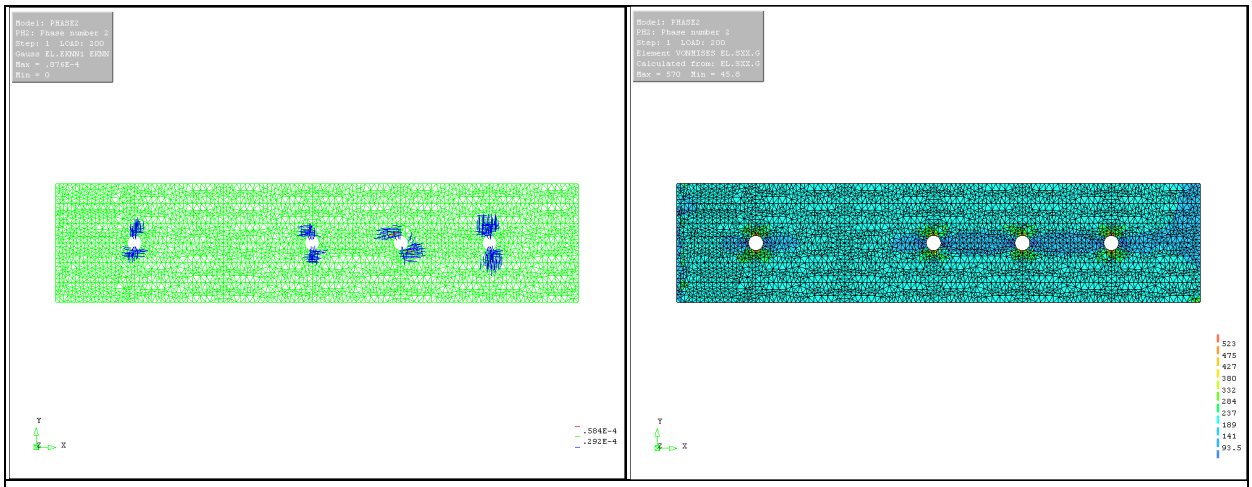

p_{impact} = 200 psi

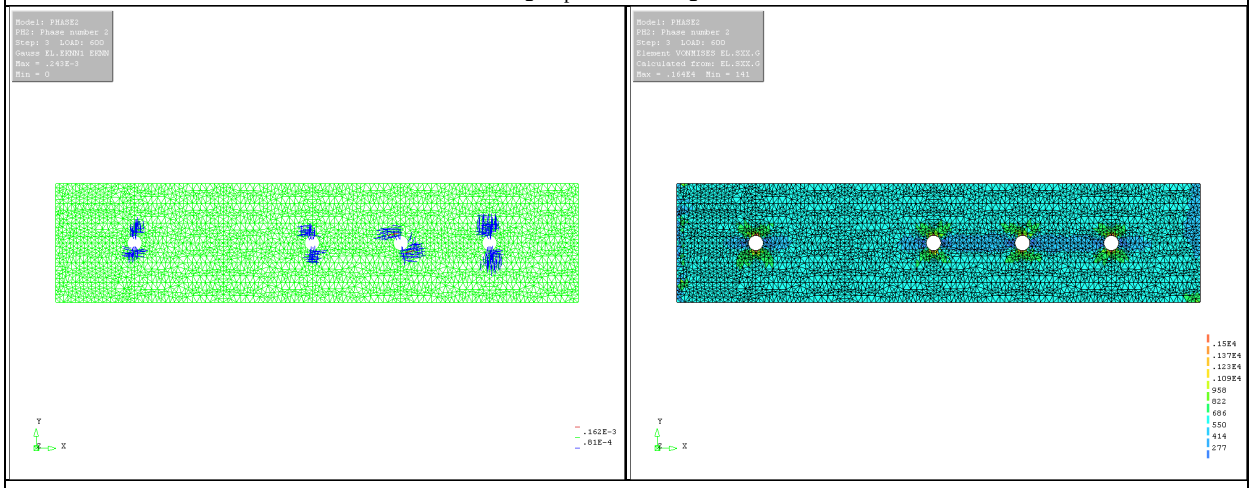

p_{impact} = 600 psi

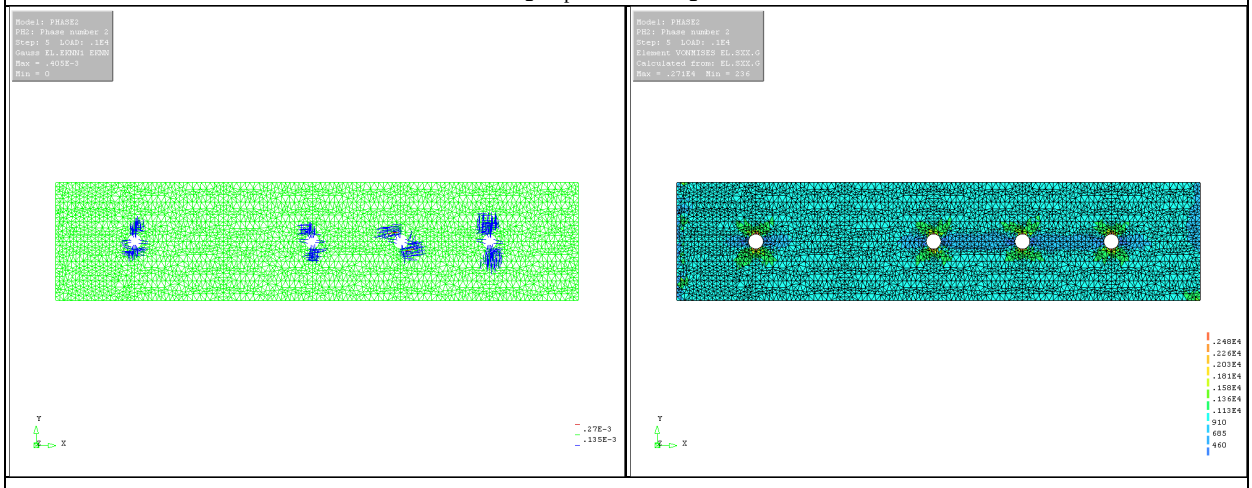

p_{impact} = 1,000 psi

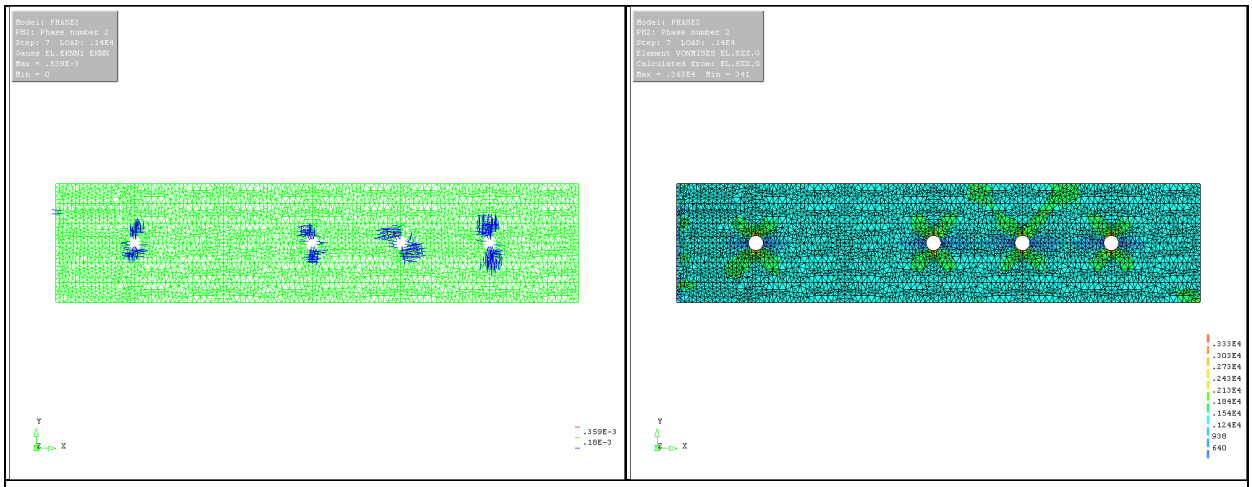

p_{impact} = 1,400 psi

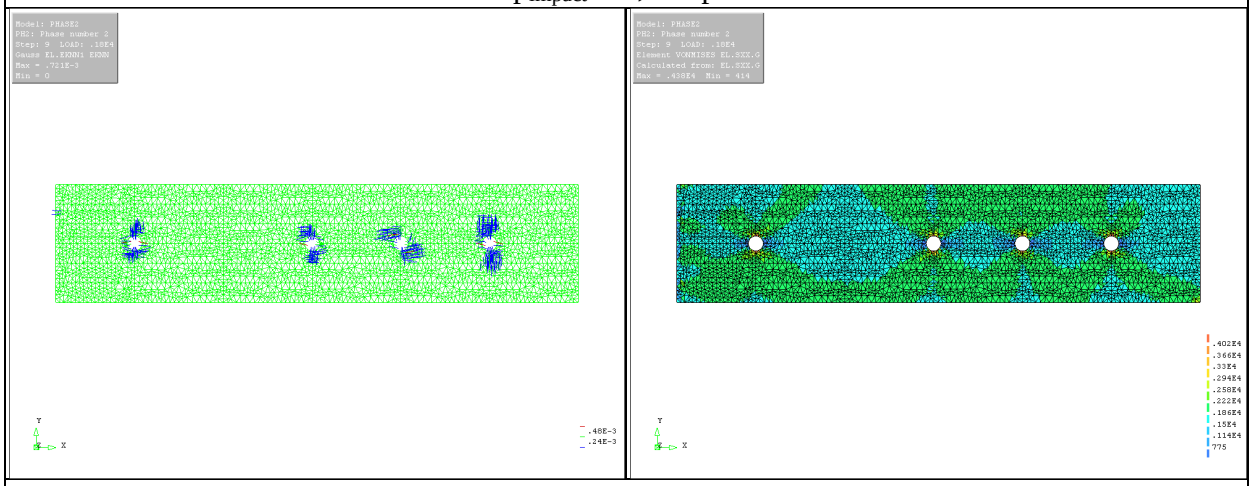

p_{impact} = 1,800 psi

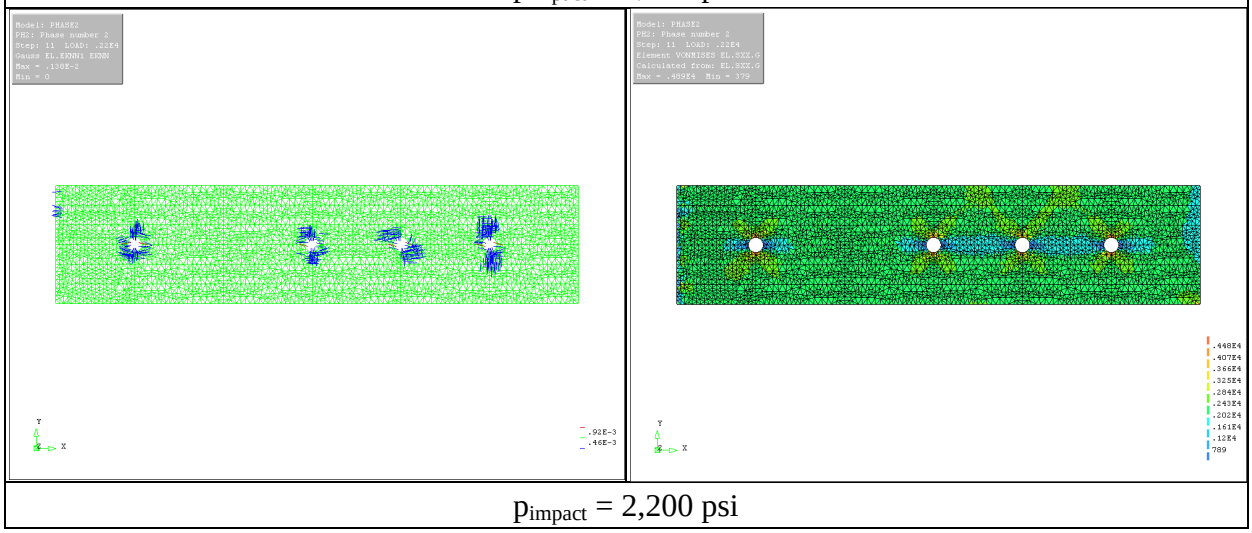

p_{impact} = 2,200 psi

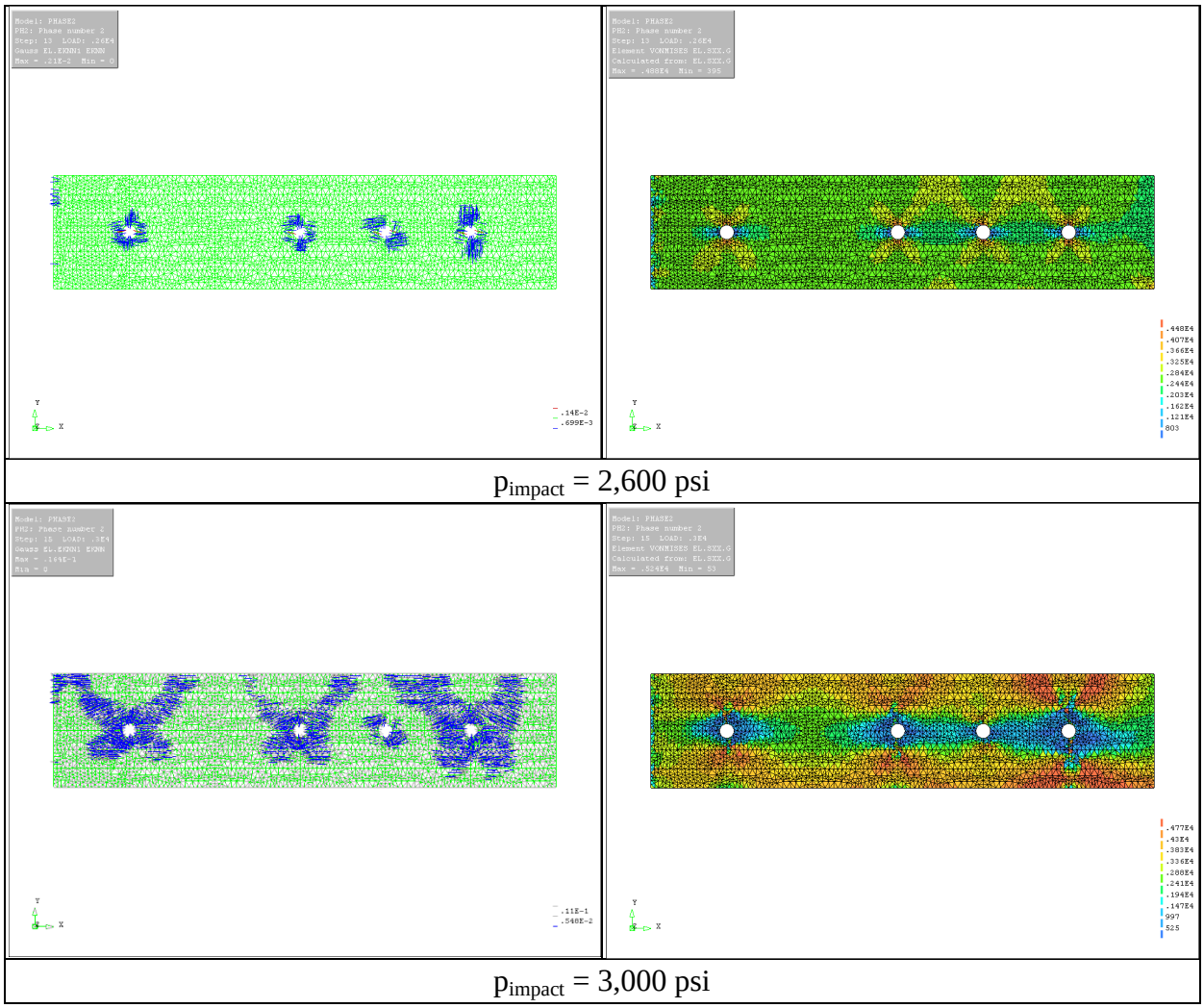

Figure D-15 Crack Patterns & Von Mises Stress Variations of FE Model
(Full Compression + Released Boundary Condition)

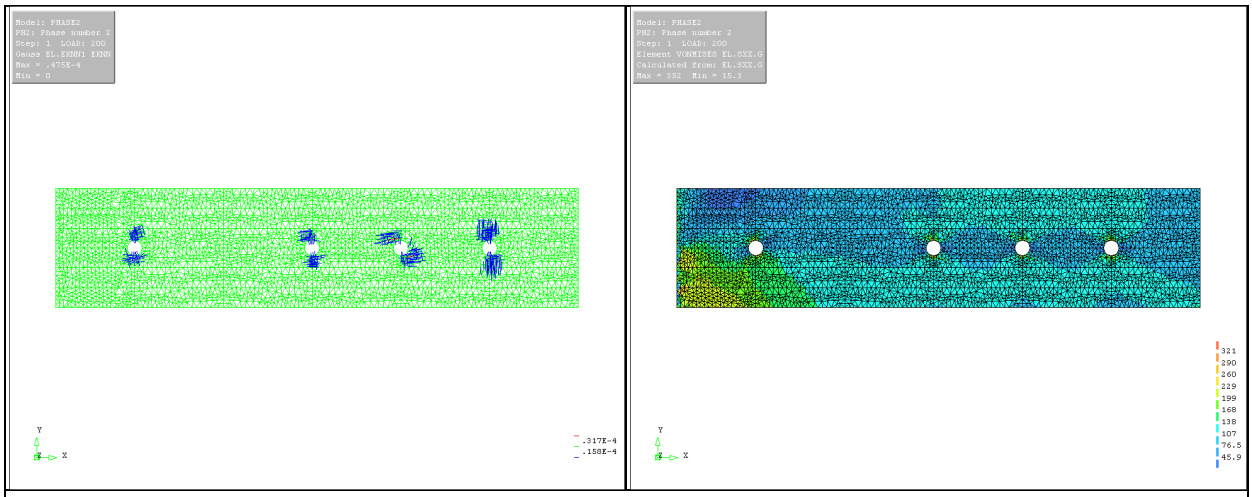

p_{impact} = 200 psi

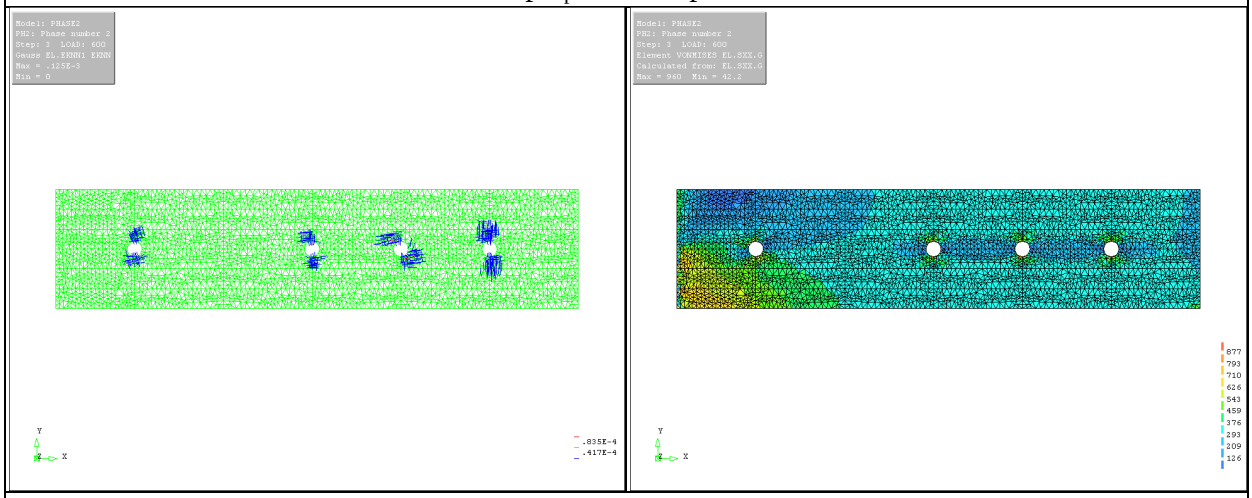

p_{impact} = 600 psi

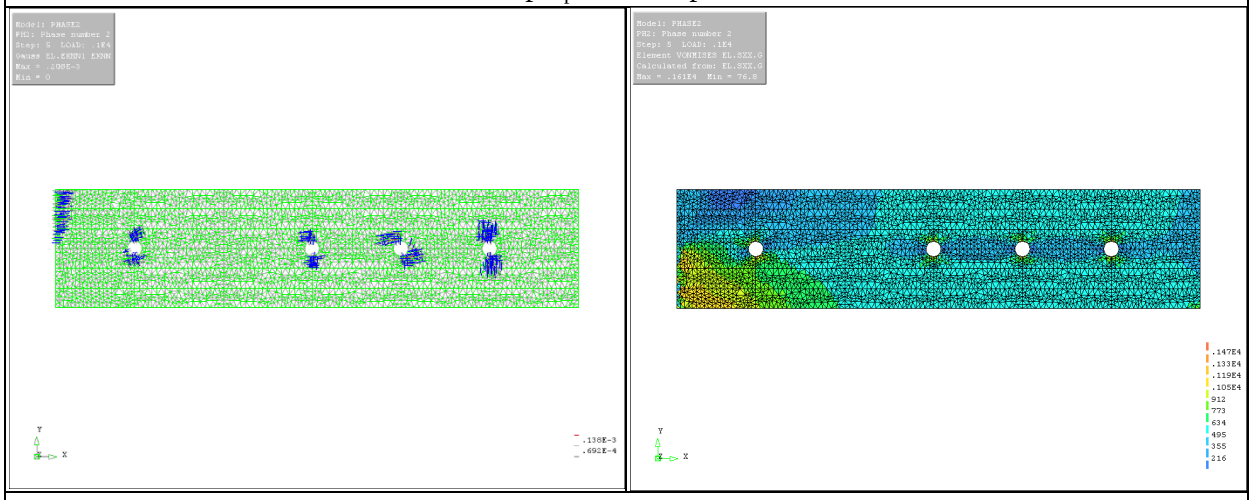

p_{impact} = 1,000 psi

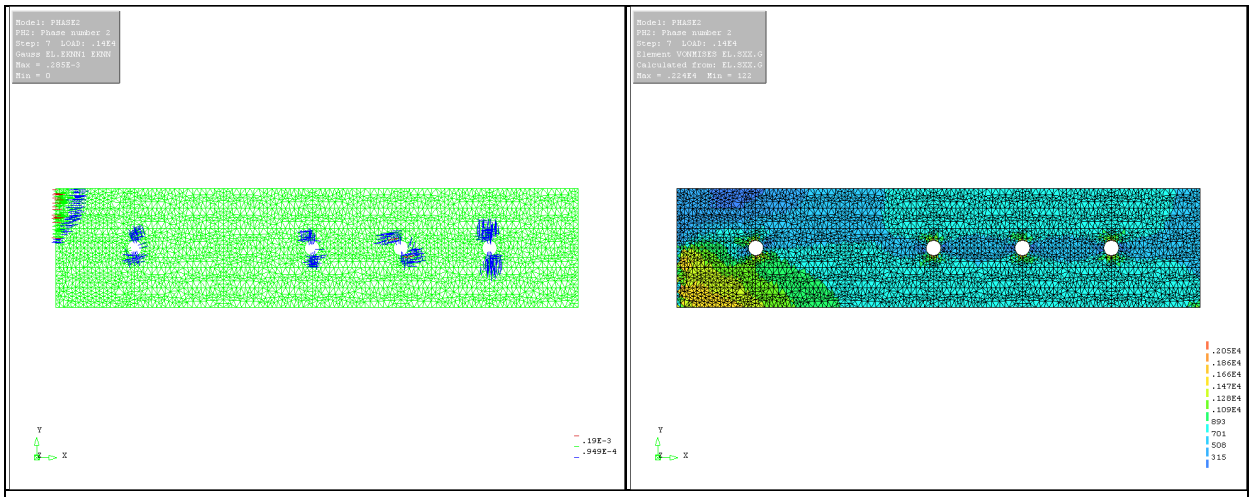

p_{impact} = 1,400 psi

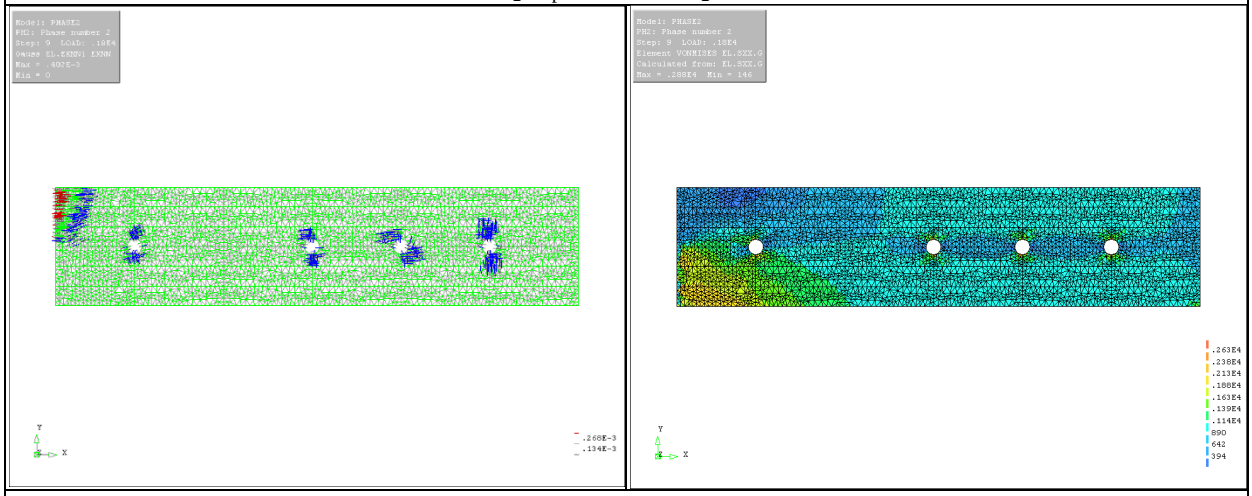

p_{impact} = 1,800 psi

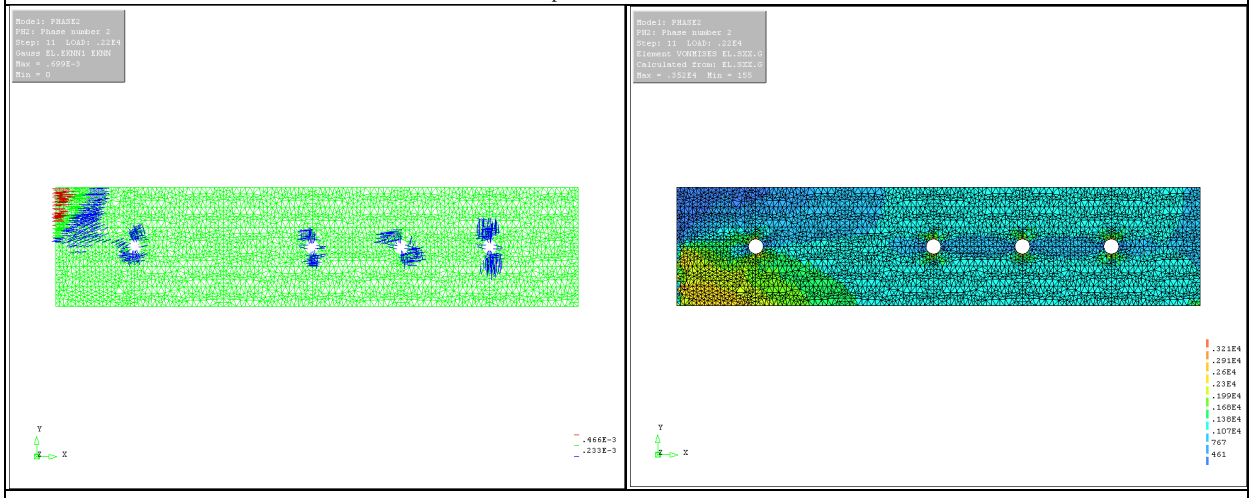

p_{impact} = 2,200 psi

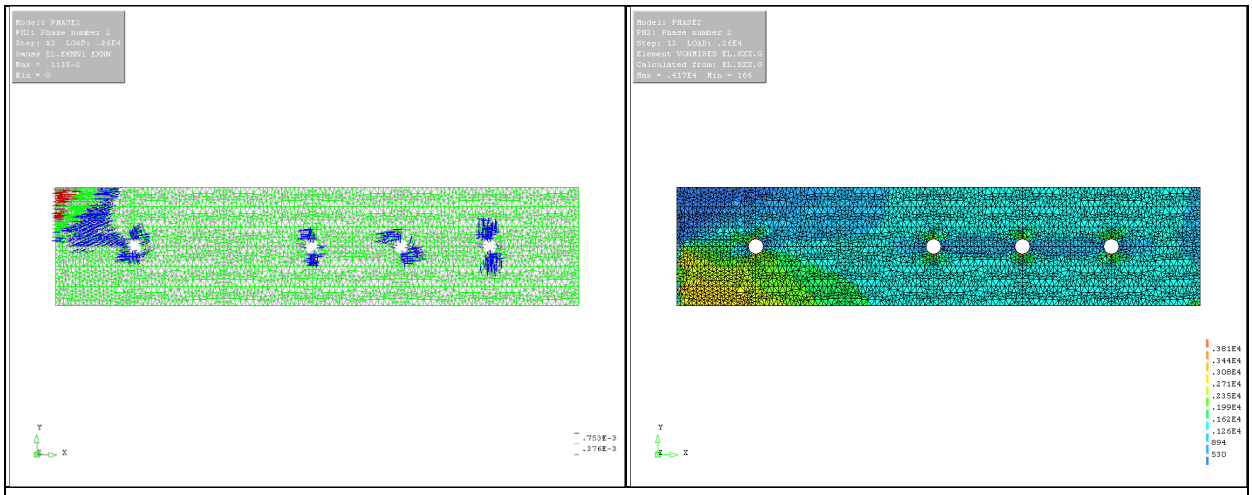

p_{impact} = 2,600 psi

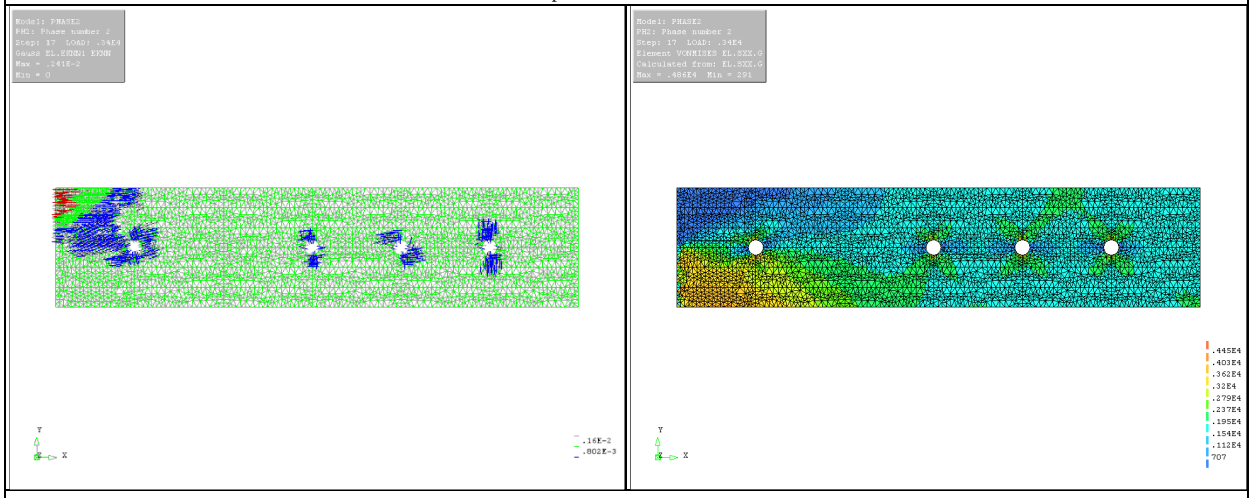

p_{impact} = 3,000 psi

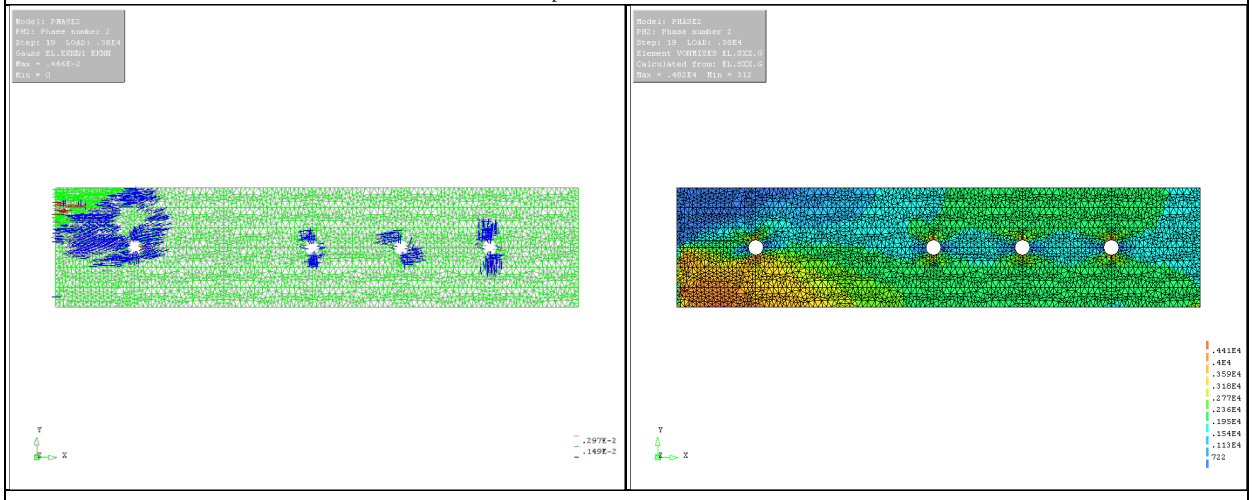

p_{impact} = 3,400 psi

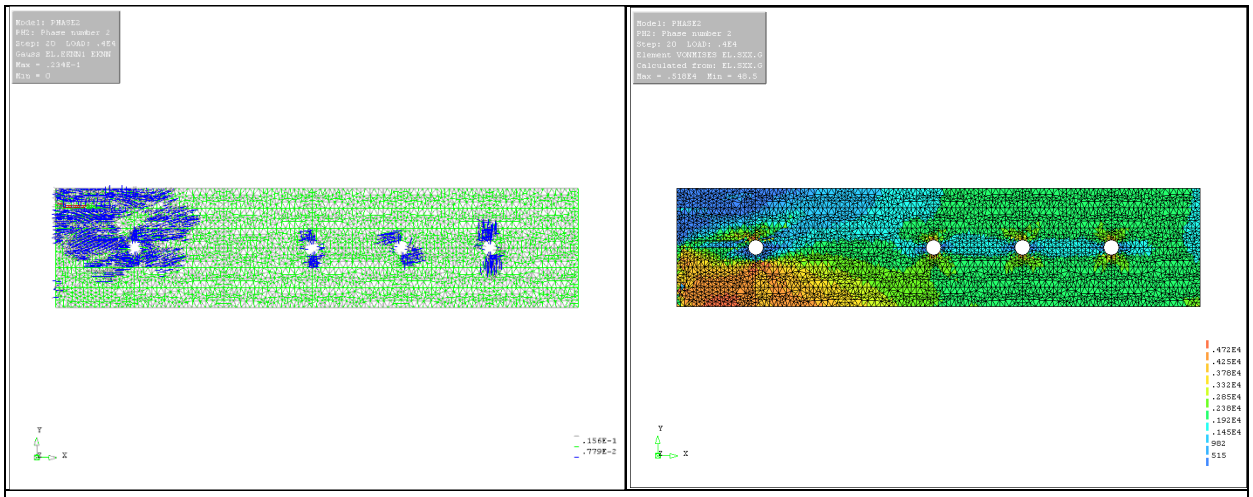

p_{impact} = 3,600 psi

Figure D-16 Crack Patterns & Von Mises Stress Variations of FE Model
(Half Compression + Released Boundary Condition)

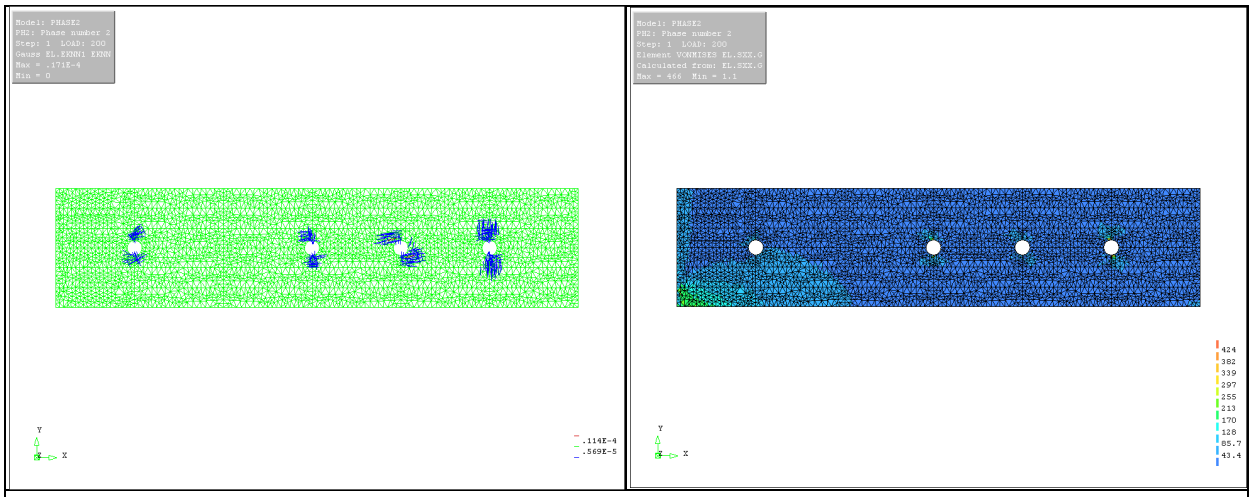

p_{impact} = 200 psi

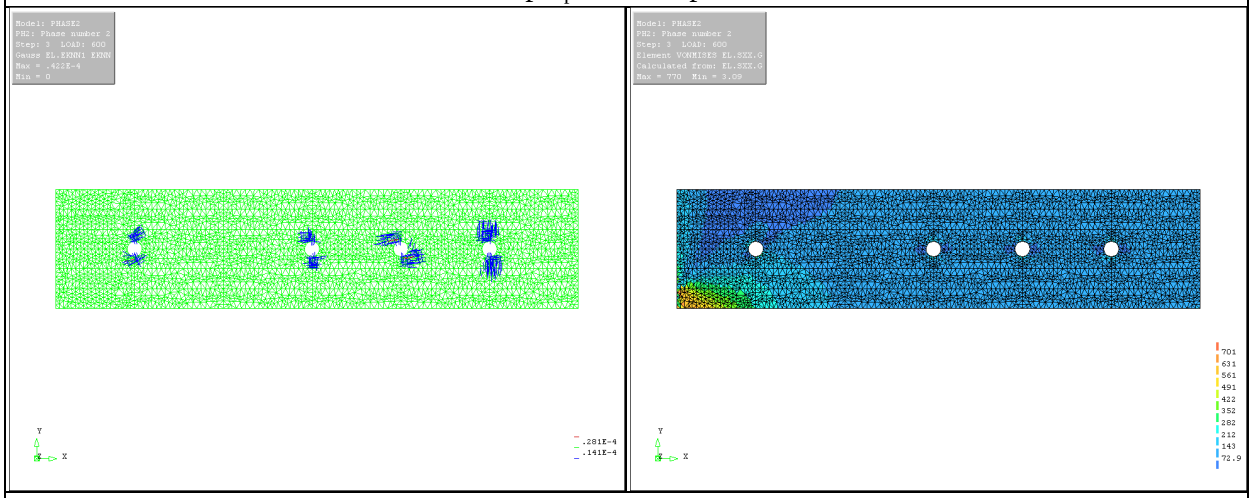

p_{impact} = 600 psi

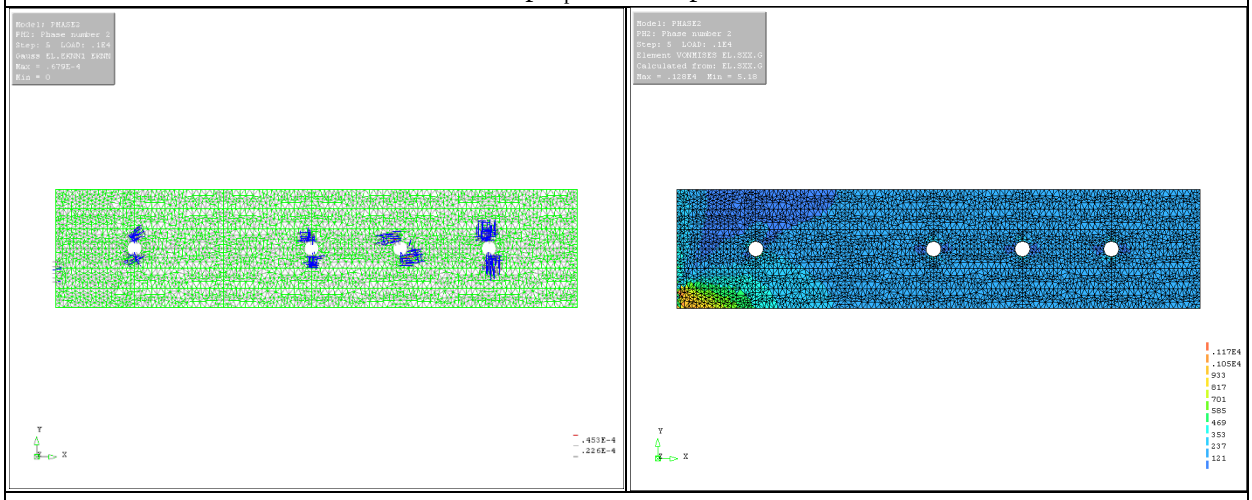

p_{impact} = 1,000 psi

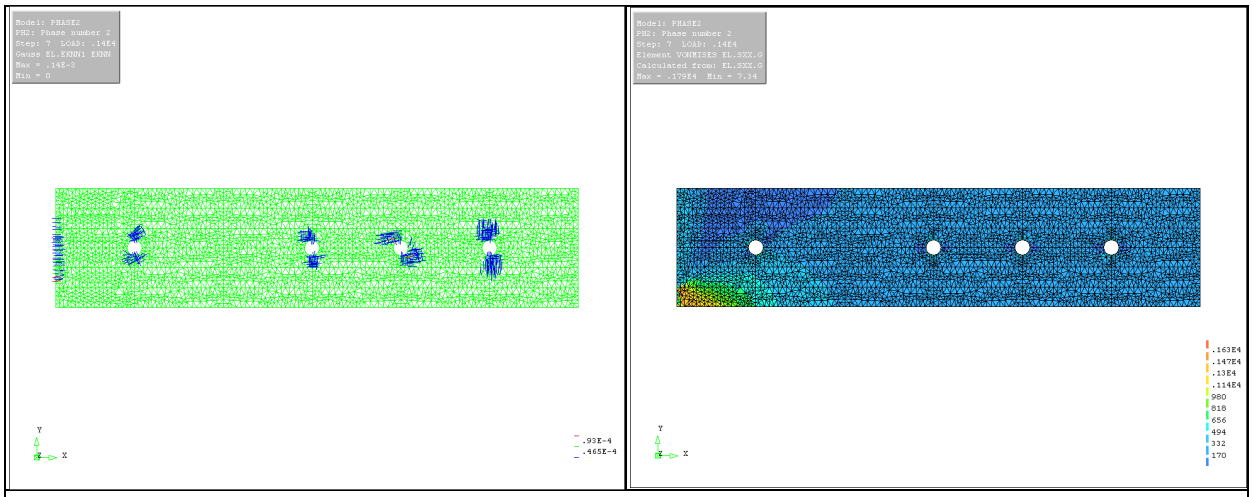

p_{impact} = 1,400 psi

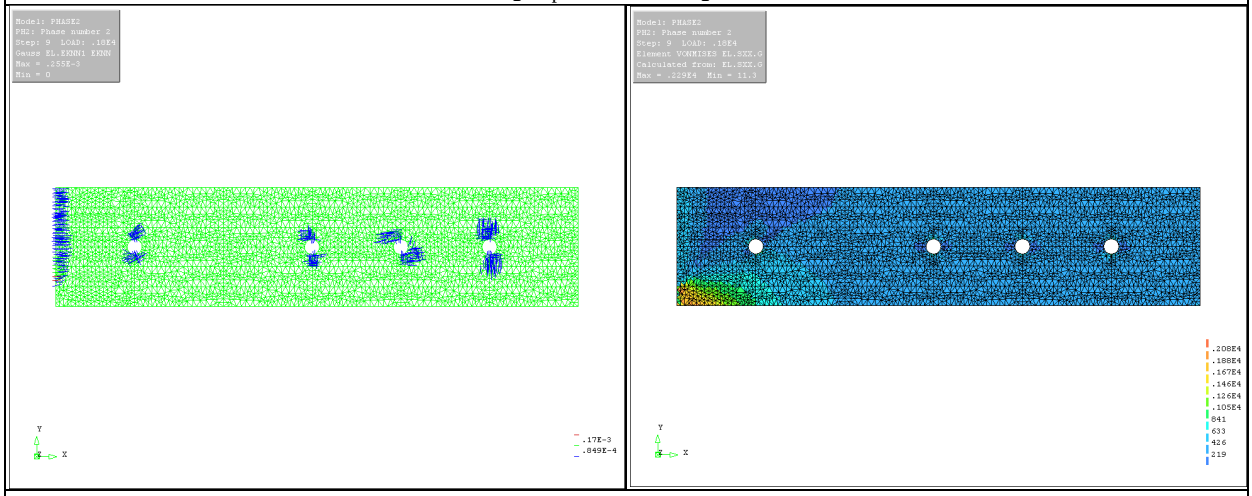

p_{impact} = 1,800 psi

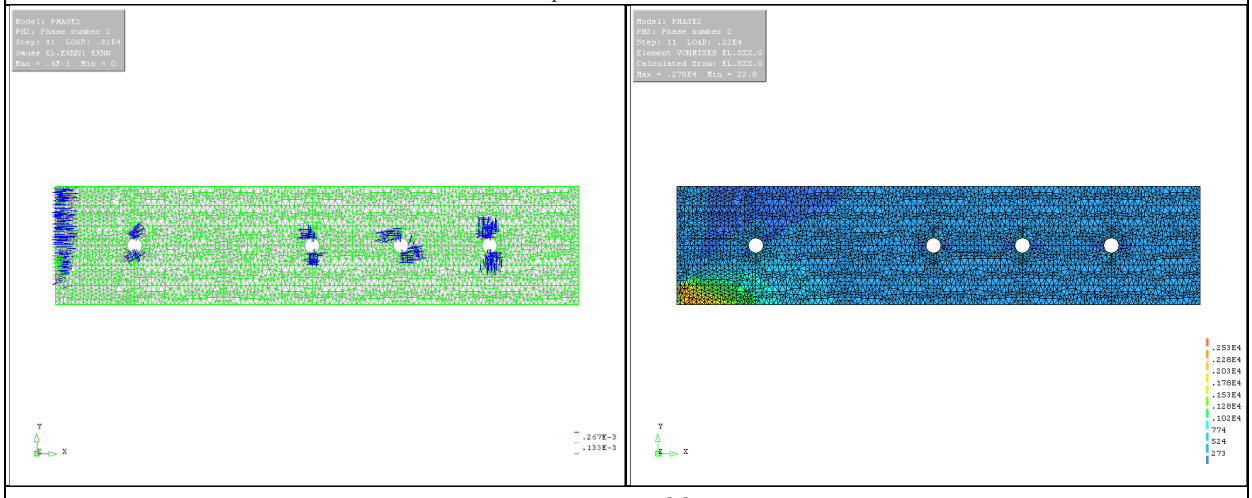

p_{impact} = 2,200 psi

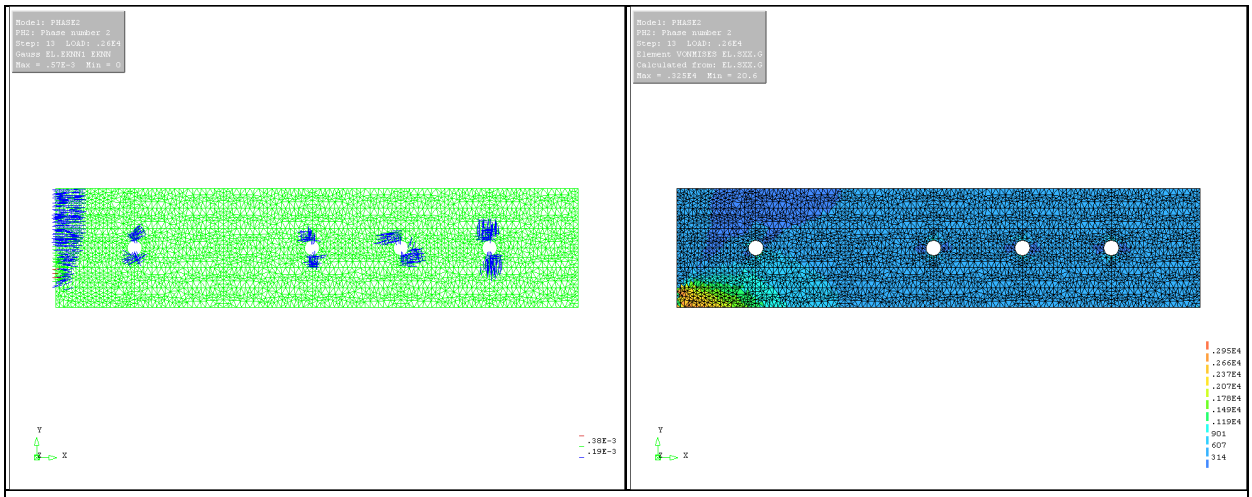

p_{impact} = 2,600 psi

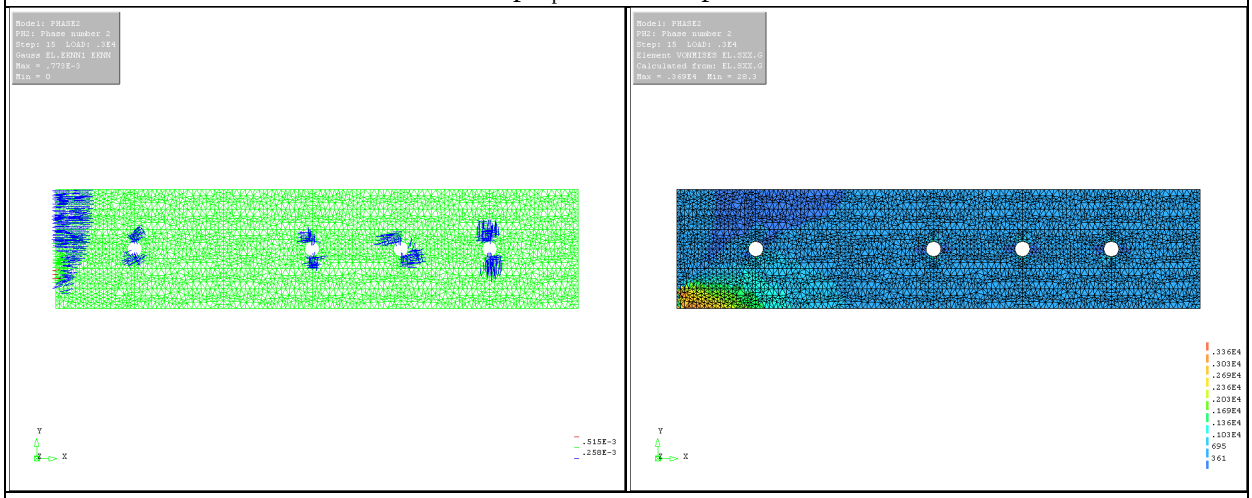

p_{impact} = 3,000 psi

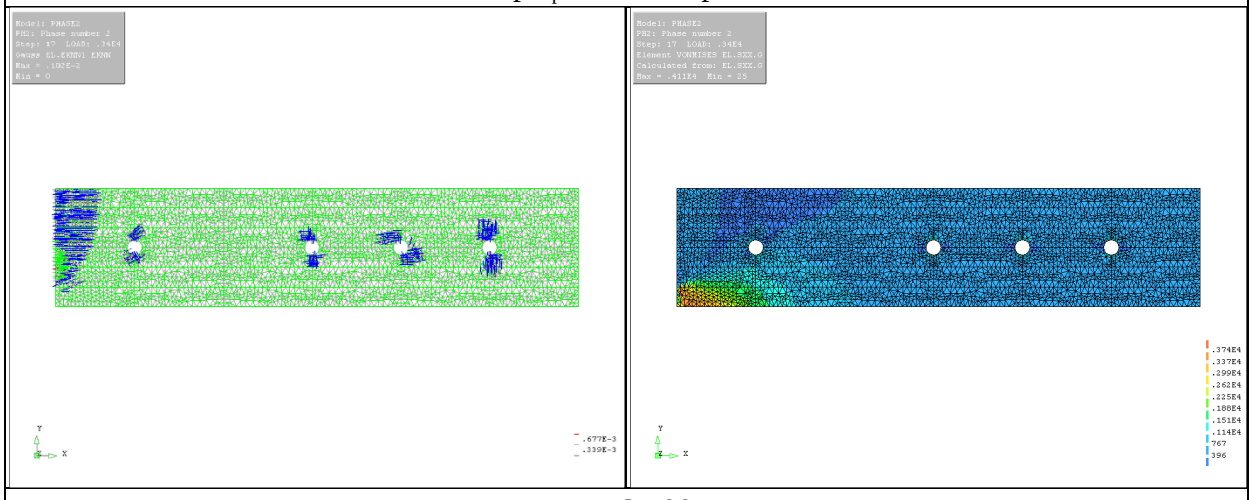

p_{impact} = 3,400 psi

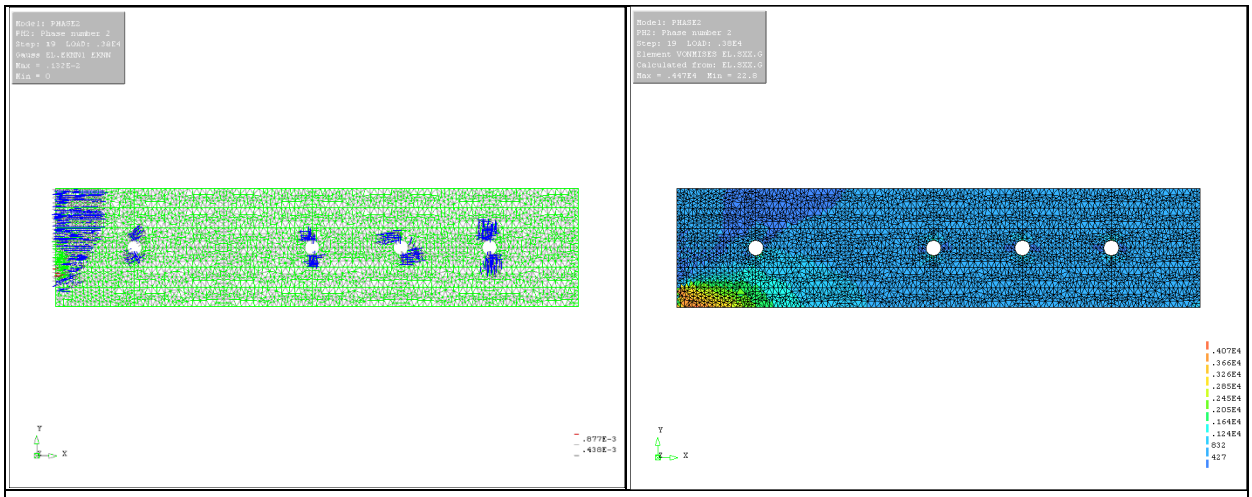

p_{impact} = 3,800 psi

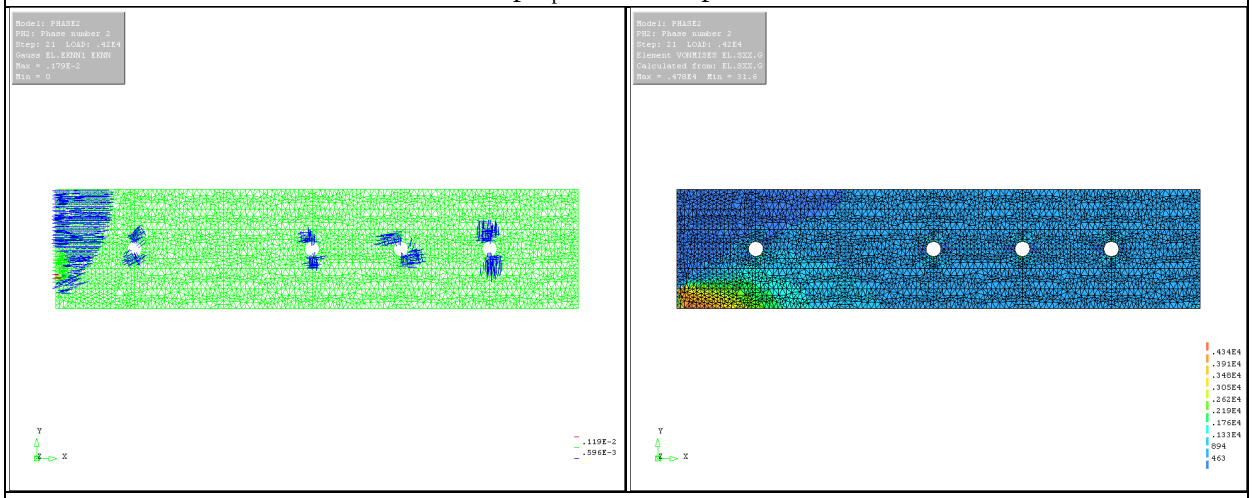

p_{impact} = 4,200 psi

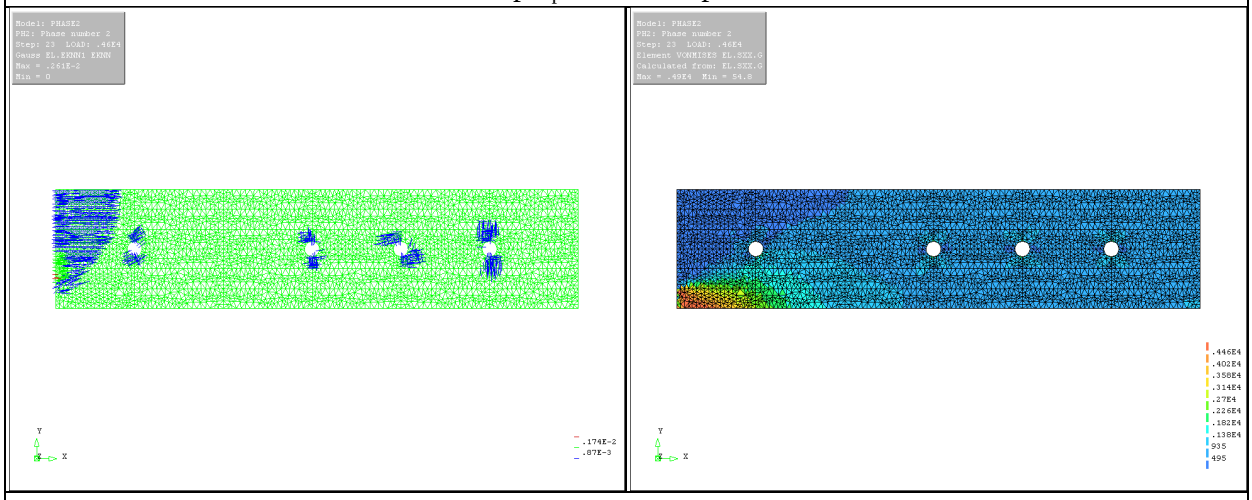

p_{impact} = 4,600 psi

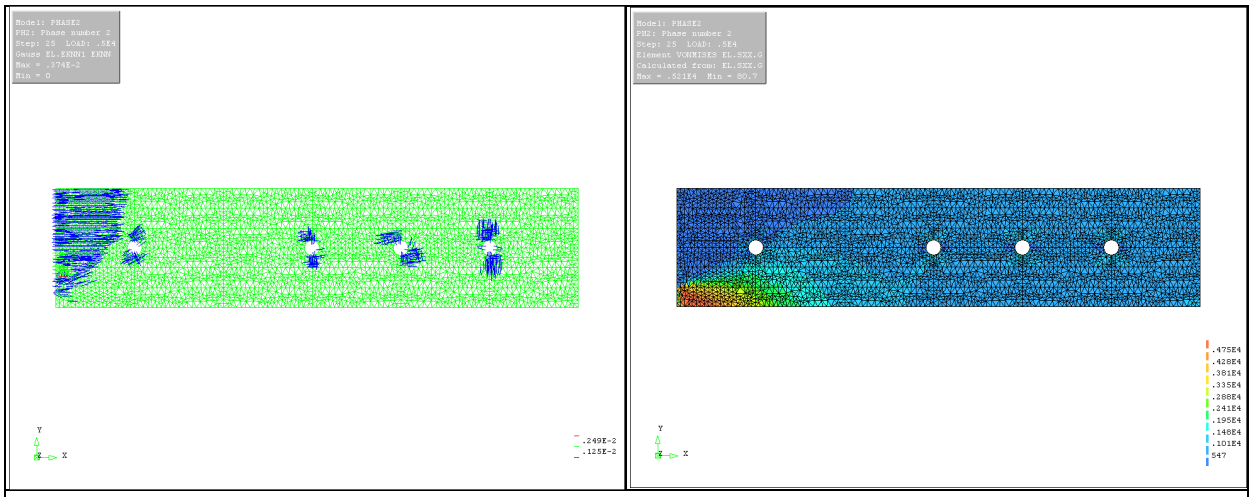

p_{impact} = 5,000 psi

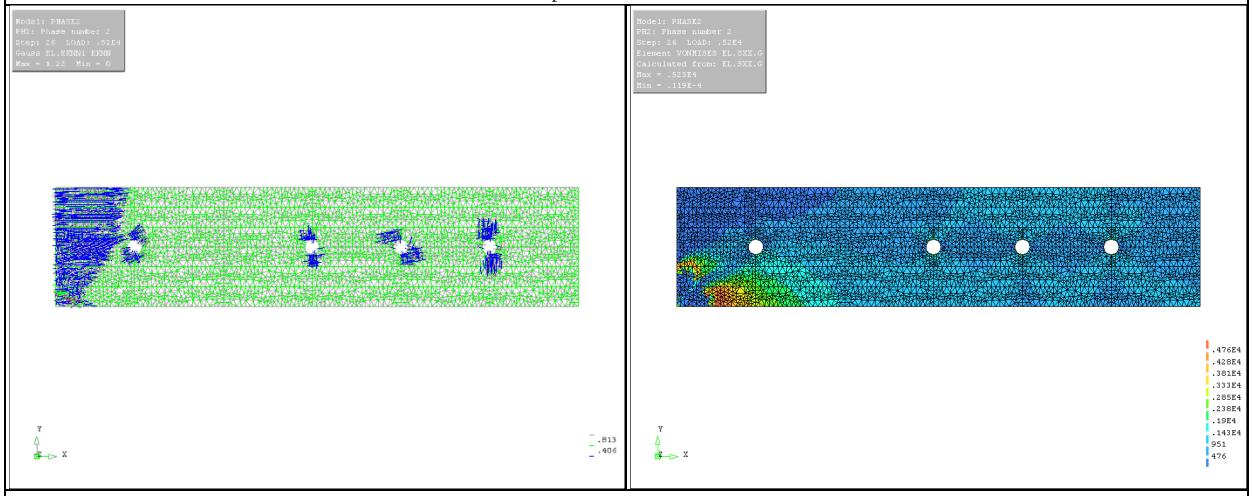

p_{impact} = 5,200 psi

Figure D-17 Crack Patterns & Von Mises Stress Variations of FE Model
(Edge Compression + Released Boundary Condition)

D.3 SIMULATION OF PROPOSED UNIT PANEL BEHAVIOR

This section presents direct comparison between analytical and experimental results with respect to load-displacement relationships. Measured displacements from the Chapter 5 unit panel static load experiments are compared with FE results in Figure D-19 to Figure D-22. Figure D-18 shows the locations of measured displacements for reference.

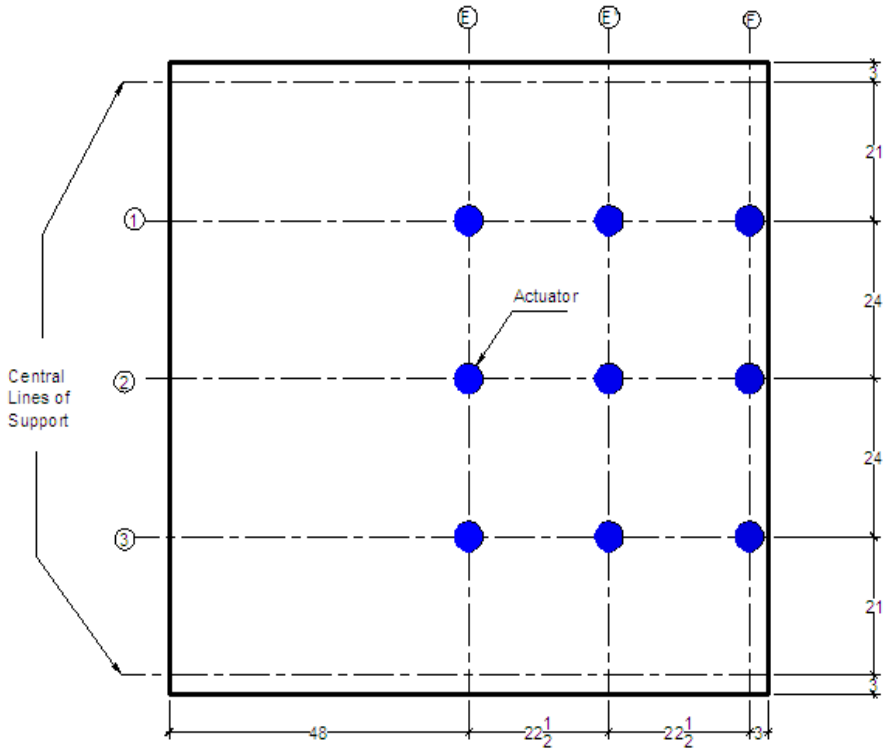

Figure D-18 Displacement Instrumentation Layout

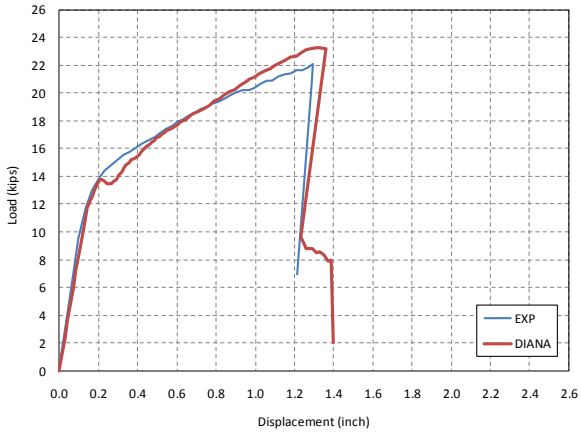

E-1

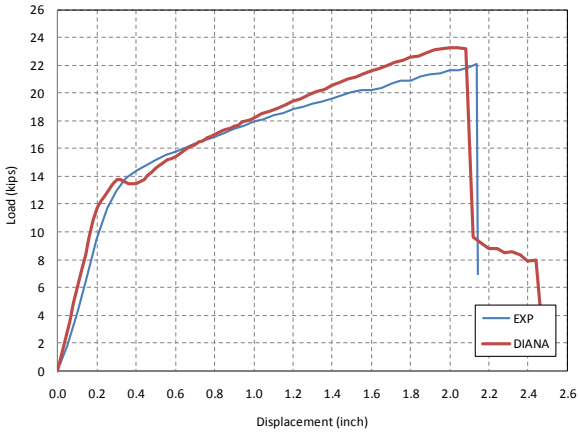

E-2

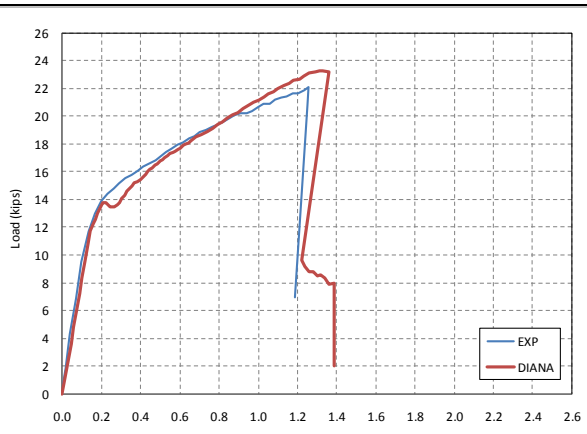

E-3

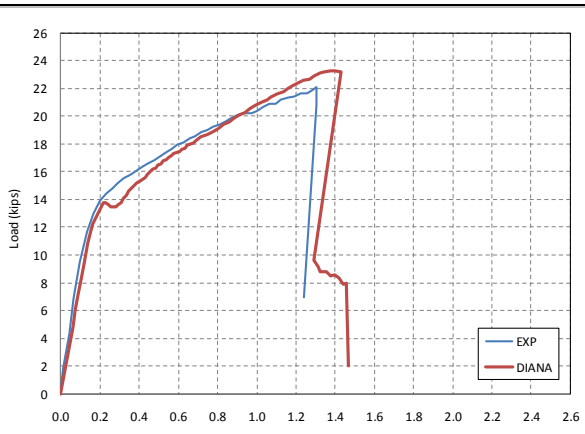

E’-1

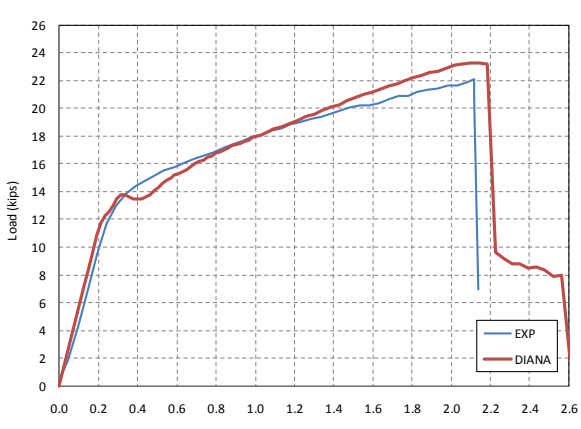

E’-2

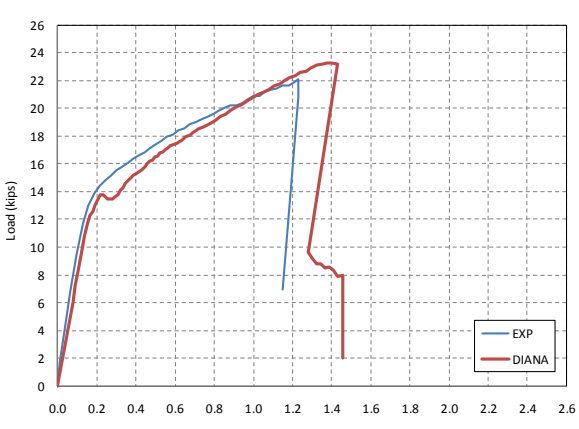

E’-3

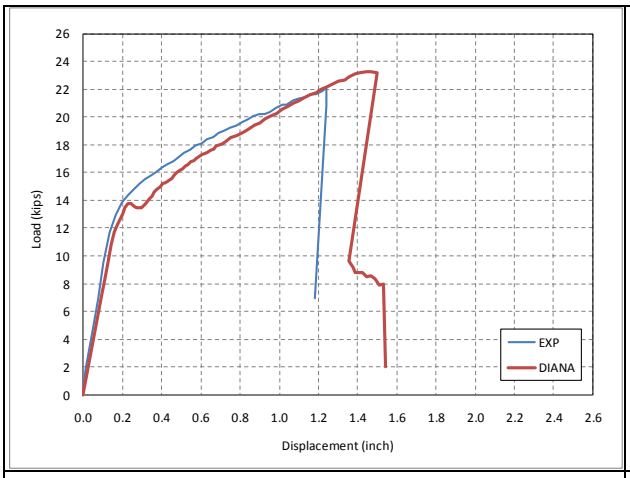

F-1

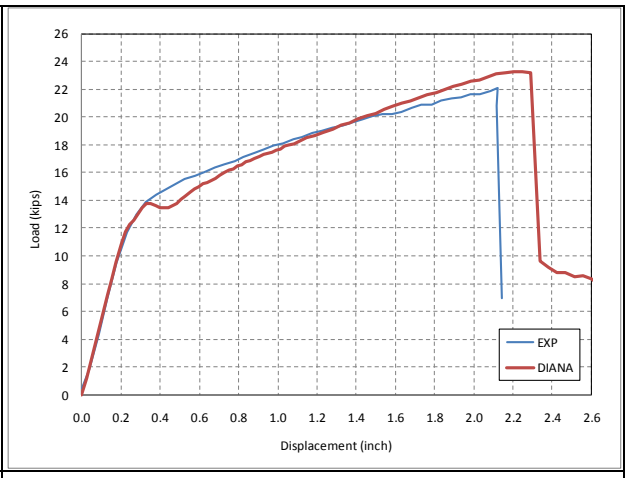

F-2

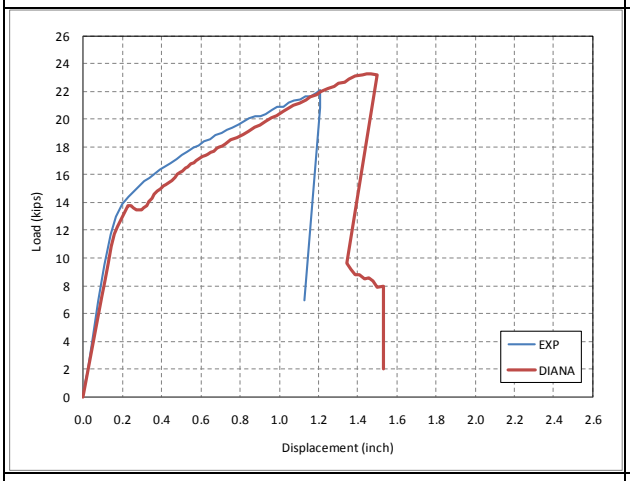

F-3

Figure D-19 Comparison of Load-Displacement for Panel ST-NC-SL

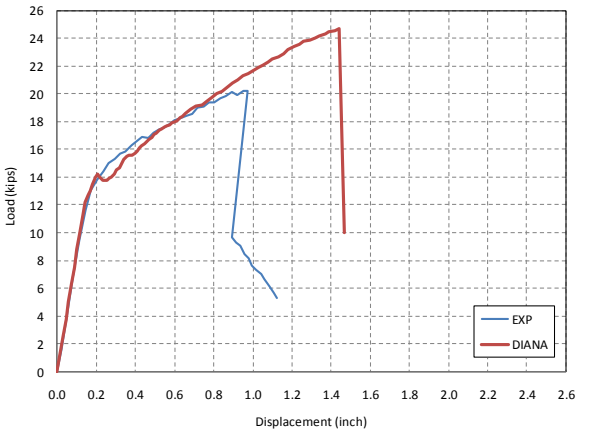

E-1

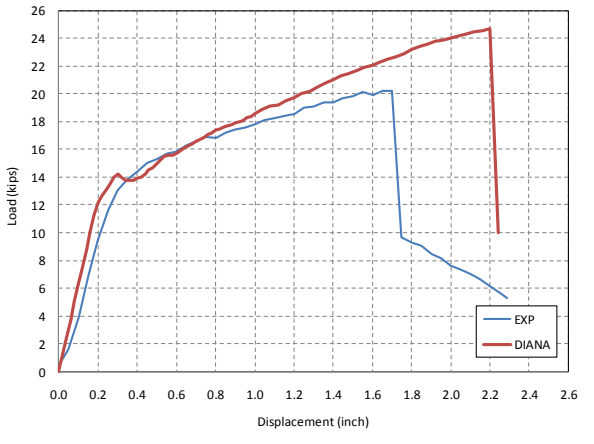

E-2

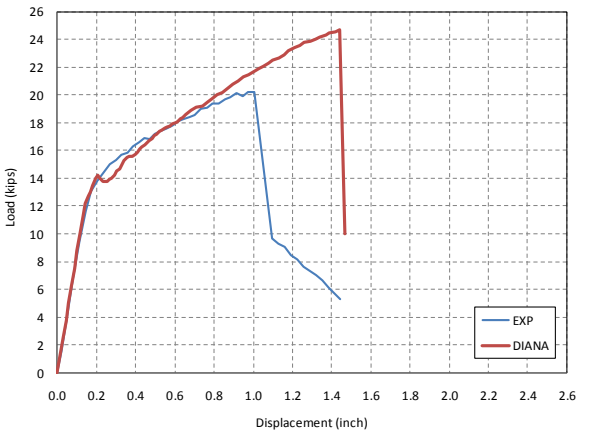

E-3

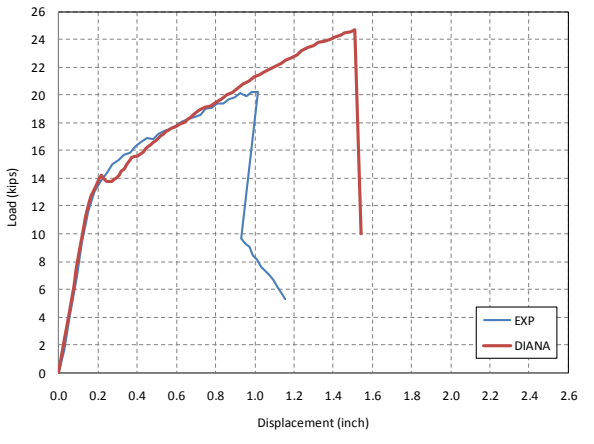

E’-1

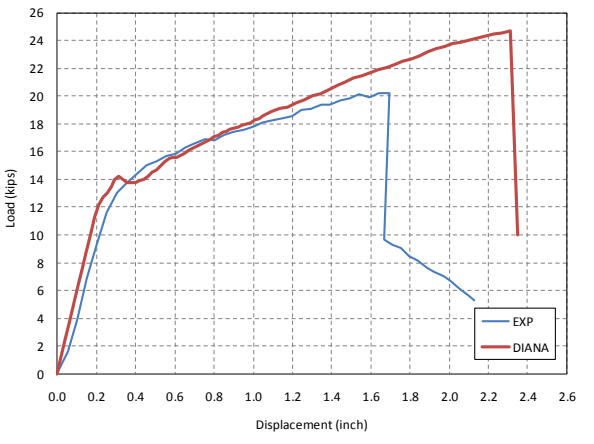

E’-2

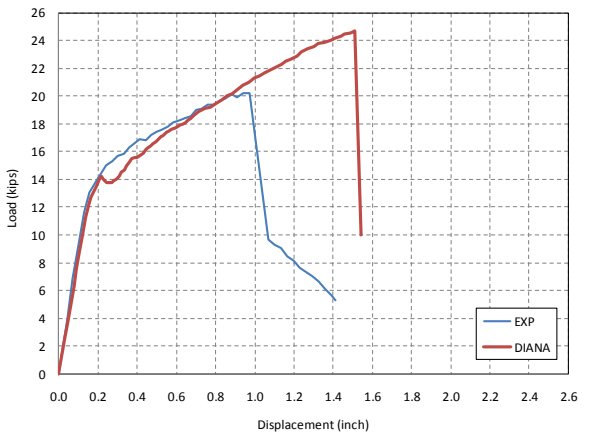

E’-3

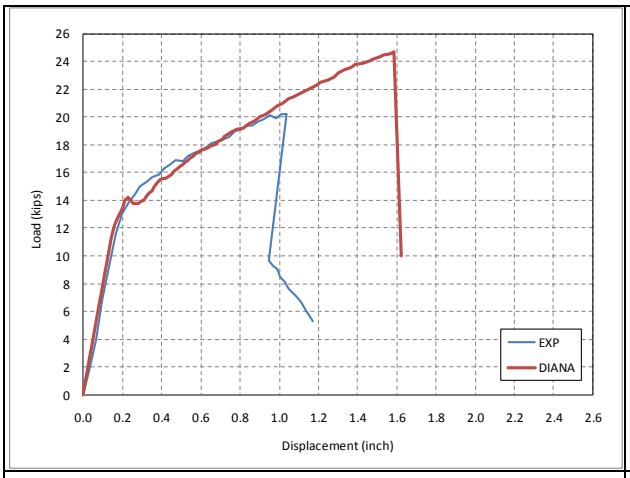

F-1

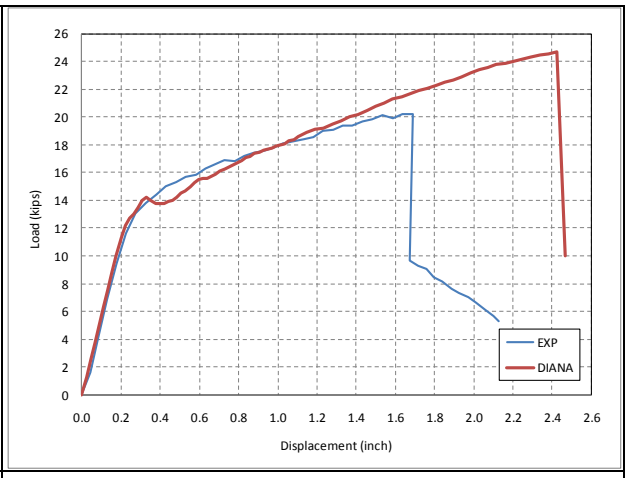

F-2

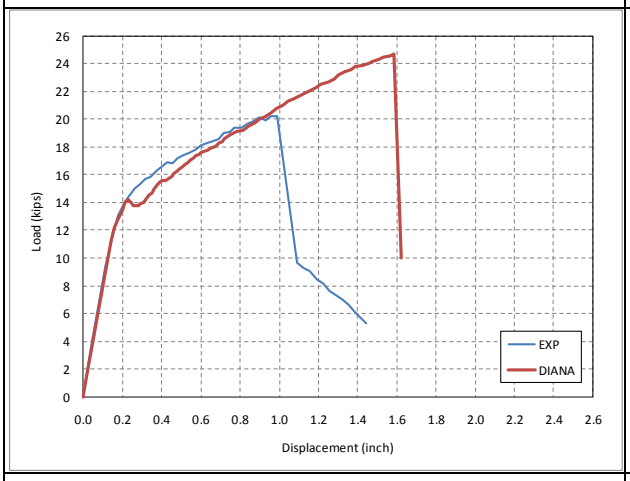

F-3

Figure D-20 Comparison of Load-Displacement for Panel ST-FRC-SL

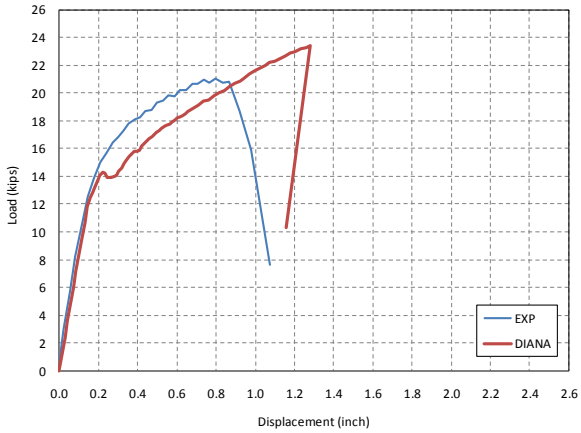

E-1

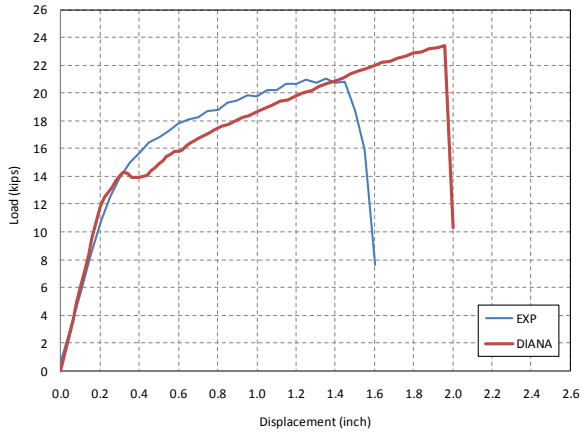

E-2

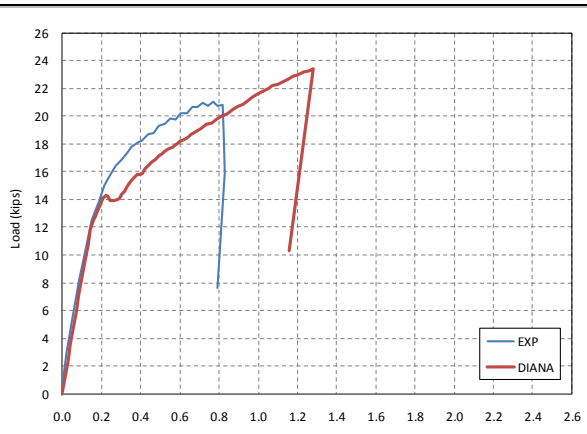

E-3

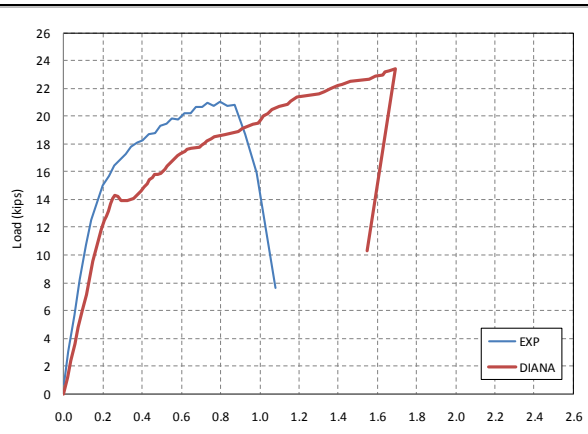

E’-1

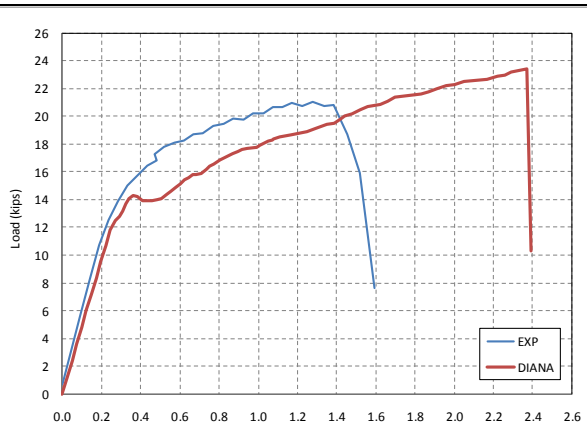

E’-2

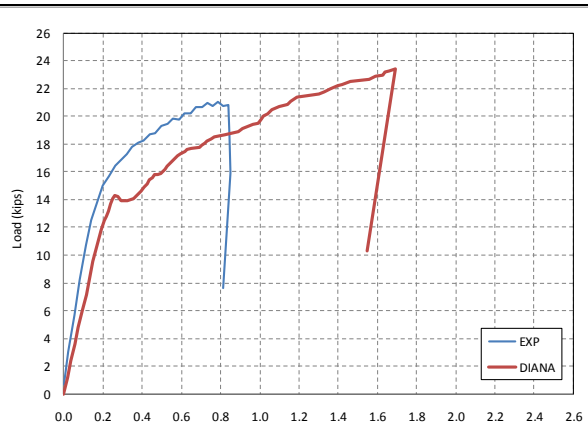

E’-3

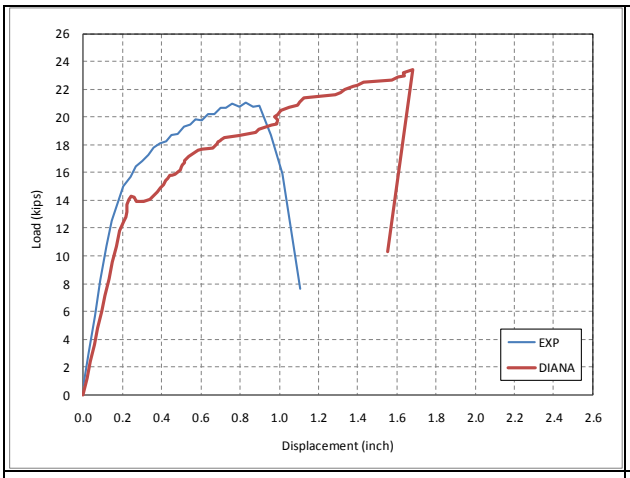

F-1

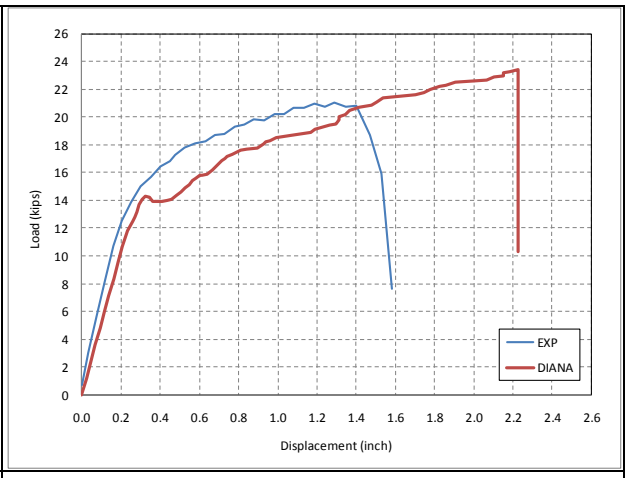

F-2

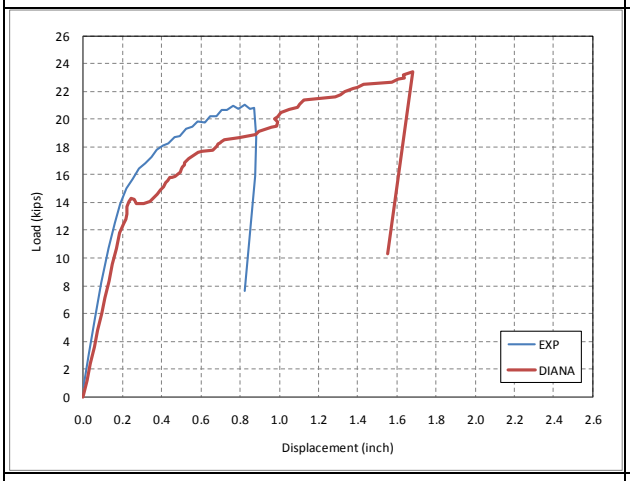

F-3

Figure D-21 Comparison of Load-Displacement for Panel CFRPT-NC-SL

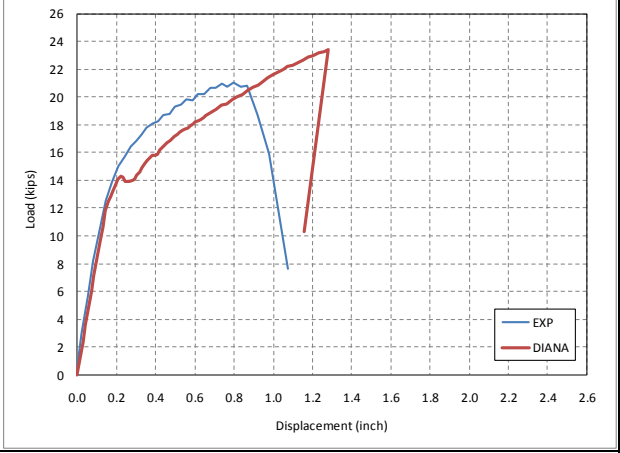

E-1

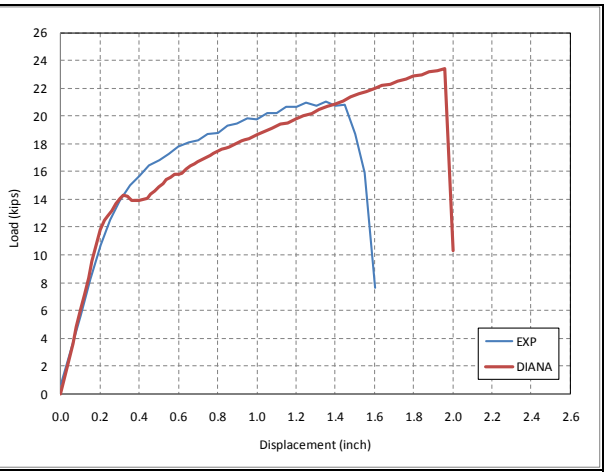

E-2

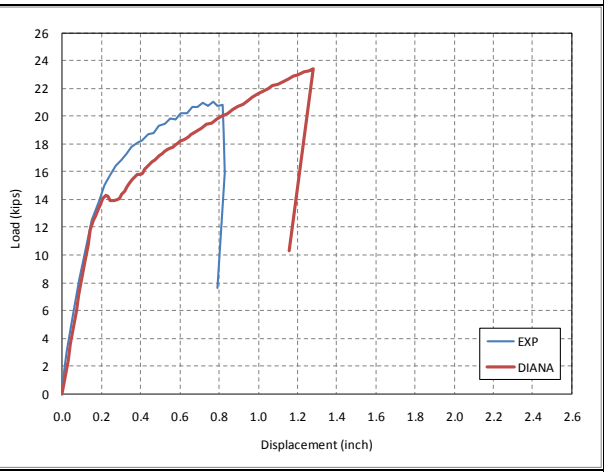

E-3

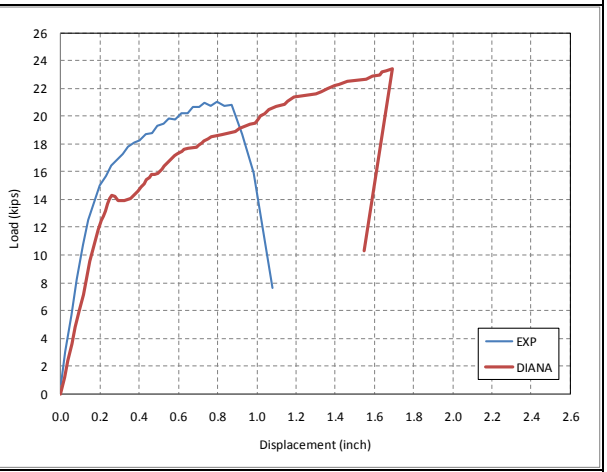

E’-1

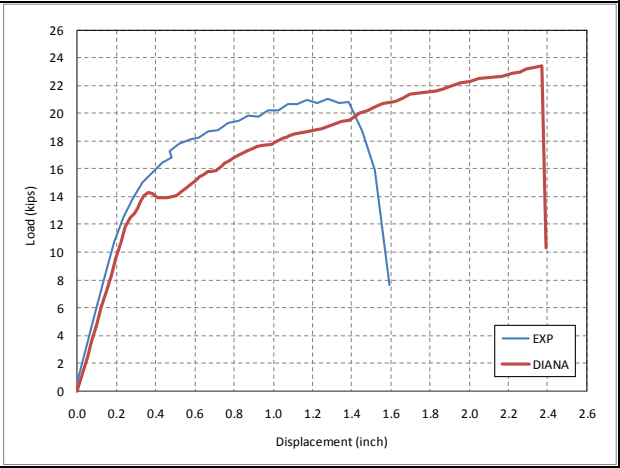

E’-2

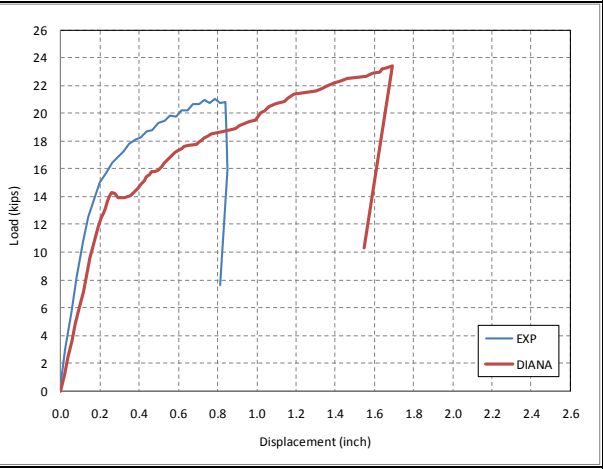

E’-3

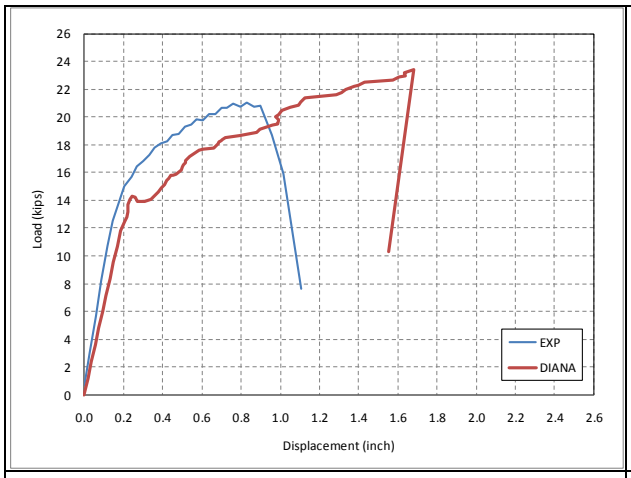

F-1

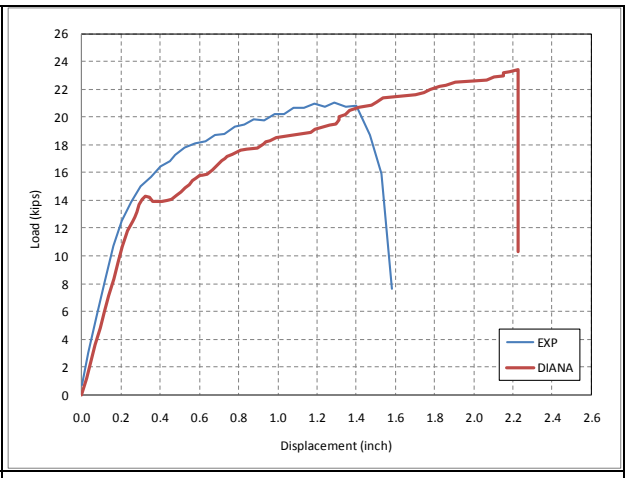

F-2

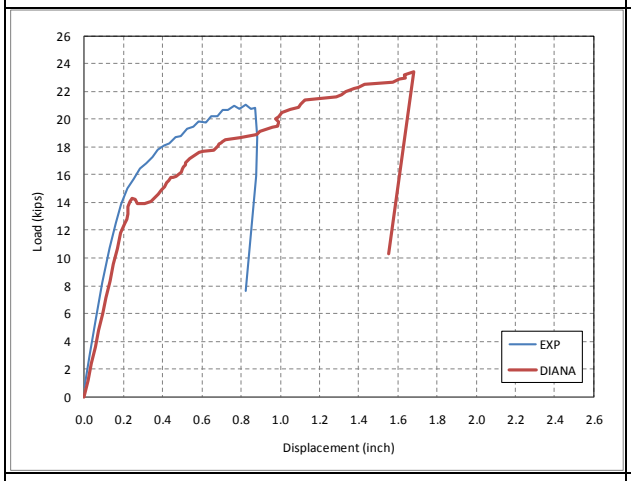

F-3

Figure D-22 Comparison of Load-Displacement for Panel CFRPT-NC-SL